

Universidade de São Paulo
Instituto de Astronomia, Geofísica e Ciências Atmosféricas
Departamento de Astronomia

Leandro Rocha Rímulo

**The life cycles of viscous decretion disks
around Be stars: fundamental disk
parameters in the SMC**

(Os ciclos de vida dos discos viscosos de decreção de estrelas
Be: parâmetros fundamentais de discos na Pequena Nuvem de
Magalhães)

São Paulo
2017

Leandro Rocha Rímulo

**The life cycles of viscous decretion disks
around Be stars: fundamental disk
parameters in the SMC**

**(Os ciclos de vida dos discos viscosos de decreção de estrelas
Be: parâmetros fundamentais de discos na Pequena Nuvem de
Magalhães)**

Tese apresentada ao Departamento de Astro-
nomia do Instituto de Astronomia, Geofísica
e Ciências Atmosféricas da Universidade de
São Paulo como requisito parcial para a ob-
tenção do título de Doutor em Ciências.

Área de Concentração: Astronomia
Orientador: Prof. Dr.
Alex Cavaliéri Carciofi

Versão Corrigida. O original encontra-se dis-
ponível na Unidade.

São Paulo
2017

To the BeACoN¹s!

¹ “Be Aficionados Collaborative Network” (<http://beacon.iag.usp.br/>).
And if you are interested in this thesis, you are one of us!

Agradecimentos/Acknowledgements

Muitas pessoas contribuíram para que este trabalho chegasse ao ponto em que chegou. Para mim, este trabalho representa apenas uma parte de uma conquista pessoal muito maior que eu tive desde que vim para São Paulo, já quase em abril de 2011, e que envolve muitas coisas íntimas às quais eu me darei o direito de não expor aqui.

Eu primeiramente agradeço imensamente ao Alex, meu orientador durante esses pouco mais de quatro anos em que trabalhamos juntos. Nesse período, desenvolvemos uma relação muito mais que profissional. Desenvolvemos uma grande amizade que eu espero que dure para sempre! Não deve ter sido fácil me orientar, já desde o começo, quando fui admitido como seu orientando de uma forma não usual. E, depois, teve o meu jeito peculiar de perder o foco e ir a fundo em algumas coisas e, muitas vezes, me dispersar por muito tempo por caminhos desnecessários! E muito obrigado pela paciência durante as minhas fases de baixa produtividade que ocorreram principalmente em 2014 e 2015, e por ainda confiar em mim, apesar daqueles dias! Este trabalho científico, brevemente apresentado nesta tese, é dedicado principalmente a você, e, em seguida, ao nosso grupo BeACoN, que espero poder se beneficiar com ele. Eu espero poder continuar colaborando profissionalmente com você por mais bastante tempo!

Eu agradeço em seguida à professora Sílvia Rossi, que se mostrou verdadeiramente uma grande amiga durante o final do meu doutorado. Agradeço pela grande empatia. Também vou guardar uma boa recordação de você para sempre!

Muito obrigado, também, professor Eduardo Janot, por me entender quando eu disse que estava descontente com o nosso projeto, estava infeliz com ele, e decidi mudar de projeto e de orientador, lá pela segunda metade de 2012. Obrigado por aceitar a minha escolha e pelos calorosos e descontraídos cumprimentos quando passamos a nos encontrar ocasionalmente pelos corredores do IAG desde então. Te desejo tudo de bom!

Agradeço imensamente à minha família por terem me dado tanto amor e compreensão, e por terem trabalhado muito para que eu conseguisse chegar até aqui. Agradeço à minha mãe por se dedicar de corpo e alma pela nossa formação - de meus irmãos Alexandre e Daniel e minha. E grande foi a sua preocupação comigo aqui em São Paulo! Obrigado por

ter me ajudado com sua presença, conselhos e até o ombro amigo nessas últimas semanas em que escrevi esta tese! Igualmente agradeço ao meu pai, também pela dedicação ao longo de nossas vidas, e por ser um grande exemplo para mim! Eu te admiro muito! Tanto que estou trilhando um caminho semelhante ao seu. Me recordei, agora, inclusive, de quando falávamos de átomos e de estrelas quando eu era pequeno. Eu suspeito que você foi essencial na minha paixão pelo entendimento da natureza. E espero um dia me tornar um profissional tão bom quanto você!

Obrigado Alexandre e Daniel, meus irmãos, pela amizade e companheirismo ao crescermos juntos. E obrigado por estarem à disposição em momentos que eu precisei, e pelas boas recepções quando eu voltava para BH. Agradeço também às minhas sobrinhas Raquel e Joana, simplesmente por serem uma alegria em nossas vidas! Vocês realmente coloriram a nossa família! Desculpem-me por eu ficar longe de vocês na maior parte do tempo!

Obrigado, tia Neusa, por também estar sempre presente em nossas vidas, e sempre disposta a ajudar. Obrigado por considerar aos meus irmãos e a mim como se fôssemos seus filhos e por nos acompanhar desde sempre! Obrigado, também, Bigode (o meu fii...). Agora, você também inventou de morar em São Paulo! Obrigado por ser sempre um primo companheiro e amigo de todos nós! Um amber!... Obrigado, também, Izabela, tia Marisa e tio Zé, igualmente pela amizade e pelo companheirismo, e pelas risadas!

E um obrigado à Pedrita, à Babi e à Bianca, que já se foram, e à Sisi que está bem velhinha!

Agradeço imensamente aos meus amigos do grupo BeACoN e demais amigos do IAG e daqui de São Paulo. Eu realmente descobri pessoas maravilhosas nesta cidade! Primeiramente, muito obrigado, Daniel Moser, pela amizade e por me aconselhar em minhas dificuldades e incertezas pessoais (pessoalmente, ou por Skype, de Nice ou de Santiago). Obrigado a você e aos seus pais pela recepção lá em Santa Catarina. Obrigado também pela ajuda computacional com o seu pacote `pyhdust` (que agora é de todos nós), por me introduzir ao `emcee` e por me auxiliar na administração da minha grade de modelos que foi gerada em semanas, pela máquina Alphacrucis, também com a ajuda de vários BeACoNs.

Muito obrigado, Bruno, pela imensa amizade desde que cheguei em SP, por se preocupar comigo e por me aconselhar nos meus momentos de crise! Acho que você teve muita sensibilidade de me perceber nesses momentos e me oferecer a sua amizade! Foi também muito bom aquele tempo em que moramos juntos no apartamento! E obrigado a você e sua família pela calorosa recepção e passeios, me fazendo me sentir parte da família!

Agradeço imensamente também à Daiane e ao Marcelo, pela descontração e pela maior intimidade que desenvolvemos especialmente nestes últimos meses de meu doutorado! Obrigado, também, André, pelo acolhimento nas recepções em sua casa e em seu casa-

mento e pelo voto de confiança recente de querer trabalhar junto comigo na continuação deste trabalho! Agradeço, enfim, a todos os BeACoNs daqui do IAG, pela ajuda mútua que damos uns aos outros e por sermos amigos, além de colaboradores. Muito obrigado, Rodrigo (Chuchu), Mohammad, Daniel Bednarski, Fellipy, Despo, Amanda, Artur, Lucas, Cyril e ao BeACoN a quem eu infelizmente tenha me esquecido de citar!

I extend my thanks to some BeACoNs that live far away. Thanks, Thomas Rivinius, for providing me the data for the execution of this work and for the nice personal meetings we had here in São Paulo, at IAG and at Alex' house, or in Canada. Thanks, Jon Bjorkman and Atsuo Okazaki, for the fruitful theoretical discussions on the physics involved in all what we were doing! And thanks, Robert Klement, for being a nice friend and collaborator from abroad! Unfortunately, I could not participate in that project Alex set for both of us, because I was too "lost" by that time! But we had nice times together here in São Paulo!

Obrigado, Fábio Mendes, dono da agência de viagens FábioTur, pela amizade que desenvolvemos, e, especialmente, por me aturar durante os vários meses que convivemos juntos no apartamento! Obrigado por me ensinar muitas coisas da "vida prática" e também pelos conselhos. Agradeço também a alegria e a descontração dos vários amigos da FábioTur: Thamirys, Luiz, Vanessa, o senhor Big, Daniel May, Arianna e demais malucos envolvidos!

Obrigado, Mille, pela amizade distante e pela imensa intimidade que tivemos, lá pelo final de 2013! Foi uma uma experiência muito bonita aquela, que eu vou guardar comigo para sempre! Te desejo muitas felicidades em seu casamento e em sua vida!

Thanks, Neenie, for the distant friendship in the last year and for listening to me in my times of solitude!

Muito obrigado, também, Ercília Zilli e Alfredo Simonetti, profissionais que têm trabalhado para me ajudar em meus conflitos internos desde 2012! Muito obrigado, seu Geraldo, dona Mariazinha e Joana, por me acolherem em momentos de grande crise e por darem muito de si, gratuitamente, no intuito de me ajudar! Desculpem-me, hoje, por estar mais distante. Sinto que esse meu distanciamento foi necessário para um apaziguamento interno nas minhas reflexões existenciais. Mas quero mandar um salve a todos os "jovens do Maria", incluindo o João e o Francisco, filhos do meu orientador Alex! Saudades de todos!

Tenho saudades, enfim, dos meus amigos da AECX, lá de Belo Horizonte! Nos vimos tão poucas vezes nesses últimos seis anos, e peço desculpas pelo meu sumisso! Vocês estão no meu coração e quero que nossa amizade dure para sempre!

Finalmente, agradeço à FAPESP (processo 2012/21518-5) e ao CNPq (processo 142411/2011-6) pelo apoio financeiro.

Esta tese/dissertação foi escrita em \LaTeX com a classe IAGTESE, para teses e dissertações do IAG.

“In principle, we can know all of mathematics. It is given to us in its entirety and does not change. ...That part of it of which we have a perfect view seems beautiful, suggesting harmony; that is that all the parts fit together although we see fragments of them only. ...Mathematics is applied to the real world and has proved fruitful. This suggests that the mathematical parts and the empirical parts are in harmony and the real world is also beautiful.”

“(...) Our total reality and total existence are beautiful and meaningful. ...We should judge reality by the little which we truly know of it. Since that part which conceptually we know fully turns out to be so beautiful, the real world of which we know so little should also be beautiful. Life may be miserable for seventy years and happy for a million years: the short period of misery may even be necessary for the whole.”

Kurt Gödel, in *A Logical Journey*, MIT Press, 1996

“Two things fill the mind with ever new and increasing wonder and awe - the starry heavens above me and the moral law within me.”

Immanuel Kant, in *Critique of Practical Reason*, 1788.

“One of the most important societal functions of modern astronomy is as a tool for education in the broadest sense. Because it is one of the most approachable of sciences, and one that consistently fascinates young people, astronomy is an excellent vehicle for introducing science and technology to children. The accessibility of the sky, the beauty of cosmic objects and the immensity of the Universe are inspirational and provide a perspective that encourages internationalism and tolerance. The excitement of astronomy has stimulated large numbers of young people to choose a career in science and technology, thereby contributing to the ‘knowledge economy’ of many countries.”

International Astronomical Union,
Astronomy for the Developing World: Strategic Plan 2010 - 2020

Resumo

Estrelas Be são estrelas massivas na sequência principal, com emissões em seus espectros que se originam de um disco circunstelar gasoso. Embora o modelo de disco viscoso de decreção (“viscous decretion disk” - VDD) seja capaz de explicar satisfatoriamente a maior parte das observações, dois ingredientes físicos: a magnitude da viscosidade (α) e a taxa de injeção de massa no disco, ainda são muito pouco conhecidos. Além disso, muito trabalho ainda precisa ser feito para que entendamos os ciclos de vida desses discos: quão rápido eles crescem e dissipam, quanto tempo eles duram, etc. As curvas de luz de estrelas Be que produzem eventos de formação e dissipação de disco oferecem uma oportunidade de se estudar os seus ciclos de vida e de estimar as propriedades fundamentais dos discos. Uma lista de procedimentos (um “pipeline”) foi desenvolvida para modelar esses eventos. Ela usa uma grade de curvas de luz sintéticas, computadas a partir de simulações hidrodinâmicas detalhadas combinadas com cálculos de transferência radiativa. A comparação entre modelos e dados foi possível utilizando-se de duas leis empíricas que descobrimos, que imitam bastante o perfil fotométrico dos eventos. Uma amostra de 54 estrelas Be do “survey” OGLE na direção da Pequena Nuvem de Magalhães (“Small Magellanic Cloud” - SMC) foi selecionada para este estudo. As taxas típicas de perda de massa e momento angular associadas aos eventos são da ordem de $\sim 10^{-10} M_{\odot} \text{ yr}^{-1}$ e $\sim 5 \times 10^{36} \text{ g cm}^2 \text{ s}^{-2}$, respectivamente. Nós demonstramos que o momento angular perdido pela estrela, mesmo para os eventos associados aos discos mais densos, ainda está abaixo que o requerido pelos melhores modelos de evolução estelar, de tal forma que as estrelas não alcancem suas velocidades de ruptura (“break-up velocities”). Nossos números oferecem, pela primeira vez, restrições aos mecanismos internos de transporte de momento angular de estrelas massivas em alta rotação. Este trabalho também aumentou em 54 vezes o número de estrelas Be cujos parâmetros α foram determinados, e ele representa a primeira determinação estatística do parâmetro α para estrelas Be. Os valores de α encontrados são, tipicamente, da ordem de alguns décimos, consistentes com os resultados recentes na literatura e com os valores encontrados para as novas anãs, mas maiores que os preditos pela teoria atual. Considerando a amostra como um todo, o parâmetro de viscosidade é aproximadamente duas vezes maior na formação ($\langle \alpha_{\text{bu}} \rangle = 0.63$) do que na dissipação ($\langle \alpha_{\text{d}} \rangle = 0.29$). Pes-

quisa futura é necessária para verificar se essa tendência é real ou um resultado de nossas considerações feitas nos modelos. Se real, este fenômeno merece ser melhor investigado, já que ele pode fornecer indícios da origem da viscosidade anômala de discos astrofísicos. No futuro próximo, nós estenderemos o nosso trabalho para estrelas Be da Grande Nuvem de Magalhães (“Large Magellanic Cloud” - LMC) e da Galáxia, através do uso dos muitos “surveys” fotométricos disponíveis que contêm coberturas temporais de anos.

Abstract

Be stars are main-sequence massive stars with emission features in their spectrum, which originates from a circumstellar gaseous disk. Even though the viscous decretion disk (VDD) model can satisfactorily explain most observations, two important physical ingredients, namely the magnitude of the viscosity (α) and the disk mass injection rate, remain poorly constrained. In addition, substantial work remains to be done in order to fully understand the life cycles of these disks: how fast they grow and dissipate, for how long they last, etc. The light curves of Be stars that undergo events of disk formation and dissipation offer an opportunity to study their life cycles and to constrain the disks' fundamental properties. A pipeline was developed to model these events that uses a grid of synthetic light curves, computed from detailed hydrodynamic simulations combined with radiative transfer calculations. Comparison between model and data was made possible by two empirical laws we discovered, which closely match the photometric behaviour of the events. A sample of 54 Be stars from the OGLE survey of the Small Magellanic Cloud (SMC) was selected for this study. The typical mass and angular momentum loss rates associated with the disk events are of the order of $\sim 10^{-10} M_{\odot} \text{yr}^{-1}$ and $\sim 5 \times 10^{36} \text{g cm}^2 \text{s}^{-2}$, respectively. We showed that the angular momentum lost by the star, even for the events with the densest disks, was still smaller than the required by the best evolutionary models so that the stars do not reach their break-up velocities. These numbers offer, for the first time, constraints on the internal angular momentum transport mechanisms of fast rotating massive stars. This work also increased the number of Be stars whose α parameters have been determined by 54 times, and it represents the first statistically significant determination of α for Be stars. The values of α found are typically of a few tenths, consistent with recent results in the literature and with the ones found in dwarf novae, but larger than the current theory predicts. Considering the sample as a whole, the viscosity parameter is roughly two times larger at build-up ($\langle \alpha_{\text{bu}} \rangle = 0.63$) than at dissipation ($\langle \alpha_{\text{d}} \rangle = 0.29$). Further work is necessary to verify whether this trend is real or a result of some of the model assumptions. If real, this is a phenomenon worth further investigation, as it may lead to clues as to the origin of anomalous viscosity in astrophysical disks. In the near future, we intend to extend our work to Be stars from

the Large Magellanic Cloud (LMC) and from the Galaxy, by making use of the many photometric surveys, with years of coverage, available.

List of Figures

1.1	H-R diagram of nearby stars.	26
1.2	Amateur image of the Pleiades open cluster, also showing H α line profile of the seven main stars.	28
1.3	<i>Left:</i> Schematic view of a Be star, with examples of spectral profiles from pole-on to shell. <i>Right:</i> Image reconstruction of the Be star ζ Tauri in H α , based on optical interferometry.	29
1.4	<i>Left:</i> V/R variations in H α of the Be star ζ Tauri. <i>Right:</i> Schematic representation of an one-armed spiral pattern.	31
1.5	Variability of the Be star δ Scorpii over more than 11 years.	32
1.6	Appearance of a gravity darkened star.	34
1.7	Evolutionary tracks for A-B type stars for $Z = 0.014$ (left) and $Z = 0.002$ (right).	35
1.8	Wind streamlines and disk formation for three disk models: WCD, MWCD and VDD.	37
1.9	A VDD model of the Be star ζ Tauri that includes global density waves.	39
1.10	Theoretical non-LTE H α line profiles for a B0e star with a Keplerian disk.	40
1.11	The formation loci of continuum emission.	41
2.1	Roche shapes of the stellar configurations, with critical ratios W varying from 0 to 1 in steps of 0.1.	60
2.2	For the same stellar models of Fig. 2.1: <i>Upper-left:</i> Flux at the surface of the stars compared to the non-rotating case as a function of the polar angle θ . <i>Upper-right:</i> Effective temperature compared to the non-rotating case as a function of θ . In dotted straight lines, values of $0.6(L/S_W\sigma)^{\frac{1}{4}}$, where S_W is the surface area of the star with parameter W . <i>Lower-left:</i> $\log g_{\text{eff}}$ compared to the non-rotating case as a function of θ . <i>Lower-right:</i> $\log T_{\text{eff}}$ versus $\log g_{\text{eff}}$. The inclinations of these curves give the β coefficient.	62

3.1	Two light curves, in photometric bands V (green) and I (red), selected from the OGLE-II and OGLE-III photometric surveys. <i>Above</i> : light curve of SMC_SC1 75701 (OGLE-II ID). <i>Below</i> : light curve of SMC_SC6 128831 (OGLE-II ID).	66
3.2	Simulation of a constant build up phase ($\Sigma_0 = 1.549\text{g cm}^{-2}$), during $\tilde{\tau}_{\text{bu}} = 30$, followed by a complete dissipation ($\Sigma_0 = 0$). Three injection radii were used: $\tilde{R}_{\text{inj}} = 1.017$ (dotted), 1.169 (dashed), 1.319 (solid).	75
3.3	Dynamical bump model with $\tilde{\tau}_{\text{bu}} = 30$	77
3.4	Simulation of a constant build up phase ($\Sigma_0 = 1.549\text{g cm}^{-2}$), during $\tilde{\tau}_{\text{bu}} = 30$, followed by a complete dissipation ($\Sigma_0 = 0$). The different colors corresponds to different instants after beginning of the build-up phase: $\tilde{\tau}+30 \sim 0$ (red), $\tilde{\tau}+30 = 0.2$ (orange), $\tilde{\tau}+30 = 1$ (green), $\tilde{\tau}+30 = 6$ (blue), $\tilde{\tau}+30 = 25$ (purple).	81
3.5	Simulation of two constant build-up phases ($\Sigma_0 = 1.549\text{g cm}^{-2}$), one during $\tilde{\tau}_{\text{bu}} = 30$ (solid line), and another during $\tilde{\tau}_{\text{bu}} = 30$ (dashed line). Both were followed by a complete dissipation ($\Sigma_0 = 0$). The different colors corresponds to different instants after beginning of the build-up phase: $\tilde{\tau} \sim 0$ (red), $\tilde{\tau} = 0.2$ (orange), $\tilde{\tau} = 1$ (green), $\tilde{\tau} = 6$ (blue), $\tilde{\tau} = 25$ (purple).	82
3.6	M. Ghoreyshi et al.'s current best results for the photometric modeling of the light curve of 28 CMa.	85
4.1	Temperatures in the cells and on the stellar surface in a simulation of near-Keplerian disk of a Be star made by HDUST.	90
4.2	HDUST's current ellipsoid stars (black) versus Roche-shaped stars with $W = 0.7$ and $W = 0.9$ (red).	91
4.3	$UBVRI$ Johnson-Cousins passbands and the limits in frequency of the SEDs generated by HDUST in this work.	92
4.4	<i>Left</i> : CMD in bands V and I of the diskless stars of Table 4.3. <i>Right</i> : diagram showing M_I (the same vertical axis of the upper-left one) versus $\alpha\tau$ (in days) for the diskless stars.	95
4.5	Examples of model I -band light curves, for several inclination angles.	97
4.6	The values of $\Delta I_{\text{bu}}^\infty$ versus $\cos i$ (left) and $\Delta V_{\text{bu}}^\infty$ versus $\cos i$ (right) for our grid.	98
4.7	Examples of the log – log derivative of $1 - \Delta I_{\text{bu}}(\tilde{\tau})/\Delta I_{\text{bu}}^\infty$ vs. $\Delta I_{\text{bu}}(\tilde{\tau})/\Delta I_{\text{bu}}^\infty$ (<i>top four panels</i>) and the log – log derivative of $\Delta I_{\text{d}}/\Delta I_{\text{d}}^0$ vs. $1 - \Delta I_{\text{d}}/\Delta I_{\text{d}}^0$, for values of $\tilde{\tau}_{\text{bu}}$ equal to 0.45, 1.5, 6 and 30 (<i>bottom four panels</i>).	99
4.8	The I - and V -band values of ξ_{bu} for our grid vs. $\cos i$	101
4.9	Selected I and V -band values of ξ_{d} for our grid vs. $\cos i$. The scaled build-up time was fixed to $\tilde{\tau}_{\text{bu}} = 2.25$	102

4.10	Selected I and V -band values of ξ_d for our grid vs. $\tilde{\tau}_{bu}$	102
5.1	V light curves and $V - R$ color curves for examples of the five modes of variability of Keller et al. (2002).	113
5.2	Examples of OGLE II light curves selected as Be star candidates: type-1 and type-1/type-2 light curves.	114
5.3	Examples of OGLE II light curves selected as Be star candidates: type-2, type-3 and type-4 light curves.	115
5.4	<i>Left:</i> CMD diagram for the selected stars from the SMC. <i>Right:</i> CMD diagram for the selected stars from the LMC.	115
5.5	Examples of SMC light curves showing clear zero point shifts between the OGLE-II and OGLE-III components.	117
5.6	Examples of SMC light curves found to have no clear inactive phase (e.g., <i>above:</i> SMC_SC4 60186) or to clearly be associated with a more complicated scenario of mass injection than the one described in the Chapter 3 (e.g., <i>below:</i> SMC_SC4 116957).	118
5.7	Color-magnitude diagram of simulated diskless stars (Table 4.3). Also shown, as errorbars, is the position of our selected stars (see eighth and ninth columns of Table 5.1).	119
6.1	Results for the selected bump of SMC_SC1 75701.	124
6.2	Results for the selected bump of SMC_SC6 128831.	125
6.3	<i>Solid line:</i> Histogram of the sum of the posterior probabilities of parameter M for all stars in our sample. <i>Dashed line:</i> IMF of Kroupa (2001) weighed by the fraction of Be stars over B stars of Martayan et al. (2007), given by the factor $M^{-2.3} f_{Be}(M)$ in Eq. (4.5.8).	128
6.4	Mean error and rms for a sample of stars from one of the fields of the OGLE-II survey.	129
6.5	Box and whisker plots of Σ_0 (above) and $t_2 - t_1$ (below) for the summed posterior probabilities of our sample of bumps, separated in six equal intervals of mass, ranging from 5 to 17 solar masses.	130
6.6	Distribution of the parameters M and Σ_0 for our sample.	131
6.7	Same as Fig. 6.5 for α_{bu} (above) and α_d (below).	131
6.8	Distribution of the two viscosity parameters α_{bu} and α_d	132
6.9	Evolution of the disk mass and mean disk temperature of the Be star 28 CMa, complementing the panels of Fig. 3.6.	133
6.10	Distributions of the steady-state mass (above) and angular momentum (below) loss rates for our sample.	135
B.1	(Star, i , Σ_0 , $\tilde{\tau}_{bu}$) = (Star 2, 90 deg, 1.37 g cm^{-2} , bu)	210

B.2	$(\text{Star}, i, \Sigma_0, \tilde{\tau}_{\text{bu}}) = (\text{Star 2}, 90 \text{ deg}, 1.37 \text{ g cm}^{-2}, \mathbf{1.5})$	211
B.3	$(\text{Star}, i, \Sigma_0, \tilde{\tau}_{\text{bu}}) = (\text{Star 2}, 90 \text{ deg}, 1.37 \text{ g cm}^{-2}, \mathbf{6})$	212
B.4	$(\text{Star}, i, \Sigma_0, \tilde{\tau}_{\text{bu}}) = (\text{Star 2}, 69.1 \text{ deg}, 1.37 \text{ g cm}^{-2}, \mathbf{bu})$	213
B.5	$(\text{Star}, i, \Sigma_0, \tilde{\tau}_{\text{bu}}) = (\text{Star 2}, 69.1 \text{ deg}, 1.37 \text{ g cm}^{-2}, \mathbf{1.5})$	214
B.6	$(\text{Star}, i, \Sigma_0, \tilde{\tau}_{\text{bu}}) = (\text{Star 2}, 69.1 \text{ deg}, 1.37 \text{ g cm}^{-2}, \mathbf{6})$	215
B.7	$(\text{Star}, i, \Sigma_0, \tilde{\tau}_{\text{bu}}) = (\text{Star 2}, 0 \text{ deg}, 1.37 \text{ g cm}^{-2}, \mathbf{bu})$	216
B.8	$(\text{Star}, i, \Sigma_0, \tilde{\tau}_{\text{bu}}) = (\text{Star 2}, 0 \text{ deg}, 1.37 \text{ g cm}^{-2}, \mathbf{1.5})$	217
B.9	$(\text{Star}, i, \Sigma_0, \tilde{\tau}_{\text{bu}}) = (\text{Star 2}, 0 \text{ deg}, 1.37 \text{ g cm}^{-2}, \mathbf{6})$	218
B.10	$(\text{Star}, i, \Sigma_0, \tilde{\tau}_{\text{bu}}) = (\text{Star 2}, 38.2 \text{ deg}, 2.50 \text{ g cm}^{-2}, \mathbf{bu})$	220
B.11	$(\text{Star}, i, \Sigma_0, \tilde{\tau}_{\text{bu}}) = (\text{Star 2}, 38.2 \text{ deg}, 2.50 \text{ g cm}^{-2}, \mathbf{1.5})$	221
B.12	$(\text{Star}, i, \Sigma_0, \tilde{\tau}_{\text{bu}}) = (\text{Star 2}, 38.2 \text{ deg}, 2.50 \text{ g cm}^{-2}, \mathbf{6})$	222
B.13	$(\text{Star}, i, \Sigma_0, \tilde{\tau}_{\text{bu}}) = (\text{Star 2}, 38.2 \text{ deg}, 1.01 \text{ g cm}^{-2}, \mathbf{bu})$	223
B.14	$(\text{Star}, i, \Sigma_0, \tilde{\tau}_{\text{bu}}) = (\text{Star 2}, 38.2 \text{ deg}, 1.01 \text{ g cm}^{-2}, \mathbf{1.5})$	224
B.15	$(\text{Star}, i, \Sigma_0, \tilde{\tau}_{\text{bu}}) = (\text{Star 2}, 38.2 \text{ deg}, 1.01 \text{ g cm}^{-2}, \mathbf{6})$	225
B.16	$(\text{Star}, i, \Sigma_0, \tilde{\tau}_{\text{bu}}) = (\text{Star 2}, 38.2 \text{ deg}, 0.41 \text{ g cm}^{-2}, \mathbf{bu})$	226
B.17	$(\text{Star}, i, \Sigma_0, \tilde{\tau}_{\text{bu}}) = (\text{Star 2}, 38.2 \text{ deg}, 0.41 \text{ g cm}^{-2}, \mathbf{1.5})$	227
B.18	$(\text{Star}, i, \Sigma_0, \tilde{\tau}_{\text{bu}}) = (\text{Star 2}, 38.2 \text{ deg}, 0.41 \text{ g cm}^{-2}, \mathbf{6})$	228

List of Tables

2.1	Conversion table between W , ω , $R_{\text{eq}}/R_{\text{pole}}$ and Υ	61
4.1	Parameters of the grid of photometric models of bumps	93
4.2	Parameters of the stellar models of Table 4.1	93
4.3	Parameters of the grid of photometric models of diskless stars	94
4.4	Values of η 's.	101
5.1	List of Be stars and their respective bumps selected for this study	120
6.1	Results of the pipeline for each star and bump of the sample	138
A.1	Empirical law parameters for band B	164
A.2	Empirical law parameters for band V	175
A.3	Empirical law parameters for band R	186
A.4	Empirical law parameters for band I	197

Contents

1. <i>Introduction</i>	25
1.1 On Be stars	27
1.1.1 The fastest rotators among non-degenerate stars	33
1.1.2 The Viscous Decretion Disk (VDD) model	37
1.1.2.1 Wind Compressed Disk	38
1.1.2.2 Magnetically Wind Compressed Disk	38
1.1.2.3 Viscous Decretion Disk	38
1.2 Dynamical VDDs	42
1.2.1 The origin of the viscosity of VDDs	43
1.2.2 Mass and angular momentum loss rates	44
1.3 Outline of this thesis	45
2. <i>Dynamical Principles of VDDs and rotating stars</i>	47
2.1 Hydrodynamical considerations	47
2.2 Thin and axisymmetric disks	49
2.2.1 An inviscid and near-Keplerian disk	49
2.2.2 On the vertical profile of thin disks	51
2.2.2.1 Vertically integrated quantities and the thin disk approximation	52
2.2.3 The alpha-disk approach to thin VDDs	53
2.3 The fast rotating star	56
2.3.1 Espinosa-Lara & Rieutord's flux prescription	60
3. <i>Viscous decretion disks around Be stars</i>	65
3.1 Main considerations	66
3.1.1 The star-disk connection	67
3.1.2 The alpha-disk code SINGLEBE	68
3.1.3 The timescale parameter τ and the time parameter $\tilde{\tau}$	70
3.2 Dynamical disk parameters	71

3.2.1	The steady-state solution of the VDD	71
3.2.2	Rates of mass and angular momentum loss	73
3.2.3	On the importance of the angular momentum loss rate	77
3.3	The mass reservoir effect	80
4.	<i>A model grid of disk formation and dissipation events</i>	87
4.1	The dynamical model grid	87
4.2	Radiative transfer models	88
4.2.1	The Monte Carlo Radiative Transfer code HDUST	89
4.2.2	Radiative transfer models	90
4.3	Empirical law	95
4.4	Fitting pipeline	103
4.5	Fitting using MCMC sampling	105
4.5.1	Statistical considerations	105
4.5.1.1	MCMC sampling with emcee	107
4.5.2	The likelihood and prior distributions of our problem	108
5.	<i>The remarkable light curves of Be stars from the Magellanic Clouds</i>	111
5.1	Selections of Be stars from the SMC and LMC	112
5.2	OGLE light curves of Be star candidates	116
5.2.1	Our selection of bumps from the SMC	116
6.	<i>Results</i>	123
6.1	SMC_SC1 75701 and SMC_SC6 128831	123
6.2	Results for the whole sample	127
6.2.1	Mass distribution	128
6.2.2	Asymptotic surface density	129
6.2.3	Disk life cycles	130
6.2.4	Viscosity parameter	132
6.2.5	Mass and angular momentum loss	135
7.	<i>Conclusions</i>	143
8.	<i>Prospectives</i>	147
	<i>Bibliography</i>	151
	<i>Appendix</i>	161
A.	<i>Long tables</i>	163

<i>B. Examples of fittings of the empirical laws</i>	<i>209</i>
B.1 (Star, $i, \Sigma_0, \tilde{\tau}_{bu}$) = (Star 2 , *, 1.37 g cm⁻² , *)	209
B.1.1 (Star, $i, \Sigma_0, \tilde{\tau}_{bu}$) = (Star 2, 90 deg , 1.37 g cm ⁻² , *)	210
B.1.2 (Star, $i, \Sigma_0, \tilde{\tau}_{bu}$) = (Star 2, 69.1 deg , 1.37 g cm ⁻² , *)	213
B.1.3 (Star, $i, \Sigma_0, \tilde{\tau}_{bu}$) = (Star 2, 0 deg , 1.37 g cm ⁻² , *)	216
B.2 (Star, $i, \Sigma_0, \tilde{\tau}_{bu}$) = (Star 2 , 38.2 deg , *, *)	219
B.2.1 (Star, $i, \Sigma_0, \tilde{\tau}_{bu}$) = (Star 2, 38.2 deg, 2.50 g cm⁻² , *)	220
B.2.2 (Star, $i, \Sigma_0, \tilde{\tau}_{bu}$) = (Star 2, 38.2 deg, 1.01 g cm⁻² , *)	223
B.2.3 (Star, $i, \Sigma_0, \tilde{\tau}_{bu}$) = (Star 2, 38.2 deg, 0.41 g cm⁻² , *)	226
 <i>C. Scientific paper</i>	 <i>229</i>

Introduction

Albert: “(...) Phosphorescence and all other organisms are made of elements that were once blended together in a star.”

Hilde: “Us too?”

Albert: “Yes, we too are stardust.”

Jostein Gaarder, in *Sophie’s World*

The stars are the main components of the visible Universe and our main sources of information about it. The study of stars, therefore, is crucial for the development of all other fields of modern astronomy.

A collection of 23000 nearby stars is summarized in the H-R diagram¹ shown in Fig. 1.1, composed of 22000 stars from the Hipparcos Catalogue together with 1000 low-luminosity stars (red and white dwarfs) from the Gliese Catalogue of Nearby Stars. The figure also shows the locations of the luminosity classes, according to the Morgan-Keenan classification, and, in the upper horizontal axis, it shows the effective temperature and modern spectral classification of the stars.

From the figure, we see that the most populated luminosity class is the Main Sequence. The main sequence is the locus of the stars that are burning hydrogen in their cores. The hydrogen burning phase is the longest phase in the life of the star, which explains why most of the randomly selected stars are found in the main sequence.

The least massive viable star (capable of hydrogen burning) has about $0.08M_{\odot}$, and its absolute magnitude is about +19. Such stars are at the bottom of the H-R diagram of Fig. 1.1. The absolute magnitude of the Sun, a G2V star, is +4.8. The heaviest stars begin their lives with masses of roughly $100M_{\odot}$ (or possibly more), and they are the Galaxy’s beacons, with absolute magnitudes above -8 , almost on the top of the H-R diagram of

¹ The most famous diagram in astronomy is the Hertzsprung-Russell diagram, or simply H-R diagram, idealized by Ejnar Hertzsprung in 1911 and, independently, by Henry Norris Russell in 1913. This diagram is a plot of luminosity (or absolute magnitude) against the colour of the stars.

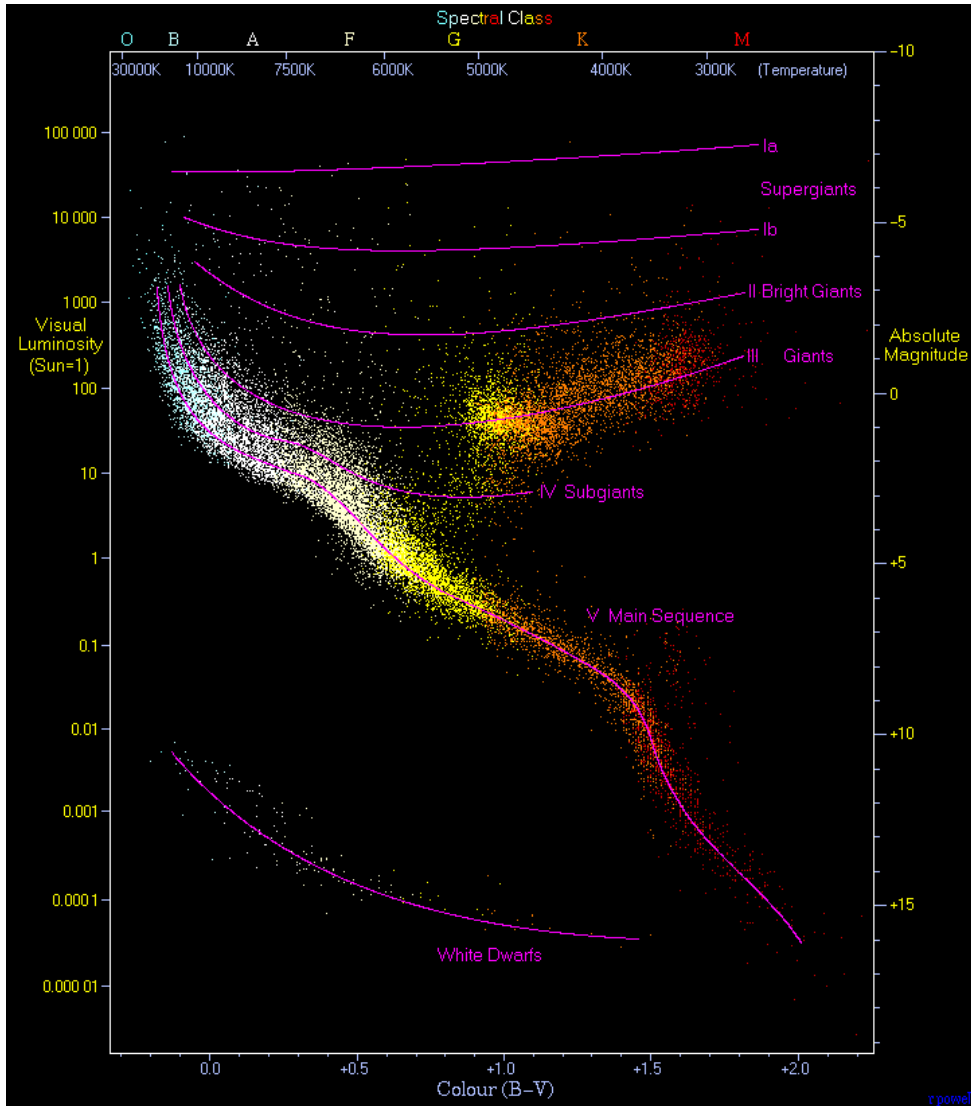


Figure 1.1: A plot of 22000 stars from the Hipparcos Catalogue together with 1000 low-luminosity stars (red and white dwarfs) from the Gliese Catalogue of Nearby Stars. (Credits: <http://www.atlasoftheuniverse.com>)

Fig. 1.1. The range of absolute magnitudes found in the stars, therefore, occupies an interval of ~ 27 magnitudes, or a factor of $\sim 6 \times 10^{10}$ in luminosity (Ledrew, 2001).

It is found that the more massive the star, the rarer it is. Nature has a preference for forming less massive stars. For stars more massive than the Sun, the work of Kroupa (2001) finds that the probability density ξ (commonly referred to as the Initial Mass Function - IMF) of a Galactic star to be formed with mass M is $\xi(M) \propto M^{-2.3}$. Consequently, OB main sequence stars, for instance, are only approximately 0.1% of the stars in the Solar neighborhood (Ledrew, 2001). Also, the more massive the star, the shorter is its life. A star with 10 times the mass of the Sun, for instance, has a lifespan ~ 120 times shorter than the life of the Sun (Granada et al., 2013).

Despite the fact that most of the stellar mass in the Galaxy is found in low-mass, dim

stars, nearly all of the light in the galaxies is emitted by the brightest stars, in such a way that our naked-eye view of the sky is strongly biased towards the brighter stars (mostly B and A typed main sequence stars, [Ledrew, 2001](#)).

Massive stars are generally defined as those with masses higher than around $8M_{\odot}$, which are the stars that will end up their lives as supernovae. Because, they are short-lived, they are usually found in or not too far away from their birth places. Massive stars are, then, typically located in regions of active star formation, such as the spiral arms of spiral galaxies.

Despite their rarity, these stars have a fundamental influence over the interstellar medium (ISM), because they are responsible for the ionization of the surrounding gas. They generate most of the ultraviolet radiation of the galaxies, which is the radiation usually detected in the observations of the farthest and most redshifted galaxies. Also, they power the far infrared of the galaxies through the heating of dust.

The usually strong stellar winds of massive stars and, later on, their supernovae, inject mechanical energy into the ISM and, also, nuclear processed material generated by their cores, during their lifetime. These stars, thus, supply the medium with new material and energy for the birth of new generations of stars.

In this work, we will focus on a group of main sequence, usually massive stars, known as “Be stars”. Be stars are found in the lower end of the group of massive stars and also a little below it. In [Fig. 1.1](#), they are found in the upper end of the main sequence (roughly between $\sim 300L_{\odot}$ and $\sim 30000L_{\odot}$). We will describe this group of peculiar stars in more detail in the next section.

1.1 On Be stars

(...) une particularité curieuse (...)
une ligne lumineuse très belle et bien
plus brillante que tout le reste du
spectre.

Father A. Secchi, 1866

In a classical, observational, and quite broad definition, a Be star is a hot star, with a B spectral type (mass ranging roughly from 3 to 17 solar masses), non-supergiant, whose spectrum has, or had at some time, one or more Balmer lines in emission ([Jaschek et al., 1981](#); [Collins, 1987](#)). In a more modern and theoretically-oriented definition, a Be star is a very rapidly rotating B star, typically with non-radial pulsations, that forms a geometrically thin viscous decretion disk (VDD) composed of an outwardly diffusing gaseous Keplerian disk that is fed by mass ejected from the central star and is governed by viscosity ([Rivinius et al., 2013](#)) and a possibly non-negligible line-driven wind ([Kee et al., 2016](#)).

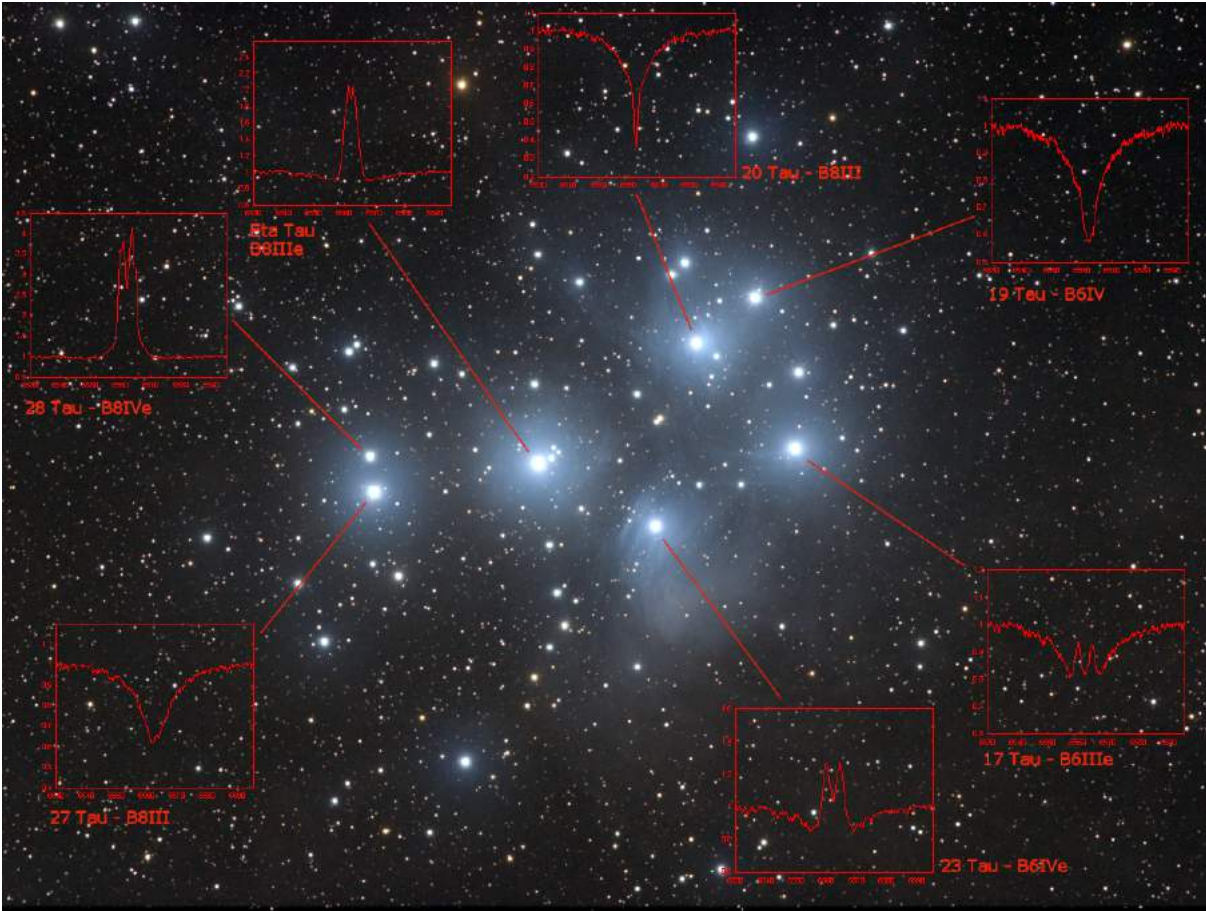


Figure 1.2: Amateur image of the Pleiades open cluster, also showing $H\alpha$ line profile of the seven main stars. Four of them (17 Tau, 23 Tau, Eta Tau and 28 Tau) are Be stars, which is evidenced from the emission features in their line profiles. Credits: <http://www.astrosurf.com/buil/us/bestar.htm>

Be stars were discovered roughly 150 years ago, in the early years of astronomical spectroscopy, by [Secchi \(1866\)](#), who noticed the $H\beta$ line in emission in the Be star γ Cassiopeiae. Like, γ Cas, some Be stars are among the brightest stars in the visible sky, which makes them interesting also for amateur astronomers (see, e.g., Fig. 1.2). It was only in the last two to three decades, however, that the understanding of Be stars has advanced from simple classifications and toy-models to more sophisticated views based on physical principles. This happened, both due to the advances in observing techniques, including the now available optical and near-infrared (near-IR) interferometry, and due to computational and theoretical advances, which allowed the construction of much more detailed and complex physical models for these stars.

Be stars are not rare. Approximately 10% of the main-sequence B stars in the Galaxy are in fact Be stars ([Rivinius et al., 2013](#)). This percentage can grow to roughly 35% when we go to the Small Magellanic Cloud and can be even higher in some young clusters ([Martayan et al., 2011](#)).

The “e” letter in the spectral classification of Be stars comes from “emission”. Indeed,

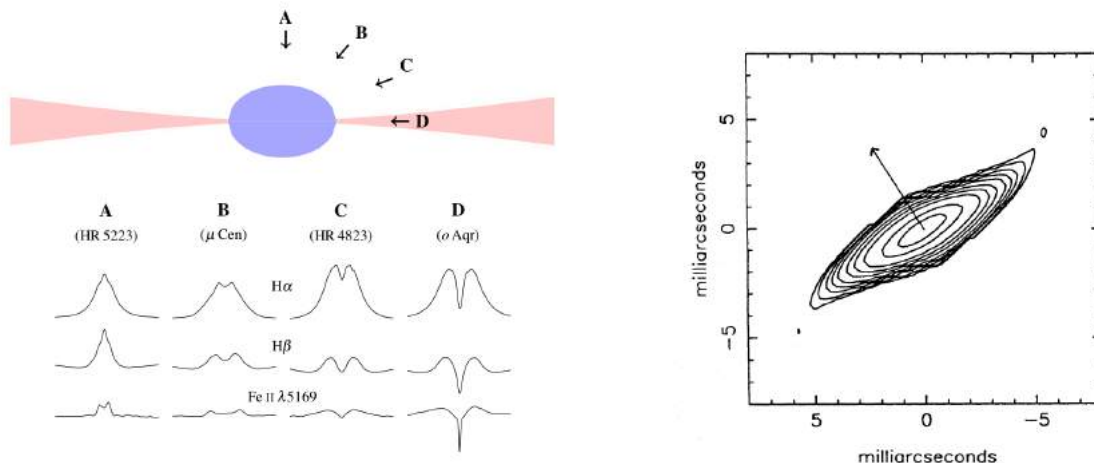


Figure 1.3: *Left:* Schematic view of a Be star with a flared disk (and an oblate fast rotating central star). Below, examples of spectral profiles from pole-on to shell Be stars are shown (*Credits:* Rivinius et al., 2013). *Right:* Image reconstruction of the Be star ζ Tauri in H α , based on optical interferometry. The arrow indicates the direction of linear polarization. (*Credits:* Quirrenbach et al., 1994)

they are easiest identified by the emission features in their spectra, examples of which are seen in Fig. 1. This extra emission comes from circumstellar material around the star. Further evidence of this material comes from the excess IR emission (e.g., Gehrz et al., 1974) and polarization (e.g., Wood et al., 1997). Furthermore, there is ample evidence that this material is not spherical, but rather distributed in a disk-like structure (Quirrenbach et al., 1994). One important example is the double-peaked profile of emission lines. The simplest explanation for this feature is a rotating and geometrically thin gaseous disk of material, as the schematic Fig. 1.3 (left panel) illustrates. The two peaks are the blueshifted (left) and redshifted (right) emission from the two opposing sides of the rotating disk. Be stars whose disks are seen nearly edge-on, which present intense absorption at the center of the line, are commonly referred to as shell stars.

Incidentally, the double-peaked shape in the Balmer lines also means that the radial velocity of the disk-like material is much smaller than the rotation velocity. If that were not the case, the significant outward radial motion would produce asymmetric line profiles with redshifted emission and blueshifted absorption that would resemble the classical P Cygni profiles for winds of high radial velocities (Porter and Rivinius, 2003). Since such profiles are not observed in the H recombination lines, the radial velocity is observationally constrained to upper limits of the order of $\sim 10\text{--}20\text{ km s}^{-1}$ (Owocki and Ud-Doula, 2003).

Despite the evidence, there was still some dispute over the non-sphericity of the circumstellar material of Be stars during the 70s and 80s (Rivinius et al., 2013). The final confirmation of the disk-like nature of the circumstellar material came from optical interferometry, beginning with the work of Quirrenbach et al. (1994), who produced the first

interferometric image of a Be star (ζ Tauri, see the right panel of Fig. 1.3), showing its highly flattened appearance.

Be stars are sometimes confused with Herbig Ae/Be stars, which are pre-main-sequence objects. These stars are still embedded in clouds of gas and dust and are accreting material, usually in the form of circumstellar disks. Be stars, however, are not pre-main-sequence objects. Their circumstellar disks originate from outbursts from the star and not from an external cloud.

An important feature of Be stars is that, due to the high effective temperatures of their central B type stars, their disks are completely ionized and devoid of dust. Therefore, their opacity comes primarily from hydrogen and free electrons (Carciofi, 2011). These opacities are much better understood than the opacities of the disks of young stellar objects (YSO), which are dominated by dust. This is an excellent advantage for using Be stars with the aim of understanding the physics of circumstellar disks of astronomical objects.

The regions above and below the equatorial disk are similar to those around a normal B-type star. They present a weak radiatively driven wind. When viewed at near pole-on angles, Be stars show weak asymmetric blueshifted UV absorption lines (weak P Cygni profiles), most typically of Si IV and C IV (Snow, 1981), only accessible from observations from space. From these lines, wind velocities and densities can be derived (Puls et al., 2008). Typical wind mass loss rates of Be stars are $\sim 10^{-11} - 10^{-9} M_{\odot} \text{ yr}^{-1}$ and typical terminal velocities are $\sim 500 - 1500 \text{ km s}^{-1}$ (Snow, 1981).

The presence of the circumstellar disk causes scattering of part of the stellar radiation by free electrons. This, together with absorption by H atoms, is the cause of the observed polarized spectrum of Be stars, which is described in details by Haubois et al. (2014). The detailed shape of the polarized continuum is very sensitive to the density of the disk material, and has been used as a density diagnostic in the literature (an example will be provided below). Furthermore, in a disk-like configuration illuminated by a central star, the net polarization will be perpendicular to the disk. This is illustrated in Fig. 1.3, which shows that the direction of the linear polarization is perpendicular to the main elongation axis determined by interferometry. Almost all Be stars emit polarized continuous light (Rivinius et al., 2013), and the percentage of linear polarization is found to be as high as 2% for some denser disks.

As mentioned above, additional evidence of the presence of the disk is the flux excess observed from visible to radio wavelengths. This excess is caused by continuum emission from the disk by both the free-free process, involving free electrons, and the free-bound recombination, involving protons and electrons.

In addition to the fact that the radial velocity of the disks of Be stars must be much smaller than the azimuthal velocity v_{ϕ} , as imposed by the symmetric double-peaked shape with a central absorption, there is another feature observed in the line profiles that sug-

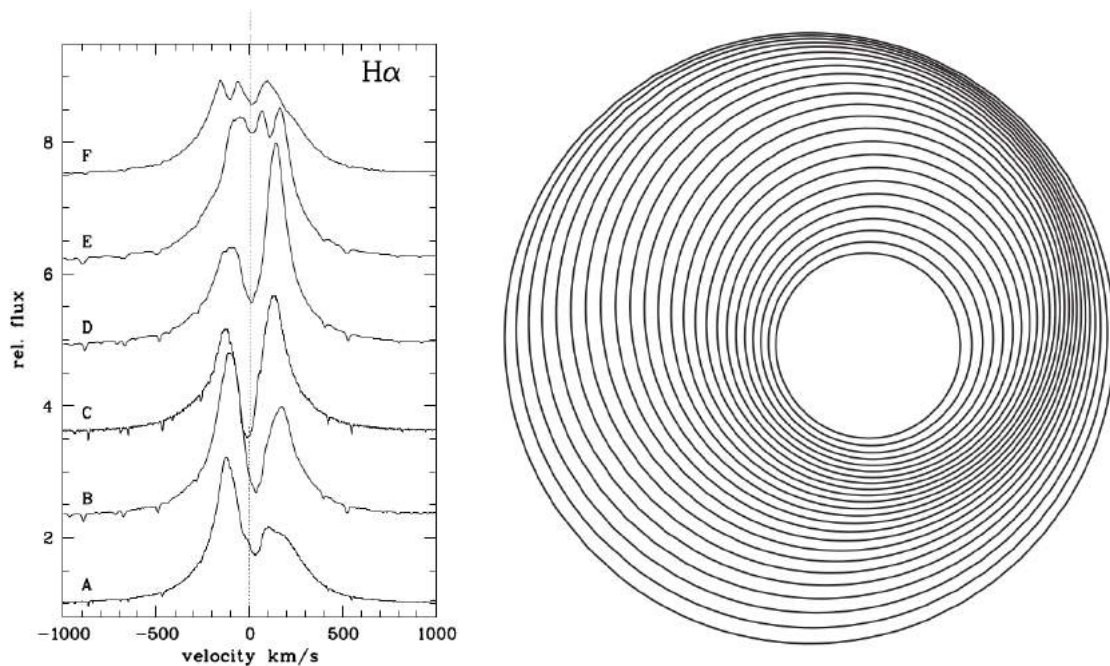


Figure 1.4: *Left:* V/R variations in H α of the Be star ζ Tauri. The period of the variations is ~ 3.8 years. (*Credits:* Štefl et al., 2009). *Right:* Schematic representation of an one-armed spiral pattern generated by elliptical (perturbed) orbits. (*Credits:* Sparke and Gallagher, 2007)

gests that the azimuthal flow must be near-Keplerian (i.e., $v_\phi \propto 1/R^{1/2}$), namely the V/R variations, which are near-periodic asymmetries in the line profiles observed in several Be stars (Okazaki, 1997). In the left panel of Fig. 1.4, V/R variations of the H α profile of ζ Tau are shown. The period of the variations for that Be star is ~ 3.8 years (Štefl et al., 2009).

The V/R variations are easily explained in the context of a Keplerian disk. In an exactly Keplerian disk, which would be the case if the fluid elements were only under a radial acceleration from a point-like central star, then the orbits of the fluid elements would be circular, with azimuthal velocities following $v_\phi \propto 1/R^{1/2}$. A global perturbation on the disk would make these orbits elliptical, forming an one-armed spiral pattern composed by the clumping of the elliptical orbits like the one sketched in Fig. 1.4 (right). For a fluid under a radial acceleration $\propto 1/r^2$, that configuration would be static (Sparke and Gallagher, 2007). The density of the disk would be greater near the clumping of the orbits and smaller away from them. However, due to several deviations from the $1/r^2$ law - e.g., from deformities of the central star from the spherical shape, or the radiative wind from the central hot star - the spiral pattern shown in the figure will precess around the star, usually in timescales much longer than the orbital periods of the orbits. The secular winding of the spiral pattern, produced by a near-Keplerian disk, explains the near periodic V/R variations, as first demonstrated by (Carciofi et al., 2009).

Finally, apart from the V/R variations, which are perturbations of a steady-state disk,

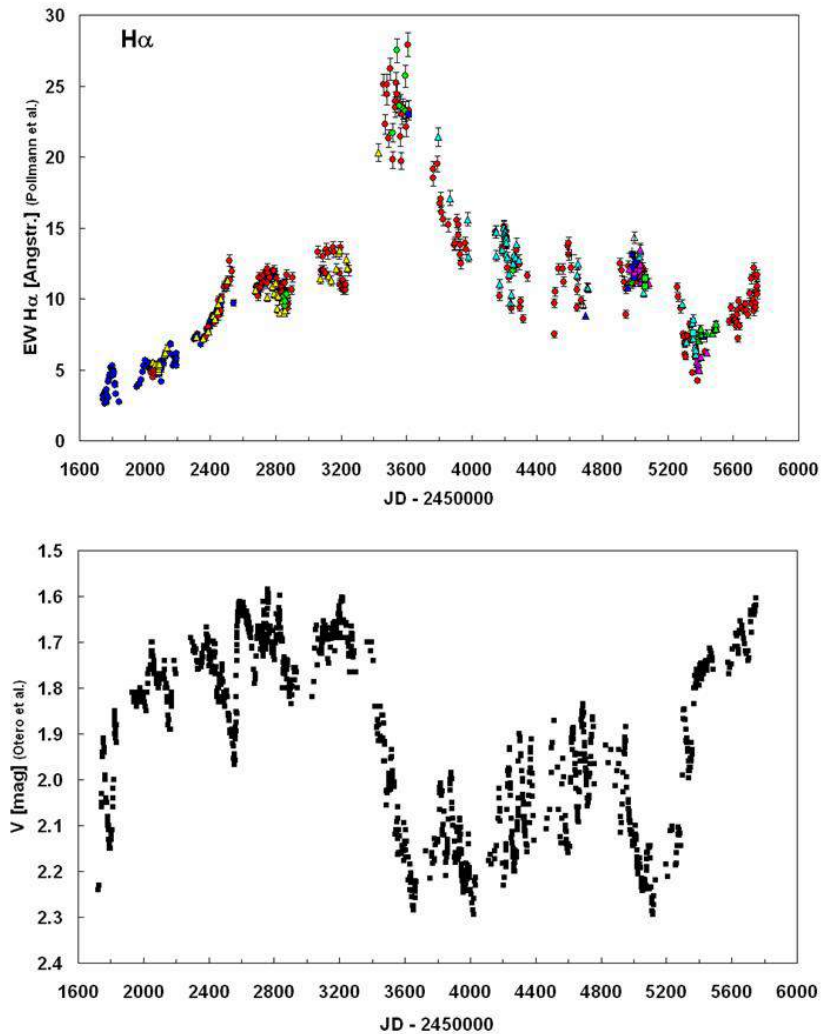


Figure 1.5: Variability of the Be star δ Scorpii over more than 11 years. *Above*: Equivalent width of the H α emission line. *Below*: V-band light curve. (Credits: https://www.aavso.org/vsots_delsco)

another striking feature of Be stars is that most are usually variable in all observables and in several timescales (days, weeks, months or even years). This variability indicates that the injection of matter and angular momentum from the star into the disk is variable, with sudden outbursts of mass injection and periods of no or negligible mass injection. As a result of that, many Be stars are known to alternate phases in which a disk is present with diskless phases, during which their spectroscopic appearance is that of a normal B star. Rivinius et al. (2016) proposes a terminology, which will be used here, in which a Be star that possesses a disk is said to be active and, conversely, when there is no detectable disk, the Be star is inactive. Two additional terms are used to distinguish the phases of active disk formation (outbursting Be star) and dissipation (dissipating Be star).

As an example of variability, in Fig. 1.5 we show measurements of the equivalent width

(EW) of the H α line (above) and the visual photometric V band (below) of the Be star δ Sco over the course of more than 11 years, during which the V magnitude varied between its inactive value ($V = 2.3$) and its maximum excess ($V = 1.59$).

From the panels, we see that a disk started forming around RJD = 1700². The continuum V -band excess, which comes from the inner regions of the disk (Carciofi, 2011), rapidly increased until around RJD = 2000. From then on, there was still a general trend of increasing, but at a slower rate, as if a plateau were being reached. The equivalent width of H α , which originates from a much larger region than the visual V band (Carciofi, 2011), increased during this time at a much slower pace. The panels also show that, apart from this general description, the evolution of the observables was filled with small-scale variability, very likely indicating that the rate of disk feeding from the star was not constant but rather variable.

Nearly around RJD = 3400, however, there was a fast decrease in the V -band excess, indicating the disappearance of the inner disk. This happened because the disk stopped being fed by the star. That resulted in an initial increase in the H α EW line due to the fact that the continuum around the line decreased just like the V -band excess. However, after the peak, the EW also started to decrease, showing that the extended disk also gradually disappeared. The light curve of δ Sco is a very irregular one. Several Be stars show light curves more well behaved, even with some periodicity in the outbursts (see, e.g., Mennickent et al., 2002; Sabogal et al., 2005).

1.1.1 The fastest rotators among non-degenerate stars

Another peculiarity of Be stars is their fast rotation, which is easily seen by their broad photospheric lines. A convenient parameter for specifying the rotational rate of a star is the ratio of the rotational velocity at the equator to the orbital velocity at the equator:

$$W = \frac{v_{\text{eq}}}{v_{\text{orb}}}, \quad (1.1.1)$$

where

$$v_{\text{orb}} = \left(\frac{GM}{R_{\text{eq}}} \right)^{\frac{1}{2}}, \quad (1.1.2)$$

where M is the mass of the star and R_{eq} is its equatorial radius. The parameter W , therefore, is a number between zero (for a non-rotating star) and one (for a star rotating at its critical limit).

Another commonly used parameter for specifying the rotational rate of a star is the ratio of the surface angular velocity to the critical surface angular velocity (assuming that the star's shape is given by the a Roche equipotential, see Sect. 2.3):

$$\omega = \frac{\Omega}{\Omega_0}, \quad (1.1.3)$$

² The reduced Julian Date (RJD) is given by RJD = JD – 2450000.

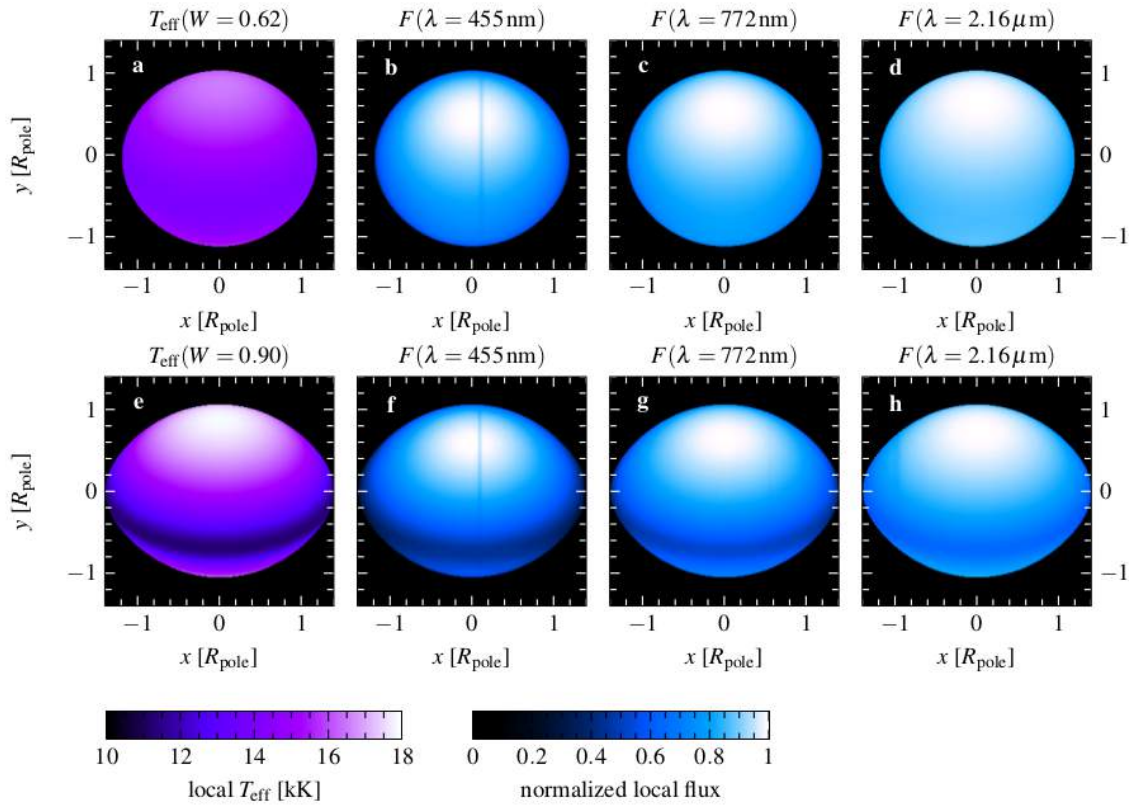


Figure 1.6: Appearance of a gravity darkened star. The temperatures shown follow the law $T_{\text{eff}} \propto g_{\text{eff}}^{\beta}$, with $\beta = 0.20$. *Upper row*: Surface appearance of a star rotating at $W = 0.62$. From left to right: Temperature and flux distributions in line free regions at $\lambda = 455\text{nm}$, $\lambda = 772\text{nm}$, and $\lambda = 2.16\mu\text{m}$. *Lower row*: Same as upper row, but for $W = 0.90$. (Credits: Rivinius et al., 2013)

where

$$\Omega_0 = \left(\frac{GM}{\left(\frac{3}{2}R_{\text{pole}}\right)^3} \right)^{\frac{1}{2}}, \quad (1.1.4)$$

where R_{pole} is the polar radius of the star.

From the compilation of the values of W of several Be stars, from several studies ranging from spectroscopic modeling, interferometric imaging and measurements of v_{eq} from Be shell stars, it was concluded that all well-studied Be stars present $W \gtrsim 0.7$, which offers a loose estimate for the minimum rotation rate necessary for a B star to become a Be star (Rivinius et al., 2013). So, fast stellar rotation is a property fundamentally linked to the so-called Be phenomenon.

The role of fast rotation for the Be phenomenon is that it reduces the effective gravity mainly at the stellar equator and facilitates mass ejection into an equatorial disk. One important effect of rotation is that the centrifugal acceleration forces the outer layers of the star, specially at lower latitudes, into an oblate shape. Furthermore, the lower

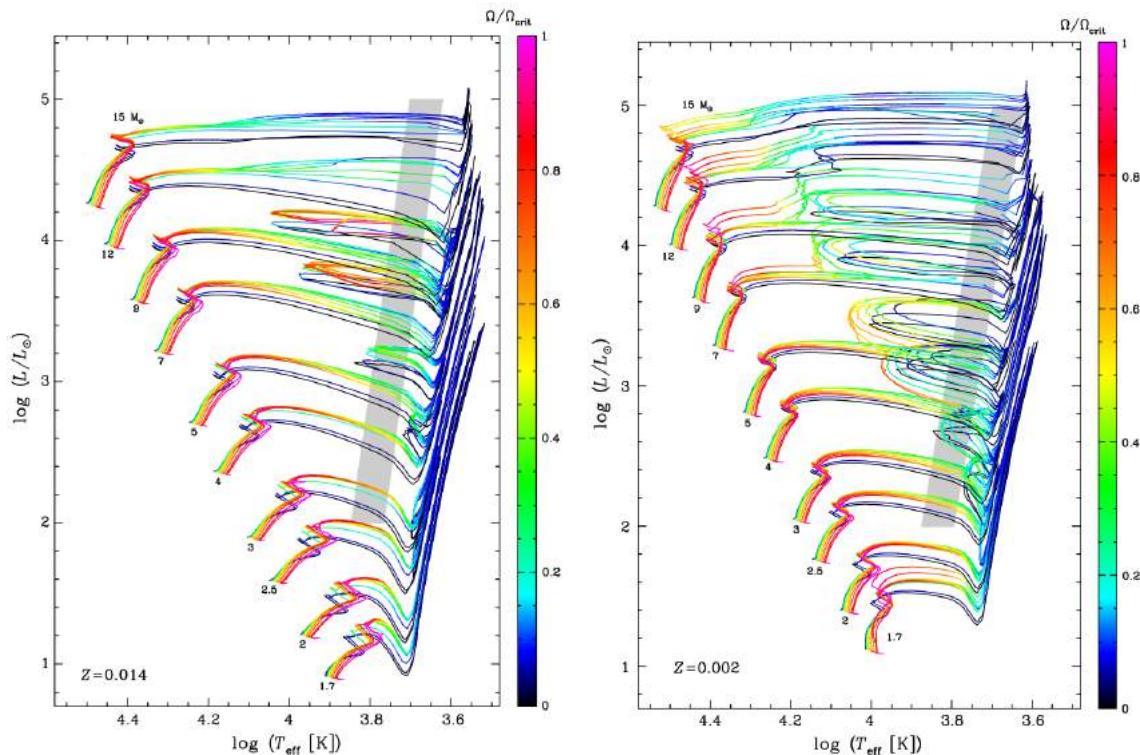


Figure 1.7: Evolutionary tracks for A-B type stars for $Z = 0.014$ (left) and $Z = 0.002$ (right), from the ZAMS to very late stages of the evolution of the stars. The colour code represents the rotational parameter ω (scales on the right of each panel). Be stars are usually found with $\omega \gtrsim 0.9$. The gray strips are the classical Cepheid instability strips. (Adapted from: [Georgy et al., 2013](#))

effective gravity near the stellar equator increases the scale height, diverting the internal flux towards the poles ([Espinosa Lara and Rieutord, 2011](#)), making them hotter while the equatorial regions become colder. Fig. 1.6 shows the shape, the temperature and the flux in three continuum bands of two stars with rotation rates given by $W = 0.62$ (above) and $W = 0.90$ (below), and with the surface temperature given by the law $T_{\text{eff}} \propto g_{\text{eff}}^{\beta}$, with $\beta = 0.20$. The distribution of the rotation rate W obtained from measurements of Galactic shell Be stars peaks around $W = 0.81$ with a standard deviation of 0.12 ([Rivinius et al., 2006](#)). Therefore, the top panels represent rotating B stars usually rotating too slowly to be Be stars, and the lower panels likely represent the rapidly rotating Be stars.

There are two proposed evolutionary channels to explain why Be stars rotate so fast. The first channel involves only an isolated star. As the rotating B star evolves on the main sequence, core contraction and internal angular momentum redistribution generally tends to enhance surface angular rotation ([Ekström et al., 2008](#); [Granada et al., 2013](#)). The near critical limit is, therefore, reached as a natural evolution of the rotating star ([Ekström et al., 2008](#)). The best rotating evolutionary models, however, require that such stars must already start as quite fast rotators already in the zero age main sequence (ZAMS). In Fig. 1.7, we show evolutionary tracks of A and B type stars for metallicities $Z = 0.014$

(left) and $Z = 0.002$ (right), from the ZAMS to very late stages of the evolution of the stars. The colors of the tracks give information of the rotational rate of the stars. The condition that Be stars are found with $W \gtrsim 0.7$ corresponds to the condition $\omega \gtrsim 0.9$ in their scale, and, therefore, the red to pink portions of the tracks are the predicted locii of Be stars in the HR-diagram.

Not much after the end of the main sequence phase, the expansion of the outer layers of the stars reduce W , which must inhibit the Be phenomenon from then on. Be stars might, thus, be a natural outcome of stars with an initial rotational velocity in the upper extreme of the initial velocity distribution.

The other proposed channel for the fast rotation of Be stars is interaction with a binary companion. The most massive stars ($M \geq 8M_{\odot}$) either are binaries (about 75%) or were so at some point of their evolution (Sana et al., 2012). It is possible that at least some fraction of the fast rotating Be stars were spun-up due to mass transfer from its binary companion (Ekström et al., 2008).

Is rotation the only key parameter to control whether a B star becomes a Be star? The answer to that is: probably no. Since several Be stars rotate still quite below the critical limit ($W \approx 1$), and since old theories of disk formation as a consequence of the winds (see Sect. 1.1.2 below) have failed to predict the general properties of the observed disks, it follows that an additional mechanism, referred to in the literature as the “Be mechanism” must operate in order to give the additional push to the near equatorial matter, in order to put it in orbit around the star. There is growing evidence that this mechanism must be stellar pulsation (Rivinius et al., 1998; Baade et al., 2016; Rivinius et al., 2016).

Why is the Be phenomenon mainly restricted to B type stars? Ekström et al. (2008) speculate that, for stars with spectral type earlier than B (O-type) stars, the intense mass and momentum loss through radiative winds prevents these stars from reaching near critical limits of surface rotation. These massive stars actually have their surfaces decelerated during their evolution in the main sequence. Following Kee et al. (2016), we would add that, even if the stars were rotating near critically, the strong radiative winds would ablate any forming disk too fast to be detected as a Be disk. Conversely, Ekström et al. (2008) also argue that, for stars with spectral type later than B (A-type stars), the meridional currents are not strong enough to accelerate the outer envelope.

Following the argument of Ekström et al. (2008), in environments of lower metallicity, the line-driven radiative mass and angular momentum loss must diminish, further extending the range of appearance of the Be phenomenon to stars of earlier type in those environments. Also, the minimum initial mass for the meridional currents become efficient enough to accelerate the surface would raise. That would also move the minimum mass for the appearance of Be stars upwards (Ekström et al., 2008).

Therefore, with their gaseous disks and fast rotation, Be stars, which some decades ago were considered to be of little relevance to the main field of hot and massive stars,

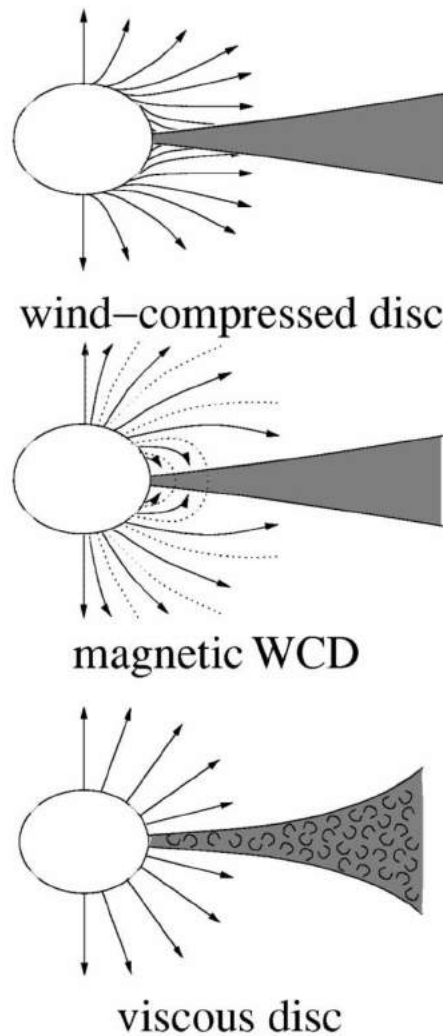


Figure 1.8: Wind streamlines and disk formation for three disk models. In the WCD, the streamlines are deflected towards the equator, creating the disk. In the MWCD, the wind is channeled by a magnetic field towards the equator, creating the disk. In the VDD, turbulence generates the disk and the wind is not important in the formation of the disk. (*Credits: Porter and Rivinius, 2003*)

turned out to be fundamental laboratories to test the physical mechanisms relevant for the evolution of the upper main sequence stars!

1.1.2 The Viscous Decretion Disk (VDD) model

Several theories were put forward to try to explain the properties of the disks of Be stars (even before they were actually confirmed interferometrically as disks in the mid nineties). As a first example, there is the toy-model used by [Waters et al. \(1987\)](#) for estimating of the mass loss rates of Be stars, using the Infrared Astronomical Satellite (IRAS) data. Their model was that of a mass conserving outflowing equatorial wind, with no other hydrodynamics involved. Coupled with a simple treatment of radiative transfer, this model offered some insight into the circumstellar properties of Be stars.

Some authors, however, still mistakenly cite their mass loss rate determinations for Be stars, which are two orders of magnitude above the now accepted values, as [Vieira et al. \(2015, 2017\)](#) have recently shown, and this work will also confirm.

Fig. 1.8, schematically shows three hydrodynamically sophisticated disk models proposed to explain the formation of Be star disks.

1.1.2.1 Wind Compressed Disk

[Bjorkman and Cassinelli \(1993\)](#) proposed a model in which the rotation of the radiation-driven wind of the fast rotating star B star would bend the flow towards the equatorial plane (due to the centrifugal and Coriolis forces). The streamlines from opposing hemispheres would, then, produce a shock at the equatorial plane, which would result in a dense region in the equatorial plane, representing the disk. This is the Wind Compressed Disk (WCD) model.

The WCD model was ruled out, however, by dynamical simulations ([Cranmer and Owocki, 1995](#); [Owocki et al., 1996](#)) that showed that the nonradial components of the line-driving force and the gravity darkening of the fast rotating star would actually inhibit the equatorial flow required by the WCD model. While ruled out from dynamical arguments, WCDs also failed to reproduce the observed IR excess and the near-Keplerian azimuthal flow that agrees with observations ([Porter and Rivinius, 2003](#)), since, in this model, the azimuthal velocity is close to angular momentum conserving ($v_\phi \propto 1/R$) and the radial outflow is too large also.

1.1.2.2 Magnetically Wind Compressed Disk

Soon later, the spirit of the WCD model was revived with the addition of magnetic fields, in the magnetically wind compressed disk (MWCD, [Cassinelli et al., 2002](#)). A key issue was the role of magnetic fields in channeling the line-driven wind of the star into the equatorial plane.

The magnetic fields that are required to significantly affect the B star wind flow are on the order of hundreds of gauss. Currently, however, there is no detection of large scale magnetic fields in Be stars, setting a lower limit of a few hundred gauss to possible large scale fields in Be stars ([Wade et al., 2012](#)). Also, simulations show that MWCDs present time dependent configurations more complicated than the expectation that the azimuthal flow must be near Keplerian. Actually, these simulations put serious doubts on the feasibility of these disks ([Owocki and Ud-Doula, 2003](#)).

1.1.2.3 Viscous Decretion Disk

In the Viscous Decretion Disk (VDD) model, the azimuthal motion is near Keplerian and a viscous mechanism produces the torque that causes the outward diffusion of mate-

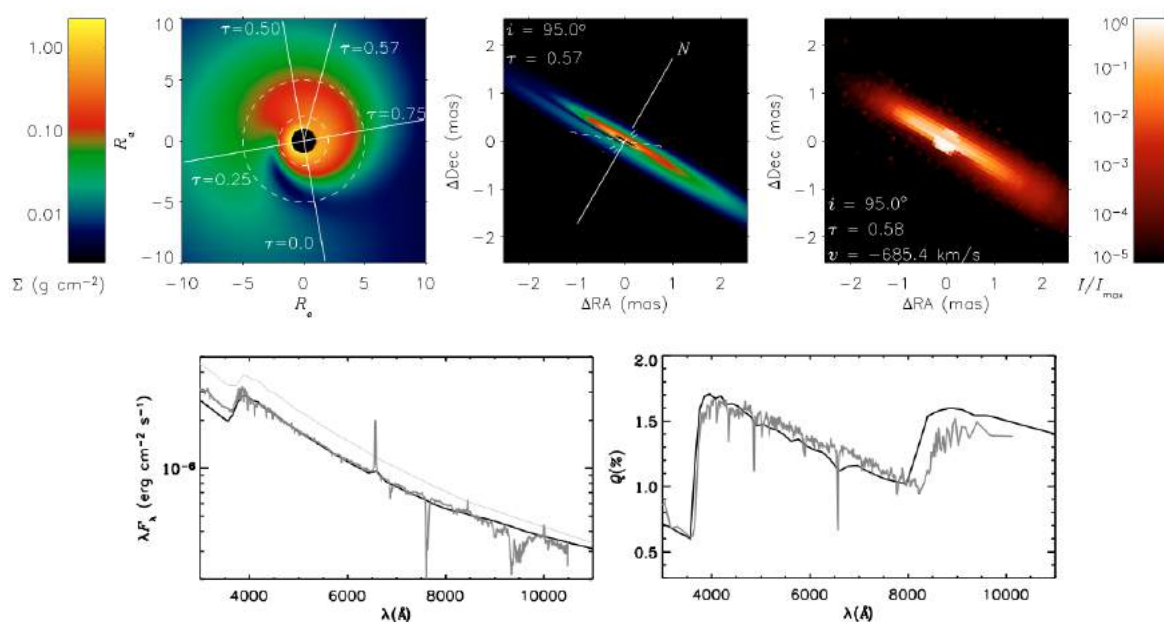


Figure 1.9: A VDD model of the Be star ζ Tauri that includes global density waves. *Above, left:* Density perturbation pattern as seen from above the disk. *Above, center:* Density perturbation pattern projected onto the plane of the sky. *Above, right:* continuum synthetic image generated by HDUST at $2.16 \mu\text{m}$, and used for interferometric fitting. *Below:* The dark grey lines are the observations of the optical spectrum (left) and optical spectropolarization (right), and the black lines represent the perturbed VDD model results. (Credits: Carciofi et al., 2009)

rial. The VDD model was first proposed by Lee et al. (1991) and further developed by Porter (1999); Okazaki (2001); Bjorkman and Carciofi (2005), and it is nearly identical, physically, to the accretion disks of pre-main-sequence objects, which are also viscous disks.

In the VDD model, the radiative wind from the star is believed not to participate in the formation of the disk. Rather, the model requires that some mechanism must put the stellar matter into orbit in the inner disk. From that point on, viscosity takes over as the mechanism governing the fate of the material, diffusing matter and angular momentum outwards, thus making the disk grow.

The VDD is the only theory to date that satisfies the whole set of observational facts. It has been demonstrated (e.g., Haubois et al., 2012) that a VDD fed roughly at a constant rate, and for a sufficiently long time (a few to several years, depending on the value of the viscosity), reaches a quasi-steady state in which the density is nearly constant in time. If the gas temperature is properly taken into consideration, the density profile is typically a complicated function of the distance from the star (e.g., Carciofi and Bjorkman, 2008). However, a usual approximation is to consider the temperature of the gas to follow a power law with the radial distance, in which case the density profile assumes a power-law

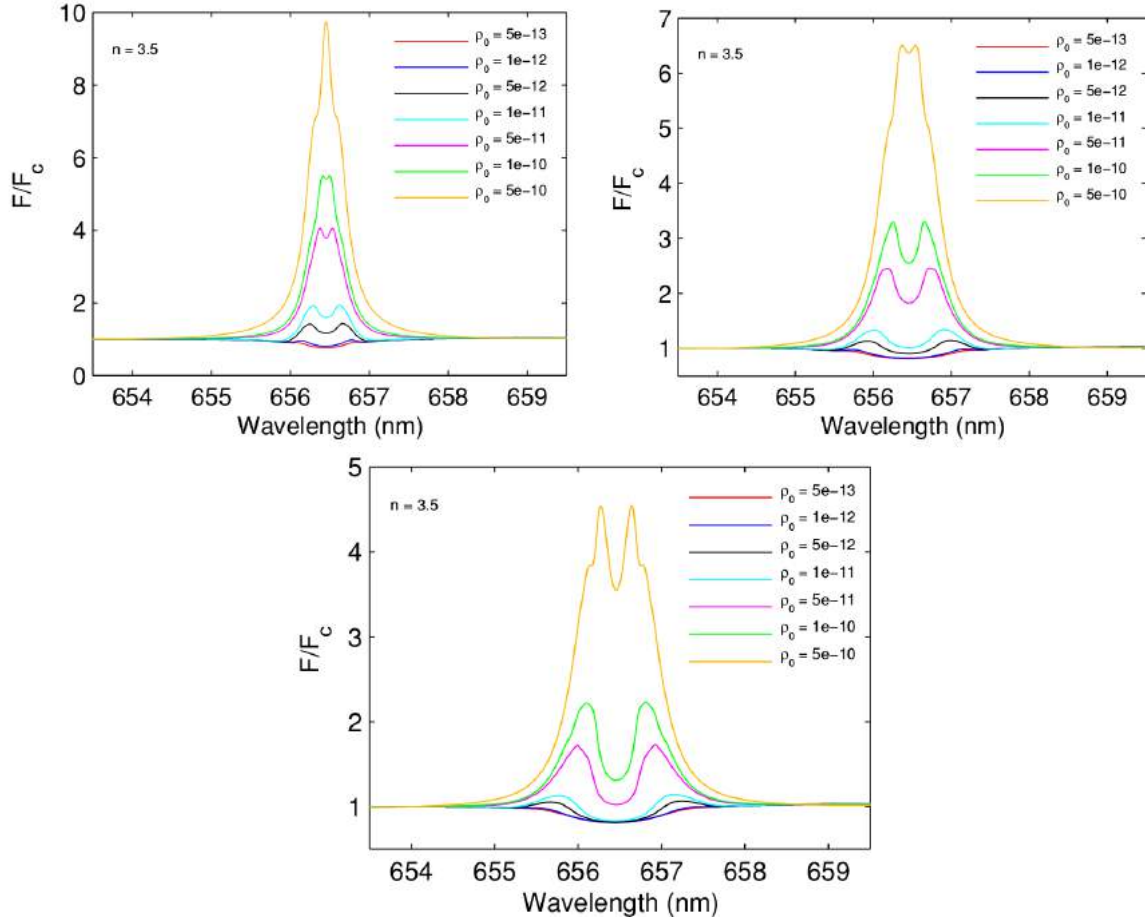


Figure 1.10: Theoretical non-LTE H α line profiles for a B0e star with a Keplerian disk and with several base densities ρ_0 , viewed at $i = 20$ deg (upper-left), $i = 45$ deg (upper-right) and $i = 70$ deg (below). (Credits: Silaj et al., 2010)

form given by

$$\rho(R, z) = \rho_0 \left(\frac{R}{R_{\text{eq}}} \right)^{-n} e^{-\frac{z^2}{2H^2}}, \quad (1.1.5)$$

where $H = (c_s/v_{\text{orb}})R^{\frac{3}{2}}$ is the disk scale height, with $c_s = (kT_{\text{disk}}/\mu m_H)^{\frac{1}{2}}$ and $v_{\text{orb}} = (GM/R_{\text{eq}})^{\frac{1}{2}}$ being respectively the isothermal sound speed and the orbital velocity at the stellar equator. For an isothermal disk, we must have $n = 7/2$ (e.g., Carciofi, 2011).

In the last decade, this simple steady-state VDD has been successful in describing the main observed features of individual Be disks (Carciofi et al., 2006, 2007; Jones et al., 2008; Carciofi et al., 2009; Klement et al., 2015) and samples of Be stars (Silaj et al., 2010; Touhami et al., 2011; Vieira et al., 2017). In Fig. 1.9, in particular, we show a fitting of a steady-state VDD with a density wave to several observables of the Be star ζ Tau (Carciofi et al., 2009), a Be star well known for its V/R variations, using the Monte Carlo radiative transfer code HDUST (Carciofi et al., 2004; Carciofi and Bjorkman, 2006, 2008).

In Fig. 1.10, we show theoretical H α line profiles of an early-type Be star made by Silaj et al. (2010), using a non-LTE radiative transfer code. For these calculations, they

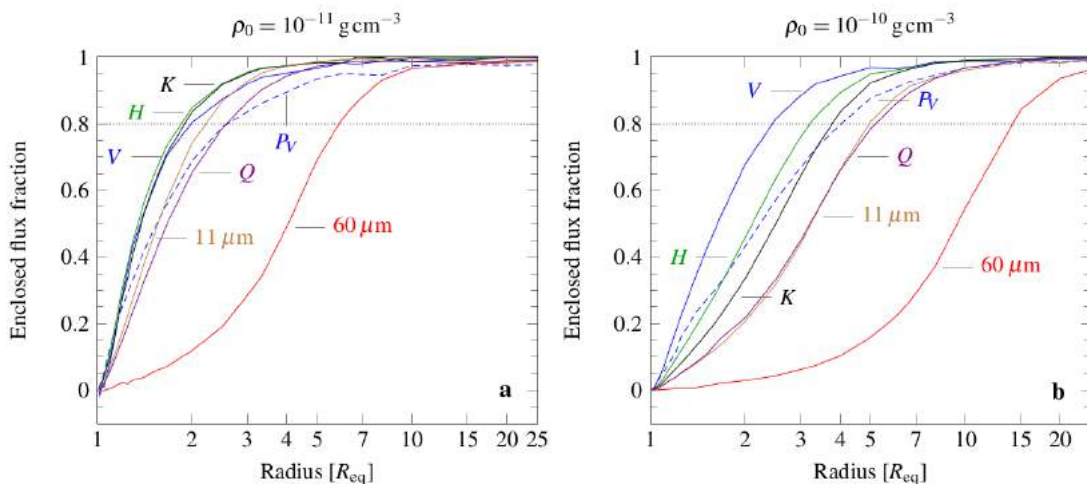


Figure 1.11: The formation loci of continuum emission for various wavelength bands for the base densities $\rho_0 = 10^{-11} \text{ g cm}^{-3}$ (left) and $\rho_0 = 10^{-10} \text{ g cm}^{-3}$ (right). Data were computed with HDUST, for a steady-state VDD seen at $i = 30 \text{ deg.}$ (Credits: Rivinius et al., 2013)

assumed Keplerian disk with a surface density law given by Eq. (1.1.5), with $n = 7/2$. From these panels, we may infer that the base density $\rho_0 = 5 \times 10^{-13} \text{ g cm}^{-3}$ is roughly the threshold density for the detection of a disk in a Be star.

Fig. 1.11, generated by HDUST, shows the locii of formation of several observables in a VDD, for two density scales. From the figures, we see that continuum visible and near-infrared observations generally probe the inner disk (between $1R_{\text{eq}}$ and $\sim 3 - 4R_{\text{eq}}$ at most). Mid to far infrared (e.g., $60 \mu\text{m}$), on the other hand, probe a much more extended region. The $\text{H}\alpha$ line (not shown in the panels) probe an area more or less similar to the $60 \mu\text{m}$ band (Carciofi, 2011).

I conclude this section reflecting on the fact that the idea of the Keplerian disk existed before the two alternative proposed disks (the WCD and the MWCD). The reason it faced skepticism due to the fact (since $W \sim 0.8$) that it required an unidentified mechanism for injecting matter at its base. Mass injection would be much easier if all Be stars were nearly critically rotating ($W \approx 1$). In that case, a simple convective layer at the (colder) equator would have the energy to produce the observed outbursts. Observations show, however that critical rotation is not the general case of Be stars. Thus, the VDD requires the “Be mechanism”: a physical mechanism able to give the additional push to the near equatorial stellar matter in order to put it into orbit. Also, the VDD requires a viscous mechanism, which needs a physical description. What is the source of this viscosity? (Since the circumstellar matter is a hot plasma, it must contain small scale magnetic fields, which must be a clue.) What is the required magnitude of this viscous mechanism? These fundamental questions are partly addressed in this thesis.

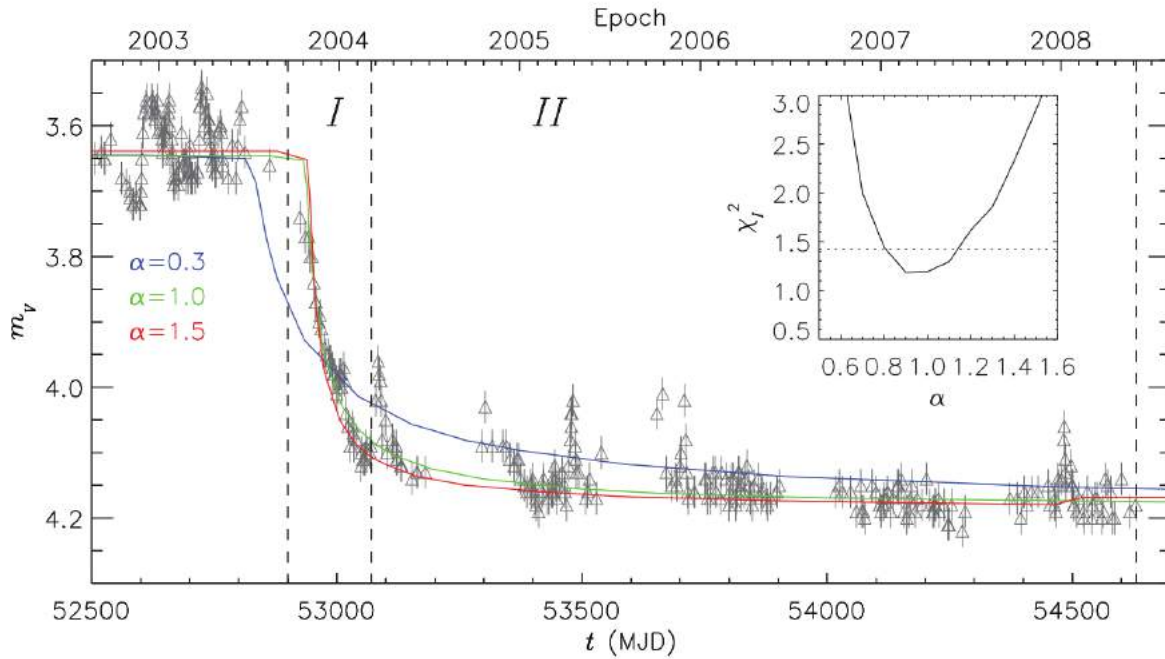


Figure 1.12: V-band light curve of the Be star 28 CMa, together with synthetic light curves of the dissipation of a VDD for different values of the viscosity parameter α . (Credits: Carciofi et al., 2012)

1.2 Dynamical VDDs

In this work, as in the most of the recent works on Be stars, the VDD model offers the conceptual framework with which Be stars disks are analyzed. Despite the great success of the VDD model, there are several open and intriguing theoretical questions about it that remain unexplained. The main ones are the identification of the “Be mechanism” producing the Be phenomom and the proper description of the viscous mechanism. Explaining both mechanisms are the key to understand the disk variability of these stars, and may hold the key to understand astrophysical disks in general.

The VDD model was always formulated in the alpha-disk formalism, in which the kinematic viscosity is scaled by the α parameter, defined such that the $R\phi$ component of the stress tensor is proportional to the gas pressure: $W_{R\phi} = -\alpha P$ (Shakura and Sunyaev, 1973).

Dynamical studies of the VDD model are recent in the literature, and still quite scarce. Jones et al. (2008), using a 1-D time-dependent treatment of the alpha-disk and a non-LTE radiative transfer code, studied the temperature and density profiles of a dynamical disk and their respective H α line profiles. Haubois et al. (2012) studied the theoretical photometric effects of time variable mass injection rates on the structure of the disk, also using an 1-D time-dependent treatment of the alpha-disk, and the radiative transfer code HDUST.

Carciofi et al. (2012) used these the time-dependent calculations of the disk surface density and the emergent flux at selected times, in order to estimate, for the first time, the α parameter for a Be circumstellar disk. The chosen star (28 CMa) passed from an active phase, that lasted from 2001 to 2003, to a dissipating phase at the end of 2003. The modeling of the dissipating phase allowed them to determine the value $\alpha = 1.0 \pm 0.2$.

Later, however, it was realized that a proper consideration of the previous history of the disk must be taken into consideration when fitting the dissipating portion of a lightcurve. This is a consequence of an effect identified during this thesis work, which we dubbed “mass reservoir effect”. The discovery of this effect was fundamental for the success of the PhD work of M. Ghoreyshi (IAG/USP) and my own. As described in Sect. 3.3, the discovery of mass reservoir effect resulted in a revision of the α parameter of the 2003 disk dissipation of 28 CMa to 0.21 ± 0.05 .

1.2.1 The origin of the viscosity of VDDs

It has been argued (Shakura and Sunyaev, 1973) that magnetic fields are the likely way in which a plasma shearing disk flow transports angular momentum from the inner rapidly rotating fluid to the outer slowly rotating fluid. Balbus and Hawley (1991) realized that the magnetorotational instability (MRI) could provide the necessary feedback to maintain a magnetic dynamo in the plasma disks (King et al., 2007). Since then, the MRI is the main theoretical bet for the mechanism that generates the necessary viscosity of alpha-disks. The reason is that simulations involving the MRI do demonstrate that a self-maintaining process which transports angular momentum in the required manner implied by the observations of such disks is feasible.

The most recent computations, however, still obtain values of α smaller than those required by observations of hot alpha disks (see below) by at least an order of magnitude, and often more (unless quite unlikely assumptions are made on the geometry of the magnetic fields). King et al. (2007) point out, however, that most of the computational limitations are likely to act in the direction of reducing α .

On the observational side, currently the largest body of evidence of values of α for hot disks comes from the light curves of dwarf novae which represent a subclass of cataclismic variables: binaries with white dwarf primaries and usually main sequence companions, which undergo outbursts at irregular intervals. In the currently most developed theory, these outbursts are due to an instability in the disk. The outbursts are episodes of enhanced mass transfer of the disk onto the primary, involving a significant part of the whole disk. The decay time of the burst is thus a measure of the viscous time scale of the disk. In the most clear-cut cases there appears to be evidence that values of $\alpha \sim 0.1 - 0.4$ are required to provide a good description of the behaviour of fully ionized, thin accretion discs (King et al., 2007).

On the opposite direction, there are observational indications from the inferred lifeti-

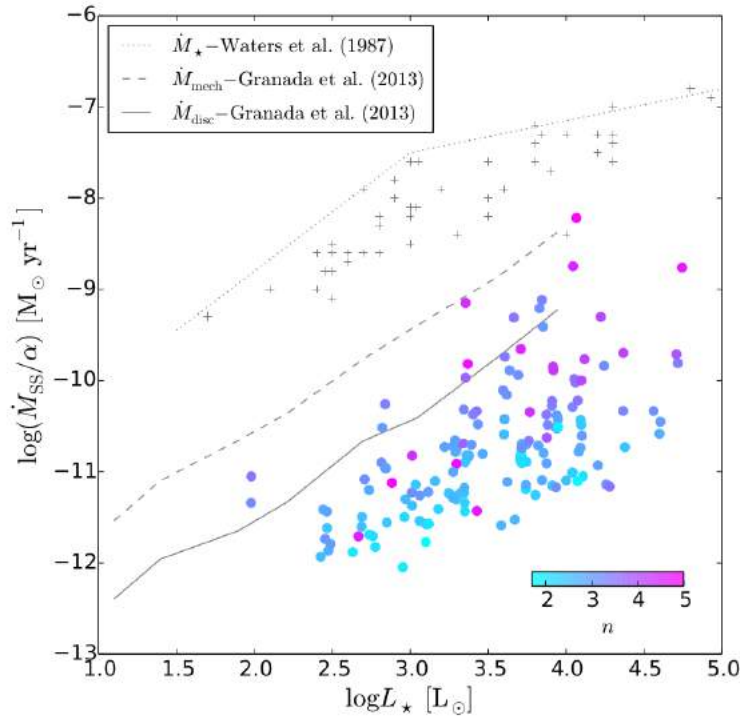


Figure 1.13: *Left:* Steady-state mass loss rate as a function of stellar luminosity. The circles are determinations of Vieira et al. (2017). The circle colors indicate the fitted n value. The solid line corresponds to the mass loss rate computed by Granada et al. (2013). The gray crosses indicate the values computed using an old toy-model by Waters et al. (1987). (Credits: Vieira et al., 2017)

mes and sizes of the much cooler and denser protostellar disks (Strom et al., 1993) that α may be rather small there, $\sim 10^{-3}$.

The recent determinations of the α parameter for 28 CMa (Sect. 3.3) are of the order of the ones estimated for the dwarf novae. The realization that the light curves of Be stars offer the key to measuring alpha directly (or as directly as possible) provided the primary motivation for this thesis work. This method of light curve fitting has brought Be disks to the small group of astrophysical objects with disk for which viscosity can be determined!

1.2.2 Mass and angular momentum loss rates

It was proposed (e.g., Ekström et al., 2008; Krtićka et al., 2011) that the disks of Be stars may provide natural mechanisms for removing large quantities of angular momentum from the fast rotating stars, preventing them from reaching the critical limit of rotation, during their main sequence evolution. The evolutionary models of Granada et al. (2013), in particular, adopted the prescription outlined by Krtićka et al. (2011): they assumed the appearance of completely formed VDDs every time their models reached a near-critical limit of rotation. The predicted mass density and the rate of angular momentum loss of

their disks were roughly similar to the ones found by [Vieira et al. \(2017\)](#), who modeled the spectral energy distribution (SED) of 80 Be stars using the VDD model (provided α a few tenths). This is illustrated in [Fig. 1.13](#).

1.3 Outline of this thesis

In this chapter we introduced the basic concepts of Be stars, and outlined the current status of the research on those objects.

The development of the VDD theory brought Be star research to a whole new level, allowing for the first time the establishment of a quantitative research where models and observations could be compared to extract meaningful information from the observations.

Recently, dynamical VDD studies demonstrated that, by modeling the temporal variability of Be stars (e.g., their light curves), it is possible to measure fundamental quantities of their disks (mass loss rates, viscosity parameters, etc.). However, to date these dynamical studies have been performed only on a single star (28 CMa).

The goal of this thesis work is to greatly increase the sample of variable Be stars studied with the dynamical VDD.

In [Chapter 2](#), we describe the main hydrodynamical equations of the VDD model in the alpha-disk formalism ([Shakura and Sunyaev, 1973](#)) and the main equations of the fast rotating star used in this work. We show how these equations are derived from the continuity principles of hydrodynamics.

In [Chapter 3](#), we describe how the star-disk connection is described in the VDD equations and we study dynamical VDDs. We show how important physical parameters of the dynamical disks are related to their steady-state counterparts, and we also link them to the mass and angular loss rates of the star. We also discuss how the history of mass injection of the disk affects its evolution, in what has been dubbed “the mass reservoir effect”.

Armed with the conclusions of the studies of dynamical disks, in [Chapter 4](#) we develop a grid of dynamical timescaled models representative of bumps usually found in the light curves of Be stars. This grid of dynamical models is expanded to include different possibilities of central stars and viewing angles in a grid of timescaled light curves, generated by a non-LTE radiative transfer treatment of the dynamical models. It is found that, for most of the viewing angles, the synthetic light curves can be approximated by empirical formulae, which can be used to fit the photometric bumps. We, therefore, describe a chain of procedures (a pipeline) for fitting the observed bumps in the light curves and extracting important parameters of the star and the disk. From these, other physical parameters described in [Chapter 3](#) can be derived.

We, then, advance to [Chapter 5](#), where we select very good examples of bumps from the catalog of Be star candidates from the SMC. We identify the bumps in the light curves

and the intervals of inactivity (with no detectable disk).

This selection of light curves and bumps is used in Chapter 6, where we fit them using the Markov Chain Monte Carlo (MCMC) technique, which is a powerful technique that allows us to see the probability distributions of the stellar and disk parameters, enabling us to derive quantities of interest and their uncertainties.

The main conclusions and perspectives of this work are outlined in Chapters 7 and 8.

Dynamical Principles of VDDs and rotating stars

If you wish to make an apple pie from scratch, you must first invent the Universe.

Carl Sagan, Cosmos TV series, 1980.

2.1 Hydrodynamical considerations

The equations that govern the evolution of a fluid's properties and its motion are conservation equations, from the laws of physics. The first conservation equation we enunciate is mass continuity, given by

$$\frac{\partial \rho}{\partial t} + \nabla \cdot (\rho \mathbf{v}) = \mathcal{S}, \quad (2.1.1)$$

where ρ is the volume density [g cm^{-3}], the vector $\rho \mathbf{v}$ is the mass flux, and the term \mathcal{S} represents any source (or sink) of mass [$\text{g cm}^{-3} \text{s}^{-1}$].

When we write the Eq. (2.1.1) as $\partial \rho / \partial t = \mathcal{S} - \nabla \cdot (\rho \mathbf{v})$, we clearly see that the equation says that, “in an infinitesimal element of fluid δV , the variation of the mass inside that volume, $\int_{\delta V} (\partial \rho / \partial t) dV$, is given by the mass that is added (or removed) there, $\int_{\delta V} \mathcal{S} dV$, minus the mass that flows away from there, $\oint_{\delta V} \rho \mathbf{v} \cdot d\mathbf{A}$ ”.

We use Eq. (2.1.1) to describe the fluid that composes the disk of the Be star. This fluid is known to be supplied by the star. So, we use the source term \mathcal{S} for describing the connection between the disk and the star and the disk and its outer medium, which is empty space.

The mass flux, $\rho \mathbf{v}$, is also equal to the volume density of linear momentum of the fluid [$\text{g cm}^{-3} \text{cm s}^{-1}$]. So, the second conservation equation we enunciate is that of linear momentum, as follows

$$\frac{\partial \rho \mathbf{v}}{\partial t} + \nabla \cdot \mathbf{\Pi} = \mathcal{F}, \quad (2.1.2)$$

where $\mathbf{\Pi}$ is the momentum flux tensor (Landau and Lifshitz, 2013) and \mathcal{F} represents the sources (or sinks) of linear momentum (usually, external forces acting on the fluid).

The momentum flux tensor, for convenience, is separated in two components given by $\mathbf{\Pi} = \rho\mathbf{v}\mathbf{v} - \boldsymbol{\sigma}$, where $\rho\mathbf{v}\mathbf{v}$ is the Reynolds tensor, related to the advective transport of momentum through the fluid and $\boldsymbol{\sigma}$ is Cauchy's stress tensor, related to non-advective mechanisms of transport of momentum (e.g., internal forces, like that resulting from the gradient of pressure).

Since the addition or removal of mass (with velocity \mathbf{v}) will also result in addition or removal of linear momentum, we subtract this contribution from \mathcal{F} and define the new force term \mathcal{F}^* , given by

$$\mathcal{F}^* = \mathcal{F} - \mathcal{S}\mathbf{v}. \quad (2.1.3)$$

Substitution of the above definitions into the equation of continuity of linear momentum leads us to

$$\begin{aligned} \frac{\partial\rho\mathbf{v}}{\partial t} + \nabla \cdot (\rho\mathbf{v}\mathbf{v} - \boldsymbol{\sigma}) &= \mathcal{F}^* + \mathcal{S}\mathbf{v} \\ \left[\mathbf{v} \frac{\partial\rho}{\partial t} + \rho \frac{\partial\mathbf{v}}{\partial t} \right] + [(\nabla \cdot \mathbf{v})\rho\mathbf{v} + \rho\mathbf{v} \cdot \nabla\mathbf{v} + (\nabla\rho \cdot \mathbf{v})\mathbf{v} - \nabla \cdot \boldsymbol{\sigma}] &= \mathcal{F}^* + \mathcal{S}\mathbf{v} \\ \left[\mathbf{v} \frac{\partial\rho}{\partial t} + \rho \frac{\partial\mathbf{v}}{\partial t} \right] + \rho\mathbf{v} \cdot \nabla\mathbf{v} + (\rho\nabla \cdot \mathbf{v})\mathbf{v} + (\nabla\rho \cdot \mathbf{v})\mathbf{v} &= \mathcal{F}^* + \mathcal{S}\mathbf{v} + \nabla \cdot \boldsymbol{\sigma} \\ \mathbf{v} \left(\frac{\partial\rho}{\partial t} + \nabla \cdot (\rho\mathbf{v}) \right) + \rho \left(\frac{\partial\mathbf{v}}{\partial t} + \mathbf{v} \cdot \nabla\mathbf{v} \right) &= \mathcal{F}^* + \mathcal{S}\mathbf{v} + \nabla \cdot \boldsymbol{\sigma}, \end{aligned}$$

from which we see that the first term in parenthesis is just the first member of the mass continuity equation, which will cancel with $\mathcal{S}\mathbf{v}$. Therefore, we end up with

$$\rho \left(\frac{\partial\mathbf{v}}{\partial t} + \mathbf{v} \cdot \nabla\mathbf{v} \right) = \mathcal{F}^* + \nabla \cdot \boldsymbol{\sigma}, \quad (2.1.4)$$

which is the Navier-Stokes equation - the analog of Newton's second law of motion for hydrodynamics (Landau and Lifshitz, 2013).

The equation of motion of the fluid (Eq. 2.1.4) says that the elements of the fluid will be accelerated due to external forces (like the gravitational force, per volume, from a point mass: $\mathcal{F}^* = -\rho(GM/r^2)\hat{\mathbf{r}}$) and internal stresses of the fluid.

The third conservation equation we enunciate is that of angular momentum (Landau and Lifshitz, 2013), given by

$$\frac{\partial\mathbf{r} \times \rho\mathbf{v}}{\partial t} + \nabla \cdot (\mathbf{r} \times \mathbf{\Pi}) = \mathbf{r} \times \mathcal{F}, \quad (2.1.5)$$

which, after some manipulation and taking the continuity of linear momentum equations into consideration (Eq. 2.1.2), results in the condition $\nabla \cdot (\mathbf{r} \times \boldsymbol{\sigma}) = \mathbf{r} \times \nabla \cdot \boldsymbol{\sigma}$, from which it follows that Cauchy's stress tensor must be symmetric:

$$\boldsymbol{\sigma} = \boldsymbol{\sigma}^T \text{ or } \sigma_{ij} = \sigma_{ji}. \quad (2.1.6)$$

In a fluid at rest, Cauchy's stress tensor becomes "hydrostatic". Therefore, it is given by $\boldsymbol{\sigma} = -P\mathbf{1}$, where $\mathbf{1}$ is the identity tensor and P is the hydrostatic pressure, which,

according to thermodynamics, is defined by an equation of state. We therefore isolate the thermodynamic pressure component from $\boldsymbol{\sigma}$, which leads us to

$$\boldsymbol{\sigma} = -P\mathbf{1} + \mathbf{W}, \quad (2.1.7)$$

where the stress tensor \mathbf{W} contains the other body forces apart from the thermodynamic pressure (e.g., viscous forces).

The set of equations that represent the elements of the stress tensor \mathbf{W} are called constitutive equations (Heinbockel, 2001). When, in particular, the stress tensor \mathbf{W} is zero, the fluid is said to be an ideal fluid (or an inviscid fluid). In that case, the Navier-Stokes (Eq. 2.1.9) is also called the Euler equation. Another common type of fluid is the newtonian fluid (Heinbockel, 2001), which is a special case of the general fluid in which the stress tensor is linear with respect to the velocity gradient tensor $\nabla\mathbf{v}$. For a newtonian fluid, \mathbf{W} is given by

$$\mathbf{W} = \rho\nu'(\nabla \cdot \mathbf{v})\mathbf{1} + 2\rho\nu\boldsymbol{\epsilon}, \quad (2.1.8)$$

where $\boldsymbol{\epsilon} = [(\nabla\mathbf{v}) + (\nabla\mathbf{v})^T]/2$ is the strain tensor, and ν and ν' are, respectively, the kinematic and bulk viscosities.

From Eq. (2.1.7), the Navier-Stokes equation is finally written as follows

$$\rho\left(\frac{\partial\mathbf{v}}{\partial t} + \mathbf{v} \cdot \nabla\mathbf{v}\right) = \mathcal{F}^* - \nabla P + \nabla \cdot \mathbf{W}. \quad (2.1.9)$$

2.2 Thin and axisymmetric disks

Theorem 1. “Assume that a cow is a uniform sphere with mass m and radius r ...”

Unknown author

In this work, we will assume that the disk is azimuthally symmetric. From the assumption of azimuthal symmetry, it follows that any derivative with respect to ϕ is zero.

We will also assume that the disk is symmetric with respect to the plane $z = 0$. From this assumption, it follows that, in our description, scalar functions are even in z . So, $\rho(z) = \rho(-z)$, $\mathcal{S}(z) = \mathcal{S}(-z)$, etc. Also, the z component of vectorial functions are odd in z : $v_z(z) = -v_z(-z)$, $\mathcal{F}_z(z) = -\mathcal{F}_z(-z)$, etc.; and tensorial functions follow the rule $\hat{\mathbf{x}}_i \cdot \mathbf{W} \cdot \hat{\mathbf{x}}_j(z) = (-1)^{\delta_{i3} + \delta_{j3}} \hat{\mathbf{x}}_i \cdot \mathbf{W} \cdot \hat{\mathbf{x}}_j(-z)$.

2.2.1 An inviscid and near-Keplerian disk

As a first instructive example of a disk, let us consider an axisymmetric and time-independent rotational flow given by $\mathbf{v} = \Omega\hat{\mathbf{z}} \times \mathbf{r}$ with $\partial\Omega/\partial t = 0$. Let us assume also that there is no viscosity, such that the stress tensor \mathbf{W} is zero.

Therefore, it follows that “material derivative” term in the Navier-Stokes equation becomes

$$\begin{aligned}
\frac{\partial \mathbf{v}}{\partial t} + \mathbf{v} \cdot \nabla \mathbf{v} &= (\boldsymbol{\Omega} \times \mathbf{r}) \cdot \nabla (\boldsymbol{\Omega} \times \mathbf{r}) \\
&= ((\boldsymbol{\Omega} \times \mathbf{r}) \cdot \nabla \boldsymbol{\Omega}) \times \mathbf{r} + \boldsymbol{\Omega} \times \{(\boldsymbol{\Omega} \times \mathbf{r}) \cdot \nabla \mathbf{r}\} \\
&= ((\boldsymbol{\Omega} \times \mathbf{r}) \cdot \nabla \boldsymbol{\Omega}) \times \mathbf{r} + \boldsymbol{\Omega} \times \{(\boldsymbol{\Omega} \times \mathbf{r}) \cdot \mathbf{1}\} \\
&= ((\boldsymbol{\Omega} \times \mathbf{r}) \cdot \nabla \boldsymbol{\Omega}) \times \mathbf{r} + \boldsymbol{\Omega} \times (\boldsymbol{\Omega} \times \mathbf{r}) \\
\frac{\partial \mathbf{v}}{\partial t} + \mathbf{v} \cdot \nabla \mathbf{v} &= ((\boldsymbol{\Omega} \times \mathbf{r}) \cdot \nabla \boldsymbol{\Omega}) \times \mathbf{r} - \Omega^2 r (\hat{\mathbf{r}} - (\hat{\mathbf{z}} \cdot \hat{\mathbf{r}}) \hat{\mathbf{z}}),
\end{aligned}$$

from which we also see that the first term of the second member vanishes, because we are considering an azimuthally symmetric flow: $((\boldsymbol{\Omega} \times \mathbf{r}) \cdot \nabla \boldsymbol{\Omega}) \times \mathbf{r} = \Omega R (\partial \Omega / \partial \phi) \hat{\boldsymbol{\phi}} = \mathbf{0}$.

The equation of motion is then given by

$$\frac{1}{\rho} \nabla P = \frac{1}{\rho} \mathcal{F}^* + \Omega^2 R \hat{\mathbf{R}}. \quad (2.2.1)$$

Taking the curl of the above equation

$$\nabla \times \left(\frac{1}{\rho} \nabla P \right) = \nabla \times \left(\frac{1}{\rho} \mathcal{F}^* \right) + \nabla \times (\Omega^2 R \hat{\mathbf{R}})$$

results in

$$\nabla c_s^2 \times \nabla \ln \rho = \nabla \times \left(\frac{1}{\rho} \mathcal{F}^* \right) + \frac{\partial}{\partial z} (\Omega^2 R) \hat{\boldsymbol{\phi}}, \quad (2.2.2)$$

where we have used the equation of state of the ideal gas, $P = \rho c_s^2$, and the assumption of axisymmetry.

Therefore, if the external force is radial (e.g., the gravitational force from a point mass, $\mathcal{F}^* = -(GM/r^2) \hat{\mathbf{r}}$), then $\nabla \times (\mathcal{F}^*/\rho) = \mathbf{0}$. Then, if the term on the left in (Eq. 2.2.2) is zero (e.g., if the disk is isothermal or polytropic), then we have $\partial \Omega / \partial z = 0$, which means that the rotational velocity is constant in cylinders.

Therefore, returning to Eq. (2.2.1), let us look only to its radial component. It is given by

$$\begin{aligned}
\Omega^2 R &= -\frac{1}{\rho} \mathcal{F}_R^* + \frac{1}{\rho} \frac{\partial P}{\partial R} \\
&= -\frac{1}{\rho} \mathcal{F}_R^* \left(1 + \left(-\frac{\rho c_s^2}{\mathcal{F}_R^*} \right) \left(\frac{\partial \ln \rho}{\partial R} + \frac{\partial \ln c_s^2}{\partial R} \right) \right),
\end{aligned} \quad (2.2.3)$$

where, in the last step, we have used the relation $P = \rho c_s^2$.

Then, in the approximation that the azimuthal motion is constant on cylinders, we may evaluate the above equation for Ω at the plane of the disk ($z = 0$). Assuming the gravitational acceleration of a point star, $\mathcal{F}^*|_{z=0} = -(GM/R^2) \hat{\mathbf{R}}$, we conclude that

$$\Omega^2 R = \frac{GM}{R^2} \left(1 + \left(\frac{R c_s^2}{GM} \right) \left(\frac{\partial \ln \rho}{\partial \ln R} + \frac{\partial \ln c_s^2}{\partial \ln R} \right) \right). \quad (2.2.4)$$

Since $v_\phi = \Omega R$, the above equation becomes

$$v_\phi^2 = v_K^2 \left(1 + \left(\frac{c_s^2}{v_K^2} \right) \left(\frac{\partial \ln \rho}{\partial \ln R} + \frac{\partial \ln c_s^2}{\partial \ln R} \right) \right), \quad (2.2.5)$$

where $v_K = v_{\text{orb}} \tilde{R}^{-\frac{1}{2}}$ is the Keplerian azimuthal velocity.

Therefore, for an inviscid isothermal/polytropic circumstellar disk whose stream lines are circular orbits, the near-Keplerian azimuthal motion is a solution. The deviations from the Keplerian motion come from the density ρ and temperature distributions, and they start to be non-negligible when the gradient of pressure becomes non negligible compared to the force of gravity.

We will see later that an isothermal VDD in steady-state has $\partial \ln \rho / \partial \ln R \approx -7/2$. Also, near the stellar equator ($R = R_{\text{eq}}$), the ratio between the isothermal sound speed and the Keplerian velocity is very small. For Be stars, we typically have $c_s / v_{\text{orb}} \approx 0.02$. However, at $R \sim 300 R_{\text{eq}}$, Eq. (2.2.5) already typically predicts $v_\phi \approx 0.5 v_K$.

2.2.2 On the vertical profile of thin disks

Interferometric observations of Be stars reveal that their disks are geometrically thin, with opening angles of a few degrees (Rivinius et al., 2013). Let us explore the properties of a thin disk, by using again the Navier-Stokes equation (Eq. 2.1.9). Isolating the gradient of pressure, we have

$$\nabla P = \mathcal{F}^* - \rho \left(\frac{\partial \mathbf{v}}{\partial t} + \mathbf{v} \cdot \nabla \mathbf{v} \right) + \nabla \cdot \mathbf{W}. \quad (2.2.6)$$

We will study the z component of that equation. Hence, multiplying by $\cdot \hat{\mathbf{z}}$ to see the vertical component of the motion, and dividing by P , we have

$$\begin{aligned} \frac{\partial \ln P}{\partial z} &= \frac{1}{P} \left(\mathcal{F}_z^* + \left(-\rho \left(\frac{\partial \mathbf{v}}{\partial t} + \mathbf{v} \cdot \nabla \mathbf{v} \right) \cdot \hat{\mathbf{z}} + \nabla \cdot \mathbf{W} \cdot \hat{\mathbf{z}} \right) \right) \\ &= \frac{1}{c_s^2} \left(\frac{1}{\rho} \mathcal{F}_z^* + \left(- \left(\frac{\partial \mathbf{v}}{\partial t} + \mathbf{v} \cdot \nabla \mathbf{v} \right) \cdot \hat{\mathbf{z}} + \frac{1}{\rho} \nabla \cdot \mathbf{W} \cdot \hat{\mathbf{z}} \right) \right). \end{aligned} \quad (2.2.7)$$

In general (e.g., Shakura and Sunyaev, 1973), it is assumed that the acceleration in the z direction is small, at least close to the denser regions of the disk, near the plane $z = 0$. Therefore, we will ignore the vertical velocity v_z and the forces due to stresses in that direction. We, therefore, have

$$\frac{\partial \ln P}{\partial z} \approx \frac{1}{c_s^2} \frac{1}{\rho} \mathcal{F}_z^*. \quad (2.2.8)$$

Eq. (2.2.8) says that the vertical component of the external force over the disk is counter balanced by the vertical gradient of the hydrostatic pressure. The scale height H of a thin disk is defined (e.g., Shakura and Sunyaev, 1973) by the gradient of pressure

with vertical height ($\partial \ln P / \partial \ln z = -z^2 / H^2$). Therefore, with the external force being the gravitational force of the central star ($\mathcal{F}^* = -\rho(GM/r^2)\hat{\mathbf{r}}$), we rewrite Eq. (2.2.8) as

$$\frac{\partial \ln \rho}{\partial z} + \frac{\partial \ln c_s^2}{\partial z} \approx -\frac{z}{H^2} \text{ where } \frac{H^2}{R^2} = \frac{c_s^2}{v_K^2} \left(1 + \left(\frac{z}{R}\right)^2\right)^{\frac{3}{2}}, \quad (2.2.9)$$

which can be integrated in z to obtain ρ :

$$\rho(R, z, t) = \rho(R, 0, t) \left(\frac{c_s^2(z=0)}{c_s^2}\right) e^{-\int_0^z \frac{z'}{H^2} dz'} \quad (2.2.10)$$

In particular, for a disk that is isothermal in height, it follows that

$$\rho(R, z, t) \approx \rho(R, 0, t) e^{-\frac{z^2}{2H^2}}, \quad (2.2.11)$$

where we have also approximated the scale height by

$$\frac{H}{R} \approx \frac{c_s}{v_K}, \quad (2.2.12)$$

which, as we have already seen in Sect. 2.2.1, is of the order of ~ 0.02 near the stellar equator (but, e.g., ~ 0.35 at $R \sim 300R_{\text{eq}}$).

Therefore, the rotating circumstellar disks with temperatures of the order of $\sim 60\%$ of the mean effective temperature of the Be star (Carciofi and Bjorkman, 2006) are thin disks, vertically sustained by hydrostatic pressure. The condition in which $c_s^2/v_K^2 \ll 1$ will be referred in this work as the ‘‘thin disk approximation’’.

2.2.2.1 Vertically integrated quantities and the thin disk approximation

The separation of the R and z components of the density of the disk (Eq. 2.2.11) suggests the usage of vertically integrated quantities for the description of the thin disk. Hence, the surface density of the disk is defined by

$$\Sigma(R, t) = \int_{-\infty}^{\infty} \rho(R, z, t) dz. \quad (2.2.13)$$

By substituting Eq. 2.2.11 into Eq. (2.2.13), we conclude that the surface density of the rotating circumstellar disk is $\Sigma(R, t) = (2\pi)^{\frac{1}{2}} H \rho(R, 0, t)$, which can be used to rewrite Eq. 2.2.11 as the relation between Σ and ρ , given by

$$\rho(R, z, t) \approx \frac{\Sigma(R, t)}{(2\pi)^{\frac{1}{2}} H} e^{-\frac{z^2}{2H^2}}, \text{ where } \frac{H}{R} \approx \frac{c_s}{v_K}. \quad (2.2.14)$$

Any other physical quantity Q , after being vertically integrated, is going to be given in terms of its averaged value $\langle Q \rangle$, as defined by the following equation:

$$\langle Q \rangle \Sigma = \int_{-\infty}^{\infty} \rho Q dz. \quad (2.2.15)$$

Since our system is symmetric with respect to the plane $z = 0$, it follows that the physical quantities Q are odd or even functions of z . If the physical quantity Q is odd in z (e.g., v_z , \mathcal{F}_z^*), then its vertically averaged quantity will be zero ($\int_{-\infty}^{\infty} \rho Q^{\text{odd}} dz = 0$), since ρ is an even function. If, however, Q is an even quantity in z (e.g., v_R , P , c_s), its vertically averaged quantity will not be zero.

2.2.3 The alpha-disk approach to thin VDDs

For describing a thin, axisymmetric and viscous disk (with $\mathbf{W} \neq \mathbf{0}$), we first start with the mass continuity equation:

$$\begin{aligned} \frac{\partial \rho}{\partial t} + \nabla \cdot (\rho \mathbf{v}) &= \mathcal{S} \\ \frac{\partial \rho}{\partial t} + \frac{1}{R} \frac{\partial}{\partial R} (R \rho v_R) + \frac{1}{R} \frac{\partial \rho v_\phi}{\partial \phi} + \frac{\partial \rho v_z}{\partial z} &= \mathcal{S} \\ \frac{\partial \rho}{\partial t} + \frac{1}{R} \frac{\partial}{\partial R} (R \rho v_R) + \frac{\partial \rho v_z}{\partial z} &= \rho \frac{\mathcal{S}}{\rho}, \end{aligned} \quad (2.2.16)$$

where, in the last step, we used the axisymmetric condition.

The vertically-integrated mass continuity equation is, then, given by

$$\frac{\partial \Sigma}{\partial t} + \frac{1}{R} \frac{\partial (R \Sigma \langle v_R \rangle)}{\partial R} = \Sigma \left\langle \frac{\mathcal{S}}{\rho} \right\rangle - 2 (\rho v_z)|_\infty, \quad (2.2.17)$$

where, besides the term containing the mass source \mathcal{S} , we see a new term, $2 (\rho v_z)|_\infty$, which is the upward mass flux, at infinity. This term may represent a disk wind, such as the ablating line-driven wind described by (Krtićka et al., 2011) in their radially extended steady-state VDD irradiated by the central star. The physical quantity $2\pi R \Sigma \langle v_R \rangle$ is the mass flux crossing the cylinder within radius R .

We now proceed to the Navier-Stokes equation (Eq. 2.1.9). It contains the advective term $\rho \mathbf{v} \cdot \nabla \mathbf{v}$. In cylindrical coordinates, it is given by

$$\begin{aligned} \rho \mathbf{v} \cdot \nabla \mathbf{v} &= \begin{pmatrix} \rho v_R & \rho v_\phi & \rho v_z \end{pmatrix} \begin{pmatrix} \frac{\partial v_R}{\partial R} & \frac{\partial v_\phi}{\partial R} & \frac{\partial v_z}{\partial R} \\ \frac{1}{R} \left(\frac{\partial v_R}{\partial \phi} - v_\phi \right) & \frac{1}{R} \left(\frac{\partial v_\phi}{\partial \phi} + v_R \right) & \frac{1}{R} \frac{\partial v_z}{\partial \phi} \\ \frac{\partial v_R}{\partial z} & \frac{\partial v_\phi}{\partial z} & \frac{\partial v_z}{\partial z} \end{pmatrix} \\ \rho \mathbf{v} \cdot \nabla \mathbf{v} &= \left(\rho v_R \frac{\partial v_R}{\partial R} + \frac{\rho v_\phi}{R} \left(\frac{\partial v_R}{\partial \phi} - v_\phi \right) + \rho v_z \frac{\partial v_R}{\partial z} \right) \hat{\mathbf{R}} + \\ &\quad \left(\rho v_R \frac{\partial v_\phi}{\partial R} + \frac{\rho v_\phi}{R} \left(\frac{\partial v_\phi}{\partial \phi} + v_R \right) + \rho v_z \frac{\partial v_\phi}{\partial z} \right) \hat{\boldsymbol{\phi}} + \\ &\quad \left(\rho v_R \frac{\partial v_z}{\partial R} + \frac{\rho v_\phi}{R} \frac{\partial v_z}{\partial \phi} + \rho v_z \frac{\partial v_z}{\partial z} \right) \hat{\mathbf{z}}, \end{aligned}$$

which, owing to the axisymmetry of our problem, simplifies to

$$\begin{aligned} \rho \mathbf{v} \cdot \nabla \mathbf{v} = & \left(\rho v_R \frac{\partial v_R}{\partial R} - \frac{\rho v_\phi^2}{R} + \rho v_z \frac{\partial v_R}{\partial z} \right) \hat{\mathbf{R}} + \\ & \left(\rho v_R \frac{\partial v_\phi}{\partial R} + \frac{\rho v_\phi v_R}{R} + \rho v_z \frac{\partial v_\phi}{\partial z} \right) \hat{\boldsymbol{\phi}} + \\ & \left(\rho v_R \frac{\partial v_z}{\partial R} + \rho v_z \frac{\partial v_z}{\partial z} \right) \hat{\mathbf{z}}. \end{aligned} \quad (2.2.18)$$

The Navier-Stokes equation also contains the term $\nabla \cdot \mathbf{W}$, the force per unit of volume over the fluid due to the stress tensor. In cylindrical coordinates, it is given by

$$\begin{aligned} \nabla \cdot \mathbf{W} = & \left(\frac{1}{R} \frac{\partial}{\partial R} (R W_{RR}) + \frac{1}{R} \frac{\partial W_{\phi R}}{\partial \phi} - \frac{W_{\phi\phi}}{R} + \frac{\partial W_{z\phi}}{\partial z} \right) \hat{\mathbf{R}} + \\ & \left(\frac{\partial W_{R\phi}}{\partial R} + \frac{1}{R} \frac{\partial W_{\phi\phi}}{\partial \phi} + \frac{W_{\phi R} + W_{R\phi}}{R} + \frac{\partial W_{z\phi}}{\partial z} \right) \hat{\boldsymbol{\phi}} + \\ & \left(\frac{1}{R} \frac{\partial}{\partial R} (R W_{Rz}) + \frac{1}{R} \frac{\partial W_{\phi z}}{\partial \phi} + \frac{\partial W_{zz}}{\partial z} \right) \hat{\mathbf{z}}, \end{aligned} \quad (2.2.19)$$

which, after invoking the axisymmetry of the problem and the fact that stress tensor \mathbf{W} is symmetric (meaning that $W_{\phi R} + W_{R\phi} = 2W_{R\phi}$), the above equation simplifies to

$$\begin{aligned} \nabla \cdot \mathbf{W} = & \left(\frac{1}{R} \frac{\partial}{\partial R} (R W_{RR}) - \frac{W_{\phi\phi}}{R} + \frac{\partial W_{z\phi}}{\partial z} \right) \hat{\mathbf{R}} + \\ & \left(\frac{1}{R^2} \frac{\partial}{\partial R} (R^2 W_{R\phi}) + \frac{\partial W_{z\phi}}{\partial z} \right) \hat{\boldsymbol{\phi}} + \\ & \left(\frac{1}{R} \frac{\partial}{\partial R} (R W_{Rz}) + \frac{\partial W_{zz}}{\partial z} \right) \hat{\mathbf{z}}. \end{aligned} \quad (2.2.20)$$

The z component of the Navier-Stokes was already addressed in Sect. 2.2.2, and resulted in the thin disk approximation. We here proceed to the ϕ component of the Navier-Stokes equation. It is given by

$$\begin{aligned} \rho \left(\frac{\partial v_\phi}{\partial t} + v_R \frac{\partial v_\phi}{\partial R} + \frac{v_\phi v_R}{R} + v_z \frac{\partial v_\phi}{\partial z} \right) &= \mathcal{F}_\phi^* - \frac{1}{R} \frac{\partial P}{\partial \phi} + \nabla \cdot \mathbf{W} \cdot \hat{\boldsymbol{\phi}} \\ \rho \left(\frac{\partial v_\phi}{\partial t} + v_R \frac{\partial v_\phi}{\partial R} + \frac{v_\phi v_R}{R} \right) &= \mathcal{F}_\phi^* + \frac{1}{R^2} \frac{\partial}{\partial R} (R^2 W_{R\phi}) + \frac{\partial W_{z\phi}}{\partial z}, \end{aligned} \quad (2.2.21)$$

where in the last step we have used the axisymmetry of the problem (to make $\partial P / \partial \phi = 0$) and the approximation that $\partial v_\phi / \partial z \approx 0$, as is the case for the azimuthal motion for the polytropic inviscid disk (see Sect. 2.2.1). Another argument for eliminating that term would be the assumption that v_z is much smaller than the other velocity components in the regions where the disk is dense, as was done in Sect 2.2.2.

By multiplying the Eq. (2.2.21) by R and integrating vertically, we obtain the following

$$\Sigma \frac{\partial}{\partial t} (Rv_\phi) + R\Sigma \langle v_R \rangle \frac{1}{R} \frac{\partial}{\partial R} (Rv_\phi) = R\Sigma \left\langle \frac{\mathcal{F}_\phi^*}{\rho} \right\rangle + \frac{1}{R} \frac{\partial}{\partial R} \left(R^2 \Sigma \left\langle \frac{W_{R\phi}}{\rho} \right\rangle \right) + 2RW_{z\phi}|_\infty. \quad (2.2.22)$$

The above equation contains the term $R\Sigma \langle v_R \rangle$, which is proportional to mass flux through the thin disk. Solving for this term, we obtain the following equation

$$R\Sigma \langle v_R \rangle = \frac{R\Sigma \left\langle \frac{\mathcal{F}_\phi^*}{\rho} \right\rangle + \frac{1}{R} \frac{\partial}{\partial R} \left(R^2 \Sigma \left\langle \frac{W_{R\phi}}{\rho} \right\rangle \right) + 2RW_{z\phi}|_\infty - \Sigma \frac{\partial}{\partial t} (Rv_\phi)}{\frac{1}{R} \frac{\partial}{\partial R} (Rv_\phi)}. \quad (2.2.23)$$

Now, it is expected from the observations of the disks of Be stars that the radial velocity must be much smaller than the azimuthal velocity: $\langle v_R \rangle \ll v_\phi$. So, for an external force whose radial component is dominated by gravity, i.e.,

$$\mathcal{F}_R^* = -\rho(GM/R^2) + \text{other small forces}, \quad (2.2.24)$$

we will have a similar situation as the one described in Sect. 2.2.1 for the azimuthal velocity v_ϕ . It follows, therefore, that the latter is approximately given by the Keplerian orbital velocity, at least in the thin disk approximation.

Therefore, assuming that $v_\phi \approx v_K$, the denominator of Eq. (2.2.23) will be given by $R^{-1} \partial(Rv_\phi) / \partial R \approx \frac{1}{2}(GM/R^3)^{\frac{1}{2}}$ and the time dependent term $\partial(Rv_\phi) / \partial t$ will approximately vanish. The mass flux is, thus, given by

$$2\pi R\Sigma \langle v_R \rangle = 4\pi \left(\frac{R^3}{GM} \right)^{\frac{1}{2}} \left(R\Sigma \left\langle \frac{\mathcal{F}_\phi^*}{\rho} \right\rangle + \frac{1}{R} \frac{\partial}{\partial R} \left(R^2 \Sigma \left\langle \frac{W_{R\phi}}{\rho} \right\rangle \right) + 2RW_{z\phi}|_\infty \right) \quad (2.2.25)$$

The above equation shows that a force in the positive ϕ direction due to the component $W_{R\phi}$ of the stress tensor or a positive component of an external force in the ϕ direction (the term containing \mathcal{F}_ϕ^*) can produce an outward mass flux, by transferring angular momentum to the fluid. (Also, a torque exerted by the outer boundary in infinity, given by the term $2RW_{z\phi}|_\infty$, can produce a mass flux.)

If the fluid of the disk is a viscous one of the newtonian kind, then, by Eq. (2.1.8), it follows that $W_{R\phi} = \rho R\nu \partial(v_\phi/R) / \partial R$, where ν is the kinematic viscosity. In the approximation that $v_\phi \approx v_K$, it follows that the $R\phi$ component of the stress tensor of the newtonian fluid is given by

$$W_{R\phi} = -\frac{3}{2}\rho\nu \left(\frac{GM}{R^3} \right)^{\frac{1}{2}}, \quad (2.2.26)$$

Instead of assuming that the fluid is newtonian, however, it is customary to scale the stress $W_{R\phi}$, which has unit of pressure, with the thermodynamic pressure P , through the dimensionless parameter α , as follows

$$W_{R\phi} = -\alpha P. \quad (2.2.27)$$

From Eqs. (2.2.26) and (2.2.27), it follows that the kinematic viscosity is related to the α parameter by the equation $\nu = (2/3)\alpha c_s H$, where H is the scale height (Eq. 2.2.12).

In this work, we will follow the definition of the α parameter given by (e.g., Eq. (2.2.27) (following, e.g., Okazaki, 2001)). In this definition of α , there is no mention to the newtonian stress tensor. However, several other works in the literature employ an alternative definition of the viscosity parameter. It is argued that the kinematic viscosity must be $\nu \leq c_s H$, since it results from momentum transport via eddies whose speed cannot be faster than the isothermal sound speed c_s and whose size cannot be bigger than the scale height H of the disk. Therefore, an alternative parameter α^* is defined by $\nu = \alpha^* c_s H$, and it is argued that $0 \leq \alpha^* \leq 1$. This alternative parameter relates to our viscosity parameter by $\alpha = (3/2)\alpha^*$.

Substitution of Eq. 2.2.27 into Eq. 2.2.25, gives

$$2\pi R \Sigma \langle v_R \rangle = 4\pi \left(\frac{R^3}{GM} \right)^{\frac{1}{2}} \left(R \Sigma \left\langle \frac{\mathcal{F}_\phi^*}{\rho} \right\rangle - \frac{1}{R} \frac{\partial}{\partial R} (R^2 \Sigma \langle \alpha c_s^2 \rangle) + 2RW_{z\phi}|_\infty \right). \quad (2.2.28)$$

In this work, we will consider that $2RW_{z\phi}|_\infty = 0$, because the outside medium of our disk system is empty space. (Gayley et al., 2001) has pointed out, however, that the non-negligible size of the aparent disk of the star together with a non-zero radial velocity may lead to the appearance of a ϕ component in the radiative line-driven force. That force can take the place of our unspecified external force \mathcal{F}_ϕ^* . We don't know if the common assumptions related to the line-force formalism apply to the generally optically thick inner portions of the disks of the Be stars. In this work, therefore, we will assume that there is no external force with a ϕ component.

From the above equation, we see that the effective viscous force in the ϕ direction is positive or negative, if the gradient of $R^2 \Sigma \langle \alpha c_s^2 \rangle$ is negative or positive, respectively. For an isothermal disk with α constant, if we assume a surface density profile $\Sigma \propto R^{-m}$, then the viscous force is positive (producing a positive mass flux - decretion) if $m > 2$, and negative (producing a negative mass flux - accretion) if $m < 2$.

2.3 The fast rotating star

In this section, we detail the main features of our stellar model used for the central star of the Be system. This stellar model will enter as input into the radiative transfer code HDUST.

The fast rotating star is a spinning fluid, under its own gravity, for which we will assume a negligible viscosity (at least for movements on timescales smaller than the evolutionary ones - Kippenhahn et al., 2012). Therefore, from the Navier-Stokes equation (Eq. 2.1.4), we write

$$\frac{1}{\rho} \nabla P = \frac{1}{\rho} \mathcal{F}^* - \frac{\partial \mathbf{v}}{\partial t} - \mathbf{v} \cdot \nabla \mathbf{v}, \quad (2.3.1)$$

where the vector $\nabla P/\rho$ is the effective gravity of the stellar configuration. The surface of a hydrostatic star, therefore, must be normal to this vector.

We will assume that the motion of the stellar fluid is axisymmetric and, at all places, circular around the axis of the star. We will, therefore, ignore complications such as convective motion or meridional circulations or stellar pulsations in our simple model. Let us, therefore, consider that the circular streamlines are given by $\mathbf{v} = \boldsymbol{\Omega} \times \mathbf{r}$ where $\boldsymbol{\Omega} = \Omega \hat{\mathbf{z}}$ is the angular velocity. As already shown in Sect. 2.2.1, it follows that

$$\frac{\partial \mathbf{v}}{\partial t} + \mathbf{v} \cdot \nabla \mathbf{v} = -\Omega^2 r (\hat{\mathbf{r}} - (\hat{\mathbf{z}} \cdot \hat{\mathbf{r}}) \hat{\mathbf{z}}) .$$

Hence, the effective gravity of the star is given by

$$\mathbf{g}_{\text{eff}} = \frac{1}{\rho} \nabla P = -\frac{GM}{r^2} \hat{\mathbf{r}} + \Omega^2 r (\hat{\mathbf{r}} - (\hat{\mathbf{z}} \cdot \hat{\mathbf{r}}) \hat{\mathbf{z}}) , \quad (2.3.2)$$

where we have assumed that the majority of the stellar mass is near its center, so $\mathcal{F}^*/\rho = -(GM/r^2)\hat{\mathbf{r}}$ is a good approximation for the gravitational acceleration acting at every point of the star. This acceleration can also be expressed as the gradient of the gravitational potential $\Phi = -GM/r$.

The last term in Eq. (2.3.2) is the centrifugal acceleration. In cylindrical coordinates, which will be very useful later in this work, this acceleration is given by $\Omega^2 R \hat{\mathbf{R}}$, from which we see that it increases linearly with the distance from the axis of rotation of the star (for a star rotating as a solid-body). Therefore, the closer a point is to the stellar equator, the more it will feel the centrifugal acceleration.

We must remember that the angular velocity in Eq. 2.3.2 may depend on the position of the fluid inside the star. It is thus a function of r and θ (in spherical coordinates) and of R and z in cylindrical coordinates. By this fact, the centrifugal acceleration cannot, in general, be defined in terms of a potential, like: $-\nabla V = \Omega^2 R \hat{\mathbf{R}}$. The centrifugal acceleration will be expressed in terms of a potential, if its curl is zero (because of the vector property: $\nabla \times \nabla V = \mathbf{0}$). Therefore, taking the curl $\nabla \times \Omega^2 R \hat{\mathbf{R}}$, results in the requirement that $\partial \Omega / \partial z = 0$, which means that the streamlines of the stellar fluid must be constant in cylinders. This is, obviously a serious restriction. An even greater restriction is that in which the stellar fluid rotates as solid body, meaning that, not even $\partial \Omega / \partial z = 0$, but $\partial \Omega / \partial R = 0$ also. In the case of a solid body rotation, one can easily show that $V = (1/2)\Omega^2 r^2 \sin^2 \theta$ is an appropriate potential that results in the centrifugal acceleration: $-\nabla V = \Omega^2 R \hat{\mathbf{R}}$. We therefore, rewrite Eq. (2.3.2) as follows

$$\frac{1}{\rho} \nabla P = -\nabla \Psi , \quad (2.3.3)$$

where

$$\Psi = -\frac{GM}{r} - \frac{1}{2} \Omega^2 r^2 \sin^2 \theta \quad (2.3.4)$$

is the Roche potential.

Now that the effective gravity of the star is given as the gradient of the potential Ψ , it follows that the surface of the star is defined by an equipotential $\Psi = \text{constant}$. It must be remembered, however, as explained above, that Eq. (2.3.2) is more general than Eqs. (2.3.3) and (2.3.4), and stars do have differential rotation. Therefore, their shapes might not be well described by the equipotentials of the Roche potential. Since the internal rotation of fast rotating stars is still poorly constrained, this effect can be potentially serious when determinations of the critical fraction W of a star is made, e.g., interferometrically (based solely on its shape).

Let us, then, follow with the determination of the shape of the star, assumed to be given by a Roche equipotential. First, we define the parameter r_0 , which has dimension of distance, and the dimensionless variable s as

$$s = \frac{r}{r_0}. \quad (2.3.5)$$

Let us assume that r_0 is the value of the polar radius of a star rotating at critical velocity. The radius of the stellar equator of that star is r'_0 . The form of this star is given by the equipotential $\Psi = \Psi_0$, and it is rotating with angular velocity Ω_0 .

Since, the star is rotating at critical velocity, it follows that the effective gravity at its equator is zero, and, therefore, $-GM/r_0'^2 + \Omega_0^2 r_0' = 0$, from which follows that $\Omega_0^2 = GM/r_0'^3$.

Now, since both the polar radius (measuring r_0) and the equatorial radius (measuring r'_0) are on the same surface $\Psi = \Psi_0$, we can eliminate r'_0 from the equality: $-GM/r_0 = -GM/r'_0 - (1/2)\Omega_0^2 r_0'^2$, from which it results that $r'_0 = (3/2)r_0$ (the ratio between the equatorial radius and the polar radius of a critically rotating star is 1.5), and we end up with the other two important parameters defined as

$$\Psi_0 = -\frac{GM}{r_0} \quad (2.3.6)$$

and

$$\Omega_0^2 = \frac{8}{27} \frac{GM}{r_0^3}. \quad (2.3.7)$$

Now, let us define the scaled Roche potential by

$$\psi = \frac{\Psi}{\Psi_0}, \quad (2.3.8)$$

and the dimensionless angular velocity by

$$\omega = \frac{\Omega}{\Omega_0 \psi^{\frac{3}{2}}}. \quad (2.3.9)$$

By substitution of all definitions into the Roche potential (Eq. 2.3.4), it follows that

$$\begin{aligned}
\frac{\Psi}{\Psi_0} = \psi &= + \frac{GM}{r} \frac{r_0}{GM} + \frac{r_0}{GM} \frac{1}{2} \Omega^2 r^2 \sin^2 \theta \\
&= + \frac{GM}{r} \frac{r_0}{GM} + \frac{r_0^3}{GM} \frac{1}{2} \Omega^2 \left(\frac{r}{r_0} \right)^2 \sin^2 \theta \\
&= + \frac{GM}{r} \frac{r_0}{GM} + \frac{8}{27} \frac{1}{\Omega_0^2} \frac{1}{2} \Omega^2 \left(\frac{r}{r_0} \right)^2 \sin^2 \theta \\
\psi &= \frac{1}{s} + \frac{4}{27} \psi^3 \omega^2 s^2 \sin^2 \theta, \tag{2.3.10}
\end{aligned}$$

from which it follows that the surface of the star, $s_\psi(\omega, \theta)$, is given by the following third order equation

$$s^3 - \frac{27}{4} \frac{1}{\psi^2 \omega^2 \sin^2 \theta} s + \frac{27}{4} \frac{1}{\psi^3 \omega^2 \sin^2 \theta} = 0, \quad \theta \neq 0, \pi \tag{2.3.11}$$

$$s = \frac{1}{\psi}, \quad \theta = 0, \pi \tag{2.3.12}$$

which, for the case of $0 \leq \omega \leq 1$, results in closed surfaces given by

$$\begin{aligned}
s_\psi &= \frac{1}{\psi}, \quad \theta = 0, \pi \\
s_\psi &= \frac{3}{\psi} \frac{1}{\omega \sin \theta} \cos \left[\frac{\pi}{3} + \frac{1}{3} \arccos(\omega \sin \theta) \right], \quad \theta \neq 0, \pi \tag{2.3.13}
\end{aligned}$$

Eq. (2.3.13) gives the analytical form of the surface of stellar configuration rotating as a solid body.

Observationally, the rotation rate of the star is better stated in terms of the critical ratio $W = \Omega R_{\text{eq}}/v_{\text{orb}}$, where $v_{\text{orb}} = (GM/R_{\text{eq}})^{\frac{1}{2}}$. (The equatorial and polar radius are given by $R_{\text{eq}} = r_0 s_{\psi, \text{eq}}$ and $R_{\text{pole}} = r_0 s_{\psi, \text{pole}}$.) Just like ω , the parameter W is also a number between 0 and 1. It is, however, better suited for comparison with observations, since $v_{\text{eq}} = \Omega R_{\text{eq}}$ can be easily estimated from them.

In Fig. 2.1, we show the forms of Roche stars with increasing values of W , from 0 to 1, in steps of 0.1. The blue shape correspond to $W = 0.8$ and the red shapes correspond to $W = 0.7$ and $W = 0.9$. The red shapes more or less correspond to the limits (within $\pm 1\sigma$) of the distribution of values of W found by Rivinius et al. (2006), by studying shell Be stars.

In some works in the literature, however, it is also common to find the Υ parameter, defined as the ratio of the equatorial velocity and the critical velocity defined by $v_{\text{crit}} = (GM/1.5R_{\text{pole}})^{\frac{1}{2}}$, which, for our Roche model, is also a number between 0 and 1. If the star, on the other hand, does not follow a Roche potential, it would be possible to obtain values beyond 1 for Υ . Therefore, the usage of this parameter should be discouraged as Rivinius et al. (2013) pointed out. The practical problem, however, with the three definitions of W , ω and Υ is that they are only equal for a specific star if they are equal to

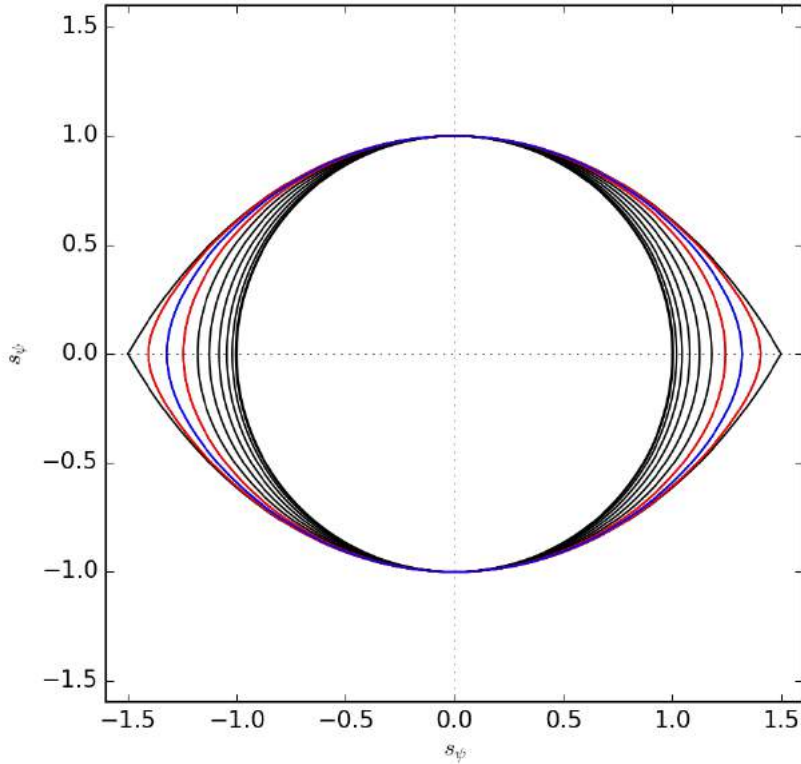


Figure 2.1: Shapes of the stellar configurations, rotating as solid bodies, with critical ratios W varying from 0 to 1 in steps of 0.1. The blue shape correspond to $W = 0.8$ and the red shapes correspond to $W = 0.7$ and $W = 0.9$. For all stars, it was chosen $\psi = 1$.

0 or 1. They differ in all other cases and that can lead to a great deal of confusion. (In this work, in particular, it was necessary to perform conversions between these parameters.) Finally, interferometrists might define the stellar rotation rate by the ratio between the equatorial radius and the polar radius, known as the oblateness of the star. For our Roche model, it is a number between 1 and 1.5.

In Table 2.3, we list the set of formulas required to convert between the four parameters: W , ω , $R_{\text{eq}}/R_{\text{pole}}$ and Υ .

2.3.1 Espinosa-Lara & Rieutord's flux prescription

Inside the star, energy is in the stellar core as the result of nuclear reactions. Outside the core, energy is not generated. It diffuses outwards until it leaves through the stellar surface. Therefore, outside the core, the energy flux \mathbf{F} must be divergenceless: $\nabla \cdot \mathbf{F} = 0$, meaning that there is no source of energy in the envelope.

For a radiative envelope, the radiative flux is given by the diffusion equation $\mathbf{F} = -\chi \nabla T$. The temperature is a function of ρ and P . If the star is barotropic, meaning, in our case, that the ρ and P are constants on an equipotential Ψ , then, it follows the

	W	ω	$\frac{R_{\text{eq}}}{R_{\text{pole}}}$	Υ
W	—	$\left(\frac{8}{\omega} \cos^3\left(\frac{\pi}{3} + \frac{1}{3} \arccos \omega\right)\right)^{\frac{1}{2}}$	$\left(2 \frac{R_{\text{eq}}}{R_{\text{pole}}} - 2\right)^{\frac{1}{2}}$	$\left(\frac{3\Upsilon}{\cos\left(3 \arccos\left(\frac{\Upsilon}{2}\right) - \pi\right)} - 2\right)^{\frac{1}{2}}$
ω	$\left(\frac{27}{8} \frac{W^2}{\left(1 + \frac{1}{2}W^2\right)^3}\right)^{\frac{1}{2}}$	—	$\left(\frac{27}{4} \frac{\left(\frac{R_{\text{eq}}}{R_{\text{pole}}} - 1\right)}{\left(\frac{R_{\text{eq}}}{R_{\text{pole}}}\right)^3}\right)^{\frac{1}{2}}$	$\cos\left(3 \arccos\left(\frac{\Upsilon}{2}\right) - \pi\right)$
$\frac{R_{\text{eq}}}{R_{\text{pole}}}$	$1 + \frac{1}{2}W^2$	$\frac{3}{\omega} \cos\left(\frac{\pi}{3} + \frac{1}{3} \arccos \omega\right)$	—	$\frac{3\Upsilon}{2 \cos\left(3 \arccos\left(\frac{\Upsilon}{2}\right) - \pi\right)}$
Υ	$\left(\frac{3}{2} \frac{W^2}{1 + \frac{1}{2}W^2}\right)^{\frac{1}{2}}$	$2 \cos\left(\frac{\pi}{3} + \frac{1}{3} \arccos \omega\right)$	$\left(3 \frac{\frac{R_{\text{eq}}}{R_{\text{pole}}} - 1}{\frac{R_{\text{eq}}}{R_{\text{pole}}}}\right)^{\frac{1}{2}}$	—

Table 2.1 - Conversion table between W , ω , $R_{\text{eq}}/R_{\text{pole}}$ and Υ .

temperature is also constant in the equipotential Ψ and $\nabla T = (\partial T / \partial \Psi) \nabla \psi$, which means that $\mathbf{F} = \chi(\partial T / \partial \Psi) \mathbf{g}_{\text{eff}}$. Then, at the surface of the star, the flux must be given by σT_{eff}^4 , from which the “von Zeipel relation” $T_{\text{eff}} \propto g_{\text{eff}}^{\frac{1}{4}}$ is obtained. However, there is a contradiction, since the effective gravity is not constant along the equipotential Ψ , in contradiction with our assumption that the temperature is constant on an equipotential. This contradiction was known since [von Zeipel \(1924\)](#), and it implies that a rotating star that is isothermal on equipotentials cannot be in radiative equilibrium.

Nevertheless, in the convective envelopes, heat is transported by buoyance, essentially following the opposing direction of the effective gravity ([Espinosa Lara and Rieutord, 2011](#)). Therefore, inspired by this fact and by the “von Zeipel” law, which also prescribed a flux in the direction of the effective gravity, [Espinosa Lara and Rieutord \(2011\)](#) suggested the following prescription for the flux transport inside the rotating star:

$$\nabla \cdot \mathbf{F} = L \delta^3(\mathbf{r}), \text{ such that } \mathbf{F} \parallel \mathbf{g}_{\text{eff}}, \quad (2.3.14)$$

that is: all the stellar luminosity is generated at the center of the star (roughly the location of the near spherical core) and, in every point, the flux follows parallel to the effective gravity. Interestingly, this prescription matches quite well with the predictions of their more detailed rotating stellar interior code ESTER ([Espinosa Lara and Rieutord, 2011](#)).

We therefore adopt their prescription in this work. The analytical solution of the problem given by Eq. (2.3.14) for a Roche star is lengthy and well described in [Espinosa Lara and Rieutord \(2011\)](#). We will only state their results here.

The flux at every point inside the star, and at the surface in particular, is given by the following equation

$$\mathbf{F} = -\frac{L}{4\pi GM} F_{\omega}(s, \theta) \mathbf{g}_{\text{eff}}, \quad (2.3.15)$$

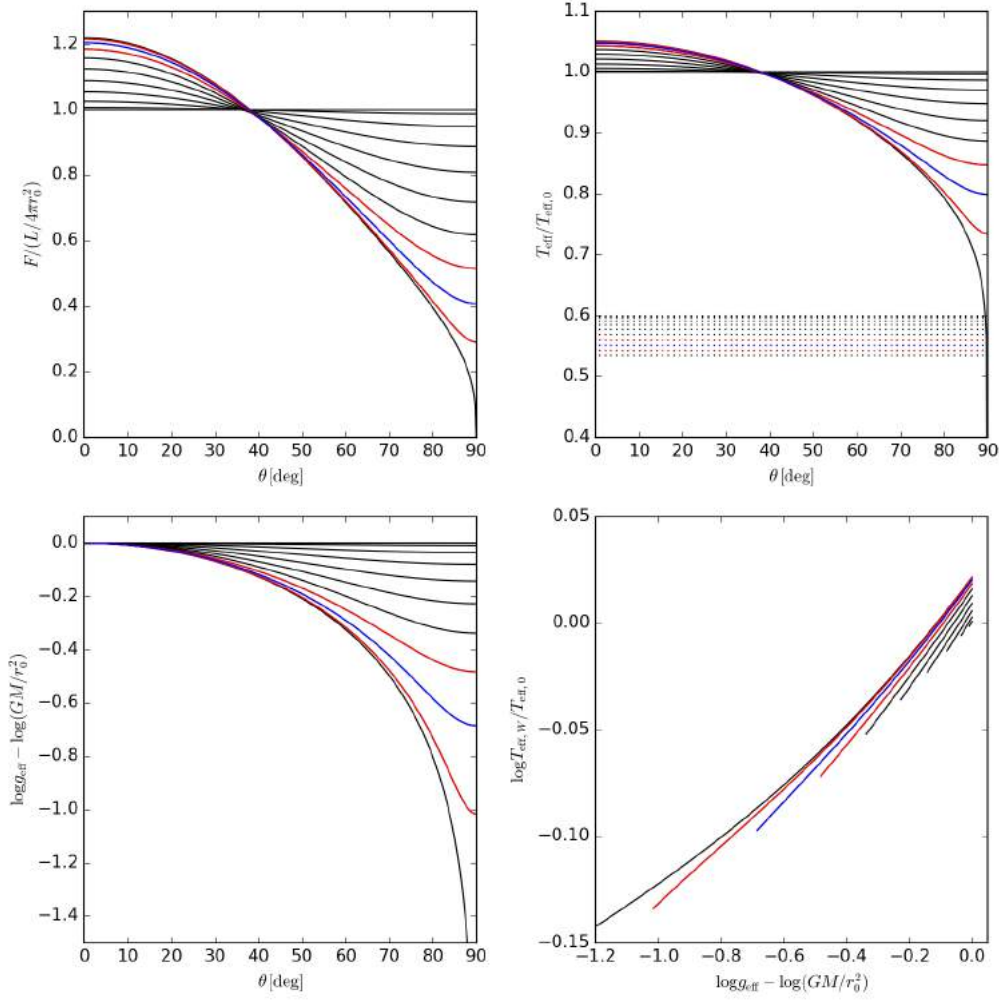


Figure 2.2: For the same stellar models of Fig. 2.1: *Upper-left*: Flux at the surface of the stars compared to the non-rotating case as a function of the polar angle θ . *Upper-right*: Effective temperature compared to the non-rotating case as a function of θ . In dotted straight lines, values of $0.6(L/S_W\sigma)^{\frac{1}{4}}$, where S_W is the surface area of the star with parameter W . *Lower-left*: $\log g_{\text{eff}}$ compared to the non-rotating case as a function of θ . *Lower-right*: $\log T_{\text{eff}}$ versus $\log g_{\text{eff}}$. The inclinations of these curves give the β coefficient.

where, the function $F_\omega(s, \theta)$ is given by

$$F_\omega(s, \theta) = \begin{cases} \frac{\tan^2 \vartheta(s, \theta)}{\tan^2 \theta} & , \quad \theta \neq 0, \frac{\pi}{2} \\ \exp\left(\frac{2^4}{3^4} \psi^3 \omega^2 s^3\right) & , \quad \theta = 0 \\ \left(1 - \frac{2^3}{3^3} \psi^3 \omega^2 s^3\right)^{-\frac{2}{3}} & , \quad \theta = \frac{\pi}{2} \end{cases} \quad (2.3.16)$$

where the function $\vartheta(s, \theta)$ is defined implicitly by the relation

$$\frac{2^3}{3^4} \psi^3 \omega^2 s^3 \cos^3 \theta + \cos \theta + \ln \tan \frac{\theta}{2} = \cos \vartheta + \ln \tan \frac{\vartheta}{2}. \quad (2.3.17)$$

In order to obtain the function $\vartheta(s, \theta)$ at any point s and θ , in this work, we applied

the following iterative method (as suggested in [Espinosa Lara, 2014](#)):

$$\vartheta_{N+1} = \vartheta_N - \frac{y_N}{\left(\frac{dy}{d\vartheta}\right)_N}, \text{ where } \vartheta_0 = \theta, \quad (2.3.18)$$

where

$$y_N = \cos \vartheta_N + \ln \tan \frac{\vartheta_N}{2} - \frac{2^3}{3^4} \psi^3 \omega^2 s^3 \cos^3 \theta - \cos \theta - \ln \tan \frac{\theta}{2}, \quad (2.3.19)$$

and

$$\left(\frac{dy}{d\vartheta}\right)_N = -\sin \vartheta_N + \frac{1}{\sin \vartheta_N}. \quad (2.3.20)$$

In Fig. 2.2, for the same stars of Fig. 2.1, we show the values of the flux (upper-left), temperature (upper-right), $\log g_{\text{eff}}$ (lower-left), relative to the non-rotating case, as a function of the polar angle θ . Clearly, rotation creates hotter polar regions and colder equatorial regions. Rotation also lowered the effective gravity at the surface of the star, specially near the equator. At the poles, however, the effective gravity remains the same as for the non-rotating case.

Also, in the lower-right panel, we show the curves of $\log T_{\text{eff}}$ versus $\log g_{\text{eff}}$. The curves are almost straight lines, meaning that, in [Espinosa-Lara & Rieutord's](#) prescription, we can still adopt the common approach $T_{\text{eff}} \propto g_{\text{eff}}^\beta$, where β is the slope of the curves shown in the lower-right panel.

The $T_{\text{eff}} \propto g_{\text{eff}}^\beta$ is already implemented in the radiative transfer code `HDUST`. Therefore, for a rotating star with parameter W , we adopted the coefficient $\beta(W)$ obtained by fitting a straight line to the $\log T_{\text{eff}}$ versus $\log g_{\text{eff}}$ curve.

Viscous decretion disks around Be stars

Every formula which expresses a law
of nature is a hymn of praise to God.

Maria Mitchell, *Life, Letters and
Journals* (1896)

The optical light curves of early-type Be stars (with spectral type ranging roughly from B0 to B4) are usually quite variable in timescales of days to years, with amplitudes of up to tenths of a magnitude (Rivinius et al., 2013). The majority of them show very irregular variability. Most show clear single bump-like features, characterized by a fast rise in brightness followed by a slower fading. Frequently, between the brightening and the fading phases some sort of plateau of nearly constant brightness is seen. Sometimes, a dip is seen, such that an initial rapid fading is followed by a slow recovery of the stellar brightness. Two examples of light curves showing these features are given in Fig. 3.1, taken from OGLE-II (Udalski et al., 1997) and OGLE-III (Udalski et al., 2008) data from two Be star candidates from the SMC, based on the selection made by Mennickent et al. (2002). Object SMC_SC1 75701 shows two brightening bumps, while object SMC_SC6 128831 shows a dip.

These bumps and dips resemble the photometric features shown in Haubois et al. (2012, e.g., their Fig. 14) of a circumstellar viscous disk that builds-up as a result of a constant rate of mass injection to the disk and, later, is left to dissipate after the cessation of the mass injection. Haubois et al. (2012) studied several disk feeding scenarios (constant vs. cyclic vs. outburst), calculated their photometric observables, and demonstrated that the bumps are disk formation/dissipation events of active Be stars seen at near pole-on inclination angles ($i \lesssim 70$ deg) while the dips are associated with near edge-on Be stars (shell stars, $i \gtrsim 70$ deg). The inclination angle plays an important role in how the stellar brightness is modified by the presence of a disk because, in the second case (edge-on), the disk is seen projected against the star and, thus, causes an attenuation of the stellar radiation. This attenuation does not happen for the pole-on case, where the net effect of the disk is to increase the optical brightness as a result of free-bound and free-free

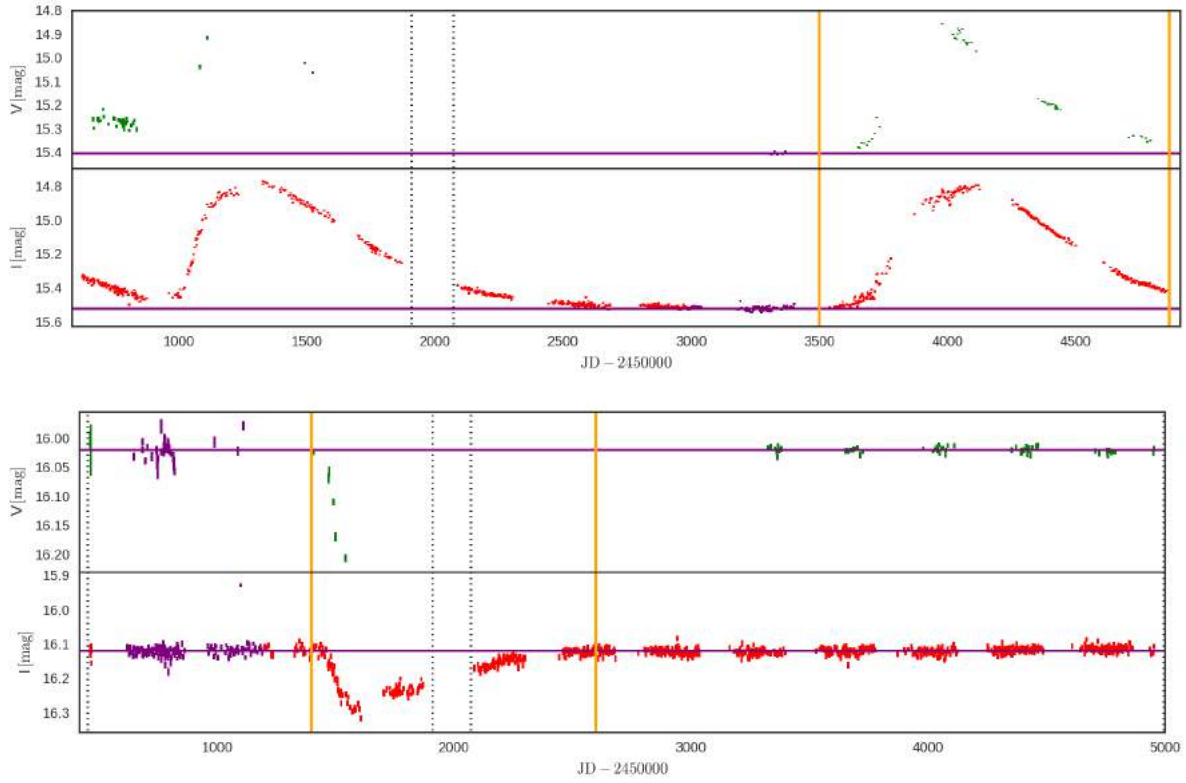


Figure 3.1: Two light curves, in photometric bands V (green) and I (red), selected from the OGLE-II and OGLE-III photometric surveys. *Above*: light curve of SMC_SC1 75701 (OGLE-II ID). *Below*: light curve of SMC_SC6 128831 (OGLE-II ID). The pair of vertical dotted straight lines near $\text{JD} - 2450000 = 2000$ separates OGLE-II from OGLE-III data. The measurements shown in purple are assumed to represent the inactive (diskless) brightness level of the Be star. Their mean is given by the horizontal purple straight lines. The pairs of vertical orange straight lines bracket our visually selected bumps.

radiation from the gas (Gehrz et al., 1974; Vieira et al., 2015)

In this chapter, we describe the basic hydrodynamical concepts of gaseous viscous Keplerian disks, with a focus on how to model the aforementioned events of disk construction and dissipation in the light curves of active Be stars.

3.1 Main considerations

The evolution of the surface density of the thin circumstellar axisymmetric disks of Be stars is described by Eq. (2.2.17), which we rewrite here:

$$\frac{\partial \Sigma}{\partial t} + \frac{1}{R} \frac{\partial}{\partial R} (R \Sigma \langle v_R \rangle) = \Sigma \left\langle \frac{\mathcal{S}}{\rho} \right\rangle - 2(\rho v_z)|_{\infty}, \quad (3.1.1)$$

where, in the circumstellar alpha-disk approach, the mass flux, $2\pi R \Sigma \langle v_R \rangle$ is given by Eq. (2.2.28).

We assume here that $2RW_{z\phi}|_{\infty}$ vanishes, because the external medium beyond the disk is empty space. We also, assume that possible azimuthal forces (e.g., the azimuthal component of a radiative line-driven force) are negligible, meaning that $\langle \mathcal{F}_{\phi}^*/\rho \rangle \approx 0$. Therefore, according to Eq. (2.2.28), the mass flux is given by

$$2\pi R\Sigma \langle v_R \rangle = -4\pi \left(\frac{R^3}{GM} \right)^{\frac{1}{2}} \frac{1}{R} \frac{\partial}{\partial R} (R^2 \Sigma \langle \alpha c_s^2 \rangle), \quad (3.1.2)$$

where $c_s^2 = kT_{\text{disk}}/\mu m_H$.

Substitution of Eqs. (3.1.2) into (3.1.1) leads to the following partial differential equation for the evolution of the surface density of the thin VDD

$$\frac{\partial \Sigma}{\partial t} = \frac{2}{R} \frac{\partial}{\partial R} \left(\left(\frac{R}{GM} \right)^{\frac{1}{2}} \frac{\partial}{\partial R} (R^2 \alpha c_s^2 \Sigma) \right) + \Sigma \left\langle \frac{\mathcal{S}}{\rho} \right\rangle - 2(\rho v_z)|_{\infty}, \quad (3.1.3)$$

where we have also considered $\langle \alpha c_s^2 \rangle \approx \alpha c_s^2$, for simplicity.

3.1.1 The star-disk connection

The source terms $\Sigma \langle \mathcal{S}/\rho \rangle$ and $-2(\rho v_z)|_{\infty}$ represent the rate of mass injected into (or removed from) the disk per unit of area. In this work, we further assume that the vertical losses of mass from the disk (see, e.g., the disk wind of Krtićka et al., 2011) are negligible ($(\rho v_z)|_{\infty} \approx 0$). The term $\Sigma \langle \mathcal{S}/\rho \rangle$, on the other hand, represents the variable mass exchange between the star and the disk and the disk and the outer medium through an outer boundary.

In this work, we assume that mass is injected from the star into a ring with radius R_{inj} and negligible thickness. Therefore, the rate of mass injection per unit of area is given by $\dot{M}_{\text{inj}}(t)/2\pi R_{\text{inj}}\delta R$, where $\delta R \rightarrow 0^+$. In addition, mass can flow away from the disk through its boundaries. Mass can fall back into the star through the inner boundary at R_{eq} , or it can leave the system at an outer boundary, R_{out} .

Therefore, the source function is given by

$$\Sigma \left\langle \frac{\mathcal{S}}{\rho} \right\rangle = \dot{M}_{\text{inj}}(t) \frac{\delta(R - R_{\text{inj}})}{2\pi R} + \text{boundaries}, \quad (3.1.4)$$

where $\dot{M}_{\text{inj}}(t)$ is the mass injection rate from the star into the disk at R_{inj} .

We assume that all mass that eventually reaches the stellar equator R_{eq} is totally absorbed by the star. Therefore, the inner boundary consists in setting $\Sigma(R_{\text{eq}}, t) = 0$. The outer boundary, on the other hand, can be interpreted as the limiting radius of the disk due to a binary companion (e.g., Okazaki et al., 2002) or due to the photoevaporation of the disk (e.g., Okazaki, 2001). Therefore, we also assume that all mass that eventually reaches the outer boundary at the radius R_{out} is totally absorbed. Therefore, at the outer boundary, as at the inner boundary, we set $\Sigma(R_{\text{out}}, t) = 0$.

The source terms contain explicit reference to the boundaries because the boundaries are just like additional rings, where mass is removed from the disk, limiting the existence of the disk to the region $R_{\text{eq}} \leq R \leq R_{\text{out}}$. Therefore, Eq. (3.1.4) with our assumptions of boundaries are completely defined by the following equation

$$\Sigma \left\langle \frac{\mathcal{S}}{\rho} \right\rangle = \dot{M}_{\text{eq}}(t) \frac{\delta(R - R_{\text{eq}})}{2\pi R} + \dot{M}_{\text{inj}}(t) \frac{\delta(R - R_{\text{inj}})}{2\pi R} + \dot{M}_{\text{out}}(t) \frac{\delta(R - R_{\text{out}})}{2\pi R}. \quad (3.1.5)$$

In the above equation, $\dot{M}_{\text{eq}}(t)$ is the rate of mass removal (since $\dot{M}_{\text{eq}}(t) \leq 0$ always) at the stellar equator. It is given by

$$\dot{M}_{\text{eq}}(t) = -4\pi \left(\frac{R_{\text{eq}}}{GM} \right)^{\frac{1}{2}} \frac{\partial}{\partial R} (\alpha c_s^2 R^2 \Sigma) \Big|_{R_{\text{eq}}^+}. \quad (3.1.6)$$

Similarly, $\dot{M}_{\text{out}}(t)$ is the rate of mass removal (since $\dot{M}_{\text{out}}(t) \leq 0$ always) at the outer radius R_{out} . It is given by

$$\dot{M}_{\text{out}}(t) = 4\pi \left(\frac{R_{\text{out}}}{GM} \right)^{\frac{1}{2}} \frac{\partial}{\partial R} (\alpha c_s^2 R^2 \Sigma) \Big|_{R_{\text{out}}^-}. \quad (3.1.7)$$

In Eq. (3.1.5), the first two terms represent the star-disk connection. The third term represents the relationship between the disk and the outer space.

The dynamical problem described by Eq. (3.1.3) was solved, in this work, using the numerical code **SINGLEBE** (Okazaki, 2007), which I studied in the beginning of this thesis and slightly modified. We address the main features of this code in Sect. 3.1.2 below. Later, we return to the modeling of dynamical disks, responsible for the observed bumps and dips (and other often more complex shapes) seen in the light curves of Be stars.

3.1.2 The alpha-disk code SINGLEBE

Eq. (3.1.3) can be multiplied by R^2 and written in the following way

$$\frac{\partial R^2 \Sigma}{\partial t} = 2 \frac{\partial}{\partial \ln R} \left(\left(\frac{1}{GMR} \right)^{\frac{1}{2}} \frac{\partial}{\partial \ln R} (\alpha c_s^2 R^2 \Sigma) \right) + \text{sources}(R). \quad (3.1.8)$$

Eq. (3.1.8) is the partial differential equation solved by **SINGLEBE** (Okazaki, 2007). **SINGLEBE** is a very simple code, if compared to other available general 3D hydrodynamical solvers. It was, nevertheless, very carefully written for the purpose of simulating the time-dependent evolution of an axisymmetric alpha-disk. It solves Eq. (3.1.8) by the FTCS (Forward-Time Central-Space) scheme. Eq. (3.1.8) is a parabolic partial differential equation, and the FTCS is known to be stable for that class of equations (Pletcher et al., 1997). The integration, therefore, is given by the following finite difference method

$$f_i^{n+1} \approx f_i^n + \left(\frac{\partial f}{\partial t} \right)_i^n dt, \quad (3.1.9)$$

where $f = R^2\Sigma$ and $(\partial f/\partial t)_i^n$ represents the second member of Eq. (3.1.8). The derivatives contained in that member (e.g., of some function $g(R)$) are evaluated as follows:

$$\left(\frac{\partial g}{\partial \ln R}\right)_i^n \approx \frac{g_{i+\frac{1}{2}}^n - g_{i-\frac{1}{2}}^n}{\ln R_{i+\frac{1}{2}} - \ln R_{i-\frac{1}{2}}}, \quad (3.1.10)$$

where $\ln R_{i+\frac{1}{2}} = (\ln R_i + \ln R_{i+1})/2$, $g_{i-\frac{1}{2}} = (g_{i-1} + g_i)/2$, and so on...

The time increment dt is defined only once at the beginning of each run, following the classic Courant-Friedrichs-Lewy (CFL) numerical stability condition: $dt = C \min\left(\left|\frac{dR}{v_R}\right|\right)$ (with the choice $C = 0.3$), calculated assuming a shock configuration. This time interval is usually several times smaller than the usual time intervals (chosen by the user) between consecutive prints of the calculations to an external file.

Following Eq. (3.1.8), SINGLEBE's radial grid was defined as a logarithmic one. At the beginning of my work, I changed it to a more general logarithm grid defined by

$$\ln \tilde{R}[i] = \ln \tilde{R}_1 + (i - i_1) \frac{\ln \tilde{R}_2 - \ln \tilde{R}_1}{i_{21}}, \quad \text{for } i = 1, 2, 3, 4, \dots, N, \quad (3.1.11)$$

where $\tilde{R} = R/R_{\text{eq}}$ and $N = i_1 + i_{21} + n_2$, and the three natural numbers $i_1 > 0$, $i_{21} > 0$ and $n_2 \geq 0$ are chosen by the user.

So, in this grid, we freely choose two radii (two real numbers) \tilde{R}_1 and \tilde{R}_2 and their indices in the grid, respectively given by i_1 and $i_1 + i_{21}$. Therefore, we in summary define that $\tilde{R}_1 = \tilde{R}[i_1]$ and $\tilde{R}_2 = \tilde{R}[i_1 + i_{21}]$. (Notice, therefore, that if $i_1 > 1$, then there are $i_1 - 1$ radii before R_1 .) Finally, we may extend the grid to n_2 radii after R_2 . Therefore, the total number of radii in the grid is given by $N = i_1 + i_{21} + n_2$. In any case, the problem has an inner boundary condition that is always in the first radius ($\tilde{R}[1]$) and an outer boundary condition that is always in the last radius ($\tilde{R}[N]$).

When the code is run, since the definition of the grid is done before the time increment dt is calculated by the CFL condition, our redefinition of the grid does not alter the stability of the calculation. (It affects the size of the timestep dt and, thus, the amount of time taken to perform the calculation.)

It is important to note here that, in the work of [Carciofi et al. \(2012\)](#), where the parameter α was first determined for a dissipating portion of the light curve of the Be star 28 CMa, we found that the grid was set with the following definition (using the notation of my new grid): " $\tilde{R}_1[10] = 1$ and $\tilde{R}_2[400] = 1000$, with the radius where mass was being injected set to $\tilde{R}_{\text{inj}} = \tilde{R}_1$ ". Therefore, the mass was being put into orbit exactly at the stellar equator, but there were 9 radial cells before it: the inner boundary was inside the star, at $\tilde{R}[1] = 0.8526$. This is clearly a physical inconsistency. The absorption of the disk matter should happen at the surface of the star. The code was in effect treating the star to be smaller, with 85.26% of its size. The bigger distance between the inner boundary and the injection radius was one of the causes that made it necessary to use a

bigger value of α to fit the dissipation of 28 CMa's light curve. (The other major cause was the fact that the authors didn't take into account the previous history of the disk, as we shall see later in Sect. 3.3)

In Ghoreyshi et al. (2016) and in this work, we defined the grid by “ $\tilde{R}_1[1] = 1$ and $\tilde{R}_2[400] = 1000$, with the injection radius set to $\tilde{R}_{\text{inj}} = \tilde{R}[2]$ (with these definitions, Eq. 3.1.11 dictates that $\tilde{R}[2] = 1.017$)”. Therefore, the inner boundary condition is at the stellar equator, as we think it should be, and mass is injected into the disk just a little distance above the equator.

3.1.3 The timescale parameter τ and the time parameter $\tilde{\tau}$

In this work, we assume that the disk is isothermal with $T_{\text{disk}} = 0.6T_{\text{eff}}$, following Carciofi and Bjorkman (2006), and that the α parameter is constant with R , but we allow it to possibly be time-dependent, as there is evidence for changing α in the disks of Be stars (see Sect. 3.3 below). Eqs. (3.1.3) and (3.1.5) can, then, be scaled in the following way

$$\frac{\partial \Sigma}{\partial t} = \frac{1}{\tau} \left\{ \frac{2}{\tilde{R}} \frac{\partial}{\partial \tilde{R}} \left[\tilde{R}^{\frac{1}{2}} \frac{\partial}{\partial \tilde{R}} \left(\tilde{R}^2 \Sigma \right) \right] + \tau \Sigma \left\langle \frac{\mathcal{S}}{\rho} \right\rangle \right\}, \quad (3.1.12)$$

where we introduce the *timescale parameter*, $\tau(t)$, given by

$$\tau(t) = \frac{1}{\alpha(t)} \left(\frac{R_{\text{eq}}^3}{GM} \right)^{\frac{1}{2}} \frac{v_{\text{orb}}^2}{c_s^2}. \quad (3.1.13)$$

The timescale parameter is proportional to the viscous timescale at the stellar equator. The viscous timescale is given by $t_{\text{vis}} = R^2/\nu$, where the viscosity ν is given by $\nu = (2/3)\alpha c_s^2 R/v_K$. Since we are in the thin disk limit ($c_s^2/v_K^2 \ll 1$), we see that τ is much larger than the orbital period at the stellar equator, given by $2\pi(R_{\text{eq}}^3/GM)^{\frac{1}{2}}$.

The solution of Eq. 3.1.12 is scaled in time by the timescale parameter, which controls how fast matter is redistributed throughout the disk and, consequently, its observational counterparts. It follows that by fitting observed light curves of Be stars, this parameter can be estimated, and once other parameters are known (R_{eq} , M , T_{disk}), the α value can be determined (e.g., Carciofi et al., 2012). This scaling relation is fundamental to this PhD thesis.

In order to generate models that do not depend on the time-dependent form of $\alpha(t)$ and also on the parameters R_{eq} , M and T_{disk} , which are related to the central star, we will define a dimensionless *time parameter*, $\tilde{\tau}(t)$, such that

$$d\tilde{\tau} = \frac{dt}{\tau(t)}, \quad (3.1.14)$$

which allows us to solve Eq. (3.1.12) in terms of $\tilde{\tau}$ instead of the physical time t . The advantage of using this new parameter is that it removes the problem of the time dependency of $\alpha(t)$ and separates it from the problem of solving Eq. (3.1.12). Consequently, it

allows us to create a grid of solutions of Eq. (3.1.12) that is independent of $\alpha(t)$, R_{eq} , M and T_{disk} (see Chapter 4).

The source term, now multiplied by τ , in Eq. (3.1.12), is given by

$$\tau\Sigma \left\langle \frac{\mathcal{S}}{\rho} \right\rangle = \left(\frac{\tau\dot{M}_{\text{inj}}}{2\pi R_{\text{eq}}^2} \right) \frac{\delta(\tilde{R} - \tilde{R}_{\text{inj}})}{\tilde{R}} + \text{boundaries}, \quad (3.1.15)$$

where the term in parenthesis is a measure of the mass injection rate in terms of the time parameter, instead of the physical time. This term has the dimension of a surface density.

Before moving on to the modeling of bump-like events like the ones in Fig. 3.1, we introduce in the next section some important parameters of the dynamical disks implied in the equations shown above.

3.2 Dynamical disk parameters

The steady-state solution of the viscous disk corresponds to the limiting case of a disk that has been fed at a constant rate for an infinitely long time. It is obtained by setting $\partial\Sigma/\partial t = 0$ (in Eq. 3.1.12 or 3.1.1) and assuming that α and \dot{M}_{inj} are time-independent.

Probably the best way to describe the fundamental parameters of a dynamical disk is by comparing their dynamical properties with their corresponding steady-state properties. We will, consequently, dedicate some effort in this section to the study of the steady-state solution of the dynamical problem of the viscous disk.

3.2.1 The steady-state solution of the VDD

Eq. (3.1.5) shows that the radius of mass injection divides the disk in two regions: a narrow region between the inner boundary and the radius of mass injection ($1 \leq \tilde{R} \leq \tilde{R}_{\text{inj}}$), and the much wider region between the radius of mass injection and the outer boundary ($\tilde{R}_{\text{inj}} \leq \tilde{R} \leq \tilde{R}_{\text{out}}$), where we have defined $\tilde{R}_{\text{inj}} = R_{\text{inj}}/R_{\text{eq}}$ and $\tilde{R}_{\text{out}} = R_{\text{out}}/R_{\text{eq}}$.

By setting $\partial\Sigma/\partial t = 0$ in Eq. (3.1.1), it follows that the steady-state disk is given by the solution of the following equation

$$\frac{\partial}{\partial R} (2\pi R\Sigma \langle v_R \rangle) = \dot{M}_{\text{inj}} \delta(R - R_{\text{inj}}), \quad 1 < \tilde{R} < \tilde{R}_{\text{out}}, \quad (3.2.1)$$

where we have used the mass source defined by Eq. (3.1.5).

The above equation says that, in steady-state, the mass flux is a constant in the region $1 < \tilde{R} < \tilde{R}_{\text{inj}}$ and another constant in the region $\tilde{R}_{\text{inj}} < \tilde{R} < \tilde{R}_{\text{out}}$. Integrating from just before R_{inj} (from R_{inj}^-) to just after R_{inj} (to R_{inj}^+) results in the following discontinuity condition

$$(2\pi R\Sigma \langle v_R \rangle) |_{R_{\text{inj}}^+} - (2\pi R\Sigma \langle v_R \rangle) |_{R_{\text{inj}}^-} = \dot{M}_{\text{inj}}, \quad (3.2.2)$$

which just means that the mass being injected at R_{inj} is flowing in both directions: inwards and outwards.

Consequently, the steady-state mass flux in the narrow region $1 < \tilde{R} < \tilde{R}_{\text{inj}}$ is given by the following constant

$$2\pi R\Sigma \langle v_R \rangle = -\dot{M}_{\text{inj}}\Xi, \quad 1 < \tilde{R} < \tilde{R}_{\text{inj}}, \quad (3.2.3)$$

where Ξ is some number between 0 and 1, representing the fraction of the injected mass that is flowing back to the star. Then, in order to satisfy the discontinuity condition given by Eq. (3.2.2), the steady-state mass flux in the wider region $\tilde{R}_{\text{inj}} < \tilde{R} < \tilde{R}_{\text{out}}$ is given by

$$2\pi R\Sigma \langle v_R \rangle = \dot{M}_{\text{inj}}(1 - \Xi), \quad \tilde{R}_{\text{inj}} < \tilde{R} < \tilde{R}_{\text{out}}. \quad (3.2.4)$$

Let us first look into the mass flux in the outer region $\tilde{R}_{\text{inj}} < \tilde{R} < \tilde{R}_{\text{out}}$. Since, in steady-state, the mass flux is constant in the whole region, it results in the following equation

$$-4\pi \left(\frac{R^3}{GM} \right)^{\frac{1}{2}} \frac{1}{R} \frac{\partial}{\partial R} (\alpha c_s^2 R^2 \Sigma) = \dot{M}_{\text{inj}}(1 - \Xi), \quad \tilde{R}_{\text{inj}} < \tilde{R} < \tilde{R}_{\text{out}}, \quad (3.2.5)$$

which, by isolating the term with the derivative on the left and, then, integrating from R_{inj} to R , results in the following steady-state profile for Σ

$$\alpha c_s^2 R^2 \Sigma - \alpha c_s^2 R_{\text{inj}}^2 \Sigma_{\text{inj}} = -\frac{(GM)^{\frac{1}{2}}}{2\pi} \dot{M}_{\text{inj}}(1 - \Xi) \left(R^{\frac{1}{2}} - R_{\text{inj}}^{\frac{1}{2}} \right), \quad \tilde{R}_{\text{inj}} < \tilde{R} < \tilde{R}_{\text{out}}. \quad (3.2.6)$$

Now, the outer boundary condition comes into play. Setting $\Sigma(R_{\text{out}}, t) = 0$ gives

$$\alpha c_s^2 R_{\text{inj}}^2 \Sigma_{\text{inj}} = \frac{(GM)^{\frac{1}{2}}}{2\pi} \dot{M}_{\text{inj}}(1 - \Xi) \left(R_{\text{out}}^{\frac{1}{2}} - R_{\text{inj}}^{\frac{1}{2}} \right), \quad (3.2.7)$$

which, substituting in Eq. (3.2.6) results in the following formula for the steady-state surface density in the region $\tilde{R}_{\text{inj}} < \tilde{R} < \tilde{R}_{\text{out}}$:

$$\Sigma = \frac{(GM)^{\frac{1}{2}} \dot{M}_{\text{inj}}(1 - \Xi)}{2\pi \alpha c_s^2} \frac{1}{R^2} \left(R_{\text{out}}^{\frac{1}{2}} - R^{\frac{1}{2}} \right), \quad \tilde{R}_{\text{inj}} < \tilde{R} < \tilde{R}_{\text{out}}. \quad (3.2.8)$$

We recognize the above equation as the equation number 24 of [Carciofi and Bjorkman \(2008\)](#). Notice, however, that their α parameter corresponds to 2/3 times our α (see the discussion on the variation in the definitions of α in Sect. 2.2.3). That is the reason the number 3π appears in their equation while the number 2π appears in our Eq. (3.2.8). Also notice that their \dot{M} corresponds to our $\dot{M}_{\text{inj}}(1 - \Xi)$. This latter quantity is the steady-state decretion rate.

In order to find the value of Ξ , we must complement our analysis with the study of the steady-state in the narrow region $1 \leq \tilde{R} \leq \tilde{R}_{\text{inj}}$. Eq. (3.2.3) implies in the following equation

$$-4\pi \left(\frac{R^3}{GM} \right)^{\frac{1}{2}} \frac{1}{R} \frac{\partial}{\partial R} (\alpha c_s^2 R^2 \Sigma) = -\dot{M}_{\text{inj}}\Xi, \quad 1 \leq \tilde{R} \leq \tilde{R}_{\text{inj}}, \quad (3.2.9)$$

which, by isolating the term with the derivative on the left and, then, integrating from R to R_{inj} , results in the following steady-state profile for Σ

$$\alpha c_s^2 R^2 \Sigma - \alpha c_s^2 R_{\text{inj}}^2 \Sigma_{\text{inj}} = -\frac{(GM)^{\frac{1}{2}}}{2\pi} \dot{M}_{\text{inj}} \Xi \left(R_{\text{inj}}^{\frac{1}{2}} - R^{\frac{1}{2}} \right), \quad 1 \leq \tilde{R} \leq \tilde{R}_{\text{inj}}. \quad (3.2.10)$$

We are using the inner boundary condition that $\Sigma(R_{\text{eq}}, t) = 0$. Therefore, from Eq. (3.2.10), it follows that we must have

$$\alpha c_s^2 R_{\text{inj}}^2 \Sigma_{\text{inj}} = \frac{(GM)^{\frac{1}{2}}}{2\pi} \dot{M}_{\text{inj}} \Xi \left(R_{\text{inj}}^{\frac{1}{2}} - R_{\text{eq}}^{\frac{1}{2}} \right). \quad (3.2.11)$$

From Eqs. (3.2.7) and (3.2.11), we can now obtain the value of Ξ . It is given by

$$\Xi = \frac{R_{\text{out}}^{\frac{1}{2}} - R_{\text{inj}}^{\frac{1}{2}}}{R_{\text{out}}^{\frac{1}{2}} - R_{\text{eq}}^{\frac{1}{2}}}, \quad (3.2.12)$$

from which we see that, since R_{inj} must be very close to R_{eq} and R_{out} must be much further away, it follows that Ξ is usually a number just a little smaller than 1 for every Be star. Therefore, in steady-state, most of the injected mass comes back to the star and is absorbed.

Substitution of Eq. (3.2.11) into Eq. (3.2.10) and of Eq. (3.2.7) into Eq. (3.2.6) finally results in the steady-state surface density of the disk:

$$\Sigma_{\text{steady}}(\tilde{R}) = \begin{cases} \frac{\Sigma_0}{\tilde{R}^2} \Xi \left(\frac{\tilde{R}^{\frac{1}{2}} - 1}{\tilde{R}_{\text{inj}}^{\frac{1}{2}} - 1} \right), & 1 \leq \tilde{R} < \tilde{R}_{\text{inj}} \\ \frac{\Sigma_0}{\tilde{R}^2} \left(\frac{\tilde{R}_{\text{out}}^{\frac{1}{2}} - \tilde{R}^{\frac{1}{2}}}{\tilde{R}_{\text{out}}^{\frac{1}{2}} - 1} \right), & \tilde{R}_{\text{inj}} \leq \tilde{R} \leq \tilde{R}_{\text{out}} \end{cases}, \quad (3.2.13)$$

where we have defined the physical quantity Σ_0 by the following equation

$$\Sigma_0 = \frac{1}{\Xi} \tilde{R}_{\text{inj}}^2 \Sigma_{\text{inj}}. \quad (3.2.14)$$

The physical quantity Σ_0 represents the surface density at $\tilde{R} = 1$, obtained by extrapolating Σ_{steady} in the domain $\tilde{R}_{\text{inj}} \leq \tilde{R} \leq \tilde{R}_{\text{out}}$ to $\tilde{R} = 1$. We will refer to this physical quantity as the *asymptotic surface density*. It is the asymptotic value reached after an infinitely long disk build-up under a constant \dot{M}_{inj} .

3.2.2 Rates of mass and angular momentum loss

Substitution of Eq. (3.2.14) into Eq. (3.2.11) shows that Σ_0 is related to \dot{M}_{inj} by the following equation

$$2\pi R_{\text{eq}} \Sigma_0 \left(\frac{R_{\text{eq}}}{\tau} \right) = \dot{M}_{\text{inj}} \left(\tilde{R}_{\text{inj}}^{\frac{1}{2}} - 1 \right) \equiv \left(-\frac{\partial M}{\partial t} \right)_{\text{typ}}. \quad (3.2.15)$$

We may extend Eq. (3.2.15) to the general case of a time-dependent $\dot{M}_{\text{inj}}(\tilde{\tau})$, which would define, by the same equation, a time dependent asymptotic surface density, $\Sigma_0(\tilde{\tau})$.

Applying Eq. (3.2.15) to Eq. (3.1.15), it follows that

$$\tau \Sigma \left\langle \frac{\mathcal{S}}{\rho} \right\rangle = \frac{\Sigma_0(\tilde{\tau})}{\tilde{R}_{\text{inj}}^{\frac{1}{2}} - 1} \frac{\delta(\tilde{R} - \tilde{R}_{\text{inj}})}{\tilde{R}} + \text{boundaries}. \quad (3.2.16)$$

The function $\Sigma_0(\tilde{\tau})$, therefore, is just another way of specifying the history of mass injection from the star into the disk. It has, however, the advantage of being a surface density, which is a quantity that may be determined from, e.g. SED analyses, in contrast to the mass injection rate and the radius of mass injection, which are parameters that cannot be directly determined.

The steady-state solution (Eq. 3.2.13) shows that, in the outer domain $\tilde{R}_{\text{inj}} \leq \tilde{R} \leq \tilde{R}_{\text{out}}$, the density profile of the disk is not altered if \tilde{R}_{inj} is changed, provided that \dot{M}_{inj} is also changed in order to maintain Σ_0 fixed, according to Eq. (3.2.15). In fact, we verified that the time-dependent solutions of Eq. (3.1.12) in the domain $\tilde{R}_{\text{inj}} \leq \tilde{R} \leq \tilde{R}_{\text{out}}$ are negligibly affected by the particular choice of \tilde{R}_{inj} and $\dot{M}_{\text{inj}}(\tilde{\tau})$, as long as the quantity $\Sigma_0(\tilde{\tau})$ is kept fixed, as Fig. 3.2 shows.

In Fig. 3.2, we show the evolution of three disk models that started from the diskless state, received a constant mass injection rate $\Sigma_0 = 1.549 \text{ g cm}^{-2}$ for a period $\tilde{\tau}_{\text{bu}} = 30$, and, after that, were left to dissipate (with $\Sigma_0 = 0$). The three disk models had different values of \tilde{R}_{inj} (and of \dot{M}_{inj} , consequently, so that Σ_0 is fixed). The upper-left panel shows the surface density profile at 5 times during the build-up phase and the upper-right panel shows the surface density profiles at 5 times during the dissipation phase. The dotted, dashed and solid curves show the models with \tilde{R}_{inj} given by 1.017, 1.169 and 1.319, respectively. It is easy to see the positions of the injection radii in the curves by the positions of the discontinuities in their derivatives, as a consequence of the delta function in Eq. 3.1.5. The upper-left and upper-right panels illustrate the fact that the evolution of the disks with the same $\Sigma_0(\tilde{\tau})$, but different \tilde{R}_{inj} and \dot{M}_{inj} are nearly indistinguishable in their domain $\tilde{R}_{\text{inj}} \leq \tilde{R} \leq \tilde{R}_{\text{out}}$. This is, we believe, in part a consequence of the fact that the dynamical solutions reach a near steady-state very quickly in the vicinity of the injection radius (Haubois et al., 2012). See, however, further discussions in Sect. 3.2.3.

Provided that mass is injected not too far from the stellar photosphere (i.e., assuming $\tilde{R}_{\text{inj}} \approx 1$), the domain $1 \leq \tilde{R} \leq \tilde{R}_{\text{inj}}$ is much narrower than the region where the continuum visual flux of Be stars is generated (see Carciofi, 2011, and Fig. 1.11), which means that the emission from this region can be ignored. Consequently, we conclude that $\Sigma_0(\tilde{\tau})$ (with the assumption that $\tilde{R}_{\text{inj}} \approx 1$) is a much better parameter for describing the mass injection history of the disk than the pair of parameters $\dot{M}_{\text{inj}}(\tilde{\tau})$ and \tilde{R}_{inj} . We will, therefore, for the remainder of this work, use the asymptotic surface density function $\Sigma_0(\tilde{\tau})$ as a measure of the mass and angular momentum injection into our disk models.

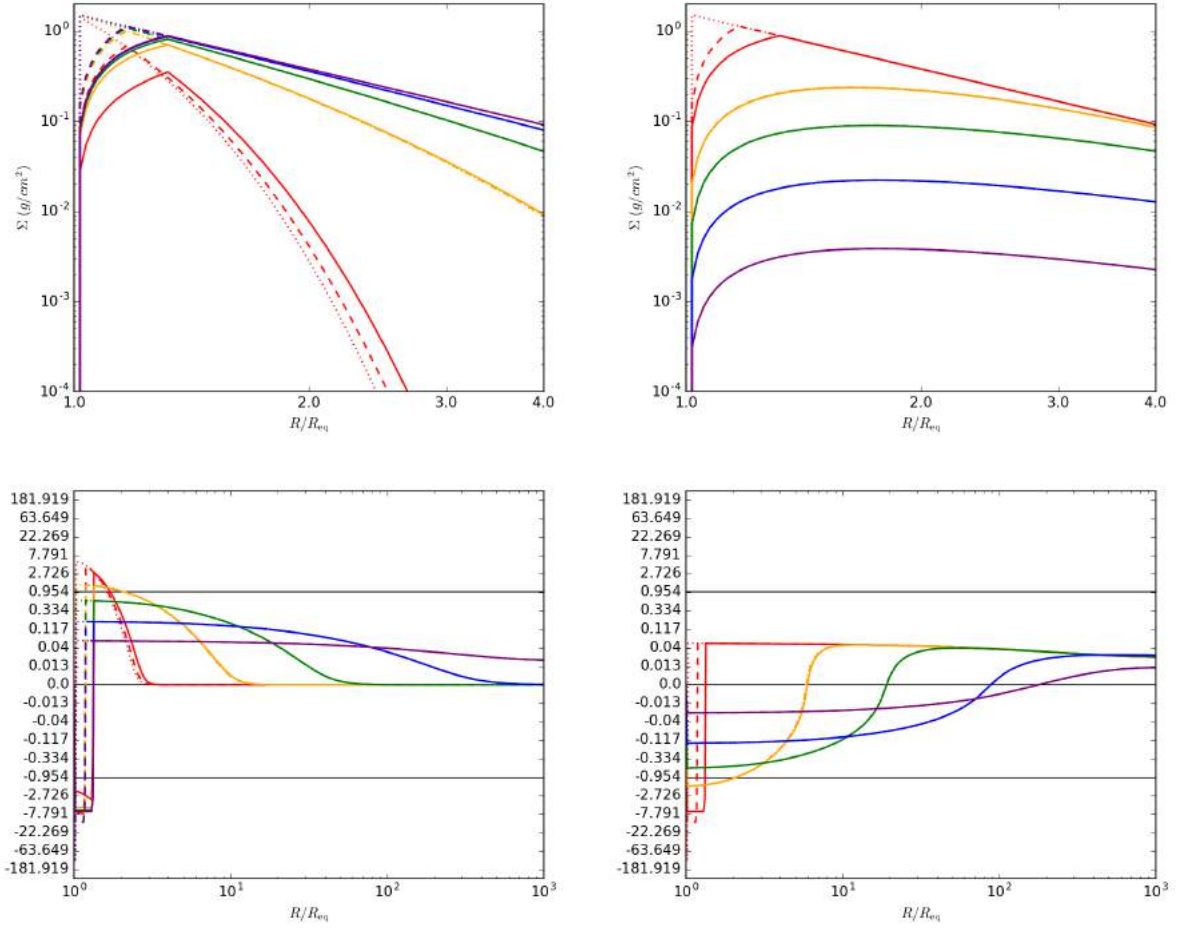


Figure 3.2: Simulation of a constant build up phase ($\Sigma_0 = 1.549 \text{ g cm}^{-2}$), during $\tilde{\tau}_{\text{bu}} = 30$, followed by a complete dissipation ($\Sigma_0 = 0$). Three injection radii were used: $\tilde{R}_{\text{inj}} = 1.017$ (dotted), 1.169 (dashed), 1.319 (solid). The different colors corresponds to different times after the beginning (*left*) or the end of injection (*right*): $\tilde{\tau} \sim 0$ (red), $\tilde{\tau} = 0.2$ (orange), $\tilde{\tau} = 1$ (green), $\tilde{\tau} = 6$ (blue), $\tilde{\tau} = 25$ (purple). *Top*: Surface density in the first 4 stellar radii, where most of the visual continuum observables are generated. *Bottom*: Mass flux, as a function of the typical decretion rate (Eq. 3.2.15), in the whole simulated disk.

The time-dependent solutions of Eq. (3.1.12) generally show that, for Be stars dynamically feeding the disk, but still far from steady-state, the mass flux close to \tilde{R}_{inj} has absolute values of the order of $(-\partial M/\partial t)_{\text{typ}}$, defined by Eq. (3.2.15). Therefore, we refer to this quantity as the *typical decretion rate*, which depends on parameters that are relatively easy to estimate from SEDs of Be stars. As an illustration of how the values of the mass flux in the disk compares with the typical decretion rate, we show, in the two lower panels of Fig. 3.2, the mass fluxes, divided by the typical decretion rate, of the simulated dynamical models.¹ Two horizontal straight lines mark the position of the

¹ The vertical axis of the plates are in arcsinh scale, to better show the smaller values, positive or

positive and negative typical decretion rates. The lower-left and lower-right panels show the mass fluxes at the 5 selected times during the build-up phase and the dissipation phase, respectively.

From the lower-left panel, we see that, in the build-up phase, the mass flux outwards begins quite high, in the vicinity of the radius of mass injection. This flux diffuses outwards, progressively diminishing its value near the mass injection radius. We see, however, that, at least during the interval $\Delta\tilde{\tau} = 1$ (comprised by the red, orange and green curves), the mass flux near the radius of mass injection is very close to the typical decretion rate. As time passes, the mass flux approaches its steady state value, given by the constant value of $\dot{M}_{\text{inj}}(1 - \Xi)$ through the whole domain $\tilde{R}_{\text{inj}} \leq \tilde{R} \leq \tilde{R}_{\text{out}}$. The purple curve (for $\tilde{\tau} = 25$), in particular, shows that at this time, there is a significant mass loss through the outer boundary, which in our models was set to $\tilde{R}_{\text{out}} = 1000$.

The lower-right panel shows that, in the dissipation phase, which started at $\tilde{\tau}_{\text{bu}} = 30$, the inner disk rapidly becomes an accretion disk. Again, at least during the first interval $\Delta\tilde{\tau} = 1$ (comprised by the red, orange and green curves), the mass flux near the radius of mass injection is very close to the negative typical decretion rate. The radius where the mass flux is zero is the ‘‘stagnation point’’ (Haubois et al., 2012). At $\tilde{\tau} = 31$, the stagnation point is already beyond $\tilde{R} = 10$. At $\tilde{\tau} = 55$, it is already beyond $\tilde{R} = 100$. Further away, however, the disk is still a decretion disk (that is: a disk with a positive mass flux). As $\tilde{\tau} \rightarrow \infty$, the mass flux tends to zero in the whole disk.

In the simulations done in this work, since the values of \dot{M}_{inj} and \tilde{R}_{inj} are of no interest and the value of \tilde{R}_{out} is quite uncertain, we arbitrarily chose $\tilde{R}_{\text{inj}} = 1.017$ and $\tilde{R}_{\text{out}} = 1000$. Eq. (3.2.15), therefore, shows that the typical decretion rate is much smaller than the mass injection rate $\dot{M}_{\text{inj}}(\tilde{\tau})$. In our case, the typical decretion rate is only $8.46 \times 10^{-3} \dot{M}_{\text{inj}}$. This means that, as seen above, the majority of the injected mass flows inwards and is absorbed by the inner boundary at the stellar equator, and only a small remaining fraction of the injected mass is responsible for the growth of the disk. These results were first obtained from SPH simulations of Be disks by Okazaki et al. (2002), who found that only about 0.1% of the injected material flows outward, as a direct result of their choice for R_{inj} .

In steady-state, only the fraction of the injected mass given by $\dot{M}_{\text{inj}}(1 - \Xi)$ is flowing outwards through the disk and crossing the outer radius R_{out} , thus leaving the system (in our case, $1 - \Xi = 2.84 \times 10^{-4}$). Since the mass of the disk is not varying in steady-state, the mass flux given by $\dot{M}_{\text{inj}}(1 - \Xi)$ is actually the rate of mass being lost by the star, which we indicate by $(-\partial M/\partial t)_{\text{steady}}$. It is easily seen that it is related to the typical decretion rate by the following equation

$$\left(-\frac{\partial M}{\partial t}\right)_{\text{steady}} = \frac{\Lambda}{\tilde{R}_{\text{out}}^{\frac{1}{2}}} \left(-\frac{\partial M}{\partial t}\right)_{\text{typ}}, \quad (3.2.17)$$

negative, and compress the regions of high absolute value in a similar way as the log scale does.

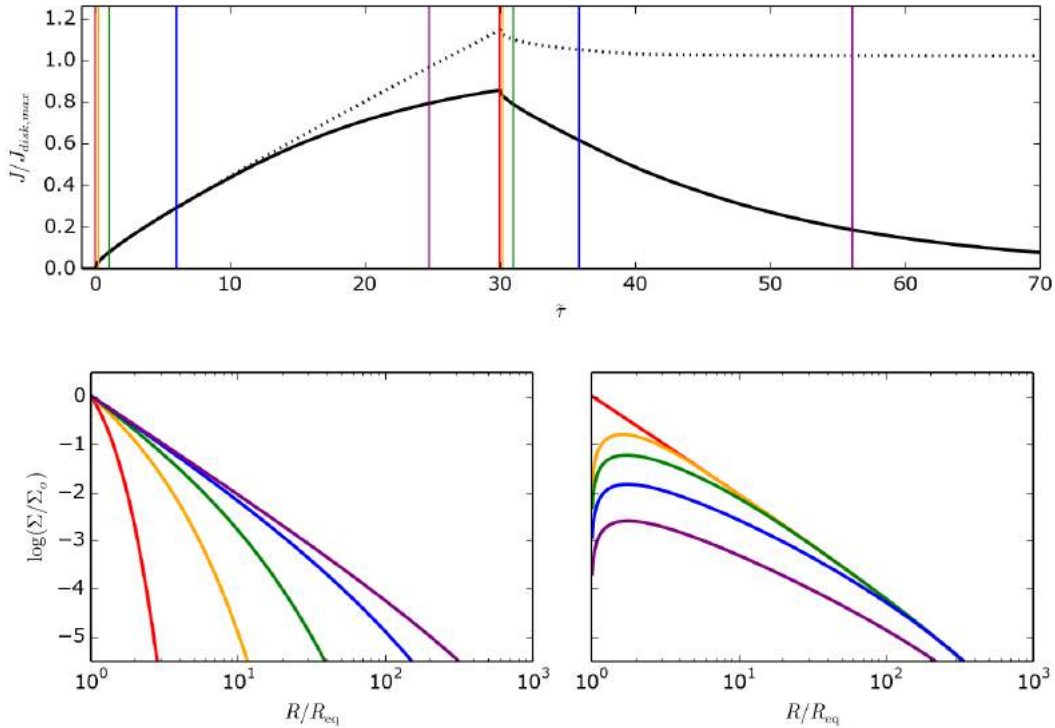


Figure 3.3: Dynamical bump model with $\tilde{\tau}_{\text{bu}} = 30$. *Above*: the amount of angular momentum in the disk (solid black curve) and the amount of angular momentum that is lost by the star (dotted black curve). Colored vertical straight lines mark the 5 instants $\tilde{\tau} = 0, 0.2, 1, 6, 25$ (during the build-up phase), and the 5 instants $\tilde{\tau} = 30, 30.2, 31, 36, 55$ (during the dissipation phase). Surface density profiles are shown at the first 5 instants (*lower-left*) and at the last 5 instants (*lower-right*).

where $\Lambda = 1/(1 - \tilde{R}_{\text{out}}^{-\frac{1}{2}})$ is a number very close to 1 for any Be disk in general. In our case, $\Lambda - 1 = 3.27 \times 10^{-2}$.

In steady-state, the angular momentum escaping the system at the outer boundary (and also ultimately being lost by the star) is $(GMR_{\text{out}})^{\frac{1}{2}} \dot{M}_{\text{inj}}(1 - \Xi)$, being given by

$$\left(-\frac{\partial J}{\partial t}\right)_{\text{steady}} = \Lambda (GMR_{\text{eq}})^{\frac{1}{2}} \left(-\frac{\partial M}{\partial t}\right)_{\text{typ}}. \quad (3.2.18)$$

Therefore, from Eq. (3.2.17) we see that knowing \tilde{R}_{out} is essential for estimating the rate of mass being lost by the star. This, however, is not the case for the rate of angular momentum being lost by the star, given by Eq. (3.2.18). It follows that the latter quantity can be much more reliably obtained from light curve modelling than the former.

3.2.3 On the importance of the angular momentum loss rate

The same model used above for Fig. 3.2 will be used again to explore some other important properties of the dynamical models.

The upper panel of Fig. 3.3 shows the amount of angular momentum in the disk, given

by

$$J_{\text{disk}} = \int_{R_{\text{eq}}}^{R_{\text{out}}} (GMR)^{\frac{1}{2}} \Sigma 2\pi R dR, \quad (3.2.19)$$

and the amount of angular momentum that is lost by the star, given by the angular momentum that is injected at the radius of mass injection minus the angular momentum that falls back to the stellar equator:

$$-\Delta J_* = \int_{t_{\text{init}}}^t \left[(GMR_{\text{inj}})^{\frac{1}{2}} \dot{M}_{\text{inj}} + (GMR_{\text{eq}})^{\frac{1}{2}} \dot{M}_{\text{eq}} \right] dt'. \quad (3.2.20)$$

By the conservation of angular momentum, the difference between the dotted and the solid curves is the angular momentum that escapes the system through the outer boundary at R_{out} . All values were scaled by the maximum angular momentum supported by the disk, which is given by

$$J_{\text{disk,max}} = \int_{R_{\text{eq}}}^{R_{\text{out}}} (GMR)^{\frac{1}{2}} \Sigma_{\text{steady}} 2\pi R dR. \quad (3.2.21)$$

The plot shows that, as the build-up process occurs, the disk's angular momentum and mass increase continuously. Eventually (in our example, roughly after $\tilde{\tau} = 10$), we see that a non-negligible amount of angular momentum starts to reach the outer radius $\tilde{R}_{\text{out}} = 1000$, thus leaving the system through the outer boundary. After the end of the build-up phase (which, in our example, happens at $\tilde{\tau} = 30$), the disk starts to dissipate: the black curve shows that the disk loses angular momentum until it reaches zero. However, as the dotted curve shows, only a fraction of the angular momentum of the disk returns to the star by re-accretion. The dotted curve tends to a non-zero value, which is the angular momentum that was lost by the star in the whole process.

This non-zero total angular momentum lost by the star was verified in our simulations, for the case of a constant α , to be given exactly by

$$-\Delta J_* = \left(-\frac{\partial J}{\partial t} \right)_{\text{steady}} \Delta t, \quad (3.2.22)$$

where Δt is the duration of the build-up time.

The two lower panels of Fig. 3.3 show surface density radial profiles in the whole disk range (the Σ profiles of Fig. 3.2 were limited only to the first four radii) at the specified times marked in the above panel. During build-up, the disk grows from the inside outward, with the inner regions reaching a near steady-state earlier than the outer parts. During dissipation, however, the disk becomes less and less dense as a whole, more or less in a self-similar way, because the entire disk is coupled by viscous forces.

It is implicit in our assumptions for the mass source (Eq. 3.1.5) that matter is injected with Keplerian velocity at R_{inj} and its removed with Keplerian velocity at R_{eq} and at R_{out} . Therefore, at the radius of mass injection, there is an angular momentum injection

rate given by $(GMR_{\text{inj}})^{\frac{1}{2}}\dot{M}_{\text{inj}}$, and at the stellar equator, there is an angular momentum removal rate given by $(GMR_{\text{eq}})^{\frac{1}{2}}\dot{M}_{\text{eq}}$. Be stars, however, do not rotate at critical velocities. Their mean rotational parameter is $W = 0.81 \pm 0.12$ (Rivinius et al., 2006). We may therefore assume that the inner boundary condition is located at just the place where the Keplerian velocity assumption starts to break down. There is strong evidence, however, at least for the Be star Achernar (Rivinius et al., 2013), the closest Be star, that the equatorial velocity may be near-Keplerian during the whole period of Be activity (build-up and dissipation). Rivinius et al. (2013) noticed a broadening in the wings of pure photospheric lines during an activity period of Achernar. I believe that it indeed makes sense that during activity the connection between the matter being injected and absorbed in the build-up phase (or being absorbed only) in the dissipation phase, might put at least the stellar equator of the star, which is a region not well separated from the disk, in a near orbital velocity. If that is the case, our adopted inner boundary condition in which matter is absorbed with azimuthal Keplerian velocity should be closer to reality.

In any case, the rate of angular momentum injected minus the rate of angular momentum absorbed is the rate of variation of the angular momentum of the star. Therefore,

$$\begin{aligned} -\frac{\partial J}{\partial t} &= \dot{J}_{\text{disk}} - (GMR_{\text{out}})^{\frac{1}{2}}\dot{M}_{\text{out}} = (GMR_{\text{inj}})^{\frac{1}{2}}\dot{M}_{\text{inj}} + (GMR_{\text{eq}})^{\frac{1}{2}}\dot{M}_{\text{eq}} \\ &= (GMR_{\text{eq}})^{\frac{1}{2}}\left(\tilde{R}_{\text{inj}}^{\frac{1}{2}}\dot{M}_{\text{inj}} + \dot{M}_{\text{eq}}\right) \\ &= (GMR_{\text{eq}})^{\frac{1}{2}}\dot{M}_{\text{inj}}\left(\tilde{R}_{\text{inj}}^{\frac{1}{2}} - \frac{-\dot{M}_{\text{eq}}}{\dot{M}_{\text{inj}}}\right). \end{aligned}$$

In steady-state, we have that $\dot{M}_{\text{eq}} = -\dot{M}_{\text{inj}}\Xi \gtrsim -\dot{M}_{\text{inj}}$, where the last approximation comes from the fact that almost all matter injected comes back to the star. Therefore, we have that the angular momentum loss rate of the star is given by

$$-\frac{\partial J}{\partial t} = \dot{J}_{\text{disk}} - (GMR_{\text{out}})^{\frac{1}{2}}\dot{M}_{\text{out}} \approx (GMR_{\text{eq}})^{\frac{1}{2}}\dot{M}_{\text{inj}}\left(\tilde{R}_{\text{inj}}^{\frac{1}{2}} - 1\right). \quad (3.2.23)$$

Eq. (3.2.15), however, says that $\alpha\Sigma_0 \propto \dot{M}_{\text{inj}}\left(\tilde{R}_{\text{inj}}^{\frac{1}{2}} - 1\right)$. Therefore, we conclude that Σ_0 , apart from a determination of α , is closely related to the net angular momentum that is injected into the disk. The product $\alpha\Sigma_0$ is just another way of specifying that physical quantity.

Also, noticing that $\dot{M}_{\text{inj}}\left(\tilde{R}_{\text{inj}}^{\frac{1}{2}} - 1\right)$ is the typical accretion rate, we may compare Eq. (3.2.23) with Eq. (3.2.18), from where we conclude that

$$-\frac{\partial J}{\partial t} \approx \left(-\frac{\partial J}{\partial t}\right)_{\text{steady}}, \quad (3.2.24)$$

which means that the angular momentum loss rate of the star is roughly given by the steady-state angular momentum loss rate.

I conclude this section reflecting on the fact that, although we commonly associate Be stars with “mass loss”, probably as a result of Be stars being traditionally linked with stellar winds, the fact is that these stars have outflowing rotating disks, and our results suggest that, in this context, it might be better to talk about “angular momentum loss”. Any future theory explaining the Be mechanism will probably be linked with the angular momentum as the fundamental physical quantity to be explained.

3.3 The mass reservoir effect

It is important to stress that the solution $\Sigma(\tilde{R}, \tilde{\tau})$ is shaped not just by the mass injection rate $\Sigma_0(\tilde{\tau})$ at the specific instant $\tilde{\tau}$, but by the whole mass injection history before the instant $\tilde{\tau}$. Therefore, the advantage of studying the relatively isolated bumps like the ones exemplified in Fig. 3.1, which started after a clear inactive phase, is that there is no disk present when the bump starts developing; thus, no previous history of mass injection has to be taken into account in the beginning of their modeling.

The light curves of several Be stars show that the duration of the build-up phase, which we refer to as the *build-up time*, is variable between Be stars and even between different bumps from the same star, ranging from a few days to years. The dissipation phase that follows, however, contrary to the build-up phase, depends on the previous history of mass injection. For this reason, the modeling of the dissipation phase must not be disconnected from the modeling of the build-up phase that happened before it. This was one of the main realizations of this thesis. One of the main consequences of this fact is what we call the “mass reservoir effect” (see also Ghoreyshi et al., 2016).

It is possible that two Be star disks with roughly the same visual magnitude have two very different total masses. This is because the visual continuum emission of a Be disk comes almost entirely from the inner parts of the disk, roughly within the very first few stellar radii (see Fig. 1.11). Depending on the magnitude of the viscosity, a disk under a constant mass injection rate from the star may effectively reach a near steady density distribution in the region of the first few stellar radii within a few months. The outer parts, however, would not have reached a near steady-state yet, and would continue to grow in density, had the mass injection continued, increasing the total mass of the disk in the process. It could take several years for these outer regions to reach a near-steady state. But despite that, the effect on the visual continuum of this growth would be barely noticeable, since these regions contribute negligibly to the visible continuum emission. This is illustrated in Fig. 3.4.

The total mass of the disk is shown in the upper panel of Fig. 3.4. We notice that, although the mass injection rate \dot{M}_{inj} is constant in the disk, during the build-up the total

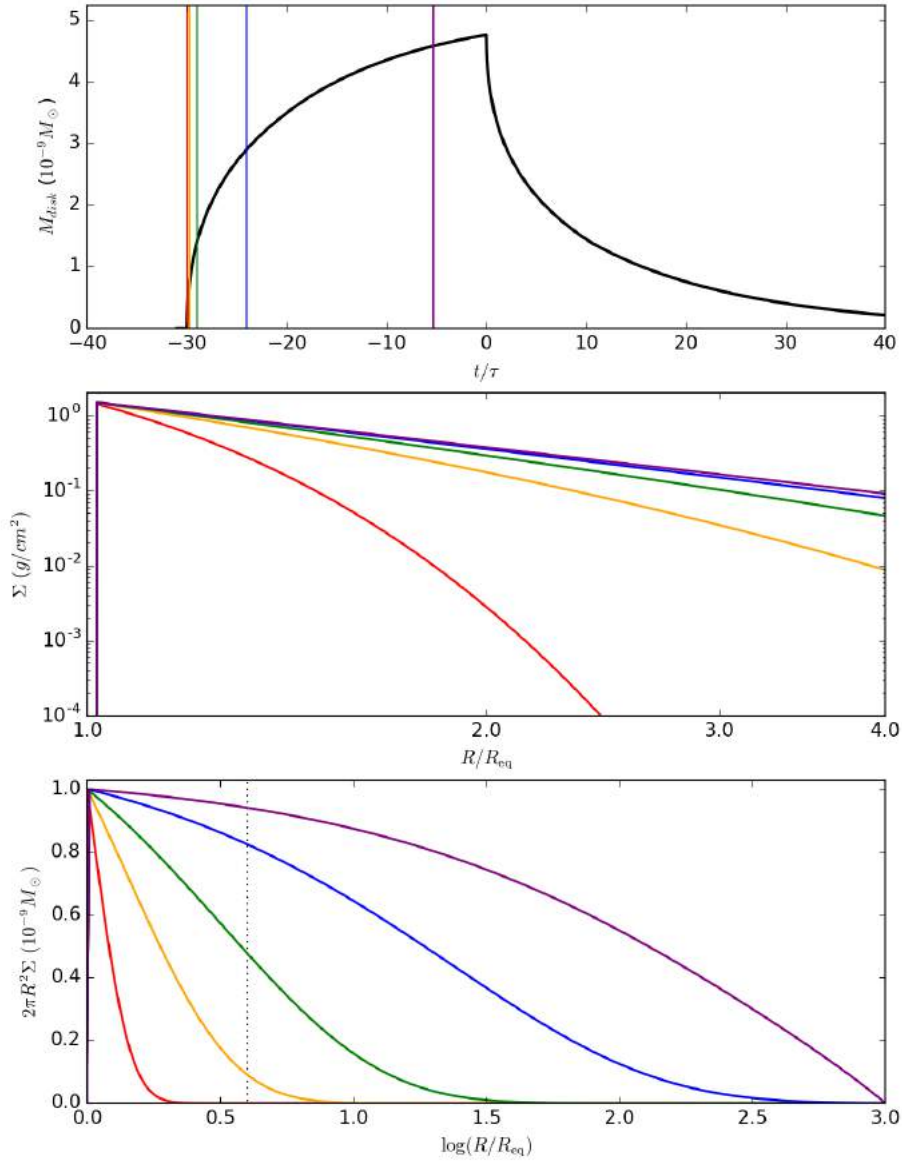


Figure 3.4: Simulation of a constant build up phase ($\Sigma_0 = 1.549 \text{ g cm}^{-2}$), during $\tilde{\tau}_{\text{bu}} = 30$, followed by a complete dissipation ($\Sigma_0 = 0$). The different colors corresponds to different instants after beginning of the build-up phase: $\tilde{\tau} + 30 \sim 0$ (red), $\tilde{\tau} + 30 = 0.2$ (orange), $\tilde{\tau} + 30 = 1$ (green), $\tilde{\tau} + 30 = 6$ (blue), $\tilde{\tau} + 30 = 25$ (purple). *Above*: Total mass of the disk. *Middle*: Surface density profile in the first four radii of the disk. *Below*: Mass distribution ($\partial M_{\text{disk}}/\partial \ln R$) of the disk.

mass of the disk continually increases but at a slower rate. This is due to the fact that the stellar equator absorbs an increasing fraction of the mass being injected, owing to the increasing angular momentum loss rate as the outer radius grows. In the middle panel

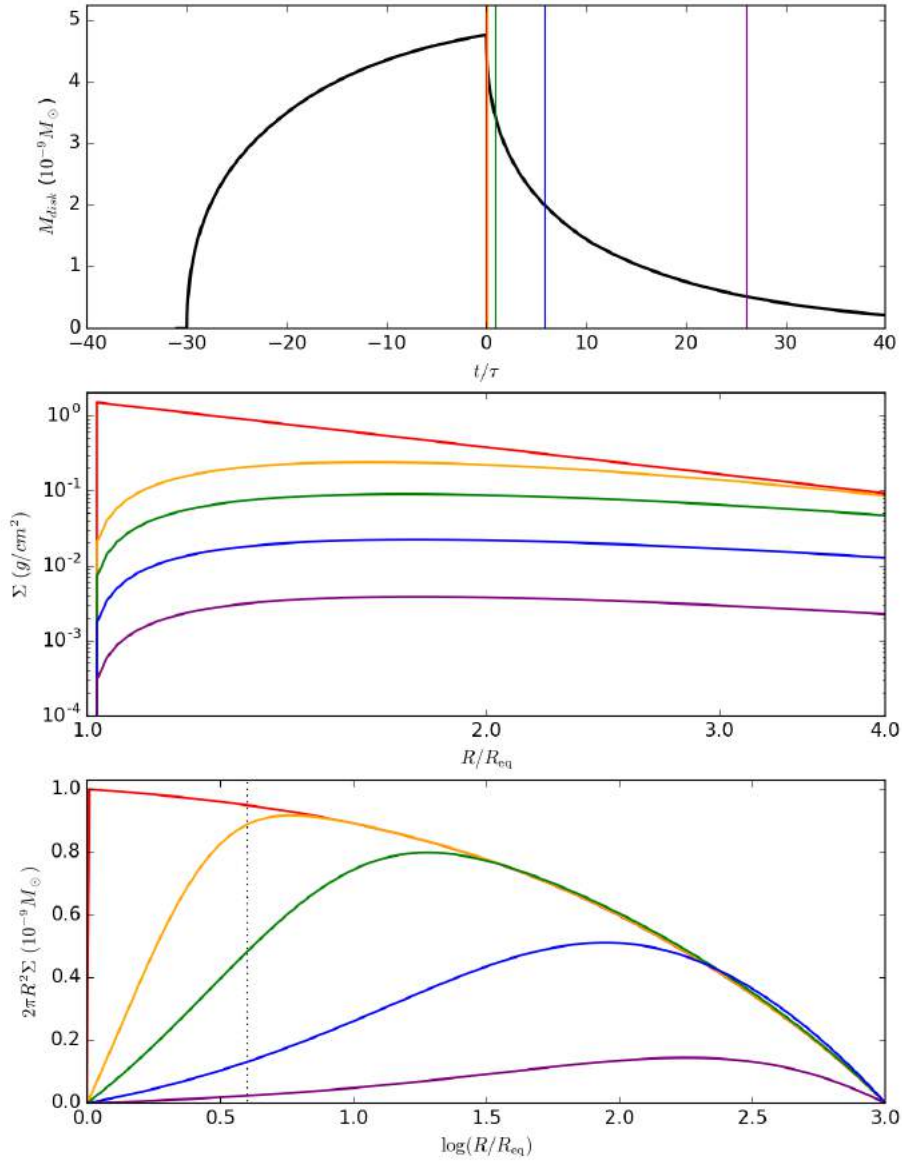


Figure 3.5: Simulation of two constant build-up phases ($\Sigma_0 = 1.549 \text{ g cm}^{-2}$), one during $\tilde{\tau}_{\text{bu}} = 30$ (solid line), and another during $\tilde{\tau}_{\text{bu}} = 30$ (dashed line). Both were followed by a complete dissipation ($\Sigma_0 = 0$). The different colors corresponds to different instants after beginning of the build-up phase: $\tilde{\tau} \sim 0$ (red), $\tilde{\tau} = 0.2$ (orange), $\tilde{\tau} = 1$ (green), $\tilde{\tau} = 6$ (blue), $\tilde{\tau} = 25$ (purple). The three panels are the same as the ones of Fig. 3.4.

of Fig. 3.4 we show the surface density of the disk, at $1 \leq \tilde{R} \leq 4$ (from where the most of the visible continuum is generated) at the five times defined in the upper panel. From this panel, we can see that, at $\tilde{\tau} + 30 = 1$ (see green curve), the inner disk has reached

a state very close to the steady-state. Therefore, the photometric visual bump (or dip) must already be reaching a plateau by this time. The upper panel shows, however, that the disk's mass is still increasing and will still increase much more, as time passes. This is further illustrated in the lower left panel of Fig. 3.4, where we plot $2\pi R^2\Sigma$ versus $\log \tilde{R}$. A dotted vertical line marks the radius $\tilde{R} = 4$. The mass of the disk is given by the integral $\int (2\pi R^2\Sigma) d \ln R$. Therefore, in the lower panel, any area below each curve and between two radii gives the amount of mass between these radii.

Now, when the mass injection rate from the star to the disk eventually stops, the viscous forces that couple all the matter in the disk lead to the reaccretion of most of the disk mass (see the lower-right panel of Fig. 3.2). In that case, we may expect that disks that are very similar in their inner regions (having, therefore, similar visual excesses) but are very different in their outer regions will have a different observed photometric dissipation, due to the fact that the inner region will be viscously coupled to the outer regions. A more massive outer disk represents a bigger reservoir of mass for the inner disk in the dissipation process.

In Fig. 3.5, it is shown that a more massive disk can supply the inner regions with mass for a longer time than a less massive outer disk, eventually making the dissipation of the more massive disk appear slower than the dissipation of the less massive one.

In the upper panel of Fig. 3.5, we compare two disk models that have been fed with the same Σ_0 but by two very different durations ($\tilde{\tau}_{\text{bu}} = 30$ and $\tilde{\tau}_{\text{bu}} = 3$). In that case, the inner regions of both disks have reached a near-steady surface density by the time of the end of the smallest build-up time ($\tilde{\tau} = 3$). The solid and dashed red lines on the middle panel show that the inner disk of these two disks are very similar, and, so, their visual photometric emission should be very similar. The upper panel, on the other hand, shows that, just before $\tilde{\tau} = 0$, the disk that had a build-up time ten times longer ended having more than twice the mass of the other.

As the dissipation phase takes place ($\tilde{\tau} > 0$), the middle panel shows that the surface density of the more massive disk diminishes at a slower rate. Therefore, the initially more massive disk should reduce its visible brightness at a slower rate. Since the viscosity parameter α influences the timescale parameter τ (see Eq. 3.1.13), we see from the middle panel that a more massive disk, when dissipating, could mimic the dissipation of a less massive disk with a smaller α . This is the effect of the mass reservoir on the determination of the α viscosity parameter of VDDs.

The contribution of the outer mass reservoir is further illustrated by the lower panel. We see that the initial distribution of mass of the two disks before the dissipation (given by the solid and dashed red curves) was very different. Since the mass flux is given by $2\pi R\Sigma \langle v_R \rangle = 2/(GMR)^{\frac{1}{2}}(\partial(\alpha c_s^2 2\pi R^2\Sigma)/\partial \ln R)$, it follows that the slope of the curves of the lower panel is a measure of the mass flux: if the distribution of mass is either locally increasing or decreasing, it means, respectively, that mass is flowing inwards or

outwards. The points of maxima of each curve are the “stagnation points” (the points where $2\pi R\Sigma \langle v_R \rangle = 0$). The lower panel, therefore, shows that the more massive disk always accretes mass back to the star at a higher rate, since the slope of the surface density at $\log \tilde{R} = 0$ is always steeper for the more massive disk. Despite that, the more massive disk still takes longer to decrease because the accretion region of this disk (the region of positive inclination in its curve) rapidly becomes increasingly bigger than the one of the less massive disk and the reservoir of mass available of the former is bigger than that of the latter.

The importance of the mass reservoir effect can be assessed by the reevaluation of the α parameter in 28 CMa by Ghoreyshi et al. (2016). Carciofi et al. (2012) modeled the 2003 dissipation phase of 28 CMa by considering a very long previous build-up time, and found that a high value of α was necessary to match the observed dissipation rate. Ghoreyshi et al. (2016) have shown that when the prior mass injection history is properly accounted for in the modeling, the value of α required to match the dissipation rate is much smaller: $\alpha = 0.21 \pm 0.05$ (M. Ghoreyshi, in preparation).

In Fig. 3.6, we show M. Ghoreyshi et al.’s² current best results for the photometric modeling of the light curve of 28 CMa, covering more than 33 years. From the first panel, we see that there are 4 major bumps. These bumps, however, contain smaller bumps in it, suggesting a more erratic mass injection rate superimposed to a more near periodic one. Their values of \dot{M}_{inj} are shown in the third panel (where they have set $\tilde{R}_{\text{inj}} = 1.017$, like we did in our models). In the first panel, we see that the dissipation of the third major bump is the dissipation previously modelled by Carciofi et al. (2012). In their modelling, Carciofi et al. (2012), who were unaware of the mass reservoir effect, used a very long build-up phase before turning the mass injection off to model the dissipation with the dynamical solutions coupled with the radiative transfer code HDUST (A. Carciofi, priv. comm.). Therefore, they required a very large value of $\alpha = 1$ in order to model the observed dissipation. In contrast, by modeling the whole available light curve, M. Ghoreyshi et al. obtained the values of α for several build-up and dissipations, properly taking the disk’s history into account.

An important fact seen in the first panel of Fig. 3.6 is that one single value of α is not able to fit all the observed bumps in the light curve. M. Ghoreyshi et al.’s results indicate that the α parameter of a Be star can be variable, at least in time. Another striking fact, related to the first, is that we see that the values of α during the build-up phase are often greater than the values of α during the dissipations. The only exception to that is the third major bump. We still don’t have an explanation for this fact and will come back to it when we discuss our own results.

The second panel of Fig. 3.6 shows the mass flux at three different radii as a function of time. This panel is a complementary version of the two lower panels of Fig. 3.2. We

² His PhD thesis is on going, with a paper in the last steps of preparation.

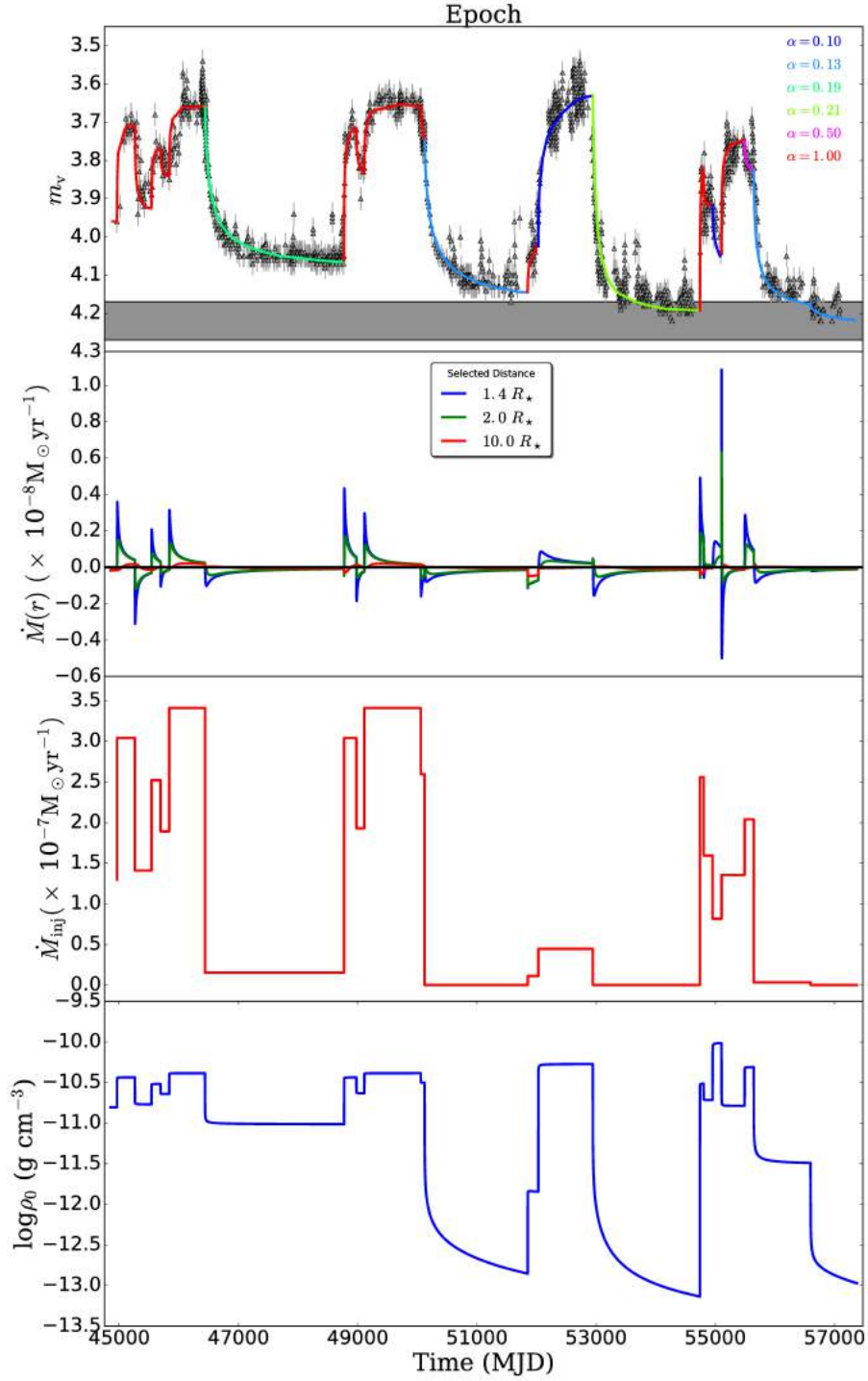


Figure 3.6: M. Ghoreyshi et al.’s current best results for the photometric modeling of the light curve of 28 CMa. *First:* A more than 33 years-long light curve of the 28 CMa with the best fitted synthetic light curve generated by a dynamical model computed with SINGLEBE feeding the radiative transfer code HDUST. The different colors correspond to different values of α used in separated portions of the curve. *Second:* Mass flux at $\tilde{R} = 1.4$ (blue), $\tilde{R} = 2.0$ (green), $\tilde{R} = 10.0$ (red), as a function of time. *Third:* Mass injection rate (\dot{M}_{inj} , with $\tilde{R}_{\text{inj}} = 1017$) into the disk as a function of time. *Fourth:* mass density at the radius of mass injection, $\rho_{\text{inj}} = \Sigma_{\text{inj}} / (2\pi)^{\frac{1}{2}} H$.

see that, after the abrupt changes in \dot{M}_{inj} (or Σ_0 , in our work), the mass flux in the inner disk abruptly changes. The absolute value of the mass flux at radii nearer to the radius of mass injection always show bigger amplitudes in the variations after the changes of \dot{M}_{inj} . At larger radii, the variations in the mass flux are smaller, meaning that the inner disk retains part of the mass flux, vary more intensely and leave less mass to the outer regions.

A model grid of disk formation and dissipation events

God used beautiful mathematics in
creating the world.

Paul Dirac, *The Cosmic Code:
Quantum Physics As The Language
Of Nature* (1982)

4.1 *The dynamical model grid*

For building a comprehensive grid of dynamical models that are solutions of Eq. 3.1.12, we make usage of the definitions of Chapter 3 that allow us to write the solution $\Sigma(\tilde{R}, \tilde{\tau})$ in terms of $\Sigma_0(\tilde{\tau})$ (see source term in Eq. 3.2.16) and the dimensionless time parameter $\tilde{\tau}$ (see Eq. 3.1.14).

As discussed in Sect. 3.3, the advantage of studying relatively isolated bumps like the ones exemplified in Fig. 3.1, which started after a clear inactive phase, is that there is no previous history of mass injection to be taken into account for the modeling, so that during build-up, the shape of the curve is controlled solely by $\Sigma_0(\tilde{\tau})$ and $\tilde{\tau}$, while at dissipation, an additional parameter, the previous disk build-up time, must be considered (see Sect 3.3). By using the time parameter (Eq. 3.1.14) instead of the physical time, our dynamical models are independent of the specific physical parameters M , T_{eff} , R_{eq} and $\alpha(t)$ of the Be star under consideration (recall that these parameters – see Eq. 3.1.13 – define the timescale parameter $\tau(t)$, which in turn makes the connection between the physical time t and the time parameter $\tilde{\tau}$.) Also, from the linearity of Eq. 3.1.12, it follows that multiplying $\Sigma_0(\tilde{\tau})$ by some constant results in the solution $\Sigma(\tilde{R}, \tilde{\tau})$ multiplied by the same constant. Consequently, the dynamical models need to be run for just one arbitrary value of Σ_0 .

For our grid of dynamical models of bumps and dips of Be stars, we assume that the stars start diskless. Then, at time $\tilde{\tau} = 0$, mass injection into the disk begins, with some asymptotic surface density ($\Sigma_0 > 0$), which lasts until $\tilde{\tau} = \tilde{\tau}_{\text{bu}}$. This last quantity is the

scaled build-up time, related to the above mentioned build-up time, but scaled by the timescale parameter. After that ($\tilde{\tau} > \tilde{\tau}_{\text{bu}}$), mass injection no longer occurs ($\Sigma_0 = 0$) and the disk dissipates.

We generated 11 dynamical models following the description given in the last paragraph, for 11 different values of $\tilde{\tau}_{\text{bu}}$, listed as the numerical values in the fourth column of Table 4.1. In addition to these dynamical models, we also generated 1 dynamical model composed only of a very long build-up phase. This model that is not of a bump (or dip) is represented in the fourth column of Table 4.1 as the $\tilde{\tau}_{\text{bu}} = \text{bu}$ model. Finally, we also generated 1 dynamical model that did not start from a diskless state, but rather from the steady-state (see Eq. 3.2.13) configuration for the given Σ_0 . This model corresponds to a bump that dissipates after an infinitely long build-up phase. In the fourth column of Table 4.1, this model is the $\tilde{\tau}_{\text{bu}} = \infty$ model.

For the models with $\tilde{\tau}_{\text{bu}} \neq \text{bu}$, it is important to remember that their build-up phases are all indistinguishable from sections of the very long build-up model described by $\tilde{\tau}_{\text{bu}} = \text{bu}$. Therefore, we only need to model specific instants of the dynamical models with $\tilde{\tau}_{\text{bu}} = \text{bu}$ to have the photometric description of the build-up phases of all the other models. We hence, only have to model the dissipation phases of the other models. These dissipation phases differ from one another because of the mass reservoir effect, outlined in Sect. 3.3.

Since the timescale parameter (Eq. 3.1.13) is roughly given by $\sim (100\text{--}200)/\alpha$ days for early Be stars with $\alpha \lesssim 1$, our chosen values of $\tilde{\tau}_{\text{bu}}$ correspond to real build-up times of at least 15 days, which brackets the observed build-up times of the sample described below (Sect. 5.2, Table 5.1).

4.2 Radiative transfer models

Having selected a set of suitable hydrodynamic bump models, the next step is to produce photometric light curves of these models.

In this work, at selected time parameters $\tilde{\tau}$, a particular dynamical model, which is a function $\Sigma(\tilde{R}, \tilde{\tau})$ is input to the Monte Carlo 3-D radiative transfer code HDUST (Carciofi et al., 2004; Carciofi and Bjorkman, 2006, 2008) which calculates the emergent spectrum of the star+disk system.

To convert between surface density and mass density, it is assumed that the disk is vertically supported by hydrostatic pressure (see Eq. 2.2.14), in which case the vertical density profile is approximately a Gaussian, and

$$\rho(\tilde{R}, z, \tilde{\tau}) = \frac{\Sigma(\tilde{R}, \tilde{\tau})}{\sqrt{2\pi}H} e^{-\frac{z^2}{2H^2}}, \quad (4.2.1)$$

where

$$\frac{H}{R_{\text{eq}}} = \left(\frac{c_s}{v_{\text{orb}}} \right) \tilde{R}^{\frac{3}{2}}, \quad (4.2.2)$$

is the scale height.

Before making further specifications in our models of bumps (and dips), let us briefly introduce the radiative transfer code **HDUST**, used in this work to generate the photometric observables associated with our dynamical models of bumps.

4.2.1 The Monte Carlo Radiative Transfer code HDUST

C.P. Dullemond, in his lecture notes¹, states: “When you hear that radiative transfer is a very challenging topic, the reason is that in many cases we do not know the values of j_ν and/or k_ν in advance. The radiation field I_ν that we wish to compute can affect the medium in such a way as to modify j_ν and k_ν . We are then faced with a “chicken or egg” effect: to compute I_ν we need to know j_ν and k_ν , and to compute j_ν and k_ν we need to know I_ν .”

HDUST is a Monte Carlo code that solves simultaneously the radiative transfer, radiative equilibrium and statistical equilibrium equations for a physical system composed of sources of radiation and an arbitrary distribution of gas (hydrogen) and dust (Carciofi et al., 2004; Carciofi and Bjorkman, 2006, 2008). The gas and dust compose the “interaction region”. This interaction region, which is the circumstellar envelope of a Be star for our purposes, is divided into several small cells where the physical properties are assumed to be constant (number of particles, kinetic temperature, velocity, velocity gradient and level populations). Consequently, the emissivity j_ν and the opacity k_ν are also constants within each cell.

The radiative transfer and radiative equilibrium problems and the statistical equilibrium problem are solved in an iterative alternating fashion. The code alternates from “global” to “local” at each iteration. The “global problem” is the Monte Carlo solution of the radiative transfer problem, where the radiation field is simulated. The “local problem” is the updating of the states of each cell to new states that are more in equilibrium with the radiation field just simulated.

For each iteration, in the radiative transfer part of the problem, the total luminosity of the physical system is divided into N “photon packets” (PP)². These N PPs will be emitted from points from the stellar surface and from the cells, and they will be propagated until they escape the envelope. During the propagation of the PPs, when one crosses the surface of a cell and is absorbed within that cell, the interaction with the gas is tracked by sampling (counting) the number of radiative transitions (e.g., bound-bound, bound-free) caused by the absorption. Then, in the rest frame of the fluid, a PP is reemitted at the same location and with the same total energy (but with a different frequency), as that of the incoming PP, in order to ensure radiative equilibrium ($\nabla \cdot \mathbf{F}_\nu = 0$) in the rest frame of the fluid.

¹ http://www.ita.uni-heidelberg.de/~dullemond/lectures/radtrans_2012/

² Actually, they are “luminosity packets”.

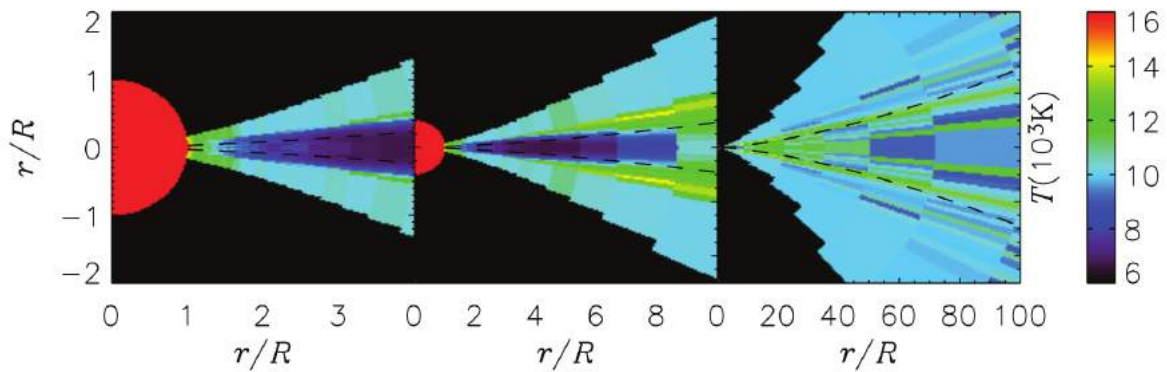


Figure 4.1: Temperatures in the cells and on the stellar surface in a simulation of near-Keplerian disk of a Be star made by HDUST. (Credits: [Carciofi and Bjorkman, 2006](#))

At the end of the radiative transfer part, the code has sampled all relevant radiative rates for all cells. Then, for each cell, a linearized scheme produces a new updated state to be used in the next iteration.

After a sufficient number of iterations, both the global and local problems converge to a self-consistent system in which the microphysics within each cell is in equilibrium with the radiation field of the whole system. In the last iteration, in particular, when the PPs escape the envelope, their luminosities are binned in into solid angle bins (corresponding to the observer’s viewing angles) and frequency bins (which will compose the synthetic SEDs).

Fig. 4.1, from [Carciofi and Bjorkman \(2006\)](#), shows the temperatures for several HDUST cells, defined in spherical coordinates, in the simulation of a Be star with its near-Keplerian circumstellar disk. The stellar surface assumed in this figure, in particular, was a spherical one.

4.2.2 Radiative transfer models

The radiative transfer part of the problem requires a stellar model, which will be the main source of radiation. The stellar model defines the physical parameters M , R_{eq} and T_{eff} , which were left unspecified in the dynamical model grid. In addition, another parameter must be specified: the inclination, i (where $i = 0$ means pole-on orientation).

As we know, one important feature of the central stars of Be stars is that they are fast rotators. Fast rotation causes the star to be oblate, with hotter poles and colder equatorial regions. The rotation rate is specified by the ratio of the rotation velocity at the equator to the Keplerian velocity at the equator, $W = v_{\text{eq}}/v_{\text{orb}}$. The ratio between the equatorial radius to the polar radius is given by $R_{\text{eq}}/R_{\text{pole}} = 1 + W^2/2$ for a Roche-shaped star. All these parameters evolve in time as a consequence of stellar evolution, and Be stars can be found in luminosity classes from V to III ([Rivinius et al., 2013](#)).

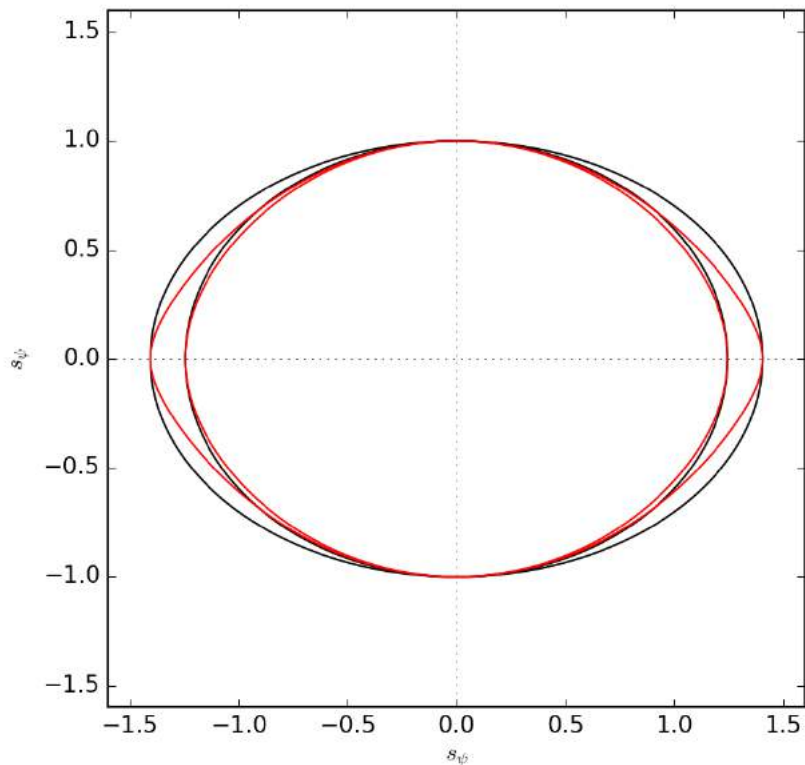


Figure 4.2: HDUST’s current ellipsoid stars (black) versus Roche-shaped stars with $W = 0.7$ and $W = 0.9$ (red).

As the sources of the physical parameters of our rotating stars, we used the evolutionary tracks generated by the Geneva stellar evolution code (Georgy et al., 2013)³. Therefore, the physical parameters of the central stars that enter as input into HDUST (e.g., R_{eq} and T_{eff}) are obtained by interpolating the tracks, in metallicity Z , stellar mass M , rotation parameter W and the age during the main sequence t/t_{MS} , where t_{MS} is the timespan of the main sequence for each stellar model.

The current version of HDUST allows for a spheroidal oblate star, with the latitude-dependent surface temperature being given by (Carciofi et al., 2008)

$$T_{\text{surf}} \propto g_{\text{eff}}^{\beta}. \quad (4.2.3)$$

In Fig. 4.2, we show the ellipsoidal shape compared to the shape given by Roche equipotentials for $W = 0.7$ and $W = 0.9$, roughly corresponding to the $\pm 1\sigma$ limits of the distribution of values of W for Galactic Be stars (Rivinius et al., 2006).

The coefficient $\beta(W)$ in Eq. (4.2.3) is calculated by fitting a straight line to the curve given by $\ln T_{\text{surf}}$ versus $\ln g_{\text{eff}}$ given by the flux theory of Espinosa Lara and Rieutord (2011) (see the lower-right panel of Fig. 2.2). For the disk scale height (Eq. 4.2.2), we assume

³ Their tracks are available online at <https://obswww.unige.ch/Recherche/evol/-Database->

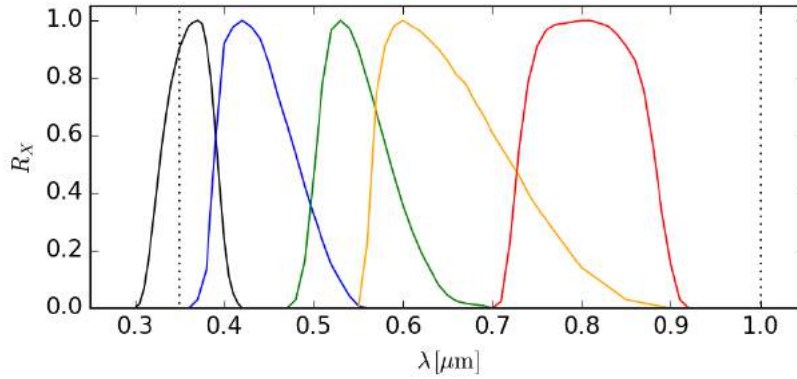


Figure 4.3: *UBVRI* Johnson-Cousins passbands from Bessell (1990), in black, blue, green, orange and red, respectively. The vertical dotted lines mark the limits in frequency of the SEDs generated by HDUST in this work.

an isothermal disk with $T_{\text{disk}} = 0.6T_{\text{eff}}$, where T_{eff} is the mean effective temperature of the star, defined by $T_{\text{eff}} = (L_*/\sigma S_*)^{1/4}$, with S_* being the surface area of the star (here calculated as the surface of the Roche equipotential).

For CCD observations (photon counting devices), a photometric observable is proportional to the number of photons arriving per units of time and area, given by

$$\int_0^\infty (\lambda/hc) F_\lambda(\lambda) R_X(\lambda) d\lambda,$$

where $F_\lambda(\lambda)$ is the flux density and $R_X(\lambda)$ is the passband of a given standard filter X . The function F_λ is one of the main outputs of the code HDUST.

The Johnson Magnitude System is a special case of a “Vega magnitude system”. Therefore, measurements in any filter X are compared to measurements of Vega in that same filter, in the following way

$$M_X = -\frac{5}{2} \log \left(\frac{\langle \lambda F_\lambda \rangle_X}{\langle \lambda F_\lambda^{\text{Vega}} \rangle_X} \right) + M_X^{\text{Vega}}, \quad (4.2.4)$$

where the magnitude of Vega is defined to be $M_X^{\text{Vega}} = 0.03$ in every filter and

$$\langle \lambda F_\lambda \rangle_X = \frac{\int_0^\infty (\lambda F_\lambda) R_X(\lambda) d\lambda}{\int_0^\infty R_X(\lambda) d\lambda}. \quad (4.2.5)$$

In order to generate synthetic magnitudes, we used the standard *BVRI* Johnson-Cousins passbands from Bessell (1990). They are sketched as the solid curves in Fig. 4.2. To calibrate our system to cgs units, we used the Vega flux from ATLAS9 model of Vega described in Castelli and Kurucz (1994), and we normalized HDUST’s flux as if the objects were at 10pc of distance.

Table 4.1 - Parameters of the grid of photometric models of bumps

Star	i [deg]	Σ_0 [g cm $^{-2}$]	$\tilde{\tau}_{\text{bu}}$
Star 1	00.0	0.30	bu
Star 2	21.8	0.41	00.15
Star 3	31.0	0.56	00.45
	38.2	0.75	00.75
	44.4	1.01	01.50
	50.0	1.37	02.25
	55.2	1.85	03.00
	60.0	2.50	04.50
	64.6		06.00
	69.1		09.00
	73.4		15.00
	77.6		30.00
	81.8		∞
	85.9		
	90.0		

Table 4.2 - Parameters of the stellar models of Table 4.1

Star	Z	M/M_{\odot}	W	t/t_{MS}	$\alpha\tau$ [d]
Star 1	0.002	7	0.81	0.5	125.3
Star 2	0.002	11	0.81	0.5	138.8
Star 3	0.002	15	0.81	0.5	160.4

The SEDs generated by HDUST were chosen, in this work, to be given in the (visual) frequency domain $0.35 - 1 \mu\text{m}$. This limit is shown in Fig. 4.3, covering the limits of the four *BVRI* passbands.

A grid of model light curves was computed using the 13×8 dynamical models described in Sect. 4.1 (third and fourth columns of Table 4.1). For each of these disk models, 17 radiative transfer models were calculated with HDUST at different instants of time parameters (not shown in the table)⁴ and 15 equally-spaced values of $\cos i$ (second column). This whole process was done for 3 different stellar models (“Star 1”, “Star 2” and “Star 3”, first column of Table 4.1). Details of the stellar models are given in Table 4.2. They

⁴ The time parameters were: 0, 0.02, 0.05, 0.09, 0.15, 0.21, 0.3, 0.6, 0.9, 1.5, 2.1, 3, 6, 9, 15, 30, ∞ . For the long build-up light curves ($\tilde{\tau}_{\text{bu}} = \text{bu}$), this list of values are for $\tilde{\tau}$. For the other cases, the list of values is for $\tilde{\tau} - \tilde{\tau}_{\text{bu}}$.

Table 4.3 - Parameters of the grid of photometric models of diskless stars

Z	M/M_{\odot}	W	t/t_{MS}	i [deg]
0.002	2.50	0.600	0.00	00.0
	3.68	0.699	0.25	27.3
	4.85	0.770	0.50	38.9
	6.00	0.833	0.75	48.2
	7.15	0.901	1.00	56.3
	8.29	0.990		63.6
	9.42			70.5
	10.54			77.2
	11.66			83.6
	12.78			90.0
	13.89			
	15.00			

were chosen to represent early B-type stars from the SMC ($Z = 0.002$), in the middle of their life in the main sequence, with the rotation parameter given by the mean value obtained for Be stars ($W = 0.81$, Rivinius et al., 2006). In the sixth column of Table 4.2, we present the values of $\alpha\tau$ (Eq. 3.1.13) for the disks of these stars (with the assumption that $T_{\text{disk}} = 0.6T_{\text{eff}}$).

In short, a single light curve is specified by taking one element of each column of Table 4.1. The end result was a grid of $3 \times 14 \times 8 \times 13 = 4368$ light curves, for each of the *BVRI* bands. A study of these light curves will be presented in Sect. 4.3 below.

We also generated a grid of inactive (diskless) stellar models. Because these models can be computed much faster than the bump models, we were able to cover a much finer grid of stellar parameters (Table 4.3). The grid is composed by models for 12 different masses (second column), 6 different rotation rates (third column), 5 equally spaced values for the age in the main sequence (fourth column) and 10 equally spaced values of $\cos i$ (fifth column), resulting in a total of $12 \times 6 \times 5 \times 10 = 3600$ photometric models for each of the *BVRI* bands.

In the left panel of Fig. 4.4, we show a color-magnitude diagram (CMD) in the *V* and *I* bands of the stellar models of Table 4.3. This figure will be used in this work to represent all the possible main sequence central stars of the Be star system. The mass of the star increases with the size of its marker. The 5 different stellar ages are seen as the groups of points move in the upper-right direction. This is better seen in the lower, less crowded, portion of the diagram. For each star, the effect changing i from 90 deg to 0 deg is to move in the upper-left direction. From this diagram, therefore, we see that

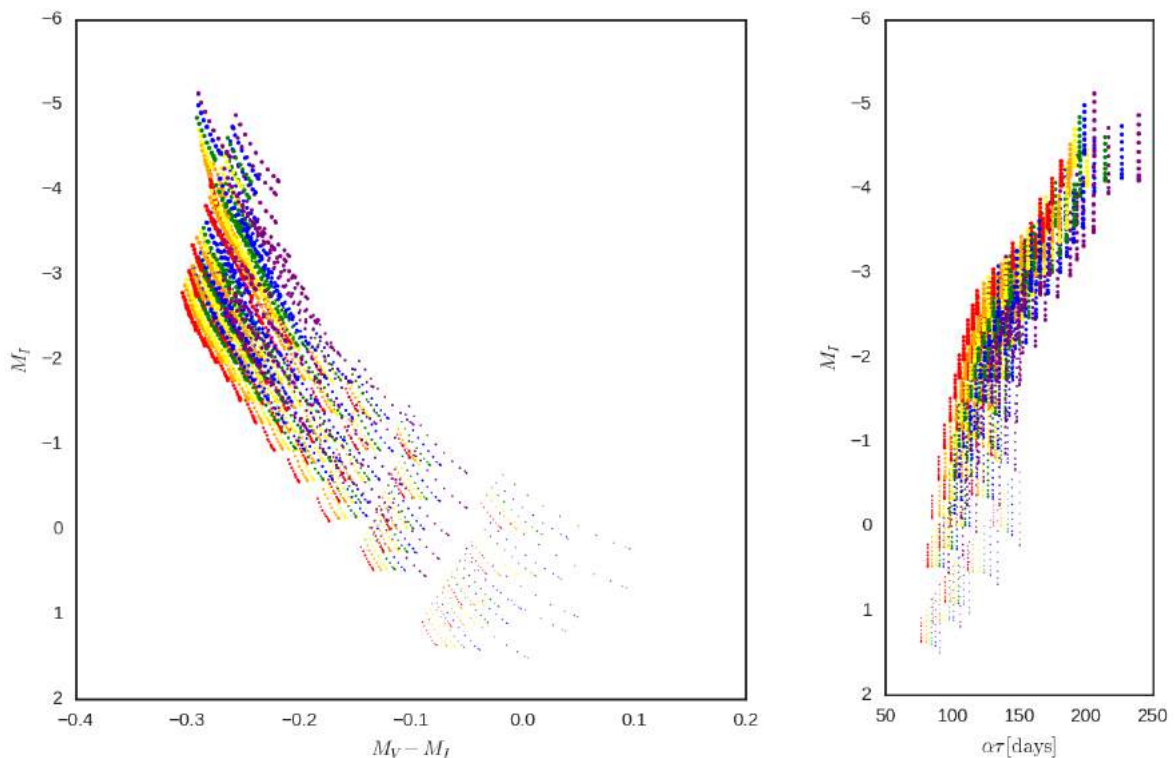


Figure 4.4: *Left*: CMD in bands V and I of the diskless stars of Table 4.3. The colors red, orange, yellow, green, blue and purple correspond to the 6 values of W in increasing order. The mass of the star increases with the size of its marker. The 5 different stellar ages are seen as the groups of points move in the upper-right direction. For each star, the effect of going from inclination angle 90 deg to 0 deg is to move in the upper-left direction. *Right*: diagram showing M_I (the same vertical axis of the upper-left one) versus $\alpha\tau$ (in days) for the diskless stars.

for stars seen pole-on, the effect of increasing W is to increase its apparent magnitude (owing to the polar brightening in the “von Zeipel effect”, the flux is enhanced in the poles - see Sect. 2.3.14) and to make it a little redder (since the temperature decreases in the equatorial regions). For stars seen edge-on, there is little variation in the apparent magnitude, but the star becomes much redder, because of the decrease in the temperature in the equatorial region.

In the right panel of Fig. 4.4, we show the same models in a diagram of M_I (the same vertical axis of the upper-left one) versus $\alpha\tau$ (in days). From this diagram, we see that the values of the disk parameter $\alpha\tau$ (Eq. 3.1.13, with the assumption that $T_{\text{disk}} = 0.6T_{\text{eff}}$) are roughly between 100 and 200 days for early Be stars.

4.3 Empirical law

In order to facilitate the comparison of the synthetic light curves (Sect. 4.2.2) with the observed ones (Sect. 5.2), we developed two empirical laws that match quite closely

the synthetic light curves for build-up and dissipation. The usefulness of these formulae will become clear in the next section.

In our discussion of the features of the light curves, it is useful to separate them in three groups: *pole-on light curves*, of stars seen at small inclination angles ($0 \leq i \lesssim 70$ deg), which should statistically correspond to the majority of the observed light curves; *edge-on light curves*, of shell stars ($i \approx 90$ deg); and, *intermediate light curves*, of stars seen at intermediate angles ($70 \lesssim i \lesssim 85$ deg – the extension of this intermediate region varies depending the photometric band under consideration and will be defined below). Pole-on light curves show an increase in apparent brightness, due to the additional flux coming from the disk. Conversely, edge-on light curves show a decrease in apparent brightness, due to obscuration of the star by the disk. The intermediate case shows the smallest variations in apparent brightness and frequently the light curve has a more complicated shape, as it is influenced by variable amounts of disk emission/absorption.

A computed light curve is a sequence of absolute magnitudes for a set of time parameters, in a given photometric band X , given by

$$M_X(\tilde{\tau}) = M_{X*} + \Delta X(\tilde{\tau}),$$

where M_{X*} is the absolute magnitude of the inactive Be star at band X , and $\Delta X(\tilde{\tau})$ is the magnitude difference caused by the disk ($\Delta X(\tilde{\tau})$ can be either positive or negative). M_{X*} can be estimated from the flux during the inactive phase (e.g., the purple points of Fig. 3.1).

A build-up light curve (for $\tilde{\tau} - \tilde{\tau}_{\text{bu}} < 0$) is denoted by $\Delta X_{\text{bu}}(\tilde{\tau})$. Its limiting value, if the build-up phase were to have an infinite duration, is denoted by $\Delta X_{\text{bu}}^{\infty}$ – the photometric excess of the disk when in steady-state. A dissipation light curve (for $\tilde{\tau} - \tilde{\tau}_{\text{bu}} \geq 0$) is denoted by $\Delta X_{\text{d}}(\tilde{\tau})$. Its value at the beginning of the dissipation ($\tilde{\tau} = \tilde{\tau}_{\text{bu}}$) is given by ΔX_{d}^0 .

Since every dynamical model starts from a diskless state and asymptotically ends at a diskless state, it follows that, regardless of the viewing angle, for every build-up light curve the quantity $\Delta X_{\text{bu}}(\tilde{\tau})/\Delta X_{\text{bu}}^{\infty}$ is a function that goes from 0 to 1 as $\tilde{\tau}$ goes from 0 to ∞ , and for every dissipation light curve, the quantity $\Delta X_{\text{d}}(\tilde{\tau})/\Delta X_{\text{d}}^0$ is a function that goes from 1 to 0 as $\tilde{\tau} - \tilde{\tau}_{\text{bu}}$ goes from 0 to ∞ .

Figure 4.5 shows examples of I -band light curves from the grid (see Table 4.1). The dashed black curves correspond to $\Delta I_{\text{bu}}/\Delta I_{\text{bu}}^{\infty}$ versus $\tilde{\tau}$. The solid curves correspond to $\Delta I_{\text{d}}/\Delta I_{\text{d}}^0$ versus $\tilde{\tau} - \tilde{\tau}_{\text{bu}}$ for four dissipating light curves with increasing scaled build-up times. Vertical colored straight lines (with the same color code as the one of Fig. 3.3) mark the times $\tilde{\tau}$ or $\tilde{\tau} - \tilde{\tau}_{\text{bu}} = 0, 0.2, 1$.

The light curves show that, at $\tilde{\tau} \approx 1$, the simulated bump has reached a significant fraction of its limiting value, and, at $\tilde{\tau} - \tilde{\tau}_{\text{bu}} \approx 1$, the bump has already fallen considerably from its previous magnitude before the beginning of the dissipation.

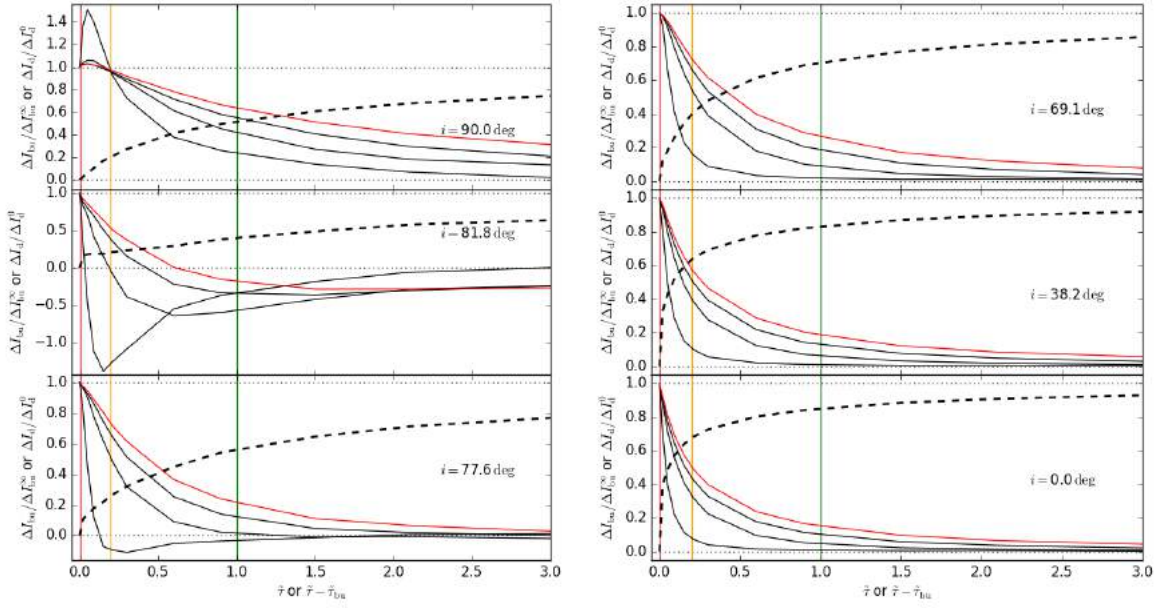


Figure 4.5: Examples of model I -band light curves, for several inclination angles, as indicated. The dashed black curves correspond to $\Delta I_{\text{bu}}/\Delta I_{\text{bu}}^\infty$ versus $\tilde{\tau}$, and the solid curves correspond to $\Delta I_{\text{d}}/\Delta I_{\text{d}}^0$ versus $\tilde{\tau} - \tilde{\tau}_{\text{bu}}$, for four dissipating light curves with scaled build-up times given by $\tilde{\tau}_{\text{bu}} = 0.15, 1.5, 6$ (in black) and $\tilde{\tau}_{\text{bu}} = 30$ (in red). Vertical colored straight lines mark the instants $\tilde{\tau}$ or $\tilde{\tau} - \tilde{\tau}_{\text{bu}} = 0, 0.2, 1$. All light curves are specifically for Star 2 and disks with $\Sigma_0 = 1.37 \text{ g cm}^{-2}$.

It can be seen in the panels that the dissipating curves with bigger scaled build-up times dissipate at slower rates. This is a consequence of the mass reservoir effect.

The light curves at near pole-on angles (the three panels from the right) show that, during the build-up phase, there is brightening due to the construction of the disk (and a usually negligible obscuration of the star by the disk), and during the dissipation phase, there is a decrease in brightening due to the disappearance of the disk. These light curves also show that, when viewed at angles closer to pole-on ($\cos i$ closer to 1), they build-up and dissipate faster. We will return to this effect below.

In the light curves at intermediate angles (middle-left and lower-left panels), both the effects of brightening from the disk and dimming from the obscuration of the star take place. The dissipations in the middle-left panel, for instance, show that, first, the gradual disappearance of the disk results in decrease in brightness. However, in time, the star becomes also less obscured by the disk and a small brightening happens.

For light curves at near edge-on angles (upper-left panel), the build-up light curves are dimmings due to obscuration of the star by the disk and the dissipation light curves are brightenings due to the disappearance of the disk and the disobscuration of the star.

The values of $\Delta I_{\text{bu}}^\infty$ and $\Delta V_{\text{bu}}^\infty$ for our grid are shown on the left and right panels of Fig. 4.6, respectively, plotted against $\cos i$. The values for the B and R bands show qualitatively similar patterns to the ones presented in this figure. Each panel shows the

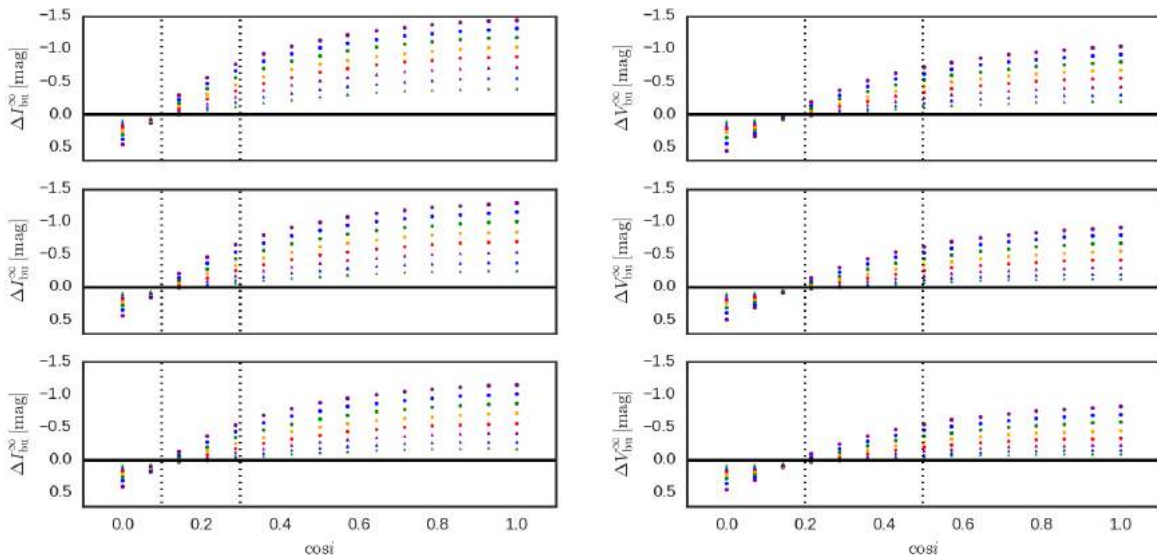


Figure 4.6: The values of $\Delta I_{\text{bu}}^{\infty}$ versus $\cos i$ (left) and $\Delta V_{\text{bu}}^{\infty}$ versus $\cos i$ (right) for our grid. In both panels, from top to bottom, the results are for Star 1, Star 2 and Star 3, respectively. Purple, blue, green, orange and red circles correspond to $\Sigma_0 = 2.50, 1.85, 1.37, 1.01, 0.75 \text{ g cm}^{-2}$. Purple, blue and green diamonds correspond to $\Sigma_0 = 0.56, 0.41, 0.30 \text{ g cm}^{-2}$. Vertical dotted lines define the region of intermediate angles for the I -band (left, $73 \lesssim i \lesssim 84 \text{ deg}$) and for the V -band (right, $60 \lesssim i \lesssim 78 \text{ deg}$).

results for a different star, and all 8 values of Σ_0 (Table 4.1) are represented in the figure by different colors and symbols. The curves monotonically increase with $\cos i$, starting with negative values at edge-on orientation and reaching a maximum for pole-on viewing. The angle for which $\Delta X_{\text{bu}}^{\infty} = 0$, where the disk excess emission is exactly matched by the absorption of photospheric light by the disk, depends both on the density scale (as shown in the figure) and (most importantly) on the band pass.

An analysis of our model grid allowed us to determine the ranges in inclination angle for which the light curve displays the intermediate behavior described above. They were determined by visual inspection of our model grid, as the angles for which the light curves present more complex shapes (see, e.g., the I -band light curves seen at $i = 81.8 \text{ deg}$ and $i = 77.6 \text{ deg}$ in Fig. 4.5). Their adopted values are 53-78 deg, 60-78 deg, 66-84 deg and 73-84 deg for the $BVRI$ bands, respectively.

For pole-on orientations, the observed excess is given by $\Delta X \approx -2.5 \log(1 + F_{\text{disk}}/F_*) \approx -F_{\text{disk}}/F_*$. Vieira et al. (2015) studied the continuum emission from gaseous disks, and showed that it can be approximated by the sum of the flux coming from an optically thick inner part (the so-called pseudophotosphere) with the contribution from an optically thin outer part, i.e.,

$$F_{\text{disk}} \propto \cos i F_{\text{thick}} + F_{\text{thin}}. \quad (4.3.1)$$

If the contribution of the optically thin part of the disk were negligible and the stellar flux, F_* , did not depend on $\cos i$ (see Fig. 4.4), ΔX would be a linear function of $\cos i$. Clearly

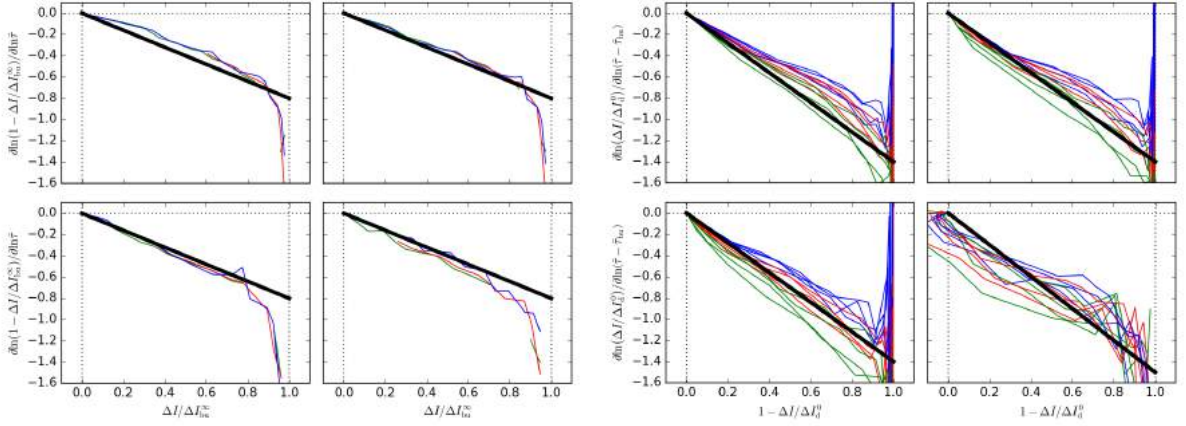


Figure 4.7: Examples of the log – log derivative of $1 - \Delta I_{\text{bu}}(\tilde{\tau})/\Delta I_{\text{bu}}^\infty$ vs. $\Delta I_{\text{bu}}(\tilde{\tau})/\Delta I_{\text{bu}}^\infty$ (top four panels) and the log – log derivative of $\Delta I_{\text{d}}/\Delta I_{\text{d}}^0$ vs. $1 - \Delta I_{\text{d}}/\Delta I_{\text{d}}^0$, for values of $\tilde{\tau}_{\text{bu}}$ equal to 0.45, 1.5, 6 and 30 (bottom four panels). They correspond to light curves of Star 2, seen at $i = 0$ deg (upper left), $i = 44.42$ deg (upper right), $i = 69.98$ deg (lower left), and $i = 90$ deg (lower right). The green, red and blue curves correspond to Σ_0 equal to 1.37, 0.75 and 0.41 g cm^{-2} . Black straight lines are the derived empirical laws.

this is not the case, and both the optically thin and thick parts of the disk contribute to observed behavior of ΔX vs. $\cos i$. This pseudo-photosphere concept will be important to understand the growth and decay rates of the light curves, discussed below. Figure 4.6 also shows that the excesses increase a little when moving from a low- to a high-mass star, for disks with the same other features. This is a consequence of the fact that the stellar flux relative to the disk flux increases with the luminosity of the star. Finally, by comparing the left and right panels of Figure 4.6, we see that, for pole-on angles, the excesses increase with the wavelength, as we notice that the excesses on the left panel are bigger than the ones on the right panel. This doesn't happen, however, for near-edge-on angles, where both $\Delta I_{\text{bu}}^\infty$ and $\Delta V_{\text{bu}}^\infty$ have similar values.

Both the pole-on and edge-on light curves have functions $\Delta X_{\text{bu}}(\tilde{\tau})/\Delta X_{\text{bu}}^\infty$ and $\Delta X_{\text{d}}(\tilde{\tau})/\Delta X_{\text{d}}^0$ that are qualitatively similar to each other, as exemplified by the upper-left and right panels of Fig. 4.5, suggesting that they could be approximated by simple and general formulas of $\tilde{\tau}$. This is illustrated in Fig. 4.7, where we compare the values of $\Delta I_{\text{bu}}(\tilde{\tau})/\Delta I_{\text{bu}}^\infty$ and $\Delta I_{\text{d}}(\tilde{\tau})/\Delta I_{\text{d}}^0$ (in the horizontal axis) with their log – log derivatives (in the vertical axis). As the panels exemplify, the curves are similar to each other in a wide range parameters ($\cos i$, Σ_0 and $\tilde{\tau}_{\text{bu}}$), and they can be roughly approximated by straight lines (shown in black). Therefore, the build-up and dissipation light curves (for inclinations not in the intermediate region) should roughly obey the following differential equations:

$$\frac{\partial \ln}{\partial \ln \tilde{\tau}} \left(1 - \frac{\Delta X_{\text{bu}}}{\Delta X_{\text{bu}}^\infty} \right) \approx -\eta_{\text{bu}} \frac{\Delta X_{\text{bu}}}{\Delta X_{\text{bu}}^\infty}, \quad (4.3.2)$$

and

$$\frac{\partial \ln}{\partial \ln(\tilde{\tau} - \tilde{\tau}_{\text{bu}})} \frac{\Delta X_{\text{d}}}{\Delta X_{\text{d}}^0} \approx -\eta_{\text{d}} \left(1 - \frac{\Delta X_{\text{d}}}{\Delta X_{\text{d}}^0} \right). \quad (4.3.3)$$

Eq. (4.3.2) is an ordinary differential equation (ODE) with the form given by $d \ln(1 - v)/d \ln x = -\eta v$. By defining the variable $y = 1 - v$, the ODE becomes $d \ln y/d \ln x = -\eta(1 - y)$, which is the exactly the form of Eq. (4.3.3). Therefore, we just have to solve the ODE

$$\frac{d \ln y}{d \ln x} = -\eta(1 - y), \quad (4.3.4)$$

which is a special case a class of non-linear ODEs called ‘‘Bernoulli equations’’⁵. The secret for solving Eq. (4.3.4) is defining $w = y^{-1}$. In that case, Eq. (4.3.4) becomes

$$\frac{dw}{w - 1} = \eta d \ln x, \quad (4.3.5)$$

which now is a linear ODE. Its solution is

$$w - 1 = (\xi x)^\eta, \quad (4.3.6)$$

where ξ is a constant of integration.

Now, returning to $y = w^{-1}$, we have the solution of Eq. (4.3.4), which corresponds to Eq. (4.3.3), and further making $v = y - 1$, we have the solution to the ODE that corresponds to Eq. (4.3.2). Therefore, the solutions of Eqs. (4.3.2) and (4.3.3) are, respectively,

$$\Delta X_{\text{bu}} = \Delta X_{\text{bu}}^\infty \left[1 - \frac{1}{1 + (\xi_{\text{bu}} \tilde{\tau})^{\eta_{\text{bu}}}} \right], \quad (4.3.7)$$

and

$$\Delta X_{\text{d}} = \Delta X_{\text{d}}^0 \left[\frac{1}{1 + (\xi_{\text{d}} (\tilde{\tau} - \tilde{\tau}_{\text{bu}}))^{\eta_{\text{d}}}} \right]. \quad (4.3.8)$$

The continuity condition given by the fact that a bump or dip has a build-up phase followed by a dissipation phase requires that

$$\Delta X_{\text{d}}^0 = \Delta X_{\text{bu}}^\infty \left[1 - \frac{1}{1 + (\xi_{\text{bu}} \tilde{\tau}_{\text{bu}})^{\eta_{\text{bu}}}} \right]. \quad (4.3.9)$$

The parameters ξ_{bu} and ξ_{d} are constants of integration whose values were determined by fitting Eqs. (4.3.7) and (4.3.8) to the computed light curves. The tables of the parameters $\Delta X_{\text{bu}}^\infty$ and the fitted parameters ξ_{bu} and ξ_{d} are given in Appendix A, in Tables A.1, A.2, A.3 and A.4 for the *BVRI* bands, respectively. Examples of plots of the light curves given by Eqs. (4.3.7) and (4.3.8) compared with the synthetic light curves generated by our grid are shown in Appendix B. As briefly explained in Appendix A, the values of the exponents η_{bu} and η_{d} were empirically determined to best match the model light curves. Their values are dependent on the photometric band, and are listed in Table 4.4.

⁵ <http://eqworld.ipmnet.ru/en/solutions/ode/ode0104.pdf>

Table 4.4 - Values of η 's.

	B	V	R	I
η_{bu} (edge-on)	0.8	0.8	0.8	0.8
(pole-on)	0.8	0.8	0.8	0.8
η_{d} (edge-on)	1.5	1.5	1.5	1.5
(pole-on)	1.1	1.2	1.3	1.4

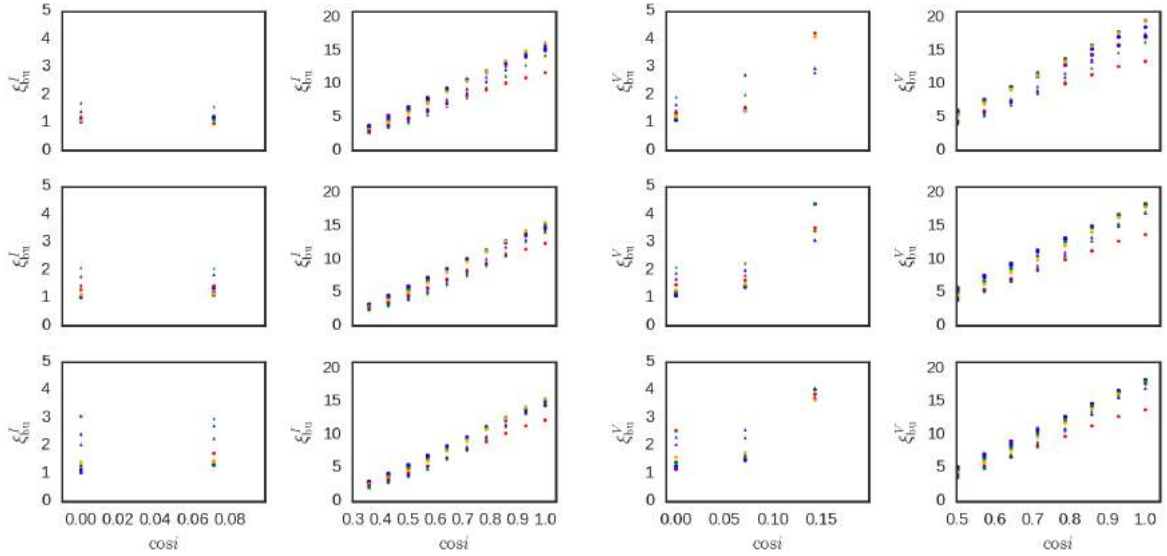


Figure 4.8: The I - and V -band values of ξ_{bu} for our grid vs. $\cos i$. *First column:* Edge-on models for the I -band. *Second column:* Pole-on models for the I -band. *Third column:* Edge-on models for the V -band. *Fourth column:* Pole-on models for the V -band. From top to bottom, the results for Star 1, 2, and 3, respectively. The markers are the same as in Fig. 4.6.

Representative I - and V -band values of ξ_{bu} and ξ_{d} for our grid are shown in Figs. 4.8, 4.9 and 4.10 (the values of ξ_{bu} and ξ_{d} for the BR bands show qualitatively similar patterns to the ones presented in these figures). Each row shows the results for a different star. The panels of the first and third columns are for edge-on models in the I and V bands, respectively. The panels of the second and fourth columns are for pole-on models in the I and V bands, respectively.

The values of ξ are directly related to the rate of photometric variations: the smaller the ξ the slower the variation (see Eqs. 4.3.7 and 4.3.8). Figure 4.8 exemplify the strong variation of ξ_{bu} with i , for the pole-on case (see second and fourth columns). This is probably due to the fact that, in the build-up process, the density grows inside-out (see lower panels of Fig. 3.3), which means that the optically thick part of the disk, which is an expanding pseudo-photosphere, forms first, and the optically thin part of the disk takes longer to be built. Since the optical excess of the disk is given by $\Delta X \propto \cos i F_{\text{thick}} +$

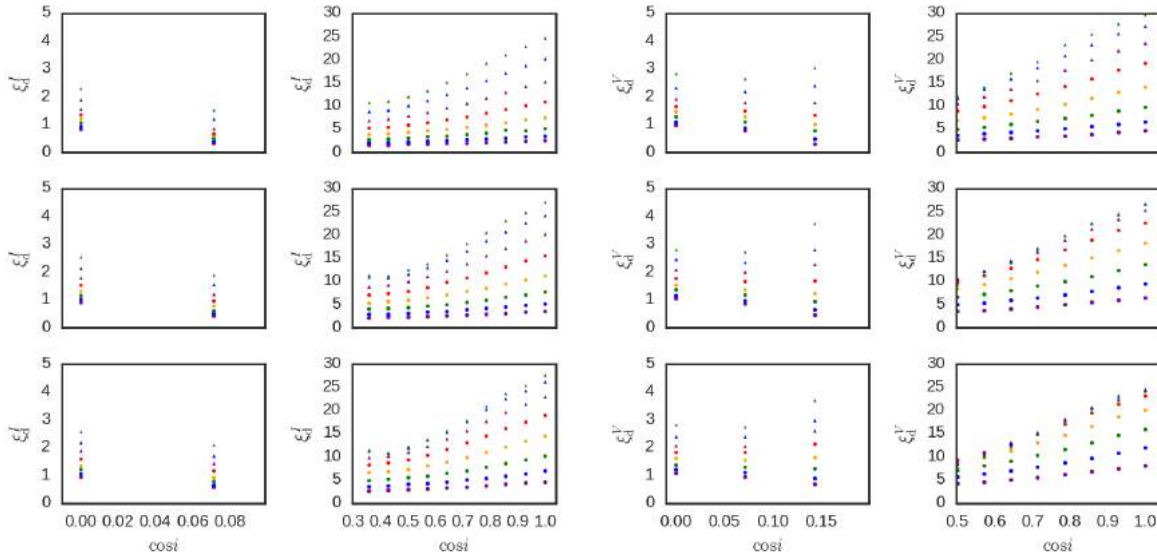


Figure 4.9: Selected I and V -band values of ξ_d for our grid vs. $\cos i$. The scaled build-up time was fixed to $\tilde{\tau}_{bu} = 2.25$. *First column:* Edge-on models for the I -band. *Second column:* Pole-on models for the I -band. *Third column:* Edge-on models for the V -band. *Fourth column:* Pole-on models for the V -band. From top to bottom, the results for Star 1, 2, and 3, respectively. The markers are the same as in Fig. 4.6.

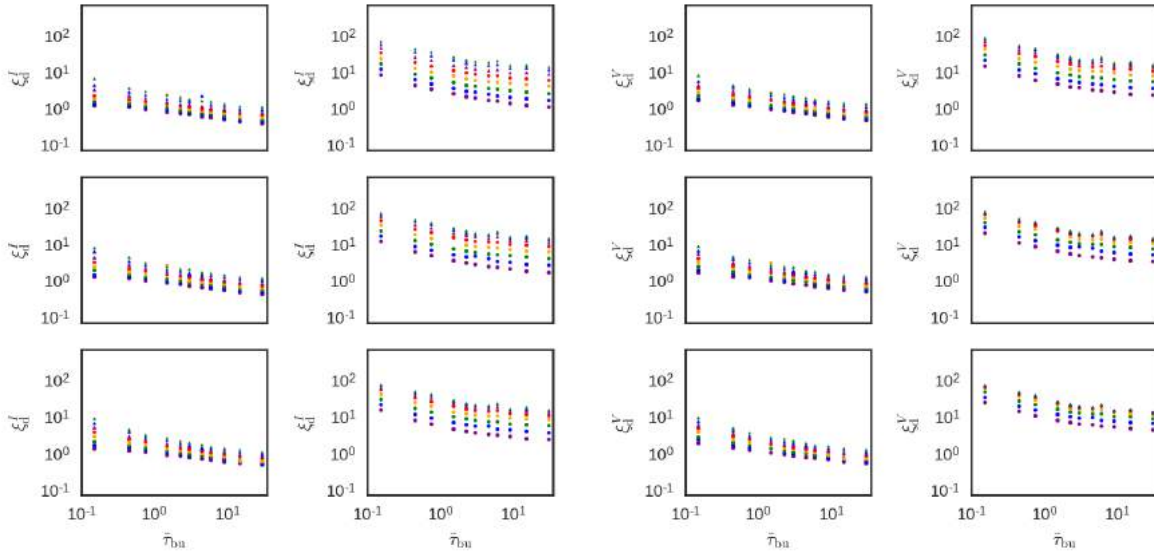


Figure 4.10: Selected I and V -band values of ξ_d for our grid vs. $\tilde{\tau}_{bu}$. *First column:* Edge-on models for the I -band with $i = 90$ deg. *Second column:* Pole-on models for the I -band with $i = 0$ deg. *Third column:* Edge-on models for the V -band with $i = 90$ deg. *Fourth column:* Pole-on models for the V -band with $i = 0$ deg. From top to bottom, the results for Star 1, 2, and 3, respectively. The markers are the same as in Fig. 4.6.

F_{thin} , it follows that, as we move from pole-on to edge-on angles, only the optically thick contribution (proportional to $\cos i$) varies. As a consequence, the observed rate of increase in flux moves from being more to less optically thick dominated.

In the dissipation process, the density rapidly adjusts to a self-similar dissipation pattern in the inner disk (see lower panels of Fig. 3.3). Therefore, the flux from the disk is the result of the decrease and disappearance of the optically thick region - transformed into an optically thin region - and the diminishing of the whole optically thin region. The pole-on values of ξ_d (second and fourth panels of Fig. 4.9) are affected by $\cos i$ to a lesser extent, when compared to the values of ξ_{bu} . In the dissipation process, by the same reasoning applied to the build-up process, since the optically thick emission is attenuated by the effect of $\cos i$, its disappearance has a reduced effect for more inclined disks and, therefore, the disk should apparently disappear at a slower rate.

The values of ξ_d also show great variation with the asymptotic surface density (Figs. 4.9 and 4.10). More specifically, increasing Σ_0 results in a light curve with a slower decay rate. This is probably due to different levels of saturation in the optically thick region. The denser the optically thick region, the bigger its optical depth and the greater the amount of time for it to turn into an optically thin region.

In addition, Fig. 4.10 shows that ξ_d strongly depends on the scaled build-up time. As expected from the mass reservoir effect (Sect. 3.3), increasing $\tilde{\tau}_{bu}$ results in smaller values of ξ_d , which implies slower decay rates.

From the above an important conclusion can be drawn: viscosity is not the only parameter affecting the rate of photometric variations in a Be light curve. The stellar parameters, the asymptotic surface density, as well as the inclination angle, all affect the observed shape of the light curve. Thus, extracting α from light curves, one of the main goals of this work, cannot be done without some knowledge about these parameters.

4.4 Fitting pipeline

So far, our model light curves were given in terms of the dimensionless time parameter, $\tilde{\tau}$. Thus, an equation is necessary to transform from the physical time t to $\tilde{\tau}$, in order to connect the real light curves to our simulated ones.

A variation in the time parameter, $d\tilde{\tau}$, is related to a variation in physical time by $d\tilde{\tau} = dt/\tau(t)$, where $\tau(t)$ depends on 3 stellar parameters (M , R_{eq} , T_{eff}) and the viscous parameter $\alpha(t)$ (Eq. 3.1.13). For a given Be star, the build-up phase starts at t_1 , and ends at t_2 , when dissipation begins. Thus, the build-up time is given by $t_2 - t_1$. In this work, following the results of Ghoreyshi et al. (2016), we explore the possibility that the viscosity parameter may be different at build-up ($\alpha(t) = \alpha_{bu}$, for $t_1 \leq t < t_2$) and dissipation ($\alpha(t) = \alpha_d$, for $t \geq t_2$). Therefore, the transformation equation from t to $\tilde{\tau}$ is

$$\tilde{\tau} = \begin{cases} \alpha_{bu} \frac{t-t_1}{\alpha\tau}, & t_1 \leq t < t_2 \\ \alpha_{bu} \frac{t_2-t_1}{\alpha\tau} + \alpha_d \frac{t-t_2}{\alpha\tau}, & t \geq t_2 \end{cases}, \quad (4.4.1)$$

which is such that, as t goes from t_1 to t_2 , $\tilde{\tau}$ goes from 0 to $\tilde{\tau}_{\text{bu}}$, given by

$$\tilde{\tau}_{\text{bu}} = \alpha_{\text{bu}} \frac{t_2 - t_1}{\alpha\tau}, \quad (4.4.2)$$

and for t larger than t_2 , we see that $\tilde{\tau} > \tilde{\tau}_{\text{bu}}$. Recall that $\alpha\tau$, defined in Eq. 3.1.13, is a quantity dependent only on the stellar parameters and the disk temperature (see the upper-right panel of Fig. 4.4 for the values of $\alpha\tau$ for the stellar models of Table 4.3).

Substitution of Eq. (4.4.1) into Eqs. (4.3.7), (4.3.8) and (4.3.9), gives the following equation for fitting an observed bump

$$\Delta X(t) = \begin{cases} \Delta X_{\text{bu}}^{\infty} \left(1 - \frac{1}{1 + [C_{\text{bu}}(t-t_1)]^{\eta_{\text{bu}}}} \right), & t_1 \leq t < t_2 \\ \Delta X_{\text{bu}}^{\infty} \left(1 - \frac{1}{1 + [C_{\text{bu}}(t_2-t_1)]^{\eta_{\text{bu}}}} \right) \frac{1}{1 + [C_{\text{d}}(t-t_2)]^{\eta_{\text{d}}}}, & t \geq t_2 \end{cases} \quad (4.4.3)$$

where

$$C_{\text{bu}} = \alpha_{\text{bu}} \frac{\xi_{\text{bu}}}{\alpha\tau}, \quad (4.4.4)$$

and

$$C_{\text{d}} = \alpha_{\text{d}} \frac{\xi_{\text{d}}}{\alpha\tau} \quad (4.4.5)$$

are coefficients related to the rate of photometric variations. The values of the parameters $\Delta X_{\text{bu}}^{\infty}$, ξ_{bu} and ξ_{d} were tabulated in Appendix A, by fitting the respective empirical laws to the model grid.

Our goal is to fit an observed light curve with Eq. 4.4.3, in order to obtain, in a self-consistent way, all the stellar and disk parameters of interest. For that, the following chain of procedures is adopted:

1. Find a light curve of a Be star that contains at least one clear inactive phase and one complete photometric bump.
2. Obtain the magnitudes X_* at the inactive phase. Subtract these magnitudes from the light curve and obtain the excesses $\Delta X(t)$.

Without a clear inactive phase, it is not possible to obtain the pure photospheric brightness (e.g., the horizontal purple straight lines in Fig. 3.1) and, consequently, it is not possible to know how much of the observed bumps represent the disk contribution to the total flux. In addition, the photometric bump must contain a completely identified build-up phase (from which the instants t_1 and t_2 can be extracted) along with a considerable fraction of the dissipation phase.

3. Fit Eq. (4.4.3) to the selected bumps, obtaining the coefficients $\Delta X_{\text{bu}}^{\infty}$, C_{bu} and C_{d} , as well as the times t_1 and t_2 for the onsets of build-up and dissipation.

4. Transform the magnitudes at the inactive phase, X_* , to absolute magnitudes, M_{X_*} , by correcting for the distance to the star and reddening at each observed band.

Given the theoretical dependence of the coefficients in Eq. 4.4.3 on the stellar parameters, the absolute magnitudes are required to estimate the stellar parameters (M , W and t/t_{MS}). From them, the parameter $\alpha\tau$ (see Eq. 3.1.13) can be estimated. Clearly, if the stellar parameters are known from some other way (e.g., by spectroscopic analysis), this requirement is no longer necessary. Unfortunately, this is not the case for our sample (see Chapter 5 below).

5. Estimate the stellar parameters, the geometric parameter ($\cos i$) and the bump parameters (Σ_0 , α_{bu} and α_{d} , for each bump) that best reproduce the fitted stellar (M_{X_*}) and bump ($\Delta X_{\text{bu}}^\infty$, C_{bu} and C_{d}) parameters (see Eqs. 4.4.4 and 4.4.5 and the parameters $\Delta X_{\text{bu}}^\infty$, ξ_{bu} and ξ_{d} from Sect. 4.3).

In practice, the above process involves several complications (e.g., estimating the goodness of the fit) that are described in the next section.

4.5 Fitting using MCMC sampling

Never tell me the odds!

Han Solo to C-3PO, in Star Wars:
The Empire Strikes Back

The task of fitting the measured stellar (M_{X_*}) and bump parameters ($\Delta X_{\text{bu}}^\infty$, C_{bu} and C_{d}) and estimating the model parameters – step 5, above – was done using the Markov-Chain Monte Carlo (MCMC) sampling technique. In this section, we describe this technique and how it was used to estimate the parameters of our models based on light curves described in Chapter 6.

4.5.1 Statistical considerations

A certain physical system will be defined by N_m model parameters. Together, they compose the N_m -dimensional vector \mathbf{m} , which represents the state of the physical system. The physical system will also be associated to N_D observed data quantities, which, together, compose the N_D -dimensional vector \mathbf{D} . When fitting models to observations, we are interested in obtaining a probabilistic distribution of states \mathbf{m} given the observed data \mathbf{D} . With such a distribution, we can calculate mean values, standard deviations, medians and percentiles, etc.

In the whole space of possibilities of our different physical systems of Be stars, there is a small subset of those systems, which we refer to as $\text{d}\mathcal{M}$, which contains a small list of

possible states, and there is also a small subset of those systems, which we refer to as $d\mathcal{D}$, which contains a small list of possible observations. The probability of getting physical systems of Be stars with states in the small set $d\mathcal{M}$ and with observed data in the small set $d\mathcal{D}$ is

$$P(d\mathcal{M} \cap d\mathcal{D}) = P(d\mathcal{M} | d\mathcal{D})P(d\mathcal{D}) = P(d\mathcal{D} | d\mathcal{M})P(d\mathcal{M}), \quad (4.5.1)$$

where we have applied the definition of conditional probabilities that say that the “probability of A and B” equals the “probability of B” times the “probability of A, given B”.

Now, these small probabilities can be rewritten in terms of probability density functions, whose interpretations are as follows:

- $P(d\mathcal{M}) \rightarrow \pi(\mathbf{m}) d^{N_m} m$, where $\pi(\mathbf{m})$ is the probability density of a Be star with the state \mathbf{m} , independent of the observations. It represents, therefore, our prior knowledge of the distribution of Be stars. We refer to $\pi(\mathbf{m})$ as the “prior distribution”.
- $P(d\mathcal{D} | d\mathcal{M}) \rightarrow L(\mathbf{D} | \mathbf{m}) d^{N_D} D$, where $L(\mathbf{D} | \mathbf{m})$ is the probability density referred to as the “likelihood of a Be star with the observed data \mathbf{D} , given the state \mathbf{m} ”. This distribution depends on the uncertainties of the observed data. The smaller those are, the sharper the likelihood of the data \mathbf{D} around the state \mathbf{m} .
- $P(d\mathcal{M} | d\mathcal{D}) \rightarrow p(\mathbf{m} | \mathbf{D}) d^{N_m} m$, where $p(\mathbf{m} | \mathbf{D})$ is our desired distribution: the probability density of a Be star with state \mathbf{m} , given the observed data \mathbf{D} . It is called the “posterior probability”: the probability obtained by multiplying our prior knowledge with the likelihood of the model after observations have been made.
- $P(d\mathcal{D}) \rightarrow g(\mathbf{D}) d^{N_D} D$, where $g(\mathbf{D})$ is just a normalizing constant for the distribution $p(\mathbf{m} | \mathbf{D})$.

Substitution of these probability density functions into Eq. (4.5.1) results in the following equation for the probability densities

$$p(\mathbf{m} | \mathbf{D}) = \frac{L(\mathbf{D} | \mathbf{m}) \pi(\mathbf{m})}{g(\mathbf{D})} \quad (4.5.2)$$

where $g(\mathbf{D}) = \int L(\mathbf{D} | \mathbf{m}) \pi(\mathbf{m}) d^{N_m} m$.

4.5.1.1 MCMC sampling with `emcee`

Spock: “Random chance seems to have operated in our favor”

McCoy: “In plain, non-Vulcan English, we’ve been lucky”

Spock: “I believe I said that, Doctor.”

Spock to McCoy in Star Trek: The Original Series, episode “The Doomsday Machine”

In statistics, the quantities of interest are usually integrals of functions ϕ , weighed by the probability density p , over a certain domain: $\int p(\mathbf{m} | \mathbf{D}) \phi(\mathbf{m}) d^{N_m} m$. If, however, the dimension of the parameter space N_m is too big and/or the probability density p is too “complicated”, the problem of calculating such integral easily becomes untractable by ordinary means.

A Markov Chain (MC) is a mathematical system that undergoes random transitions from one state to another on a state space. The next state depends only on the current state and not on the sequence of events that preceded it. A Markov Chain, therefore, is a memoriless process.

Some MCs have stationary distributions. For these MCs, the stationary distributions will be asymptotically reached by the states after a sufficiently large number of iterations, regardless of the initial state of the chain. One example of such a Markov Chain is the one that is constructed by the famous “Metropolis algorithm”. In that algorithm, a certain probability density function is given as input and a Markov Chain is generated in which the states converge to a sample distributed according to the probability density that was given⁶.

What the Metropolis algorithm does is exactly the purpose of any Markov Chain Monte Carlo (MCMC) algorithm. MCMC methods are, therefore, a class of algorithms, which utilize random numbers, for generating samples of states $\{\mathbf{m}_r\}_{r=1}^R$ from a probability distribution $p(\mathbf{m} | \mathbf{D})$ which is given as input. They construct a Markov chain that has the distribution $p(\mathbf{m} | \mathbf{D})$ as its stationary distribution (MacKay, 2003). The output of the MCMC algorithm is the sample of states $\{\mathbf{m}_r\}_{r=1}^R$.

In the stationary distribution, the states are more densely distributed where the probability density is higher. In fact the stationary sample is such that $p(\mathbf{m}_r | \mathbf{D}) d^{N_m} m_r \rightarrow \frac{1}{R}$, where $d^{N_m} m_r$ is a measure of the hypervolume occupied by a single state. Therefore, one of the most important consequences of this fact is the ease of calculating the aforementi-

⁶ The Metropolis algorithm was presented in 1953, in a work whose main purpose was the numerical calculation of the equation of state for a system of rigid spheres in two dimensions.

oned integrals required for statistical analysis, namely

$$\int p(\mathbf{m} | \mathbf{D}) \phi(\mathbf{m}) d^{N_m} m \rightarrow \frac{1}{R} \sum_{r=1}^R \phi(\mathbf{m}_r). \quad (4.5.3)$$

One final and crucial feature of MCMC algorithms (such as the Metropolis algorithm) is that the probability density $p(\mathbf{m} | \mathbf{D})$, which is given as input, does not need to be normalized, because the algorithms deal only with ratios of these distributions. Therefore, we don't need to calculate the integral $g(\mathbf{D})$ in Eq. 4.5.2. If we had to perform such a calculation, there would be no advantage in the MCMC technique.

In this work, we use `emcee` (Foreman-Mackey et al., 2013), which is Python implementation of the Affine Invariant MCMC Ensemble sampler of Goodman and Weare (2010). Other samplers, however, are also available in `emcee`, like the classic Metropolis Algorithm, for example. In the context of `emcee`, the “states” are referred to as “walkers”. According to the `emcee` website⁷: “Walkers are the members of the ensemble. They are almost like separate Metropolis-Hastings chains but, of course, the proposal distribution for a given walker depends on the positions of all the other walkers in the ensemble.”

When `emcee` is used for approximating a multi-dimensional posterior probability density, the ensemble of “walkers” starts to move around the N_m -dimensional space, according to the MCMC algorithm. There will be a certain number of MC iterations required before a near stationary state, according to the probability density $p(\mathbf{m} | \mathbf{D})$, is reached by the walkers. This first phase where the walkers move towards the regions of high probability is called the “burn-in” phase, and its resulting sampling is discarded because it is not the desired stationary sampling. It is usually a trial-and-error problem to determine the minimum number of steps that are needed to converge to the stationary distribution within an acceptable error. After the burn-in, the walkers are well localized near the most likely regions after which their subsequent positions are then recorded. This is the sampling phase of the Markov Chain, which never ends. This chain of states is used as the sample of the desired distribution $p(\mathbf{m} | \mathbf{D})$.

4.5.2 The likelihood and prior distributions of our problem

In our fitting procedure for each light curve containing N_{bumps} identified bumps, there are $4 + 5N_{\text{bumps}}$ model parameters. These are the 3 stellar parameters (M , t/t_{MS} , W), the geometric parameter ($\cos i$), and, for each bump in the light curve, there are 5 additional parameters: the initial times of the build-up and dissipation phases (t_1 and t_2), the asymptotic surface density (Σ_0), and the viscosity parameters during the build-up and dissipation phases (α_{bu} and α_{d}). The state space of our system is thus a $(4 + 5N_{\text{bumps}})$ -dimensional space, and the problem of estimating these $4 + 5N_{\text{bumps}}$ model parameters,

⁷ <http://dan.iel.fm/emcee/current/>

which can be represented by the $(4 + 5N_{\text{bumps}})$ -dimensional vector \mathbf{m} , can be addressed by MCMC sampling of the probability distribution of these models, given the data \mathbf{D} from the light curves.

We assume that the errors of each of the observations in the light curves follow a Gaussian distribution and, therefore, the likelihood of a Be star with the observed data, given some model parameters, is

$$L(\mathbf{D} | \mathbf{m}) \propto e^{-\frac{1}{2}\chi^2}, \quad (4.5.4)$$

where

$$\chi^2 = \chi_{\text{diskless}}^2 + \chi_{\text{bump}}^2, \quad (4.5.5)$$

and

$$\chi_{\text{diskless}}^2 = \sum_{\text{bands}} \frac{(M_{X^*}^{\text{model}} - M_{X^*}^{\text{obs}})^2}{\sigma^2(M_{X^*}^{\text{obs}})}, \quad (4.5.6)$$

and

$$\chi_{\text{bump}}^2 = \sum_{\text{bands}} \sum_{\text{bumps}} \frac{1}{N_t} \sum_{i=1}^{N_t} \frac{(\Delta X_i^{\text{model}} - \Delta X_i^{\text{obs}})^2}{\sigma^2(\Delta X_i^{\text{obs}})}, \quad (4.5.7)$$

where N_t is the number of datapoints for a given bump at a given photometric band.

From Eq. (4.5.7), we see that the goodness of the fit for each bump is given by the reduced chi-square of a model light curve with respect to the data points. The sums in Eqs. (4.5.6) and (4.5.7) then show that each magnitude during inactivity and each bump in each band are treated with equal weight in the final χ^2 used in the likelihood function (Eq. 4.5.5).

The prior distribution π represents our prior knowledge of the distribution of Be stars. We assume it to be

$$\pi(\mathbf{m}) \propto M^{-2.3} f_{\text{Be}}(M) e^{-\frac{(W - \langle W \rangle)^2}{2\sigma_W^2}}, \quad (4.5.8)$$

where the factor $M^{-2.3}$ is the initial mass function (IMF) of Kroupa (2001), and $f_{\text{Be}}(M)$ represents the fraction of Be stars relative to the number of B stars, estimated by Martayan et al. (2007, their Fig. 6). Finally, the Gaussian factor comes from the distribution of rotational velocities in the sample of Be stars, here estimated from Rivinius et al. (2006), assuming $\langle W \rangle = 0.81$ and $\sigma_W = 0.12$.

For sampling of the model parameters, we have chosen $50 \times (4 + 5N_{\text{bumps}})$ “walkers”, for each light curve. For a randomly chosen set of parameters sampled by `emcee` in the course of the simulation, the corresponding stellar and bump observables are calculated by a multidimensional linear interpolation of the model grid (see the tables in Appendix A and the diskless models of Table 4.3). During the raffle of parameters the prior probability is set to zero if one of the sampled values lies outside of this allowed range (Tables 4.1 and 4.3). We found that 1000 iterations in the burn-in phase is sufficient for the convergence of all our models.

In Chapter 5 we present a selection of light curves of Be stars from the SMC, and measure their stellar and bump quantities (steps 1 to 4 of the pipeline). Later, in Chapter 6, we apply step 5 of the pipeline, as described in Sect 4.4, in order to estimate the relevant parameters of the selected Be stars.

The remarkable light curves of Be stars from the Magellanic Clouds

Look how they shine for you

Guy Berryman, in the song “Yellow”,
from Coldplay

From the previous chapters, we conclude that the most reliable and direct way of estimating the α viscosity parameter is to consider time-dependent disk behavior, where the diffusive effect of viscosity will have clear observational counterparts. Therefore, light curves of long temporal coverage, such as the ones given by microlensing or planetary transit surveys are excellent instruments to study the dynamical processes acting on the disk, as it builds-up and dissipates. Also, our studies have shown that other important byproducts of studying the light curves of Be stars are the estimations of the mass and angular momentum loss rates of the star. These physical quantities are important estimates for stellar evolutionary models and may give us clues about the “Be mechanism”.

In 1986, astronomer Bohdan Paczyński proposed to use of gravitational microlensing to look for dark matter in the form of massive compact halo objects (MACHOs). By observing fields crowded with background stars, a MACHO would be detected when passing nearly in front of a background star and causing the star to appear brighter in a very distinct way (Aubourg et al., 1993). Since then, microlensing surveys like OGLE (Udalski et al., 1992), MACHO (Alcock et al., 1997) and EROS (Aubourg et al., 1993) resulted in light curves of millions of stars. It suffices to say that MACHOs were indeed found soon after the campaigns started. But, what is important for our work is that many thousands of light curves of variable Be stars, with years of coverage, were recorded in these campaigns.

In the recent decades, astronomers also started to detect exoplanets (planets far outside our Solar System). One of the methods of detecting such planets is the “transit method”, in which a planet in an edge-on orbit around the star passes in front of the star, causing a minute dimming. Periodic dimmings are the signature of planets orbiting other

stars. OGLE-TR-56b was the first exoplanet discovered by the transit method alone, in November 2002¹, and in the last ten to fifteen years, there has been an enormous increase in the number of high precision photometric surveys, looking for transits of exoplanets. Some of these surveys are ground based, like KELT (Pepper et al., 2007) and SuperWASP (Pollacco et al., 2006). Some are space missions, like CoRoT² and Kepler³. In order to find transiting planets at the moment of transit, and, later, to establish that they are periodic, the photometric surveys must continuously cover portions of sky containing many stars for long periods of time. Consequently, light curves of many Be stars with years of coverage were also recorded by these surveys.

This chapter is devoted to a description of the features of light curves of Be star candidates from the Magellanic Clouds and to a selection of some of these light curves. We obtained hundreds of light curves from the OGLE-II (Udalski et al., 1997) and OGLE-III (Udalski, 2003; Udalski et al., 2008) photometric surveys, for stars selected from catalogs of Be star candidates in the SMC (Mennickent et al., 2002) and the LMC (Sabogal et al., 2005). We ultimately, selected light curves for 54 SMC Be star candidates containing clear inactive phases and 81 bumps and dips.

5.1 Selections of Be stars from the SMC and LMC

Keller et al. (2002) selected 1279 light curves from the MACHO photometric survey from the Large Magellanic Cloud (LMC) galaxy which were believed to be light curves of variable Be stars. They did so by: 1) selecting light curves with colors and magnitudes in regions that correspond to the locations of Be stars in color-magnitude diagrams (CMD); 2) selecting (automatically) from these light curves the ones that satisfied a certain criterium of variability; and 3) excluding the “contaminants” (e.g., eclipsing binaries) by visual inspection. The remaining 1279 light curves showed the following morphologies, illustrated in Fig. 5.1:

- mode 1 - “bumper events”
- mode 2 - “flicker events”
- mode 3 - “step events”
- mode 4 - “baseline variations”
- mode 5 - “fading events”

¹ The exoplanet HD 209458 b (sometimes unofficially called “Osiris”), however, discovered in November 1999 by the “radial velocity method”, was also found to be transiting before the discovery of OGLE-TR-56b

² <https://corot.cnes.fr/en/COROT/index.htm>

³ https://www.nasa.gov/mission_pages/kepler/main/index.html

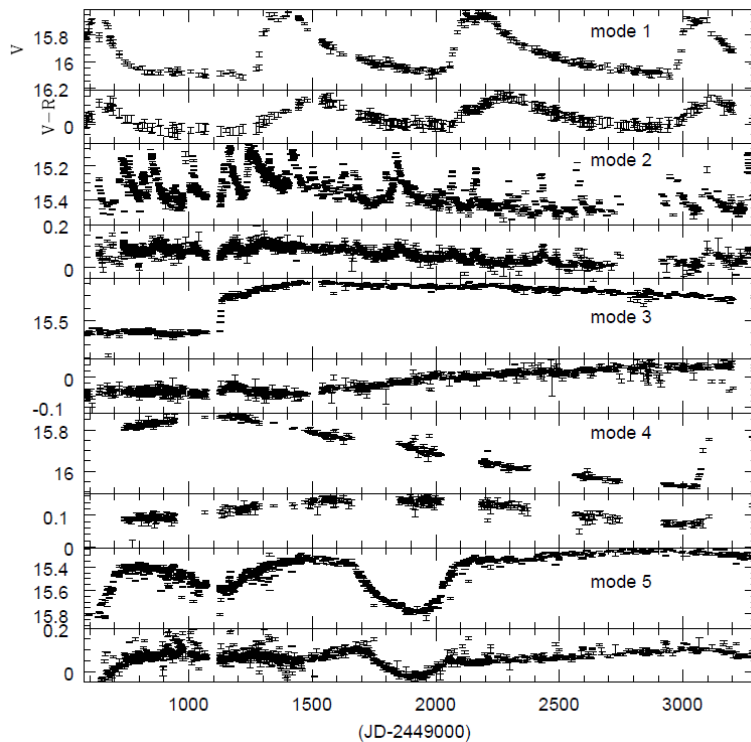


Figure 5.1: V light curves and $V - R$ color curves for examples of the five modes of variability of Keller et al. (2002).

In fact, several different modes frequently appear in the light curves for a single star.

A subset of 102 of those stars also were examined spectroscopically in a limited number of instances. The majority (91%) of the spectroscopic sample was found to exhibit Balmer emission lines in at least one epoch. Therefore, it was confirmed that at least $\sim 90\%$ of the light curves obtained by their photometric selection method were Be stars.

Mennickent et al. (2002) selected 1056 OGLE-II light curves of Be star candidates from the Small Magellanic Cloud (SMC) galaxy, with a method similar to the one of Keller et al. (2002). They also: 1) selected light curves inside regions in CMDs; and 2) visually inspected the light curves, removing spurious variables, Cepheids and eclipsing binaries. They classified the morphologies of their light curves in a little different way, shown in Figs. 5.2 and 5.3:

- Type-1 events (showing sharp outbursts or hump-like outbursts, roughly corresponding to mode 1 and mode 2 events of Keller et al. (2002))
- Type-2 events (showing “high” and “low” states, roughly corresponding to the mode 3 events of Keller et al. (2002))
- Type-3 events (showing periodic or near-periodic events)
- Type-4 events (showing non-periodic outbursts)

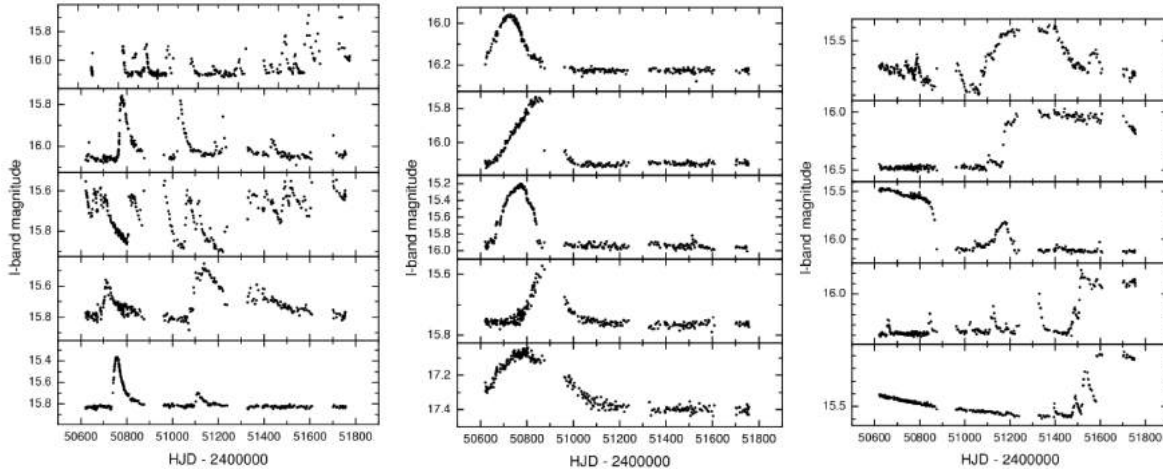


Figure 5.2: Examples of OGLE II light curves selected as Be star candidates. *Left*: Type-1 light curves showing sharp outbursts. *Middle*: Type-1 light curves showing hump-like outbursts. *Right*: Type-1/Type-2 light curves showing outbursts and “high” and “low” states. (Credits: Mennickent et al., 2002)

The authors found that the majority of the light curves fall into the type-4 category. In fact, the relative fraction of these light curves was: 64.9% objects showing type-4 light curves, 13.2% objects showing type-1 light curves, 14.6% showing type-2 light curves, and 7.4% stars showing type-3 light curves. Figure 5.4 (left) shows the distributions of these objects in a color-magnitude diagram, together with a main sequence track.

In a continuation of the previous work, Sabogal et al. (2005) selected 2446 OGLE-II light curves of Be star candidates of from the LMC galaxy. They found 60.0% type-4, 23.1% type-1, 6.1% type-2, 6.1% type-3 and 4.0% type-1/type-2 light curves. Figure 5.4 (right) shows the distributions of their objects also in a color-magnitude diagram, together with a main sequence track. As for the case of the selection of Mennickent et al. (2002), we see that their objects occur mostly for very late O-type stars and early B-type stars.

The type-4 light curves should correspond to Be stars showing episodes of mass injection more complicated than the simple build-up followed by dissipation scenario described in Sect. 4.1.

Most interesting for us is the type-1 group ($\sim 13\%$ of the sample), composed by light curves that show single sharp or hump-like bumps, like the bumps of the light curve of SMC_SC1 75701 (Fig. 3.1). These bumps should be the result of single nearly continuous episodes of mass injection followed by dissipation of the disk, like the theoretical scenario explored in Sect. 4.1. The “bumper events” and “flicker events” of Mennickent et al. (2002) more or less correspond to the bumps of type-1 light curves, but also to features of the more irregular type-4 light curves. The bumpers have durations of a few hundred days, while the flicker events are faster, with durations of a few dozens of days. Dips like the one exemplified by the light curve of SMC_SC6 128831 (Fig. 3.1) were called “fading events” by Mennickent et al. (2002). The frequency of these events was much smaller than that of the bumpers (Mennickent et al., 2002), which is in accordance with the picture

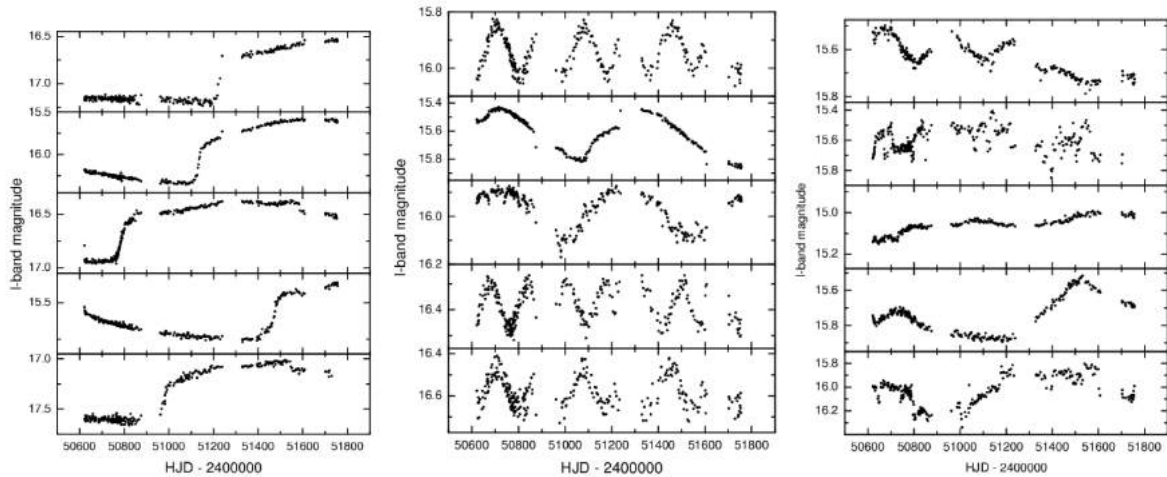


Figure 5.3: Examples of OGLE II light curves selected as Be star candidates. *Left*: Type-2 light curves showing “high” and “low” states. *Middle*: Type-3 light curves showing periodic oscillations. *Right*: Type-4 light curves showing random variability. (Credits: Mennickent et al., 2002)

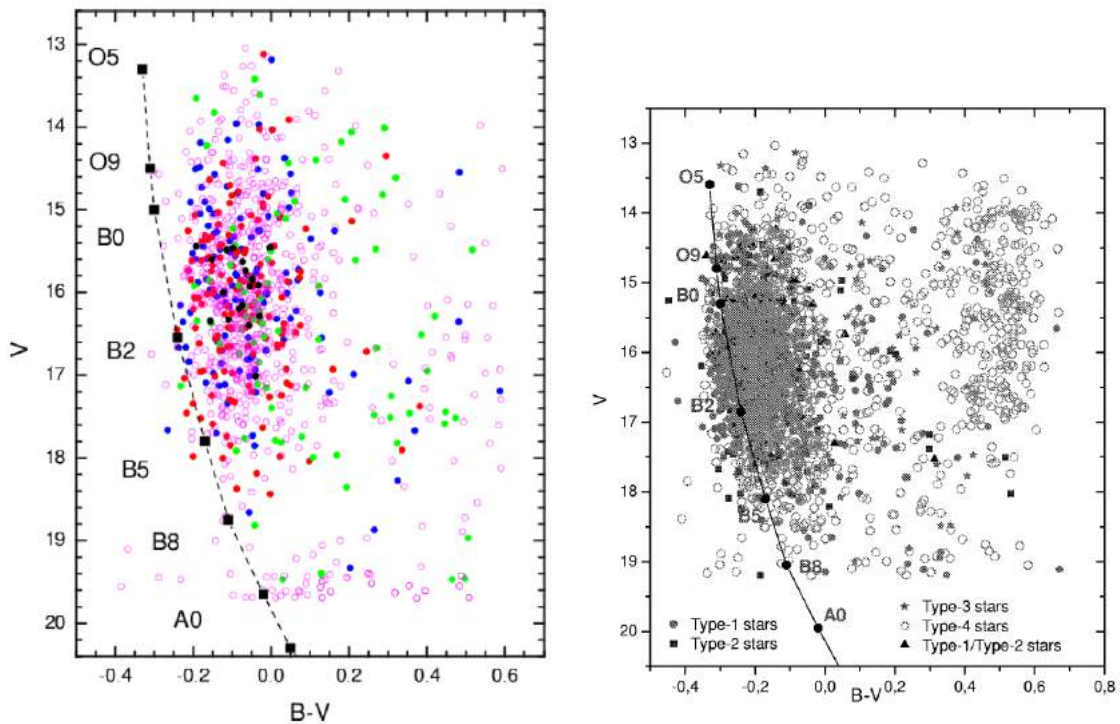


Figure 5.4: *Left*: CMD diagram for the selected stars from the SMC. Blue dots correspond to type-1 stars, red dots to type-2 stars, green dots to type-3 stars, circles to type-4 stars and black dots to type-1/type-2 stars. A main sequence track is shown for reference. (Credits: Mennickent et al., 2002) *Right*: CMD diagram for the selected stars from the LMC. A main sequence track is shown for reference. (Credits: Sabogal et al., 2005)

that fading events are associated with the less numerous shell stars.

The type-2 group ($\sim 14\%$ of the sample of Mennickent et al. (2002)), containing light curves showing high and low plateaus, also has some interesting cases for our purposes.

High plateaus are usually the photometric result of a longer build-up process in which a near steady-state has been reached in the inner disk. The low plateaus are frequently the portions of the light curve during inactive phases.

Paul et al. (2012) studied the spectral properties of stars from the catalogues of Mennickent et al. (2002) and Sabogal et al. (2005). For the candidates from the SMC, they found that the majority of type-1 and type-2 light curves belong to early B type stars with emission features characteristic of circumstellar material (Paul et al., 2012). Therefore, these light curves are very likely from Be stars. For the candidates of the LMC, however, there wasn't a clear emission feature for a fraction of the type-1 light curves.

5.2 OGLE light curves of Be star candidates

In this work, we used both the catalogs of Be star candidates of Mennickent et al. (2002) and Sabogal et al. (2005), and, later, we focused just on the former.

In 2012, our collaborators Thomas Rivinius and Xavier Haubois downloaded public *I*-band light curves of the Be star candidates of these two catalogs, from the OGLE-II survey⁴. Later, they contacted the OGLE team, in order to obtain the data in the other bands and the OGLE-III data for the stars in the catalogs. They were kindly sent by Igor Soszyński from the OGLE team, who provided the *V*- and *B*-band OGLE-II data of the stars and the corresponding OGLE-III *V*- and *I*-band data for a fraction of the stars, obtained by cross-identifications. The OGLE-II portions of the light curves range roughly from January 1997 to December 2000. The OGLE-III portions of the light curves range roughly from June 2001 to May 2009. Our resulting light curves, therefore, covered roughly 12 years.

5.2.1 Our selection of bumps from the SMC

The light curves were visually inspected according to the criteria of item 1, Sect. 4.4; i.e., light curves with at least one clear inactive phase and one bump. In this initial work we focussed on well-behaved light curves with clear bumps. We also avoided the short events (flickers, with build-up times $\lesssim 15$ days), due to the fact that most of them are poorly sampled.

We selected light curves from the catalogue of Be star candidates from the SMC of Mennickent et al. (2002). Due to a callibration issue between the OGLE-II and OGLE-III portions of the light curves, namely a shift in the zero points present in some of the light curves, it was necessary to find separate intervals of inactivity in both the OGLE-II and OGLE-III portions of several light curves to correct the problem. Fig. 5.5 shows examples of light curves with such zero point shifts.

⁴ <http://ogledb.astrouw.edu.pl/~ogle/photdb/>

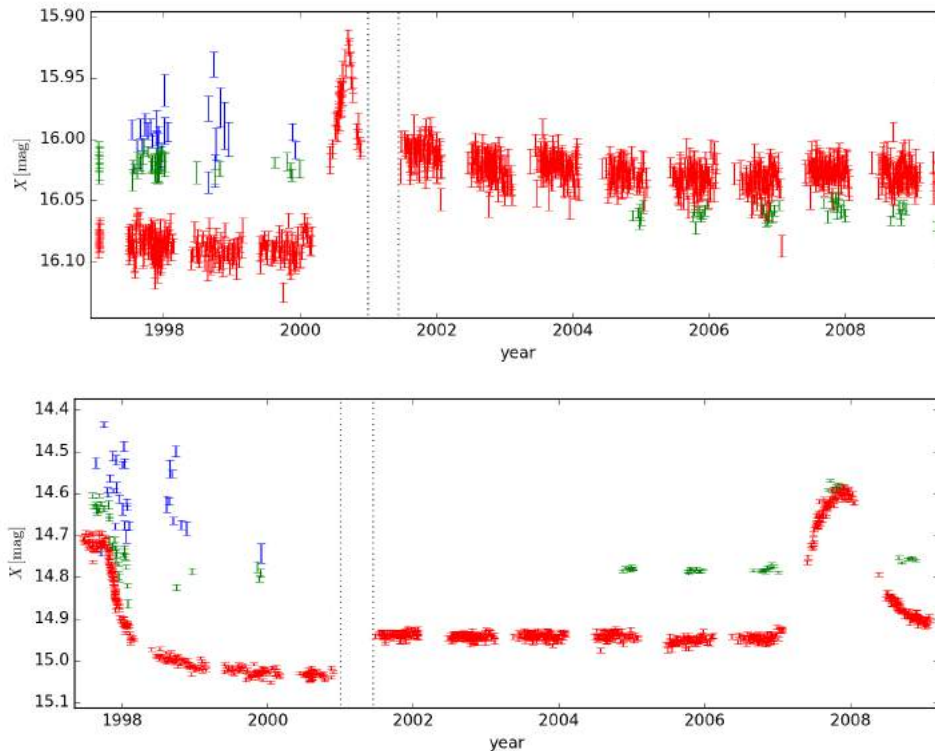


Figure 5.5: Examples of SMC light curves showing clear zero point shifts between the OGLE-II and OGLE-III components. The blue, green and red points correspond to the B , V and I bands, respectively. Above: SMC_SC5 21134. Below: SMC_SC8 183240. Both light curves in this figure were used in this work (see Table 5.1).

Several other light curves failed to meet the criteria of item 1 of Sect. 4.4. In Fig. 5.6, we show an example of a light curve without a clear inactive phase (above) and a light curve (below), probably belonging to the type-4 category, without a clear dissipation phase and with variability that suggests a more complicated scenario of mass injection than the one described in the Chapter 3.

The end result was a sample of 54 stars, containing 81 selected bumps, shown in Table 5.1. In the table, horizontal lines separate the data for each of the 54 stars. Each row in the table contain the data for each of the 81 selected bumps. The fifth and sixth columns in the table contain the beginning and ending of the selected inactive interval for the light curve. The seventh, eighth and ninth columns contain the B_* , V_* and I_* magnitudes obtained at the inactive phase for the light curve. Due to the nature of the OGLE survey, the B_* and V_* magnitudes are not available for all sources. The eleventh column contains the bands that were considered in the fitting process of the specific bumps, depending on the availability of measurements in each band. The last two columns are initial visual estimates of t_1 and t_2 , which were used as input for `emcee`.

As explained in Sect. 4.4, the magnitudes at the inactive phase are necessary to set the baseline level of the light curves, which will be used to get an estimate of the stellar

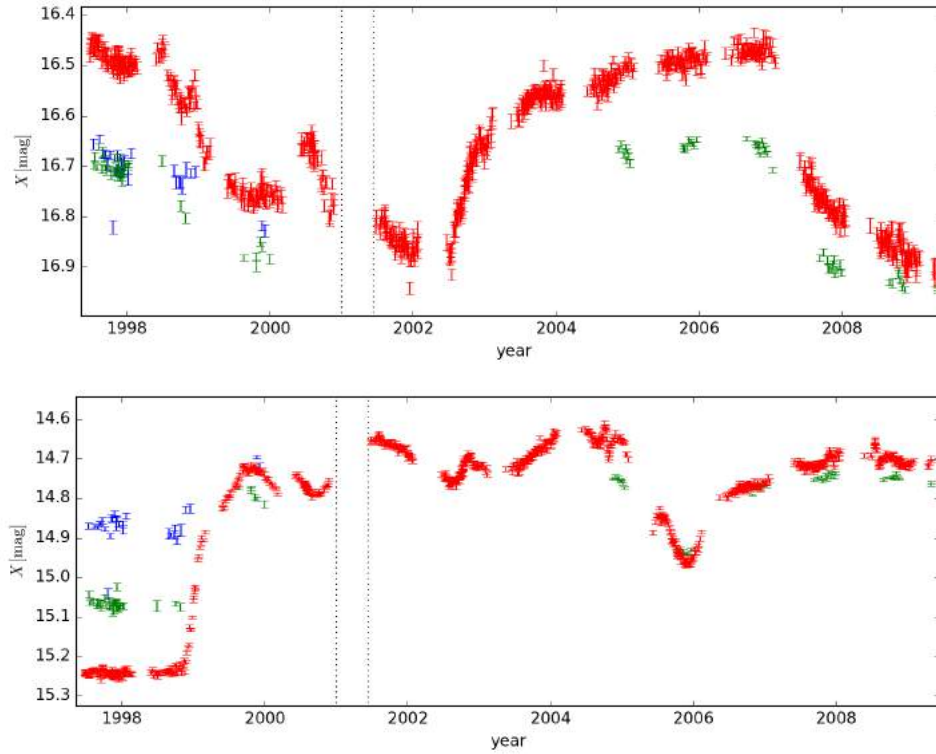


Figure 5.6: Examples of SMC light curves found to have no clear inactive phase (e.g., *above*: SMC_SC4 60186) or to clearly be associated with a more complicated scenario of mass injection than the one described in the Chapter 3 (e.g., *below*: SMC_SC4 116957). The blue, green and red points correspond to the *B*, *V* and *I* bands, respectively.

parameters. In order to do the latter, these apparent magnitudes must be color-corrected and converted to absolute magnitudes by the standard formula $M_{X^*} = X_* - (5 \log d - 5) - A_X$. We adopted as the distance to the SMC $d = 60.3 \pm 3.8$ kpc from [Hilditch et al. \(2005\)](#). The mean *V*-band reddening of the bright stars over the whole SMC is $A_V = 0.470 \pm 0.326$ ([Zaritsky et al., 2004](#)). The reddening in the other bands were obtained by the relations A_X/A_V given by [Gordon et al. \(2003\)](#).

The color-magnitude diagram (CMD) of Fig. 5.7 compares the grid of diskless models (Table 4.3) to our sample of Be stars. Most of the stars lie in the upper right corner of the CMD, which means that the majority of our sample is comprised of early-type Be stars, as further discussed in Chapter 6.

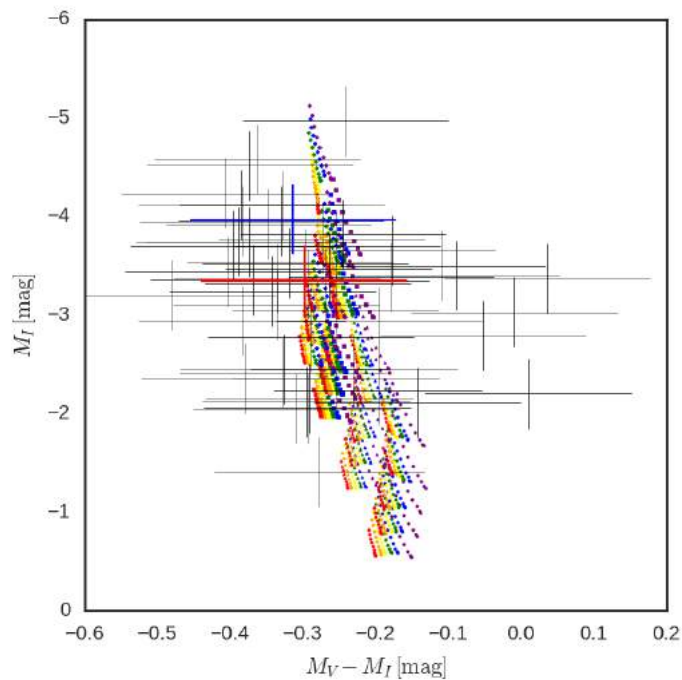


Figure 5.7: Color-magnitude diagram of simulated diskless stars (Table 4.3). Circles, triangles, squares and diamonds correspond to stellar models with $M = 6.0, 8.3, 11.7, 15.0 M_{\odot}$, respectively. The colors red, orange, yellow, green, blue and purple correspond, respectively, to the 6 values of W in increasing order. The 5 different stellar ages are seen as the groups of points move in the upper-right direction. For each star, the effect of going from an inclination angle of 90 deg to 0 deg is to move in the upper-left direction. Also shown, with errorbars, are the positions of our selected stars (see eighth and ninth columns of Table 5.1). The blue and red errorbars mark the positions of SMC_SC1 75701 and SMC_SC6 128831, respectively.

Table 5.1 - List of Be stars and their respective bumps selected for this study

OGLE-II		OGLE-III		diskless interval		B_*	V_*	I_*	Bump	Bands	Bump interval	
Field	ID	Field	ID	(JD-2450000)					ID		(JD-2450000)	
smc_sc1	7612	smc133.4	8877	600	1300	15.926±0.01	16.164±0.009	16.443±0.009	01	<i>I</i>	1420	2000
									02	<i>I</i>	3250	3800
smc_sc1	60553	smc128.6	57	3000	3500	—	15.418±0.003	15.601±0.007	01	<i>V I</i>	3500	5000
smc_sc1	75701	smc125.7	20383	3000	3500	—	15.397±0.003	15.51±0.006	01	<i>V I</i>	3650	5000
smc_sc1	92262	smc128.6	147	3500	3800	—	15.623±0.003	15.811±0.007	01	<i>I</i>	2600	3100
									02	<i>V I</i>	3900	5000
smc_sc2	94939	smc125.3	52	1000	1100	15.832±0.008	15.991±0.013	16.126±0.007	01	<i>I</i>	1100	2000
smc_sc3	5719	smc125.1	20231	2980	3020	—	—	16.233±0.01	01	<i>I</i>	1200	4500
smc_sc3	15970	smc125.2	28056	700	750	15.282±0.01	15.412±0.006	15.541±0.006	01	<i>B V I</i>	750	2000
									02	<i>I</i>	2200	3500
									03	<i>V I</i>	4000	5000
smc_sc3	71445	smc125.2	34818	700	800	16.227±0.01	16.425±0.009	16.608±0.012	01	<i>I</i>	1450	2400
									02	<i>I</i>	4400	4700
smc_sc3	125899	smc125.2	6200	3500	3750	—	15.837±0.004	15.956±0.008	01	<i>I</i>	2320	3400
smc_sc3	197941	smc125.3	25034	4000	4060	—	15.671±0.003	15.724±0.006	01	<i>V I</i>	2350	4000
smc_sc4	22859	smc125.4	22723	700	1200	17.068±0.013	17.133±0.012	17.129±0.015	01	<i>V I</i>	1200	3500
smc_sc4	71499	smc100.7	34896	1000	1450	15.414±0.011	15.553±0.007	15.597±0.006	01	<i>V I</i>	1430	2400
									02	<i>V I</i>	2900	4400
smc_sc4	120783	smc100.6	7129	4250	4500	—	14.401±0.003	14.442±0.005	01	<i>V I</i>	2750	4500
smc_sc4	127840	smc100.6	38372	3500	4500	—	14.853±0.003	15.026±0.006	01	<i>I</i>	2800	3500
smc_sc4	156248	smc100.8	14683	1000	1200	15.91±0.01	15.964±0.007	15.852±0.006	01	<i>I</i>	1320	2300
smc_sc4	156251	smc100.8	14642	600	680	14.881±0.005	15.13±0.007	15.338±0.005	01	<i>B V I</i>	650	1200
									02	<i>V I</i>	3170	3600
									03	<i>V I</i>	3770	4600
smc_sc4	159829	smc100.8	37214	4450	4500	—	15.895±0.005	15.959±0.009	01	<i>I</i>	2600	3000
									02	<i>V I</i>	3430	4500
smc_sc4	159857	smc100.8	45127	3000	3500	—	15.626±0.004	15.8±0.008	01	<i>I</i>	780	1400

Table 5.1 - continued.

OGLE-II		OGLE-III		diskless interval		B_*	V_*	I_*	Bump	Bands	Bump interval	
Field	ID	Field	ID	(JD-2450000)					ID		(JD-2450000)	
									02	<i>V I</i>	3600	4300
smc_sc4	163828	smc100.7	8813	600	700	17.171±0.009	17.164±0.009	16.953±0.013	01	<i>B V I</i>	700	2400
smc_sc4	167554	smc100.7	51098	3000	4500	—	17.258±0.009	17.2±0.016	01	<i>I</i>	1620	1900
									02	<i>V I</i>	4700	5000
smc_sc4	171253	smc100.7	42620	700	1200	15.674±0.01	15.714±0.009	15.691±0.006	01	<i>I</i>	1410	1900
									02	<i>V I</i>	3245	4000
smc_sc4	175272	smc100.6	7362	3950	4000	—	16.579±0.005	16.431±0.009	01	<i>I</i>	2600	3800
smc_sc4	179053	smc100.6	38443	0	1000	16.304±0.009	16.339±0.009	16.148±0.008	01	<i>I</i>	1300	2400
smc_sc5	11453	smc100.8	14734	3300	3400	—	15.871±0.004	15.779±0.008	01	<i>I</i>	3400	5000
smc_sc5	21117	smc100.8	52883	3650	3750	—	16.051±0.004	16.143±0.009	01	<i>V I</i>	970	2000
									02	<i>I</i>	2200	2800
									03	<i>I</i>	2900	3400
									04	<i>V I</i>	3850	5000
smc_sc5	21134	smc100.8	45175	1000	1500	15.994±0.013	16.023±0.006	16.091±0.007	01	<i>I</i>	1600	2000
smc_sc5	32377	smc100.7	50838	4050	4100	—	15.844±0.003	15.941±0.008	01	<i>I</i>	3030	3400
									02	<i>I</i>	4350	5000
smc_sc5	43650	smc100.6	15248	1400	2000	17.177±0.013	17.214±0.01	17.305±0.017	01	<i>V I</i>	750	2000
									02	<i>V I</i>	2550	5000
smc_sc5	54851	smc100.5	14725	600	850	16.264±0.01	16.311±0.009	16.366±0.008	01	<i>B V I</i>	850	2000
									02	<i>I</i>	2120	3600
									03	<i>V I</i>	3650	5000
smc_sc5	65500	smc101.8	21127	1000	1500	16.034±0.011	15.981±0.007	15.959±0.006	01	<i>B V I</i>	600	1000
smc_sc5	129535	smc100.6	53957	4700	4800	—	16.923±0.008	16.953±0.013	01	<i>V I</i>	3300	5000
smc_sc5	145724	smc101.8	21370	3000	3200	—	—	17.116±0.019	01	<i>I</i>	3230	5000
smc_sc5	180034	smc100.1	27826	3900	4100	—	16.436±0.005	16.431±0.009	01	<i>V I</i>	4120	5000
smc_sc5	260841	smc100.1	36050	800	900	15.858±0.011	16.013±0.008	16.182±0.008	01	<i>I</i>	1500	2200
									02	<i>V I</i>	3800	4800

Table 5.1 - continued.

OGLE-II		OGLE-III		diskless interval		B_*	V_*	I_*	Bump	Bands	Bump interval	
Field	ID	Field	ID	(JD-2450000)					ID		(JD-2450000)	
smc_sc5	260957	smc100.1	36101	1200	1700	16.747±0.009	16.917±0.009	17.043±0.015	01	V I	3620	5000
smc_sc5	266088	smc100.2	9240	700	750	17.227±0.012	17.315±0.01	17.408±0.016	01	B V I	750	2000
smc_sc5	276982	smc100.3	9403	4400	4500	—	15.993±0.005	15.757±0.008	01	V I	3030	4500
smc_sc5	282963	smc100.3	9408	1000	1500	15.431±0.009	15.591±0.006	15.665±0.005	01	I	1600	4300
smc_sc6	11085	smc100.1	36096	700	1100	15.52±0.01	15.667±0.007	15.863±0.006	01	V I	1400	2000
									02	V I	3900	5000
smc_sc6	17538	smc100.2	9240	0	750	17.213±0.012	17.315±0.013	17.424±0.015	01	V I	800	3000
smc_sc6	42440	smc100.3	56046	700	1100	16.867±0.012	17.01±0.011	17.19±0.017	01	I	1400	3500
smc_sc6	99991	smc100.1	43700	1300	1800	15.755±0.007	15.923±0.007	16.126±0.009	01	I	650	1400
									02	I	1800	2500
									03	I	3150	4000
									04	I	4200	5000
smc_sc6	105368	smc100.2	17645	600	1200	16.462±0.011	16.592±0.008	16.681±0.011	01	V I	1150	2000
									02	I	2700	4000
smc_sc6	116294	smc100.2	49901	0	900	16.775±0.012	16.958±0.01	17.085±0.013	01	I	985	2000
smc_sc6	128831	smc100.3	55954	600	1200	15.849±0.009	16.018±0.007	16.116±0.007	01	I	1445	2600
smc_sc6	199611	smc100.3	29080	600	1300	15.265±0.011	15.447±0.008	15.594±0.006	01	I	1500	2000
smc_sc6	272665	smc106.6	26640	1000	1500	17.784±0.016	17.962±0.016	18.04±0.029	01	I	1620	4500
smc_sc7	57131	smc105.6	33029	1200	2000	16.037±0.015	16.127±0.008	16.269±0.008	01	I	2780	3500
smc_sc8	183240	smc105.2	32029	3000	4000	—	14.783±0.003	14.946±0.005	01	V I	4150	4800
smc_sc9	105383	smc110.6	114	1000	1300	16.115±0.01	16.264±0.007	16.4±0.009	01	V I	1240	3500
									02	V I	3780	4800
smc_sc9	168422	smc113.7	6330	4700	4850	—	17.002±0.009	17.057±0.014	01	V I	2700	4850
smc_sc10	8906	smc110.6	22338	4500	5000	—	15.253±0.003	15.382±0.006	01	I	2935	3300
									02	V I	3650	3710
smc_sc11	28090	smc113.2	4458	4500	5000	—	15.248±0.004	15.433±0.006	01	V I	2300	4500
smc_sc11	46587	smc110.3	16096	600	1000	17.087±0.013	17.248±0.01	17.343±0.021	01	I	1110	4500

Results

I hate being “allowed for”, as if I were some incalculable quantity in an astronomical equation.

Dorothy L. Sayers and Robert Eustace, *The Documents in the Case*

In this section, the results obtained by applying the pipeline (Sects. 4.4 and 4.5) to the stars and bumps of our sample are described. Initially, the results for the two objects of Fig. 3.1 are examined in detail (Sect. 6.1), followed by an analysis of the results obtained for the entire sample (Sect. 6.2).

6.1 *SMC_SC1 75701 and SMC_SC6 128831*

The results for SMC_SC1 75701 and SMC_SC6 128831 are shown in Figs. 6.1 and 6.2, respectively. For SMC_SC1 75701 there was enough data for both the I and V bands to allow these two light curves to be fitted simultaneously. For SMC_SC6 128831, however, only I -band data was available. The times for the beginning of the build-up (t_1) and dissipation (t_2) are fitted quantities in the pipeline, but an initial estimate for them is provided to `emcee` by graphically analyzing each light curve. These estimates are shown as the purple and orange segments in the horizontal straight lines in the figure. As explained in Sect. 4.5.1.1, in the MCMC sampling, after a sufficient number of iterations, a stationary sample is obtained, for which the model parameters are more concentrated in the regions of higher posterior probability. In the plots we show 100 sets of randomly selected model curves obtained after the stationary sample was reached. The dispersion of the curves gives a visual measure of the goodness of the fits.

The goodness of the fit can be quantitatively assessed from the distribution of the posterior probabilities of each fitted parameter shown in Figs. 6.1 and 6.2. The main diagonal of the triangular diagram plots the distributions of the stellar (M , t/t_{MS} and W), geometrical ($\cos i$), and bump (Σ_0 , α_{bu} and α_{d}) parameters, and they can be used to

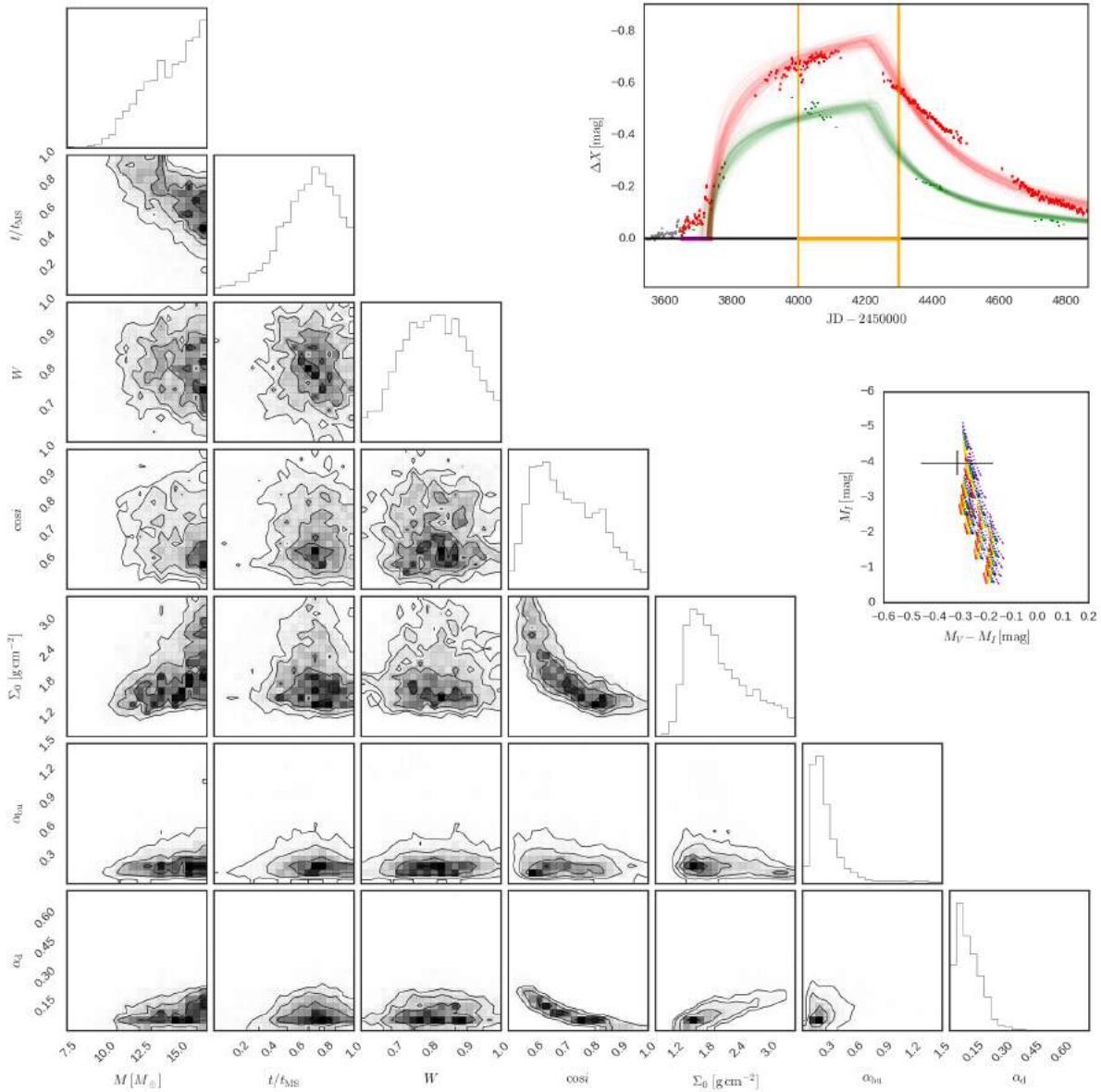


Figure 6.1: *Upper-right*: Light curve of SMC_SC1 75701. Thin lines: 100 model curves randomly selected from the stationary sample of the `emcee` code. The red (green) color indicates the I (V) band. The purple and orange time intervals marked in the horizontal straight lines are the allowed intervals for the model parameters t_1 and t_2 , respectively. *Middle-right*: CMD displaying the model grid of inactive Be stars and the position of SMC_SC1 75701 (see Fig. 5.7 for details). *Below*: Results of the `emcee` run for SMC_SC1 75701. Histogram distributions of the posterior probabilities (top panels) and two-by-two correlations of the stellar (M , t/t_{MS} and W), geometrical ($\cos i$), and bump (Σ_0 , α_{bu} and α_{d}) parameters (off-diagonal panels). The parameters t_1 and t_2 were not shown for convenience. The normalized density contour levels shown in the off-diagonal panels are 12%, 39%, 68%, 87% of the peak probability.

assess how well-constrained each parameter is. The images below the diagonal show how the parameters correlate with each other.

The stellar parameters (M , t/t_{MS} and W) are mainly constrained by the magnitudes

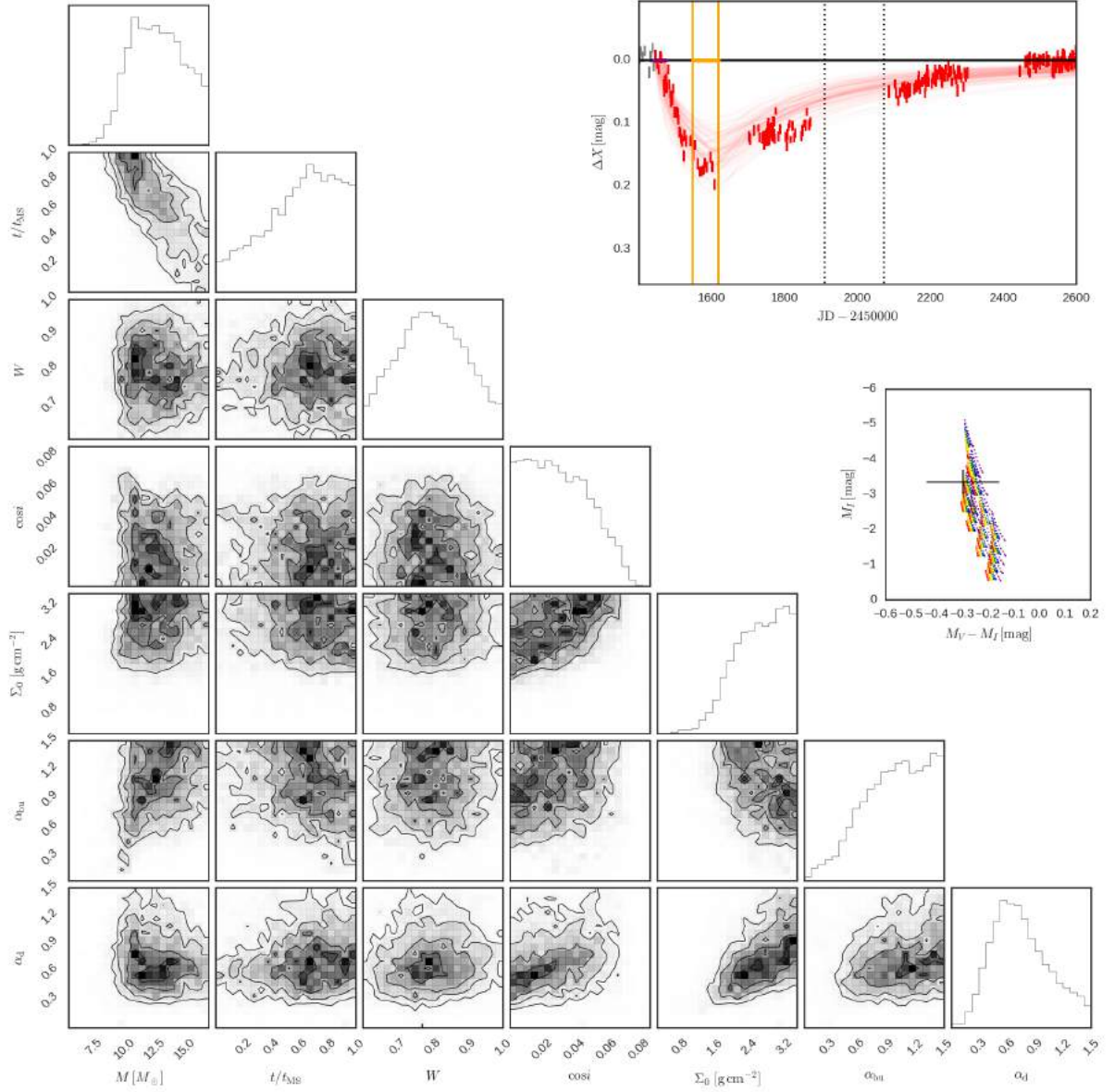


Figure 6.2: Same as Fig. 6.1 for SMC_SC6 128831.

at the inactive phase. In Fig. 6.1, the three leftmost histograms along the diagonal have broad distributions, which means that these parameters are not well constrained. The first histogram shows that SMC_SC1 75701 is an early Be star, probably even more massive than the available stellar models (Table 4.3). This agrees with the position of the star in the CMD (Fig. 5.7). The mass is anti-correlated with the main sequence age (see $t/t_{\text{MS}} \times M$ plane), as expected from the fact that a less massive but more evolved star can have a similar absolute magnitude to that of a younger, more massive star.

The bump parameters (Σ_0 , α_{bu} and α_{d}) are mainly constrained by the shape of the observed bump. Roughly, the amplitude of the bump depends mostly on Σ_0 (and $\cos i$,

see Fig. 4.6), while the value of viscosity parameter in each phase controls the rate of brightness variation. For SMC_SC1 75701, Σ_0 has a broad distribution peaking around $\sim 1.5 \text{ g cm}^{-2}$, indicating a quite dense disk, close to the densest cases in the sample of Vieira et al. (2017) for the same spectral type. This fact can also be inferred from Fig. 4.6, given the large observed $\Delta I_{\text{bu}}^\infty$. The best-fit viscosity parameters are $\alpha_{\text{bu}} = 0.24_{-0.08}^{+0.18}$ and $\alpha_{\text{d}} = 0.11_{-0.05}^{+0.08}$.

Of the three bump parameters derived for SMC_SC1 75701, Σ_0 and α_{d} clearly anti-correlate with $\cos i$, while α_{bu} shows no strong sign of correlation. In fact, an anti-correlation of these three parameters with $\cos i$ is expected, as a consequence of the dependency of $\Delta X_{\text{bu}}^\infty$, ξ_{bu} and ξ_{d} , defined in Sect. 4.3, on $\cos i$. Fig. 4.6 shows that, if the star is seen more pole-on (higher values of $\cos i$), smaller values of Σ_0 are required in order to obtain the fitted $\Delta X_{\text{bu}}^\infty$, hence the strong anti-correlation seen in the $\Sigma_0 \times \cos i$ plane. Eq. (4.4.4) shows that the fitted coefficient C_{bu} is proportional to the product of α_{bu} and ξ_{bu} , and it was shown (second and fourth columns of panels of Fig. 4.8) that disks seen more pole-on (higher values of $\cos i$) appear to build-up faster (having higher values of ξ_{bu}). Therefore, for higher values of $\cos i$, smaller values of α_{bu} are required to obtain the fitted C_{bu} , which would produce an anti-correlation in the $\alpha_{\text{bu}} \times \cos i$ plane. Even though this last anti-correlation was not observed for SMC_SC1 75701, it is clearly seen for many objects of our sample, for instance, SMC_SC3 71445 and SMC_SC3 125899 (see Figs. C11 and C13 from the paper in Appendix C). Eq. (4.4.5) shows that C_{d} is proportional to the product of α_{d} and ξ_{d} , and it was shown in the second and fourth columns of panels of Fig. 4.9 that the more pole-on and the less dense the disk, the faster the rate of brightness variation in the dissipation, thus the anti-correlation seen in the $\alpha_{\text{d}} \times \cos i$ plane. Finally, the plane $\alpha_{\text{d}} \times \Sigma_0$ shows a correlation which is a consequence of the above mentioned relationship between ξ_{d} with Σ_0 .

The results for SMC_SC6 128831 (Fig. 6.2) indicate a less massive star ($M = 12.2_{-2.2}^{+2.7} M_\odot$) surrounded by a much more massive disk ($\Sigma_0 = 2.6_{-0.6}^{+0.5} \text{ g cm}^{-2}$). SMC_SC6 128831 is an example of a dip, which means that this Be star is seen at a near edge-on angles, with $\cos i$ being well constrained. The very steep build-up phase of SMC_SC6 128831 hints to large mass injection rate and viscosity during build-up, as confirmed by the fifth and sixth histograms along the diagonal of Fig. 6.2. The viscosity parameter during dissipation was found to be $\alpha_{\text{d}} = 0.69_{-0.27}^{+0.34}$. The plane $\alpha_{\text{d}} \times \Sigma_0$ shows a correlation, just as for the case of SMC_SC1 75701, which is a consequence of the relationship between ξ_{d} with Σ_0 , also expected for near-edge-on inclinations (see Fig. 4.9).

For SMC_SC6 128831 a positive correlation between Σ_0 , α_{bu} and α_{d} with $\cos i$ was observed. Fig. 4.6 shows that, if the star moves away from the edge-on case ($\cos i = 0$), bigger values of Σ_0 are required in order to obtain the fitted $\Delta X_{\text{bu}}^\infty$, hence the correlation seen in the $\Sigma_0 \times \cos i$ plane. The first column of panels of Fig. 4.8 (for the *I*-band) show that, for the edge-on case there is no strong variation of ξ_{bu} with $\cos i$. The third column

of panels (for the V -band), however, show an increase of ξ_{bu} with $\cos i$, which does not affect the estimates for this dip, since there are no measurements in the V -band for this dip. In any case, however, in both the first and third columns of panels, there is the trend that a more tenuous disk appears to build faster, especially when the star is hotter. Therefore, since Eq. 4.4.4 shows that $C_{\text{bu}} \propto \alpha_{\text{bu}} \xi_{\text{bu}}$, it follows that, with the increase of Σ_0 with $\cos i$, the function ξ_{bu} decreases and, hence, α_{bu} increases. Finally, Eq. 4.4.5 shows that $C_{\text{d}} \propto \alpha_{\text{d}} \xi_{\text{d}}$ and Fig. 4.10 shows that ξ_{d} decreases with $\cos i$ and Σ_0 . Therefore, as Σ_0 increases with $\cos i$, it follows that ξ_{d} decreases and, hence, α_{d} must increase. Similar trends were found for the other two edge-on stars in our sample (SMC_SC1 92262, Figs. C4 and C5, and SMC_SC4 179053, Fig. C34 from the paper in Appendix C).

In general, the histograms of Fig. 6.2 are broader than the ones in Fig. 6.1, indicating that parameters are more poorly constrained than for SMC_SC1 75701. There are two main reasons for this. First, only I -band data was available for this star, which has a negative impact on the pipeline’s ability to constrain the stellar parameters. The MCMC method ensures that the uncertainties in the stellar parameters are properly propagated into the other model parameters. Second, the fact that the dips have smaller amplitudes than the bumps of pole-on stars, even for higher values of Σ_0 , is a great disadvantage, because the bump amplitude is much closer to the noise level of the measurements.

The results of the pipeline for all stars in Table 5.1 are shown in Figs. C1 to C79, in the paper in Appendix C. The best-fit model parameters for all stars and bumps are listed in Table 6.1.

6.2 Results for the whole sample

Geordi: “Suddenly it’s like the laws of physics went right out the window.”

Q: “And why shouldn’t they?”

They’re so inconvenient!”

Georgi to Q, in Star Trek: The Next Generation, episode “True Q”

As seen previously, the scarcity of information about the central star (one, two, or at most 3 photometric bands only) causes a poor determination of its fundamental stellar parameters, which, owing to the nature of the MCMC method, propagates onto the disk parameters. The main result of this work, therefore, does not lie on the individual determination of the bump parameters, but on the statistical properties of the sample as a whole.

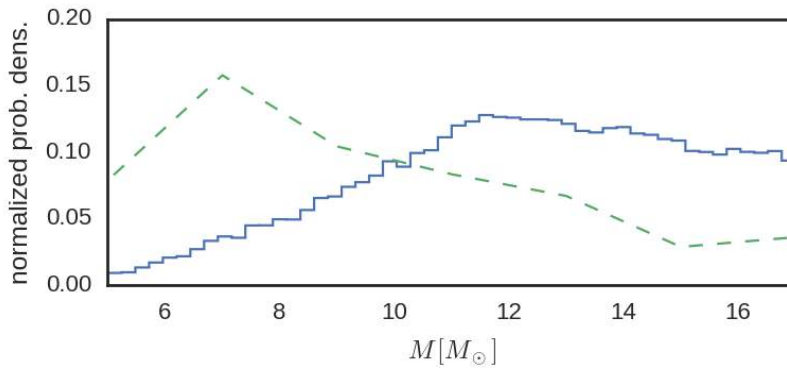


Figure 6.3: *Solid line*: Histogram of the sum of the posterior probabilities of parameter M for all stars in our sample. *Dashed line*: IMF of Kroupa (2001) weighed by the fraction of Be stars over B stars of Martayan et al. (2007), given by the factor $M^{-2.3} f_{\text{Be}}(M)$ in Eq. (4.5.8).

6.2.1 Mass distribution

Let us initially discuss the properties of our sample, in order to determine whether it represents a typical population of Be stars in SMC, or whether one or more selection biases were introduced.

Our selection of stars and bumps comes from the catalogue of visual photometric Be star candidates of Mennickent et al. (2002), where the candidate stars were selected according to the expected location of Be stars in color-magnitude diagrams and according to the observed variability in the light curves. In Fig. 6.3, we show the sum of the posterior probabilities of parameter M for all our sample of stars (solid line). Clearly, most of our stars are early-type Be stars, in agreement to the position of our sample in the CMD (Fig. 5.7). We also show the factor $\propto M^{-2.3} f_{\text{Be}}(M)$ of Eq. 4.5.8 (dashed line). We recall that this factor was assumed as a prior in the MCMC fitting, and it represents our current knowledge about the populations of Be stars in the SMC. The green curve shows that, although the fraction of Be stars over B stars ($f_{\text{Be}}(M)$, estimated by Martayan et al. (2007) from a cluster of the SMC) generally increases with M , the higher probability of the formation of less massive stars expressed in the IMF of Kroupa (2001) results in a bigger incidence of late type over early type Be stars. Our sample, therefore, is biased towards more massive stars.

This bias likely has several reasons:

1. The typical apparent I -band magnitudes of a B0 and a B9 star in the SMC are ~ 15.5 and ~ 19.5 , with rms uncertainties given by $\gtrsim 0.005$ and $\gtrsim 0.15$, respectively (Wyrzykowski et al., 2009, and see also Fig. 6.4). Consequently, it is more difficult to detect small amplitude bumps for late-type Be stars.
2. Late-type Be stars tend to have more tenuous disks than early-type ones (Vieira

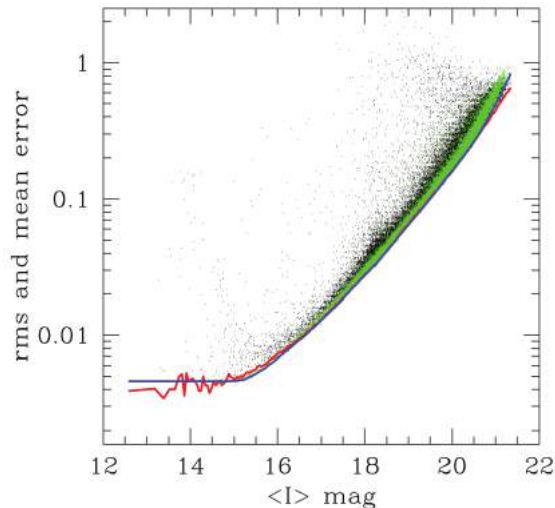


Figure 6.4: Mean error (green) and rms (black) for a sample of stars from one of the fields of the OGLE-II survey. (Credits: [Wyrzykowski et al., 2009](#))

[et al., 2017](#), see also next subsections), and therefore should develop bumps with much smaller amplitudes.

3. Late-type Be stars tend to show less variability ([Rivinius et al., 2013](#), see also next subsections), which would make it less probable to identify bumps in their light curves.

6.2.2 Asymptotic surface density

In the upper panel of Fig. 6.5 we show how Σ_0 varies with stellar mass in our sample, demonstrating a clear tendency toward denser disks around the more massive stars. [Vieira et al. \(2017\)](#) have shown that, for the Be stars in the MW, the incidence of denser disks increases with the mass of the stars. Comparison of our results with the ones of [Vieira et al.](#) are shown in Fig. 6.6. While our sample is biased towards large masses, their sample is more evenly distributed in mass. Another difference is that our results are all concentrated in a region of high disk density, while theirs cover a much wider range of densities for all spectral types. The reason for this lies in the fact that for this initial study we selected light curves with large and well-defined bumps, disregarding low-amplitude and short-duration ones. In fact, the detection of tenuous disks by [Vieira et al.](#) was only possible because they studied the SED in the IR (typically between 9 and 60 μm), where the disk emission is much stronger than in the visible range. Therefore, all but the most dense of their disks would be too tenuous to generate appreciable photometric excesses in the visual photometric bands, suitable for our fitting procedure.

We conclude that our sample of visual bumps should represent the upper limit for the densities found in the disks of SMC Be stars. In the Milky Way (MW), these large

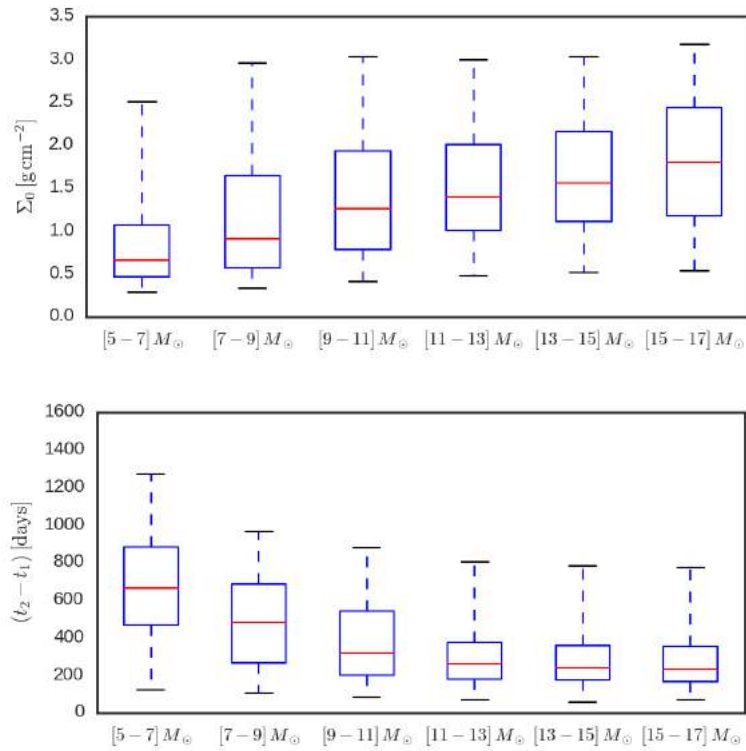


Figure 6.5: Boxplots of Σ_0 (above) and $t_2 - t_1$ (below) for the summed posterior probabilities of our sample of bumps, separated in six equal intervals of mass, ranging from 5 to 17 solar masses. The middle line of the boxes mark the median (50%) of the samples. The lower and upper ends of the boxes mark 25% and 75% of the samples. The lower and upper whiskers mark 5% and 95% of the samples.

densities are only found in early type Be stars. The median of the Σ_0 for our sample is $\langle \Sigma_0 \rangle = 1.44_{-0.75}^{+1.01} \text{ g cm}^{-2}$. Furthermore, there may be some indication that the Be stars in the SMC may have more massive disks, on average, than their MW counterparts, in line with results from the literature that report higher H α equivalent widths in the SMC Be stars than in the MW (Martayan et al., 2007). This last point, however, should be viewed with some caution given the large biases present in our sample.

6.2.3 Disk life cycles

In the lower panel of Fig. 6.5, we plot the distribution of the build-up time, $t_2 - t_1$, versus the stellar mass. We see that the duration of the bump is much shorter for massive stars, which indicates that these stars are much more variable than their late type siblings. Similar findings were reported in the MW (e.g. Rivinius et al., 2013). For a complete characterization of the disk life cycles we would require a full census of the number of bumps present during the timespan of OGLE-II and OGLE-III observations (roughly 12 years). Unfortunately, this cannot be done for our sample because in this study we selected only the well-defined bumps. The median of the build-up time for our sample is $\langle t_2 - t_1 \rangle = 305_{-171}^{+351}$ days.

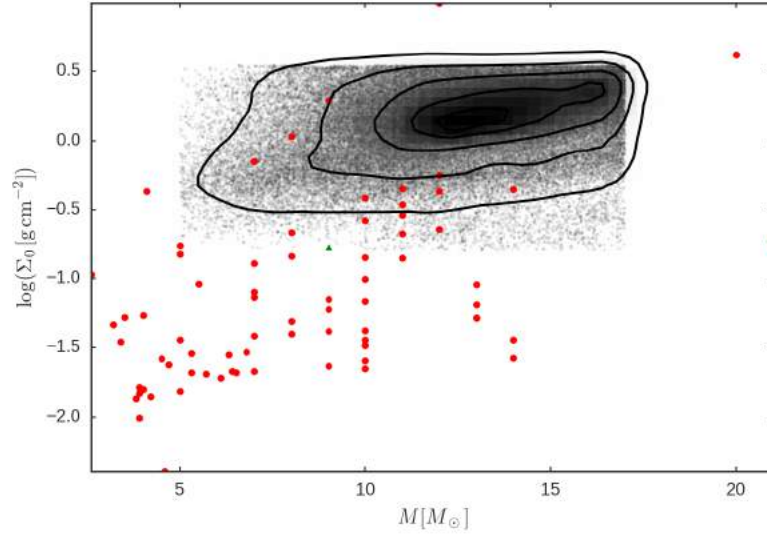


Figure 6.6: Distribution of the parameters M and Σ_0 for our sample. The contour levels are the same as in Fig. 6.1. The red dots correspond to the surface densities at the base of the disk of MW Be stars, measured by Vieira et al. (2017). The green triangle corresponds to the initial state of the ablating disk model of Kee et al. (2016) for a B2e star.

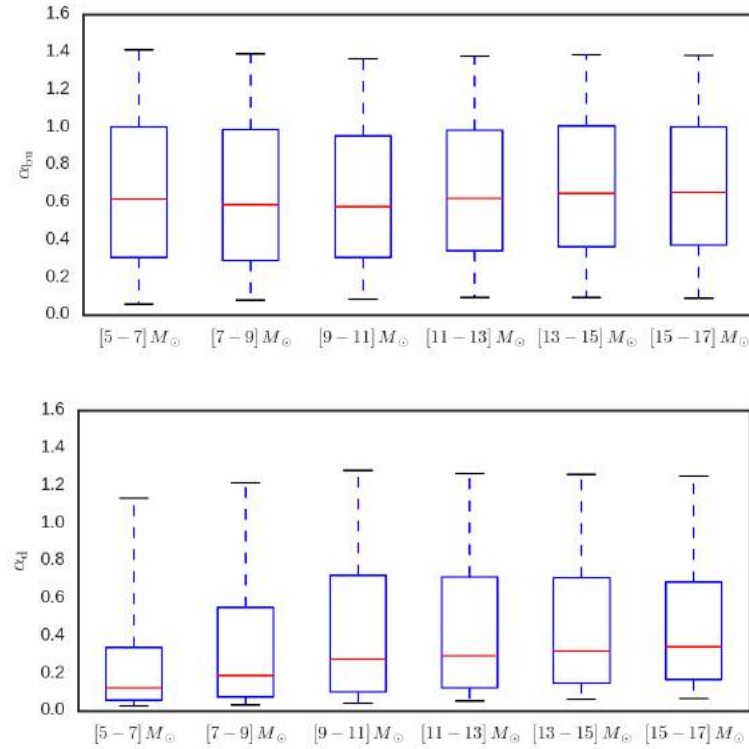


Figure 6.7: Same as Fig. 6.5 for α_{bu} (above) and α_d (below).

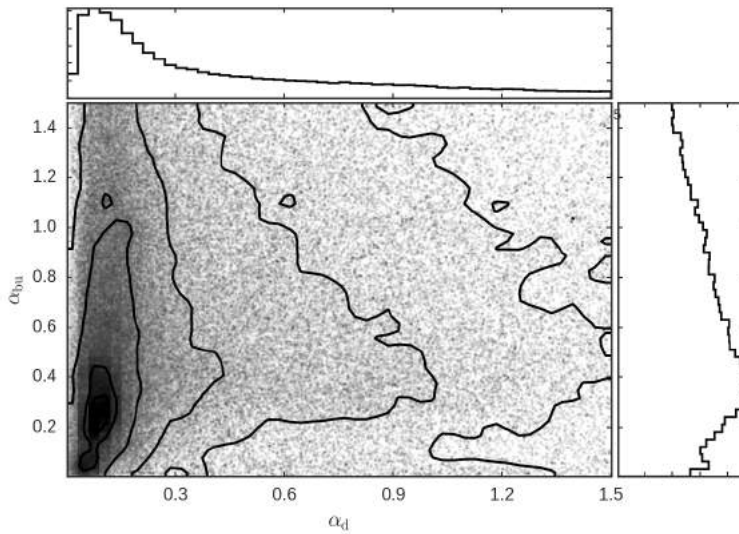


Figure 6.8: Distribution of the two viscosity parameters α_{bu} and α_{d} . The histograms above and on the right are the projections for α_{d} and α_{bu} , respectively. The contour levels are the same as in Fig. 6.1.

6.2.4 Viscosity parameter

The majority of our determinations of the viscosity parameter had broad uncertainty distributions, and it was found that the errors in the determinations of α_{bu} were generally greater than those of α_{d} . Considering the sample as a whole, we find that there is no variation of α_{bu} with the stellar mass (Fig. 6.7, top), but there is a slight hint that α_{d} may grow with the stellar mass (Fig. 6.7, bottom). Furthermore, we find that on average the viscosity parameter is roughly two times larger at build-up than at dissipation ($\langle \alpha_{\text{bu}} \rangle = 0.63^{+0.52}_{-0.39}$ vs. $\langle \alpha_{\text{d}} \rangle = 0.29^{+0.61}_{-0.20}$).

The estimated values of α in the range of a few tenths to one are in agreement with the usual values obtained for the hot and variable disks of dwarf novae (King et al., 2007; Kotko and Lasota, 2012). They are, however, an order of magnitude or more above the usual values obtained in magnetohydrodynamic (MHD) simulations, where the magnetorotational instability (MRI, Balbus and Hawley, 1991) is the main theoretical assumption for the mechanism that generates the necessary viscosity (King et al., 2007).

In Fig. 6.8, we show the distributions of α_{bu} (right) and α_{d} (above) and the distribution in the $\alpha_{\text{bu}} \times \alpha_{\text{d}}$ plane. We found that, for most of the bumps, there was a correlation between α_{bu} and α_{d} , with values of α_{bu} greater than values of α_{d} being more likely. This trend can be seen in the darker areas of the $\alpha_{\text{bu}} \times \alpha_{\text{d}}$ plane. Ghoreyshi and Carciofi (2017) modeled several build-up and dissipation phases of the Be star 28 CMa and found the same trend for that star.

It is unclear whether the higher likelihood of $\alpha_{\text{bu}} > \alpha_{\text{d}}$ is really a phenomenon or a result of the approximations employed in this work. One key approximation made in our model is that the hydrodynamical equations are solved assuming that the entire disk

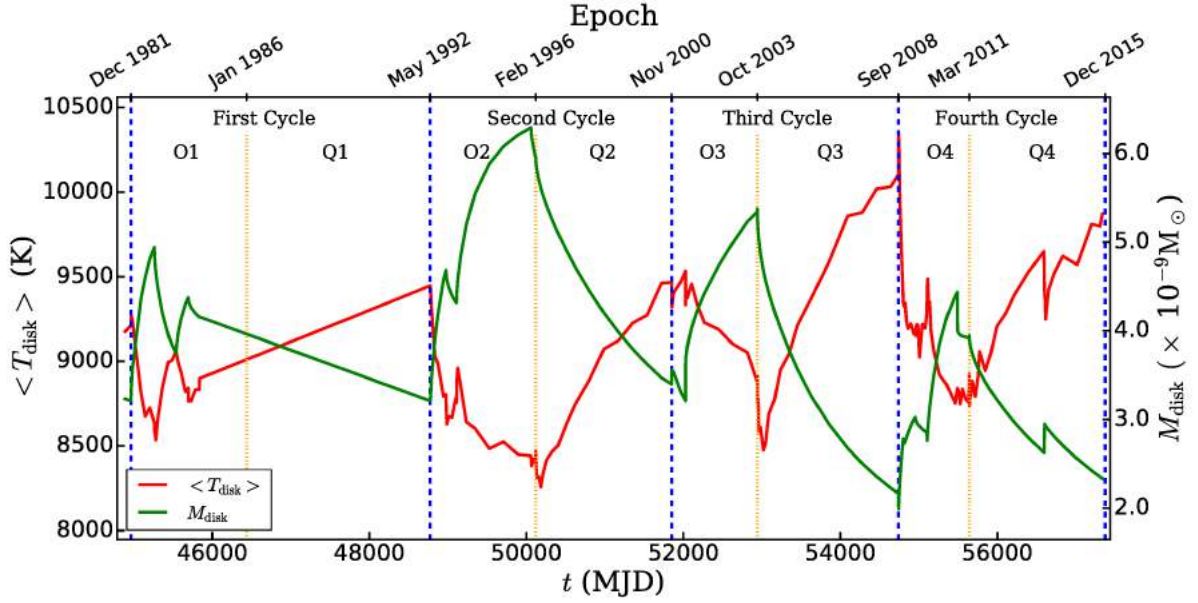


Figure 6.9: Evolution of the disk mass and mean disk temperature of the Be star 28 CMa, complementing the panels of Fig. 3.6. The green curve shows the total mass of the disk. The red curve shows the mean temperature of the disk, calculated by Eq. (6.2.1). (Credits: M. Ghoreyshi, priv. comm.)

is isothermal. Earlier studies, however, (e.g., Jones et al., 2004; Carciofi and Bjorkman, 2006) have shown the disk to be highly non-isothermal, which means that c_s in Eq. 3.1.2 is a complicated function both of R and time. There is not any strong correlation between the viscosity parameters and the temperatures of the disks, because in Fig. 6.7 we do not see strong correlations between the viscosity parameters and the mass of the stars. However, the fitted parameters C_{bu} and C_d are proportional to $\alpha_{bu}c_s^2$ and $\alpha_dc_s^2$, respectively (see Eqs. 3.1.13, 4.4.4, and 4.4.5). Therefore, if we erroneously underestimated the temperature during build-up phase, characterized by a surface density that starts from zero and then increases, and overestimated the temperature during dissipation, where the density starts higher and begins to decrease, that might contribute to our determination of $\alpha_{bu} > \alpha_d$ being more likely.

The Fig. 6.9 was very recently generated by M. Ghoreyshi (priv. comm.). It must be compared with the modeling of the light curve of 28 CMa in Fig. 3.6. The green curve shows the total mass of the disk of his dynamical model of the star 28 CMa. During the build-up phases, the mass of the disk increases and then decreases during the dissipation phases. The red curve shows the average temperature of the disk, given by

$$\langle T_{\text{disk}} \rangle = \frac{\sum_{\text{cells}} \rho_i T_{i,\text{disk}} \delta V_i}{\sum_{\text{cells}} \rho_i \delta V_i}, \quad (6.2.1)$$

where the average was made over all the cells of the interaction region of HDUST. The volume of each cell is given by δV_i .

The red curve, therefore, shows that, at the beginning of the build-up phases, the mean temperature of the disk is usually higher, and it decreases as time passes and the disk becomes denser, especially in the equatorial plane. Conversely, at the beginning of the dissipations, the mean temperature is usually lower, and it increases as time passes and the disk becomes tenuous. These observed variations in temperature, around 10 – 20%, may help explaining physically why $\alpha_{\text{bu}} > \alpha_{\text{d}}$ was found to be more likely. It does not invalidate the conclusion that indeed $\alpha_{\text{bu}} > \alpha_{\text{d}}$, however.

Another approximation is that the possible effects of line forces were neglected. Recently, [Kee et al. \(2016\)](#) simulated the effects of a line-driving on the disks of early B-type stars. They showed that the line-driving was able to ablate and destroy the disk in timescales compatible with the observed large-amplitude photometric variations of Be stars. They argued that the presence of the line-driven ablation might be the cause of the apparent abnormal value estimated for α by [Carciofi et al. \(2012\)](#); [Ghoreyshi and Carciofi \(2017\)](#), and this work. Future work must explore if the viscous force and the line force working together can reproduce the variability of Be stars with smaller values of α .

The line force acting on an outwardly diffusing near-Keplerian optically thin disk under irradiation by the hot star will have a positive component in the azimuthal direction, giving angular momentum to the gas ([Gayley et al., 2001](#)). It is possible that this additional source of angular momentum may help viscosity in pushing material outwards during the build-up phase and act to oppose to the reaccretion of the inner disk during dissipation, thus contributing to the observed trend of $\alpha_{\text{bu}} > \alpha_{\text{d}}$. We expect, however, that for our low-metallicity SMC Be stars, the possible effect of the line force will be greatly diminished. Furthermore, so far all studies of the effects of line forces in gaseous Keplerian disks assumed that the gas is optically thin, which is not the case for the inner parts of the disk, near the equatorial plane. The green triangle in [Fig. 6.6](#) marks the mass and density at the stellar equator of the initial state of the ablating disk model of [Kee et al. \(2016\)](#) for a B2e star. Our calculations show that their initial state would generate only a modest excess $\Delta I = -0.1$ mag, if seen pole-on.

On the other hand, it is possible that an opposite scenario might happen. The line force might operate to ablate the tenuous material above the disk plane. These regions would receive radiation from the stellar surface and radiation reprocessed by the optically thick disk, behaving as a sink of mass and angular momentum from the disk (e.g. [Krtićka et al., 2011](#)). In that case, the line-driven wind would actually slow down the build-up phase, because it would take a longer time for the disk to reach a near steady-state, and would speed up the dissipation phase. If the above were true, that would result in $\alpha_{\text{bu}} < \alpha_{\text{d}}$, contrary to the results of [Ghoreyshi and Carciofi \(2017\)](#) and this work.

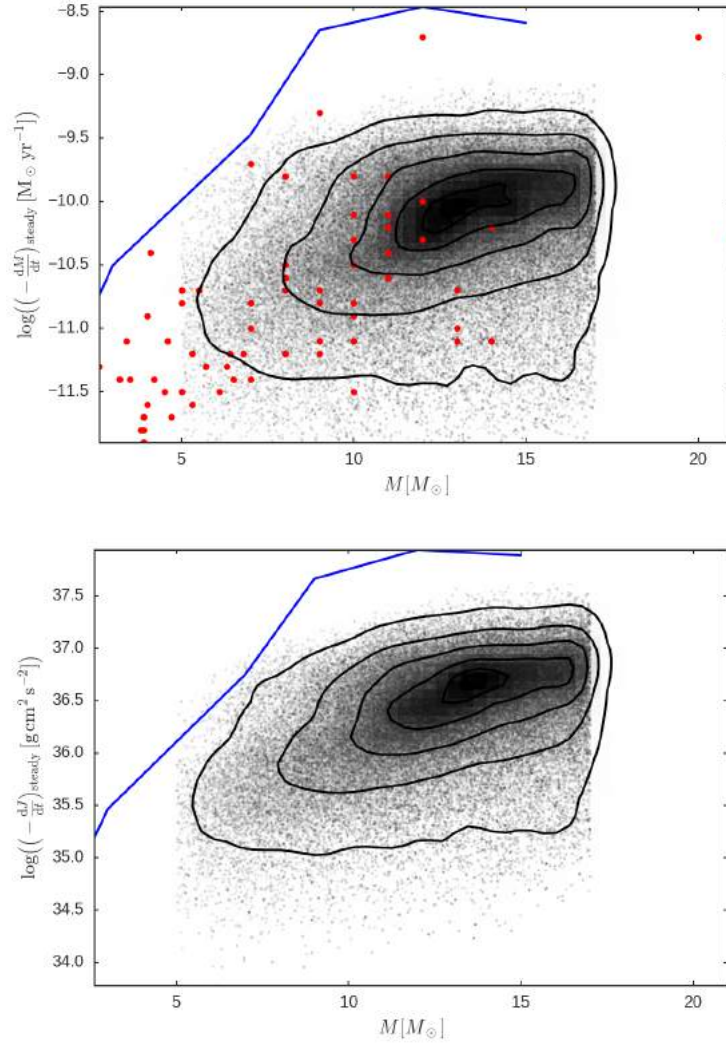


Figure 6.10: Distributions of the steady-state mass (above) and angular momentum (below) loss rates for our sample. The contour levels are the same as in Fig. 6.1. The red dots (upper panel) are the values of $(-\partial M/\partial t)_{\text{steady}}$, calculated from the results of Vieira et al. (2017) for MW Be stars. The blue curves are the estimations made by Granada et al. (2013) of the steady-state mass and angular momentum loss of their $Z = 0.002$ stars during their episodes of disk formation.

6.2.5 Mass and angular momentum loss

Although the disks of Be stars in our sample are generally not in steady-state, their steady-state mass and angular momentum loss rates (Eqs. 3.2.17 and 3.2.18) are useful estimates of the actual quantities that are lost by the star after the bump event ends (see Sect 3.2). The panels of Fig. 6.10 show our distributions of the steady-state mass (above) and angular momentum (below) loss rates. For the calculation of $(-\partial M/\partial t)_{\text{steady}}$, we considered the radius of the outer boundary to be given by the radius at which the disk outflow becomes angular momentum conserving (which can be seen as an outer radius of the viscous disk), estimated as $\tilde{R}_{\text{out}} = 0.3(v_{\text{orb}}/c_s)^2$ by Krtićka et al. (2011). The red dots

(upper panel) are the estimates of $(-\partial M/\partial t)_{\text{steady}}$ made from the results of [Vieira et al. \(2017\)](#) for MW Be stars, assuming that $\alpha = 1$.

The steady-state mass and angular momentum loss rates for our densest bumps are of the order of $\sim 10^{-10} M_{\odot} \text{ yr}^{-1}$ and $\sim 5 \times 10^{36} \text{ g cm}^2 \text{ s}^{-2}$, respectively. The typical decretion rate, which estimates the flux of mass in the disk near the stellar equator, is an order of magnitude higher than $(-\partial M/\partial t)_{\text{steady}}$, being of the order of $\sim 10^{-9} M_{\odot} \text{ yr}^{-1}$, which also corresponds to the upper limit of the observed wind mass loss rate of B stars ([Snow, 1981](#); [Puls et al., 2008](#)). Values of the typical decretion rate and steady-state angular momentum loss rate are given in the eleventh and twelfth columns of [Table 6.1](#), respectively. The total angular momentum lost by the star as a consequence of the bump, $-\Delta J_*$, is given by $(-\partial J/\partial t)_{\text{steady}}$ times the build-up time (Eq. [3.2.22](#)), and the total mass lost is simply $-\Delta M_* = -\Delta J_*/(GM R_{\text{out}})^{\frac{1}{2}}$, if we still approximate the VDD as a Keplerian disk at R_{out} .

If we consider that a typical bump has a build-up time of roughly one year, then the mass and angular momentum lost by the star as a consequence of one dense complete bump are of the order of $\sim 10^{-10} M_{\odot}$ and $\sim 10^{44} \text{ g cm}^2 \text{ s}^{-1}$ (or ~ 0.01 Moon masses and $\sim 10^{-3}$ times Earth's orbital angular momentum around the Sun, respectively). The VDD is, thus, a physical mechanism capable of extracting a large quantity of angular momentum from the outer layers of the star, without requiring the loss of too much mass. It is, therefore, a rotational breaking mechanism for the outer layers. The angular momentum lost by the star for each individual bump is given in the thirteenth column of [Table 6.1](#).

It has been proposed (e.g., [Krtićka et al., 2011](#)) that, during the evolution of the star, the formation of the VDD might be a natural mechanism to extract angular momentum from the outer layers of the star, preventing them from exceeding the break up velocity. [Granada et al. \(2013\)](#) assumed the appearance of a steady-state VDD in the Geneva stellar evolution code every time the outer layers of the star reached $W > 0.88$ ($\omega > 0.99$, in their notation, where $\omega = \Omega/(8GM/27R_{\text{pole}}^3)^{\frac{1}{2}}$). The blue curves in [Fig. 6.10](#) are the estimates made by [Granada et al. \(2013\)](#) of the steady-state mass and angular momentum loss of their $Z = 0.002$ stars during their episodes of disk formation. It is remarkable that our estimates of $(-\partial M/\partial t)_{\text{steady}}$ and $(-\partial J/\partial t)_{\text{steady}}$ made using our dynamical VDD models of bumps in the light curves of Be stars and the estimations of $(-\partial M/\partial t)_{\text{steady}}$ made using near-IR SED fitting by [Vieira et al. \(2017\)](#) are both similar to the estimates of these physical quantities made by [Granada et al. \(2013\)](#), by assuming that the disks are formed when a certain criterion of maximum surface angular velocity in the evolving stars is reached, though our results are still below (by an order of magnitude for $M \gtrsim 12M_{\odot}$) their results. That means that, even if $\alpha = 1$ in their disks, they will still have to be denser than ours in order for them to extract the required angular momentum from the star. Also, the red dots from are for the assumption of $\alpha = 1$ in their VDDs, which means that they must be roughly the upper limits of their determinations of $(-\partial M/\partial t)_{\text{steady}}$.

It is therefore an important fact that the compatibility of our three works require that $\alpha_{\text{bu}} \sim 1$, which was obtained in our results.

The fact that the curves of [Granada et al. \(2013\)](#) lie up to one order of magnitude above our results and the ones of [Vieira et al.](#) suggests that their assumed disks were made much too dense to be able to remove the needed angular momentum. The evolutionary models of [Granada et al. \(2013\)](#) with the disk prescription only generated decretion disks if their initial rotation rate was $W_{\text{ZAMS}} > 0.66$ (or $\omega_{\text{ZAMS}} > 0.9$) and if $W > 0.88$ was reached. That happened during $\lesssim 0.1\%$ of the stars' life in the main sequence. The authors showed however that by lowering the maximum velocity criterion of one of their models to a maximum velocity that is satisfied by most Be stars, they could make the appearance of disks with a frequency more compatible with the fraction of Be stars found in clusters. The obtained mass and angular momentum loss rates didn't change appreciably from the obtained with previous models, however. This may lead us to believe that the lowering of the maximum velocity criterion may not explain why their required disks are denser than the observed ones.

The authors pointed that the inclusion of other mechanisms taking place inside the star (e.g., magnetic coupling between the core and the envelope) would lead to faster surface rotation, enhancing the integrated time of appearance of decretion disks. Our results, however, seem to point in the other direction. Maybe, the internal coupling assumed in their evolutionary models is too strong, resulting in an excessive transport of angular momentum from the contracting core to the outer layers, resulting in the necessity of creating a too dense VDD in order to extract angular momentum from the surface of the star and prevent it from breaking-up.

We conclude that, although the Be phenomenon is probably a powerful velocity breaking mechanism for the outer layers of the star, its effect on the star as a whole is expected to be modest. Our determinations of angular momentum loss show that, even if the Be phenomenon happened during $\sim 30\%$ of the stellar main sequence lifetime, and the integrated time of all build-up phases were $\sim 30\%$ of that time, that would lead to the removal of $\sim 1\%$ of the initial angular momentum of the star, which, for fast rotating stars of masses from $7M_{\odot}$ to $15M_{\odot}$ is of $8 - 30 \times 10^{51} \text{ g cm}^2 \text{ s}^{-1}$ ([Granada et al., 2013](#)).

Table 6.1 - Results of the pipeline for each star and bump of the sample

OGLE-II ID	Bump ID	M/M_{\odot}	t/t_{MS}	W	$\cos i$	Σ_0 [g cm $^{-2}$]	α_{bu}	α_{d}	$\tilde{\tau}_{\text{bu}}$	$(-\frac{\partial M}{\partial t})_{\text{typ}}$ [$10^{-9} \times M_{\odot} \text{ yr}^{-1}$]	$(-\frac{\partial J}{\partial t})_{\text{std}}$ [$10^{36} \times \text{ g cm}^2 \text{ s}^{-2}$]	$-\Delta J_*$ [$10^{44} \times \text{ g cm}^2 \text{ s}^{-1}$]
smc_sc1 7612	01	$12.8^{+2.6}_{-2.6}$	$0.5^{+0.3}_{-0.3}$	$0.81^{+0.11}_{-0.1}$	$0.36^{+0.11}_{-0.04}$	$1.1^{+1.3}_{-0.6}$	$0.33^{+0.68}_{-0.24}$	$0.65^{+0.54}_{-0.41}$	$0.15^{+0.32}_{-0.11}$	$0.62^{+0.65}_{-0.38}$	$1.09^{+1.35}_{-0.68}$	$0.07^{+0.08}_{-0.04}$
	02					$1.3^{+1.2}_{-0.7}$	$0.38^{+0.64}_{-0.27}$	$0.62^{+0.53}_{-0.4}$	$0.15^{+0.28}_{-0.1}$	$0.77^{+0.8}_{-0.45}$	$1.35^{+1.66}_{-0.81}$	$0.07^{+0.08}_{-0.04}$
smc_sc1 60553	01	$12.7^{+2.8}_{-1.9}$	$0.7^{+0.2}_{-0.3}$	$0.81^{+0.1}_{-0.11}$	$0.66^{+0.12}_{-0.1}$	$1.6^{+0.7}_{-0.4}$	$1.25^{+0.18}_{-0.25}$	$0.09^{+0.04}_{-0.03}$	$2.76^{+0.5}_{-0.57}$	$4.32^{+2.2}_{-1.54}$	$8.24^{+5.62}_{-3.31}$	$2.63^{+1.73}_{-1.05}$
smc_sc1 75701	01	$14.7^{+1.7}_{-2.3}$	$0.7^{+0.2}_{-0.2}$	$0.81^{+0.1}_{-0.1}$	$0.7^{+0.15}_{-0.1}$	$1.9^{+0.8}_{-0.4}$	$0.24^{+0.18}_{-0.08}$	$0.11^{+0.08}_{-0.05}$	$0.66^{+0.48}_{-0.22}$	$1.15^{+1.06}_{-0.52}$	$2.47^{+2.62}_{-1.24}$	$1.03^{+1.08}_{-0.52}$
smc_sc1 92262	01	$12.7^{+2.5}_{-1.8}$	$0.6^{+0.2}_{-0.3}$	$0.8^{+0.11}_{-0.09}$	$0.03^{+0.03}_{-0.02}$	$1.5^{+1.0}_{-0.9}$	$0.47^{+0.6}_{-0.29}$	$0.84^{+0.4}_{-0.38}$	$0.53^{+0.63}_{-0.34}$	$1.07^{+1.62}_{-0.56}$	$2.01^{+2.83}_{-1.06}$	$0.31^{+0.4}_{-0.16}$
	02					$2.4^{+0.4}_{-0.5}$	$0.99^{+0.26}_{-0.23}$	$0.94^{+0.35}_{-0.3}$	$1.2^{+0.58}_{-0.37}$	$4.42^{+2.72}_{-1.42}$	$8.36^{+6.38}_{-3.24}$	$1.51^{+1.01}_{-0.62}$
smc_sc2 94939	01	$12.2^{+2.7}_{-2.3}$	$0.6^{+0.2}_{-0.3}$	$0.81^{+0.1}_{-0.11}$	$0.45^{+0.13}_{-0.07}$	$2.4^{+0.7}_{-0.8}$	$0.88^{+0.42}_{-0.45}$	$0.69^{+0.43}_{-0.33}$	$1.15^{+0.53}_{-0.56}$	$3.44^{+2.61}_{-1.75}$	$6.05^{+5.42}_{-3.17}$	$1.06^{+0.92}_{-0.56}$
smc_sc3 5719	01	$12.3^{+2.7}_{-2.3}$	$0.6^{+0.3}_{-0.3}$	$0.81^{+0.1}_{-0.11}$	$0.38^{+0.11}_{-0.05}$	$2.6^{+0.5}_{-0.8}$	$0.72^{+0.42}_{-0.33}$	$0.47^{+0.36}_{-0.22}$	$3.83^{+2.41}_{-1.72}$	$3.25^{+2.3}_{-1.77}$	$5.73^{+4.5}_{-3.18}$	$4.09^{+3.25}_{-2.27}$
smc_sc3 15970	01	$13.5^{+1.5}_{-1.3}$	$0.8^{+0.1}_{-0.2}$	$0.87^{+0.07}_{-0.09}$	$0.63^{+0.05}_{-0.03}$	$1.1^{+0.2}_{-0.1}$	$0.89^{+0.31}_{-0.45}$	$0.13^{+0.05}_{-0.04}$	$1.64^{+0.67}_{-0.79}$	$2.52^{+1.15}_{-1.14}$	$5.31^{+3.1}_{-2.54}$	$1.55^{+0.95}_{-0.74}$
	02					$1.4^{+0.2}_{-0.2}$	$0.85^{+0.29}_{-0.31}$	$0.17^{+0.04}_{-0.04}$	$1.92^{+0.77}_{-0.7}$	$2.89^{+1.38}_{-1.03}$	$6.17^{+3.61}_{-2.52}$	$2.24^{+1.22}_{-0.92}$
	03					$1.2^{+0.2}_{-0.1}$	$1.1^{+0.25}_{-0.3}$	$0.12^{+0.05}_{-0.05}$	$2.62^{+0.83}_{-0.9}$	$3.27^{+1.37}_{-1.12}$	$6.97^{+3.75}_{-2.73}$	$2.62^{+1.66}_{-1.18}$
smc_sc3 71445	01	$11.2^{+2.7}_{-2.3}$	$0.5^{+0.3}_{-0.3}$	$0.81^{+0.1}_{-0.1}$	$0.43^{+0.09}_{-0.06}$	$2.5^{+0.6}_{-0.6}$	$0.57^{+0.41}_{-0.25}$	$0.75^{+0.37}_{-0.31}$	$1.11^{+0.8}_{-0.48}$	$2.14^{+1.74}_{-1.0}$	$3.42^{+3.2}_{-1.7}$	$0.83^{+0.77}_{-0.41}$
	02					$1.4^{+0.7}_{-0.5}$	$0.65^{+0.53}_{-0.34}$	$1.05^{+0.31}_{-0.38}$	$0.47^{+0.41}_{-0.24}$	$1.38^{+0.91}_{-0.61}$	$2.19^{+1.74}_{-1.02}$	$0.2^{+0.17}_{-0.09}$
smc_sc3 125899	01	$13.4^{+2.3}_{-2.4}$	$0.6^{+0.2}_{-0.3}$	$0.82^{+0.1}_{-0.11}$	$0.37^{+0.17}_{-0.06}$	$1.7^{+0.9}_{-0.7}$	$0.7^{+0.54}_{-0.44}$	$0.41^{+0.33}_{-0.22}$	$0.89^{+0.7}_{-0.53}$	$2.14^{+2.11}_{-1.32}$	$4.04^{+4.74}_{-2.55}$	$0.73^{+0.88}_{-0.46}$
smc_sc3 197941	01	$12.0^{+2.5}_{-1.8}$	$0.8^{+0.2}_{-0.2}$	$0.82^{+0.1}_{-0.11}$	$0.57^{+0.15}_{-0.05}$	$0.8^{+0.3}_{-0.2}$	$0.4^{+0.52}_{-0.23}$	$0.1^{+0.04}_{-0.04}$	$1.43^{+1.79}_{-0.81}$	$0.69^{+0.82}_{-0.38}$	$1.3^{+1.69}_{-0.75}$	$0.66^{+0.85}_{-0.38}$
smc_sc4 22859	01	$9.5^{+2.5}_{-2.1}$	$0.4^{+0.3}_{-0.3}$	$0.81^{+0.1}_{-0.11}$	$0.64^{+0.19}_{-0.1}$	$0.4^{+0.2}_{-0.1}$	$0.66^{+0.57}_{-0.51}$	$0.04^{+0.64}_{-0.02}$	$3.5^{+3.15}_{-2.71}$	$0.27^{+0.26}_{-0.19}$	$0.35^{+0.42}_{-0.25}$	$0.21^{+0.25}_{-0.15}$
smc_sc4 71499	01	$14.5^{+1.8}_{-2.2}$	$0.7^{+0.2}_{-0.2}$	$0.82^{+0.1}_{-0.09}$	$0.54^{+0.07}_{-0.03}$	$1.3^{+0.5}_{-0.3}$	$0.7^{+0.46}_{-0.35}$	$0.25^{+0.11}_{-0.08}$	$0.96^{+0.66}_{-0.47}$	$2.15^{+1.3}_{-0.94}$	$4.6^{+3.3}_{-2.26}$	$0.94^{+0.67}_{-0.46}$
smc_sc4 71499	02					$1.5^{+0.5}_{-0.3}$	$0.64^{+0.47}_{-0.34}$	$0.19^{+0.06}_{-0.06}$	$1.16^{+0.83}_{-0.63}$	$2.18^{+1.77}_{-1.0}$	$4.59^{+4.38}_{-2.23}$	$1.26^{+1.19}_{-0.61}$
smc_sc4 120783	01	$15.2^{+1.2}_{-1.8}$	$0.9^{+0.1}_{-0.1}$	$0.84^{+0.09}_{-0.1}$	$0.64^{+0.2}_{-0.11}$	$0.7^{+0.3}_{-0.2}$	$0.63^{+0.54}_{-0.43}$	$0.11^{+0.06}_{-0.05}$	$1.56^{+1.33}_{-1.06}$	$1.47^{+1.37}_{-0.93}$	$3.67^{+3.63}_{-2.41}$	$1.53^{+1.46}_{-1.01}$
smc_sc4 127840	01	$14.3^{+1.7}_{-1.8}$	$0.9^{+0.1}_{-0.2}$	$0.83^{+0.09}_{-0.11}$	$0.6^{+0.15}_{-0.09}$	$2.6^{+0.5}_{-0.6}$	$0.4^{+0.23}_{-0.15}$	$0.85^{+0.4}_{-0.41}$	$0.54^{+0.3}_{-0.19}$	$3.19^{+2.4}_{-1.53}$	$7.35^{+6.28}_{-3.72}$	$1.6^{+1.3}_{-0.8}$
smc_sc4 156248	01	$12.3^{+2.8}_{-1.9}$	$0.7^{+0.2}_{-0.3}$	$0.81^{+0.09}_{-0.1}$	$0.07^{+0.02}_{-0.04}$	$1.3^{+1.4}_{-0.9}$	$0.5^{+0.73}_{-0.34}$	$0.78^{+0.43}_{-0.41}$	$1.44^{+1.98}_{-1.0}$	$0.83^{+3.31}_{-0.56}$	$1.6^{+6.2}_{-1.07}$	$0.63^{+2.39}_{-0.43}$
smc_sc4 156251	01	$15.3^{+1.2}_{-1.7}$	$0.7^{+0.1}_{-0.2}$	$0.83^{+0.1}_{-0.1}$	$0.76^{+0.08}_{-0.07}$	$2.2^{+0.4}_{-0.4}$	$0.4^{+0.16}_{-0.11}$	$0.78^{+0.4}_{-0.33}$	$0.37^{+0.14}_{-0.1}$	$2.52^{+1.17}_{-0.91}$	$5.83^{+3.14}_{-2.42}$	$0.86^{+0.48}_{-0.37}$
	02					$1.5^{+0.2}_{-0.2}$	$0.65^{+0.29}_{-0.18}$	$0.61^{+0.35}_{-0.21}$	$0.62^{+0.25}_{-0.16}$	$2.7^{+1.46}_{-0.98}$	$6.27^{+3.88}_{-2.6}$	$0.94^{+0.57}_{-0.39}$
	03					$2.5^{+0.4}_{-0.4}$	$0.8^{+0.42}_{-0.33}$	$0.49^{+0.18}_{-0.13}$	$0.96^{+0.47}_{-0.36}$	$5.27^{+2.84}_{-2.16}$	$11.98^{+7.6}_{-5.13}$	$2.31^{+1.45}_{-0.92}$
smc_sc4 159829	01	$13.1^{+2.6}_{-2.3}$	$0.6^{+0.3}_{-0.3}$	$0.8^{+0.11}_{-0.1}$	$0.61^{+0.1}_{-0.07}$	$2.0^{+0.7}_{-0.5}$	$1.07^{+0.28}_{-0.34}$	$0.25^{+0.1}_{-0.08}$	$1.47^{+0.48}_{-0.48}$	$3.91^{+1.91}_{-1.44}$	$7.21^{+4.56}_{-2.97}$	$1.37^{+0.84}_{-0.56}$
	02					$2.1^{+0.6}_{-0.4}$	$0.96^{+0.36}_{-0.36}$	$0.67^{+0.31}_{-0.24}$	$2.26^{+0.84}_{-0.77}$	$3.64^{+1.99}_{-1.56}$	$6.74^{+4.54}_{-3.15}$	$2.18^{+1.49}_{-1.0}$

Table 6.1 - continued.

OGLE-II ID	Bump ID	M/M_{\odot}	t/t_{MS}	W	$\cos i$	Σ_0 [g cm $^{-2}$]	α_{bu}	α_{d}	$\tilde{\tau}_{\text{bu}}$	$(-\frac{\partial M}{\partial t})_{\text{typ}}$ [$10^{-9} \times M_{\odot} \text{ yr}^{-1}$]	$(-\frac{\partial J}{\partial t})_{\text{std}}$ [$10^{36} \times \text{ g cm}^2 \text{ s}^{-2}$]	$-\Delta J_*$ [$10^{44} \times \text{ g cm}^2 \text{ s}^{-1}$]
smc_sc4 159857	01	$13.7^{+1.9}_{-2.3}$	$0.7^{+0.2}_{-0.3}$	$0.81^{+0.1}_{-0.1}$	$0.55^{+0.08}_{-0.03}$	$0.6^{+1.0}_{-0.2}$	$0.42^{+0.64}_{-0.32}$	$0.66^{+0.46}_{-0.35}$	$0.28^{+0.45}_{-0.22}$	$0.62^{+0.5}_{-0.36}$	$1.22^{+1.15}_{-0.75}$	$0.12^{+0.11}_{-0.07}$
	02					$1.0^{+0.6}_{-0.2}$	$0.7^{+0.48}_{-0.43}$	$0.34^{+0.56}_{-0.16}$	$0.42^{+0.28}_{-0.27}$	$1.38^{+0.94}_{-0.65}$	$2.7^{+2.24}_{-1.36}$	$0.22^{+0.19}_{-0.11}$
smc_sc4 163828	01	$9.7^{+2.4}_{-2.0}$	$0.4^{+0.4}_{-0.3}$	$0.79^{+0.11}_{-0.1}$	$0.71^{+0.14}_{-0.08}$	$0.7^{+0.2}_{-0.1}$	$0.53^{+0.58}_{-0.33}$	$0.06^{+0.05}_{-0.02}$	$3.42^{+3.83}_{-2.13}$	$0.43^{+0.5}_{-0.25}$	$0.59^{+0.78}_{-0.36}$	$0.44^{+0.58}_{-0.26}$
smc_sc4 167554	01	$9.9^{+2.4}_{-2.1}$	$0.4^{+0.3}_{-0.2}$	$0.82^{+0.1}_{-0.1}$	$0.63^{+0.12}_{-0.09}$	$0.9^{+0.7}_{-0.3}$	$0.54^{+0.51}_{-0.36}$	$0.6^{+0.45}_{-0.29}$	$0.45^{+0.42}_{-0.3}$	$0.59^{+0.46}_{-0.31}$	$0.82^{+0.76}_{-0.46}$	$0.08^{+0.08}_{-0.04}$
	02					$1.6^{+0.7}_{-0.5}$	$0.42^{+0.47}_{-0.21}$	$0.86^{+0.41}_{-0.37}$	$0.42^{+0.5}_{-0.2}$	$0.86^{+0.82}_{-0.41}$	$1.19^{+1.44}_{-0.61}$	$0.14^{+0.15}_{-0.07}$
smc_sc4 171253	01	$14.3^{+1.9}_{-2.5}$	$0.6^{+0.2}_{-0.3}$	$0.81^{+0.11}_{-0.11}$	$0.58^{+0.13}_{-0.06}$	$0.3^{+1.2}_{-0.1}$	$0.29^{+0.74}_{-0.28}$	$0.81^{+0.44}_{-0.49}$	$0.24^{+0.6}_{-0.23}$	$0.16^{+0.3}_{-0.12}$	$0.32^{+0.65}_{-0.23}$	$0.04^{+0.07}_{-0.03}$
	02					$0.3^{+0.8}_{-0.1}$	$0.48^{+0.66}_{-0.44}$	$0.64^{+0.52}_{-0.42}$	$0.31^{+0.45}_{-0.29}$	$0.29^{+0.32}_{-0.2}$	$0.58^{+0.7}_{-0.4}$	$0.05^{+0.06}_{-0.04}$
smc_sc4 175272	01	$12.1^{+2.8}_{-2.4}$	$0.5^{+0.3}_{-0.3}$	$0.81^{+0.1}_{-0.1}$	$0.38^{+0.12}_{-0.06}$	$1.8^{+0.8}_{-0.7}$	$0.75^{+0.49}_{-0.39}$	$0.48^{+0.29}_{-0.23}$	$2.31^{+1.52}_{-1.21}$	$2.07^{+1.73}_{-1.16}$	$3.52^{+3.33}_{-2.05}$	$1.37^{+1.31}_{-0.8}$
smc_sc4 179053	01	$12.6^{+2.6}_{-2.3}$	$0.6^{+0.3}_{-0.4}$	$0.8^{+0.11}_{-0.11}$	$0.02^{+0.02}_{-0.02}$	$2.1^{+0.7}_{-0.6}$	$0.96^{+0.37}_{-0.52}$	$1.1^{+0.27}_{-0.32}$	$2.14^{+1.11}_{-1.16}$	$3.1^{+1.84}_{-1.32}$	$5.5^{+4.29}_{-2.58}$	$1.74^{+1.19}_{-0.86}$
smc_sc5 11453	01	$13.6^{+2.2}_{-2.3}$	$0.7^{+0.2}_{-0.3}$	$0.81^{+0.11}_{-0.11}$	$0.38^{+0.12}_{-0.06}$	$1.8^{+0.7}_{-0.7}$	$0.9^{+0.38}_{-0.4}$	$0.26^{+0.15}_{-0.11}$	$4.17^{+1.82}_{-1.74}$	$3.3^{+2.78}_{-1.81}$	$6.49^{+6.33}_{-3.7}$	$4.41^{+4.36}_{-2.51}$
smc_sc5 21117	01	$13.5^{+1.9}_{-1.7}$	$0.7^{+0.1}_{-0.2}$	$0.84^{+0.09}_{-0.1}$	$0.52^{+0.04}_{-0.02}$	$1.3^{+0.3}_{-0.2}$	$0.5^{+0.32}_{-0.17}$	$0.61^{+0.48}_{-0.32}$	$0.64^{+0.39}_{-0.23}$	$1.46^{+1.04}_{-0.57}$	$2.97^{+2.63}_{-1.34}$	$0.56^{+0.47}_{-0.26}$
	02					$1.8^{+0.5}_{-0.4}$	$0.58^{+0.4}_{-0.26}$	$0.17^{+0.08}_{-0.05}$	$0.85^{+0.55}_{-0.38}$	$2.44^{+1.63}_{-1.04}$	$4.99^{+3.88}_{-2.39}$	$1.08^{+0.78}_{-0.51}$
	03					$1.9^{+0.6}_{-0.5}$	$0.57^{+0.28}_{-0.19}$	$0.35^{+0.23}_{-0.13}$	$0.57^{+0.28}_{-0.18}$	$2.53^{+1.34}_{-1.01}$	$5.13^{+3.52}_{-2.37}$	$0.76^{+0.54}_{-0.35}$
	04					$1.3^{+0.2}_{-0.2}$	$0.87^{+0.36}_{-0.3}$	$0.16^{+0.07}_{-0.05}$	$3.11^{+1.26}_{-1.03}$	$2.65^{+1.36}_{-1.09}$	$5.36^{+3.51}_{-2.46}$	$2.83^{+1.95}_{-1.29}$
smc_sc5 21134	01	$12.7^{+2.5}_{-2.4}$	$0.6^{+0.2}_{-0.3}$	$0.8^{+0.11}_{-0.09}$	$0.38^{+0.15}_{-0.06}$	$0.8^{+1.4}_{-0.4}$	$0.4^{+0.68}_{-0.33}$	$0.18^{+0.26}_{-0.11}$	$0.34^{+0.59}_{-0.28}$	$0.54^{+0.58}_{-0.36}$	$0.97^{+1.22}_{-0.66}$	$0.12^{+0.15}_{-0.08}$
smc_sc5 32377	01	$13.3^{+2.3}_{-2.2}$	$0.7^{+0.2}_{-0.3}$	$0.81^{+0.1}_{-0.11}$	$0.34^{+0.06}_{-0.03}$	$1.9^{+0.9}_{-0.7}$	$0.71^{+0.45}_{-0.4}$	$0.66^{+0.48}_{-0.33}$	$0.3^{+0.28}_{-0.17}$	$2.53^{+2.18}_{-1.38}$	$4.93^{+4.81}_{-2.77}$	$0.31^{+0.3}_{-0.17}$
	02					$2.2^{+0.8}_{-0.6}$	$0.51^{+0.41}_{-0.24}$	$0.32^{+0.15}_{-0.12}$	$0.84^{+0.69}_{-0.38}$	$2.31^{+1.89}_{-1.12}$	$4.49^{+4.36}_{-2.34}$	$1.08^{+1.03}_{-0.56}$
smc_sc5 43650	01	$10.7^{+3.0}_{-2.6}$	$0.4^{+0.3}_{-0.3}$	$0.81^{+0.1}_{-0.11}$	$0.55^{+0.09}_{-0.04}$	$0.5^{+1.2}_{-0.2}$	$0.35^{+0.75}_{-0.3}$	$0.39^{+0.71}_{-0.3}$	$0.61^{+1.32}_{-0.53}$	$0.24^{+0.33}_{-0.16}$	$0.35^{+0.59}_{-0.23}$	$0.07^{+0.12}_{-0.05}$
	02					$0.6^{+0.2}_{-0.2}$	$0.72^{+0.53}_{-0.53}$	$0.53^{+0.67}_{-0.42}$	$6.35^{+4.94}_{-4.65}$	$0.5^{+0.45}_{-0.33}$	$0.71^{+0.83}_{-0.46}$	$0.74^{+0.92}_{-0.47}$
smc_sc5 54851	01	$11.7^{+1.6}_{-1.5}$	$0.7^{+0.1}_{-0.1}$	$0.78^{+0.1}_{-0.08}$	$0.62^{+0.04}_{-0.01}$	$1.3^{+0.3}_{-0.2}$	$0.38^{+0.35}_{-0.14}$	$0.11^{+0.04}_{-0.03}$	$0.82^{+0.73}_{-0.3}$	$1.06^{+0.78}_{-0.42}$	$1.95^{+1.69}_{-0.9}$	$0.59^{+0.5}_{-0.28}$
	02					$1.3^{+0.2}_{-0.2}$	$0.48^{+0.42}_{-0.21}$	$0.12^{+0.04}_{-0.03}$	$1.19^{+0.99}_{-0.54}$	$1.28^{+1.07}_{-0.58}$	$2.33^{+2.28}_{-1.18}$	$0.8^{+0.79}_{-0.41}$
	03					$1.1^{+0.2}_{-0.1}$	$0.51^{+0.25}_{-0.2}$	$0.05^{+0.01}_{-0.01}$	$2.11^{+0.99}_{-0.8}$	$1.12^{+0.7}_{-0.49}$	$2.04^{+1.52}_{-0.97}$	$1.19^{+0.88}_{-0.57}$
smc_sc5 65500	01	$12.1^{+2.9}_{-2.4}$	$0.6^{+0.2}_{-0.3}$	$0.81^{+0.1}_{-0.1}$	$0.71^{+0.13}_{-0.08}$	$1.7^{+0.6}_{-0.4}$	$0.7^{+0.38}_{-0.34}$	$0.26^{+0.13}_{-0.1}$	$0.44^{+0.24}_{-0.19}$	$2.07^{+1.66}_{-1.02}$	$3.7^{+3.62}_{-2.05}$	$0.32^{+0.31}_{-0.17}$
smc_sc5 129535	01	$9.4^{+2.2}_{-2.0}$	$0.5^{+0.3}_{-0.3}$	$0.81^{+0.1}_{-0.11}$	$0.58^{+0.13}_{-0.06}$	$0.7^{+0.2}_{-0.2}$	$0.65^{+0.52}_{-0.37}$	$0.25^{+0.36}_{-0.13}$	$3.88^{+3.02}_{-2.29}$	$0.58^{+0.54}_{-0.32}$	$0.8^{+0.86}_{-0.46}$	$0.56^{+0.6}_{-0.33}$
smc_sc5 145724	01	$9.2^{+2.1}_{-1.8}$	$0.5^{+0.3}_{-0.3}$	$0.81^{+0.1}_{-0.1}$	$0.4^{+0.13}_{-0.06}$	$2.6^{+0.7}_{-1.0}$	$0.88^{+0.4}_{-0.46}$	$0.16^{+0.19}_{-0.08}$	$3.87^{+1.89}_{-1.98}$	$2.6^{+2.03}_{-1.55}$	$3.46^{+3.23}_{-2.12}$	$1.79^{+1.7}_{-1.11}$
smc_sc5 180034	01	$12.6^{+2.6}_{-2.6}$	$0.4^{+0.3}_{-0.3}$	$0.8^{+0.1}_{-0.1}$	$0.62^{+0.17}_{-0.09}$	$1.0^{+0.5}_{-0.3}$	$0.4^{+0.65}_{-0.25}$	$0.22^{+0.17}_{-0.09}$	$0.97^{+1.54}_{-0.57}$	$0.68^{+0.81}_{-0.4}$	$1.17^{+1.57}_{-0.71}$	$0.36^{+0.47}_{-0.22}$

Table 6.1 - continued.

OGLE-II ID	Bump ID	M/M_{\odot}	t/t_{MS}	W	$\cos i$	Σ_0 [g cm $^{-2}$]	α_{bu}	α_{d}	$\tilde{\tau}_{\text{bu}}$	$(-\frac{\partial M}{\partial t})_{\text{typ}}$ [$10^{-9} \times$ $M_{\odot} \text{ yr}^{-1}$]	$(-\frac{\partial J}{\partial t})_{\text{std}}$ [$10^{36} \times$ g cm $^2 \text{ s}^{-2}$]	$-\Delta J_*$ [$10^{44} \times$ g cm $^2 \text{ s}^{-1}$]
smc_sc5 260841	01	$12.7^{+2.4}_{-2.0}$	$0.6^{+0.2}_{-0.3}$	$0.83^{+0.09}_{-0.1}$	$0.54^{+0.08}_{-0.03}$	$0.6^{+0.4}_{-0.1}$	$0.8^{+0.42}_{-0.49}$	$0.07^{+0.58}_{-0.03}$	$1.42^{+0.81}_{-0.93}$	$0.86^{+0.71}_{-0.45}$	$1.58^{+1.61}_{-0.88}$	$0.38^{+0.38}_{-0.22}$
	02					$0.5^{+0.2}_{-0.1}$	$0.78^{+0.4}_{-0.41}$	$0.08^{+0.78}_{-0.04}$	$2.49^{+1.47}_{-1.38}$	$0.78^{+0.6}_{-0.41}$	$1.44^{+1.39}_{-0.82}$	$0.64^{+0.64}_{-0.36}$
smc_sc5 260957	01	$9.4^{+2.5}_{-1.9}$	$0.5^{+0.3}_{-0.3}$	$0.82^{+0.1}_{-0.11}$	$0.58^{+0.13}_{-0.06}$	$1.3^{+0.4}_{-0.3}$	$0.64^{+0.46}_{-0.3}$	$0.05^{+0.02}_{-0.02}$	$2.41^{+1.92}_{-1.1}$	$1.07^{+0.89}_{-0.57}$	$1.48^{+1.49}_{-0.85}$	$0.66^{+0.68}_{-0.38}$
smc_sc5 266088	01	$8.8^{+2.4}_{-2.1}$	$0.4^{+0.4}_{-0.3}$	$0.8^{+0.1}_{-0.1}$	$0.71^{+0.14}_{-0.08}$	$0.7^{+0.4}_{-0.2}$	$0.29^{+0.73}_{-0.22}$	$0.07^{+0.07}_{-0.03}$	$1.53^{+3.83}_{-1.17}$	$0.23^{+0.46}_{-0.15}$	$0.31^{+0.58}_{-0.21}$	$0.18^{+0.34}_{-0.12}$
smc_sc5 276982	01	$15.2^{+1.3}_{-2.0}$	$0.5^{+0.2}_{-0.2}$	$0.81^{+0.1}_{-0.11}$	$0.78^{+0.11}_{-0.11}$	$1.0^{+0.4}_{-0.3}$	$0.05^{+0.18}_{-0.03}$	$0.06^{+0.05}_{-0.02}$	$0.25^{+0.8}_{-0.13}$	$0.13^{+0.26}_{-0.06}$	$0.26^{+0.57}_{-0.14}$	$0.17^{+0.34}_{-0.09}$
smc_sc5 282963	01	$13.8^{+2.1}_{-2.4}$	$0.7^{+0.2}_{-0.3}$	$0.82^{+0.1}_{-0.11}$	$0.37^{+0.11}_{-0.05}$	$1.5^{+0.7}_{-0.5}$	$0.69^{+0.47}_{-0.35}$	$0.44^{+0.29}_{-0.19}$	$5.52^{+3.69}_{-2.75}$	$2.46^{+1.98}_{-1.47}$	$5.05^{+4.7}_{-3.2}$	$6.01^{+5.53}_{-3.82}$
smc_sc6 11085	01	$15.7^{+1.0}_{-2.0}$	$0.6^{+0.2}_{-0.3}$	$0.82^{+0.09}_{-0.1}$	$0.69^{+0.07}_{-0.07}$	$2.3^{+0.6}_{-0.4}$	$0.63^{+0.47}_{-0.26}$	$0.16^{+0.09}_{-0.05}$	$0.87^{+0.63}_{-0.36}$	$3.17^{+2.3}_{-1.35}$	$6.76^{+5.89}_{-3.13}$	$1.39^{+1.2}_{-0.65}$
	02					$2.5^{+0.6}_{-0.6}$	$0.65^{+0.43}_{-0.24}$	$0.34^{+0.2}_{-0.1}$	$1.04^{+0.63}_{-0.36}$	$3.66^{+2.39}_{-1.49}$	$7.79^{+6.18}_{-3.49}$	$1.82^{+1.43}_{-0.8}$
smc_sc6 17538	01	$8.8^{+2.5}_{-2.1}$	$0.3^{+0.3}_{-0.2}$	$0.81^{+0.1}_{-0.1}$	$0.62^{+0.17}_{-0.1}$	$0.8^{+0.4}_{-0.2}$	$0.63^{+0.55}_{-0.45}$	$0.1^{+0.12}_{-0.05}$	$3.15^{+2.77}_{-2.3}$	$0.5^{+0.49}_{-0.29}$	$0.61^{+0.74}_{-0.36}$	$0.33^{+0.41}_{-0.2}$
smc_sc6 42440	01	$9.4^{+2.6}_{-2.1}$	$0.4^{+0.4}_{-0.3}$	$0.8^{+0.11}_{-0.11}$	$0.37^{+0.14}_{-0.06}$	$1.8^{+0.8}_{-0.8}$	$0.76^{+0.49}_{-0.41}$	$0.2^{+0.16}_{-0.11}$	$2.4^{+1.65}_{-1.29}$	$1.5^{+1.6}_{-0.83}$	$2.01^{+2.62}_{-1.15}$	$0.75^{+0.97}_{-0.44}$
smc_sc6 99991	01	$13.0^{+2.2}_{-2.2}$	$0.7^{+0.2}_{-0.2}$	$0.82^{+0.1}_{-0.1}$	$0.34^{+0.04}_{-0.03}$	$1.6^{+0.6}_{-0.5}$	$0.53^{+0.41}_{-0.23}$	$0.94^{+0.33}_{-0.28}$	$0.64^{+0.51}_{-0.27}$	$1.82^{+1.03}_{-0.72}$	$3.54^{+2.38}_{-1.6}$	$0.61^{+0.41}_{-0.27}$
	02					$1.8^{+0.7}_{-0.4}$	$0.67^{+0.42}_{-0.32}$	$0.75^{+0.31}_{-0.26}$	$1.07^{+0.73}_{-0.49}$	$2.42^{+1.7}_{-1.06}$	$4.68^{+3.84}_{-2.24}$	$1.09^{+0.85}_{-0.52}$
	03					$1.8^{+0.5}_{-0.4}$	$0.51^{+0.4}_{-0.22}$	$0.82^{+0.33}_{-0.27}$	$0.81^{+0.63}_{-0.34}$	$1.89^{+1.26}_{-0.77}$	$3.64^{+2.95}_{-1.66}$	$0.82^{+0.65}_{-0.36}$
	04					$1.7^{+0.6}_{-0.5}$	$0.42^{+0.53}_{-0.18}$	$0.94^{+0.28}_{-0.26}$	$0.78^{+1.0}_{-0.36}$	$1.56^{+1.05}_{-0.66}$	$3.04^{+2.29}_{-1.44}$	$0.8^{+0.61}_{-0.37}$
smc_sc6 105368	01	$12.4^{+2.7}_{-2.5}$	$0.5^{+0.2}_{-0.3}$	$0.82^{+0.11}_{-0.1}$	$0.53^{+0.05}_{-0.03}$	$1.0^{+0.4}_{-0.2}$	$0.56^{+0.5}_{-0.32}$	$0.2^{+0.12}_{-0.07}$	$1.03^{+0.9}_{-0.59}$	$0.89^{+0.79}_{-0.45}$	$1.52^{+1.66}_{-0.81}$	$0.36^{+0.39}_{-0.19}$
	02					$1.5^{+0.7}_{-0.5}$	$0.24^{+0.45}_{-0.12}$	$0.22^{+0.2}_{-0.09}$	$0.56^{+1.02}_{-0.27}$	$0.65^{+0.76}_{-0.31}$	$1.17^{+1.53}_{-0.63}$	$0.34^{+0.43}_{-0.18}$
smc_sc6 116294	01	$9.2^{+2.3}_{-1.8}$	$0.5^{+0.3}_{-0.3}$	$0.81^{+0.1}_{-0.11}$	$0.4^{+0.14}_{-0.06}$	$2.6^{+0.7}_{-1.0}$	$0.89^{+0.38}_{-0.38}$	$0.18^{+0.19}_{-0.09}$	$2.39^{+1.03}_{-1.09}$	$2.67^{+2.3}_{-1.5}$	$3.63^{+3.66}_{-2.09}$	$1.13^{+1.13}_{-0.65}$
smc_sc6 128831	01	$12.2^{+2.7}_{-2.2}$	$0.6^{+0.2}_{-0.3}$	$0.8^{+0.11}_{-0.09}$	$0.03^{+0.02}_{-0.02}$	$2.6^{+0.5}_{-0.6}$	$0.98^{+0.35}_{-0.4}$	$0.69^{+0.34}_{-0.27}$	$0.82^{+0.32}_{-0.36}$	$4.18^{+2.2}_{-1.72}$	$7.47^{+4.69}_{-3.44}$	$0.84^{+0.61}_{-0.4}$
smc_sc6 199611	01	$13.8^{+2.1}_{-2.0}$	$0.8^{+0.2}_{-0.3}$	$0.81^{+0.1}_{-0.1}$	$0.37^{+0.12}_{-0.06}$	$1.4^{+1.4}_{-0.7}$	$0.47^{+0.62}_{-0.33}$	$0.34^{+0.34}_{-0.18}$	$0.35^{+0.48}_{-0.25}$	$1.48^{+1.51}_{-0.91}$	$3.03^{+3.73}_{-1.93}$	$0.34^{+0.42}_{-0.21}$
smc_sc6 272665	01	$7.0^{+1.8}_{-1.2}$	$0.4^{+0.3}_{-0.3}$	$0.8^{+0.11}_{-0.1}$	$0.37^{+0.14}_{-0.05}$	$0.7^{+0.4}_{-0.2}$	$0.68^{+0.54}_{-0.46}$	$0.08^{+0.25}_{-0.05}$	$5.97^{+5.43}_{-4.09}$	$0.37^{+0.37}_{-0.22}$	$0.4^{+0.46}_{-0.24}$	$0.37^{+0.42}_{-0.24}$
smc_sc7 57131	01	$12.1^{+2.6}_{-2.2}$	$0.6^{+0.3}_{-0.3}$	$0.81^{+0.1}_{-0.1}$	$0.39^{+0.12}_{-0.06}$	$2.0^{+0.7}_{-0.7}$	$0.78^{+0.45}_{-0.39}$	$0.74^{+0.41}_{-0.35}$	$1.69^{+0.98}_{-0.81}$	$2.48^{+1.97}_{-1.36}$	$4.32^{+3.9}_{-2.46}$	$1.26^{+1.11}_{-0.73}$
smc_sc8 183240	01	$14.7^{+1.6}_{-1.8}$	$0.8^{+0.1}_{-0.2}$	$0.82^{+0.1}_{-0.11}$	$0.64^{+0.18}_{-0.11}$	$0.7^{+0.3}_{-0.2}$	$0.63^{+0.51}_{-0.38}$	$0.25^{+0.21}_{-0.12}$	$1.1^{+0.86}_{-0.63}$	$1.37^{+1.24}_{-0.8}$	$3.2^{+3.22}_{-1.94}$	$0.92^{+0.89}_{-0.54}$
smc_sc9 105383	01	$13.2^{+2.6}_{-2.5}$	$0.5^{+0.2}_{-0.3}$	$0.83^{+0.09}_{-0.1}$	$0.56^{+0.08}_{-0.05}$	$1.9^{+0.8}_{-0.5}$	$0.52^{+0.5}_{-0.25}$	$0.1^{+0.04}_{-0.03}$	$1.17^{+1.2}_{-0.58}$	$1.82^{+1.58}_{-0.86}$	$3.36^{+3.43}_{-1.76}$	$1.01^{+1.07}_{-0.51}$
	02					$1.8^{+0.5}_{-0.4}$	$0.86^{+0.38}_{-0.39}$	$0.1^{+0.05}_{-0.03}$	$1.76^{+0.73}_{-0.75}$	$2.58^{+1.8}_{-1.15}$	$4.75^{+4.14}_{-2.38}$	$1.3^{+1.12}_{-0.62}$
smc_sc9 168422	01	$9.4^{+2.3}_{-2.0}$	$0.4^{+0.3}_{-0.3}$	$0.82^{+0.1}_{-0.11}$	$0.61^{+0.16}_{-0.08}$	$0.5^{+0.4}_{-0.2}$	$0.56^{+0.62}_{-0.45}$	$0.08^{+0.12}_{-0.04}$	$2.15^{+2.35}_{-1.71}$	$0.33^{+0.41}_{-0.22}$	$0.44^{+0.63}_{-0.3}$	$0.2^{+0.29}_{-0.13}$
smc_sc10 8906	01	$13.9^{+2.0}_{-2.1}$	$0.8^{+0.1}_{-0.2}$	$0.81^{+0.11}_{-0.1}$	$0.58^{+0.1}_{-0.05}$	$2.0^{+1.0}_{-0.7}$	$0.79^{+0.44}_{-0.34}$	$0.47^{+0.26}_{-0.18}$	$0.16^{+0.1}_{-0.07}$	$3.88^{+2.17}_{-1.57}$	$8.2^{+5.63}_{-3.7}$	$0.26^{+0.19}_{-0.12}$

Table 6.1 - continued.

OGLE-II ID	Bump ID	M/M_{\odot}	t/t_{MS}	W	$\cos i$	Σ_0 [g cm $^{-2}$]	α_{bu}	α_{d}	$\tilde{\tau}_{\text{bu}}$	$(-\frac{\partial M}{\partial t})_{\text{typ}}$ [$10^{-9} \times$ $M_{\odot} \text{ yr}^{-1}$]	$(-\frac{\partial J}{\partial t})_{\text{std}}$ [$10^{36} \times$ g cm $^2 \text{ s}^{-2}$]	$-\Delta J_*$ [$10^{44} \times$ g cm $^2 \text{ s}^{-1}$]
	02					$1.8^{+0.7}_{-0.6}$	$0.81^{+0.39}_{-0.35}$	$0.92^{+0.34}_{-0.32}$	$0.06^{+0.03}_{-0.02}$	$3.39^{+2.05}_{-1.5}$	$7.26^{+5.01}_{-3.55}$	$0.09^{+0.06}_{-0.04}$
smc_sc11 28090	01	$13.7^{+2.1}_{-2.1}$	$0.8^{+0.1}_{-0.2}$	$0.83^{+0.09}_{-0.11}$	$0.56^{+0.12}_{-0.05}$	$1.7^{+0.8}_{-0.5}$	$0.1^{+0.1}_{-0.05}$	$0.12^{+0.05}_{-0.05}$	$0.41^{+0.37}_{-0.18}$	$0.48^{+0.41}_{-0.23}$	$1.02^{+1.01}_{-0.54}$	$0.64^{+0.64}_{-0.34}$
smc_sc11 46587	01	$9.0^{+2.5}_{-2.1}$	$0.4^{+0.4}_{-0.3}$	$0.81^{+0.1}_{-0.11}$	$0.39^{+0.19}_{-0.07}$	$0.9^{+0.7}_{-0.4}$	$0.6^{+0.57}_{-0.43}$	$0.36^{+0.51}_{-0.22}$	$4.02^{+3.88}_{-2.89}$	$0.55^{+0.58}_{-0.34}$	$0.72^{+0.91}_{-0.47}$	$0.55^{+0.7}_{-0.36}$

Conclusions

Though my soul may set in darkness,
it will rise in perfect light;
I have loved the stars too fondly to be
fearful of the night.

Sarah Williams, last lines of the
fourth paragraph of the poem *The
Old Astronomer to His Pupil*.

Be stars can be selected from the bulk of light curves from photometric surveys by their characteristic magnitudes and colors and by their quite irregular variability of a few tenths of a magnitude at optical wavelenths (e.g., [Mennickent et al., 2002](#); [Paul et al., 2012](#)). The variability is understood to be due to variable rates of disk feeding by the central fast rotating star.

We presented a new method to model the light curves of Be stars with the goal of extracting quantitative information about the fundamental parameters of their disks, such as the viscosity parameter, α , and the asymptotic surface density (Σ_0). We demonstrated that the new parameter Σ_0 , the asymptotic surface density, which can be thought to correspond to the steady-state surface density of the disk at the stellar equator, is a much more useful way of expressing the mass injection rate and the net angular momentum injection rate of the star into the disk than the pair given by the mass injection rate and the radius of mass injection. Also, we took advantage of the scaling relations of the equation that governs the diffusion of mass through the disk, in order to generate a grid of dynamical models that is independent of the viscosity parameter α , which in this work, was assumed to be time-dependent.

The method we developed uses a large pre-computed grid of synthetic Be light curves, calculated using detailed hydrodynamic calculations coupled with three-dimensional NLTE radiative transfer calculations. The comparison between the model grid and the observed light curves was made possible by the identification of two empirical laws that consists of simple formulas that closely match the photometric behaviour during disk build-up and dissipation.

An initial analysis of our model grid allowed us to draw important conclusions about the properties of viscous decretion discs (VDD) around Be stars, and their effect on the stellar SED as they evolve in time:

- The viscosity parameter α is the most important parameter controlling the observed rate of photometric variations in Be light curves, but it is not the only one. Stellar parameters (mass, radius and effective temperature), as well as the disk viewing angle and density level, all contribute to change the rate of brightness variations in complicated ways, which means that if meaningful information about α is to be extracted from the data, these parameters must be estimated somehow;
- We identified a previously unknown effect, dubbed the mass-reservoir effect, which also controls the rate of photometric variations during phases of disk dissipation. This effect is a consequence of the fact that VDDs build a mass reservoir in their outer regions, which is unnoticed at short wavelengths (e.g., visible). The longer the build-up phase of a disk, the bigger its mass reservoir. When mass injection from the star stops and reaccrretion occurs, the reservoir feeds the inner disk with mass. Clearly, the larger the reservoir, the longer it will be able to supply mass to the inner disk, and the slower the photometric dissipation will appear.

We applied our fitting pipeline to a sample of light curves of 54 Be star candidates from the SMC (Mennickent et al., 2002) containing 81 clearly identified events of disk formation/dissipation (here referred to as bumps). The light curves come from OGLE-II and OGLE-III data, covering roughly 12 years. A Markov Chain Monte Carlo (MCMC) technique was used to properly estimate the posterior probabilities of each fitted parameter.

It was found that our sample is biased towards early type Be stars, likely because these stars are more variable and their disks are denser, resulting in clearer bumps. Also, photometric uncertainties increase for late type Be stars. Since our sample was selected based on the appearance of their bumps, we conclude that our Be disks must be among the densest found for Be stars in the SMC. We verified an increase of Σ_0 with the stellar mass and the median for our whole sample is $\langle \Sigma_0 \rangle = 1.44_{-0.75}^{+1.01} \text{ g cm}^{-2}$. Our results may suggest that Be disks in the SMC are denser than their siblings in the Galaxy, in line with H α surveys that found stronger line emission in the SMC than in our Galaxy.

The durations of the build-up phases become shorter for more massive stars, which indicates that, as was already observed in the Galaxy, late-type Be stars are less variable than early-type ones. The median of the build-up time for our sample is $\langle t_2 - t_1 \rangle = 305_{-171}^{+351}$ days.

We obtained, for the first time, estimates of α for a statistically significant sample of Be stars. In our work, we explored the possibility that the viscosity parameter might be different at build-up (α_{bu}) and dissipation (α_{d}). We found no significant variation of α_{bu}

with the stellar mass (Fig. 6.7, top), but some evidence points to a correlation between α_d with M (Fig. 6.7, bottom). Furthermore, we find that on average the viscosity parameter is larger at build-up than at dissipation. The medians of the two viscosity parameters are $\langle\alpha_{bu}\rangle = 0.63^{+0.52}_{-0.39}$ and $\langle\alpha_d\rangle = 0.29^{+0.61}_{-0.20}$. These values are in agreement in magnitude with the determinations of Carciofi et al. (2012) and Ghoreyshi and Carciofi (2017) for the Galactic Be star 28 CMa. They are also similar to the values of α usually found in cataclysmic variables (King et al., 2007; Kotko and Lasota, 2012).

The trend that $\alpha_{bu} > \alpha_d$ was also seen by Ghoreyshi and Carciofi (2017) in the different cycles of activity of the Be star 28 CMa. Further work is necessary to establish whether this trend is real or simply a result of our model assumptions. In particular, two important physical effects were ignored in this work, namely the fact that Be disks are non-isothermal and the line forces known to act on the disk material. This last point, however, is likely of little importance for Be stars in the SMC, given their low metallicity. The α determinations made in this work should help in investigating the physical mechanisms producing the anomalous viscosity in circumstellar disks environments.

It must be further emphasised that in this work what is really measured are the timescales for disk build-up and dissipation. Under the assumption that viscosity is the only driving mechanism operating on the disk, these timescales can in turn be converted to estimates of the viscosity parameter. The presence of other driving mechanisms (such as the aforementioned ablation) might affect the determination of α in unpredictable ways.

The steady-state mass loss rate for the bumps is of the order of $\sim 10^{-10} M_{\odot} \text{ yr}^{-1}$. The typical decretion rate is of the order of $\sim 10^{-9} M_{\odot} \text{ yr}^{-1}$. These values are in agreement with the upper limit of the observed wind mass loss rate of B stars (Snow, 1981; Puls et al., 2008). In addition, these values roughly agree in magnitude with the work of Vieira et al. (2017), who studied a sample of 80 Galactic Be stars.

The steady-state angular momentum loss rate for the bumps, however, was found to be of the order of $\sim 5 \times 10^{36} \text{ g cm}^2 \text{ s}^{-2}$, which is roughly one order of magnitude below the angular momentum loss rates required by the Geneva evolutionary models (see Fig. 6.10), so the evolving star does not reach its break-up velocity. Therefore, our results, for the first time, put constraints on the internal mechanisms of angular momentum transport of massive fast rotating stars.

Prospectives

That is the exploration that awaits you! Not mapping stars and studying nebula, but charting the unknown possibilities of existence.

Q to Picard, in *Star Trek: The Next Generation*, episode “All Good Things...”

It’s not a silly question if you can’t answer it.

Jostein Gaarder, *Sophie’s World*

There are observational and theoretical future perspectives for this work.

On the observational side, the first obvious continuation is the modelling of the light curves containing bumps and inactive phases of the LMC, using the catalog of Be star candidates of [Sabogal et al. \(2005\)](#). We are already working on this project.

Our work, however, has shown that it is important to make an effort to remove the biases of our samples, by trying to include late-type Be stars and smaller-amplitude bumps. It is possible to find smaller amplitude bumps in the light curves of the catalogs of [Mennickent et al. \(2002\)](#) and [Sabogal et al. \(2005\)](#), but, for such bumps, the uncertainties will be more comparable in size with the amplitude of the bump, making the determinations of all the disk parameters more uncertain. We can, however, extend our light curves by adding OGLE-IV data, which is a continuation of the OGLE project ([Udalski et al., 2015](#)), for the stars of the catalogs of [Mennickent et al. \(2002\)](#) and [Sabogal et al. \(2005\)](#) and combine them with the near-infrared light curves of the VISTA Magellanic Survey (VMC) ([Cioni et al., 2011](#)). Since the flux excess in Be stars increases for longer wavelengths, with VMC data, we should be able to obtain bumps in the infrared that are associated with less dense disks, which would have much smaller amplitudes in the visual

light curves of OGLE-IV. The OGLE-IV and VMC surveys started in March 2010 and November 2009, respectively. In both surveys, the data is collected mostly from August to January, because of the position of the Magellanic Clouds in the sky. VMC, however, only guarantees at least 12 measurements in the K_s band ($\sim 2 - 2.4 \mu\text{m}$) in this period, which hopefully means a measurement once every ~ 15 days.

The metallicity of the stars in the Magellanic Clouds is smaller than the galactic ones. The effects of the line-driven force in these regions, must, therefore, be less pronounced, and, hence, the disks of Be stars in these regions are essentially driven by viscosity. This is a great important justification for studying Be stars in the SMC and LMC. Despite that, we should however, extend our studies to the Galaxy, where there are many photometric surveys being carried out today, usually with smaller telescopes, limited to $V \sim 13 - 14$ mag. With the releases of parallaxes (distances) of the Gaia spacecraft¹, we can have the distances of each individual star whose light curve came from these Galactic stellar variability surveys. Such surveys are general variability surveys like ASAS (Pojmanski, 1997) or HATNet (Bakos et al., 2002) and surveys primarily focusing on planetary transits, like KELT (Pepper et al., 2007) and SuperWASP (Pollacco et al., 2006).

Finally, it is also important to obtain a better estimate of the central star properties, e.g., via spectroscopic modelling or using stars belonging to clusters with known ages. Our current analysis was limited by the amount of information available on the central stars. This can be done for Galactic stars and for stars in the LMC and SMC, though, in the latter cases, bigger telescopes are required. Spectra and multicolor polarimetry of Galactic southern stars can be made by our group with the Brazilian telescopes at Observatório Pico dos Dias (OPD). In the near future, optical broad-band polarimetry will also be available from the SOUTH-POL survey (Magalhães et al., 2012), which will image the entire southern sky (from the Cerro Tololo Inter-American Observatory - CTIO). Polarimetry gives us information about the density of the disk, and, specially, constraints on its inclination angle.

From the theoretical side, one primary future prospective is the non-isothermal treatment of the disk evolution. Recent results show that the non-isothermality of the disk can affect all our determinations, as shown in Fig. 6.9. The non-isothermal treatment of the disk shouldn't be difficult to implement. It could be done with SINGLEBE and HDUST working in a "predictor-corrector" way involving a few iterations.

We must, however, investigate the importance of line-driving in our viscous decretion disk formalism, especially when dealing with stars from the Galaxy. In particular, how will ablation, as suggested by the work of Kee et al. (2016) or by the work of Krtićka et al. (2011) affect the evolution of viscous disks of early Be stars?

In this work, we have shown that the angular momentum lost by early Be stars, even in the case of the most massive disks, are still below the angular momentum loss that the

¹ <http://sci.esa.int/gaia/>

Geneva stellar evolutionary models ([Granada et al., 2013](#)) require so that rotating stars do not exceed their break-up velocities during the main sequence evolution. Could this be an observational constraint to their internal angular momentum transport, implying their transport is too efficient? With our increasing sample of Be stars with angular momentum loss estimates, we hope to collaborate with the Geneva team in testing their evolutionary models in the future.

Finally, with our estimates of the α parameter, we hope to attract the attention of turbulence theoreticians. Is it possible for the MRI to generate the observed viscosities? Or, since this and other work on Be stars have shown that late-type Be stars have more stable disks, could the turbulence be induced instead by the stellar radiation?

Bibliography

- Alcock C., Allsman R. A., Alves D., Axelrod T. S., Becker A. C., Bennett D. P., Cook K. H., Freeman K. C., Griest K., Guern J., Lehner M. J., Marshall S. L., Peterson B. A., Pratt M. R., Quinn P. J., Rodgers A. W., Stubbs C. W., Sutherland W., Welch D. L., The MACHO Project Large Magellanic Cloud Microlensing Results from the First Two Years and the Nature of the Galactic Dark Halo, *ApJ*, 1997, vol. 486, p. 697
- Aubourg E., Bareyre P., Bréhin e. a., Evidence for gravitational microlensing by dark objects in the Galactic halo, *Nature*, 1993, vol. 365, p. 623
- Baade D., Rivinius T., Pigulski A., Carciofi A. C., Martayan C., Moffat A. F. J., Wade G. A., Weiss W. W., Grunhut J., Handler G., Kuschnig R., Mehner A., Pablo H., Popowicz A., Rucinski S., Whittaker G., Short-term variability and mass loss in Be stars. I. BRITe satellite photometry of η and μ Centauri, *A&A*, 2016, vol. 588, p. A56
- Bakos G. Á., Lázár J., Papp I., Sári P., Green E. M., System Description and First Light Curves of the Hungarian Automated Telescope, an Autonomous Observatory for Variability Search, *PASP*, 2002, vol. 114, p. 974
- Balbus S. A., Hawley J. F., A powerful local shear instability in weakly magnetized disks. I - Linear analysis. II - Nonlinear evolution, *ApJ*, 1991, vol. 376, p. 214
- Bessell M. S., UBVRI passbands, *PASP*, 1990, vol. 102, p. 1181
- Bjorkman J. E., Circumstellar Disks. In *Stellar Atmospheres: Theory and Observations* , vol. 497 of *Lecture Notes in Physics*, Berlin Springer Verlag, 1997, p. 239
- Bjorkman J. E., Carciofi A. C., Modeling the Structure of Hot Star Disks. In *The Nature and Evolution of Disks Around Hot Stars* , vol. 337 of *Astronomical Society of the Pacific Conference Series*, 2005, p. 75
- Bjorkman J. E., Cassinelli J. P., Equatorial disk formation around rotating stars due to Ram pressure confinement by the stellar wind, *ApJ*, 1993, vol. 409, p. 429

- Carciofi A. C., The circumstellar discs of Be stars. In *Active OB Stars: Structure, Evolution, Mass Loss, and Critical Limits*, vol. 272 of IAU Symposium, 2011, p. 325
- Carciofi A. C., Bjorkman J. E., Non-LTE Monte Carlo Radiative Transfer. I. The Thermal Properties of Keplerian Disks around Classical Be Stars, *ApJ*, 2006, vol. 639, p. 1081
- Carciofi A. C., Bjorkman J. E., Non-LTE Monte Carlo Radiative Transfer. II. Nonisothermal Solutions for Viscous Keplerian Disks, *ApJ*, 2008, vol. 684, p. 1374
- Carciofi A. C., Bjorkman J. E., Magalhães A. M., Effects of Grain Size on the Spectral Energy Distribution of Dusty Circumstellar Envelopes, *ApJ*, 2004, vol. 604, p. 238
- Carciofi A. C., Bjorkman J. E., Otero S. A., Okazaki A. T., Štefl S., Rivinius T., Baade D., Haubois X., The First Determination of the Viscosity Parameter in the Circumstellar Disk of a Be Star, *ApJ*, 2012, vol. 744, p. L15
- Carciofi A. C., Domiciano de Souza A., Magalhães A. M., Bjorkman J. E., Vakili F., On the Determination of the Rotational Oblateness of Achernar, *ApJ*, 2008, vol. 676, p. L41
- Carciofi A. C., Magalhães A. M., Leister N. V., Bjorkman J. E., Levenhagen R. S., Achernar: Rapid Polarization Variability as Evidence of Photospheric and Circumstellar Activity, *ApJ*, 2007, vol. 671, p. L49
- Carciofi A. C., Miroschnichenko A. S., Kusakina A. V., Bjorkman J. E., Bjorkman K. S., Marang F., Kuratov K. S., García-Lario P., Calderón J. V. P., Fabregat J., Magalhães A. M., Properties of the δ Scorpii Circumstellar Disk from Continuum Modeling, *ApJ*, 2006, vol. 652, p. 1617
- Carciofi A. C., Okazaki A. T., Le Bouquin J.-B., Štefl S., Rivinius T., Baade D., Bjorkman J. E., Hummel C. A., Cyclic variability of the circumstellar disk of the Be star ζ Tauri. II. Testing the 2D global disk oscillation model, *A&A*, 2009, vol. 504, p. 915
- Cassinelli J. P., Brown J. C., Maheswaran M., Miller N. A., Telfer D. C., A Magnetically Torqued Disk Model for Be Stars, *ApJ*, 2002, vol. 578, p. 951
- Castelli F., Kurucz R. L., Model atmospheres for VEGA, *A&A*, 1994, vol. 281, p. 817
- Cioni M.-R. L., Clementini G., Girardi L. e. a., The VMC survey. I. Strategy and first data, *A&A*, 2011, vol. 527, p. A116
- Collins II G. W., The use of terms and definitions in the study of Be stars. In *IAU Colloq. 92: Physics of Be Stars*, 1987, p. 3

- Cranmer S. R., Owocki S. P., The effect of oblateness and gravity darkening on the radiation driving in winds from rapidly rotating B stars, *ApJ*, 1995, vol. 440, p. 308
- Ekström S., Meynet G., Maeder A., Barblan F., Evolution towards the critical limit and the origin of Be stars, *A&A*, 2008, vol. 478, p. 467
- Espinosa Lara F., Theory of stellar distortion by fast rotators. In *EAS Publications Series*, vol. 69 of *EAS Publications Series*, 2014, p. 297
- Espinosa Lara F., Rieutord M., Gravity darkening in rotating stars, *A&A*, 2011, vol. 533, p. A43
- Foreman-Mackey D., Hogg D. W., Lang D., Goodman J., emcee: The MCMC Hammer, *PASP*, 2013, vol. 125, p. 306
- Gayley K. G., Ignace R., Owocki S. P., Line Forces in Keplerian Circumstellar Disks and Precession of Nearly Circular Orbits, *ApJ*, 2001, vol. 558, p. 802
- Gehrz R. D., Hackwell J. A., Jones T. W., Infrared observations of Be stars from 2.3 to 19.5 microns., *ApJ*, 1974, vol. 191, p. 675
- Georgy C., Ekström S., Granada A., Meynet G., Mowlavi N., Eggenberger P., Maeder A., Populations of rotating stars. I. Models from 1.7 to 15 M_{\odot} at $Z = 0.014, 0.006,$ and 0.002 with Ω/Ω_{crit} between 0 and 1, *A&A*, 2013, vol. 553, p. A24
- Ghoreyshi M. R., Carciofi A. C., Analysis of the V-Band Light Curve of the Be Star ω CMA with the Viscous Decretion Disk Model. In *Astronomical Society of the Pacific Conference Series*, vol. 508 of *Astronomical Society of the Pacific Conference Series*, 2017, p. 323
- Ghoreyshi M. R., Carciofi A. C., Bjorkman J., Rivinius T., Baade D., Štefl S., Okazaki A., Modeling the Complete Lightcurve of ω CMA. In *Bright Emissaries: Be Stars as Messengers of Star-Disk Physics*, vol. 506 of *Astronomical Society of the Pacific Conference Series*, 2016, p. 315
- Goodman J., Weare J., Ensemble samplers with affine invariance, *Communications in applied mathematics and computational science*, 2010, vol. 5, p. 65
- Gordon K. D., Clayton G. C., Misselt K. A., Landolt A. U., Wolff M. J., A Quantitative Comparison of the Small Magellanic Cloud, Large Magellanic Cloud, and Milky Way Ultraviolet to Near-Infrared Extinction Curves, *ApJ*, 2003, vol. 594, p. 279
- Granada A., Ekström S., Georgy C., Krtićka J., Owocki S., Meynet G., Maeder A., Populations of rotating stars. II. Rapid rotators and their link to Be-type stars, *A&A*, 2013, vol. 553, p. A25

- Haubois X., Carciofi A. C., Rivinius T., Okazaki A. T., Bjorkman J. E., Dynamical Evolution of Viscous Disks around Be Stars. I. Photometry, *ApJ*, 2012, vol. 756, p. 156
- Haubois X., Mota B. C., Carciofi A. C., Draper Z. H., Wisniewski J. P., Bednarski D., Rivinius T., Dynamical Evolution of Viscous Disks around Be Stars. II. Polarimetry, *ApJ*, 2014, vol. 785, p. 12
- Heinbockel J., Introduction to Tensor Calculus and Continuum Mechanics. Trafford, 2001
- Hilditch R. W., Howarth I. D., Harries T. J., Forty eclipsing binaries in the Small Magellanic Cloud: fundamental parameters and Cloud distance, *MNRAS*, 2005, vol. 357, p. 304
- Jaschek M., Slettebak A., Jaschek C., , 1981 Be star terminology. *Be Star Newsletter*
- Jones C. E., Sigut T. A. A., Marlborough J. M., Iron line cooling of Be star circumstellar discs, *MNRAS*, 2004, vol. 352, p. 841
- Jones C. E., Sigut T. A. A., Porter J. M., The circumstellar envelopes of Be stars: viscous disc dynamics, *MNRAS*, 2008, vol. 386, p. 1922
- Jones C. E., Tycner C., Sigut T. A. A., Benson J. A., Hutter D. J., A Parameter Study of Classical Be Star Disk Models Constrained by Optical Interferometry, *ApJ*, 2008, vol. 687, p. 598
- Kee N. D., Owocki S., Sundqvist J. O., Line-driven ablation of circumstellar discs - I. Optically thin decretion discs of classical Oe/Be stars, *MNRAS*, 2016, vol. 458, p. 2323
- Keller S. C., Bessell M. S., Cook K. H., Geha M., Syphers D., Blue Variable Stars from the MACHO Database. I. Photometry and Spectroscopy of the Large Magellanic Cloud Sample, *AJ*, 2002, vol. 124, p. 2039
- King A. R., Pringle J. E., Livio M., Accretion disc viscosity: how big is alpha?, *MNRAS*, 2007, vol. 376, p. 1740
- Kippenhahn R., Weigert A., Weiss A., *Stellar Structure and Evolution*, 2012
- Klement R., Carciofi A. C., Rivinius T., Panoglou D., Vieira R. G., Bjorkman J. E., Štefl S., Tycner C., Faes D. M., Korčáková D., Müller A., Zavala R. T., Curé M., Multitechnique testing of the viscous decretion disk model. I. The stable and tenuous disk of the late-type Be star β CMi, *A&A*, 2015, vol. 584, p. A85
- Kotko I., Lasota J.-P., The viscosity parameter α and the properties of accretion disc outbursts in close binaries, *A&A*, 2012, vol. 545, p. A115

- Kroupa P., On the variation of the initial mass function, *MNRAS*, 2001, vol. 322, p. 231
- Krtićka J., Owocki S. P., Meynet G., Mass and angular momentum loss via decretion disks, *A&A*, 2011, vol. 527, p. A84
- Landau L., Lifshitz E., *Fluid Mechanics*. No. v. 6, Elsevier Science, 2013
- Ledrew G., *The Real Starry Sky*, *JRASC*, 2001, vol. 95, p. 32
- Lee U., Osaki Y., Saio H., Viscous excretion discs around Be stars, *MNRAS*, 1991, vol. 250, p. 432
- MacKay D., *Information Theory, Inference and Learning Algorithms*. Cambridge University Press, 2003
- Magalhães A. M., de Oliveira C. M., Carciofi A., Costa R., Dal Pino E. M. G., Diaz M., Ferrari T., Fernandez C., Gomes A. L., Marrara L., Pereyrac A., Ribeiro N. L., Rodrigues C. V., Rubinho M. S., Seriacopi D. B., Taylor K., *South Pol: Revealing the polarized southern sky*. In *American Institute of Physics Conference Series* , vol. 1429 of *American Institute of Physics Conference Series*, 2012, p. 244
- Martayan C., Floquet M., Hubert A. M., Gutiérrez-Soto J., Fabregat J., Neiner C., Mekkas M., *Be stars and binaries in the field of the SMC open cluster NGC 330 with VLT-FLAMES*, *A&A*, 2007, vol. 472, p. 577
- Martayan C., Frémat Y., Hubert A.-M., Floquet M., Zorec J., Neiner C., *Effects of metallicity, star-formation conditions, and evolution in B and Be stars. II. Small Magellanic Cloud, field of NGC 330*, *A&A*, 2007, vol. 462, p. 683
- Martayan C., Rivinius T., Baade D., Hubert A.-M., Zorec J., *Populations of Be stars: stellar evolution of extreme stars*. In *Active OB Stars: Structure, Evolution, Mass Loss, and Critical Limits* , vol. 272 of *IAU Symposium*, 2011, p. 242
- Mennickent R. E., Pietrzyński G., Gieren W., Szewczyk O., *On Be star candidates and possible blue pre-main sequence objects in the Small Magellanic Cloud*, *A&A*, 2002, vol. 393, p. 887
- Okazaki A. T., *On the confinement of one-armed oscillations in discs of Be stars.*, *A&A*, 1997, vol. 318, p. 548
- Okazaki A. T., *Viscous Transonic Decretion in Disks of Be Stars*, *PASJ*, 2001, vol. 53, p. 119
- Okazaki A. T., *Theory vs. Observation of Circumstellar Disks and Their Formation*. In *Active OB-Stars: Laboratories for Stellare and Circumstellar Physics* , vol. 361 of *Astronomical Society of the Pacific Conference Series*, 2007, p. 230

- Okazaki A. T., Bate M. R., Ogilvie G. I., Pringle J. E., Viscous effects on the interaction between the coplanar decretion disc and the neutron star in Be/X-ray binaries, *MNRAS*, 2002, vol. 337, p. 967
- Owocki S., Ud-Doula A., Magnetic Spin-Up of Line-Driven Stellar Winds. In *Magnetic Fields in O, B and A Stars: Origin and Connection to Pulsation, Rotation and Mass Loss*, vol. 305 of *Astronomical Society of the Pacific Conference Series*, 2003, p. 350
- Owocki S. P., Cranmer S. R., Gayley K. G., Inhibition of Wind Compressed Disk Formation by Nonradial Line-Forces in Rotating Hot-Star Winds, *ApJ*, 1996, vol. 472, p. L115
- Paul K. T., Subramaniam A., Mathew B., Mennickent R. E., Sabogal B., Study of candidate Be stars in the Magellanic Clouds using near-infrared photometry and optical spectroscopy, *MNRAS*, 2012, vol. 421, p. 3622
- Pepper J., Pogge R. W., DePoy D. L., Marshall J. L., Stanek K. Z., Stutz A. M., Poindexter S., Siverd R., O'Brien T. P., Trueblood M., Trueblood P., The Kilodegree Extremely Little Telescope (KELT): A Small Robotic Telescope for Large-Area Synoptic Surveys, *PASP*, 2007, vol. 119, p. 923
- Pletcher R., Tannehill J., Anderson D., *Computational Fluid Mechanics and Heat Transfer*, Second Edition. Series in Computational and Physical Processes in Mechanics and Thermal Sciences, Taylor & Francis, 1997
- Pojmanski G., The All Sky Automated Survey, *Acta Astron.*, 1997, vol. 47, p. 467
- Pollacco D. L., Skillen I., Collier Cameron e. a., The WASP Project and the SuperWASP Cameras, *PASP*, 2006, vol. 118, p. 1407
- Porter J. M., On outflowing viscous disc models for Be stars, *A&A*, 1999, vol. 348, p. 512
- Porter J. M., Rivinius T., Classical Be Stars, *PASP*, 2003, vol. 115, p. 1153
- Puls J., Vink J. S., Najarro F., Mass loss from hot massive stars, *A&A Rev.*, 2008, vol. 16, p. 209
- Quirrenbach A., Buscher D. F., Mozurkewich D., Hummel C. A., Armstrong J. T., Maximum-entropy maps of the Be shell star zeta Tauri from optical long-baseline interferometry, *A&A*, 1994, vol. 283, p. L13
- Rivinius T., Baade D., Carciofi A. C., Short-term variability and mass loss in Be stars. II. Physical taxonomy of photometric variability observed by the Kepler spacecraft, *A&A*, 2016, vol. 593, p. A106

- Rivinius T., Baade D., Steff S., Stahl O., Wolf B., Kaufer A., Stellar and circumstellar activity of the Be star MU Centauri. I. Line emission outbursts, *A&A*, 1998, vol. 333, p. 125
- Rivinius T., Baade D., Townsend R. H. D., Carciofi A. C., Šteff S., Variable rotational line broadening in the Be star Achernar, *A&A*, 2013, vol. 559, p. L4
- Rivinius T., Carciofi A. C., Martayan C., Classical Be stars. Rapidly rotating B stars with viscous Keplerian decretion disks, *A&A Rev.*, 2013, vol. 21, p. 69
- Rivinius T., Šteff S., Baade D., Bright Be-shell stars, *A&A*, 2006, vol. 459, p. 137
- Sabogal B. E., Mennickent R. E., Pietrzyński G., Gieren W., Be star candidates in the Large Magellanic Cloud: the catalogue and comparison with the Small Magellanic Cloud sample, *MNRAS*, 2005, vol. 361, p. 1055
- Sana H., de Mink S. E., de Koter A., Langer N., Evans C. J., Gieles M., Gosset E., Izzard R. G., Le Bouquin J.-B., Schneider F. R. N., Binary Interaction Dominates the Evolution of Massive Stars, *Science*, 2012, vol. 337, p. 444
- Secchi A., Schreiben des Herrn Prof. Secchi, Directors der Sternwarte des Collegio Romano, an den Herausgeber, *Astronomische Nachrichten*, 1866, vol. 68, p. 63
- Shakura N. I., Sunyaev R. A., Black holes in binary systems. Observational appearance., *A&A*, 1973, vol. 24, p. 337
- Silaj J., Jones C. E., Tycner C., Sigut T. A. A., Smith A. D., A Systematic Study of H α Profiles of Be Stars, *ApJS*, 2010, vol. 187, p. 228
- Snow Jr. T. P., Stellar winds and mass-loss rates from Be stars, *ApJ*, 1981, vol. 251, p. 139
- Sparke L. S., Gallagher III J. S., *Galaxies in the Universe: An Introduction*. Cambridge University Press, 2007
- Strom S. E., Edwards S., Skrutskie M. F., Evolutionary time scales for circumstellar disks associated with intermediate- and solar-type stars. In *Protostars and Planets III*, 1993, p. 837
- Touhami Y., Gies D. R., Schaefer G. H., The Infrared Continuum Sizes of Be Star Disks, *ApJ*, 2011, vol. 729, p. 17
- Udalski A., The Optical Gravitational Lensing Experiment. Real Time Data Analysis Systems in the OGLE-III Survey, *Acta Astron.*, 2003, vol. 53, p. 291

- Udalski A., Kubiak M., Szymanski M., Optical Gravitational Lensing Experiment. OGLE-2 – the Second Phase of the OGLE Project, *Acta Astron.*, 1997, vol. 47, p. 319
- Udalski A., Szymanski M., Kaluzny J., Kubiak M., Mateo M., The Optical Gravitational Lensing Experiment, *Acta Astron.*, 1992, vol. 42, p. 253
- Udalski A., Szymanski M. K., Soszynski I., Poleski R., The Optical Gravitational Lensing Experiment. Final Reductions of the OGLE-III Data, *Acta Astron.*, 2008, vol. 58, p. 69
- Udalski A., Szymański M. K., Szymański G., OGLE-IV: Fourth Phase of the Optical Gravitational Lensing Experiment, *Acta Astron.*, 2015, vol. 65, p. 1
- Štefl S., Rivinius T., Carciofi A. C., Le Bouquin J.-B., Baade D., Bjorkman K. S., Heselbach E., Hummel C. A., Okazaki A. T., Pollmann E., Rantakyrö F., Wisniewski J. P., Cyclic variability of the circumstellar disk of the Be star ζ Tauri. I. Long-term monitoring observations, *A&A*, 2009, vol. 504, p. 929
- Vieira R. G., Carciofi A. C., Bjorkman J. E., The pseudo-photosphere model for the continuum emission of gaseous discs, *MNRAS*, 2015, vol. 454, p. 2107
- Vieira R. G., Carciofi A. C., Bjorkman J. E., Rivinius T., Baade D., Rímulo L. R., The life cycles of Be viscous decretion discs: time-dependent modelling of infrared continuum observations, *MNRAS*, 2017, vol. 464, p. 3071
- von Zeipel H., The radiative equilibrium of a rotating system of gaseous masses, *MNRAS*, 1924, vol. 84, p. 665
- Wade G. A., Grunhut J. H., MiMeS Collaboration The MiMeS Survey of Magnetism in Massive Stars. In *Circumstellar Dynamics at High Resolution*, vol. 464 of *Astronomical Society of the Pacific Conference Series*, 2012, p. 405
- Waters L. B. F. M., Cote J., Lamers H. J. G. L. M., IRAS observations of Be stars. II - Far-IR characteristics and mass loss rates, *A&A*, 1987, vol. 185, p. 206
- Wood K., Bjorkman K. S., Bjorkman J. E., Deriving the Geometry of Be Star Circumstellar Envelopes from Continuum Spectropolarimetry. I. The Case of ζ Tauri, *ApJ*, 1997, vol. 477, p. 926
- Wyrzykowski L., Kozłowski S., Skowron J., Belokurov V., Smith M. C., Udalski A., Szymański M. K., Kubiak M., Pietrzyński G., Soszyński I., Szewczyk O., Żebruń K., The OGLE view of microlensing towards the Magellanic Clouds - I. A trickle of events in the OGLE-II LMC data, *MNRAS*, 2009, vol. 397, p. 1228

Zaritsky D., Harris J., Thompson I. B., Grebel E. K., The Magellanic Clouds Photometric Survey: The Large Magellanic Cloud Stellar Catalog and Extinction Map, *AJ*, 2004, vol. 128, p. 1606

Appendix

Appendix A

Long tables

Here we present the parameters $\Delta X_{\text{bu}}^\infty$, ξ_{bu} and ξ_{d} of the empirical laws given by Eqs. (4.3.7) and (4.3.8), and with η 's given by Table 4.4, for the *BVRI* bands in Tables A.1, A.2, A.3 and A.4, respectively.

The fits were performed with the MCMC `emcee` code (Sect. 4.5). The values in the tables are for the fits with the highest probability. The standard deviations from the fits were small for edge-on and pole-on angles (see forth column of the tables). The standard deviations from the fits of light curves of intermediate angles were high (and the residuals also) and they were the best measure in the definition of the region of intermediate angles for each band (see the extensions of the regions of intermediate angles for each band in the text of Sect. 4.3).

For the intermediate angles, in particular, the η used was the one for “edge-on” in Table 4.4 if $\Delta X_{\text{bu}}^\infty$ was positive and the one from “pole-on” in that table if $\Delta X_{\text{bu}}^\infty$ was negative.

The values given in Table 4.4 were the values that gave the best fittings (like the ones exemplified in Appendix B) for the greatest number of light curves.

Table A.1 - Empirical law parameters for band B.

Star	Σ_0 [g cm ⁻²]	cos i	$\tilde{\tau}_{bu}$ ang. type	bu		0.15	0.45	0.75	1.50	2.25	3.00	4.50	6.00	9.00	15.00	30.00	∞
				ΔB_{bu}^∞	ξ_{bu}^B	ξ_d^B											
S1	2.5	0.0	edge-on	0.511	1.232	2.02	1.56	1.375	1.15	1.024	0.952	0.846	0.785	0.707	0.611	0.555	0.535
S1	2.5	0.071	edge-on	0.363	1.603	2.03	1.485	1.287	1.047	0.929	0.853	0.759	0.697	0.631	0.542	0.491	0.466
S1	2.5	0.143	edge-on	0.156	7.166	2.686	1.758	1.398	1.003	0.822	0.76	0.662	0.584	0.506	0.413	0.374	0.34
S1	2.5	0.215	interm.	-0.025	4.25	3.513	1.801	1.183	2.419	71.635	75.725	153.281	272.649	255.478	84.525	45.069	35.747
S1	2.5	0.286	interm.	-0.185	0.769	155.721	18.299	11.439	7.662	5.885	5.178	4.045	3.732	3.617	3.184	2.792	2.994
S1	2.5	0.357	interm.	-0.312	1.931	10.595	7.183	5.953	4.712	4.03	3.587	3.007	2.833	2.676	2.381	2.138	2.226
S1	2.5	0.429	interm.	-0.416	3.477	10.616	6.947	5.559	4.415	3.837	3.464	2.933	2.773	2.602	2.338	2.11	2.171
S1	2.5	0.5	interm.	-0.498	5.407	11.771	7.266	5.75	4.549	3.98	3.594	3.122	2.932	2.758	2.464	2.243	2.291
S1	2.5	0.571	interm.	-0.566	7.522	13.058	7.813	6.198	4.877	4.256	3.875	3.368	3.173	2.989	2.672	2.463	2.495
S1	2.5	0.643	pole-on	-0.625	9.756	14.636	8.597	6.779	5.32	4.663	4.254	3.725	3.52	3.284	2.973	2.748	2.788
S1	2.5	0.714	pole-on	-0.673	12.049	16.554	9.566	7.512	5.891	5.163	4.714	4.168	3.929	3.672	3.322	3.068	3.097
S1	2.5	0.786	pole-on	-0.712	14.292	18.555	10.687	8.414	6.577	5.765	5.251	4.666	4.422	4.124	3.743	3.455	3.477
S1	2.5	0.857	pole-on	-0.746	16.451	21.096	12.034	9.453	7.378	6.466	5.909	5.267	5.007	4.63	4.195	3.894	3.914
S1	2.5	0.928	pole-on	-0.773	18.691	24.098	13.651	10.698	8.285	7.227	6.629	5.932	5.647	5.18	4.691	4.374	4.433
S1	2.5	1.0	pole-on	-0.794	20.472	27.2	15.255	11.939	9.202	7.988	7.309	6.589	6.24	5.72	5.225	4.878	5.016
S1	1.85	0.0	edge-on	0.413	1.251	2.424	1.838	1.607	1.318	1.154	1.082	0.999	0.911	0.808	0.703	0.638	0.619
S1	1.85	0.071	edge-on	0.306	1.613	2.489	1.83	1.535	1.248	1.074	1.013	0.896	0.823	0.743	0.651	0.584	0.571
S1	1.85	0.143	edge-on	0.157	4.792	3.161	2.285	1.806	1.357	1.149	1.029	0.811	0.776	0.697	0.616	0.534	0.528
S1	1.85	0.215	interm.	0.015	469.674	4.309	2.719	1.995	1.213	0.938	3.7	0.382	5.935	0.361	16.244	36.156	8.417
S1	1.85	0.286	interm.	-0.124	0.59	43.077	58.661	19.877	10.796	7.894	6.67	6.381	5.694	4.771	3.963	3.581	3.412
S1	1.85	0.357	interm.	-0.237	1.794	15.156	8.289	6.988	5.409	4.626	4.143	3.996	3.691	3.269	2.824	2.565	2.531
S1	1.85	0.429	interm.	-0.332	3.442	14.041	8.325	6.879	5.383	4.656	4.142	3.988	3.679	3.314	2.892	2.682	2.66
S1	1.85	0.5	interm.	-0.408	5.51	15.669	9.051	7.438	5.798	5.039	4.487	4.277	3.998	3.614	3.179	2.946	2.914
S1	1.85	0.571	interm.	-0.473	7.837	17.521	10.028	8.206	6.405	5.556	4.99	4.734	4.432	4.029	3.566	3.321	3.276
S1	1.85	0.643	pole-on	-0.528	10.319	19.698	11.333	9.201	7.127	6.251	5.612	5.304	4.987	4.541	4.07	3.779	3.739
S1	1.85	0.714	pole-on	-0.573	12.938	22.365	12.755	10.407	8.074	7.044	6.389	5.996	5.624	5.145	4.615	4.322	4.301
S1	1.85	0.786	pole-on	-0.611	15.658	25.441	14.548	11.794	9.165	7.958	7.203	6.758	6.326	5.826	5.276	4.951	4.994
S1	1.85	0.857	pole-on	-0.642	18.312	29.255	16.661	13.435	10.334	8.978	8.124	7.633	7.145	6.576	6.029	5.691	5.837
S1	1.85	0.928	pole-on	-0.667	20.872	33.733	19.016	15.265	11.64	10.092	9.213	8.664	8.086	7.475	6.941	6.542	6.817
S1	1.85	1.0	pole-on	-0.686	22.881	38.355	21.483	17.226	13.051	11.276	10.114	9.767	9.079	8.372	7.871	7.397	7.781
S1	1.37	0.0	edge-on	0.329	1.304	2.926	2.109	1.822	1.495	1.328	1.222	1.105	1.017	0.921	0.805	0.731	0.714
S1	1.37	0.071	edge-on	0.254	1.636	3.011	2.133	1.833	1.471	1.321	1.193	1.072	0.985	0.893	0.775	0.714	0.696
S1	1.37	0.143	edge-on	0.146	3.827	3.818	2.702	2.271	1.735	1.531	1.346	1.2	1.12	0.977	0.851	0.777	0.761
S1	1.37	0.215	interm.	0.036	90.464	5.094	3.486	2.808	2.008	1.822	1.412	1.395	1.289	0.917	0.896	0.866	0.815
S1	1.37	0.286	interm.	-0.08	0.482	14.374	328.28	199.606	20.143	11.852	10.675	6.22	5.928	6.413	4.721	3.953	3.614

Table A.1 - continued.

Star	Σ_0 [g cm ⁻²]	cos i	$\tilde{\tau}_{\text{bu}}$ ang. type	bu			0.15	0.45	0.75	1.50	2.25	3.00	4.50	6.00	9.00	15.00	30.00	∞
				$\Delta B_{\text{bu}}^\infty$	ξ_{bu}^B	ξ_{d}^B												
S1	1.37	0.357	interm.	-0.177	1.787	24.461	10.48	8.302	5.968	5.253	4.785	4.129	3.892	3.808	3.23	2.931	2.844	
S1	1.37	0.429	interm.	-0.262	3.468	17.74	10.537	8.522	6.399	5.547	5.149	4.505	4.264	4.062	3.545	3.286	3.198	
S1	1.37	0.5	interm.	-0.332	5.483	19.517	11.696	9.427	7.185	6.274	5.833	5.141	4.864	4.65	4.046	3.755	3.778	
S1	1.37	0.571	interm.	-0.391	7.876	22.373	13.264	10.682	8.164	7.214	6.601	5.902	5.594	5.294	4.718	4.373	4.445	
S1	1.37	0.643	pole-on	-0.44	10.508	25.776	15.174	12.253	9.347	8.25	7.624	6.816	6.507	6.144	5.492	5.111	5.239	
S1	1.37	0.714	pole-on	-0.482	13.285	29.779	17.297	14.11	10.658	9.45	8.708	7.862	7.554	7.082	6.349	5.931	6.185	
S1	1.37	0.786	pole-on	-0.515	16.154	34.411	19.994	16.024	12.336	10.809	10.042	9.083	8.798	8.193	7.41	6.96	7.327	
S1	1.37	0.857	pole-on	-0.543	19.074	40.04	23.065	18.571	14.173	12.435	11.461	10.434	10.242	9.363	8.618	8.012	8.72	
S1	1.37	0.928	pole-on	-0.565	22.011	46.584	26.792	21.498	16.251	14.186	12.99	12.03	12.019	10.647	10.013	9.223	10.334	
S1	1.37	1.0	pole-on	-0.58	24.289	53.4	30.568	24.635	18.443	15.867	14.514	13.669	13.804	11.928	11.377	10.423	12.057	
S1	1.01	0.0	edge-on	0.26	1.364	3.437	2.417	2.088	3.123	1.516	1.4	1.232	1.149	1.043	0.841	0.839	0.842	
S1	1.01	0.071	edge-on	0.208	1.594	3.547	2.51	2.142	2.87	1.551	1.423	1.252	1.161	1.056	0.84	0.844	0.848	
S1	1.01	0.143	edge-on	0.132	3.075	4.495	3.249	2.769	2.776	1.928	1.758	1.54	1.45	1.304	1.054	1.042	1.056	
S1	1.01	0.215	interm.	0.048	16.107	6.121	4.479	3.745	56.935	2.609	2.429	2.079	2.133	1.888	1.552	1.619	1.727	
S1	1.01	0.286	interm.	-0.046	0.384	26.954	110.929	381.087	286.612	79.824	19.037	11.967	7.118	6.707	6.712	3.021	2.581	
S1	1.01	0.357	interm.	-0.128	1.652	82.201	11.828	9.155	9.959	5.699	5.035	4.7	4.275	3.837	3.943	3.112	2.889	
S1	1.01	0.429	interm.	-0.202	3.266	21.087	11.998	9.509	9.861	6.53	5.912	5.428	5.043	4.573	4.522	3.827	3.648	
S1	1.01	0.5	interm.	-0.262	5.086	23.464	13.865	11.24	10.559	7.608	7.059	6.313	6.052	5.493	5.338	4.682	4.611	
S1	1.01	0.571	interm.	-0.314	7.212	27.125	16.133	13.094	11.883	8.888	8.214	7.459	7.147	6.644	6.309	5.612	5.705	
S1	1.01	0.643	pole-on	-0.357	9.637	31.688	18.734	15.38	13.408	10.399	9.666	8.773	8.51	7.872	7.377	6.669	7.163	
S1	1.01	0.714	pole-on	-0.393	12.152	37.111	21.927	18.078	15.006	12.196	11.262	10.267	10.196	9.377	8.56	7.88	9.047	
S1	1.01	0.786	pole-on	-0.422	15.018	44.002	25.979	21.177	17.023	14.226	13.112	11.95	11.956	10.921	9.878	9.235	11.175	
S1	1.01	0.857	pole-on	-0.445	17.938	51.401	30.354	24.916	19.173	16.424	15.152	13.767	14.091	12.639	11.385	10.65	13.754	
S1	1.01	0.928	pole-on	-0.463	20.658	60.802	35.672	29.305	21.723	18.636	17.092	15.91	16.612	14.485	13.099	12.202	16.826	
S1	1.01	1.0	pole-on	-0.473	22.891	70.496	41.114	33.665	24.425	20.773	18.827	18.111	19.127	16.094	14.811	13.705	19.92	
S1	0.75	0.0	edge-on	0.204	1.468	4.324	2.839	2.404	1.939	1.695	1.567	1.397	1.292	1.183	1.042	0.948	0.931	
S1	0.75	0.071	edge-on	0.167	1.765	4.425	2.967	2.495	2.019	1.772	1.638	1.465	1.345	1.242	1.091	0.981	0.968	
S1	0.75	0.143	edge-on	0.112	3.131	5.397	3.776	3.202	2.604	2.265	2.097	1.912	1.759	1.617	1.468	1.344	1.318	
S1	0.75	0.215	interm.	0.046	80.87	7.398	5.169	4.539	3.67	3.371	3.361	3.087	2.947	3.476	2.616	2.537	2.577	
S1	0.75	0.286	interm.	-0.022	39.937	21.617	60.179	180.416	363.804	327.329	366.691	247.691	99.498	37.139	20.082	12.447	3.774	
S1	0.75	0.357	interm.	-0.09	1.659	234.545	16.004	9.981	6.795	5.873	4.704	4.506	4.203	3.71	3.158	2.798	2.914	
S1	0.75	0.429	interm.	-0.149	3.018	26.246	13.634	10.765	8.098	7.148	6.355	5.776	5.449	4.93	4.639	4.039	4.213	
S1	0.75	0.5	interm.	-0.2	4.531	26.875	15.551	12.762	9.719	8.58	7.823	7.114	6.883	6.193	5.692	5.265	5.582	
S1	0.75	0.571	interm.	-0.242	6.105	30.787	18.843	15.26	11.784	10.3	9.42	8.588	8.492	7.613	6.878	6.519	6.961	
S1	0.75	0.643	pole-on	-0.278	7.927	37.009	22.443	18.222	13.976	12.388	11.315	10.223	10.267	9.102	8.388	7.888	8.832	

Table A.1 - continued.

Star	Σ_0 [g cm ⁻²]	cos i	$\tilde{\tau}_{bu}$ ang. type	bu		0.15	0.45	0.75	1.50	2.25	3.00	4.50	6.00	9.00	15.00	30.00	∞
				ΔB_{bu}^∞	ξ_{bu}^B	ξ_d^B											
S1	0.75	0.714	pole-on	-0.307	9.676	43.557	26.679	21.866	16.711	14.65	13.376	12.234	12.351	10.716	10.042	9.394	10.905
S1	0.75	0.786	pole-on	-0.33	11.4	51.798	31.817	25.889	19.893	17.469	15.794	14.251	14.919	12.51	11.989	11.013	13.405
S1	0.75	0.857	pole-on	-0.347	13.112	61.387	37.811	30.967	23.249	19.912	18.031	16.609	17.544	14.39	13.949	12.648	16.391
S1	0.75	0.928	pole-on	-0.36	14.656	72.95	44.345	36.76	26.421	22.601	20.335	19.261	21.001	16.179	16.398	14.444	19.954
S1	0.75	1.0	pole-on	-0.366	15.691	83.592	51.718	42.315	29.767	25.099	22.42	21.575	23.96	17.699	18.538	16.006	23.423
S1	0.56	0.0	edge-on	0.16	1.543	5.083	3.389	2.8	2.186	1.933	1.784	1.575	1.45	1.337	1.152	1.068	1.033
S1	0.56	0.071	edge-on	0.134	1.745	4.924	3.558	2.928	2.3	2.042	1.893	1.69	1.538	1.415	1.235	1.132	1.093
S1	0.56	0.143	edge-on	0.093	2.75	6.245	4.489	3.776	3.066	2.717	2.519	2.284	2.125	1.979	1.743	1.636	1.578
S1	0.56	0.215	interm.	0.044	6.942	8.044	6.403	5.75	4.693	4.443	4.154	4.159	3.76	3.633	3.298	3.334	3.238
S1	0.56	0.286	interm.	-0.007	67.764	81.412	40.885	117.976	231.031	258.856	351.47	297.635	328.064	293.562	266.423	284.651	258.177
S1	0.56	0.357	interm.	-0.062	1.556	299.725	23.977	10.324	6.464	4.99	4.293	3.571	3.549	2.963	2.861	2.459	2.722
S1	0.56	0.429	interm.	-0.107	3.151	35.694	14.542	11.33	7.978	6.88	6.225	5.507	5.491	4.968	4.62	4.03	4.459
S1	0.56	0.5	interm.	-0.146	4.659	31.372	17.101	13.491	10.224	8.905	7.98	7.183	7.287	6.482	5.982	5.47	6.088
S1	0.56	0.571	interm.	-0.179	6.464	34.22	19.973	16.41	12.705	10.942	10.234	8.909	9.149	8.034	7.36	7.043	7.886
S1	0.56	0.643	pole-on	-0.206	8.467	40.658	24.707	20.285	15.267	13.284	12.394	10.977	11.314	9.876	9.221	8.562	10.187
S1	0.56	0.714	pole-on	-0.228	10.856	49.07	29.892	24.37	18.679	16.15	15.012	13.269	13.85	11.802	11.029	10.294	12.736
S1	0.56	0.786	pole-on	-0.245	13.35	58.049	35.679	29.818	22.331	19.487	17.627	15.539	16.912	13.933	13.233	12.233	15.958
S1	0.56	0.857	pole-on	-0.257	16.109	69.184	42.401	35.768	26.147	22.415	20.316	18.251	20.275	15.84	15.627	13.811	19.785
S1	0.56	0.928	pole-on	-0.265	18.969	82.209	51.033	43.337	30.001	25.218	22.586	21.285	23.922	17.756	18.331	16.087	24.183
S1	0.56	1.0	pole-on	-0.267	20.724	93.501	59.484	49.343	33.391	27.182	24.706	23.785	28.089	19.59	20.667	17.62	28.36
S1	0.41	0.0	edge-on	0.124	1.734	6.102	3.922	3.296	2.54	2.229	2.021	1.811	1.624	1.502	1.291	1.205	1.154
S1	0.41	0.071	edge-on	0.106	1.85	6.036	4.097	3.433	2.756	2.356	2.162	1.944	1.705	1.612	1.397	1.297	1.269
S1	0.41	0.143	edge-on	0.075	2.682	7.005	5.217	4.365	3.528	3.278	2.976	2.763	2.507	2.442	2.126	1.949	1.945
S1	0.41	0.215	interm.	0.038	6.274	16.04	7.643	6.67	5.841	5.475	5.241	4.9	4.844	4.75	4.288	4.308	4.147
S1	0.41	0.286	interm.	0.001	298.321	115.416	57.898	145.617	126.343	223.322	282.342	264.2	302.723	303.543	305.299	310.457	323.879
S1	0.41	0.357	interm.	-0.04	1.76	302.226	174.255	21.389	6.557	4.004	3.518	3.264	3.293	2.227	2.185	1.689	2.079
S1	0.41	0.429	interm.	-0.073	3.405	102.958	15.902	12.009	7.445	6.486	5.661	5.162	5.26	4.133	4.002	3.574	4.219
S1	0.41	0.5	interm.	-0.102	4.598	33.656	17.297	13.691	10.436	8.561	7.613	7.165	7.195	5.92	5.819	5.088	5.935
S1	0.41	0.571	interm.	-0.125	6.359	37.578	21.466	17.126	12.585	11.062	10.058	9.147	9.375	7.817	7.518	6.942	8.133
S1	0.41	0.643	pole-on	-0.145	8.444	42.85	25.447	21.023	15.901	13.536	12.399	11.171	11.661	9.775	9.323	8.548	10.586
S1	0.41	0.714	pole-on	-0.16	10.609	51.83	31.001	25.966	19.521	16.645	15.16	13.755	14.321	11.719	11.604	10.596	13.468
S1	0.41	0.786	pole-on	-0.171	13.262	61.077	38.581	31.76	23.543	20.293	18.124	16.462	17.674	13.981	13.702	12.352	17.41
S1	0.41	0.857	pole-on	-0.179	16.006	73.851	45.109	37.971	27.697	23.618	20.737	19.086	21.435	16.205	16.295	14.441	21.814
S1	0.41	0.928	pole-on	-0.183	18.986	88.284	55.612	44.724	31.551	26.597	23.706	21.985	25.667	17.919	19.415	16.318	26.992
S1	0.41	1.0	pole-on	-0.182	21.209	99.68	63.632	53.344	35.447	29.091	25.337	25.031	29.871	19.711	21.596	18.456	31.369

Table A.1 - continued.

Star	Σ_0 [g cm ⁻²]	cos i	$\tilde{\tau}_{\text{bu}}$ ang. type	bu		0.15	0.45	0.75	1.50	2.25	3.00	4.50	6.00	9.00	15.00	30.00	∞
				$\Delta B_{\text{bu}}^\infty$	ξ_{bu}^B	ξ_{d}^B											
S1	0.3	0.0	edge-on	0.096	6.629	7.678	4.542	3.661	2.884	2.474	2.284	1.97	1.809	1.699	1.474	1.322	1.251
S1	0.3	0.071	edge-on	0.082	1.908	7.744	4.674	3.865	3.059	2.635	2.411	2.15	1.955	1.84	1.564	1.459	1.395
S1	0.3	0.143	edge-on	0.058	2.771	12.337	5.854	4.887	4.111	3.79	3.456	3.04	2.86	2.804	2.441	2.31	2.211
S1	0.3	0.215	interm.	0.03	36.55	32.934	9.423	7.624	6.956	6.679	6.504	6.155	5.74	5.888	5.256	5.308	5.2
S1	0.3	0.286	interm.	0.003	282.936	228.636	150.817	157.266	138.707	227.599	198.369	260.657	281.333	295.088	309.106	257.1	259.74
S1	0.3	0.357	interm.	-0.025	20.874	319.978	267.356	166.275	41.016	7.152	11.906	5.109	4.425	4.918	2.171	1.793	1.99
S1	0.3	0.429	interm.	-0.05	3.491	180.182	20.781	11.975	6.718	6.148	4.69	5.022	4.799	3.69	3.538	3.494	3.701
S1	0.3	0.5	interm.	-0.069	4.77	46.535	17.842	13.784	9.149	8.463	7.194	6.472	6.893	5.532	5.253	4.418	5.418
S1	0.3	0.571	interm.	-0.086	6.126	39.222	22.698	17.548	12.305	10.786	9.251	8.511	9.033	7.278	6.994	6.311	7.719
S1	0.3	0.643	pole-on	-0.099	8.16	46.058	25.705	21.561	15.212	13.641	11.73	10.621	11.186	9.461	8.896	8.081	10.783
S1	0.3	0.714	pole-on	-0.109	10.172	54.44	31.811	26.222	18.999	16.963	14.692	13.042	14.276	11.471	11.129	10.063	13.474
S1	0.3	0.786	pole-on	-0.116	12.715	62.874	40.385	31.587	23.429	20.542	17.778	15.928	17.711	13.653	13.155	11.843	17.061
S1	0.3	0.857	pole-on	-0.12	15.634	76.752	47.51	39.025	27.428	23.989	20.049	19.089	21.911	15.561	16.023	13.834	22.137
S1	0.3	0.928	pole-on	-0.122	18.332	90.184	58.474	46.453	32.451	26.737	23.067	21.902	26.817	17.337	18.328	16.042	27.296
S1	0.3	1.0	pole-on	-0.12	20.383	113.511	64.429	52.943	34.938	29.936	26.434	24.125	30.351	20.279	20.827	17.738	32.619
S2	2.5	0.0	edge-on	0.474	1.176	2.092	1.629	1.478	1.2	1.086	0.996	0.904	0.833	0.757	0.658	0.595	0.58
S2	2.5	0.071	edge-on	0.346	1.525	2.052	1.586	1.403	1.142	1.022	0.936	0.84	0.788	0.702	0.606	0.543	0.531
S2	2.5	0.143	edge-on	0.166	4.842	2.573	1.919	1.638	1.226	1.049	0.917	0.795	0.752	0.638	0.562	0.467	0.458
S2	2.5	0.215	interm.	0.01	439.245	3.327	2.168	1.674	1.016	0.809	0.598	0.802	0.478	4.605	0.291	47.653	31.689
S2	2.5	0.286	interm.	-0.134	0.687	122.926	40.367	16.438	8.664	6.749	5.816	4.758	4.183	3.93	3.241	3.01	2.772
S2	2.5	0.357	interm.	-0.25	2.01	16.376	8.374	6.546	4.942	4.226	3.878	3.37	3.042	2.803	2.436	2.267	2.149
S2	2.5	0.429	interm.	-0.346	3.736	13.696	8.034	6.434	4.92	4.225	3.887	3.428	3.142	2.925	2.523	2.331	2.251
S2	2.5	0.5	interm.	-0.423	5.811	14.751	8.587	6.842	5.281	4.557	4.189	3.699	3.468	3.172	2.789	2.593	2.507
S2	2.5	0.571	interm.	-0.487	8.099	16.529	9.427	7.57	5.796	5.038	4.673	4.136	3.879	3.573	3.152	2.915	2.848
S2	2.5	0.643	pole-on	-0.542	10.579	18.593	10.598	8.493	6.481	5.668	5.241	4.683	4.381	4.034	3.57	3.335	3.284
S2	2.5	0.714	pole-on	-0.587	13.121	20.974	11.9	9.547	7.322	6.374	5.912	5.306	4.965	4.571	4.089	3.82	3.8
S2	2.5	0.786	pole-on	-0.623	15.636	23.851	13.445	10.804	8.273	7.189	6.638	5.977	5.645	5.18	4.673	4.392	4.432
S2	2.5	0.857	pole-on	-0.653	18.094	27.384	15.338	12.273	9.327	8.159	7.448	6.787	6.448	5.899	5.374	5.063	5.179
S2	2.5	0.928	pole-on	-0.677	20.495	31.508	17.44	13.917	10.557	9.147	8.449	7.704	7.407	6.735	6.197	5.813	6.016
S2	2.5	1.0	pole-on	-0.695	22.348	35.837	19.778	15.671	11.812	10.193	9.446	8.693	8.424	7.535	7.036	6.584	6.95
S2	1.85	0.0	edge-on	0.375	1.242	2.563	1.88	1.66	1.358	1.189	1.866	1.427	0.952	0.84	0.736	0.677	0.653
S2	1.85	0.071	edge-on	0.286	1.56	2.532	1.865	1.636	1.319	1.15	1.513	1.182	0.917	0.821	0.712	0.647	0.621
S2	1.85	0.143	edge-on	0.156	3.891	3.198	2.281	1.961	1.497	1.275	1.262	1.098	0.955	0.868	0.743	0.663	0.641
S2	1.85	0.215	interm.	0.031	265.893	4.293	2.789	2.331	1.594	1.305	0.725	0.801	0.895	0.781	0.648	0.55	0.539
S2	1.85	0.286	interm.	-0.093	0.876	59.812	348.518	77.876	16.625	11.526	17.326	11.39	5.987	4.897	4.187	3.692	3.429

Table A.1 - continued.

Star	Σ_0 [g cm ⁻²]	cos i	$\tilde{\tau}_{\text{bu}}$ ang. type	bu		0.15	0.45	0.75	1.50	2.25	3.00	4.50	6.00	9.00	15.00	30.00	∞
				$\Delta B_{\text{bu}}^\infty$	ξ_{bu}^B	ξ_{d}^B											
S2	1.85	0.357	interm.	-0.195	1.804	23.258	10.965	7.849	5.927	5.229	6.512	5.374	3.805	3.349	2.961	2.733	2.658
S2	1.85	0.429	interm.	-0.282	3.366	16.386	9.948	7.79	6.116	5.299	6.13	5.197	4.017	3.63	3.21	2.991	2.938
S2	1.85	0.5	interm.	-0.352	5.33	18.053	10.964	8.708	6.699	5.914	6.495	5.648	4.547	4.135	3.665	3.416	3.407
S2	1.85	0.571	interm.	-0.41	7.558	20.234	12.345	9.763	7.567	6.654	7.137	6.334	5.137	4.719	4.225	3.981	3.997
S2	1.85	0.643	pole-on	-0.459	9.941	23.452	14.034	11.099	8.552	7.597	8.066	7.176	5.922	5.43	4.925	4.612	4.727
S2	1.85	0.714	pole-on	-0.5	12.498	26.851	15.934	12.744	9.79	8.644	9.123	8.222	6.786	6.299	5.742	5.395	5.589
S2	1.85	0.786	pole-on	-0.532	15.154	31.201	18.357	14.509	11.263	9.899	10.435	9.524	7.865	7.254	6.664	6.25	6.63
S2	1.85	0.857	pole-on	-0.559	17.796	36.203	21.096	16.789	12.896	11.295	11.971	10.985	9.165	8.317	7.799	7.242	7.832
S2	1.85	0.928	pole-on	-0.58	20.28	42.311	24.416	19.502	14.882	12.931	13.836	12.845	10.719	9.512	9.008	8.307	9.288
S2	1.85	1.0	pole-on	-0.594	22.485	48.582	27.978	22.24	16.778	14.456	15.838	14.756	12.397	10.654	10.304	9.421	10.738
S2	1.37	0.0	edge-on	0.296	1.346	3.236	2.204	1.909	1.524	1.371	1.262	1.13	1.044	0.949	0.834	0.754	0.732
S2	1.37	0.071	edge-on	0.235	1.602	3.21	2.238	1.915	1.54	1.387	1.279	1.129	1.046	0.962	0.841	0.757	0.735
S2	1.37	0.143	edge-on	0.14	3.383	3.88	2.811	2.374	1.873	1.624	1.503	1.328	1.231	1.125	0.981	0.891	0.861
S2	1.37	0.215	interm.	0.045	27.624	5.394	3.731	3.122	2.35	2.007	1.875	1.758	1.569	1.394	1.298	1.199	1.175
S2	1.37	0.286	interm.	-0.058	0.37	17.181	184.088	369.423	117.264	30.251	17.269	10.318	8.286	6.203	4.262	3.82	3.907
S2	1.37	0.357	interm.	-0.144	1.624	54.387	12.599	8.742	6.796	5.734	4.922	4.34	4.151	3.689	3.243	2.932	2.957
S2	1.37	0.429	interm.	-0.219	3.124	19.171	11.227	8.884	6.923	6.104	5.496	4.913	4.662	4.288	3.792	3.507	3.571
S2	1.37	0.5	interm.	-0.28	4.96	20.904	12.723	10.22	7.913	6.967	6.308	5.74	5.466	5.016	4.52	4.199	4.358
S2	1.37	0.571	interm.	-0.331	7.008	24.248	14.736	11.828	9.163	8.116	7.384	6.683	6.46	5.851	5.347	5.03	5.249
S2	1.37	0.643	pole-on	-0.374	9.34	28.247	17.084	13.777	10.758	9.421	8.637	7.885	7.617	6.951	6.334	5.921	6.337
S2	1.37	0.714	pole-on	-0.409	11.918	33.003	19.981	16.073	12.478	10.986	10.088	9.139	9.05	8.105	7.508	6.976	7.646
S2	1.37	0.786	pole-on	-0.436	14.567	38.642	23.394	18.931	14.662	12.793	11.726	10.658	10.692	9.364	8.817	8.149	9.204
S2	1.37	0.857	pole-on	-0.458	17.288	46.06	27.26	22.053	16.97	14.689	13.577	12.378	12.537	10.734	10.272	9.459	11.029
S2	1.37	0.928	pole-on	-0.475	19.983	54.043	32.467	26.191	19.613	16.828	15.202	14.294	14.818	12.233	12.044	10.879	13.282
S2	1.37	1.0	pole-on	-0.485	22.142	62.649	37.166	30.233	22.149	18.758	16.994	16.247	17.017	13.625	13.733	12.208	15.59
S2	1.01	0.0	edge-on	0.233	1.435	3.999	2.618	2.202	3.514	1.548	1.438	1.27	1.177	1.072	0.989	0.85	0.836
S2	1.01	0.071	edge-on	0.19	1.683	3.935	2.718	2.265	3.083	1.621	1.491	1.315	1.212	1.117	1.007	0.882	0.867
S2	1.01	0.143	edge-on	0.123	3.064	4.784	3.523	2.849	2.693	2.011	1.883	1.673	1.554	1.431	1.298	1.142	1.107
S2	1.01	0.215	interm.	0.049	13.351	6.561	4.746	3.925	3.033	2.866	2.892	2.558	2.441	2.446	2.138	2.001	1.979
S2	1.01	0.286	interm.	-0.029	2.708	14.693	37.049	137.399	424.271	315.092	292.634	195.054	102.215	22.719	18.167	2.791	3.537
S2	1.01	0.357	interm.	-0.101	1.467	259.545	15.297	9.403	20.985	5.215	4.626	4.006	3.961	3.462	3.374	2.827	2.767
S2	1.01	0.429	interm.	-0.162	2.962	22.369	12.518	9.851	14.56	6.406	5.8	5.225	4.998	4.43	4.242	3.726	3.792
S2	1.01	0.5	interm.	-0.212	4.673	23.673	13.984	11.6	14.779	7.699	6.986	6.339	6.17	5.506	5.221	4.731	4.847
S2	1.01	0.571	interm.	-0.255	6.527	27.975	16.77	13.581	16.429	9.157	8.442	7.587	7.498	6.737	6.375	5.769	6.144
S2	1.01	0.643	pole-on	-0.29	8.683	32.796	20.262	16.511	18.859	10.956	10.112	9.1	9.094	8.14	7.592	6.997	7.802

Table A.1 - continued.

Star	Σ_0 [g cm ⁻²]	cos i	$\tilde{\tau}_{\text{bu}}$ ang. type	bu		0.15	0.45	0.75	1.50	2.25	3.00	4.50	6.00	9.00	15.00	30.00	∞
				$\Delta B_{\text{bu}}^\infty$	ξ_{bu}^B	ξ_{d}^B											
S2	1.01	0.714	pole-on	-0.318	11.137	38.903	23.88	19.334	21.689	13.076	12.054	10.741	11.032	9.542	9.056	8.37	9.748
S2	1.01	0.786	pole-on	-0.34	13.69	46.334	28.727	23.265	25.74	15.464	14.09	12.66	13.035	11.161	10.542	9.748	12.203
S2	1.01	0.857	pole-on	-0.357	16.369	55.388	33.799	27.716	29.973	17.907	16.209	14.677	15.534	12.772	12.223	11.31	15.033
S2	1.01	0.928	pole-on	-0.369	19.178	65.621	40.794	33.008	35.623	20.254	18.139	17.2	18.52	14.462	14.033	13.021	18.471
S2	1.01	1.0	pole-on	-0.374	21.168	75.637	46.756	38.126	40.767	22.643	20.087	19.373	21.644	16.098	15.748	14.639	21.924
S2	0.75	0.0	edge-on	0.184	1.576	4.89	3.246	2.566	2.012	1.779	1.611	1.425	1.324	1.212	1.058	0.964	0.929
S2	0.75	0.071	edge-on	0.154	2.571	4.94	3.303	2.669	2.126	1.878	1.727	1.533	1.385	1.292	1.13	1.035	0.992
S2	0.75	0.143	edge-on	0.104	3.154	6.076	4.101	3.486	2.775	2.503	2.313	2.059	1.908	1.773	1.544	1.413	1.395
S2	0.75	0.215	interm.	0.047	36.958	7.829	5.846	5.023	4.214	3.888	3.779	3.47	3.348	3.261	3.028	2.815	2.863
S2	0.75	0.286	interm.	-0.009	86.537	27.113	22.479	61.17	217.786	292.935	346.778	324.308	291.774	328.82	266.675	285.246	200.053
S2	0.75	0.357	interm.	-0.067	2.125	292.144	14.571	8.467	5.492	4.06	3.621	3.076	3.189	2.446	2.303	2.098	2.361
S2	0.75	0.429	interm.	-0.116	5.253	25.276	12.05	9.707	7.149	5.928	5.309	4.788	4.792	4.12	3.742	3.47	3.845
S2	0.75	0.5	interm.	-0.156	4.331	24.282	14.08	11.723	8.936	7.719	7.026	6.461	6.322	5.504	5.178	4.763	5.283
S2	0.75	0.571	interm.	-0.19	5.759	29.753	17.512	14.303	11.086	9.64	8.709	7.86	8.048	6.911	6.502	6.007	6.871
S2	0.75	0.643	pole-on	-0.217	7.527	35.084	21.167	17.687	13.44	11.717	10.758	9.576	9.898	8.481	7.983	7.552	8.843
S2	0.75	0.714	pole-on	-0.239	9.28	42.264	25.937	21.312	16.368	14.178	12.823	11.521	12.162	10.239	9.67	8.901	11.019
S2	0.75	0.786	pole-on	-0.256	11.139	50.542	31.64	25.785	19.488	16.821	15.278	13.716	14.603	11.939	11.574	10.485	13.824
S2	0.75	0.857	pole-on	-0.267	12.945	61.005	37.636	31.148	23.004	19.599	17.711	15.99	17.553	13.613	13.579	12.246	16.985
S2	0.75	0.928	pole-on	-0.275	14.651	73.65	45.157	37.168	26.583	22.224	19.997	18.656	20.924	15.528	16.062	14.025	21.037
S2	0.75	1.0	pole-on	-0.277	15.9	84.388	52.038	43.606	30.116	24.608	21.956	21.235	24.577	17.226	18.179	15.7	24.905
S2	0.56	0.0	edge-on	0.146	1.768	5.922	3.706	3.104	2.346	2.003	1.84	1.623	1.514	1.357	1.193	1.082	1.043
S2	0.56	0.071	edge-on	0.124	1.931	5.9	3.848	3.219	2.456	2.19	1.952	1.738	1.609	1.503	1.293	1.159	1.13
S2	0.56	0.143	edge-on	0.087	3.021	7.147	4.901	4.017	3.341	2.929	2.72	2.438	2.301	2.1	1.848	1.733	1.712
S2	0.56	0.215	interm.	0.043	7.945	10.513	7.025	5.996	5.401	4.972	5.062	4.526	4.406	4.017	3.875	3.916	3.637
S2	0.56	0.286	interm.	0.001	303.242	74.999	75.387	106.844	134.995	149.373	199.023	218.112	280.769	280.838	267.656	305.094	317.231
S2	0.56	0.357	interm.	-0.045	1.33	277.759	114.138	9.369	3.832	3.162	2.696	2.393	2.311	1.819	1.718	1.518	1.564
S2	0.56	0.429	interm.	-0.082	2.902	30.865	12.207	9.141	6.152	5.321	4.556	4.282	4.285	3.441	3.339	2.991	3.362
S2	0.56	0.5	interm.	-0.113	4.26	25.641	14.412	11.764	8.35	7.305	6.768	6.002	6.135	5.052	4.83	4.333	5.184
S2	0.56	0.571	interm.	-0.137	5.929	30.078	17.769	14.449	10.856	9.682	8.823	7.898	7.851	6.583	6.503	5.766	7.002
S2	0.56	0.643	pole-on	-0.158	7.964	34.717	21.712	18.034	13.375	11.913	10.516	9.793	10.095	8.416	8.002	7.275	9.07
S2	0.56	0.714	pole-on	-0.173	10.048	42.396	26.576	21.915	16.57	14.466	13.073	11.701	12.423	10.25	9.819	8.848	11.322
S2	0.56	0.786	pole-on	-0.184	12.688	52.645	32.977	27.353	20.128	17.127	15.673	14.229	15.276	11.996	11.875	10.564	14.514
S2	0.56	0.857	pole-on	-0.192	15.265	63.25	39.24	33.407	23.673	20.165	18.042	16.48	18.354	13.719	13.859	12.381	17.832
S2	0.56	0.928	pole-on	-0.196	18.43	76.227	47.869	40.6	27.254	22.857	20.396	19.098	22.549	15.624	16.437	14.036	22.526
S2	0.56	1.0	pole-on	-0.195	20.291	90.359	55.015	46.336	31.098	25.179	22.551	21.986	25.838	17.237	18.91	16.109	27.239

Table A.1 - continued.

Star	Σ_0 [g cm ⁻²]	cos i	$\tilde{\tau}_{\text{bu}}$ ang. type	bu		0.15	0.45	0.75	1.50	2.25	3.00	4.50	6.00	9.00	15.00	30.00	∞
				$\Delta B_{\text{bu}}^\infty$	ξ_{bu}^B	ξ_{d}^B											
S2	0.41	0.0	edge-on	0.115	1.904	7.171	4.311	3.435	2.7	2.316	2.124	1.818	1.672	1.57	1.335	1.24	1.178
S2	0.41	0.071	edge-on	0.098	2.067	7.067	4.533	3.718	2.851	2.486	2.306	1.99	1.832	1.717	1.454	1.32	1.271
S2	0.41	0.143	edge-on	0.07	3.097	8.688	5.691	4.766	3.875	3.518	3.28	2.75	2.69	2.566	2.215	2.074	1.996
S2	0.41	0.215	interm.	0.036	8.048	14.475	8.436	7.527	6.394	6.246	6.334	5.479	5.337	5.536	4.914	4.872	4.674
S2	0.41	0.286	interm.	0.006	325.941	89.774	81.513	90.26	99.567	141.653	188.049	209.869	286.666	235.39	230.728	290.957	290.017
S2	0.41	0.357	interm.	-0.028	10.088	287.946	242.767	102.114	7.584	3.114	5.681	2.252	2.275	1.467	1.46	1.366	1.348
S2	0.41	0.429	interm.	-0.055	3.329	114.263	12.059	8.003	5.633	4.619	3.772	3.863	3.625	2.921	2.65	2.339	2.753
S2	0.41	0.5	interm.	-0.077	4.307	29.424	13.731	10.788	7.741	6.513	5.69	5.379	5.472	4.579	4.078	3.838	4.58
S2	0.41	0.571	interm.	-0.095	5.868	30.188	16.67	13.849	10.111	8.789	7.415	7.287	7.434	6.16	5.751	5.159	6.273
S2	0.41	0.643	pole-on	-0.109	7.822	35.267	21.863	17.339	13.074	11.052	9.856	9.108	9.634	7.692	7.469	6.853	8.54
S2	0.41	0.714	pole-on	-0.12	10.025	44.073	26.144	20.859	16.166	13.69	12.224	11.079	11.898	9.47	9.263	8.399	11.015
S2	0.41	0.786	pole-on	-0.128	12.318	52.375	33.204	26.75	19.56	16.682	14.793	13.212	14.833	11.13	11.143	10.25	14.394
S2	0.41	0.857	pole-on	-0.132	15.307	64.978	40.873	33.01	23.509	19.348	17.585	15.595	18.522	13.11	13.34	11.903	17.927
S2	0.41	0.928	pole-on	-0.134	18.504	77.366	50.087	40.975	27.268	22.705	18.944	18.613	22.076	14.894	15.82	13.596	22.54
S2	0.41	1.0	pole-on	-0.132	20.159	91.097	56.338	46.712	31.317	25.464	22.132	21.343	26.003	16.783	18.339	15.431	26.966
S2	0.3	0.0	edge-on	0.089	2.091	9.205	5.304	4.089	3.018	2.581	2.365	2.155	1.888	1.737	1.482	1.388	1.3
S2	0.3	0.071	edge-on	0.076	2.22	9.892	5.421	4.307	3.248	2.934	2.562	2.257	2.087	1.861	1.593	1.497	1.407
S2	0.3	0.143	edge-on	0.054	3.422	13.301	6.616	5.706	4.384	4.092	3.74	3.487	3.051	2.875	2.513	2.439	2.388
S2	0.3	0.215	interm.	0.029	8.308	57.184	12.846	9.437	7.939	8.206	7.161	7.142	6.838	6.387	6.21	5.895	5.674
S2	0.3	0.286	interm.	0.007	307.856	203.145	124.363	155.981	171.274	197.938	198.094	237.045	252.117	219.426	262.68	265.888	275.838
S2	0.3	0.357	interm.	-0.016	23.143	312.535	273.005	212.32	90.758	55.577	28.266	9.299	4.793	5.332	5.018	1.528	2.431
S2	0.3	0.429	interm.	-0.037	2.777	207.001	18.72	8.347	5.176	3.951	3.775	3.405	3.355	2.88	2.696	2.484	2.452
S2	0.3	0.5	interm.	-0.053	4.14	53.104	12.064	9.987	7.447	5.975	5.064	4.803	4.707	4.314	4.08	3.398	3.942
S2	0.3	0.571	interm.	-0.065	5.834	41.648	16.446	13.099	9.3	7.795	7.088	6.629	6.822	5.761	5.22	4.76	5.514
S2	0.3	0.643	pole-on	-0.075	7.744	34.31	19.568	16.838	11.785	10.028	8.938	8.274	8.57	6.841	6.979	6.219	7.64
S2	0.3	0.714	pole-on	-0.082	10.174	44.878	24.973	20.991	15.308	12.632	11.7	10.075	10.94	8.871	8.431	7.646	9.809
S2	0.3	0.786	pole-on	-0.087	12.535	54.745	30.6	25.89	18.027	15.717	14.676	12.441	13.39	10.553	10.663	9.16	12.86
S2	0.3	0.857	pole-on	-0.09	15.468	61.628	38.204	32.028	22.615	18.307	16.882	14.675	16.241	12.438	12.865	11.296	16.315
S2	0.3	0.928	pole-on	-0.09	18.484	82.989	49.643	40.948	26.098	21.175	18.687	17.448	21.523	14.221	15.183	12.587	21.251
S2	0.3	1.0	pole-on	-0.087	20.741	101.189	58.898	44.898	30.347	24.686	21.457	20.741	25.81	15.901	17.759	15.213	26.203
S3	2.5	0.0	edge-on	0.441	1.268	2.346	1.728	1.501	1.245	1.116	1.02	0.918	0.851	0.773	0.671	0.612	0.599
S3	2.5	0.071	edge-on	0.335	1.647	2.367	1.717	1.505	1.235	1.089	1.004	0.897	0.827	0.75	0.648	0.587	0.569
S3	2.5	0.143	edge-on	0.176	4.705	3.127	2.178	1.826	1.396	1.19	1.071	0.94	0.868	0.762	0.708	0.58	0.572
S3	2.5	0.215	interm.	0.035	432.992	4.364	2.806	2.236	1.536	1.241	1.074	0.913	0.815	0.646	0.534	0.463	0.47
S3	2.5	0.286	interm.	-0.1	0.445	6.067	327.9	54.278	12.528	8.669	6.986	5.667	4.825	4.15	3.349	3.085	2.92

Table A.1 - continued.

Star	Σ_0 [g cm ⁻²]	cos i	$\tilde{\tau}_{\text{bu}}$ ang. type	bu		0.15	0.45	0.75	1.50	2.25	3.00	4.50	6.00	9.00	15.00	30.00	∞
				$\Delta B_{\text{bu}}^\infty$	ξ_{bu}^B	ξ_{d}^B											
S3	2.5	0.357	interm.	-0.208	1.626	14.578	8.246	6.452	4.925	4.161	3.807	3.409	3.104	2.826	2.456	2.228	2.193
S3	2.5	0.429	interm.	-0.299	3.207	12.613	8.285	6.522	5.059	4.377	4.004	3.572	3.306	3.004	2.641	2.423	2.361
S3	2.5	0.5	interm.	-0.371	5.155	14.692	8.967	7.245	5.573	4.825	4.42	3.977	3.704	3.376	2.965	2.762	2.715
S3	2.5	0.571	interm.	-0.43	7.44	16.888	10.178	8.143	6.27	5.431	5.002	4.528	4.205	3.854	3.428	3.205	3.174
S3	2.5	0.643	pole-on	-0.481	9.84	19.358	11.605	9.245	7.108	6.222	5.705	5.177	4.844	4.44	3.957	3.736	3.743
S3	2.5	0.714	pole-on	-0.522	12.448	22.405	13.144	10.546	8.113	7.058	6.51	5.926	5.596	5.148	4.609	4.354	4.401
S3	2.5	0.786	pole-on	-0.555	15.02	25.833	15.065	12.031	9.207	8.036	7.465	6.771	6.479	5.908	5.367	5.068	5.185
S3	2.5	0.857	pole-on	-0.582	17.654	30.114	17.272	13.73	10.526	9.173	8.505	7.812	7.531	6.834	6.249	5.868	6.143
S3	2.5	0.928	pole-on	-0.605	20.1	35.058	20.046	15.866	12.118	10.528	9.711	9.011	8.765	7.825	7.251	6.817	7.274
S3	2.5	1.0	pole-on	-0.62	22.173	40.392	22.95	18.203	13.758	11.855	10.965	10.266	10.141	8.857	8.319	7.779	8.479
S3	1.85	0.0	edge-on	0.35	1.369	2.767	1.994	1.716	1.397	1.214	1.156	1.565	1.025	0.888	0.754	0.688	0.668
S3	1.85	0.071	edge-on	0.277	1.65	2.689	2.067	1.77	1.429	1.231	1.173	1.397	1.014	0.9	0.77	0.698	0.673
S3	1.85	0.143	edge-on	0.163	3.84	3.571	2.677	2.263	1.723	1.451	1.393	1.318	1.149	1.044	0.883	0.799	0.782
S3	1.85	0.215	interm.	0.051	48.782	4.976	3.695	3.008	2.203	1.799	1.793	1.231	1.393	1.312	1.162	1.04	1.065
S3	1.85	0.286	interm.	-0.062	1.791	8.808	94.101	335.001	112.286	23.027	13.138	15.957	6.758	4.677	3.31	3.045	2.637
S3	1.85	0.357	interm.	-0.156	1.45	39.382	8.783	6.684	5.19	4.834	4.063	5.185	3.571	3.113	2.645	2.512	2.391
S3	1.85	0.429	interm.	-0.236	2.976	16.038	9.175	7.374	5.785	5.246	4.636	5.205	3.972	3.553	3.1	2.942	2.883
S3	1.85	0.5	interm.	-0.301	4.821	17.968	10.55	8.498	6.62	5.964	5.285	5.786	4.608	4.186	3.695	3.499	3.51
S3	1.85	0.571	interm.	-0.354	6.942	20.867	12.231	9.85	7.706	6.895	6.275	6.565	5.341	4.925	4.38	4.154	4.243
S3	1.85	0.643	pole-on	-0.4	9.326	24.407	14.312	11.464	8.899	7.988	7.333	7.575	6.259	5.81	5.207	4.958	5.178
S3	1.85	0.714	pole-on	-0.436	11.877	28.481	16.569	13.46	10.337	9.303	8.545	8.726	7.328	6.785	6.175	5.823	6.157
S3	1.85	0.786	pole-on	-0.466	14.551	33.419	19.445	15.617	12.002	10.752	9.941	10.086	8.475	7.917	7.212	6.835	7.366
S3	1.85	0.857	pole-on	-0.489	17.291	39.165	22.883	18.296	13.981	12.479	11.468	11.769	9.922	9.076	8.5	7.982	8.924
S3	1.85	0.928	pole-on	-0.507	19.97	46.229	26.82	21.489	16.244	14.247	13.101	13.796	11.623	10.387	9.972	9.236	10.653
S3	1.85	1.0	pole-on	-0.519	22.005	53.872	31.133	25.052	18.479	16.08	14.706	16.156	13.352	11.73	11.433	10.512	12.609
S3	1.37	0.0	edge-on	0.278	1.509	3.667	2.399	1.967	1.594	1.399	1.292	1.15	1.067	0.972	0.844	0.772	0.747
S3	1.37	0.071	edge-on	0.227	1.781	3.719	2.47	2.088	1.677	1.475	1.354	1.229	1.119	1.019	0.886	0.822	0.787
S3	1.37	0.143	edge-on	0.144	3.543	4.607	3.289	2.695	2.153	1.886	1.716	1.549	1.411	1.288	1.134	1.045	1.013
S3	1.37	0.215	interm.	0.058	19.401	6.536	4.678	4.0	3.18	2.815	2.633	2.432	2.255	2.12	1.914	1.793	1.727
S3	1.37	0.286	interm.	-0.031	5.526	9.847	9.498	76.933	342.854	290.933	221.112	81.665	7.668	3.727	1.951	1.158	1.109
S3	1.37	0.357	interm.	-0.111	1.244	239.28	8.161	6.266	4.757	4.201	3.75	3.298	3.011	2.76	2.461	2.267	2.347
S3	1.37	0.429	interm.	-0.179	2.752	16.321	9.608	7.822	5.947	5.292	4.774	4.262	4.121	3.688	3.382	3.109	3.191
S3	1.37	0.5	interm.	-0.234	4.53	19.63	11.424	9.421	7.361	6.456	5.961	5.318	5.087	4.645	4.24	3.969	4.115
S3	1.37	0.571	interm.	-0.28	6.574	23.198	13.862	11.375	8.793	7.791	7.075	6.419	6.271	5.59	5.187	4.85	5.189
S3	1.37	0.643	pole-on	-0.318	8.809	27.682	16.724	13.522	10.406	9.253	8.48	7.674	7.604	6.828	6.277	5.885	6.399

Table A.1 - continued.

Star	Σ_0 [g cm ⁻²]	cos i	$\tilde{\tau}_{\text{bu}}$ ang. type	bu		0.15	0.45	0.75	1.50	2.25	3.00	4.50	6.00	9.00	15.00	30.00	∞
				$\Delta B_{\text{bu}}^\infty$	ξ_{bu}^B	ξ_{d}^B											
S3	1.37	0.714	pole-on	-0.349	11.361	33.493	19.745	16.209	12.513	11.017	10.127	9.056	9.11	8.042	7.564	6.969	7.939
S3	1.37	0.786	pole-on	-0.373	14.068	39.581	23.713	19.283	14.758	12.909	11.88	10.708	10.975	9.441	8.973	8.316	9.687
S3	1.37	0.857	pole-on	-0.391	16.824	46.753	28.049	23.091	17.412	15.158	13.806	12.599	13.093	10.896	10.581	9.687	11.78
S3	1.37	0.928	pole-on	-0.405	19.706	56.269	33.623	27.285	20.141	17.268	15.639	14.749	15.584	12.302	12.425	11.143	14.378
S3	1.37	1.0	pole-on	-0.412	21.812	65.678	39.096	32.205	23.139	19.365	17.445	16.678	18.157	13.93	14.306	12.687	16.991
S3	1.01	0.0	edge-on	0.22	1.677	4.456	2.74	2.351	1.819	1.605	1.466	1.3	1.19	1.039	0.793	0.823	0.864
S3	1.01	0.071	edge-on	0.184	1.961	4.485	2.859	2.521	1.941	1.731	1.558	1.384	1.277	1.102	0.855	0.886	0.921
S3	1.01	0.143	edge-on	0.124	3.512	5.36	3.868	3.253	2.585	2.31	2.14	1.9	1.749	1.542	1.319	1.26	1.288
S3	1.01	0.215	interm.	0.059	12.199	8.03	5.565	5.322	4.385	3.942	3.58	3.406	3.215	3.081	3.024	2.724	2.653
S3	1.01	0.286	interm.	-0.007	50.443	18.865	11.819	23.682	191.658	250.512	268.387	311.962	362.139	330.088	250.75	201.314	154.863
S3	1.01	0.357	interm.	-0.075	1.477	293.44	11.987	4.559	3.631	3.23	2.811	2.524	2.503	2.235	2.489	1.765	1.719
S3	1.01	0.429	interm.	-0.129	2.572	18.672	10.325	7.458	5.553	4.987	4.639	4.135	3.942	3.735	3.811	2.947	2.883
S3	1.01	0.5	interm.	-0.174	4.259	20.428	12.744	9.822	7.235	6.55	6.112	5.44	5.374	4.96	4.959	4.124	3.892
S3	1.01	0.571	interm.	-0.211	6.237	24.792	15.623	12.157	9.01	8.377	7.606	6.74	6.786	6.223	6.212	5.355	5.116
S3	1.01	0.643	pole-on	-0.242	8.386	29.898	19.064	14.83	10.973	10.178	9.302	8.311	8.37	7.653	7.624	6.695	6.59
S3	1.01	0.714	pole-on	-0.266	10.74	37.261	23.199	18.138	15.06	12.152	11.279	10.0	10.222	9.126	8.965	8.226	8.612
S3	1.01	0.786	pole-on	-0.284	13.437	44.864	27.835	22.421	15.774	14.693	13.278	11.941	12.5	10.668	10.452	9.757	11.393
S3	1.01	0.857	pole-on	-0.298	16.18	53.436	33.472	26.436	18.62	17.092	15.517	14.032	15.117	12.4	12.266	11.358	14.909
S3	1.01	0.928	pole-on	-0.307	19.276	64.504	40.153	31.813	21.555	19.6	17.597	16.373	18.226	13.911	14.077	13.209	19.288
S3	1.01	1.0	pole-on	-0.31	21.398	74.777	47.218	37.514	24.851	21.688	19.626	18.809	21.265	15.603	15.978	14.93	23.966
S3	0.75	0.0	edge-on	0.176	1.815	5.542	3.426	2.764	2.108	1.824	1.684	1.476	1.34	1.235	1.078	0.976	0.935
S3	0.75	0.071	edge-on	0.149	2.087	5.436	3.521	2.875	2.243	1.932	1.793	1.561	1.428	1.326	1.162	1.054	1.013
S3	0.75	0.143	edge-on	0.104	3.648	6.419	4.71	3.853	3.056	2.705	2.467	2.246	2.08	1.94	1.69	1.576	1.512
S3	0.75	0.215	interm.	0.053	20.664	9.426	6.89	6.116	5.303	4.905	4.69	4.326	4.177	4.161	3.88	3.758	3.577
S3	0.75	0.286	interm.	0.004	356.927	18.097	16.503	25.969	65.733	92.01	79.814	197.844	250.789	246.588	281.701	261.543	309.774
S3	0.75	0.357	interm.	-0.049	1.054	291.849	65.815	6.04	2.75	2.402	2.079	1.94	1.798	1.483	1.399	1.209	1.343
S3	0.75	0.429	interm.	-0.092	2.474	18.485	8.929	6.928	5.317	4.493	3.939	3.613	3.573	3.086	2.831	2.399	2.889
S3	0.75	0.5	interm.	-0.128	3.987	21.163	11.868	9.668	7.303	6.372	5.802	5.217	5.173	4.481	4.173	3.709	4.217
S3	0.75	0.571	interm.	-0.156	5.628	24.693	15.043	12.451	9.213	8.29	7.385	6.687	6.83	5.9	5.515	5.038	5.771
S3	0.75	0.643	pole-on	-0.181	26.476	31.885	18.944	15.527	11.707	10.267	9.353	8.366	8.67	7.477	6.882	6.358	7.677
S3	0.75	0.714	pole-on	-0.198	9.091	39.644	23.076	19.193	14.396	12.773	11.588	10.15	10.843	9.025	8.609	7.795	9.782
S3	0.75	0.786	pole-on	-0.212	10.935	47.095	28.963	23.509	17.553	15.363	13.788	12.238	13.193	10.627	10.397	9.304	12.479
S3	0.75	0.857	pole-on	-0.221	13.043	56.462	34.728	28.951	20.574	17.849	16.188	14.474	16.017	12.358	12.399	10.863	15.519
S3	0.75	0.928	pole-on	-0.227	14.785	67.829	42.224	34.796	23.834	20.378	18.204	16.962	19.661	14.071	14.574	12.509	19.364
S3	0.75	1.0	pole-on	-0.227	15.86	79.722	49.792	40.896	26.983	22.788	20.079	19.462	22.703	15.762	16.784	14.31	23.162

Table A.1 - continued.

Star	Σ_0 [g cm ⁻²]	cos i	$\tilde{\tau}_{bu}$ ang. type	bu		0.15	0.45	0.75	1.50	2.25	3.00	4.50	6.00	9.00	15.00	30.00	∞
				ΔB_{bu}^∞	ξ_{bu}^B	ξ_d^B											
S3	0.56	0.0	edge-on	0.141	2.13	6.563	3.973	3.212	2.439	2.104	1.918	1.631	1.525	1.412	1.197	1.112	1.047
S3	0.56	0.071	edge-on	0.121	2.349	6.243	4.0	3.327	2.65	2.219	2.049	1.768	1.612	1.506	1.291	1.185	1.138
S3	0.56	0.143	edge-on	0.086	3.704	7.507	5.086	4.428	3.581	3.125	2.872	2.607	2.405	2.305	2.009	1.807	1.742
S3	0.56	0.215	interm.	0.047	9.193	11.029	8.03	7.33	6.268	6.006	5.696	5.436	5.079	5.152	4.911	4.581	4.534
S3	0.56	0.286	interm.	0.009	365.41	55.16	50.157	40.616	95.565	98.997	143.33	119.122	192.469	186.694	218.694	263.552	246.734
S3	0.56	0.357	interm.	-0.033	5.873	306.846	160.575	54.689	4.754	2.178	1.934	1.87	1.778	1.411	1.134	1.075	1.121
S3	0.56	0.429	interm.	-0.065	2.332	57.008	8.829	6.539	4.503	3.938	3.546	3.239	3.119	2.647	2.468	2.144	2.406
S3	0.56	0.5	interm.	-0.091	3.932	20.754	11.95	8.802	6.623	5.715	5.213	4.812	4.698	4.12	3.76	3.404	3.879
S3	0.56	0.571	interm.	-0.113	5.651	24.769	15.281	11.985	8.883	7.81	6.894	6.29	6.459	5.454	5.016	4.717	5.352
S3	0.56	0.643	pole-on	-0.13	7.79	31.581	18.711	15.627	11.369	9.764	8.936	8.169	8.211	6.969	6.59	6.041	7.351
S3	0.56	0.714	pole-on	-0.143	9.964	38.52	23.66	19.245	14.121	12.299	11.304	9.748	10.581	8.687	8.306	7.567	9.732
S3	0.56	0.786	pole-on	-0.153	12.53	47.235	29.41	23.755	17.327	15.158	13.366	12.055	12.795	10.069	9.945	8.912	12.361
S3	0.56	0.857	pole-on	-0.159	15.582	57.173	36.377	28.742	20.667	17.83	15.517	14.186	16.289	11.727	11.777	10.668	15.485
S3	0.56	0.928	pole-on	-0.162	18.334	70.888	44.058	36.161	24.178	20.218	17.568	16.626	19.451	13.529	14.135	12.24	19.463
S3	0.56	1.0	pole-on	-0.16	20.801	81.44	50.908	41.672	27.224	22.355	19.287	19.053	22.702	15.114	16.404	13.912	23.57
S3	0.41	0.0	edge-on	0.112	2.263	8.008	4.447	3.848	2.793	2.355	2.163	1.884	1.706	1.559	1.345	1.228	1.178
S3	0.41	0.071	edge-on	0.096	2.491	7.714	4.608	4.092	2.897	2.502	2.292	1.986	1.853	1.677	1.45	1.32	1.28
S3	0.41	0.143	edge-on	0.068	3.902	9.475	5.886	4.98	3.872	3.497	3.319	2.93	2.691	2.459	2.192	2.045	2.017
S3	0.41	0.215	interm.	0.038	9.563	27.387	9.429	8.185	7.225	6.733	6.897	6.655	6.202	5.86	5.521	5.513	5.491
S3	0.41	0.286	interm.	0.01	320.824	83.257	83.327	117.251	119.065	150.311	151.839	149.581	221.303	203.425	245.279	262.177	279.242
S3	0.41	0.357	interm.	-0.019	10.135	301.436	268.45	136.486	68.11	19.446	14.775	3.627	1.86	1.642	1.857	1.384	1.258
S3	0.41	0.429	interm.	-0.044	2.279	141.313	9.649	6.459	4.745	3.814	3.211	3.103	3.012	2.477	2.431	2.023	2.131
S3	0.41	0.5	interm.	-0.064	3.605	27.428	11.575	8.592	6.298	5.424	4.841	4.512	4.462	3.753	3.462	3.021	3.39
S3	0.41	0.571	interm.	-0.079	5.382	28.304	14.146	11.459	8.327	7.415	6.694	6.007	5.945	5.185	4.686	4.322	4.959
S3	0.41	0.643	pole-on	-0.092	7.559	33.025	18.585	14.861	10.802	9.393	8.421	7.612	7.946	6.458	6.248	5.745	7.539
S3	0.41	0.714	pole-on	-0.1	9.811	38.678	23.148	18.36	13.754	11.435	10.557	9.342	9.891	8.191	7.892	6.907	9.005
S3	0.41	0.786	pole-on	-0.107	12.368	49.245	28.926	22.453	17.287	14.174	12.725	11.167	12.382	9.863	9.673	8.36	11.935
S3	0.41	0.857	pole-on	-0.11	15.427	59.898	35.694	29.841	20.596	17.185	15.365	13.712	15.07	11.365	11.201	10.002	14.717
S3	0.41	0.928	pole-on	-0.111	18.374	72.148	44.098	34.626	24.072	19.39	17.568	15.598	18.814	13.051	13.835	11.407	18.667
S3	0.41	1.0	pole-on	-0.109	20.701	85.31	50.408	41.701	27.209	21.072	19.652	18.874	22.257	14.288	15.637	12.966	22.916
S3	0.3	0.0	edge-on	0.086	2.51	10.071	5.338	4.146	3.095	2.704	2.356	2.102	1.917	1.775	1.507	1.354	1.374
S3	0.3	0.071	edge-on	0.074	2.799	10.38	5.336	4.229	3.38	2.82	2.523	2.225	1.972	1.887	1.6	1.43	1.418
S3	0.3	0.143	edge-on	0.054	7.093	19.248	6.661	5.439	4.555	4.105	3.76	3.19	3.09	2.749	2.363	2.333	2.271
S3	0.3	0.215	interm.	0.03	15.224	50.475	11.63	13.3	9.945	8.398	7.71	7.277	7.227	7.159	6.435	6.621	6.294
S3	0.3	0.286	interm.	0.009	275.284	212.519	132.991	149.15	215.419	218.448	224.952	270.133	250.52	234.845	244.373	277.698	270.83

Table A.1 - continued.

Star	Σ_0 [g cm ⁻²]	$\cos i$	$\tilde{\tau}_{\text{bu}}$ ang. type	bu		0.15	0.45	0.75	1.50	2.25	3.00	4.50	6.00	9.00	15.00	30.00	∞
				$\Delta B_{\text{bu}}^\infty$	ξ_{bu}^B	ξ_{d}^B											
S3	0.3	0.357	interm.	-0.011	76.221	297.838	317.487	244.71	158.067	107.346	73.889	25.574	13.273	24.816	8.619	6.064	2.316
S3	0.3	0.429	interm.	-0.031	2.524	245.67	42.41	8.272	5.767	3.87	3.641	3.162	3.287	2.587	2.399	2.142	2.114
S3	0.3	0.5	interm.	-0.044	7.095	74.876	14.197	9.121	6.902	5.733	4.83	4.441	4.158	3.69	3.512	2.991	3.172
S3	0.3	0.571	interm.	-0.055	5.344	31.969	14.738	11.345	8.041	7.136	6.592	5.914	5.589	4.772	4.654	4.112	4.643
S3	0.3	0.643	pole-on	-0.064	7.244	33.166	18.436	14.348	10.288	8.967	8.136	7.332	7.632	6.331	5.917	5.444	6.053
S3	0.3	0.714	pole-on	-0.07	9.471	40.31	22.668	18.742	12.826	11.489	10.443	8.738	9.355	7.954	7.102	6.689	8.549
S3	0.3	0.786	pole-on	-0.074	12.379	47.613	27.649	22.859	16.0	14.289	12.948	10.607	11.86	9.141	9.079	8.072	10.714
S3	0.3	0.857	pole-on	-0.076	15.545	62.145	35.322	28.246	19.235	16.176	14.603	13.57	14.625	10.332	11.2	9.238	14.182
S3	0.3	0.928	pole-on	-0.076	19.46	70.216	42.11	35.428	21.956	19.208	16.643	15.213	18.835	12.603	13.076	11.288	17.93
S3	0.3	1.0	pole-on	-0.074	21.146	94.419	52.726	42.628	25.751	21.395	19.229	18.697	21.384	14.09	15.347	12.911	22.254

Table A.2 - Empirical law parameters for band V.

Star	Σ_0 [g cm ⁻²]	cos i	$\tilde{\tau}_{bu}$ ang. type	bu		0.15	0.45	0.75	1.50	2.25	3.00	4.50	6.00	9.00	15.00	30.00	∞
				ΔV_{bu}^∞	ξ_{bu}^V	ξ_d^V											
S1	2.5	0.0	edge-on	0.554	1.086	1.915	1.484	1.327	1.106	0.99	0.911	0.827	0.767	0.69	0.598	0.539	0.52
S1	2.5	0.071	edge-on	0.33	1.453	1.611	1.22	1.09	0.872	0.772	0.704	0.645	0.586	0.526	0.449	0.402	0.386
S1	2.5	0.143	edge-on	0.039	133.16	1.59	1.002	0.804	0.405	0.294	0.233	0.22	0.221	0.21	0.207	0.206	0.208
S1	2.5	0.215	interm.	-0.197	0.662	133.572	22.539	10.466	6.261	4.714	4.261	3.261	3.012	2.813	2.431	2.128	2.189
S1	2.5	0.286	interm.	-0.378	1.663	10.671	5.867	4.442	3.454	2.898	2.628	2.183	2.023	1.879	1.653	1.457	1.479
S1	2.5	0.357	interm.	-0.521	2.869	8.264	5.079	3.984	3.109	2.637	2.403	2.032	1.878	1.749	1.547	1.368	1.388
S1	2.5	0.429	interm.	-0.636	4.315	8.559	5.072	3.954	3.087	2.634	2.51	2.057	1.912	1.778	1.578	1.4	1.41
S1	2.5	0.5	pole-on	-0.725	6.032	9.145	5.266	4.098	3.19	2.724	2.494	2.15	2.005	1.853	1.638	1.478	1.483
S1	2.5	0.571	pole-on	-0.8	7.78	9.825	5.572	4.331	3.353	2.873	2.631	2.287	2.125	1.973	1.754	1.586	1.592
S1	2.5	0.643	pole-on	-0.863	9.548	10.686	5.988	4.643	3.582	3.075	2.821	2.464	2.293	2.129	1.886	1.722	1.721
S1	2.5	0.714	pole-on	-0.915	11.253	11.628	6.478	5.011	3.859	3.315	3.046	2.671	2.485	2.295	2.051	1.881	1.882
S1	2.5	0.786	pole-on	-0.957	12.886	12.764	7.048	5.453	4.181	3.606	3.302	2.905	2.71	2.526	2.24	2.065	2.054
S1	2.5	0.857	pole-on	-0.992	14.471	14.03	7.71	5.948	4.561	3.921	3.606	3.181	2.97	2.763	2.455	2.262	2.235
S1	2.5	0.928	pole-on	-1.02	15.985	15.516	8.439	6.509	4.975	4.288	3.933	3.482	3.255	3.016	2.668	13.603	2.433
S1	2.5	1.0	pole-on	-1.042	17.182	16.997	9.184	7.077	5.383	4.631	4.248	3.771	3.51	3.243	2.88	2.653	2.665
S1	1.85	0.0	edge-on	0.446	1.099	2.11	1.695	1.483	1.24	1.11	1.037	0.959	0.877	0.777	0.678	0.611	0.593
S1	1.85	0.071	edge-on	0.279	1.433	1.81	1.447	1.245	1.025	0.897	0.833	0.731	0.666	0.606	0.524	0.474	0.461
S1	1.85	0.143	edge-on	0.059	16.404	1.733	1.242	0.949	0.618	0.486	0.357	0.278	0.248	0.223	0.213	0.231	0.214
S1	1.85	0.215	interm.	-0.14	0.524	21.848	225.622	27.261	11.375	8.674	7.176	5.569	5.526	4.633	4.047	3.51	3.286
S1	1.85	0.286	interm.	-0.302	1.503	19.785	8.325	6.238	4.568	3.963	3.495	3.038	2.924	2.645	2.327	2.109	2.021
S1	1.85	0.357	interm.	-0.434	2.648	12.049	6.789	5.354	4.103	3.526	3.176	2.816	2.675	2.426	2.152	1.958	1.902
S1	1.85	0.429	interm.	-0.542	4.086	11.957	6.777	5.373	4.094	3.553	3.189	2.853	2.731	2.477	2.196	2.006	1.951
S1	1.85	0.5	pole-on	-0.626	5.841	12.631	7.105	5.614	4.294	3.707	3.34	3.009	2.862	2.613	2.325	2.138	2.084
S1	1.85	0.571	pole-on	-0.696	7.696	13.687	8.634	6.016	4.587	3.967	3.59	3.244	3.086	2.806	2.502	2.31	2.26
S1	1.85	0.643	pole-on	-0.756	9.647	14.908	8.244	6.531	4.968	4.305	3.886	3.537	3.354	3.064	2.734	2.517	2.468
S1	1.85	0.714	pole-on	-0.804	11.582	16.31	9.0	7.121	5.418	4.701	4.246	3.882	3.666	3.358	3.0	2.765	2.71
S1	1.85	0.786	pole-on	-0.844	13.523	17.997	9.919	7.817	5.945	5.164	4.649	4.262	4.005	3.69	3.282	3.034	2.981
S1	1.85	0.857	pole-on	-0.876	15.388	19.923	10.934	8.637	6.533	5.683	5.091	4.669	4.375	4.02	3.603	3.356	3.324
S1	1.85	0.928	pole-on	-0.903	17.164	22.179	12.118	9.511	7.169	6.186	5.558	5.09	4.758	4.392	3.98	3.713	3.707
S1	1.85	1.0	pole-on	-0.922	18.632	24.346	13.225	10.373	7.733	6.672	6.006	5.55	5.171	4.792	4.372	4.085	4.097
S1	1.37	0.0	edge-on	0.349	1.182	2.589	1.998	1.725	1.42	1.285	1.169	1.056	0.98	0.892	0.772	0.703	0.682
S1	1.37	0.071	edge-on	0.231	1.491	2.246	1.738	1.488	1.199	1.089	0.972	0.878	0.797	0.733	0.628	0.581	0.541
S1	1.37	0.143	edge-on	0.067	7.82	2.08	1.663	1.307	0.874	0.78	0.609	0.55	0.488	0.371	0.297	0.262	0.239
S1	1.37	0.215	interm.	-0.097	0.385	35.384	181.665	293.433	41.206	20.395	15.691	11.083	8.905	8.882	7.118	6.27	6.269
S1	1.37	0.286	interm.	-0.237	1.351	41.667	11.926	8.575	6.259	5.244	4.835	4.172	3.746	3.568	3.138	2.897	2.813

Table A.2 - continued.

Star	Σ_0 [g cm ⁻²]	cos i	$\tilde{\tau}_{\text{bu}}$ ang. type	bu		0.15	0.45	0.75	1.50	2.25	3.00	4.50	6.00	9.00	15.00	30.00	∞
				$\Delta V_{\text{bu}}^\infty$	ξ_{bu}^V	ξ_{d}^V											
S1	1.37	0.357	interm.	-0.355	2.488	17.615	8.93	7.063	5.419	4.642	4.322	3.778	3.481	3.297	2.886	2.668	2.594
S1	1.37	0.429	interm.	-0.454	3.908	16.13	8.985	7.201	5.513	4.75	4.412	3.905	3.607	3.403	2.996	2.77	2.711
S1	1.37	0.5	pole-on	-0.533	5.627	17.064	9.556	7.657	5.849	5.065	4.718	4.176	3.886	3.652	3.233	3.004	2.918
S1	1.37	0.571	pole-on	-0.598	7.561	18.532	10.363	8.275	6.323	5.522	5.09	4.569	4.251	3.976	3.542	3.275	3.221
S1	1.37	0.643	pole-on	-0.653	9.641	20.389	11.401	9.009	6.974	6.059	5.605	5.021	4.693	4.391	3.899	3.646	3.594
S1	1.37	0.714	pole-on	-0.698	11.788	22.509	12.545	10.044	7.684	6.706	6.16	5.553	5.194	4.857	4.347	4.04	4.043
S1	1.37	0.786	pole-on	-0.735	13.887	24.957	13.963	11.162	8.469	7.398	6.783	6.102	5.729	5.374	4.832	4.529	4.558
S1	1.37	0.857	pole-on	-0.765	15.977	27.961	15.528	12.339	9.307	8.102	7.445	6.741	6.375	5.985	5.406	5.062	5.164
S1	1.37	0.928	pole-on	-0.789	17.967	31.178	17.246	13.633	10.302	8.92	8.208	7.533	7.122	6.631	6.059	5.671	5.823
S1	1.37	1.0	pole-on	-0.806	19.653	34.745	19.06	14.978	11.309	9.792	8.961	8.299	7.89	7.281	6.705	6.25	6.516
S1	1.01	0.0	edge-on	0.277	1.221	3.215	2.274	1.994	3.139	1.463	1.33	1.186	1.121	1.016	0.819	0.81	0.813
S1	1.01	0.071	edge-on	0.193	1.437	2.786	1.996	1.729	2.431	1.272	1.136	1.044	0.97	0.886	0.714	0.696	0.691
S1	1.01	0.143	edge-on	0.076	4.093	2.567	1.874	1.593	9.552	1.022	0.925	0.731	0.74	0.649	0.511	0.46	0.456
S1	1.01	0.215	interm.	-0.051	0.308	24.353	65.201	149.974	419.396	240.774	85.372	41.539	29.832	22.875	18.312	16.394	14.361
S1	1.01	0.286	interm.	-0.169	1.315	193.793	21.198	13.531	15.254	7.395	6.508	5.96	5.173	4.853	4.363	3.901	3.66
S1	1.01	0.357	interm.	-0.273	2.359	23.994	12.492	9.409	10.106	6.198	5.588	5.17	4.681	4.319	3.979	3.566	3.359
S1	1.01	0.429	interm.	-0.363	3.636	21.137	12.184	9.565	9.683	6.382	5.832	5.337	4.932	4.511	4.227	3.77	3.572
S1	1.01	0.5	pole-on	-0.435	5.24	22.067	12.906	10.183	9.894	6.895	6.333	5.802	5.396	4.958	4.636	4.179	3.956
S1	1.01	0.571	pole-on	-0.494	7.103	24.186	14.102	11.266	10.543	7.566	6.962	6.405	5.978	5.483	5.18	4.663	4.469
S1	1.01	0.643	pole-on	-0.545	9.181	26.897	15.65	12.485	11.27	8.387	7.725	7.105	6.665	6.216	5.785	5.276	5.171
S1	1.01	0.714	pole-on	-0.587	11.34	30.176	17.383	13.917	12.223	9.356	8.582	7.908	7.524	6.95	6.459	5.942	6.034
S1	1.01	0.786	pole-on	-0.62	13.511	33.946	19.403	15.519	13.294	10.5	9.603	8.846	8.501	7.866	7.18	6.704	7.02
S1	1.01	0.857	pole-on	-0.647	15.677	38.601	21.891	17.351	14.496	11.706	10.671	9.93	9.599	8.877	8.015	7.512	8.261
S1	1.01	0.928	pole-on	-0.669	17.747	43.814	24.518	19.626	15.769	12.981	11.778	11.093	10.862	9.929	8.917	8.413	9.686
S1	1.01	1.0	pole-on	-0.683	19.516	48.695	27.39	21.806	16.998	14.16	12.849	12.236	12.109	10.93	9.795	9.245	11.125
S1	0.75	0.0	edge-on	0.214	1.337	4.101	2.699	2.309	1.908	1.666	1.53	1.383	1.72	1.164	1.024	0.933	0.905
S1	0.75	0.071	edge-on	0.156	1.546	3.566	2.376	2.037	1.697	1.487	1.374	1.225	1.133	1.045	0.912	0.833	0.795
S1	0.75	0.143	edge-on	0.071	4.218	3.445	2.248	1.946	1.527	1.345	1.258	1.089	0.997	0.887	0.782	0.707	0.633
S1	0.75	0.215	interm.	-0.023	21.076	5.588	18.905	29.11	113.856	280.209	318.189	337.261	344.856	329.168	311.936	253.2	273.522
S1	0.75	0.286	interm.	-0.121	3.789	371.885	46.003	24.051	13.451	10.945	9.278	7.996	7.152	6.749	5.695	5.121	5.317
S1	0.75	0.357	interm.	-0.206	2.13	40.286	17.027	12.512	9.164	7.897	7.029	6.351	5.995	5.535	4.941	4.55	4.704
S1	0.75	0.429	interm.	-0.283	3.239	27.996	15.585	12.197	9.297	8.147	7.423	6.72	6.293	5.872	5.281	4.922	5.064
S1	0.75	0.5	pole-on	-0.346	4.539	28.169	16.502	13.055	10.054	8.965	8.031	7.343	7.036	6.518	5.909	5.496	5.756
S1	0.75	0.571	pole-on	-0.398	5.938	30.234	18.131	14.571	11.251	9.921	8.96	8.274	7.923	7.328	6.675	6.284	6.638
S1	0.75	0.643	pole-on	-0.443	7.376	34.678	20.437	16.347	12.632	11.184	10.244	9.351	9.077	8.327	7.573	7.139	7.68

Table A.2 - continued.

Star	Σ_0 [g cm ⁻²]	cos i	$\tilde{\tau}_{bu}$ ang. type	bu		0.15	0.45	0.75	1.50	2.25	3.00	4.50	6.00	9.00	15.00	30.00	∞
				ΔV_{bu}^∞	ξ_{bu}^V	ξ_d^V											
S1	0.75	0.714	pole-on	-0.479	8.781	38.989	22.943	18.565	14.352	12.645	11.54	10.54	10.353	9.379	8.663	8.115	8.88
S1	0.75	0.786	pole-on	-0.508	10.153	44.306	26.022	21.175	16.264	14.28	13.05	11.869	11.828	10.543	9.784	9.139	10.321
S1	0.75	0.857	pole-on	-0.531	11.42	51.093	29.734	23.994	18.346	15.928	14.571	13.406	13.479	11.68	11.122	10.264	11.932
S1	0.75	0.928	pole-on	-0.548	12.654	58.104	33.636	27.524	20.404	17.732	15.947	14.872	15.264	12.862	12.526	11.387	13.761
S1	0.75	1.0	pole-on	-0.558	13.455	64.339	37.9	30.867	22.416	19.197	17.25	16.433	17.137	13.914	13.82	12.434	15.555
S1	0.56	0.0	edge-on	0.168	1.448	5.049	3.392	2.807	2.241	1.934	1.801	1.587	1.475	1.336	1.166	1.074	1.045
S1	0.56	0.071	edge-on	0.127	1.574	4.636	2.975	2.476	2.047	1.788	1.639	1.481	1.343	1.249	1.076	0.989	0.955
S1	0.56	0.143	edge-on	0.067	2.954	4.545	3.086	2.565	2.021	1.788	1.612	1.44	1.293	1.248	1.013	0.973	0.916
S1	0.56	0.215	interm.	-0.001	274.53	20.445	10.237	2.494	5.778	28.446	7.976	26.151	73.211	38.128	182.118	168.69	318.603
S1	0.56	0.286	interm.	-0.079	1.075	383.395	289.324	65.948	25.425	17.385	14.724	11.369	10.861	8.899	8.333	6.985	7.464
S1	0.56	0.357	interm.	-0.146	2.125	86.034	22.353	15.881	11.205	9.472	8.645	7.478	7.495	6.382	6.261	5.59	5.775
S1	0.56	0.429	interm.	-0.207	3.255	37.889	18.478	14.81	11.094	9.405	8.836	7.93	7.801	6.909	6.471	5.997	6.32
S1	0.56	0.5	pole-on	-0.259	4.515	35.683	19.43	15.837	12.006	10.523	9.915	8.82	8.749	7.738	7.355	6.799	7.331
S1	0.56	0.571	pole-on	-0.302	5.978	37.039	21.971	17.649	13.687	11.989	11.072	9.999	9.945	8.768	8.373	7.824	8.586
S1	0.56	0.643	pole-on	-0.339	7.729	41.26	24.895	20.054	15.582	13.677	12.726	11.385	11.501	10.099	9.628	8.915	10.037
S1	0.56	0.714	pole-on	-0.368	9.62	47.656	28.452	23.145	17.848	15.58	14.434	12.961	13.242	11.425	10.978	10.178	11.854
S1	0.56	0.786	pole-on	-0.392	11.628	54.714	32.704	26.812	20.532	17.731	16.506	14.616	15.357	12.876	12.506	11.518	13.985
S1	0.56	0.857	pole-on	-0.41	13.757	62.445	37.738	30.75	23.118	20.034	18.356	16.49	17.441	14.278	14.091	12.822	16.28
S1	0.56	0.928	pole-on	-0.422	15.999	71.541	43.121	35.285	25.841	21.893	19.934	18.425	19.926	15.667	15.891	14.204	19.013
S1	0.56	1.0	pole-on	-0.428	17.632	78.909	48.439	39.859	28.093	23.624	21.38	20.334	22.466	16.985	17.431	15.332	21.573
S1	0.41	0.0	edge-on	0.13	1.649	6.44	4.274	3.442	2.707	2.314	2.083	1.877	1.731	1.578	1.399	1.279	1.229
S1	0.41	0.071	edge-on	0.102	2.735	6.249	3.815	3.058	2.483	2.186	1.983	1.768	1.624	1.48	1.314	1.179	1.129
S1	0.41	0.143	edge-on	0.06	2.817	7.0	4.117	3.367	2.571	2.396	2.183	1.849	1.799	1.649	1.431	1.346	1.245
S1	0.41	0.215	interm.	0.011	149.565	24.593	4.546	3.665	3.786	2.522	2.626	2.072	6.533	9.096	8.673	10.053	5.361
S1	0.41	0.286	interm.	-0.045	1.4	362.898	353.755	335.245	154.378	55.241	35.387	22.913	19.432	14.82	11.265	9.655	10.924
S1	0.41	0.357	interm.	-0.095	2.084	266.384	30.626	20.579	13.134	10.575	9.154	8.543	8.205	7.028	6.59	5.915	6.739
S1	0.41	0.429	interm.	-0.14	3.072	49.409	22.049	17.001	12.397	10.641	9.745	8.854	8.677	7.691	6.9	6.598	7.319
S1	0.41	0.5	pole-on	-0.179	4.333	38.625	22.612	18.227	13.841	11.691	10.915	9.934	9.939	8.738	8.109	7.542	8.561
S1	0.41	0.571	pole-on	-0.212	5.651	41.764	25.018	20.124	15.512	13.565	12.513	11.419	11.54	10.189	9.395	8.877	10.161
S1	0.41	0.643	pole-on	-0.24	7.337	46.138	28.836	23.234	17.95	15.819	14.497	13.122	13.335	11.762	10.911	10.099	12.29
S1	0.41	0.714	pole-on	-0.262	9.056	55.028	33.633	27.206	20.807	18.329	16.794	14.948	15.775	13.46	12.555	11.731	14.627
S1	0.41	0.786	pole-on	-0.279	11.081	61.276	38.619	31.802	24.266	20.892	19.41	17.151	18.247	14.991	14.34	13.229	17.448
S1	0.41	0.857	pole-on	-0.292	13.461	71.761	44.683	36.85	27.585	23.203	21.374	19.241	21.233	16.671	16.23	14.847	20.764
S1	0.41	0.928	pole-on	-0.3	15.833	83.217	51.511	42.796	30.327	25.717	22.897	21.368	23.936	18.116	18.344	16.247	24.2
S1	0.41	1.0	pole-on	-0.302	17.488	92.261	57.278	47.959	33.244	27.31	24.507	23.434	26.94	19.379	20.06	17.618	27.455

Table A.2 - continued.

Star	Σ_0 [g cm ⁻²]	cos i	$\tilde{\tau}_{bu}$ ang. type	bu		0.15	0.45	0.75	1.50	2.25	3.00	4.50	6.00	9.00	15.00	30.00	∞
				ΔV_{bu}^∞	ξ_{bu}^V	ξ_d^V											
S1	0.3	0.0	edge-on	0.1	1.936	9.085	4.943	4.025	3.134	2.834	2.498	2.206	2.01	1.865	1.604	1.51	1.396
S1	0.3	0.071	edge-on	0.081	1.996	9.436	4.634	3.536	2.979	2.634	2.447	2.08	1.883	1.783	1.543	1.4	1.356
S1	0.3	0.143	edge-on	0.051	6.703	10.1	4.801	4.039	3.445	3.059	2.67	2.461	2.281	2.176	1.864	1.776	1.639
S1	0.3	0.215	interm.	0.015	49.051	30.672	6.287	5.351	4.925	9.582	4.035	4.836	4.095	3.563	3.308	3.099	2.543
S1	0.3	0.286	interm.	-0.022	23.392	291.483	331.434	331.024	345.051	280.35	325.328	255.225	233.685	169.548	159.107	65.214	66.312
S1	0.3	0.357	interm.	-0.058	1.905	330.425	72.23	33.506	14.405	11.447	10.273	8.829	8.876	6.82	6.459	5.752	6.978
S1	0.3	0.429	interm.	-0.09	2.982	92.594	25.331	19.548	12.272	10.391	9.688	8.971	9.128	7.513	7.054	6.504	7.852
S1	0.3	0.5	pole-on	-0.119	4.059	47.283	24.352	19.359	14.043	12.162	11.205	10.236	10.5	8.823	8.449	7.942	9.348
S1	0.3	0.571	pole-on	-0.142	5.246	45.722	27.135	22.115	16.395	14.185	12.957	11.723	12.333	10.577	9.924	9.166	11.142
S1	0.3	0.643	pole-on	-0.161	6.867	50.497	30.993	25.762	18.863	17.161	15.249	13.772	14.588	12.244	11.616	10.655	13.587
S1	0.3	0.714	pole-on	-0.177	8.518	57.053	35.669	30.168	22.572	19.609	17.511	15.877	17.155	14.08	13.701	12.547	16.381
S1	0.3	0.786	pole-on	-0.189	10.423	68.1	41.975	35.065	26.279	23.283	20.405	18.126	20.024	15.922	15.587	14.197	19.926
S1	0.3	0.857	pole-on	-0.196	12.489	78.97	48.703	40.943	30.174	25.503	22.935	20.738	23.127	17.355	17.587	15.708	23.647
S1	0.3	0.928	pole-on	-0.202	14.776	91.468	57.457	47.5	33.024	27.77	25.216	23.18	26.876	19.308	20.126	17.622	28.346
S1	0.3	1.0	pole-on	-0.201	16.328	100.854	63.168	52.547	35.603	29.669	26.208	25.382	29.634	20.219	21.455	18.659	32.012
S2	2.5	0.0	edge-on	0.491	1.068	1.95	1.512	1.397	1.178	1.055	0.979	0.871	0.812	0.738	0.646	0.583	0.566
S2	2.5	0.071	edge-on	0.31	1.411	1.646	1.285	1.187	0.977	0.855	0.793	0.694	0.647	0.581	0.504	0.45	0.429
S2	2.5	0.143	edge-on	0.066	16.148	1.603	1.132	0.926	0.634	0.473	0.4	0.3	0.273	0.225	0.208	0.207	0.209
S2	2.5	0.215	interm.	-0.144	0.471	10.801	296.749	31.832	12.019	8.961	7.349	5.941	5.165	4.7	3.796	3.73	3.433
S2	2.5	0.286	interm.	-0.306	1.43	23.954	8.599	6.159	4.427	3.815	3.451	3.013	2.74	2.524	2.156	2.076	1.976
S2	2.5	0.357	interm.	-0.438	2.595	12.495	6.747	5.276	3.876	3.37	3.075	2.679	2.502	2.328	1.999	1.891	1.811
S2	2.5	0.429	interm.	-0.545	4.04	11.887	6.702	5.22	3.908	3.379	3.101	2.758	2.542	2.351	2.054	1.925	1.859
S2	2.5	0.5	pole-on	-0.628	5.79	12.411	6.961	5.463	4.085	3.551	3.265	2.893	2.682	2.484	2.181	2.048	1.972
S2	2.5	0.571	pole-on	-0.697	7.614	13.397	7.433	5.841	4.389	3.791	3.496	3.119	2.898	2.687	2.363	2.208	2.137
S2	2.5	0.643	pole-on	-0.755	9.502	14.515	8.037	6.34	4.749	4.126	3.814	3.392	3.151	2.934	2.588	2.414	2.337
S2	2.5	0.714	pole-on	-0.803	11.439	15.996	8.785	6.923	5.213	4.508	4.172	3.728	3.479	3.227	2.841	2.649	2.564
S2	2.5	0.786	pole-on	-0.84	13.244	17.573	9.664	7.61	5.717	4.96	4.577	4.105	3.832	3.535	3.137	2.929	2.825
S2	2.5	0.857	pole-on	-0.872	14.967	19.471	10.663	8.404	6.29	5.461	5.012	4.512	4.197	3.876	3.437	3.2	3.144
S2	2.5	0.928	pole-on	-0.898	16.735	21.709	11.794	9.269	6.915	5.942	5.45	4.924	4.587	4.243	3.785	3.549	3.513
S2	2.5	1.0	pole-on	-0.916	18.154	23.936	12.927	10.111	7.515	6.429	5.902	5.348	5.031	4.624	4.18	3.917	3.898
S2	1.85	0.0	edge-on	0.39	1.12	2.297	1.799	1.583	1.338	1.159	1.899	1.418	0.925	0.828	0.718	0.65	0.636
S2	1.85	0.071	edge-on	0.261	1.386	1.926	1.541	1.36	1.121	0.971	1.259	0.976	0.74	0.675	0.594	0.525	0.513
S2	1.85	0.143	edge-on	0.081	6.369	1.794	1.43	1.186	0.839	0.655	0.541	0.457	0.397	0.343	0.287	0.239	0.233
S2	1.85	0.215	interm.	-0.094	0.381	7.409	82.173	327.703	41.561	24.369	40.595	19.877	11.885	9.505	7.688	7.105	6.591
S2	1.85	0.286	interm.	-0.238	1.347	55.645	13.374	9.192	6.467	5.383	6.7	5.345	3.889	3.594	3.147	2.944	2.814

Table A.2 - continued.

Star	Σ_0 [g cm ⁻²]	cos i	$\tilde{\tau}_{bu}$ ang. type	bu		0.15	0.45	0.75	1.50	2.25	3.00	4.50	6.00	9.00	15.00	30.00	∞
				ΔV_{bu}^∞	ξ_{bu}^V	ξ_d^V											
S2	1.85	0.357	interm.	-0.359	2.444	18.396	9.231	7.124	5.331	4.653	5.366	4.462	3.481	3.211	2.824	2.639	2.544
S2	1.85	0.429	interm.	-0.459	3.817	16.032	8.983	7.083	5.353	4.686	5.172	4.434	3.589	3.308	2.921	2.718	2.623
S2	1.85	0.5	pole-on	-0.537	5.466	16.646	9.466	7.448	5.679	4.97	5.35	4.628	3.82	3.532	3.129	2.925	2.825
S2	1.85	0.571	pole-on	-0.602	7.272	18.012	10.201	8.084	6.158	5.379	5.71	4.964	4.177	3.834	3.438	3.183	3.105
S2	1.85	0.643	pole-on	-0.656	9.182	19.716	11.168	8.88	6.741	5.918	6.191	5.426	4.578	4.227	3.777	3.515	3.471
S2	1.85	0.714	pole-on	-0.701	11.209	21.949	12.271	9.767	7.415	6.503	6.773	5.992	5.032	4.679	4.178	3.92	3.898
S2	1.85	0.786	pole-on	-0.736	13.137	24.325	13.629	10.788	8.177	7.17	7.45	6.648	5.559	5.179	4.66	4.372	4.398
S2	1.85	0.857	pole-on	-0.765	15.028	27.189	15.09	11.961	9.01	7.895	8.223	7.401	6.152	5.734	5.214	4.892	4.975
S2	1.85	0.928	pole-on	-0.788	16.854	30.509	16.774	13.237	9.938	8.708	9.08	8.261	6.865	6.38	5.836	5.46	5.623
S2	1.85	1.0	pole-on	-0.804	18.397	33.904	18.528	14.585	10.916	9.536	9.986	9.146	7.597	7.008	6.452	6.042	6.283
S2	1.37	0.0	edge-on	0.306	1.213	2.888	2.064	1.779	1.485	1.373	1.219	1.11	1.016	0.937	0.814	0.746	0.721
S2	1.37	0.071	edge-on	0.216	1.439	2.496	1.766	1.563	1.292	1.174	1.068	0.954	0.876	0.806	0.694	0.635	0.613
S2	1.37	0.143	edge-on	0.084	4.395	2.343	1.632	1.445	1.083	0.939	0.806	0.704	0.626	0.554	0.452	0.402	0.386
S2	1.37	0.215	interm.	-0.051	18.068	6.4	28.129	70.457	389.707	322.05	204.138	70.283	46.205	37.748	25.417	20.498	18.642
S2	1.37	0.286	interm.	-0.175	1.197	300.31	24.376	15.083	9.471	7.952	6.911	6.046	5.556	5.021	4.393	4.076	3.923
S2	1.37	0.357	interm.	-0.28	2.256	26.285	12.681	9.629	7.139	6.154	5.573	4.991	4.66	4.27	3.766	3.507	3.451
S2	1.37	0.429	interm.	-0.37	3.5	20.787	11.833	9.41	7.128	6.2	5.67	5.127	4.792	4.447	3.948	3.684	3.618
S2	1.37	0.5	pole-on	-0.442	5.019	21.445	12.458	10.029	7.617	6.671	6.076	5.537	5.2	4.82	4.294	4.024	4.008
S2	1.37	0.571	pole-on	-0.501	6.773	23.159	13.483	10.907	8.331	7.295	6.658	6.078	5.738	5.305	4.774	4.488	4.514
S2	1.37	0.643	pole-on	-0.551	8.707	25.88	15.037	12.048	9.198	8.075	7.387	6.729	6.414	5.936	5.381	5.044	5.138
S2	1.37	0.714	pole-on	-0.591	10.622	28.854	16.589	13.395	10.2	8.967	8.211	7.535	7.216	6.659	6.05	5.719	5.862
S2	1.37	0.786	pole-on	-0.622	12.733	32.567	18.644	14.955	11.403	10.025	9.218	8.423	8.134	7.464	6.834	6.425	6.696
S2	1.37	0.857	pole-on	-0.648	14.817	36.812	20.96	16.753	12.801	11.174	10.28	9.454	9.239	8.309	7.709	7.218	7.649
S2	1.37	0.928	pole-on	-0.668	16.743	41.983	23.658	18.959	14.31	12.435	11.367	10.602	10.411	9.229	8.646	8.064	8.741
S2	1.37	1.0	pole-on	-0.681	18.376	46.681	26.488	21.12	15.791	13.655	12.392	11.735	11.577	10.082	9.625	8.87	9.86
S2	1.01	0.0	edge-on	0.24	1.304	3.798	2.474	2.048	3.537	1.526	1.407	1.267	1.174	1.071	0.981	0.846	0.831
S2	1.01	0.071	edge-on	0.177	1.503	3.416	2.305	1.852	2.577	1.383	1.262	1.143	1.059	0.976	0.872	0.77	0.745
S2	1.01	0.143	edge-on	0.083	3.426	3.247	2.319	1.833	1.697	1.247	1.129	1.013	0.931	0.839	0.713	0.642	0.6
S2	1.01	0.215	interm.	-0.018	15.939	4.34	2.491	1.754	453.771	120.727	120.839	313.361	354.819	351.847	391.27	338.331	342.653
S2	1.01	0.286	interm.	-0.12	1.076	371.419	63.721	29.739	40.315	11.927	10.432	8.5	7.807	6.886	6.076	5.443	5.492
S2	1.01	0.357	interm.	-0.207	2.117	41.955	16.721	12.137	18.522	7.683	6.987	6.252	5.813	5.433	4.865	4.471	4.427
S2	1.01	0.429	interm.	-0.283	3.309	26.699	14.468	11.441	15.513	7.731	7.108	6.388	6.074	5.639	5.085	4.719	4.742
S2	1.01	0.5	pole-on	-0.345	4.68	26.956	15.545	12.384	15.259	8.434	7.759	7.055	6.761	6.197	5.66	5.293	5.45
S2	1.01	0.571	pole-on	-0.397	6.312	28.912	17.006	13.788	16.059	9.347	8.652	7.849	7.598	6.985	6.373	6.033	6.239
S2	1.01	0.643	pole-on	-0.441	8.092	32.281	19.235	15.549	17.452	10.655	9.773	8.856	8.634	7.88	7.244	6.845	7.245

Table A.2 - continued.

Star	Σ_0 [g cm ⁻²]	cos i	$\tilde{\tau}_{bu}$ ang. type	bu		0.15	0.45	0.75	1.50	2.25	3.00	4.50	6.00	9.00	15.00	30.00	∞
				ΔV_{bu}^∞	ξ_{bu}^V	ξ_d^V											
S2	1.01	0.714	pole-on	-0.476	10.036	36.726	21.777	17.459	19.41	12.004	11.036	10.003	9.862	8.899	8.218	7.739	8.51
S2	1.01	0.786	pole-on	-0.503	12.111	42.375	25.006	19.962	21.902	13.498	12.474	11.253	11.274	10.015	9.262	8.764	10.009
S2	1.01	0.857	pole-on	-0.524	14.185	48.305	28.332	22.908	24.994	15.16	13.879	12.738	12.857	11.105	10.376	9.835	11.642
S2	1.01	0.928	pole-on	-0.54	16.387	55.129	32.548	26.204	28.196	16.776	15.309	14.255	14.707	12.27	11.607	10.936	13.679
S2	1.01	1.0	pole-on	-0.549	17.988	61.609	36.436	29.331	31.395	18.344	16.6	15.811	16.514	13.41	12.758	12.004	15.593
S2	0.75	0.0	edge-on	0.188	1.475	4.719	3.068	2.527	2.009	1.764	1.609	1.434	1.335	1.222	1.06	0.971	0.946
S2	0.75	0.071	edge-on	0.145	1.643	4.272	2.817	2.384	1.886	1.66	1.526	1.356	1.271	1.153	0.998	0.905	0.885
S2	0.75	0.143	edge-on	0.077	3.524	4.093	2.963	2.448	1.956	1.689	1.6	1.369	1.262	1.162	1.026	0.919	0.871
S2	0.75	0.215	interm.	0.005	336.352	7.907	2.756	2.229	1.52	5.069	3.137	5.304	22.756	22.214	19.381	43.606	79.95
S2	0.75	0.286	interm.	-0.076	0.911	360.73	380.807	133.713	30.347	21.307	16.602	12.782	11.627	9.813	8.065	7.193	7.681
S2	0.75	0.357	interm.	-0.146	1.92	106.683	22.127	15.675	10.69	9.169	8.144	7.271	6.952	6.113	5.629	5.175	5.582
S2	0.75	0.429	interm.	-0.207	3.062	34.684	17.588	13.851	10.118	8.972	8.4	7.379	7.257	6.497	5.919	5.572	6.026
S2	0.75	0.5	pole-on	-0.258	4.209	31.707	18.142	14.664	11.239	9.802	9.055	8.294	8.105	7.322	6.826	6.322	6.863
S2	0.75	0.571	pole-on	-0.301	5.56	34.468	20.188	16.555	12.629	11.186	10.363	9.354	9.297	8.373	7.734	7.262	8.028
S2	0.75	0.643	pole-on	-0.337	6.991	38.566	22.962	18.828	14.42	12.811	11.862	10.637	10.782	9.505	8.885	8.312	9.44
S2	0.75	0.714	pole-on	-0.365	8.476	43.447	26.419	21.764	16.694	14.765	13.548	12.116	12.444	10.843	10.232	9.548	11.126
S2	0.75	0.786	pole-on	-0.387	9.962	50.305	30.65	24.973	19.28	16.831	15.41	13.882	14.364	12.199	11.594	10.757	13.082
S2	0.75	0.857	pole-on	-0.404	11.385	58.831	35.411	28.925	21.565	18.939	17.149	15.606	16.435	13.479	13.252	12.11	15.297
S2	0.75	0.928	pole-on	-0.415	12.799	66.737	40.793	33.686	24.281	20.955	18.804	17.544	18.935	14.849	14.869	13.396	17.881
S2	0.75	1.0	pole-on	-0.42	13.822	74.687	45.528	37.618	26.695	22.653	20.292	19.308	21.404	16.074	16.4	14.626	20.385
S2	0.56	0.0	edge-on	0.149	1.686	6.276	3.666	3.005	2.383	2.08	1.89	1.678	1.535	1.423	1.231	1.104	1.079
S2	0.56	0.071	edge-on	0.119	1.814	5.289	3.424	2.855	2.265	2.008	1.829	1.604	1.492	1.354	1.171	1.084	1.053
S2	0.56	0.143	edge-on	0.071	3.1	5.646	3.817	3.165	2.523	2.272	2.082	1.829	1.686	1.559	1.372	1.265	1.237
S2	0.56	0.215	interm.	0.016	96.7	6.807	4.295	4.077	2.776	2.53	3.373	2.275	2.011	1.914	3.416	1.671	2.679
S2	0.56	0.286	interm.	-0.044	0.854	294.461	358.954	349.209	234.876	124.04	58.212	22.779	22.118	13.555	12.199	9.6	11.248
S2	0.56	0.357	interm.	-0.096	1.834	276.853	28.206	18.612	11.734	10.098	8.615	7.444	7.434	6.243	5.737	5.374	5.806
S2	0.56	0.429	interm.	-0.144	2.989	40.893	19.31	15.547	11.21	9.516	8.623	7.762	7.864	6.743	6.317	5.917	6.502
S2	0.56	0.5	pole-on	-0.183	4.195	36.276	20.238	16.843	12.157	10.494	9.794	8.99	8.878	7.64	7.328	6.908	7.704
S2	0.56	0.571	pole-on	-0.217	5.581	38.007	22.14	18.401	14.021	12.236	11.439	10.234	10.316	9.033	8.531	7.948	9.153
S2	0.56	0.643	pole-on	-0.244	7.255	42.508	26.094	21.462	16.262	14.216	13.117	11.831	12.129	10.425	9.88	9.285	10.958
S2	0.56	0.714	pole-on	-0.265	9.073	48.724	29.948	24.825	19.046	16.428	15.136	13.574	14.105	11.892	11.525	10.624	13.17
S2	0.56	0.786	pole-on	-0.282	11.105	56.865	35.139	29.018	22.024	18.904	17.529	15.597	16.48	13.638	13.122	12.035	15.641
S2	0.56	0.857	pole-on	-0.294	13.326	64.931	40.622	33.786	24.823	21.416	19.497	17.408	19.176	14.997	15.061	13.523	18.541
S2	0.56	0.928	pole-on	-0.302	15.445	75.752	47.371	38.849	27.468	23.444	21.241	19.686	22.299	16.427	16.805	15.097	21.976
S2	0.56	1.0	pole-on	-0.304	17.164	84.639	52.681	44.164	30.159	25.278	22.968	21.495	24.875	17.673	18.6	16.22	25.0

Table A.2 - continued.

Star	Σ_0 [g cm ⁻²]	cos i	$\tilde{\tau}_{bu}$ ang. type	bu		0.15	0.45	0.75	1.50	2.25	3.00	4.50	6.00	9.00	15.00	30.00	∞
				ΔV_{bu}^∞	ξ_{bu}^V	ξ_d^V											
S2	0.41	0.0	edge-on	0.116	1.896	7.522	4.512	3.675	2.736	2.469	2.177	2.002	1.753	1.603	1.401	1.266	1.237
S2	0.41	0.071	edge-on	0.096	1.999	6.776	4.302	3.454	2.689	2.364	2.201	1.982	1.736	1.59	1.362	1.27	1.231
S2	0.41	0.143	edge-on	0.062	3.085	7.187	4.667	3.908	3.182	2.818	2.625	2.363	2.094	1.98	1.762	1.599	1.566
S2	0.41	0.215	interm.	0.021	37.804	10.442	6.215	4.929	4.314	4.323	3.883	3.944	3.167	3.175	3.062	2.888	2.575
S2	0.41	0.286	interm.	-0.02	21.593	268.917	239.523	324.944	324.551	322.077	317.659	259.741	260.622	189.349	185.505	94.257	152.022
S2	0.41	0.357	interm.	-0.059	4.249	302.072	82.821	26.328	11.901	8.77	7.702	6.549	7.074	5.593	5.272	4.485	5.875
S2	0.41	0.429	interm.	-0.093	2.755	65.286	20.213	15.257	11.099	8.784	8.143	7.386	7.585	6.575	5.925	5.404	6.55
S2	0.41	0.5	pole-on	-0.122	3.959	36.693	20.287	16.163	12.379	10.609	9.689	8.772	8.959	7.673	7.2	6.56	7.892
S2	0.41	0.571	pole-on	-0.146	5.347	39.121	23.133	18.927	14.502	12.223	11.52	10.359	10.603	9.066	8.641	8.037	9.708
S2	0.41	0.643	pole-on	-0.166	6.811	44.023	27.695	22.289	16.931	14.43	13.5	12.181	12.786	10.847	10.167	9.468	11.764
S2	0.41	0.714	pole-on	-0.181	8.635	51.723	31.547	26.554	19.881	17.152	15.927	14.071	14.983	12.566	11.864	11.004	14.285
S2	0.41	0.786	pole-on	-0.192	10.663	59.942	38.119	31.186	23.14	19.912	18.493	16.073	17.768	14.05	13.69	12.397	17.077
S2	0.41	0.857	pole-on	-0.2	12.868	69.134	44.123	36.675	26.337	22.457	20.526	18.136	20.525	15.633	15.747	13.863	20.656
S2	0.41	0.928	pole-on	-0.205	15.073	81.691	50.583	42.513	29.982	24.507	22.434	20.337	24.046	17.061	17.849	15.395	24.288
S2	0.41	1.0	pole-on	-0.205	17.021	90.056	56.384	48.238	32.262	26.583	24.145	22.732	26.92	18.477	19.852	16.797	28.544
S2	0.3	0.0	edge-on	0.091	2.117	9.949	5.242	4.385	3.203	2.818	2.668	2.201	2.022	1.806	1.609	1.484	1.403
S2	0.3	0.071	edge-on	0.075	2.264	8.803	5.314	4.056	3.231	2.727	2.484	2.174	2.039	1.82	1.7	1.491	1.431
S2	0.3	0.143	edge-on	0.051	3.426	12.037	6.329	4.894	3.863	3.751	3.329	2.736	2.758	2.474	2.175	2.051	1.989
S2	0.3	0.215	interm.	0.022	27.543	35.64	9.342	7.595	6.311	6.958	6.545	5.195	4.698	4.581	4.67	4.16	4.247
S2	0.3	0.286	interm.	-0.002	253.213	237.789	262.702	230.98	251.482	286.709	323.315	309.025	315.638	311.241	309.117	302.371	290.763
S2	0.3	0.357	interm.	-0.033	3.904	289.436	253.746	106.557	32.994	12.027	6.712	6.082	7.019	4.564	4.09	3.624	4.194
S2	0.3	0.429	interm.	-0.058	2.657	195.814	19.712	14.194	9.435	7.712	6.974	6.526	6.848	5.576	5.187	4.753	5.454
S2	0.3	0.5	pole-on	-0.078	3.844	54.268	19.034	16.026	10.856	9.394	8.691	8.122	8.487	7.225	6.558	6.049	7.244
S2	0.3	0.571	pole-on	-0.095	5.146	39.503	21.97	17.902	13.055	11.565	10.905	9.718	10.275	8.543	8.09	7.453	9.13
S2	0.3	0.643	pole-on	-0.109	6.8	45.633	25.308	21.711	16.247	14.09	12.83	11.773	12.162	10.447	9.756	8.852	11.229
S2	0.3	0.714	pole-on	-0.119	8.487	53.309	31.471	25.876	19.397	16.861	15.506	13.741	14.95	11.921	11.581	10.642	13.97
S2	0.3	0.786	pole-on	-0.127	10.504	61.341	37.133	30.87	23.55	19.832	18.205	15.841	17.561	13.857	13.587	12.104	17.44
S2	0.3	0.857	pole-on	-0.132	12.785	71.414	44.02	37.424	26.206	22.653	20.499	17.785	21.317	15.448	15.321	13.51	20.783
S2	0.3	0.928	pole-on	-0.134	15.35	81.429	52.192	42.396	29.76	24.381	21.825	20.274	24.853	16.914	17.585	15.109	25.3
S2	0.3	1.0	pole-on	-0.133	17.102	92.391	57.563	48.408	32.661	26.716	24.041	22.697	27.633	17.77	19.671	16.382	28.901
S3	2.5	0.0	edge-on	0.444	1.153	2.216	1.62	1.426	1.195	1.08	1.0	0.898	0.84	0.77	0.672	0.61	0.59
S3	2.5	0.071	edge-on	0.302	1.478	1.951	1.436	1.264	1.025	0.942	0.873	0.762	0.722	0.651	0.557	0.505	0.484
S3	2.5	0.143	edge-on	0.094	8.908	2.075	1.395	1.158	0.769	0.679	0.593	0.458	0.435	0.344	0.28	0.236	0.225
S3	2.5	0.215	interm.	-0.095	0.301	1.993	17.955	363.272	54.149	24.363	17.5	13.647	10.592	9.513	7.373	6.569	6.082
S3	2.5	0.286	interm.	-0.247	1.19	52.831	12.116	8.319	5.898	4.789	4.232	3.908	3.467	3.207	2.8	2.577	2.479

Table A.2 - continued.

Star	Σ_0 [g cm ⁻²]	cos i	$\tilde{\tau}_{bu}$ ang. type	bu		0.15	0.45	0.75	1.50	2.25	3.00	4.50	6.00	9.00	15.00	30.00	∞
				ΔV_{bu}^∞	ξ_{bu}^V	ξ_d^V											
S3	2.5	0.357	interm.	-0.371	2.283	15.031	8.191	6.317	4.806	4.069	3.679	3.377	3.032	2.821	2.471	2.289	2.2
S3	2.5	0.429	interm.	-0.474	3.627	13.415	7.925	6.211	4.767	4.075	3.711	3.375	3.098	2.87	2.529	2.324	2.249
S3	2.5	0.5	pole-on	-0.553	5.258	14.299	8.263	6.518	5.003	4.306	3.928	3.582	3.261	3.049	2.683	2.482	2.408
S3	2.5	0.571	pole-on	-0.617	7.079	15.48	8.914	7.006	5.387	4.642	4.243	3.879	3.575	3.318	2.914	2.702	2.626
S3	2.5	0.643	pole-on	-0.672	8.985	16.947	9.69	7.654	5.894	5.074	4.654	4.232	3.917	3.64	3.196	2.985	2.92
S3	2.5	0.714	pole-on	-0.717	10.911	18.793	10.674	8.399	6.447	5.591	5.123	4.654	4.308	3.993	3.545	3.298	3.25
S3	2.5	0.786	pole-on	-0.752	12.836	20.893	11.817	9.28	7.101	6.161	5.622	5.117	4.748	4.413	3.939	3.683	3.664
S3	2.5	0.857	pole-on	-0.781	14.71	23.394	13.13	10.308	7.801	6.735	6.173	5.618	5.268	4.899	4.391	4.125	4.131
S3	2.5	0.928	pole-on	-0.804	16.529	26.355	14.561	11.373	8.564	7.415	6.792	6.246	5.894	5.455	4.92	4.614	4.67
S3	2.5	1.0	pole-on	-0.821	17.935	29.282	16.005	12.452	9.419	8.142	7.471	6.896	6.541	6.01	5.474	5.136	5.222
S3	1.85	0.0	edge-on	0.351	1.268	2.73	1.876	1.633	1.574	1.208	1.121	1.551	0.995	0.869	0.746	0.677	0.657
S3	1.85	0.071	edge-on	0.254	1.522	2.465	1.686	1.482	1.231	1.096	1.027	1.152	0.868	0.785	0.666	0.607	0.584
S3	1.85	0.143	edge-on	0.102	5.195	2.603	1.688	1.431	1.096	0.907	0.839	0.691	0.599	0.549	0.464	0.392	0.385
S3	1.85	0.215	interm.	-0.048	0.263	2.551	1.19	12.635	349.911	346.199	285.015	157.802	233.58	35.652	24.057	19.565	17.572
S3	1.85	0.286	interm.	-0.182	1.025	321.375	20.003	12.834	8.385	6.731	6.222	6.81	4.675	4.284	3.796	3.456	3.358
S3	1.85	0.357	interm.	-0.293	2.093	19.991	10.545	8.203	6.195	5.33	4.891	5.281	3.938	3.658	3.245	2.98	2.918
S3	1.85	0.429	interm.	-0.386	3.389	17.155	10.142	8.112	6.226	5.391	4.971	5.16	4.095	3.81	3.375	3.114	3.066
S3	1.85	0.5	pole-on	-0.459	4.948	17.963	10.736	8.581	6.65	5.763	5.328	5.471	4.403	4.102	3.655	3.407	3.359
S3	1.85	0.571	pole-on	-0.519	6.73	19.793	11.707	9.35	7.199	6.293	5.835	5.934	4.864	4.549	4.054	3.782	3.758
S3	1.85	0.643	pole-on	-0.57	8.629	21.995	12.884	10.345	7.986	6.976	6.474	6.515	5.413	5.063	4.542	4.258	4.283
S3	1.85	0.714	pole-on	-0.611	10.646	24.665	14.294	11.451	8.839	7.747	7.209	7.233	6.036	5.666	5.124	4.812	4.898
S3	1.85	0.786	pole-on	-0.643	12.736	27.859	15.932	12.719	9.798	8.69	8.036	8.017	6.747	6.343	5.794	5.43	5.565
S3	1.85	0.857	pole-on	-0.67	14.776	31.561	17.964	14.253	10.941	9.669	8.983	8.977	7.612	7.11	6.534	6.117	6.36
S3	1.85	0.928	pole-on	-0.69	16.731	35.82	20.183	16.098	12.264	10.815	9.985	10.024	8.468	7.899	7.386	6.869	7.254
S3	1.85	1.0	pole-on	-0.705	18.351	40.04	22.595	18.025	13.573	11.879	10.915	11.109	9.411	8.692	8.19	7.615	8.224
S3	1.37	0.0	edge-on	0.277	1.403	3.162	2.265	1.899	1.541	1.382	1.267	1.135	1.043	0.97	0.836	0.766	0.757
S3	1.37	0.071	edge-on	0.208	1.608	2.968	2.113	1.797	1.457	1.298	1.191	1.076	0.974	0.924	0.785	0.723	0.701
S3	1.37	0.143	edge-on	0.099	4.03	3.061	2.216	1.866	1.404	1.231	1.126	0.991	0.872	0.828	0.686	0.629	0.601
S3	1.37	0.215	interm.	-0.013	27.074	3.112	2.066	1.435	21.489	12.787	71.901	124.609	271.485	330.026	364.861	351.673	336.885
S3	1.37	0.286	interm.	-0.127	0.902	405.536	53.22	22.724	12.135	9.857	8.4	6.862	6.561	5.615	5.155	4.611	4.505
S3	1.37	0.357	interm.	-0.221	1.944	33.399	13.449	10.247	7.553	6.554	5.901	5.344	5.068	4.536	4.146	3.791	3.848
S3	1.37	0.429	interm.	-0.302	3.147	22.111	12.511	9.991	7.632	6.691	6.09	5.495	5.27	4.739	4.358	4.048	4.106
S3	1.37	0.5	pole-on	-0.368	4.617	22.742	13.302	10.694	8.259	7.184	6.705	6.077	5.776	5.284	4.841	4.532	4.639
S3	1.37	0.571	pole-on	-0.421	6.315	24.75	14.733	11.863	9.188	8.041	7.436	6.766	6.533	5.939	5.466	5.103	5.321
S3	1.37	0.643	pole-on	-0.466	8.132	28.027	16.507	13.312	10.384	9.066	8.4	7.638	7.379	6.714	6.237	5.836	6.152

Table A.2 - continued.

Star	Σ_0 [g cm ⁻²]	cos i	$\tilde{\tau}_{bu}$ ang. type	bu		0.15	0.45	0.75	1.50	2.25	3.00	4.50	6.00	9.00	15.00	30.00	∞
				ΔV_{bu}^∞	ξ_{bu}^V	ξ_d^V											
S3	1.37	0.714	pole-on	-0.503	10.144	32.099	18.713	15.128	11.73	10.299	9.504	8.673	8.409	7.644	7.093	6.639	7.117
S3	1.37	0.786	pole-on	-0.531	12.259	36.778	21.292	17.203	13.249	11.634	10.719	9.821	9.639	8.594	8.058	7.538	8.196
S3	1.37	0.857	pole-on	-0.554	14.39	42.092	24.304	19.669	14.953	13.093	12.097	11.057	11.035	9.65	9.145	8.484	9.515
S3	1.37	0.928	pole-on	-0.571	16.474	48.14	27.812	22.419	16.947	14.58	13.313	12.442	12.615	10.718	10.342	9.488	10.995
S3	1.37	1.0	pole-on	-0.582	18.145	54.206	31.401	25.388	18.699	15.981	14.603	13.894	14.151	11.717	11.566	10.452	12.501
S3	1.01	0.0	edge-on	0.218	1.576	4.418	2.614	2.265	1.802	1.609	1.463	1.318	1.209	1.049	0.806	0.824	0.866
S3	1.01	0.071	edge-on	0.171	1.758	4.057	2.499	2.162	1.724	1.529	1.436	1.27	1.18	1.032	0.792	0.806	0.84
S3	1.01	0.143	edge-on	0.093	3.648	4.435	2.821	2.376	1.857	1.629	1.516	1.346	1.266	1.112	0.845	0.847	0.867
S3	1.01	0.215	interm.	0.012	368.035	5.059	3.065	2.411	1.808	1.482	1.293	2.427	1.067	2.74	54.434	3.144	32.643
S3	1.01	0.286	interm.	-0.079	0.763	365.893	355.31	138.749	27.084	15.916	12.267	9.454	8.569	7.593	7.002	5.785	5.186
S3	1.01	0.357	interm.	-0.155	1.794	60.869	17.66	12.351	8.776	7.521	6.872	6.038	5.735	5.357	5.256	4.458	4.142
S3	1.01	0.429	interm.	-0.222	2.991	25.998	15.118	11.691	8.718	7.705	7.131	6.402	6.165	5.735	5.557	4.876	4.568
S3	1.01	0.5	pole-on	-0.277	4.314	26.223	15.958	12.572	9.672	8.6	7.922	7.18	7.001	6.505	6.204	5.619	5.299
S3	1.01	0.571	pole-on	-0.322	5.9	28.863	17.821	14.218	10.868	9.793	9.067	8.188	8.071	7.437	7.106	6.488	6.239
S3	1.01	0.643	pole-on	-0.36	7.722	32.97	20.694	16.536	12.39	11.223	10.366	9.473	9.37	8.558	8.169	7.537	7.467
S3	1.01	0.714	pole-on	-0.391	9.659	38.52	23.468	18.785	14.172	12.987	11.868	10.743	10.828	9.767	9.27	8.706	9.034
S3	1.01	0.786	pole-on	-0.414	11.833	44.117	27.324	21.8	16.209	14.702	13.613	12.253	12.576	11.02	10.519	9.976	11.108
S3	1.01	0.857	pole-on	-0.432	14.002	51.365	31.783	25.114	18.481	16.653	15.23	13.825	14.418	12.285	11.795	11.226	13.67
S3	1.01	0.928	pole-on	-0.445	16.22	59.757	36.474	29.143	20.893	18.58	16.8	15.692	16.651	13.584	13.126	12.577	16.906
S3	1.01	1.0	pole-on	-0.452	17.888	67.128	41.234	33.068	23.281	20.175	18.139	17.356	18.705	14.675	14.355	13.873	19.944
S3	0.75	0.0	edge-on	0.173	2.556	5.438	3.358	2.718	2.097	1.83	1.677	1.481	1.363	1.238	1.073	0.986	0.947
S3	0.75	0.071	edge-on	0.139	13.39	4.981	3.121	2.628	2.1	1.822	1.636	1.466	1.357	1.23	1.083	0.985	0.951
S3	0.75	0.143	edge-on	0.084	3.864	5.301	3.713	3.011	2.454	2.122	1.914	1.727	1.622	1.516	1.268	1.169	1.136
S3	0.75	0.215	interm.	0.023	300.67	6.624	4.416	3.857	3.033	2.821	2.494	2.3	2.017	2.136	1.784	1.608	1.525
S3	0.75	0.286	interm.	-0.045	23.252	139.143	321.736	315.791	244.091	88.21	30.455	15.025	12.459	7.941	7.003	5.882	6.743
S3	0.75	0.357	interm.	-0.104	1.666	244.644	20.397	13.682	9.019	7.691	6.818	6.316	5.777	5.054	4.835	4.301	4.809
S3	0.75	0.429	interm.	-0.157	2.787	32.002	15.727	12.859	9.372	8.14	7.384	6.709	6.601	5.77	5.504	4.999	5.582
S3	0.75	0.5	pole-on	-0.201	3.992	29.357	17.281	13.685	10.782	9.371	8.637	7.769	7.781	6.805	6.399	6.01	6.64
S3	0.75	0.571	pole-on	-0.238	5.261	32.846	19.224	16.054	12.333	10.921	10.021	9.103	9.048	8.047	7.514	7.055	7.977
S3	0.75	0.643	pole-on	-0.268	6.709	37.497	22.645	18.535	14.254	12.635	11.68	10.465	10.666	9.34	8.85	8.251	9.613
S3	0.75	0.714	pole-on	-0.292	8.188	43.906	26.726	21.693	16.818	14.835	13.518	12.147	12.54	10.766	10.301	9.541	11.554
S3	0.75	0.786	pole-on	-0.31	9.851	50.87	31.1	25.726	19.521	17.013	15.469	13.945	14.666	12.286	11.878	10.883	13.768
S3	0.75	0.857	pole-on	-0.323	11.326	58.962	36.305	30.156	22.229	19.418	17.455	15.84	17.023	13.586	13.498	12.187	16.328
S3	0.75	0.928	pole-on	-0.332	12.817	68.713	42.653	34.944	25.119	21.332	19.245	17.886	19.77	14.947	15.411	13.651	19.373
S3	0.75	1.0	pole-on	-0.335	13.793	76.675	47.536	39.373	27.598	23.178	20.904	19.86	22.407	16.233	17.076	14.882	22.104

Table A.2 - continued.

Star	Σ_0 [g cm ⁻²]	cos i	$\tilde{\tau}_{bu}$ ang. type	bu		0.15	0.45	0.75	1.50	2.25	3.00	4.50	6.00	9.00	15.00	30.00	∞
				ΔV_{bu}^∞	ξ_{bu}^V	ξ_d^V											
S3	0.56	0.0	edge-on	0.14	2.051	6.695	4.028	3.188	2.415	2.07	1.916	1.686	1.55	1.402	1.203	1.099	1.053
S3	0.56	0.071	edge-on	0.114	2.291	6.086	3.904	3.119	2.431	2.051	1.884	1.688	1.522	1.385	1.2	1.09	1.056
S3	0.56	0.143	edge-on	0.073	3.755	6.43	4.446	3.769	2.825	2.593	2.347	2.121	1.915	1.787	1.555	1.427	1.412
S3	0.56	0.215	interm.	0.028	21.886	12.265	5.962	5.161	4.335	3.897	3.732	3.592	3.465	3.281	2.901	2.729	2.655
S3	0.56	0.286	interm.	-0.02	1.123	132.367	208.905	284.623	338.139	281.278	301.255	224.137	183.059	70.93	43.61	13.014	18.173
S3	0.56	0.357	interm.	-0.067	14.537	325.208	25.652	14.935	8.075	6.663	5.807	5.252	5.196	4.32	4.145	3.826	4.015
S3	0.56	0.429	interm.	-0.107	2.579	35.327	15.558	12.131	9.181	7.768	7.131	6.371	6.421	5.494	5.109	4.833	5.431
S3	0.56	0.5	pole-on	-0.14	3.861	30.681	17.209	14.045	10.498	9.175	8.543	7.621	7.742	6.764	6.204	5.874	6.83
S3	0.56	0.571	pole-on	-0.167	5.384	32.45	19.976	16.369	12.557	10.948	10.137	9.17	9.299	8.108	7.644	7.156	8.397
S3	0.56	0.643	pole-on	-0.19	6.977	38.387	24.01	19.718	14.982	13.013	12.093	10.948	11.227	9.592	9.136	8.448	10.245
S3	0.56	0.714	pole-on	-0.207	8.867	45.73	27.923	23.441	17.887	15.346	14.23	12.569	13.265	11.324	10.654	9.964	12.467
S3	0.56	0.786	pole-on	-0.221	10.941	53.329	33.007	27.994	21.094	18.177	16.476	14.659	16.07	12.738	12.35	11.424	15.104
S3	0.56	0.857	pole-on	-0.23	13.264	61.922	38.905	32.791	23.854	20.522	18.744	16.608	18.799	14.345	14.357	12.864	18.351
S3	0.56	0.928	pole-on	-0.235	15.691	73.506	46.107	38.21	26.823	22.43	20.127	19.059	21.809	15.626	16.576	14.302	21.879
S3	0.56	1.0	pole-on	-0.236	17.098	81.331	52.288	43.666	29.813	24.434	21.819	21.025	24.893	16.898	18.064	15.663	25.292
S3	0.41	0.0	edge-on	0.11	2.307	8.402	4.724	3.502	2.811	2.381	2.149	1.908	1.717	1.587	1.393	1.255	1.181
S3	0.41	0.071	edge-on	0.091	2.581	8.5	4.467	3.626	2.803	2.397	2.197	1.928	1.723	1.59	1.364	1.335	1.19
S3	0.41	0.143	edge-on	0.061	4.076	9.511	5.0	4.161	3.485	2.973	2.774	2.489	2.353	2.204	1.888	1.783	1.663
S3	0.41	0.215	interm.	0.028	16.843	15.085	8.089	6.132	5.852	4.982	5.451	4.914	4.324	4.763	4.29	4.11	3.858
S3	0.41	0.286	interm.	-0.003	165.259	163.355	128.627	242.953	279.614	315.214	305.845	317.557	317.957	286.987	292.766	266.256	272.771
S3	0.41	0.357	interm.	-0.039	1.251	316.693	208.97	40.881	11.084	6.14	5.084	4.59	3.886	3.443	2.812	2.865	3.281
S3	0.41	0.429	interm.	-0.068	2.415	121.595	14.802	12.246	8.208	7.01	6.21	5.672	5.33	4.748	4.449	4.031	4.658
S3	0.41	0.5	pole-on	-0.092	3.621	29.185	16.456	13.794	10.021	8.564	7.475	7.37	7.256	6.181	5.708	5.19	6.238
S3	0.41	0.571	pole-on	-0.111	5.155	32.787	20.024	17.018	12.244	10.504	9.427	8.651	8.954	7.554	7.205	6.666	7.947
S3	0.41	0.643	pole-on	-0.128	6.744	37.29	24.2	19.609	14.946	12.735	11.718	10.591	11.148	9.402	8.779	8.22	9.941
S3	0.41	0.714	pole-on	-0.14	8.523	44.255	27.631	23.75	17.846	15.182	14.067	12.313	13.34	10.744	10.568	9.738	12.595
S3	0.41	0.786	pole-on	-0.149	10.889	54.078	34.564	28.505	21.059	17.896	16.621	14.292	16.042	12.706	12.318	11.005	15.46
S3	0.41	0.857	pole-on	-0.155	13.142	61.87	40.27	33.843	24.676	20.581	18.863	16.441	18.88	14.143	14.338	12.47	19.055
S3	0.41	0.928	pole-on	-0.158	15.791	73.549	48.385	39.504	27.946	23.108	20.361	19.169	22.539	15.413	16.342	14.131	22.916
S3	0.41	1.0	pole-on	-0.157	17.771	84.497	54.619	45.637	29.64	24.655	22.602	20.852	25.033	16.86	18.137	15.468	26.368
S3	0.3	0.0	edge-on	0.086	2.521	10.8	5.439	4.289	3.21	2.821	2.452	2.204	1.92	1.811	1.556	1.445	1.345
S3	0.3	0.071	edge-on	0.073	7.165	10.862	5.372	4.291	3.083	2.724	2.484	2.17	1.951	1.816	1.574	1.438	1.376
S3	0.3	0.143	edge-on	0.05	6.508	13.379	6.101	5.22	4.057	3.692	3.482	3.043	2.661	2.578	2.102	2.103	1.976
S3	0.3	0.215	interm.	0.025	25.24	24.912	12.875	9.155	7.614	6.928	6.98	7.046	5.691	6.423	6.354	5.409	4.817
S3	0.3	0.286	interm.	0.004	305.739	243.11	214.845	207.806	263.286	259.612	295.337	276.393	293.276	298.49	347.519	319.183	302.918

Table A.2 - continued.

Star	Σ_0 [g cm ⁻²]	$\cos i$	$\tilde{\tau}_{bu}$ ang. type	bu		0.15	0.45	0.75	1.50	2.25	3.00	4.50	6.00	9.00	15.00	30.00	∞
				ΔV_{bu}^∞	ξ_{bu}^V	ξ_d^V											
S3	0.3	0.357	interm.	-0.022	2.038	287.759	279.586	187.871	91.745	35.998	13.321	22.24	5.453	4.366	3.98	3.111	2.942
S3	0.3	0.429	interm.	-0.042	7.086	221.119	25.216	11.154	8.325	6.259	5.886	4.82	5.048	4.057	3.884	3.473	3.753
S3	0.3	0.5	pole-on	-0.06	3.525	65.868	16.802	11.967	8.927	7.957	7.169	6.136	6.572	5.471	5.234	4.784	5.633
S3	0.3	0.571	pole-on	-0.073	5.035	34.597	19.538	15.025	11.271	9.958	8.932	8.138	8.293	6.831	6.767	6.052	7.316
S3	0.3	0.643	pole-on	-0.084	6.787	36.945	23.551	18.826	13.68	12.122	10.846	9.519	10.393	8.487	8.209	7.622	9.1
S3	0.3	0.714	pole-on	-0.092	8.636	43.626	27.443	22.363	16.717	14.751	13.157	11.816	12.639	10.315	9.863	8.922	12.157
S3	0.3	0.786	pole-on	-0.099	10.605	52.726	33.155	27.676	20.166	17.492	15.517	13.556	15.333	11.625	11.969	10.618	14.494
S3	0.3	0.857	pole-on	-0.102	13.583	68.489	40.698	33.467	23.345	19.788	17.628	15.847	18.444	12.777	13.564	11.88	18.513
S3	0.3	0.928	pole-on	-0.104	15.989	77.767	47.803	39.676	27.285	22.232	19.516	18.357	21.986	14.389	15.775	13.365	22.467
S3	0.3	1.0	pole-on	-0.103	17.978	84.642	54.665	44.383	29.413	24.037	21.045	20.382	24.704	16.015	17.795	14.361	26.463

Table A.3 - Empirical law parameters for band R .

Star	Σ_0 [g cm $^{-2}$]	$\cos i$	$\tilde{\tau}_{bu}$ ang. type	bu		0.15	0.45	0.75	1.50	2.25	3.00	4.50	6.00	9.00	15.00	30.00	∞
				ΔR_{bu}^∞	ξ_{bu}^R	ξ_d^R											
S1	2.5	0.0	edge-on	0.555	1.039	1.697	1.412	1.327	1.091	0.989	0.924	0.832	0.768	0.693	0.599	0.541	0.528
S1	2.5	0.071	edge-on	0.258	1.392	1.203	1.028	0.982	0.791	0.703	0.64	0.577	0.521	0.466	0.4	0.353	0.34
S1	2.5	0.143	interm.	-0.115	0.31	2.224	123.391	206.692	11.032	6.508	5.421	3.892	3.449	3.056	2.593	2.141	2.17
S1	2.5	0.215	interm.	-0.372	1.268	11.275	4.649	3.37	2.502	2.088	1.846	1.557	1.44	1.296	1.115	0.957	0.959
S1	2.5	0.286	interm.	-0.565	2.251	6.222	3.723	2.899	2.182	1.846	1.655	1.403	1.295	1.173	1.009	0.876	0.873
S1	2.5	0.357	interm.	-0.715	3.425	6.127	3.671	2.875	2.158	1.836	1.645	1.4	1.298	1.178	1.017	0.886	0.88
S1	2.5	0.429	pole-on	-0.834	4.848	6.51	3.786	2.928	2.213	1.882	1.694	1.453	1.344	1.219	1.055	0.926	0.924
S1	2.5	0.5	pole-on	-0.925	6.436	6.961	3.954	3.077	2.306	1.97	1.77	1.528	1.414	1.284	1.113	0.983	0.982
S1	2.5	0.571	pole-on	-1.002	8.029	7.473	4.176	3.238	2.435	2.071	1.872	1.622	1.503	1.364	1.188	1.054	1.05
S1	2.5	0.643	pole-on	-1.066	9.572	8.059	4.442	3.441	2.588	2.205	1.992	1.732	1.608	1.462	1.276	1.136	1.129
S1	2.5	0.714	pole-on	-1.118	11.074	8.709	4.755	3.677	2.755	2.356	2.13	1.859	1.727	1.572	1.375	1.232	1.221
S1	2.5	0.786	pole-on	-1.16	12.466	9.411	5.109	3.937	2.956	2.524	2.289	1.999	1.858	1.691	1.486	1.335	1.315
S1	2.5	0.857	pole-on	-1.194	13.78	10.238	5.508	4.245	3.17	2.716	2.464	2.161	2.008	1.829	1.603	1.442	1.413
S1	2.5	0.928	pole-on	-1.222	15.014	11.14	5.937	4.579	3.418	2.92	2.646	2.33	2.167	1.97	1.716	1.546	1.53
S1	2.5	1.0	pole-on	-1.242	16.088	12.022	6.376	4.899	3.66	3.122	2.835	2.5	2.323	2.095	1.832	1.656	1.657
S1	1.85	0.0	edge-on	0.442	1.08	1.906	1.613	1.459	1.211	1.096	1.026	0.948	0.863	0.775	0.676	0.612	0.594
S1	1.85	0.071	edge-on	0.215	1.433	1.402	1.353	1.064	0.873	0.787	0.728	0.626	0.589	0.534	0.455	0.403	0.388
S1	1.85	0.143	interm.	-0.079	0.281	31.897	64.645	160.186	150.699	28.03	33.604	9.09	8.317	6.593	5.355	4.037	3.889
S1	1.85	0.215	interm.	-0.306	1.119	21.96	7.059	4.862	3.557	2.948	2.62	2.123	2.012	1.881	1.614	1.407	1.35
S1	1.85	0.286	interm.	-0.484	2.027	9.758	5.07	3.884	2.967	2.503	2.242	1.909	1.798	1.654	1.432	1.274	1.217
S1	1.85	0.357	interm.	-0.625	3.109	8.783	4.92	3.813	2.916	2.473	2.229	1.914	1.805	1.66	1.438	1.294	1.237
S1	1.85	0.429	pole-on	-0.738	4.465	9.119	5.088	3.94	2.993	2.546	2.311	2.003	1.886	1.722	1.503	1.352	1.303
S1	1.85	0.5	pole-on	-0.824	6.011	9.736	5.375	4.15	3.151	2.683	2.423	2.119	1.99	1.829	1.596	1.444	1.394
S1	1.85	0.571	pole-on	-0.896	7.624	10.447	5.687	4.418	3.351	2.844	2.561	2.268	2.138	1.954	1.711	1.554	1.501
S1	1.85	0.643	pole-on	-0.957	9.259	11.274	6.105	4.738	3.587	3.059	2.783	2.459	2.308	2.109	1.848	1.678	1.624
S1	1.85	0.714	pole-on	-1.006	10.846	12.181	6.601	5.113	3.872	3.314	2.986	2.656	2.49	2.281	1.995	1.818	1.764
S1	1.85	0.786	pole-on	-1.045	12.38	13.265	7.168	5.552	4.186	3.584	3.229	2.904	2.704	2.468	2.164	1.971	1.917
S1	1.85	0.857	pole-on	-1.077	13.833	14.474	7.777	6.013	4.535	3.875	3.495	3.128	2.916	2.664	2.344	2.153	2.102
S1	1.85	0.928	pole-on	-1.103	15.269	15.842	8.449	6.535	4.897	4.182	3.783	3.365	3.14	2.878	2.558	2.359	2.317
S1	1.85	1.0	pole-on	-1.122	16.431	17.238	9.103	7.043	5.238	4.455	4.055	3.625	3.371	3.116	2.777	2.566	3.342
S1	1.37	0.0	edge-on	0.347	1.13	2.431	1.935	1.707	1.38	1.258	1.137	1.043	0.961	0.879	0.765	0.695	0.679
S1	1.37	0.071	edge-on	0.179	1.483	1.698	1.46	1.297	1.012	0.951	0.824	0.764	0.688	0.631	0.532	0.484	0.458
S1	1.37	0.143	interm.	-0.047	0.217	53.941	0.809	17.997	274.593	289.029	327.173	143.024	35.083	23.924	16.595	12.093	12.666
S1	1.37	0.215	interm.	-0.246	0.962	46.853	10.7	7.182	5.017	3.995	3.69	3.184	2.833	2.605	2.25	2.036	1.97
S1	1.37	0.286	interm.	-0.407	1.797	14.751	6.672	5.229	3.979	3.297	3.077	2.679	2.429	2.243	1.952	1.789	1.724

Table A.3 - continued.

Star	Σ_0 [g cm ⁻²]	cos i	$\tilde{\tau}_{\text{bu}}$ ang. type	bu		0.15	0.45	0.75	1.50	2.25	3.00	4.50	6.00	9.00	15.00	30.00	∞
				$\Delta R_{\text{bu}}^\infty$	ξ_{bu}^R	ξ_{d}^R											
S1	1.37	0.357	interm.	-0.538	2.812	12.204	6.48	5.112	3.933	3.293	3.081	2.696	2.456	2.277	1.982	1.819	1.756
S1	1.37	0.429	pole-on	-0.642	4.106	12.34	6.758	5.334	4.088	3.461	3.209	2.825	2.575	2.408	2.101	1.924	1.864
S1	1.37	0.5	pole-on	-0.724	5.645	13.247	7.181	5.693	4.349	3.709	3.427	3.049	2.771	2.576	2.253	2.075	2.015
S1	1.37	0.571	pole-on	-0.792	7.283	14.264	7.704	6.13	4.662	3.994	3.683	3.269	3.007	2.807	2.442	2.25	2.198
S1	1.37	0.643	pole-on	-0.848	9.031	15.442	8.384	6.648	5.05	4.334	3.959	3.558	3.32	3.033	2.671	2.466	2.419
S1	1.37	0.714	pole-on	-0.894	10.746	16.876	9.147	7.241	5.49	4.72	4.33	3.869	3.586	3.312	2.924	2.721	2.683
S1	1.37	0.786	pole-on	-0.931	12.437	18.475	9.996	7.906	5.959	5.132	4.698	4.197	3.9	3.634	3.23	3.006	2.986
S1	1.37	0.857	pole-on	-0.96	14.129	20.353	10.945	8.637	6.45	5.562	5.09	4.561	4.238	3.999	3.557	3.324	3.309
S1	1.37	0.928	pole-on	-0.983	15.672	22.445	12.019	9.401	6.983	6.04	5.54	5.008	4.643	4.388	3.929	3.668	3.672
S1	1.37	1.0	pole-on	-1.001	17.025	24.338	12.985	10.101	7.584	6.535	5.997	5.456	5.085	4.77	4.297	4.007	4.036
S1	1.01	0.0	edge-on	0.272	1.172	2.942	2.144	1.923	3.033	1.44	1.307	1.174	1.105	1.014	0.825	0.803	0.803
S1	1.01	0.071	edge-on	0.152	1.379	2.108	1.638	1.524	1.936	1.116	0.986	0.886	0.825	0.768	0.619	0.606	0.582
S1	1.01	0.143	interm.	-0.011	116.039	33.347	6.766	0.708	360.643	13.046	51.753	175.924	175.217	327.419	289.309	319.12	294.908
S1	1.01	0.215	interm.	-0.176	0.982	179.383	22.092	12.31	15.49	5.884	5.258	4.676	4.022	3.725	3.213	2.887	2.774
S1	1.01	0.286	interm.	-0.316	1.772	22.44	9.882	7.18	8.113	4.452	4.059	3.706	3.29	2.997	2.72	2.41	2.31
S1	1.01	0.357	interm.	-0.434	2.686	16.567	9.034	6.934	7.278	4.462	4.085	3.718	3.364	3.029	2.843	2.504	2.381
S1	1.01	0.429	pole-on	-0.532	3.843	16.31	9.377	7.296	7.222	4.749	4.35	3.94	3.608	3.252	3.073	2.712	2.559
S1	1.01	0.5	pole-on	-0.609	5.288	17.49	10.039	7.834	7.473	5.132	4.696	4.278	3.919	3.549	3.372	2.977	2.796
S1	1.01	0.571	pole-on	-0.671	6.971	19.111	10.828	8.5	7.853	5.594	5.116	4.659	4.307	3.877	3.731	3.303	3.088
S1	1.01	0.643	pole-on	-0.724	8.72	20.955	11.845	9.291	8.335	6.097	5.593	5.104	4.724	4.335	4.119	3.697	3.45
S1	1.01	0.714	pole-on	-0.767	10.518	23.021	12.996	10.202	8.954	6.672	6.124	5.633	5.241	4.819	4.559	4.127	3.889
S1	1.01	0.786	pole-on	-0.801	12.32	25.616	14.29	11.193	9.598	7.362	6.724	6.214	5.815	5.381	5.04	4.605	4.411
S1	1.01	0.857	pole-on	-0.829	14.155	28.382	15.676	12.271	10.311	8.127	7.418	6.888	6.458	6.042	5.559	5.114	5.054
S1	1.01	0.928	pole-on	-0.85	15.824	31.6	17.251	13.568	11.042	8.925	8.12	7.577	7.176	6.743	6.103	5.656	5.755
S1	1.01	1.0	pole-on	-0.865	17.281	34.698	18.881	14.86	11.822	9.697	8.815	8.3	7.899	7.391	6.638	6.193	6.533
S1	0.75	0.0	edge-on	0.211	1.297	3.817	2.61	2.206	1.832	1.646	1.522	1.377	1.266	1.154	1.018	0.939	0.912
S1	0.75	0.071	edge-on	0.124	45.219	2.836	1.995	1.681	1.43	1.296	1.209	1.074	0.989	0.905	0.79	0.72	0.682
S1	0.75	0.143	interm.	0.004	290.788	10.903	1.872	1.012	0.712	2.896	0.484	0.384	13.49	2.416	39.135	92.047	76.254
S1	0.75	0.215	interm.	-0.127	0.855	380.042	53.847	28.987	13.626	10.343	8.487	7.054	6.371	5.537	4.731	4.136	4.309
S1	0.75	0.286	interm.	-0.243	1.995	40.242	14.516	10.672	7.198	6.084	5.44	4.773	4.423	4.063	3.601	3.209	3.3
S1	0.75	0.357	interm.	-0.345	2.404	23.79	12.11	9.389	6.893	5.901	5.308	4.789	4.493	4.168	3.688	3.356	3.451
S1	0.75	0.429	pole-on	-0.432	3.416	22.201	12.275	9.681	7.263	6.303	5.744	5.196	4.882	4.516	4.041	3.72	3.82
S1	0.75	0.5	pole-on	-0.502	4.588	23.106	13.131	10.408	7.904	6.913	6.289	5.711	5.365	4.987	4.501	4.19	4.299
S1	0.75	0.571	pole-on	-0.56	5.796	25.123	14.32	11.417	8.681	7.6	6.965	6.316	5.989	5.577	5.048	4.682	4.863
S1	0.75	0.643	pole-on	-0.609	7.028	27.986	15.838	12.662	9.656	8.474	7.715	7.069	6.719	6.228	5.695	5.306	5.538

Table A.3 - continued.

Star	Σ_0 [g cm ⁻²]	cos i	$\tilde{\tau}_{bu}$ ang. type	bu		0.15	0.45	0.75	1.50	2.25	3.00	4.50	6.00	9.00	15.00	30.00	∞
				ΔR_{bu}^∞	ξ_{bu}^R	ξ_d^R											
S1	0.75	0.714	pole-on	-0.648	8.246	31.122	17.557	14.055	10.716	9.416	8.615	7.87	7.564	6.972	6.395	5.957	6.283
S1	0.75	0.786	pole-on	-0.678	9.314	34.905	19.686	15.765	11.922	10.527	9.594	8.803	8.496	7.774	7.134	6.681	7.1
S1	0.75	0.857	pole-on	-0.702	10.436	39.115	21.915	17.542	13.287	11.692	10.643	9.775	9.565	8.596	8.003	7.411	8.057
S1	0.75	0.928	pole-on	-0.721	11.348	44.069	24.619	19.769	14.755	12.812	11.647	10.827	10.685	9.412	8.885	8.206	9.09
S1	0.75	1.0	pole-on	-0.733	12.18	48.527	27.192	21.86	16.08	13.928	12.64	11.866	11.822	10.234	9.765	8.971	10.101
S1	0.56	0.0	edge-on	0.165	1.406	5.123	3.211	2.712	2.187	1.888	1.756	1.609	1.459	1.36	1.186	1.08	1.045
S1	0.56	0.071	edge-on	0.102	1.583	3.919	2.476	2.218	1.737	1.532	1.468	1.3	1.177	1.109	0.927	0.89	0.833
S1	0.56	0.143	interm.	0.015	47.45	17.431	2.455	1.456	1.08	0.895	0.834	0.738	0.907	0.591	0.354	1.107	0.392
S1	0.56	0.215	interm.	-0.084	2.009	387.039	310.062	103.078	32.535	21.994	17.082	12.192	11.832	9.412	8.904	7.258	6.955
S1	0.56	0.286	interm.	-0.176	10.93	95.752	22.097	14.374	9.84	8.011	7.214	6.213	5.967	5.302	4.963	4.393	4.401
S1	0.56	0.357	interm.	-0.258	2.412	34.162	15.383	11.585	8.649	7.373	6.818	6.054	5.902	5.25	4.906	4.453	4.577
S1	0.56	0.429	pole-on	-0.331	3.376	28.385	15.292	11.878	9.158	7.988	7.335	6.568	6.382	5.784	5.371	4.958	5.107
S1	0.56	0.5	pole-on	-0.391	4.527	29.037	16.327	13.117	9.996	8.838	8.128	7.283	7.151	6.501	6.078	5.581	5.821
S1	0.56	0.571	pole-on	-0.441	5.884	31.521	18.099	14.473	11.194	9.861	9.152	8.215	8.083	7.317	6.845	6.349	6.675
S1	0.56	0.643	pole-on	-0.483	7.41	34.996	20.239	16.346	12.623	11.116	10.31	9.239	9.193	8.28	7.761	7.196	7.716
S1	0.56	0.714	pole-on	-0.517	9.151	39.613	22.972	18.542	14.239	12.528	11.574	10.405	10.434	9.283	8.727	8.116	8.843
S1	0.56	0.786	pole-on	-0.543	10.94	44.746	25.92	21.056	16.106	14.119	13.002	11.619	11.758	10.392	9.85	9.102	10.194
S1	0.56	0.857	pole-on	-0.563	12.738	51.025	29.396	23.869	18.027	15.674	14.394	13.063	13.315	11.409	11.052	10.077	11.696
S1	0.56	0.928	pole-on	-0.578	14.593	57.555	33.516	27.005	19.936	17.159	15.723	14.474	15.001	12.509	12.224	11.13	13.317
S1	0.56	1.0	pole-on	-0.586	16.081	63.496	36.895	29.949	21.777	18.636	16.912	15.814	16.674	13.501	13.447	12.096	14.926
S1	0.41	0.0	edge-on	0.127	1.623	6.6	4.18	3.279	2.644	2.349	2.127	1.874	1.73	1.616	1.413	1.294	1.236
S1	0.41	0.071	edge-on	0.084	1.702	5.633	3.278	2.744	2.237	1.907	1.827	1.615	1.469	1.353	1.197	1.087	1.038
S1	0.41	0.143	interm.	0.022	13.014	13.282	5.113	2.182	1.668	1.544	1.45	1.225	1.097	1.105	0.894	0.757	0.718
S1	0.41	0.215	interm.	-0.048	0.84	344.892	375.408	367.815	256.422	133.704	56.625	37.85	33.934	21.351	17.801	15.952	15.218
S1	0.41	0.286	interm.	-0.116	1.586	293.954	38.255	22.373	13.907	10.425	9.169	8.15	7.557	6.556	5.846	5.507	5.73
S1	0.41	0.357	interm.	-0.18	2.299	52.135	20.217	14.865	10.568	8.91	8.14	7.438	7.168	6.265	5.797	5.399	5.717
S1	0.41	0.429	pole-on	-0.237	3.129	36.663	18.701	14.669	11.073	9.521	8.714	8.03	7.804	6.936	6.436	6.113	6.437
S1	0.41	0.5	pole-on	-0.284	4.145	35.565	20.075	16.084	12.266	10.61	9.852	8.997	8.856	7.836	7.31	6.914	7.479
S1	0.41	0.571	pole-on	-0.324	5.384	37.776	22.269	17.937	13.83	12.123	11.121	10.16	10.131	8.967	8.387	7.851	8.74
S1	0.41	0.643	pole-on	-0.357	6.85	42.123	25.234	20.741	15.89	13.883	12.775	11.6	11.69	10.234	9.625	8.987	10.221
S1	0.41	0.714	pole-on	-0.384	8.478	47.486	29.016	23.668	18.139	15.861	14.559	13.135	13.328	11.65	10.918	10.251	11.927
S1	0.41	0.786	pole-on	-0.404	10.323	54.762	33.354	27.306	20.591	17.978	16.502	14.765	15.289	13.017	12.432	11.438	13.916
S1	0.41	0.857	pole-on	-0.419	12.229	61.699	38.021	31.162	23.196	20.001	18.248	16.533	17.449	14.257	13.944	12.743	16.209
S1	0.41	0.928	pole-on	-0.43	14.242	71.018	43.389	35.243	25.709	21.8	19.731	18.294	19.767	15.666	15.52	13.941	18.685
S1	0.41	1.0	pole-on	-0.434	15.782	78.434	47.884	39.436	28.054	23.368	21.113	20.079	22.136	16.711	16.969	15.109	21.18

Table A.3 - continued.

Star	Σ_0 [g cm ⁻²]	cos i	$\tilde{\tau}_{\text{bu}}$ ang. type	bu		0.15	0.45	0.75	1.50	2.25	3.00	4.50	6.00	9.00	15.00	30.00	∞
				$\Delta R_{\text{bu}}^\infty$	ξ_{bu}^R	ξ_{d}^R											
S1	0.3	0.0	edge-on	0.098	1.925	8.572	5.132	4.037	3.268	2.799	2.602	2.281	2.07	1.944	1.699	1.545	1.493
S1	0.3	0.071	edge-on	0.068	2.066	7.578	4.245	3.418	2.738	2.45	2.229	1.986	1.839	1.673	1.452	1.337	1.282
S1	0.3	0.143	interm.	0.025	33.485	29.979	3.789	3.139	2.682	2.426	2.106	1.909	1.805	1.738	1.482	1.396	1.218
S1	0.3	0.215	interm.	-0.023	24.573	303.837	307.811	335.109	307.23	350.268	338.568	318.0	323.62	291.891	212.128	194.633	172.367
S1	0.3	0.286	interm.	-0.072	1.463	332.586	174.486	44.976	17.801	13.797	11.546	9.183	9.535	7.39	6.669	5.91	6.583
S1	0.3	0.357	interm.	-0.117	2.146	116.398	26.503	17.923	11.771	9.944	8.899	8.011	7.983	6.669	6.319	5.81	6.463
S1	0.3	0.429	pole-on	-0.159	2.95	44.126	22.13	16.989	12.009	10.467	9.551	8.621	8.856	7.422	7.071	6.669	7.42
S1	0.3	0.5	pole-on	-0.194	3.899	39.62	23.196	18.143	13.455	11.895	10.965	9.806	10.088	8.581	8.293	7.715	8.746
S1	0.3	0.571	pole-on	-0.223	4.989	43.488	25.857	20.73	15.539	13.585	12.542	11.131	11.695	9.939	9.456	8.758	10.305
S1	0.3	0.643	pole-on	-0.247	6.279	48.903	29.301	23.924	17.932	15.799	14.507	12.929	13.636	11.51	10.999	10.292	12.342
S1	0.3	0.714	pole-on	-0.266	7.739	55.494	33.881	27.828	21.003	18.256	16.673	14.847	15.698	12.993	12.654	11.712	14.578
S1	0.3	0.786	pole-on	-0.281	9.521	62.401	39.25	32.352	24.159	20.885	19.06	16.721	18.253	14.68	14.332	13.078	17.33
S1	0.3	0.857	pole-on	-0.291	11.307	72.88	45.256	36.997	26.975	23.13	21.222	18.775	20.855	16.427	16.25	14.546	20.448
S1	0.3	0.928	pole-on	-0.298	13.171	82.222	51.2	42.574	30.049	25.449	22.912	21.135	23.911	17.779	17.941	16.096	23.861
S1	0.3	1.0	pole-on	-0.299	14.651	90.028	56.237	47.015	32.122	27.265	24.288	22.909	26.665	18.899	20.027	17.339	27.151
S2	2.5	0.0	edge-on	0.482	1.05	1.853	1.481	1.338	1.157	1.041	0.968	0.871	0.808	0.733	0.636	0.577	0.561
S2	2.5	0.071	edge-on	0.243	1.482	1.355	1.099	0.997	0.854	0.73	0.682	0.611	0.549	0.488	0.427	0.376	0.356
S2	2.5	0.143	interm.	-0.066	0.214	0.896	0.496	1.402	191.779	242.205	54.859	19.734	15.819	12.076	8.234	7.163	6.403
S2	2.5	0.215	interm.	-0.305	0.931	35.152	8.647	5.709	3.772	3.188	2.877	2.43	2.234	2.084	1.755	1.627	1.546
S2	2.5	0.286	interm.	-0.483	1.807	10.64	5.368	4.082	2.982	2.559	2.335	2.012	1.875	1.727	1.476	1.361	1.306
S2	2.5	0.357	interm.	-0.622	2.874	9.055	5.085	3.933	2.884	2.494	2.272	1.97	1.844	1.698	1.454	1.347	1.294
S2	2.5	0.429	pole-on	-0.733	4.163	9.195	5.18	4.033	2.956	2.561	2.326	2.038	1.905	1.755	1.515	1.4	1.34
S2	2.5	0.5	pole-on	-0.818	5.657	9.758	5.394	4.218	3.118	2.691	2.458	2.15	2.006	1.852	1.607	1.483	1.428
S2	2.5	0.571	pole-on	-0.888	7.19	10.427	5.752	4.49	3.317	2.866	2.613	2.297	2.141	1.977	1.724	1.582	1.531
S2	2.5	0.643	pole-on	-0.948	8.746	11.306	6.172	4.82	3.558	3.072	2.813	2.476	2.318	2.134	1.864	1.716	1.656
S2	2.5	0.714	pole-on	-0.995	10.27	12.264	6.665	5.211	3.849	3.322	3.044	2.68	2.512	2.315	2.024	1.852	1.796
S2	2.5	0.786	pole-on	-1.033	11.75	13.33	7.226	5.644	4.172	3.6	3.304	2.915	2.727	2.51	2.187	2.011	1.952
S2	2.5	0.857	pole-on	-1.063	13.157	14.617	7.857	6.132	4.521	3.905	3.569	3.176	2.947	2.7	2.362	2.196	2.128
S2	2.5	0.928	pole-on	-1.088	14.475	15.962	8.551	6.672	4.913	4.221	3.852	3.42	3.174	2.918	2.58	2.412	2.343
S2	2.5	1.0	pole-on	-1.106	15.596	17.387	9.24	7.182	5.25	4.512	4.121	3.669	3.42	3.158	2.797	2.623	2.564
S2	1.85	0.0	edge-on	0.38	1.107	2.274	1.754	1.563	1.318	1.154	1.846	1.397	0.909	0.822	0.718	0.646	0.63
S2	1.85	0.071	edge-on	0.207	1.428	1.743	1.338	1.197	0.992	0.87	0.979	0.792	0.611	0.59	0.499	0.446	0.423
S2	1.85	0.143	interm.	-0.026	0.228	1.373	0.741	0.568	4.992	52.513	451.067	428.242	349.056	350.952	73.585	38.014	35.516
S2	1.85	0.215	interm.	-0.234	0.856	110.487	15.69	8.89	5.617	4.551	6.555	4.934	3.214	2.946	2.528	2.361	2.244
S2	1.85	0.286	interm.	-0.396	1.686	16.208	7.581	5.581	4.073	3.495	4.443	3.544	2.61	2.364	2.045	1.895	1.833

Table A.3 - continued.

Star	Σ_0 [g cm ⁻²]	cos i	$\tilde{\tau}_{\text{bu}}$ ang. type	bu		0.15	0.45	0.75	1.50	2.25	3.00	4.50	6.00	9.00	15.00	30.00	∞
				$\Delta R_{\text{bu}}^{\infty}$	ξ_{bu}^R	ξ_{d}^R											
S2	1.85	0.357	interm.	-0.527	2.679	12.45	6.827	5.256	3.953	3.356	4.034	3.313	2.568	2.347	2.053	1.883	1.817
S2	1.85	0.429	pole-on	-0.63	3.941	12.358	7.062	5.442	4.032	3.517	3.984	3.358	2.687	2.456	2.152	1.975	1.911
S2	1.85	0.5	pole-on	-0.712	5.372	13.12	7.446	5.757	4.334	3.762	4.12	3.519	2.881	2.628	2.292	2.123	2.054
S2	1.85	0.571	pole-on	-0.78	6.894	14.213	7.974	6.181	4.648	4.04	4.353	3.745	3.103	2.827	2.477	2.287	2.24
S2	1.85	0.643	pole-on	-0.836	8.526	15.483	8.593	6.711	5.053	4.396	4.667	4.041	3.366	3.069	2.702	2.5	2.461
S2	1.85	0.714	pole-on	-0.88	10.138	16.893	9.394	7.307	5.507	4.795	5.028	4.383	3.659	3.355	2.966	2.759	2.731
S2	1.85	0.786	pole-on	-0.916	11.752	18.556	10.266	7.993	6.001	5.207	5.451	4.79	3.987	3.687	3.262	3.051	3.027
S2	1.85	0.857	pole-on	-0.944	13.244	20.494	11.216	8.719	6.507	5.639	5.925	5.261	4.343	4.047	3.614	3.378	3.363
S2	1.85	0.928	pole-on	-0.967	14.659	22.652	12.234	9.478	7.047	6.147	6.422	5.774	4.749	4.439	3.986	3.72	3.737
S2	1.85	1.0	pole-on	-0.983	15.914	24.807	13.26	10.25	7.642	6.659	6.946	6.246	5.175	4.848	4.377	4.085	4.12
S2	1.37	0.0	edge-on	0.298	1.173	2.676	2.008	1.751	1.457	1.317	1.217	1.097	1.005	0.922	0.813	0.747	0.715
S2	1.37	0.071	edge-on	0.175	1.404	2.067	1.59	1.352	1.115	1.043	0.938	0.84	0.761	0.693	0.599	0.55	0.518
S2	1.37	0.143	interm.	0.003	328.395	2.085	0.993	0.75	0.492	0.461	0.366	0.462	12.359	16.67	81.543	166.375	190.78
S2	1.37	0.215	interm.	-0.168	0.811	347.723	35.466	18.141	9.954	7.574	6.547	5.537	4.96	4.392	3.766	3.439	3.315
S2	1.37	0.286	interm.	-0.31	1.597	28.54	10.68	7.946	5.663	4.768	4.345	3.842	3.546	3.212	2.806	2.564	2.516
S2	1.37	0.357	interm.	-0.427	2.506	17.766	9.15	7.204	5.4	4.626	4.194	3.737	3.488	3.179	2.788	2.579	2.517
S2	1.37	0.429	pole-on	-0.524	3.672	16.704	9.334	7.435	5.615	4.843	4.429	3.929	3.663	3.373	2.977	2.752	2.702
S2	1.37	0.5	pole-on	-0.6	5.069	17.563	9.924	7.936	5.994	5.193	4.745	4.257	3.976	3.654	3.25	3.023	2.976
S2	1.37	0.571	pole-on	-0.662	6.592	19.135	10.745	8.588	6.504	5.617	5.148	4.628	4.362	4.014	3.567	3.339	3.311
S2	1.37	0.643	pole-on	-0.714	8.229	20.895	11.754	9.381	7.106	6.162	5.625	5.099	4.807	4.44	3.965	3.735	3.71
S2	1.37	0.714	pole-on	-0.755	9.961	23.088	12.893	10.246	7.739	6.746	6.194	5.623	5.315	4.921	4.432	4.162	4.157
S2	1.37	0.786	pole-on	-0.788	11.656	25.61	14.147	11.204	8.514	7.418	6.809	6.234	5.901	5.456	4.936	4.639	4.687
S2	1.37	0.857	pole-on	-0.814	13.335	28.468	15.639	12.34	9.392	8.193	7.529	6.876	6.571	6.024	5.492	5.162	5.265
S2	1.37	0.928	pole-on	-0.834	14.977	31.684	17.29	13.673	10.369	9.015	8.26	7.615	7.314	6.643	6.099	5.725	5.882
S2	1.37	1.0	pole-on	-0.848	16.278	35.02	18.975	15.049	11.337	9.819	8.984	8.338	8.035	7.233	6.701	6.253	6.521
S2	1.01	0.0	edge-on	0.233	1.27	3.556	2.383	2.01	3.447	1.531	1.383	1.251	1.159	1.068	0.972	0.861	0.832
S2	1.01	0.071	edge-on	0.145	1.46	2.712	1.992	1.601	2.095	1.242	1.132	1.004	0.919	0.858	0.747	0.682	0.647
S2	1.01	0.143	interm.	0.02	17.791	2.369	1.465	1.08	0.555	0.661	0.554	0.418	0.353	0.311	5.289	0.246	0.229
S2	1.01	0.215	interm.	-0.113	0.756	395.739	227.78	51.239	54.204	14.723	12.257	9.767	8.532	7.296	6.183	5.533	5.409
S2	1.01	0.286	interm.	-0.23	1.531	50.323	15.738	11.113	18.602	6.429	5.821	5.171	4.817	4.335	3.831	3.465	3.417
S2	1.01	0.357	interm.	-0.331	2.378	24.6	12.165	9.338	13.371	5.963	5.529	4.973	4.606	4.226	3.806	3.493	3.421
S2	1.01	0.429	pole-on	-0.417	3.419	21.976	12.149	9.487	12.221	6.309	5.807	5.251	4.964	4.574	4.124	3.806	3.735
S2	1.01	0.5	pole-on	-0.486	4.682	22.221	12.929	10.323	12.222	6.83	6.323	5.749	5.454	5.048	4.567	4.252	4.18
S2	1.01	0.571	pole-on	-0.542	6.153	24.402	14.163	11.231	12.898	7.551	6.965	6.364	6.06	5.609	5.12	4.777	4.73
S2	1.01	0.643	pole-on	-0.588	7.78	27.337	15.65	12.457	13.938	8.394	7.775	7.102	6.81	6.294	5.74	5.345	5.394

Table A.3 - continued.

Star	Σ_0 [g cm ⁻²]	cos i	$\tilde{\tau}_{\text{bu}}$ ang. type	bu		0.15	0.45	0.75	1.50	2.25	3.00	4.50	6.00	9.00	15.00	30.00	∞
				$\Delta R_{\text{bu}}^{\infty}$	ξ_{bu}^R	ξ_{d}^R											
S2	1.01	0.714	pole-on	-0.626	9.506	30.328	17.488	13.912	15.279	9.379	8.679	7.916	7.645	7.005	6.423	6.035	6.158
S2	1.01	0.786	pole-on	-0.655	11.276	34.165	19.581	15.593	16.98	10.486	9.656	8.865	8.578	7.804	7.148	6.74	7.061
S2	1.01	0.857	pole-on	-0.678	13.049	38.679	22.028	17.532	18.955	11.645	10.7	9.857	9.642	8.635	7.977	7.512	8.113
S2	1.01	0.928	pole-on	-0.695	14.807	43.413	24.654	19.636	21.319	12.843	11.782	10.952	10.807	9.498	8.827	8.318	9.34
S2	1.01	1.0	pole-on	-0.705	16.244	48.376	27.596	21.888	23.518	13.971	12.738	12.012	11.967	10.314	9.646	9.116	10.575
S2	0.75	0.0	edge-on	0.183	7.558	4.753	2.989	2.497	1.994	1.783	1.638	1.44	1.365	1.236	1.077	0.994	0.965
S2	0.75	0.071	edge-on	0.121	1.545	3.854	2.448	2.057	1.663	1.501	1.395	1.239	1.133	1.067	0.921	0.852	0.801
S2	0.75	0.143	interm.	0.03	36.995	3.633	2.038	1.54	1.216	1.095	0.97	0.791	0.708	0.646	0.53	0.494	0.408
S2	0.75	0.215	interm.	-0.07	2.467	332.743	380.503	334.162	102.391	41.729	30.877	21.607	19.333	14.513	11.794	10.574	10.219
S2	0.75	0.286	interm.	-0.162	1.467	219.94	26.915	16.655	10.54	8.511	7.582	6.598	6.234	5.529	4.938	4.558	4.602
S2	0.75	0.357	interm.	-0.245	2.254	34.882	15.404	12.116	8.756	7.579	6.858	6.147	5.92	5.357	4.784	4.447	4.565
S2	0.75	0.429	pole-on	-0.317	3.173	26.89	14.996	11.911	9.074	7.918	7.25	6.529	6.346	5.775	5.256	4.924	5.1
S2	0.75	0.5	pole-on	-0.376	4.241	27.958	16.066	12.778	9.889	8.675	8.0	7.28	7.057	6.463	5.906	5.556	5.757
S2	0.75	0.571	pole-on	-0.424	5.432	30.246	17.647	14.38	11.101	9.764	8.945	8.103	7.962	7.272	6.699	6.324	6.604
S2	0.75	0.643	pole-on	-0.464	6.869	34.014	19.968	16.108	12.488	11.029	10.119	9.156	9.053	8.185	7.586	7.139	7.626
S2	0.75	0.714	pole-on	-0.496	8.058	38.037	22.522	18.266	14.112	12.379	11.417	10.267	10.325	9.212	8.606	8.04	8.797
S2	0.75	0.786	pole-on	-0.521	9.373	43.446	25.516	20.749	16.029	14.01	12.849	11.625	11.733	10.368	9.65	9.031	10.136
S2	0.75	0.857	pole-on	-0.54	10.668	49.278	29.07	23.624	17.907	15.532	14.296	12.959	13.296	11.401	10.875	10.062	11.604
S2	0.75	0.928	pole-on	-0.553	11.785	56.316	33.095	27.039	19.892	17.128	15.588	14.483	15.025	12.47	12.146	11.06	13.303
S2	0.75	1.0	pole-on	-0.56	12.746	62.284	36.973	30.038	21.798	18.576	16.822	15.859	16.664	13.472	13.346	12.117	15.058
S2	0.56	0.0	edge-on	0.144	1.639	6.418	3.775	3.112	2.368	2.087	1.906	1.729	1.569	1.451	1.263	1.14	1.114
S2	0.56	0.071	edge-on	0.1	1.771	5.533	3.237	2.736	2.135	1.855	1.733	1.505	1.402	1.303	1.121	1.033	0.978
S2	0.56	0.143	interm.	0.036	4.695	4.977	2.84	2.363	1.882	1.597	1.57	1.329	1.186	1.156	0.947	0.853	0.793
S2	0.56	0.215	interm.	-0.038	0.476	168.26	321.904	381.947	364.11	348.434	290.264	190.167	146.107	80.261	45.77	33.63	36.244
S2	0.56	0.286	interm.	-0.109	1.339	332.336	49.748	25.696	14.325	10.882	9.411	8.039	7.533	6.363	5.882	5.369	5.913
S2	0.56	0.357	interm.	-0.173	2.126	49.841	19.5	14.391	10.286	8.658	7.806	7.009	6.803	5.993	5.531	5.185	5.575
S2	0.56	0.429	pole-on	-0.229	3.045	33.688	17.666	13.822	10.274	9.062	8.29	7.6	7.347	6.54	6.048	5.757	6.174
S2	0.56	0.5	pole-on	-0.276	4.119	32.485	18.958	15.102	11.589	10.074	9.296	8.627	8.385	7.49	6.968	6.514	7.175
S2	0.56	0.571	pole-on	-0.316	5.319	35.056	20.903	17.069	13.175	11.548	10.586	9.579	9.585	8.509	8.028	7.474	8.39
S2	0.56	0.643	pole-on	-0.348	6.761	39.338	23.824	19.263	15.015	13.147	12.21	10.881	11.056	9.734	9.125	8.58	9.76
S2	0.56	0.714	pole-on	-0.373	8.375	44.447	27.369	22.382	17.171	15.09	13.716	12.435	12.71	11.041	10.482	9.811	11.465
S2	0.56	0.786	pole-on	-0.393	10.095	51.756	31.581	25.894	19.615	17.103	15.746	13.958	14.674	12.451	11.836	10.991	13.369
S2	0.56	0.857	pole-on	-0.408	11.843	59.323	36.152	29.457	22.097	19.049	17.454	15.677	16.789	13.654	13.376	12.203	15.577
S2	0.56	0.928	pole-on	-0.417	13.755	67.92	41.301	33.715	24.572	21.032	18.979	17.6	18.946	14.985	15.007	13.504	18.064
S2	0.56	1.0	pole-on	-0.421	15.236	75.21	46.288	37.788	26.924	22.651	20.495	19.369	21.282	16.149	16.478	14.594	20.515

Table A.3 - continued.

Star	Σ_0 [g cm ⁻²]	cos i	$\tilde{\tau}_{bu}$ ang. type	bu		0.15	0.45	0.75	1.50	2.25	3.00	4.50	6.00	9.00	15.00	30.00	∞
				ΔR_{bu}^∞	ξ_{bu}^R	ξ_d^R											
S2	0.41	0.0	edge-on	0.112	1.935	8.472	4.609	3.763	2.921	2.519	2.327	2.029	1.881	1.732	1.505	1.343	1.296
S2	0.41	0.071	edge-on	0.082	2.067	9.228	3.995	3.494	2.642	2.298	2.1	1.87	1.702	1.571	1.349	1.256	1.222
S2	0.41	0.143	interm.	0.037	4.308	17.941	4.187	3.453	2.699	2.493	2.366	2.091	1.889	1.778	1.537	1.422	1.308
S2	0.41	0.215	interm.	-0.011	44.0	93.927	67.974	48.985	227.074	269.978	281.241	331.199	354.934	355.519	372.308	336.071	355.621
S2	0.41	0.286	interm.	-0.065	1.265	379.497	260.822	73.954	22.046	12.715	10.597	8.739	8.428	6.748	6.065	5.683	6.42
S2	0.41	0.357	interm.	-0.112	1.994	145.965	22.583	15.451	10.908	8.712	7.855	6.927	7.057	6.095	5.827	5.237	5.995
S2	0.41	0.429	pole-on	-0.154	2.832	38.705	19.132	14.814	11.014	9.345	8.544	7.798	7.979	6.939	6.449	6.04	6.861
S2	0.41	0.5	pole-on	-0.188	3.855	35.666	20.481	16.329	12.666	10.665	9.986	9.056	9.092	7.973	7.561	6.999	8.002
S2	0.41	0.571	pole-on	-0.218	4.951	38.226	22.991	18.769	14.302	12.416	11.431	10.426	10.61	9.232	8.709	8.246	9.597
S2	0.41	0.643	pole-on	-0.241	6.317	43.092	26.495	21.551	16.572	14.465	13.324	11.966	12.407	10.725	10.199	9.514	11.463
S2	0.41	0.714	pole-on	-0.26	7.843	49.809	30.624	25.481	19.266	16.633	15.347	13.681	14.616	12.271	11.633	10.913	13.665
S2	0.41	0.786	pole-on	-0.274	9.682	57.08	36.064	29.99	22.389	19.361	17.697	15.665	16.89	13.9	13.479	12.293	16.14
S2	0.41	0.857	pole-on	-0.284	11.444	67.317	41.565	34.643	25.543	21.754	19.762	17.554	19.552	15.311	15.211	13.769	19.16
S2	0.41	0.928	pole-on	-0.29	13.498	76.004	48.105	40.008	28.174	23.64	21.45	19.854	22.506	16.743	17.112	15.216	22.299
S2	0.41	1.0	pole-on	-0.29	14.886	84.552	53.673	44.424	30.668	25.603	22.888	21.856	25.234	18.042	18.955	16.543	25.495
S2	0.3	0.0	edge-on	0.087	2.258	11.13	5.969	4.542	3.457	3.023	2.813	2.477	2.184	2.018	1.743	1.635	1.506
S2	0.3	0.071	edge-on	0.066	2.316	16.954	5.338	4.597	3.211	2.814	2.56	2.376	2.186	1.901	1.666	1.5	1.483
S2	0.3	0.143	interm.	0.035	4.542	25.531	7.858	4.961	3.962	3.392	3.189	3.049	2.739	2.589	2.178	2.132	1.993
S2	0.3	0.215	interm.	0.003	272.158	104.073	63.064	44.972	63.831	48.231	41.32	83.104	83.31	116.621	174.194	98.484	226.288
S2	0.3	0.286	interm.	-0.035	14.722	301.471	332.21	300.923	133.822	36.703	21.968	7.545	8.942	5.506	5.245	4.14	5.116
S2	0.3	0.357	interm.	-0.068	2.918	268.645	24.879	16.041	8.674	7.468	7.248	5.81	5.994	5.097	4.645	4.218	5.174
S2	0.3	0.429	pole-on	-0.097	2.667	58.759	18.488	14.642	10.561	9.065	8.107	7.135	7.35	6.398	6.16	5.793	6.512
S2	0.3	0.5	pole-on	-0.122	3.639	38.261	19.432	16.473	11.727	10.159	9.584	8.466	8.827	7.599	7.173	6.629	7.871
S2	0.3	0.571	pole-on	-0.142	4.8	38.68	22.732	18.764	14.06	12.365	11.412	10.162	10.645	9.219	8.812	8.158	9.761
S2	0.3	0.643	pole-on	-0.159	6.032	43.462	26.855	22.459	16.573	14.575	13.758	12.12	12.594	10.796	10.385	9.515	11.967
S2	0.3	0.714	pole-on	-0.172	7.598	50.52	31.684	26.66	19.922	17.393	15.93	13.853	14.979	12.653	12.056	10.954	14.572
S2	0.3	0.786	pole-on	-0.181	9.401	60.261	37.757	31.872	23.547	20.268	18.545	16.172	17.808	14.271	13.926	12.751	17.471
S2	0.3	0.857	pole-on	-0.187	11.213	70.29	44.027	37.071	27.372	22.709	20.584	18.292	20.926	15.823	16.121	14.356	21.131
S2	0.3	0.928	pole-on	-0.191	13.449	80.831	52.382	42.001	30.407	26.019	22.562	21.024	24.384	17.298	18.013	16.001	25.077
S2	0.3	1.0	pole-on	-0.19	14.975	90.335	58.125	48.582	33.396	27.529	24.032	23.027	27.135	18.889	20.091	17.509	29.158
S3	2.5	0.0	edge-on	0.43	1.111	2.038	1.578	1.394	1.197	1.07	1.011	0.9	0.845	0.767	0.671	0.61	0.596
S3	2.5	0.071	edge-on	0.248	1.465	1.635	1.252	1.103	0.929	0.839	0.786	0.685	0.647	0.576	0.485	0.436	0.418
S3	2.5	0.143	interm.	-0.007	32.88	1.266	0.838	0.628	0.284	0.251	0.227	11.713	32.329	151.561	279.528	340.224	336.806
S3	2.5	0.215	interm.	-0.228	0.761	258.086	16.731	9.416	5.833	4.677	4.053	3.546	3.133	2.891	2.521	2.27	2.177
S3	2.5	0.286	interm.	-0.396	1.593	15.166	6.911	5.187	3.859	3.277	2.938	2.624	2.381	2.201	1.924	1.748	1.682

Table A.3 - continued.

Star	Σ_0 [g cm ⁻²]	cos i	$\tilde{\tau}_{\text{bu}}$ ang. type	bu		0.15	0.45	0.75	1.50	2.25	3.00	4.50	6.00	9.00	15.00	30.00	∞
				$\Delta R_{\text{bu}}^\infty$	ξ_{bu}^R	ξ_{d}^R											
S3	2.5	0.357	interm.	-0.529	2.591	11.102	6.194	4.846	3.652	3.148	2.825	2.553	2.317	2.139	1.876	1.707	1.651
S3	2.5	0.429	pole-on	-0.635	3.813	11.164	6.288	4.94	3.734	3.218	2.901	2.627	2.395	2.21	1.938	1.775	1.718
S3	2.5	0.5	pole-on	-0.716	5.308	11.743	6.599	5.185	3.932	3.395	3.076	2.771	2.549	2.351	2.062	1.886	1.834
S3	2.5	0.571	pole-on	-0.784	6.795	12.699	7.066	5.54	4.196	3.633	3.302	2.973	2.739	2.529	2.219	2.031	1.98
S3	2.5	0.643	pole-on	-0.841	8.376	13.783	7.646	5.979	4.534	3.925	3.582	3.223	2.98	2.741	2.41	2.211	2.154
S3	2.5	0.714	pole-on	-0.886	9.9	15.084	8.32	6.503	4.925	4.272	3.892	3.505	3.235	2.976	2.625	2.417	2.373
S3	2.5	0.786	pole-on	-0.921	11.448	16.578	9.069	7.104	5.366	4.651	4.226	3.803	3.524	3.241	2.868	2.653	2.633
S3	2.5	0.857	pole-on	-0.95	12.967	18.247	9.941	7.757	5.827	5.031	4.568	4.118	3.826	3.54	3.154	2.935	2.908
S3	2.5	0.928	pole-on	-0.973	14.381	20.174	10.873	8.451	6.3	5.439	4.945	4.496	4.199	3.889	3.474	3.237	3.231
S3	2.5	1.0	pole-on	-0.99	15.534	22.03	11.811	9.124	6.801	5.883	5.36	4.899	4.592	4.238	3.809	3.552	3.558
S3	1.85	0.0	edge-on	0.338	1.208	2.562	1.793	1.574	1.323	1.183	1.119	1.539	0.977	0.866	0.748	0.675	0.672
S3	1.85	0.071	edge-on	0.211	1.45	2.099	1.491	1.284	1.101	0.967	0.919	0.99	0.734	0.689	0.595	0.532	0.52
S3	1.85	0.143	interm.	0.021	144.362	1.807	1.085	0.81	0.566	0.424	0.32	2.919	3.128	0.252	0.233	13.478	0.298
S3	1.85	0.215	interm.	-0.162	0.679	376.35	43.653	20.109	10.055	7.149	6.321	7.18	4.812	4.262	3.69	3.34	3.193
S3	1.85	0.286	interm.	-0.311	1.476	24.349	9.811	7.333	5.226	4.39	3.993	4.441	3.275	2.966	2.584	2.378	2.284
S3	1.85	0.357	interm.	-0.433	2.407	15.051	8.264	6.593	4.899	4.189	3.823	4.093	3.185	2.903	2.542	2.343	2.269
S3	1.85	0.429	pole-on	-0.532	3.57	14.577	8.443	6.712	5.073	4.366	3.976	4.162	3.339	3.049	2.676	2.475	2.399
S3	1.85	0.5	pole-on	-0.609	4.983	15.563	8.908	7.127	5.387	4.674	4.264	4.377	3.589	3.283	2.886	2.686	2.603
S3	1.85	0.571	pole-on	-0.671	6.526	16.784	9.62	7.675	5.819	5.047	4.629	4.695	3.891	3.578	3.161	2.949	2.89
S3	1.85	0.643	pole-on	-0.723	8.185	18.52	10.52	8.358	6.331	5.516	5.058	5.09	4.255	3.926	3.5	3.27	3.218
S3	1.85	0.714	pole-on	-0.765	9.902	20.37	11.501	9.164	6.901	6.029	5.545	5.569	4.692	4.328	3.892	3.63	3.608
S3	1.85	0.786	pole-on	-0.798	11.618	22.67	12.656	10.03	7.557	6.65	6.085	6.108	5.139	4.791	4.324	4.055	4.04
S3	1.85	0.857	pole-on	-0.825	13.265	25.2	13.944	11.001	8.307	7.28	6.74	6.701	5.684	5.31	4.807	4.511	4.542
S3	1.85	0.928	pole-on	-0.846	14.796	28.136	15.326	12.117	9.166	8.024	7.425	7.337	6.264	5.847	5.36	5.003	5.074
S3	1.85	1.0	pole-on	-0.86	16.103	31.026	16.863	13.281	10.019	8.765	8.111	8.006	6.832	6.403	5.907	5.512	5.637
S3	1.37	0.0	edge-on	0.265	1.36	3.109	2.181	1.883	1.537	1.347	1.255	1.131	1.048	0.97	0.839	0.764	0.753
S3	1.37	0.071	edge-on	0.176	1.539	2.597	1.731	1.584	1.311	1.148	1.061	0.968	0.894	0.82	0.709	0.65	0.631
S3	1.37	0.143	interm.	0.037	12.814	2.133	1.502	1.15	0.888	0.693	0.594	0.486	0.446	0.397	0.29	0.256	0.301
S3	1.37	0.215	interm.	-0.109	0.57	361.024	322.719	66.478	22.642	15.591	12.597	9.501	8.447	7.243	6.228	5.454	5.111
S3	1.37	0.286	interm.	-0.234	1.364	50.044	14.073	10.047	6.93	5.856	5.398	4.634	4.307	3.882	3.527	3.187	3.109
S3	1.37	0.357	interm.	-0.341	2.232	21.112	10.796	8.434	6.295	5.47	5.029	4.444	4.145	3.804	3.414	3.151	3.123
S3	1.37	0.429	pole-on	-0.43	3.316	18.737	10.671	8.621	6.522	5.706	5.275	4.715	4.434	4.081	3.645	3.408	3.376
S3	1.37	0.5	pole-on	-0.5	4.641	19.875	11.523	9.274	7.074	6.191	5.703	5.117	4.841	4.468	4.039	3.786	3.766
S3	1.37	0.571	pole-on	-0.557	6.156	21.846	12.677	10.114	7.755	6.79	6.264	5.657	5.406	4.973	4.499	4.226	4.239
S3	1.37	0.643	pole-on	-0.605	7.8	24.275	13.935	11.149	8.546	7.469	6.943	6.304	6.004	5.526	5.055	4.749	4.806

Table A.3 - continued.

Star	Σ_0 [g cm ⁻²]	cos i	$\tilde{\tau}_{bu}$ ang. type	bu		0.15	0.45	0.75	1.50	2.25	3.00	4.50	6.00	9.00	15.00	30.00	∞
				ΔR_{bu}^∞	ξ_{bu}^R	ξ_d^R											
S3	1.37	0.714	pole-on	-0.644	9.487	27.03	15.474	12.395	9.495	8.334	7.74	7.017	6.736	6.195	5.677	5.34	5.461
S3	1.37	0.786	pole-on	-0.674	11.309	30.658	17.252	13.729	10.569	9.307	8.624	7.822	7.563	6.898	6.365	5.98	6.188
S3	1.37	0.857	pole-on	-0.697	13.057	34.3	19.377	15.436	11.816	10.331	9.566	8.73	8.484	7.657	7.13	6.686	7.015
S3	1.37	0.928	pole-on	-0.716	14.718	38.9	21.721	17.271	13.142	11.436	10.508	9.727	9.531	8.454	7.943	7.42	7.913
S3	1.37	1.0	pole-on	-0.728	16.189	42.935	24.058	19.24	14.467	12.49	11.473	10.723	10.574	9.216	8.807	8.159	8.872
S3	1.01	0.0	edge-on	0.208	1.536	4.228	2.508	2.244	1.757	1.558	1.435	1.3	1.182	1.042	0.809	0.825	0.869
S3	1.01	0.071	edge-on	0.144	1.691	3.596	2.254	1.926	1.555	1.392	1.276	1.152	1.037	0.94	0.732	0.739	0.768
S3	1.01	0.143	interm.	0.045	6.267	3.031	2.149	1.686	1.247	1.089	1.01	0.832	0.741	0.693	0.552	0.511	0.45
S3	1.01	0.215	interm.	-0.065	0.435	151.384	347.381	358.071	221.179	62.808	39.44	27.073	21.717	16.41	12.843	11.273	11.489
S3	1.01	0.286	interm.	-0.164	1.276	228.21	23.412	14.452	9.193	7.747	6.787	6.086	5.695	5.246	4.944	4.208	3.908
S3	1.01	0.357	interm.	-0.253	2.117	29.897	14.193	10.606	7.812	6.84	6.301	5.635	5.355	5.01	4.694	4.135	3.822
S3	1.01	0.429	pole-on	-0.328	3.144	24.063	13.666	10.777	8.058	7.195	6.6	6.035	5.73	5.376	5.09	4.543	4.205
S3	1.01	0.5	pole-on	-0.39	4.346	24.963	14.47	11.659	8.816	7.91	7.29	6.647	6.428	6.007	5.654	5.131	4.755
S3	1.01	0.571	pole-on	-0.441	5.768	27.239	16.323	12.962	9.74	8.819	8.199	7.481	7.191	6.718	6.336	5.846	5.432
S3	1.01	0.643	pole-on	-0.482	7.331	30.281	18.426	14.544	10.946	9.979	9.224	8.377	8.162	7.628	7.126	6.68	6.275
S3	1.01	0.714	pole-on	-0.516	9.023	34.865	20.674	16.473	12.254	11.276	10.393	9.443	9.29	8.52	8.033	7.577	7.368
S3	1.01	0.786	pole-on	-0.541	10.963	39.279	23.536	18.679	13.753	12.666	11.704	10.604	10.533	9.528	8.946	8.56	8.619
S3	1.01	0.857	pole-on	-0.562	12.755	44.847	26.765	21.383	15.488	14.127	13.011	11.909	11.967	10.561	9.931	9.596	10.343
S3	1.01	0.928	pole-on	-0.576	14.559	50.898	30.291	24.111	17.183	15.636	14.286	13.236	13.48	11.582	10.997	10.695	12.486
S3	1.01	1.0	pole-on	-0.584	16.079	56.76	33.892	27.139	19.095	16.996	15.521	14.613	15.097	12.597	12.002	11.686	14.84
S3	0.75	0.0	edge-on	0.165	1.775	5.494	3.369	2.7	2.136	1.821	1.665	1.492	1.357	1.259	1.08	1.005	0.952
S3	0.75	0.071	edge-on	0.119	2.456	4.959	2.993	2.441	1.918	1.685	1.532	1.376	1.254	1.162	0.989	0.912	0.887
S3	0.75	0.143	interm.	0.047	72.016	5.388	2.872	2.386	1.847	1.573	1.436	1.286	1.146	1.073	0.904	0.875	0.759
S3	0.75	0.215	interm.	-0.032	0.685	17.847	77.842	149.225	325.394	365.041	331.854	289.993	262.962	204.098	97.153	52.742	64.379
S3	0.75	0.286	interm.	-0.109	1.136	345.504	41.878	23.186	12.506	9.728	8.656	7.193	6.914	6.044	5.33	4.98	5.139
S3	0.75	0.357	interm.	-0.179	1.948	43.177	16.252	12.497	8.97	7.897	7.24	6.4	6.239	5.558	5.167	4.745	5.053
S3	0.75	0.429	pole-on	-0.24	2.887	28.932	15.466	12.545	9.535	8.418	7.746	6.99	6.845	6.187	5.65	5.304	5.681
S3	0.75	0.5	pole-on	-0.291	3.921	29.464	16.81	13.661	10.721	9.386	8.665	7.875	7.684	6.974	6.492	6.06	6.592
S3	0.75	0.571	pole-on	-0.333	5.038	32.02	18.914	15.51	12.029	10.694	9.853	9.001	8.833	8.027	7.397	6.964	7.643
S3	0.75	0.643	pole-on	-0.368	6.354	35.716	21.497	17.722	13.815	12.139	11.267	10.241	10.217	9.13	8.506	8.01	8.944
S3	0.75	0.714	pole-on	-0.394	7.659	41.145	24.85	20.467	15.744	13.961	12.855	11.634	11.682	10.342	9.714	9.065	10.43
S3	0.75	0.786	pole-on	-0.415	9.066	47.395	28.637	23.681	18.128	15.857	14.599	13.137	13.464	11.629	11.075	10.245	12.214
S3	0.75	0.857	pole-on	-0.431	10.391	54.232	33.036	27.19	20.428	17.723	16.25	14.728	15.468	12.974	12.448	11.464	14.259
S3	0.75	0.928	pole-on	-0.441	11.596	62.61	38.185	31.331	22.754	19.621	17.781	16.492	17.603	14.177	14.04	12.637	16.49
S3	0.75	1.0	pole-on	-0.446	12.551	69.219	42.721	34.972	24.963	21.146	19.222	18.238	19.792	15.284	15.522	13.819	18.775

Table A.3 - continued.

Star	Σ_0 [g cm ⁻²]	cos i	$\tilde{\tau}_{\text{bu}}$ ang. type	bu		0.15	0.45	0.75	1.50	2.25	3.00	4.50	6.00	9.00	15.00	30.00	∞
				$\Delta R_{\text{bu}}^\infty$	ξ_{bu}^R	ξ_{d}^R											
S3	0.56	0.0	edge-on	0.133	2.1	6.909	4.034	3.269	2.46	2.172	1.958	1.729	1.549	1.415	1.241	1.112	1.12
S3	0.56	0.071	edge-on	0.099	2.323	5.869	3.63	2.973	2.262	1.961	1.841	1.596	1.416	1.324	1.149	1.079	1.022
S3	0.56	0.143	interm.	0.047	5.323	6.27	3.823	3.064	2.564	2.174	2.046	1.782	1.633	1.465	1.314	1.17	1.137
S3	0.56	0.215	interm.	-0.006	98.48	48.064	32.346	18.991	42.695	131.568	101.633	177.814	325.464	273.318	306.937	326.084	373.702
S3	0.56	0.286	interm.	-0.068	0.981	328.351	275.117	50.522	15.956	11.161	9.296	7.426	7.616	5.605	4.98	4.885	5.381
S3	0.56	0.357	interm.	-0.12	1.845	126.827	19.059	13.57	9.561	8.011	7.282	6.532	6.56	5.664	5.161	4.765	5.429
S3	0.56	0.429	pole-on	-0.167	2.715	32.915	17.008	13.465	10.08	8.868	8.113	7.374	7.344	6.424	5.999	5.654	6.194
S3	0.56	0.5	pole-on	-0.207	3.784	32.283	18.408	15.034	11.622	9.911	9.269	8.435	8.506	7.481	7.037	6.566	7.439
S3	0.56	0.571	pole-on	-0.239	4.983	34.506	20.734	17.3	13.187	11.722	10.798	9.734	9.922	8.661	8.151	7.665	8.782
S3	0.56	0.643	pole-on	-0.265	6.506	39.788	24.248	20.008	15.64	13.616	12.572	11.355	11.621	10.078	9.502	8.942	10.536
S3	0.56	0.714	pole-on	-0.286	8.105	44.793	28.466	23.614	17.874	15.787	14.458	12.903	13.746	11.585	11.012	10.262	12.46
S3	0.56	0.786	pole-on	-0.301	9.968	54.121	33.28	27.307	20.79	18.063	16.659	14.915	15.71	13.025	12.526	11.637	14.831
S3	0.56	0.857	pole-on	-0.313	11.856	61.256	38.49	32.436	23.579	20.393	18.695	16.754	18.111	14.394	14.281	13.066	17.49
S3	0.56	0.928	pole-on	-0.32	13.922	70.824	44.232	37.067	26.438	22.53	20.286	18.873	20.888	15.957	16.164	14.451	20.506
S3	0.56	1.0	pole-on	-0.321	15.411	79.81	49.902	41.553	28.885	24.547	22.101	20.728	23.474	17.186	17.873	15.712	23.55
S3	0.41	0.0	edge-on	0.105	2.427	8.698	4.803	3.771	2.964	2.414	2.245	1.981	1.757	1.638	1.413	1.304	1.214
S3	0.41	0.071	edge-on	0.08	2.71	7.933	4.574	3.501	2.755	2.301	2.111	1.854	1.712	1.528	1.357	1.241	1.17
S3	0.41	0.143	interm.	0.043	7.445	10.59	4.949	4.085	3.28	2.735	2.519	2.333	2.201	2.01	1.766	1.552	1.555
S3	0.41	0.215	interm.	0.007	333.075	59.533	17.523	10.113	19.306	18.251	43.639	44.982	47.865	36.603	45.399	97.2	128.88
S3	0.41	0.286	interm.	-0.036	1.278	267.83	329.431	251.665	89.12	33.193	8.92	6.602	6.563	4.511	3.538	3.435	4.308
S3	0.41	0.357	interm.	-0.074	1.731	251.3	21.281	14.2	8.071	7.318	6.136	5.604	5.601	4.801	4.267	3.859	4.731
S3	0.41	0.429	pole-on	-0.108	2.579	39.259	16.665	13.197	9.651	8.31	7.476	6.735	6.959	5.956	5.462	5.043	5.949
S3	0.41	0.5	pole-on	-0.136	3.614	32.946	17.615	14.937	11.161	9.844	9.137	8.122	8.172	7.207	6.807	6.195	7.421
S3	0.41	0.571	pole-on	-0.159	4.768	35.288	21.558	18.008	13.371	11.717	10.635	9.721	9.995	8.772	8.182	7.561	9.213
S3	0.41	0.643	pole-on	-0.178	6.198	40.287	24.982	20.951	15.965	13.964	12.866	11.551	12.067	10.519	9.543	9.117	11.116
S3	0.41	0.714	pole-on	-0.193	7.859	46.985	30.09	24.682	18.787	16.835	15.104	13.226	14.173	11.819	11.318	10.544	13.699
S3	0.41	0.786	pole-on	-0.204	9.64	54.519	35.35	29.793	22.211	18.767	17.637	15.292	16.683	13.502	13.028	12.066	16.398
S3	0.41	0.857	pole-on	-0.211	11.548	64.428	41.225	34.702	25.58	21.807	19.61	17.421	19.65	15.194	14.98	13.736	19.8
S3	0.41	0.928	pole-on	-0.215	13.925	75.523	49.161	40.439	28.423	24.155	21.648	19.874	23.044	16.652	16.903	15.248	23.614
S3	0.41	1.0	pole-on	-0.215	15.405	84.909	54.794	46.141	31.872	26.266	23.612	22.097	26.136	18.345	18.971	16.761	27.18
S3	0.3	0.0	edge-on	0.083	2.738	11.146	5.776	4.479	3.536	2.827	2.522	2.266	2.023	1.836	1.588	1.478	1.405
S3	0.3	0.071	edge-on	0.065	2.946	11.526	5.577	4.296	3.334	2.714	2.506	2.195	1.965	1.755	1.585	1.431	1.352
S3	0.3	0.143	interm.	0.038	6.151	32.57	6.733	5.037	3.919	3.443	3.298	3.081	2.627	2.57	2.436	2.136	2.05
S3	0.3	0.215	interm.	0.011	258.681	108.756	35.583	27.638	28.321	10.69	28.17	12.691	20.98	24.884	47.17	38.056	33.244
S3	0.3	0.286	interm.	-0.016	36.733	285.486	351.892	289.83	302.828	255.101	163.407	102.901	66.299	63.9	27.776	17.91	15.12

Table A.3 - continued.

Star	Σ_0 [g cm ⁻²]	$\cos i$	$\tilde{\tau}_{\text{bu}}$ ang. type	bu		0.15	0.45	0.75	1.50	2.25	3.00	4.50	6.00	9.00	15.00	30.00	∞
				$\Delta R_{\text{bu}}^\infty$	ξ_{bu}^R	ξ_{d}^R											
S3	0.3	0.357	interm.	-0.044	6.538	299.593	89.591	16.511	6.79	6.159	4.706	4.767	4.52	3.574	3.429	2.947	3.449
S3	0.3	0.429	pole-on	-0.068	2.34	102.95	15.375	11.219	8.182	7.11	5.985	5.7	5.962	4.873	4.494	4.36	5.056
S3	0.3	0.5	pole-on	-0.087	3.465	33.147	16.447	13.274	9.85	8.817	7.88	7.414	7.474	6.363	6.12	5.672	6.49
S3	0.3	0.571	pole-on	-0.102	4.59	33.046	19.643	16.391	12.28	11.167	9.785	9.102	9.416	7.866	7.668	7.049	8.585
S3	0.3	0.643	pole-on	-0.116	6.123	40.372	24.034	20.057	15.284	13.374	12.032	10.924	11.483	9.675	9.183	8.747	10.611
S3	0.3	0.714	pole-on	-0.126	7.57	47.655	30.016	24.782	17.844	16.102	14.574	13.131	13.679	11.363	10.898	10.273	13.022
S3	0.3	0.786	pole-on	-0.133	9.682	57.568	35.664	29.712	21.445	19.029	17.342	15.256	16.567	12.954	12.82	11.781	16.479
S3	0.3	0.857	pole-on	-0.137	11.867	67.902	42.214	35.192	25.556	22.08	19.388	17.999	19.594	14.977	15.107	13.587	20.005
S3	0.3	0.928	pole-on	-0.14	13.972	78.273	49.504	41.57	28.276	24.006	21.262	20.408	23.851	16.182	17.133	14.933	24.394
S3	0.3	1.0	pole-on	-0.138	15.822	91.102	57.142	47.459	31.915	26.726	23.673	23.09	26.81	18.255	19.193	17.09	28.878

Table A.4 - Empirical law parameters for band I.

Star	Σ_0 [g cm ⁻²]	cos i	$\tilde{\tau}_{bu}$ ang. type	bu		0.15	0.45	0.75	1.50	2.25	3.00	4.50	6.00	9.00	15.00	30.00	∞
				ΔI_{bu}^∞	ξ_{bu}^I	ξ_d^I											
S1	2.5	0.0	edge-on	0.454	1.063	1.4	1.252	1.121	0.938	0.839	0.784	0.697	0.648	0.579	0.5	0.45	0.432
S1	2.5	0.071	edge-on	0.12	21.853	1.984	0.539	0.486	0.388	0.314	0.307	0.263	0.232	0.215	0.212	0.207	0.203
S1	2.5	0.143	interm.	-0.293	1.018	15.196	5.665	4.093	2.891	2.515	2.124	1.799	1.665	1.441	1.226	1.063	1.043
S1	2.5	0.215	interm.	-0.569	1.8	6.039	3.318	2.664	2.013	1.753	1.532	1.303	1.21	1.063	0.911	0.79	0.78
S1	2.5	0.286	interm.	-0.77	2.737	5.139	3.12	2.5	1.9	1.638	1.446	1.234	1.141	1.007	0.868	0.756	0.868
S1	2.5	0.357	pole-on	-0.925	3.853	5.263	3.152	2.514	1.902	1.632	1.448	1.243	1.135	1.015	0.877	0.765	0.753
S1	2.5	0.429	pole-on	-1.043	5.234	5.594	3.253	2.572	1.943	1.666	1.482	1.275	1.175	1.047	0.904	0.795	0.781
S1	2.5	0.5	pole-on	-1.138	6.636	5.966	3.384	2.676	2.012	1.723	1.537	1.324	1.221	1.094	0.946	0.832	0.814
S1	2.5	0.571	pole-on	-1.215	8.027	6.356	3.551	2.789	2.1	1.798	1.606	1.386	1.279	1.148	0.996	0.879	0.858
S1	2.5	0.643	pole-on	-1.278	9.42	6.795	3.744	2.937	2.21	1.887	1.69	1.463	1.349	1.214	1.054	0.934	0.911
S1	2.5	0.714	pole-on	-1.329	10.785	7.3	3.975	3.099	2.333	1.991	1.784	1.552	1.432	1.29	1.118	0.994	0.968
S1	2.5	0.786	pole-on	-1.369	11.997	7.798	4.221	3.293	2.47	2.112	1.897	1.647	1.523	1.371	1.187	1.06	1.242
S1	2.5	0.857	pole-on	-1.402	13.18	8.419	4.494	3.499	2.62	2.239	2.009	1.755	1.621	1.461	1.258	1.124	1.11
S1	2.5	0.928	pole-on	-1.428	14.278	9.06	4.806	3.727	2.785	2.38	2.14	1.871	1.725	1.545	1.34	1.194	1.206
S1	2.5	1.0	pole-on	-1.447	15.159	9.688	5.102	3.948	2.954	2.52	2.264	1.978	1.82	1.631	1.421	1.277	1.269
S1	1.85	0.0	edge-on	0.376	1.057	1.527	1.391	1.221	1.051	0.946	0.875	0.804	0.748	0.645	0.558	0.504	0.487
S1	1.85	0.071	edge-on	0.11	1.211	13.371	0.598	0.558	0.456	0.394	0.361	0.316	0.281	0.225	0.209	0.205	0.206
S1	1.85	0.143	interm.	-0.23	0.98	27.056	9.613	6.069	4.224	3.401	3.017	2.374	2.253	2.178	1.89	1.599	1.543
S1	1.85	0.215	interm.	-0.477	1.698	9.667	4.557	3.536	2.688	2.266	2.034	1.698	1.613	1.5	1.296	1.132	1.086
S1	1.85	0.286	interm.	-0.666	2.549	7.51	4.16	3.266	2.502	2.119	1.92	1.617	1.526	1.41	1.218	1.079	1.039
S1	1.85	0.357	pole-on	-0.813	3.598	7.418	4.19	3.3	2.505	2.126	1.922	1.651	1.547	1.422	1.228	1.096	1.055
S1	1.85	0.429	pole-on	-0.928	4.876	7.79	4.335	3.399	2.573	2.187	1.982	1.715	1.602	1.457	1.273	1.135	1.096
S1	1.85	0.5	pole-on	-1.017	6.34	8.279	4.547	3.56	2.684	2.287	2.075	1.803	1.681	1.534	1.335	1.191	1.152
S1	1.85	0.571	pole-on	-1.09	7.787	8.817	4.815	3.741	2.82	2.404	2.184	1.91	1.775	1.617	1.407	1.265	1.22
S1	1.85	0.643	pole-on	-1.151	9.238	9.437	5.109	3.974	2.995	2.548	2.319	2.031	1.89	1.722	1.506	1.343	1.306
S1	1.85	0.714	pole-on	-1.2	10.659	10.138	5.44	4.242	3.185	2.722	2.472	2.18	2.014	1.834	1.592	1.434	1.393
S1	1.85	0.786	pole-on	-1.239	11.945	10.899	5.835	4.534	3.403	2.906	2.642	2.329	2.152	1.952	1.702	1.542	1.503
S1	1.85	0.857	pole-on	-1.27	13.224	11.762	6.251	4.867	3.649	3.113	2.821	2.483	2.294	2.085	1.834	1.665	1.624
S1	1.85	0.928	pole-on	-1.295	14.452	12.72	6.743	5.22	3.895	3.312	3.012	2.656	2.453	2.237	1.982	1.8	1.758
S1	1.85	1.0	pole-on	-1.313	15.43	13.716	7.204	5.565	4.121	3.496	3.194	2.834	2.618	2.402	2.128	1.939	1.897
S1	1.37	0.0	edge-on	0.301	1.077	1.777	1.637	1.427	1.198	1.06	0.964	0.88	0.812	0.734	0.637	0.574	0.562
S1	1.37	0.071	edge-on	0.097	1.136	5.749	0.748	0.69	0.547	0.499	0.409	0.363	0.336	0.295	0.239	0.228	0.211
S1	1.37	0.143	interm.	-0.177	0.966	49.409	15.458	9.703	6.163	4.976	4.504	3.984	3.513	3.179	2.777	2.453	2.414
S1	1.37	0.215	interm.	-0.398	1.562	15.069	6.292	4.759	3.553	2.99	2.801	2.457	2.207	2.046	1.796	1.594	1.548
S1	1.37	0.286	interm.	-0.571	2.324	10.896	5.49	4.308	3.297	2.785	2.613	2.288	2.072	1.921	1.66	1.514	1.465

Table A.4 - continued.

Star	Σ_0 [g cm ⁻²]	cos i	$\tilde{\tau}_{\text{bu}}$ ang. type	bu		0.15	0.45	0.75	1.50	2.25	3.00	4.50	6.00	9.00	15.00	30.00	∞
				$\Delta I_{\text{bu}}^{\infty}$	ξ_{bu}^I	ξ_{d}^I											
S1	1.37	0.357	pole-on	-0.709	3.299	10.117	5.51	4.366	3.33	2.825	2.643	2.318	2.107	1.947	1.689	1.539	1.493
S1	1.37	0.429	pole-on	-0.817	4.551	10.475	5.758	4.556	3.468	2.951	2.742	2.422	2.197	2.029	1.766	1.611	1.563
S1	1.37	0.5	pole-on	-0.902	5.972	11.121	6.086	4.813	3.652	3.113	2.884	2.552	2.332	2.144	1.863	1.702	1.672
S1	1.37	0.571	pole-on	-0.972	7.447	11.951	6.466	5.12	3.872	3.318	3.059	2.714	2.487	2.287	1.992	1.818	1.797
S1	1.37	0.643	pole-on	-1.029	8.994	12.839	6.946	5.489	4.156	3.565	3.271	2.902	2.67	2.449	2.147	1.968	1.95
S1	1.37	0.714	pole-on	-1.075	10.506	13.896	7.482	5.907	4.446	3.834	3.497	3.109	2.87	2.651	2.33	2.142	2.122
S1	1.37	0.786	pole-on	-1.112	11.955	15.041	8.086	6.374	4.761	4.116	3.739	3.34	3.08	2.873	2.532	2.334	2.32
S1	1.37	0.857	pole-on	-1.141	13.452	16.35	8.745	6.882	5.094	4.774	4.023	3.618	3.316	3.125	2.758	2.548	2.625
S1	1.37	0.928	pole-on	-1.164	14.701	17.828	9.432	7.363	5.482	4.722	4.348	3.904	3.599	3.388	3.008	2.782	2.775
S1	1.37	1.0	pole-on	-1.181	15.853	19.246	10.073	7.866	5.89	5.081	4.666	4.204	3.89	3.66	3.258	3.013	3.034
S1	1.01	0.0	edge-on	0.244	1.061	2.177	1.833	1.608	2.685	1.223	1.099	0.997	0.926	0.85	0.688	0.67	0.668
S1	1.01	0.071	edge-on	0.09	0.958	6.421	0.772	0.77	3.086	0.593	0.506	0.451	0.432	0.392	0.32	0.306	0.276
S1	1.01	0.143	interm.	-0.12	1.188	194.001	35.226	20.488	312.754	8.72	7.534	6.487	5.675	5.62	3.921	3.932	4.218
S1	1.01	0.215	interm.	-0.304	1.642	24.275	9.95	7.013	7.88	4.182	3.811	3.415	3.098	2.873	2.46	2.227	2.167
S1	1.01	0.286	interm.	-0.458	2.326	15.77	7.939	5.983	6.394	3.807	3.475	3.145	2.85	2.607	2.349	2.075	2.016
S1	1.01	0.357	pole-on	-0.585	3.201	14.069	7.762	6.012	6.035	3.866	3.546	3.19	2.931	2.639	2.448	2.144	2.065
S1	1.01	0.429	pole-on	-0.689	4.321	14.238	8.061	6.26	6.018	4.07	3.724	3.364	3.071	2.771	2.621	2.282	2.188
S1	1.01	0.5	pole-on	-0.768	5.733	15.057	8.507	6.652	6.191	4.332	3.963	3.578	3.287	2.963	2.833	2.48	2.344
S1	1.01	0.571	pole-on	-0.834	7.235	16.231	9.119	7.126	6.456	4.627	4.254	3.837	3.532	3.181	3.083	2.702	2.536
S1	1.01	0.643	pole-on	-0.888	8.849	17.579	9.815	7.679	6.776	4.995	4.578	4.167	3.835	3.486	3.364	2.973	2.769
S1	1.01	0.714	pole-on	-0.932	10.459	19.158	10.64	8.291	7.192	5.433	4.952	4.544	4.196	3.831	3.688	3.275	3.048
S1	1.01	0.786	pole-on	-0.967	12.031	20.903	11.497	8.933	7.625	5.896	5.386	4.951	4.586	4.218	4.036	3.613	3.347
S1	1.01	0.857	pole-on	-0.995	13.586	22.838	12.447	9.707	8.092	6.425	5.868	5.409	5.028	4.656	4.404	3.97	3.715
S1	1.01	0.928	pole-on	-1.017	15.027	25.077	13.568	10.567	8.608	7.001	6.386	5.896	5.506	5.132	4.785	4.344	4.118
S1	1.01	1.0	pole-on	-1.032	16.238	27.287	14.704	11.484	9.101	7.565	6.885	6.381	6.004	5.626	5.205	4.736	4.562
S1	0.75	0.0	edge-on	0.19	1.18	2.62	2.032	1.781	1.519	1.353	1.261	1.121	1.046	0.953	0.834	0.755	0.741
S1	0.75	0.071	edge-on	0.074	12.03	17.98	0.979	0.87	0.773	0.683	0.652	0.568	0.511	0.469	0.406	0.371	0.315
S1	0.75	0.143	interm.	-0.085	1.082	350.767	105.624	51.595	26.323	19.517	15.252	12.489	10.898	9.179	8.009	6.858	7.292
S1	0.75	0.215	interm.	-0.235	1.5	41.868	16.12	11.146	7.482	6.187	5.402	4.787	4.41	4.006	3.494	3.201	3.194
S1	0.75	0.286	interm.	-0.366	2.102	24.097	11.232	8.452	6.08	5.222	4.688	4.216	3.904	3.593	3.166	2.907	2.933
S1	0.75	0.357	pole-on	-0.479	2.891	19.926	10.418	8.131	6.025	5.248	4.725	4.291	3.984	3.672	3.272	2.987	3.083
S1	0.75	0.429	pole-on	-0.572	3.848	19.543	10.738	8.43	6.323	5.524	5.003	4.535	4.241	3.928	3.527	3.237	3.334
S1	0.75	0.5	pole-on	-0.647	4.963	20.183	11.386	8.959	6.765	5.912	5.386	4.894	4.601	4.288	3.876	3.56	3.66
S1	0.75	0.571	pole-on	-0.709	6.074	21.805	12.272	9.673	7.296	6.428	5.853	5.347	5.017	4.698	4.251	3.939	4.059
S1	0.75	0.643	pole-on	-0.76	7.184	23.721	13.318	10.553	7.998	7.037	6.419	5.874	5.554	5.178	4.71	4.367	4.508

Table A.4 - continued.

Star	Σ_0 [g cm ⁻²]	cos i	$\tilde{\tau}_{\text{bu}}$ ang. type	bu		0.15	0.45	0.75	1.50	2.25	3.00	4.50	6.00	9.00	15.00	30.00	∞
				$\Delta I_{\text{bu}}^{\infty}$	ξ_{bu}^I	ξ_{d}^I											
S1	0.75	0.714	pole-on	-0.801	8.261	26.17	14.523	11.528	8.762	7.733	7.056	6.467	6.137	5.692	5.195	4.827	5.001
S1	0.75	0.786	pole-on	-0.833	9.254	28.757	15.994	12.675	9.628	8.49	7.769	7.179	6.781	6.271	5.745	5.354	5.602
S1	0.75	0.857	pole-on	-0.858	10.177	31.976	17.593	14.019	10.591	9.314	8.538	7.818	7.492	6.88	6.332	5.906	6.188
S1	0.75	0.928	pole-on	-0.877	11.04	35.398	19.436	15.508	11.642	10.151	9.291	8.585	8.26	7.496	6.98	6.455	6.876
S1	0.75	1.0	pole-on	-0.89	11.737	38.964	21.295	16.981	12.647	10.982	10.011	9.352	9.026	8.104	7.611	7.023	7.566
S1	0.56	0.0	edge-on	0.15	1.225	3.699	2.573	2.222	1.806	1.55	1.445	1.312	1.213	1.101	0.977	0.883	0.853
S1	0.56	0.071	edge-on	0.066	1.019	7.318	1.449	1.196	0.969	0.849	0.79	0.715	0.634	0.608	0.49	0.461	0.41
S1	0.56	0.143	interm.	-0.051	1.928	381.264	376.479	318.794	140.186	63.793	43.878	34.391	30.578	22.931	22.407	17.355	17.879
S1	0.56	0.215	interm.	-0.169	1.753	76.124	25.621	17.641	11.45	9.317	8.209	7.028	6.62	5.953	5.379	4.908	4.769
S1	0.56	0.286	interm.	-0.276	2.23	36.449	15.365	11.395	8.156	7.095	6.375	5.645	5.381	4.882	4.482	4.096	4.082
S1	0.56	0.357	pole-on	-0.37	2.938	26.9	13.474	10.485	7.873	6.861	6.332	5.633	5.412	4.911	4.563	4.212	4.204
S1	0.56	0.429	pole-on	-0.451	3.856	24.868	13.617	10.793	8.291	7.261	6.708	6.009	5.809	5.317	4.931	4.553	4.619
S1	0.56	0.5	pole-on	-0.518	4.976	25.507	14.452	11.627	8.929	7.887	7.26	6.547	6.34	5.819	5.395	5.014	5.123
S1	0.56	0.571	pole-on	-0.572	6.317	27.646	15.744	12.676	9.81	8.63	8.038	7.251	7.028	6.437	6.025	5.563	5.744
S1	0.56	0.643	pole-on	-0.617	7.779	30.497	17.428	13.986	10.843	9.631	8.851	8.009	7.795	7.143	6.659	6.221	6.452
S1	0.56	0.714	pole-on	-0.654	9.35	33.969	19.37	15.662	12.038	10.638	9.811	8.858	8.684	7.923	7.39	6.884	7.269
S1	0.56	0.786	pole-on	-0.682	11.087	37.998	21.666	17.489	13.429	11.789	10.847	9.821	9.686	8.747	8.217	7.608	8.145
S1	0.56	0.857	pole-on	-0.704	12.776	42.524	24.218	19.527	14.819	12.987	11.954	10.859	10.792	9.562	9.06	8.382	9.139
S1	0.56	0.928	pole-on	-0.72	14.442	47.534	27.139	21.745	16.371	14.201	12.943	11.906	12.031	10.408	9.997	9.144	10.252
S1	0.56	1.0	pole-on	-0.73	15.886	52.197	29.865	24.07	17.791	15.26	13.935	12.984	13.188	11.188	10.878	9.93	11.384
S1	0.41	0.0	edge-on	0.118	1.42	5.001	3.209	2.676	2.154	1.908	1.74	2.565	1.439	1.33	1.114	1.057	1.005
S1	0.41	0.071	edge-on	0.058	1.26	7.226	1.847	1.485	1.222	1.203	1.07	0.923	0.817	0.803	0.663	0.587	0.56
S1	0.41	0.143	interm.	-0.024	19.26	369.438	357.644	393.141	351.139	357.482	353.622	302.004	283.801	265.512	222.534	194.568	207.02
S1	0.41	0.215	interm.	-0.113	1.817	312.347	52.736	32.552	20.401	15.359	13.298	11.684	10.861	9.077	8.346	7.607	7.534
S1	0.41	0.286	interm.	-0.195	2.225	62.018	23.286	16.296	11.517	9.453	8.617	7.674	7.429	6.519	5.956	5.614	5.702
S1	0.41	0.357	pole-on	-0.268	2.85	39.753	18.258	13.866	10.402	8.815	8.155	7.416	7.347	6.356	5.985	5.602	5.784
S1	0.41	0.429	pole-on	-0.334	3.667	32.578	17.605	13.909	10.72	9.227	8.532	7.793	7.626	6.759	6.419	5.984	6.278
S1	0.41	0.5	pole-on	-0.388	4.654	33.179	18.63	14.903	11.606	10.062	9.345	8.523	8.372	7.472	7.052	6.735	7.01
S1	0.41	0.571	pole-on	-0.434	5.824	34.908	20.25	16.527	12.853	11.167	10.364	9.421	9.33	8.364	7.878	7.391	7.928
S1	0.41	0.643	pole-on	-0.471	7.189	38.581	22.517	18.37	14.289	12.5	11.578	10.535	10.51	9.327	8.772	8.256	9.063
S1	0.41	0.714	pole-on	-0.502	8.75	43.351	25.333	20.882	16.095	13.988	12.959	11.715	11.757	10.32	9.842	9.174	10.328
S1	0.41	0.786	pole-on	-0.525	10.491	48.54	28.75	23.443	18.084	15.607	14.47	13.023	13.349	11.457	10.943	10.194	11.702
S1	0.41	0.857	pole-on	-0.543	12.243	54.903	32.614	26.456	20.038	17.202	15.854	14.426	14.888	12.536	12.111	11.167	13.415
S1	0.41	0.928	pole-on	-0.555	14.107	61.094	36.506	29.774	22.042	18.768	17.249	15.899	16.683	13.608	13.382	12.205	15.182
S1	0.41	1.0	pole-on	-0.561	15.566	67.4	40.623	32.816	24.04	20.264	18.406	17.321	18.492	14.572	14.667	13.166	17.017

Table A.4 - continued.

Star	Σ_0 [g cm ⁻²]	cos i	$\tilde{\tau}_{bu}$ ang. type	bu		0.15	0.45	0.75	1.50	2.25	3.00	4.50	6.00	9.00	15.00	30.00	∞
				ΔI_{bu}^∞	ξ_{bu}^I	ξ_d^I											
S1	0.3	0.0	edge-on	0.092	1.707	7.568	4.105	3.496	2.656	2.303	2.062	1.894	1.741	1.532	1.327	1.267	1.21
S1	0.3	0.071	edge-on	0.049	1.586	8.412	2.515	2.172	1.697	1.519	1.328	1.226	1.121	0.977	0.887	0.809	0.739
S1	0.3	0.143	interm.	-0.006	262.998	257.732	207.881	87.268	147.275	153.166	130.709	269.441	209.981	190.875	284.33	292.273	354.845
S1	0.3	0.215	interm.	-0.069	1.859	396.074	236.68	110.909	41.262	31.431	24.993	21.607	19.627	16.916	14.718	12.524	14.065
S1	0.3	0.286	interm.	-0.129	2.179	215.382	37.138	24.661	15.45	12.908	11.356	10.226	9.904	8.659	7.837	7.128	7.936
S1	0.3	0.357	pole-on	-0.183	2.751	60.082	24.264	17.647	12.707	10.745	10.037	8.913	8.908	7.856	7.28	6.734	7.325
S1	0.3	0.429	pole-on	-0.232	3.488	43.245	22.176	16.803	12.704	11.053	10.214	9.237	9.257	8.209	7.724	7.192	7.91
S1	0.3	0.5	pole-on	-0.273	4.304	40.066	22.831	17.971	13.596	11.966	11.141	10.156	10.269	9.011	8.435	7.918	8.907
S1	0.3	0.571	pole-on	-0.307	5.368	41.783	24.477	19.909	15.235	13.367	12.394	11.355	11.433	10.063	9.526	8.862	10.097
S1	0.3	0.643	pole-on	-0.336	6.594	46.368	27.482	22.245	17.147	15.059	13.931	12.499	12.951	11.282	10.618	10.028	11.656
S1	0.3	0.714	pole-on	-0.359	7.96	51.09	31.072	25.5	19.415	16.995	15.611	13.963	14.822	12.564	11.967	11.101	13.472
S1	0.3	0.786	pole-on	-0.377	9.498	57.514	35.559	29.133	22.032	19.194	17.58	15.74	16.833	13.897	13.356	12.313	15.538
S1	0.3	0.857	pole-on	-0.39	11.176	64.91	40.502	33.482	24.631	21.068	19.246	17.429	18.969	15.252	14.897	13.509	18.006
S1	0.3	0.928	pole-on	-0.398	12.903	73.11	46.018	37.939	26.893	22.956	20.727	19.14	21.514	16.277	16.478	14.759	20.714
S1	0.3	1.0	pole-on	-0.4	14.353	80.199	50.037	41.993	29.199	24.651	22.154	20.954	23.719	17.483	18.02	15.85	23.311
S2	2.5	0.0	edge-on	0.427	1.019	1.518	1.332	1.2	1.034	0.917	0.842	0.752	0.703	0.638	0.56	0.502	0.476
S2	2.5	0.071	edge-on	0.145	1.35	0.716	0.688	0.624	0.514	0.448	0.394	0.337	0.315	0.268	0.238	0.217	0.208
S2	2.5	0.143	interm.	-0.211	0.698	53.819	15.003	8.81	5.323	4.468	3.792	3.331	2.968	2.705	2.199	2.056	1.997
S2	2.5	0.215	interm.	-0.467	1.428	11.553	4.895	3.771	2.776	2.435	2.176	1.921	1.756	1.61	1.352	1.249	1.209
S2	2.5	0.286	interm.	-0.656	2.271	8.026	4.256	3.352	2.507	2.201	1.969	1.741	1.601	1.464	1.236	1.145	1.109
S2	2.5	0.357	pole-on	-0.801	3.303	7.676	4.258	3.337	2.488	2.169	1.96	1.73	1.591	1.451	1.234	1.141	1.103
S2	2.5	0.429	pole-on	-0.912	4.599	7.945	4.373	3.427	2.558	2.222	2.015	1.759	1.635	1.493	1.329	1.176	1.136
S2	2.5	0.5	pole-on	-1.002	5.953	8.399	4.574	3.566	2.663	2.313	2.094	1.846	1.711	1.562	1.337	1.23	1.191
S2	2.5	0.571	pole-on	-1.075	7.326	8.902	4.831	3.773	2.803	2.438	2.206	1.943	1.796	1.647	1.416	1.302	1.258
S2	2.5	0.643	pole-on	-1.134	8.725	9.54	5.144	4.008	2.976	2.594	2.34	2.06	1.92	1.758	1.513	1.384	1.339
S2	2.5	0.714	pole-on	-1.181	10.101	10.265	5.511	4.281	3.178	2.758	2.501	2.208	2.054	1.872	1.615	1.481	1.43
S2	2.5	0.786	pole-on	-1.218	11.375	11.046	5.911	4.59	3.398	2.953	2.677	2.369	2.199	2.001	1.727	1.592	1.536
S2	2.5	0.857	pole-on	-1.248	12.603	11.931	6.343	4.939	3.644	3.158	2.87	2.532	2.348	2.134	1.844	1.718	1.657
S2	2.5	0.928	pole-on	-1.272	13.723	12.941	6.844	5.305	3.911	3.382	3.055	2.699	2.5	2.28	1.984	1.859	1.795
S2	2.5	1.0	pole-on	-1.288	14.698	13.931	7.344	5.661	4.164	3.576	3.237	2.866	2.669	2.452	2.137	2.003	1.937
S2	1.85	0.0	edge-on	0.344	1.04	1.745	1.472	1.345	1.144	1.019	1.649	1.212	0.784	0.712	0.614	0.561	0.537
S2	1.85	0.071	edge-on	0.135	1.175	0.867	0.8	0.743	0.618	0.53	0.563	0.471	0.373	0.341	0.275	0.251	0.239
S2	1.85	0.143	interm.	-0.146	0.769	309.93	38.392	18.141	9.437	6.731	9.322	6.918	4.602	4.285	3.672	3.306	3.169
S2	1.85	0.215	interm.	-0.371	1.444	18.92	7.449	5.391	3.836	3.199	4.182	3.443	2.386	2.238	1.941	1.749	1.692
S2	1.85	0.286	interm.	-0.547	2.192	11.748	5.9	4.584	3.399	2.902	3.528	2.885	2.176	2.012	1.761	1.589	1.548

Table A.4 - continued.

Star	Σ_0 [g cm ⁻²]	cos i	$\tilde{\tau}_{\text{bu}}$ ang. type	bu		0.15	0.45	0.75	1.50	2.25	3.00	4.50	6.00	9.00	15.00	30.00	∞
				$\Delta I_{\text{bu}}^{\infty}$	ξ_{bu}^I	ξ_{d}^I											
S2	1.85	0.357	pole-on	-0.685	3.181	10.582	5.785	4.54	3.382	2.892	3.358	2.793	2.188	2.016	1.76	1.597	1.55
S2	1.85	0.429	pole-on	-0.793	4.367	10.744	5.992	4.682	3.49	2.999	3.361	2.835	2.28	2.094	1.826	1.679	1.611
S2	1.85	0.5	pole-on	-0.878	5.705	11.346	6.259	4.926	3.686	3.163	3.462	2.947	2.409	2.195	1.924	1.751	1.706
S2	1.85	0.571	pole-on	-0.948	7.124	12.113	6.667	5.223	3.916	3.364	3.624	3.105	2.566	2.341	2.05	1.87	1.823
S2	1.85	0.643	pole-on	-1.005	8.556	13.01	7.144	5.606	4.201	3.625	3.842	3.321	2.758	2.508	2.201	2.015	1.98
S2	1.85	0.714	pole-on	-1.051	9.995	14.082	7.684	6.019	4.511	3.897	4.094	3.563	2.955	2.704	2.377	2.19	2.156
S2	1.85	0.786	pole-on	-1.086	11.38	15.284	8.298	6.507	4.86	4.194	4.384	3.831	3.18	2.931	2.585	2.386	2.358
S2	1.85	0.857	pole-on	-1.115	12.68	16.616	8.979	7.009	5.212	4.494	4.7	4.142	3.434	3.187	2.818	2.608	2.583
S2	1.85	0.928	pole-on	-1.137	13.931	18.143	9.691	7.517	5.583	4.835	5.065	4.483	3.715	3.463	3.085	2.849	2.834
S2	1.85	1.0	pole-on	-1.153	14.941	19.676	10.375	8.058	5.984	5.213	5.413	4.836	4.0	3.751	3.331	3.094	3.093
S2	1.37	0.0	edge-on	0.276	1.064	2.222	1.669	1.493	1.284	1.16	1.071	0.953	0.889	0.808	0.693	0.634	0.619
S2	1.37	0.071	edge-on	0.119	1.11	1.164	0.905	0.812	0.706	0.626	0.596	0.505	0.45	0.425	0.347	0.307	0.295
S2	1.37	0.143	interm.	-0.098	0.773	360.567	214.455	58.226	23.045	16.313	13.143	10.171	9.481	8.067	6.891	6.106	5.662
S2	1.37	0.215	interm.	-0.287	1.383	31.803	11.997	8.246	5.581	4.756	4.238	3.719	3.435	3.127	2.778	2.527	2.441
S2	1.37	0.286	interm.	-0.443	2.088	17.436	8.372	6.418	4.638	4.046	3.66	3.251	3.007	2.755	2.424	2.232	2.158
S2	1.37	0.357	pole-on	-0.569	2.971	14.45	7.879	6.206	4.615	4.022	3.651	3.271	3.028	2.765	2.439	2.252	2.184
S2	1.37	0.429	pole-on	-0.671	4.107	14.473	8.108	6.412	4.791	4.195	3.798	3.407	3.161	2.892	2.563	2.369	2.312
S2	1.37	0.5	pole-on	-0.751	5.429	15.193	8.548	6.774	5.083	4.436	4.031	3.614	3.374	3.099	2.744	2.55	2.498
S2	1.37	0.571	pole-on	-0.817	6.825	16.312	9.151	7.258	5.434	4.724	4.305	3.899	3.635	3.346	2.972	2.778	2.727
S2	1.37	0.643	pole-on	-0.87	8.393	17.691	9.854	7.799	5.837	5.091	4.643	4.197	3.945	3.645	3.256	3.052	2.995
S2	1.37	0.714	pole-on	-0.913	9.908	19.269	10.701	8.415	6.297	5.523	5.046	4.585	4.305	3.989	3.575	3.354	3.322
S2	1.37	0.786	pole-on	-0.946	11.45	21.055	11.574	9.087	6.825	5.994	5.493	4.996	4.721	4.373	3.93	3.691	3.653
S2	1.37	0.857	pole-on	-0.972	12.917	23.01	12.53	9.893	7.45	6.56	5.981	5.477	5.171	4.787	4.318	4.074	4.035
S2	1.37	0.928	pole-on	-0.993	14.277	25.369	13.635	10.825	8.14	7.138	6.526	5.975	5.678	5.219	4.742	4.448	4.458
S2	1.37	1.0	pole-on	-1.007	15.437	27.722	14.893	11.762	8.826	7.713	7.035	6.491	6.174	5.662	5.152	4.846	4.879
S2	1.01	0.0	edge-on	0.217	1.134	2.859	2.026	1.702	3.005	1.33	1.199	1.078	1.012	0.917	0.823	0.729	0.725
S2	1.01	0.071	edge-on	0.103	1.154	1.475	1.198	1.041	1.211	0.795	0.714	0.628	0.575	0.51	0.431	0.389	0.386
S2	1.01	0.143	interm.	-0.058	0.85	368.933	364.626	340.066	167.139	60.072	42.972	33.082	27.503	22.452	16.792	15.109	15.449
S2	1.01	0.215	interm.	-0.21	1.442	61.551	19.531	12.999	20.885	7.07	6.239	5.619	5.118	4.608	4.024	3.691	3.595
S2	1.01	0.286	interm.	-0.343	2.053	27.42	11.779	8.7	12.837	5.469	5.007	4.487	4.166	3.816	3.362	3.117	3.015
S2	1.01	0.357	pole-on	-0.454	2.849	20.41	10.599	8.214	10.723	5.325	4.906	4.44	4.141	3.878	3.411	3.154	3.058
S2	1.01	0.429	pole-on	-0.547	3.887	19.243	10.733	8.444	10.186	5.592	5.133	4.664	4.395	4.044	3.647	3.383	3.291
S2	1.01	0.5	pole-on	-0.621	5.13	20.075	11.409	8.95	10.271	5.965	5.508	5.03	4.74	4.39	3.978	3.697	3.592
S2	1.01	0.571	pole-on	-0.68	6.524	21.679	12.272	9.7	10.745	6.488	5.978	5.489	5.209	4.825	4.373	4.078	3.972
S2	1.01	0.643	pole-on	-0.73	8.055	23.65	13.359	10.582	11.463	7.134	6.564	6.034	5.725	5.295	4.831	4.514	4.411

Table A.4 - continued.

Star	Σ_0 [g cm ⁻²]	cos i	$\tilde{\tau}_{bu}$ ang. type	bu		0.15	0.45	0.75	1.50	2.25	3.00	4.50	6.00	9.00	15.00	30.00	∞
				ΔI_{bu}^∞	ξ_{bu}^I	ξ_d^I											
S2	1.01	0.714	pole-on	-0.77	9.65	26.017	14.681	11.561	12.465	7.823	7.223	6.633	6.315	5.902	5.321	5.002	4.931
S2	1.01	0.786	pole-on	-0.8	11.272	28.77	16.168	12.747	13.686	8.613	7.949	7.291	6.988	6.435	5.877	5.53	5.534
S2	1.01	0.857	pole-on	-0.824	12.854	31.991	17.866	14.15	15.111	9.477	8.723	8.028	7.728	7.058	6.472	6.083	6.226
S2	1.01	0.928	pole-on	-0.843	14.343	35.663	19.893	15.677	16.932	10.364	9.503	8.806	8.537	7.71	7.085	6.685	6.987
S2	1.01	1.0	pole-on	-0.854	15.648	39.201	21.883	17.245	18.547	11.255	10.268	9.636	9.367	8.338	7.706	7.27	7.806
S2	0.75	0.0	edge-on	0.172	1.277	3.82	2.488	2.158	1.722	1.529	1.417	1.259	1.162	1.057	0.934	0.859	0.831
S2	0.75	0.071	edge-on	0.089	1.417	2.289	1.449	1.354	1.096	0.974	0.909	0.804	0.731	0.681	0.574	0.544	0.474
S2	0.75	0.143	interm.	-0.027	17.157	340.71	341.251	334.517	357.927	327.209	368.398	315.749	334.291	289.413	172.27	131.98	135.304
S2	0.75	0.215	interm.	-0.148	1.407	232.811	37.709	24.071	14.534	11.516	9.96	8.57	8.04	7.02	6.203	5.661	5.562
S2	0.75	0.286	interm.	-0.255	1.974	41.962	16.955	12.329	8.672	7.481	6.762	6.011	5.677	5.157	4.619	4.293	4.338
S2	0.75	0.357	pole-on	-0.349	2.674	28.193	13.75	10.753	8.107	7.062	6.457	5.816	5.548	5.067	4.589	4.317	4.339
S2	0.75	0.429	pole-on	-0.429	3.559	25.072	13.798	10.886	8.417	7.376	6.753	6.121	5.891	5.396	4.931	4.652	4.712
S2	0.75	0.5	pole-on	-0.495	4.584	25.659	14.54	11.628	9.011	7.965	7.341	6.659	6.447	5.911	5.413	5.134	5.228
S2	0.75	0.571	pole-on	-0.548	5.723	27.46	15.814	12.736	9.867	8.753	8.066	7.35	7.127	6.532	6.002	5.677	5.824
S2	0.75	0.643	pole-on	-0.591	6.953	30.174	17.486	14.101	10.93	9.749	8.943	8.107	7.911	7.238	6.668	6.32	6.568
S2	0.75	0.714	pole-on	-0.627	8.177	33.836	19.513	15.727	12.187	10.763	9.93	9.037	8.851	8.049	7.436	7.026	7.41
S2	0.75	0.786	pole-on	-0.654	9.391	38.041	21.756	17.565	13.521	11.941	10.958	9.999	9.89	8.85	8.27	7.772	8.351
S2	0.75	0.857	pole-on	-0.674	10.542	42.526	24.516	19.727	15.058	13.172	12.121	11.077	11.041	9.734	9.167	8.58	9.396
S2	0.75	0.928	pole-on	-0.689	11.6	47.892	27.505	22.127	16.661	14.47	13.167	12.219	12.29	10.595	10.15	9.396	10.532
S2	0.75	1.0	pole-on	-0.698	12.437	52.744	30.506	24.585	18.215	15.638	14.213	13.314	13.601	11.426	11.107	10.179	11.778
S2	0.56	0.0	edge-on	0.136	1.463	5.058	3.071	2.595	2.027	1.8	1.658	1.493	1.337	1.241	1.085	0.989	0.956
S2	0.56	0.071	edge-on	0.077	1.44	3.237	2.052	1.668	1.364	1.22	1.154	1.016	0.902	0.843	0.743	0.671	0.63
S2	0.56	0.143	interm.	-0.005	272.023	138.955	130.118	21.999	57.785	125.824	102.085	158.814	160.852	183.146	207.901	261.9	384.925
S2	0.56	0.215	interm.	-0.097	1.471	375.635	129.786	49.43	28.347	21.308	17.846	14.542	13.798	11.709	10.261	9.194	9.309
S2	0.56	0.286	interm.	-0.18	1.99	87.426	25.367	17.413	12.022	10.03	9.002	7.965	7.731	6.733	6.143	5.68	5.987
S2	0.56	0.357	pole-on	-0.255	2.65	40.046	18.238	13.968	10.337	8.877	8.144	7.306	7.128	6.423	5.88	5.535	5.867
S2	0.56	0.429	pole-on	-0.321	3.46	33.582	17.286	13.596	10.495	9.215	8.406	7.719	7.474	6.768	6.296	5.917	6.242
S2	0.56	0.5	pole-on	-0.375	4.467	31.951	17.893	14.568	11.366	9.979	9.16	8.347	8.237	7.415	6.925	6.518	6.961
S2	0.56	0.571	pole-on	-0.419	5.687	34.471	19.78	16.044	12.459	11.026	10.217	9.265	9.146	8.229	7.703	7.237	7.834
S2	0.56	0.643	pole-on	-0.456	7.055	37.507	21.955	18.024	13.907	12.295	11.416	10.343	10.306	9.221	8.601	8.137	8.92
S2	0.56	0.714	pole-on	-0.485	8.537	42.563	24.785	20.22	15.601	13.819	12.75	11.51	11.582	10.245	9.649	9.055	10.13
S2	0.56	0.786	pole-on	-0.508	10.179	47.488	28.023	22.966	17.601	15.509	14.207	12.833	13.056	11.318	10.815	10.038	11.625
S2	0.56	0.857	pole-on	-0.525	11.885	53.992	31.842	26.088	19.687	17.125	15.708	14.191	14.644	12.441	11.983	11.061	13.281
S2	0.56	0.928	pole-on	-0.536	13.631	60.335	35.983	29.353	21.696	18.724	16.94	15.731	16.524	13.519	13.315	12.057	15.093
S2	0.56	1.0	pole-on	-0.541	15.049	66.842	40.098	32.975	23.739	20.177	18.348	17.271	18.294	14.501	14.537	13.105	16.986

Table A.4 - continued.

Star	Σ_0 [g cm ⁻²]	cos i	$\tilde{\tau}_{\text{bu}}$ ang. type	bu		0.15	0.45	0.75	1.50	2.25	3.00	4.50	6.00	9.00	15.00	30.00	∞
				$\Delta I_{\text{bu}}^{\infty}$	ξ_{bu}^I	ξ_{d}^I											
S2	0.41	0.0	edge-on	0.107	1.778	7.37	4.022	3.151	2.389	2.147	1.919	1.731	1.63	1.508	1.27	1.162	1.118
S2	0.41	0.071	edge-on	0.066	1.839	6.877	2.895	2.19	1.763	1.561	1.405	1.245	1.165	1.066	0.926	0.852	0.777
S2	0.41	0.143	interm.	0.006	218.244	173.68	8.838	10.744	2.003	2.321	2.345	2.753	6.179	1.137	3.384	13.625	9.71
S2	0.41	0.215	interm.	-0.056	2.272	402.819	352.642	294.352	127.967	65.303	41.882	34.841	32.814	25.119	20.787	18.907	21.096
S2	0.41	0.286	interm.	-0.117	1.853	277.276	42.278	28.17	17.432	13.957	11.6	10.538	9.747	8.697	7.977	7.242	7.94
S2	0.41	0.357	pole-on	-0.172	2.478	53.924	23.783	17.247	12.426	10.93	9.617	8.752	8.624	7.642	7.006	6.63	7.24
S2	0.41	0.429	pole-on	-0.221	3.246	39.901	20.792	16.536	12.459	10.8	9.738	9.049	8.898	7.928	7.403	6.959	7.709
S2	0.41	0.5	pole-on	-0.262	4.157	37.358	21.374	17.364	13.253	11.663	10.578	9.818	9.797	8.706	8.151	7.702	8.626
S2	0.41	0.571	pole-on	-0.297	5.213	39.017	23.635	19.008	14.771	12.977	11.873	10.913	10.95	9.677	9.125	8.617	9.827
S2	0.41	0.643	pole-on	-0.325	6.512	43.192	26.29	21.513	16.468	14.689	13.369	12.236	12.47	10.938	10.287	9.684	11.341
S2	0.41	0.714	pole-on	-0.347	7.937	48.595	29.959	24.594	18.873	16.58	15.117	13.743	14.195	12.152	11.534	10.913	13.131
S2	0.41	0.786	pole-on	-0.364	9.559	54.779	34.303	28.491	21.424	18.851	17.02	15.178	16.164	13.538	12.951	12.031	15.199
S2	0.41	0.857	pole-on	-0.377	11.071	61.677	39.221	32.179	24.063	20.767	18.599	17.103	18.414	14.944	14.492	13.323	17.557
S2	0.41	0.928	pole-on	-0.384	13.059	70.288	44.618	36.932	26.353	22.574	20.434	18.896	20.945	16.049	16.04	14.503	20.22
S2	0.41	1.0	pole-on	-0.386	14.374	77.664	49.56	40.97	28.772	24.192	21.735	20.644	23.298	17.128	17.553	15.75	22.806
S2	0.3	0.0	edge-on	0.085	2.094	9.2	5.088	3.7	2.924	2.54	2.404	1.989	1.867	1.691	1.493	1.337	1.305
S2	0.3	0.071	edge-on	0.056	2.069	22.387	3.663	2.774	2.169	1.896	1.706	1.556	1.426	1.335	1.131	1.027	0.983
S2	0.3	0.143	interm.	0.015	28.663	86.052	22.89	3.341	1.782	1.562	1.544	2.58	1.766	0.987	0.784	0.74	1.279
S2	0.3	0.215	interm.	-0.026	15.087	312.214	385.12	376.617	349.31	344.988	304.981	282.656	268.111	266.812	170.255	118.163	134.329
S2	0.3	0.286	interm.	-0.069	1.763	319.228	166.416	54.149	24.306	18.569	15.181	13.252	13.048	10.681	9.368	8.708	9.934
S2	0.3	0.357	pole-on	-0.108	2.414	114.346	31.085	21.486	13.671	11.434	10.591	9.304	9.526	8.277	7.605	7.0	8.001
S2	0.3	0.429	pole-on	-0.143	3.078	46.652	23.809	18.574	13.094	11.268	10.452	9.506	9.761	8.472	7.893	7.346	8.589
S2	0.3	0.5	pole-on	-0.172	3.931	41.249	23.628	19.105	14.199	12.577	11.315	10.38	10.77	9.374	8.662	8.147	9.507
S2	0.3	0.571	pole-on	-0.197	4.914	43.395	25.467	21.194	16.051	13.756	12.85	11.564	11.996	10.542	9.847	9.172	11.013
S2	0.3	0.643	pole-on	-0.217	6.158	46.093	28.819	24.136	17.94	15.803	14.617	13.281	13.771	11.839	11.045	10.481	12.846
S2	0.3	0.714	pole-on	-0.233	7.516	51.475	33.141	27.749	20.786	18.108	16.677	14.801	15.686	13.442	12.63	11.843	15.162
S2	0.3	0.786	pole-on	-0.244	9.166	59.337	38.604	32.206	24.24	20.574	18.749	16.682	18.146	14.874	14.262	13.21	17.694
S2	0.3	0.857	pole-on	-0.253	10.858	68.774	43.889	36.467	26.768	23.182	20.859	18.712	20.718	16.298	15.995	14.649	20.951
S2	0.3	0.928	pole-on	-0.258	12.746	77.298	50.416	42.083	29.42	24.822	22.427	20.735	23.688	17.571	17.844	15.793	24.438
S2	0.3	1.0	pole-on	-0.257	14.215	85.198	54.973	46.554	32.295	27.125	23.932	22.913	26.258	18.895	19.601	17.212	27.863
S3	2.5	0.0	edge-on	0.394	1.031	1.557	1.371	1.239	1.037	0.961	0.904	0.802	0.737	0.679	0.604	0.545	0.516
S3	2.5	0.071	edge-on	0.172	1.311	0.891	0.798	0.703	0.61	0.575	0.538	0.469	0.413	0.362	0.297	0.271	0.248
S3	2.5	0.143	interm.	-0.131	0.505	355.747	111.373	32.372	12.431	9.071	7.634	6.227	5.662	4.734	4.174	3.626	3.637
S3	2.5	0.215	interm.	-0.367	1.247	18.304	7.083	5.165	3.749	3.169	2.837	2.556	2.494	2.111	1.867	1.674	1.658
S3	2.5	0.286	interm.	-0.547	2.03	10.622	5.459	4.227	3.199	2.725	2.469	2.234	2.068	1.856	1.639	1.478	1.461

Table A.4 - continued.

Star	Σ_0 [g cm ⁻²]	cos i	$\tilde{\tau}_{\text{bu}}$ ang. type	bu		0.15	0.45	0.75	1.50	2.25	3.00	4.50	6.00	9.00	15.00	30.00	∞
				$\Delta I_{\text{bu}}^{\infty}$	ξ_{bu}^I	ξ_{d}^I											
S3	2.5	0.357	pole-on	-0.687	2.991	9.48	5.289	4.139	3.135	2.686	2.439	2.204	2.039	1.837	1.62	1.455	1.443
S3	2.5	0.429	pole-on	-0.796	4.206	9.721	5.427	4.262	3.211	2.768	2.505	2.263	2.098	1.898	1.668	1.518	1.489
S3	2.5	0.5	pole-on	-0.88	5.552	10.248	5.672	4.458	3.361	2.9	2.639	2.373	2.195	1.991	1.752	1.593	1.56
S3	2.5	0.571	pole-on	-0.951	6.935	10.89	6.021	4.72	3.556	3.063	2.799	2.52	2.336	2.116	1.858	1.69	1.658
S3	2.5	0.643	pole-on	-1.008	8.339	11.722	6.444	5.041	3.795	3.278	2.994	2.682	2.497	2.256	1.979	1.807	1.775
S3	2.5	0.714	pole-on	-1.054	9.706	12.649	6.907	5.419	4.075	3.512	3.207	2.889	2.679	2.428	2.129	1.943	1.927
S3	2.5	0.786	pole-on	-1.089	11.053	13.719	7.459	5.844	4.422	3.789	3.453	3.096	2.872	2.599	2.291	2.105	2.087
S3	2.5	0.857	pole-on	-1.118	12.331	14.939	8.077	6.311	4.728	4.063	3.699	3.317	3.078	2.801	2.486	2.29	2.276
S3	2.5	0.928	pole-on	-1.14	13.495	16.308	8.739	6.799	5.048	4.367	3.957	3.573	3.324	3.04	2.708	2.5	2.491
S3	2.5	1.0	pole-on	-1.156	14.511	17.669	9.397	7.271	5.381	4.646	4.249	3.845	3.598	3.286	2.933	2.716	2.712
S3	1.85	0.0	edge-on	0.312	1.133	1.908	1.61	1.406	1.193	1.059	0.992	1.385	0.874	0.766	0.658	0.597	0.586
S3	1.85	0.071	edge-on	0.154	1.282	0.995	0.994	0.876	0.755	0.662	0.606	0.604	0.462	0.442	0.381	0.343	0.33
S3	1.85	0.143	interm.	-0.08	9.907	386.921	337.555	328.99	51.106	25.672	18.63	22.235	13.597	10.571	8.5	7.333	7.036
S3	1.85	0.215	interm.	-0.28	1.219	37.36	11.504	8.17	5.306	4.379	4.063	4.426	3.224	2.974	2.669	2.416	2.347
S3	1.85	0.286	interm.	-0.442	1.945	16.631	7.75	5.982	4.332	3.672	3.424	3.63	2.8	2.564	2.304	2.079	2.02
S3	1.85	0.357	pole-on	-0.572	2.844	13.631	7.239	5.752	4.24	3.658	3.369	3.519	2.802	2.561	2.263	2.063	2.018
S3	1.85	0.429	pole-on	-0.677	3.97	13.443	7.433	5.884	4.369	3.787	3.479	3.578	2.906	2.664	2.355	2.157	2.094
S3	1.85	0.5	pole-on	-0.756	5.315	14.024	7.785	6.197	4.643	4.019	3.682	3.738	3.088	2.824	2.495	2.283	2.243
S3	1.85	0.571	pole-on	-0.822	6.754	14.928	8.297	6.591	4.947	4.287	3.934	3.969	3.302	3.026	2.685	2.464	2.428
S3	1.85	0.643	pole-on	-0.876	8.25	16.175	8.942	7.081	5.324	4.629	4.232	4.257	3.563	3.29	2.914	2.708	2.658
S3	1.85	0.714	pole-on	-0.919	9.746	17.523	9.678	7.663	5.749	4.989	4.582	4.602	3.858	3.583	3.193	2.954	2.956
S3	1.85	0.786	pole-on	-0.952	11.239	19.085	10.525	8.269	6.198	5.385	4.975	4.96	4.183	3.913	3.497	3.247	3.225
S3	1.85	0.857	pole-on	-0.979	12.654	20.888	11.388	8.917	6.697	5.865	5.437	5.369	4.569	4.273	3.84	3.582	3.558
S3	1.85	0.928	pole-on	-1.0	13.975	22.869	12.356	9.683	7.291	6.382	5.932	5.825	4.958	4.665	4.213	3.922	3.928
S3	1.85	1.0	pole-on	-1.014	15.114	24.925	13.372	10.519	7.921	6.916	6.444	6.274	5.354	5.066	4.597	4.276	4.308
S3	1.37	0.0	edge-on	0.247	1.275	2.364	1.865	1.606	1.37	1.204	1.098	0.986	0.922	0.843	0.732	0.671	0.658
S3	1.37	0.071	edge-on	0.132	1.319	1.415	1.182	1.029	0.915	0.794	0.71	0.636	0.587	0.547	0.465	0.421	0.398
S3	1.37	0.143	interm.	-0.042	0.363	329.683	187.713	333.113	358.463	304.895	221.239	144.276	64.324	42.353	31.543	25.272	23.788
S3	1.37	0.215	interm.	-0.206	1.179	69.821	20.301	13.347	8.078	6.77	6.111	5.282	4.918	4.398	3.888	3.599	3.432
S3	1.37	0.286	interm.	-0.346	1.85	24.566	10.684	8.233	5.896	5.078	4.713	4.137	3.886	3.554	3.138	2.923	2.812
S3	1.37	0.357	pole-on	-0.462	2.656	18.497	9.642	7.589	5.647	4.963	4.581	4.065	3.827	3.507	3.116	2.907	2.829
S3	1.37	0.429	pole-on	-0.558	3.728	17.508	9.783	7.83	5.862	5.136	4.759	4.258	4.003	3.688	3.287	3.081	3.059
S3	1.37	0.5	pole-on	-0.632	5.009	18.242	10.354	8.29	6.226	5.471	5.063	4.565	4.298	3.963	3.559	3.357	3.309
S3	1.37	0.571	pole-on	-0.694	6.39	19.518	11.165	8.888	6.701	5.891	5.463	4.937	4.658	4.332	3.911	3.674	3.64
S3	1.37	0.643	pole-on	-0.744	7.933	21.439	12.087	9.64	7.261	6.413	5.962	5.405	5.136	4.746	4.288	4.059	4.037

Table A.4 - continued.

Star	Σ_0 [g cm ⁻²]	cos i	$\tilde{\tau}_{\text{bu}}$ ang. type	bu		0.15	0.45	0.75	1.50	2.25	3.00	4.50	6.00	9.00	15.00	30.00	∞
				$\Delta I_{\text{bu}}^{\infty}$	ξ_{bu}^I	ξ_{d}^I											
S3	1.37	0.714	pole-on	-0.785	9.493	23.375	13.14	10.459	7.969	7.041	6.537	5.931	5.643	5.217	4.745	4.487	4.485
S3	1.37	0.786	pole-on	-0.815	11.123	25.708	14.434	11.487	8.769	7.742	7.159	6.512	6.215	5.733	5.243	4.95	4.997
S3	1.37	0.857	pole-on	-0.84	12.647	28.512	15.864	12.664	9.646	8.501	7.871	7.173	6.868	6.3	5.783	5.455	5.559
S3	1.37	0.928	pole-on	-0.859	14.168	31.713	17.555	14.001	10.617	9.317	8.616	7.895	7.599	6.896	6.378	6.036	6.173
S3	1.37	1.0	pole-on	-0.871	15.442	35.148	19.376	15.356	11.62	10.146	9.313	8.617	8.341	7.487	6.985	6.556	6.823
S3	1.01	0.0	edge-on	0.196	1.415	3.302	2.157	1.902	1.549	1.339	1.285	1.118	1.043	0.92	0.705	0.719	0.766
S3	1.01	0.071	edge-on	0.112	1.461	2.114	1.548	1.222	1.053	0.933	0.894	0.771	0.712	0.636	0.521	0.492	0.511
S3	1.01	0.143	interm.	-0.011	86.852	66.19	53.3	90.994	126.957	159.528	97.415	177.626	275.382	371.677	371.207	368.948	330.415
S3	1.01	0.215	interm.	-0.141	1.18	327.171	37.047	24.943	14.889	11.385	9.6	8.568	7.83	6.831	5.936	5.627	5.423
S3	1.01	0.286	interm.	-0.255	1.807	39.77	15.474	11.677	8.258	7.087	6.289	5.67	5.32	4.918	4.537	4.089	3.855
S3	1.01	0.357	pole-on	-0.353	2.583	25.148	12.802	10.081	7.487	6.649	5.951	5.469	5.136	4.863	4.492	4.043	3.83
S3	1.01	0.429	pole-on	-0.438	3.516	22.711	12.746	10.162	7.729	6.846	6.278	5.73	5.448	5.155	4.781	4.373	4.088
S3	1.01	0.5	pole-on	-0.505	4.702	23.627	13.59	10.885	8.265	7.362	6.763	6.206	5.943	5.65	5.228	4.79	4.436
S3	1.01	0.571	pole-on	-0.56	6.058	25.221	14.686	11.87	8.98	8.081	7.428	6.853	6.518	6.192	5.757	5.341	4.905
S3	1.01	0.643	pole-on	-0.606	7.571	27.813	16.306	13.03	9.78	8.927	8.218	7.566	7.261	6.875	6.365	5.989	5.489
S3	1.01	0.714	pole-on	-0.642	9.181	31.029	18.019	14.427	10.794	9.914	9.093	8.378	8.092	7.58	7.041	6.729	6.17
S3	1.01	0.786	pole-on	-0.67	10.841	34.783	20.208	16.12	11.883	10.959	10.067	9.284	8.971	8.371	7.777	7.469	7.007
S3	1.01	0.857	pole-on	-0.692	12.524	38.939	22.644	18.099	13.143	12.134	11.112	10.291	10.042	9.175	8.549	8.283	8.052
S3	1.01	0.928	pole-on	-0.708	14.154	43.886	25.404	20.246	14.528	13.31	12.146	11.327	11.172	10.011	9.388	9.137	9.414
S3	1.01	1.0	pole-on	-0.718	15.515	48.891	28.279	22.471	15.84	14.46	13.149	12.415	12.334	10.828	10.162	9.978	11.02
S3	0.75	0.0	edge-on	0.156	3.06	4.352	2.816	2.335	1.811	1.581	1.469	1.293	1.171	1.08	0.932	0.862	0.82
S3	0.75	0.071	edge-on	0.095	1.735	3.088	1.939	1.674	1.327	1.159	1.066	0.968	0.854	0.804	0.686	0.626	0.577
S3	0.75	0.143	interm.	0.006	331.307	36.647	11.183	10.463	0.617	18.53	1.38	3.534	6.625	17.973	20.537	14.236	14.528
S3	0.75	0.215	interm.	-0.091	3.438	391.969	228.459	57.025	29.26	22.56	18.249	14.852	13.612	11.928	10.424	9.155	9.466
S3	0.75	0.286	interm.	-0.18	1.715	82.52	23.872	15.958	11.141	9.349	8.628	7.495	7.107	6.382	5.943	5.42	5.605
S3	0.75	0.357	pole-on	-0.26	2.424	35.567	16.747	12.595	9.568	8.305	7.621	6.956	6.629	6.088	5.621	5.222	5.442
S3	0.75	0.429	pole-on	-0.33	3.277	29.32	16.037	12.611	9.802	8.653	8.018	7.293	7.053	6.446	5.983	5.593	5.841
S3	0.75	0.5	pole-on	-0.387	4.246	29.025	16.736	13.529	10.544	9.386	8.658	7.973	7.694	7.062	6.563	6.178	6.524
S3	0.75	0.571	pole-on	-0.434	5.361	31.471	18.512	14.868	11.637	10.388	9.559	8.778	8.611	7.82	7.276	6.837	7.31
S3	0.75	0.643	pole-on	-0.473	6.581	34.816	20.699	16.659	13.022	11.626	10.716	9.799	9.662	8.75	8.181	7.671	8.272
S3	0.75	0.714	pole-on	-0.504	7.768	39.064	23.126	18.917	14.626	12.986	12.017	10.91	10.849	9.759	9.122	8.538	9.491
S3	0.75	0.786	pole-on	-0.528	9.07	44.233	26.264	21.328	16.791	14.515	13.348	12.209	12.188	10.78	10.221	9.489	10.772
S3	0.75	0.857	pole-on	-0.546	10.241	50.048	29.805	24.179	18.407	16.055	14.738	13.523	13.715	11.791	11.392	10.459	12.308
S3	0.75	0.928	pole-on	-0.558	11.376	56.329	33.654	27.469	20.423	17.598	16.122	14.937	15.502	12.834	12.598	11.494	13.966
S3	0.75	1.0	pole-on	-0.564	12.272	62.403	37.599	30.712	22.353	19.05	17.358	16.426	17.222	13.898	13.888	12.498	15.763

Table A.4 - continued.

Star	Σ_0 [g cm ⁻²]	cos i	$\tilde{\tau}_{bu}$ ang. type	bu		0.15	0.45	0.75	1.50	2.25	3.00	4.50	6.00	9.00	15.00	30.00	∞
				ΔI_{bu}^∞	ξ_{bu}^I	ξ_d^I											
S3	0.56	0.0	edge-on	0.126	2.039	5.87	3.326	2.869	2.127	1.883	1.682	1.462	1.339	1.237	1.078	0.956	0.932
S3	0.56	0.071	edge-on	0.082	2.254	4.444	2.372	2.039	1.61	1.435	1.265	1.113	1.008	0.954	0.821	0.731	0.703
S3	0.56	0.143	interm.	0.016	88.597	10.385	5.566	1.319	0.866	0.867	0.729	0.606	0.496	0.474	0.444	0.429	0.741
S3	0.56	0.215	interm.	-0.052	1.001	331.716	353.645	346.738	186.359	58.832	46.865	33.787	33.434	25.692	22.568	18.609	19.871
S3	0.56	0.286	interm.	-0.119	1.659	305.531	40.924	25.651	15.7	12.316	11.183	9.521	9.304	7.879	7.299	6.729	7.169
S3	0.56	0.357	pole-on	-0.181	2.324	51.874	21.578	16.007	11.623	9.898	9.281	8.258	8.006	7.133	6.58	6.279	6.702
S3	0.56	0.429	pole-on	-0.235	3.167	37.218	19.567	14.896	11.753	10.168	9.309	8.561	8.381	7.555	7.04	6.67	7.132
S3	0.56	0.5	pole-on	-0.28	4.148	34.691	20.093	16.212	12.568	11.031	10.197	9.351	9.27	8.299	7.809	7.36	8.092
S3	0.56	0.571	pole-on	-0.318	5.295	36.448	21.982	17.807	14.014	12.299	11.49	10.342	10.375	9.297	8.805	8.166	9.186
S3	0.56	0.643	pole-on	-0.349	6.627	40.531	24.59	20.25	15.69	13.867	12.907	11.673	11.811	10.429	9.85	9.277	10.586
S3	0.56	0.714	pole-on	-0.374	8.191	45.631	27.912	23.035	17.697	15.579	14.538	13.065	13.456	11.708	11.046	10.365	12.216
S3	0.56	0.786	pole-on	-0.393	9.822	51.88	31.928	26.225	20.343	17.673	16.274	14.571	15.286	12.893	12.362	11.438	14.172
S3	0.56	0.857	pole-on	-0.406	11.636	58.829	36.48	30.108	22.547	19.582	17.989	16.305	17.288	14.139	13.803	12.756	16.334
S3	0.56	0.928	pole-on	-0.415	13.412	66.617	41.572	34.426	25.089	21.41	19.482	17.994	19.628	15.318	15.428	13.912	18.872
S3	0.56	1.0	pole-on	-0.418	14.816	73.54	46.783	38.435	27.107	23.03	20.936	19.662	21.882	16.644	16.996	15.019	21.586
S3	0.41	0.0	edge-on	0.102	2.41	7.767	4.348	3.249	2.571	2.171	1.897	1.676	1.564	1.412	1.251	1.094	1.033
S3	0.41	0.071	edge-on	0.07	2.7	6.353	3.331	2.458	1.877	1.702	1.512	1.308	1.232	1.117	0.942	0.864	0.829
S3	0.41	0.143	interm.	0.023	22.766	27.121	2.725	2.133	1.581	1.429	1.233	1.071	0.963	0.859	0.725	0.613	0.62
S3	0.41	0.215	interm.	-0.024	5.515	255.471	264.821	315.4	339.96	361.019	322.734	305.578	272.437	296.26	245.389	191.993	162.864
S3	0.41	0.286	interm.	-0.071	1.534	360.395	172.611	44.942	23.101	18.209	14.909	12.309	11.041	9.989	8.92	8.02	9.064
S3	0.41	0.357	pole-on	-0.115	2.221	134.63	25.941	18.958	12.722	11.282	9.922	8.974	8.719	7.658	7.313	6.739	7.588
S3	0.41	0.429	pole-on	-0.154	3.017	44.534	20.907	16.705	12.745	10.855	10.037	9.245	9.08	8.2	7.58	7.127	8.05
S3	0.41	0.5	pole-on	-0.187	3.975	37.972	22.308	17.761	13.599	12.081	11.017	10.127	10.053	9.028	8.471	8.009	9.116
S3	0.41	0.571	pole-on	-0.215	5.026	40.4	23.967	20.05	15.302	13.682	12.391	11.337	11.433	10.13	9.606	9.019	10.589
S3	0.41	0.643	pole-on	-0.237	6.393	44.407	26.933	22.864	17.527	15.375	14.137	12.791	13.283	11.482	10.82	10.25	12.267
S3	0.41	0.714	pole-on	-0.256	7.937	50.186	31.271	26.031	20.105	17.714	16.285	14.442	15.187	12.919	12.336	11.51	14.464
S3	0.41	0.786	pole-on	-0.269	9.679	57.877	36.552	30.103	22.993	20.237	18.311	16.329	17.438	14.444	13.915	12.99	16.952
S3	0.41	0.857	pole-on	-0.278	11.432	65.73	42.375	34.617	25.723	22.479	20.271	18.403	20.189	15.81	15.548	14.185	19.832
S3	0.41	0.928	pole-on	-0.284	13.457	73.564	48.068	39.927	28.529	24.25	21.98	20.266	22.96	16.997	17.477	15.478	23.259
S3	0.41	1.0	pole-on	-0.284	14.72	83.029	53.384	45.304	31.218	26.106	23.527	22.286	25.72	18.47	19.202	16.934	26.69
S3	0.3	0.0	edge-on	0.082	15.313	10.277	4.996	3.731	3.003	2.563	2.208	1.96	1.745	1.601	1.434	1.24	1.206
S3	0.3	0.071	edge-on	0.059	2.989	10.465	4.166	3.066	2.405	2.09	1.778	1.638	1.447	1.271	1.139	1.044	0.983
S3	0.3	0.143	interm.	0.026	12.967	27.117	11.664	3.557	2.306	2.025	1.8	1.586	1.395	1.321	1.092	1.009	0.905
S3	0.3	0.215	interm.	-0.003	209.896	118.636	129.681	114.352	97.154	150.596	218.312	226.937	268.823	281.904	297.38	325.499	370.601
S3	0.3	0.286	interm.	-0.038	1.358	285.498	358.619	231.412	104.761	46.5	38.687	16.196	18.594	12.336	10.262	8.416	11.358

Table A.4 - continued.

Star	Σ_0 [g cm ⁻²]	$\cos i$	$\tilde{\tau}_{\text{bu}}$	ang. type	bu		0.15	0.45	0.75	1.50	2.25	3.00	4.50	6.00	9.00	15.00	30.00	∞
					$\Delta I_{\text{bu}}^\infty$	ξ_{bu}^I	ξ_{d}^I											
S3	0.3	0.357		pole-on	-0.068	2.107	276.818	38.972	24.38	13.669	11.446	9.822	9.063	8.924	7.653	6.878	6.39	7.563
S3	0.3	0.429		pole-on	-0.096	2.858	55.426	22.347	17.028	12.664	10.858	10.102	8.911	9.09	7.852	7.357	6.837	7.876
S3	0.3	0.5		pole-on	-0.119	3.761	39.24	21.958	18.275	13.603	11.713	11.088	9.909	10.013	8.833	8.269	7.808	9.392
S3	0.3	0.571		pole-on	-0.138	4.843	38.879	24.442	20.42	15.403	13.508	12.489	11.317	11.876	10.378	9.437	8.92	10.902
S3	0.3	0.643		pole-on	-0.154	6.292	44.199	28.503	23.322	18.059	15.605	14.594	12.808	13.629	11.708	11.192	10.414	13.009
S3	0.3	0.714		pole-on	-0.167	7.657	51.276	33.098	27.639	20.555	17.934	16.442	14.873	15.678	13.241	12.558	11.727	15.46
S3	0.3	0.786		pole-on	-0.175	9.429	59.954	39.476	32.346	24.34	20.823	19.089	16.714	18.258	14.774	14.494	13.208	18.527
S3	0.3	0.857		pole-on	-0.182	11.312	67.738	45.228	37.07	27.192	23.547	21.288	18.963	21.26	16.293	16.22	14.616	22.089
S3	0.3	0.928		pole-on	-0.185	13.282	78.588	51.55	43.563	30.5	25.321	23.048	21.081	24.774	17.634	18.403	16.014	26.138
S3	0.3	1.0		pole-on	-0.184	14.856	88.985	57.125	48.268	32.583	27.649	24.818	23.477	27.958	19.201	20.303	17.894	30.033

Appendix B

Examples of fittings of the empirical laws

Here we give examples of synthetic light curves fitted with Eqs. (4.3.7) and (4.3.8), with the η 's given by Table 4.4. The figures on this appendix have 8 panels disposed in 4 columns and 2 lines. The panels for the *BVRI* filters are, respectively, the panels of the first, second, third and fourth columns. In the panels from the first line, the synthetic light curves generated by HDUST are the dots connected by dashed segments and the best fit of the empirical law to the synthetic light curves are the solid curves. The panels from the second line show the residuals of the fit from the respective above panels.

In the following sections, each light curve is defined by the vector $(\text{Star}, i, \Sigma_0, \tilde{\tau}_{\text{bu}})$ (corresponding to one element of each column of Table 4.1). For simplicity, we decided to show only light curves of Star 2 (the light curves of the other stars are qualitatively similar).

B.1 $(\text{Star}, i, \Sigma_0, \tilde{\tau}_{\text{bu}}) = (\mathbf{Star\ 2}, *, \mathbf{1.37\ g\ cm^{-2}}, *)$

In this section, we fix Σ_0 and, varying i , we show three examples of fittings for each i (the examples are for $\tilde{\tau}_{\text{bu}} = \text{bu}, 1.5, 6$).

B.1.1 $(\text{Star}, i, \Sigma_0, \tilde{\tau}_{\text{bu}}) = (\text{Star 2}, \mathbf{90 \text{ deg}}, 1.37 \text{ g cm}^{-2}, *)$

Three examples of fittings for $i = 90 \text{ deg}$.

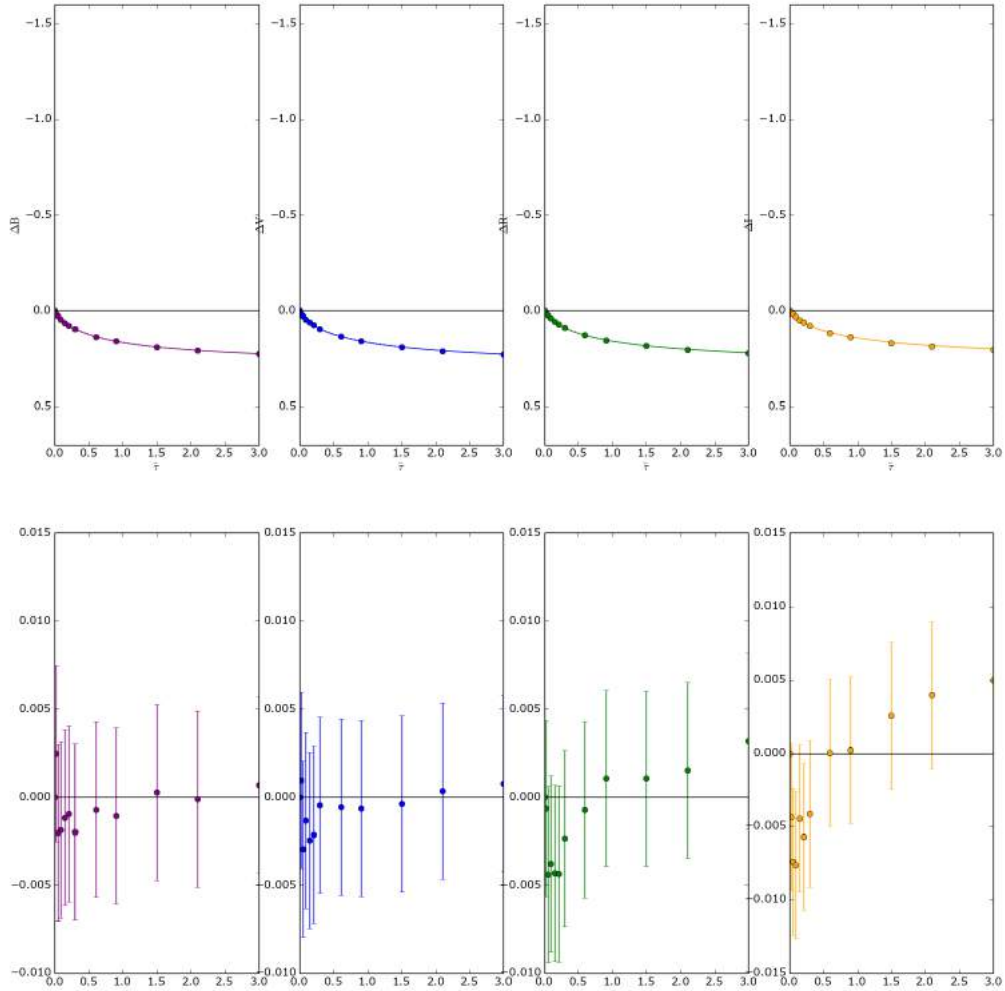
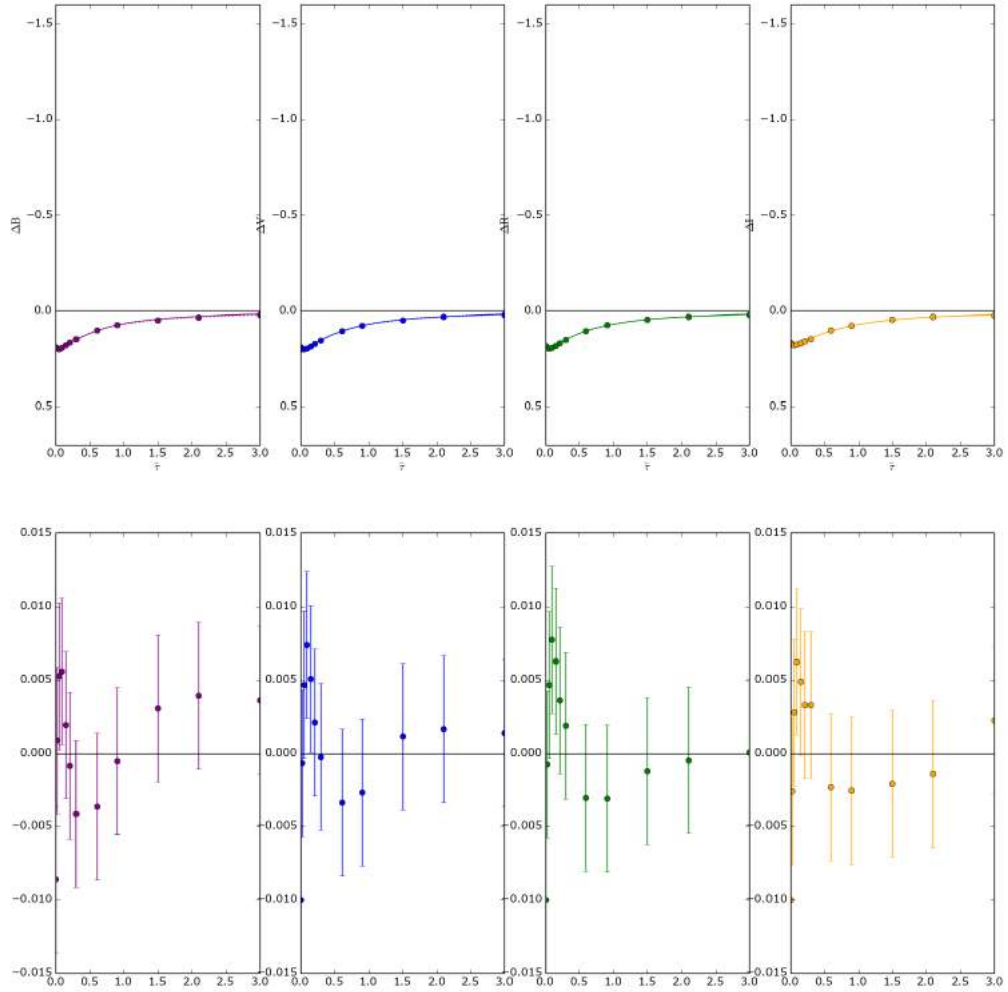


Figure B.1: $(\text{Star}, i, \Sigma_0, \tilde{\tau}_{\text{bu}}) = (\text{Star 2}, 90 \text{ deg}, 1.37 \text{ g cm}^{-2}, \text{bu})$

Figure B.2: $(\text{Star}, i, \Sigma_0, \tilde{\tau}_{\text{bu}}) = (\text{Star 2}, 90 \text{ deg}, 1.37 \text{ g cm}^{-2}, \mathbf{1.5})$

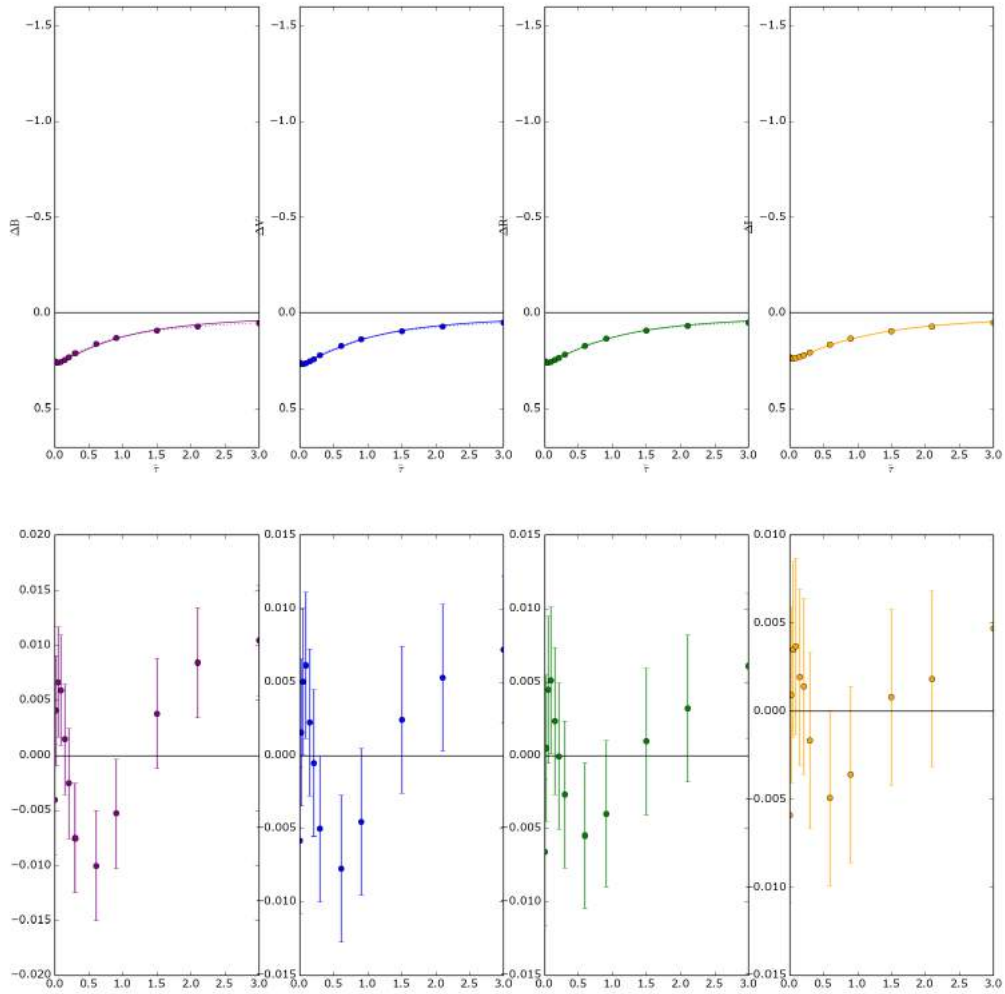


Figure B.3: $(\text{Star}, i, \Sigma_0, \tilde{\tau}_{\text{bu}}) = (\text{Star 2}, 90 \text{ deg}, 1.37 \text{ g cm}^{-2}, \mathbf{6})$

B.1.2 $(\text{Star}, i, \Sigma_0, \tilde{\tau}_{\text{bu}}) = (\text{Star 2}, \mathbf{69.1 \text{ deg}}, 1.37 \text{ g cm}^{-2}, *)$

Three examples of fittings for $i = 69.1 \text{ deg}$.

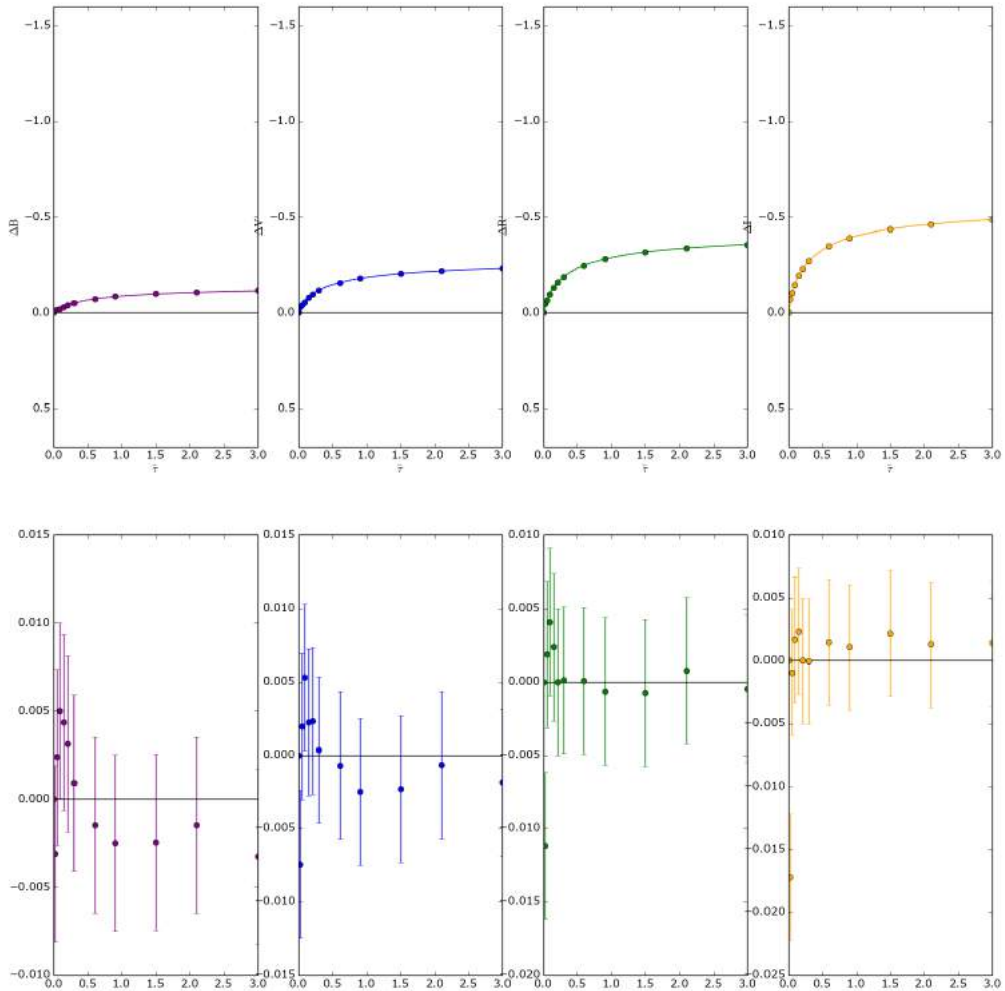


Figure B.4: $(\text{Star}, i, \Sigma_0, \tilde{\tau}_{\text{bu}}) = (\text{Star 2}, 69.1 \text{ deg}, 1.37 \text{ g cm}^{-2}, \text{bu})$

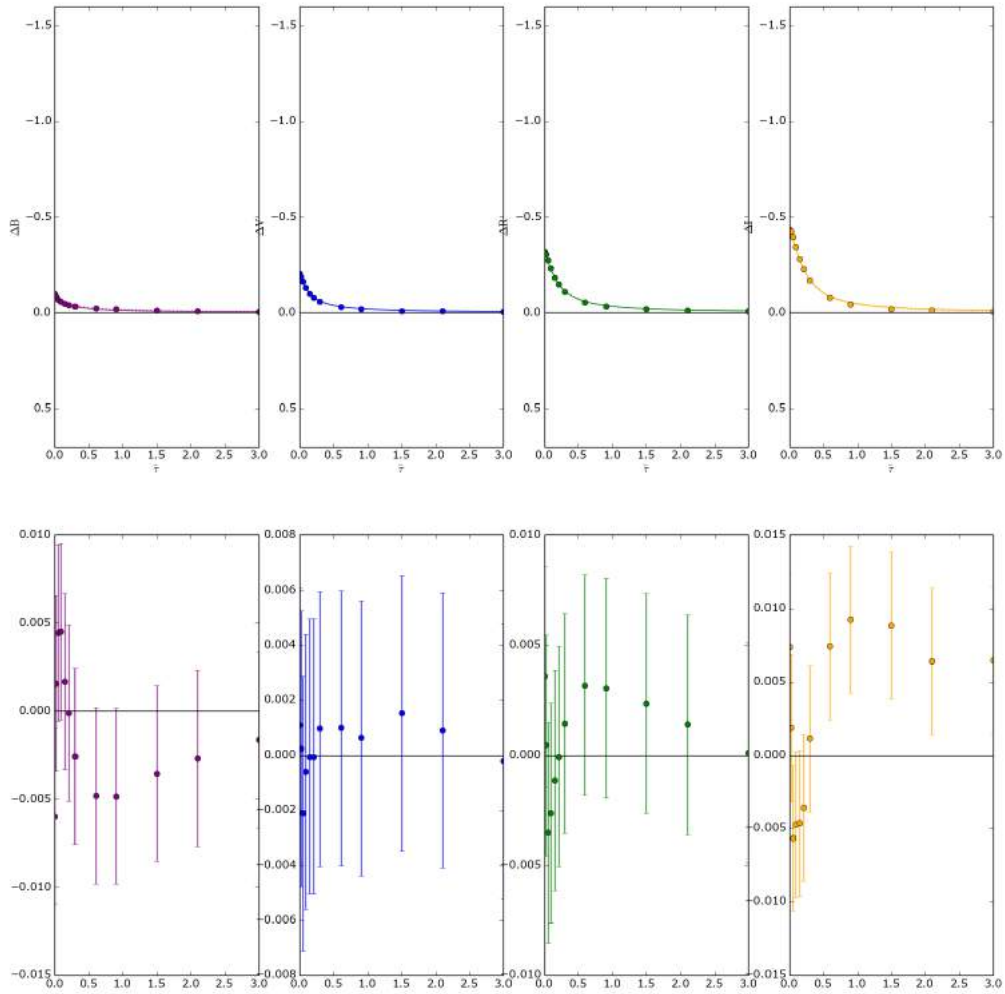


Figure B.5: $(\text{Star}, i, \Sigma_0, \tilde{\tau}_{\text{bu}}) = (\text{Star 2}, 69.1 \text{ deg}, 1.37 \text{ g cm}^{-2}, \mathbf{1.5})$

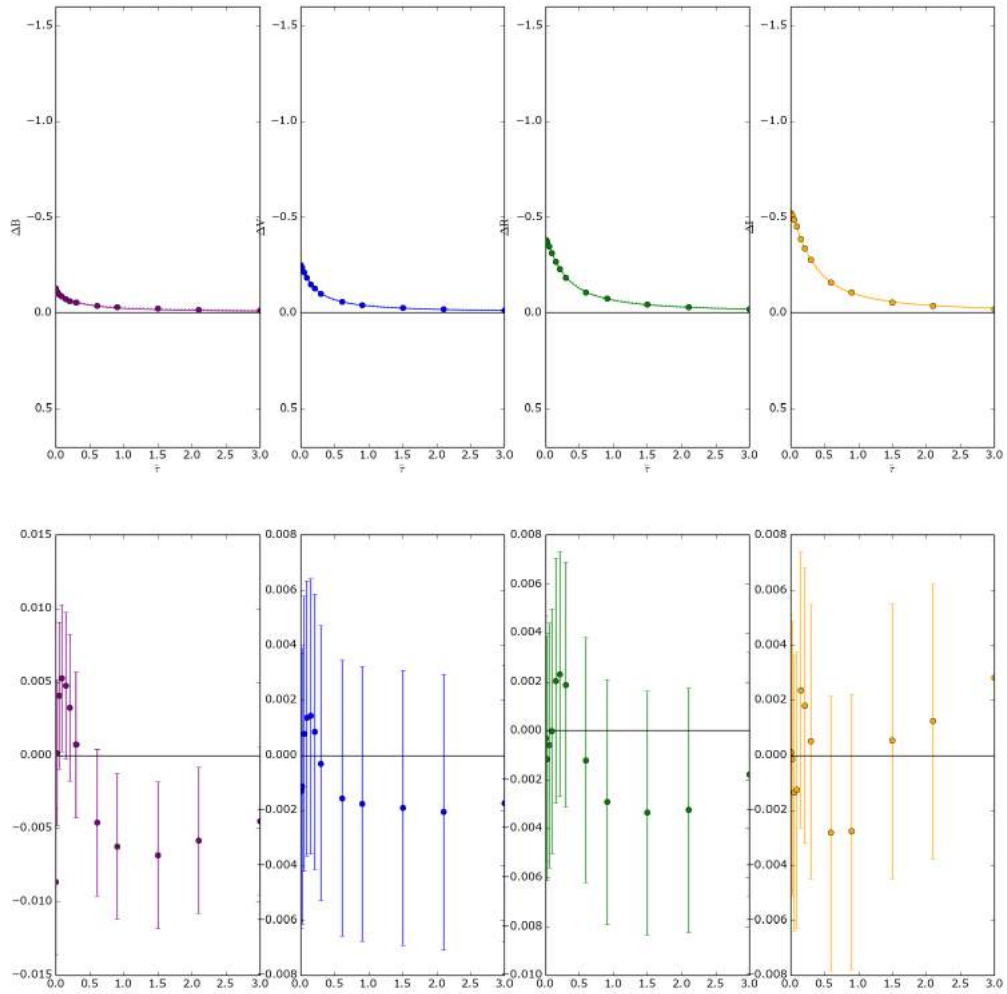


Figure B.6: $(\text{Star}, i, \Sigma_0, \tilde{\tau}_{\text{bu}}) = (\text{Star 2}, 69.1 \text{ deg}, 1.37 \text{ g cm}^{-2}, \mathbf{6})$

B.1.3 $(\text{Star}, i, \Sigma_0, \tilde{\tau}_{\text{bu}}) = (\text{Star 2}, \mathbf{0 \text{ deg}}, 1.37 \text{ g cm}^{-2}, *)$

Three examples of fittings for $i = 0 \text{ deg}$.

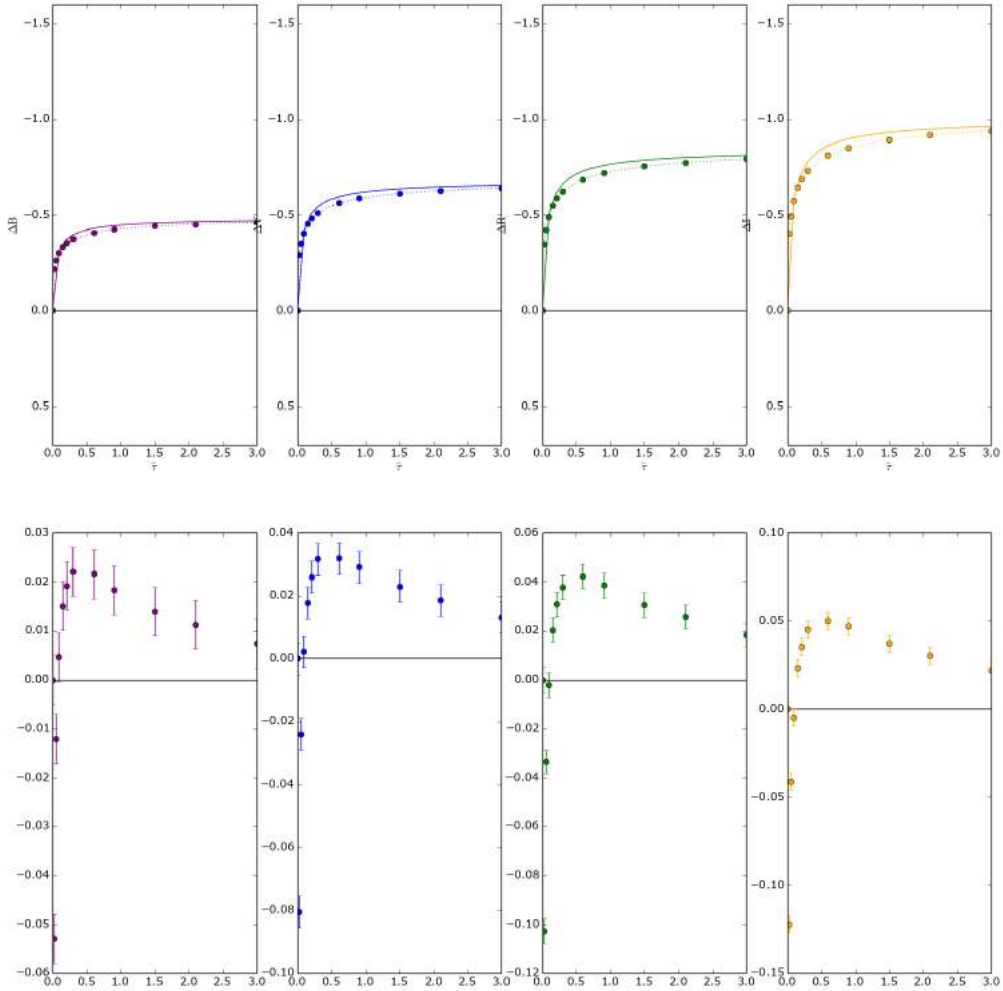
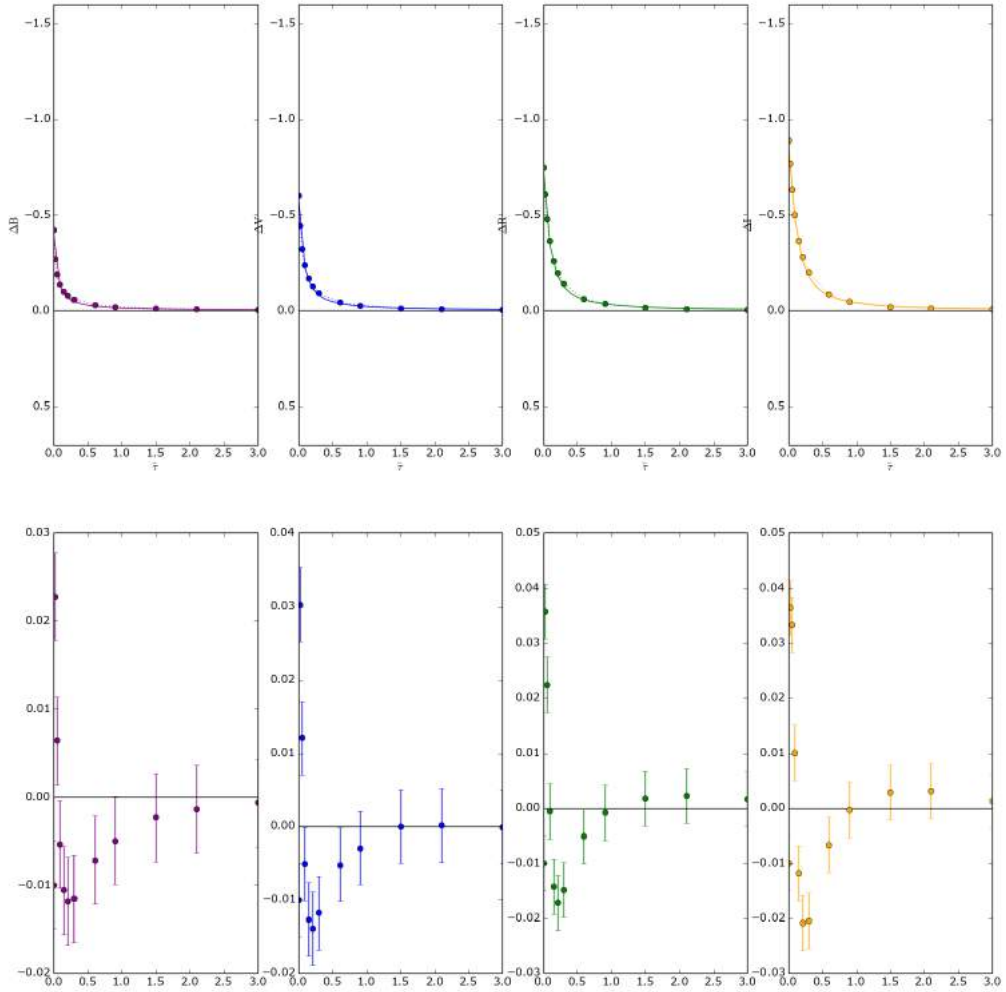


Figure B.7: $(\text{Star}, i, \Sigma_0, \tilde{\tau}_{\text{bu}}) = (\text{Star 2}, 0 \text{ deg}, 1.37 \text{ g cm}^{-2}, \text{bu})$

Figure B.8: $(\text{Star}, i, \Sigma_0, \tilde{\tau}_{\text{bu}}) = (\text{Star 2}, 0 \text{ deg}, 1.37 \text{ g cm}^{-2}, 1.5)$

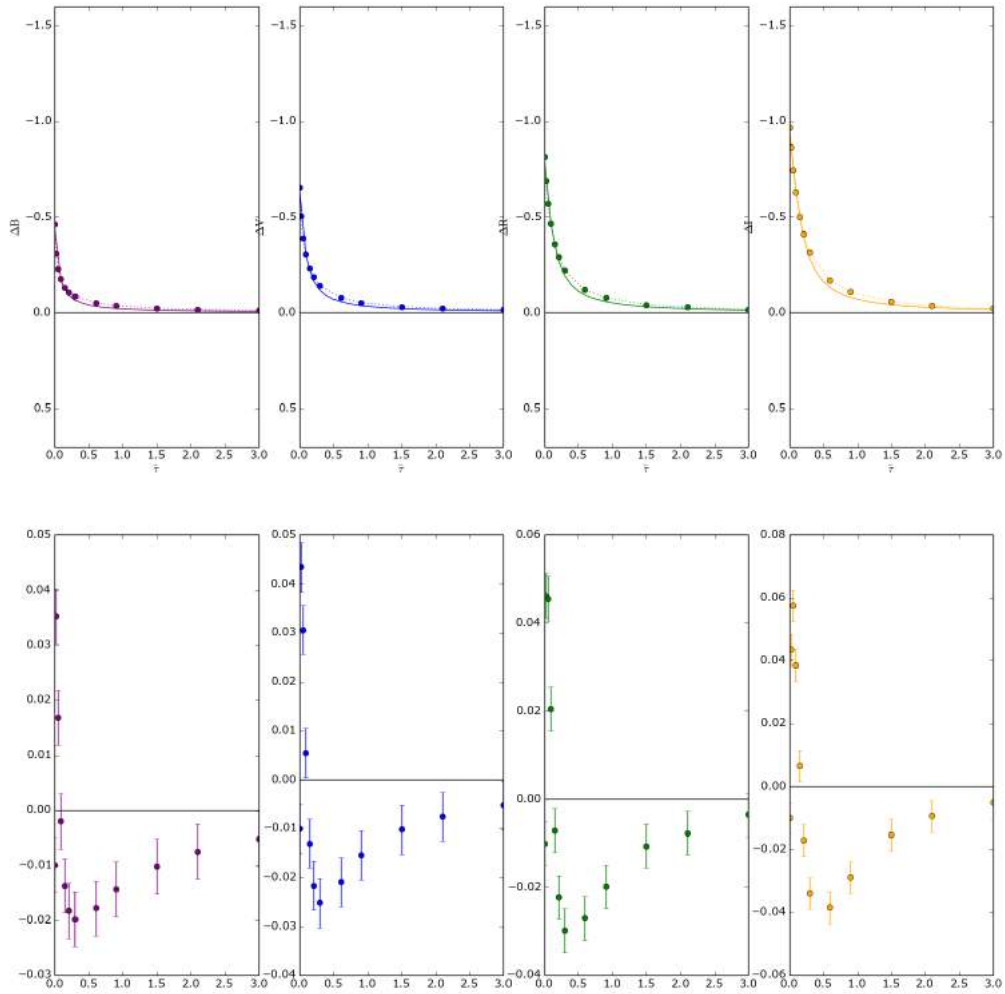


Figure B.9: $(\text{Star}, i, \Sigma_0, \tilde{\tau}_{\text{bu}}) = (\text{Star 2}, 0 \text{ deg}, 1.37 \text{ g cm}^{-2}, \mathbf{6})$

B.2 $(\text{Star}, i, \Sigma_0, \tilde{\tau}_{\text{bu}}) = (\text{Star } 2, 38.2 \text{ deg}, *, *)$

In this section, we fix i and, varying Σ_0 , we show three examples of fittings for each Σ_0 (the examples are for $\tilde{\tau}_{\text{bu}} = \text{bu}, 1.5, 6$).

B.2.1 $(\text{Star}, i, \Sigma_0, \tilde{\tau}_{\text{bu}}) = (\text{Star 2}, 38.2 \text{ deg}, 2.50 \text{ g cm}^{-2}, *)$

Three examples of fittings for $\Sigma_0 = 2.50 \text{ g cm}^{-2}$.

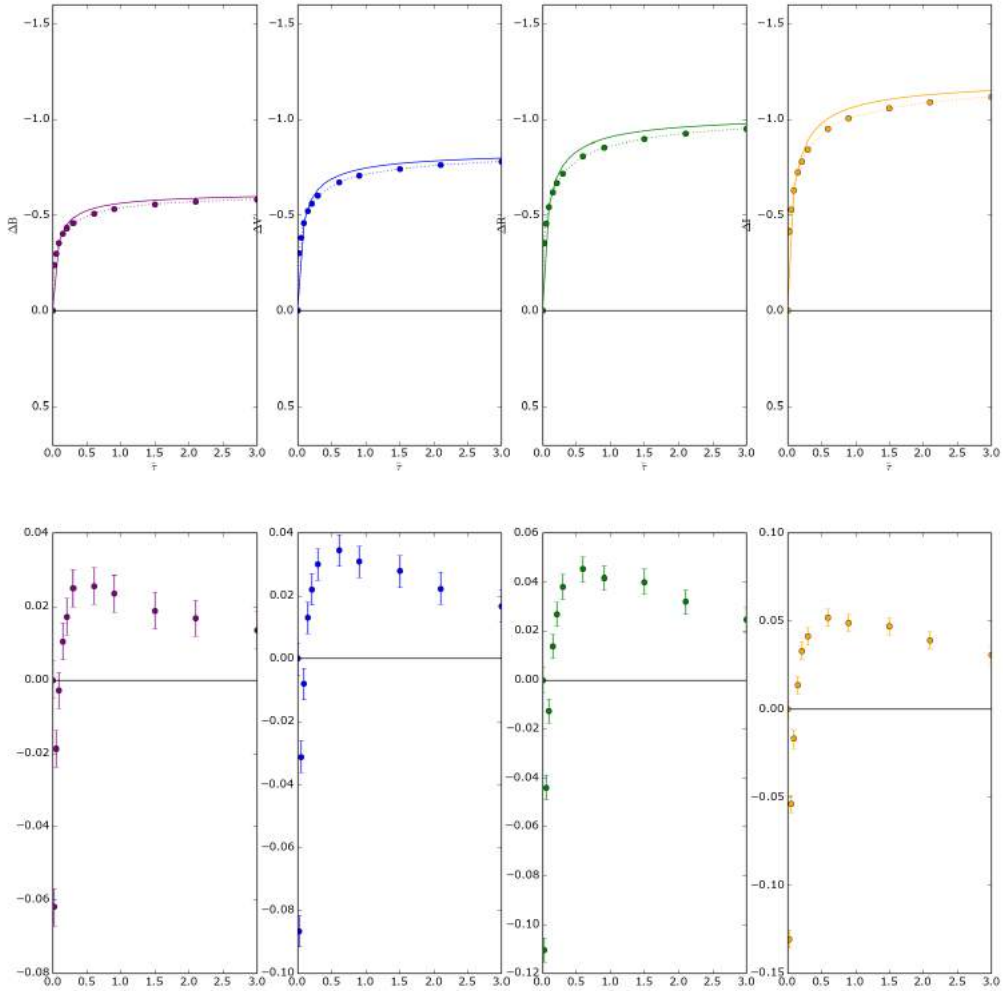


Figure B.10: $(\text{Star}, i, \Sigma_0, \tilde{\tau}_{\text{bu}}) = (\text{Star 2}, 38.2 \text{ deg}, 2.50 \text{ g cm}^{-2}, \text{bu})$

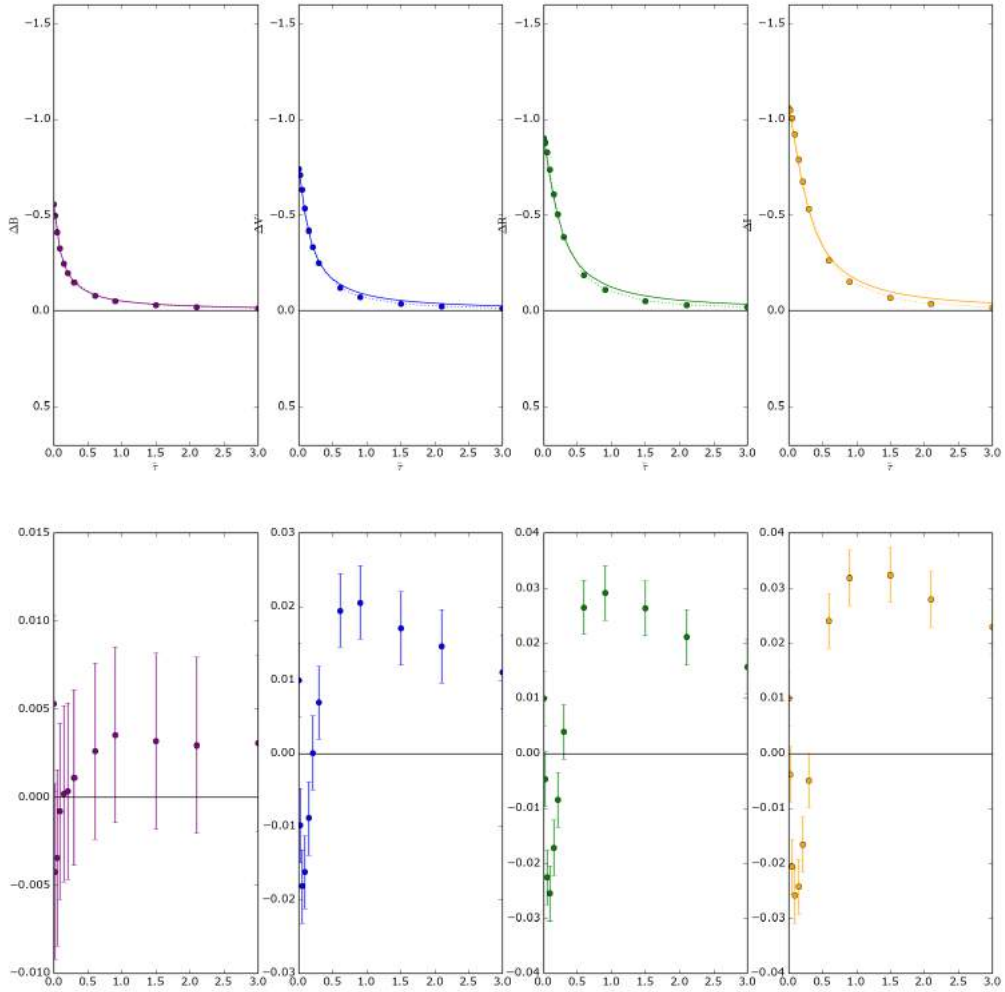


Figure B.11: (Star, i , Σ_0 , $\tilde{\tau}_{\text{bu}}$) = (Star 2, 38.2 deg, 2.50 g cm^{-2} , **1.5**)

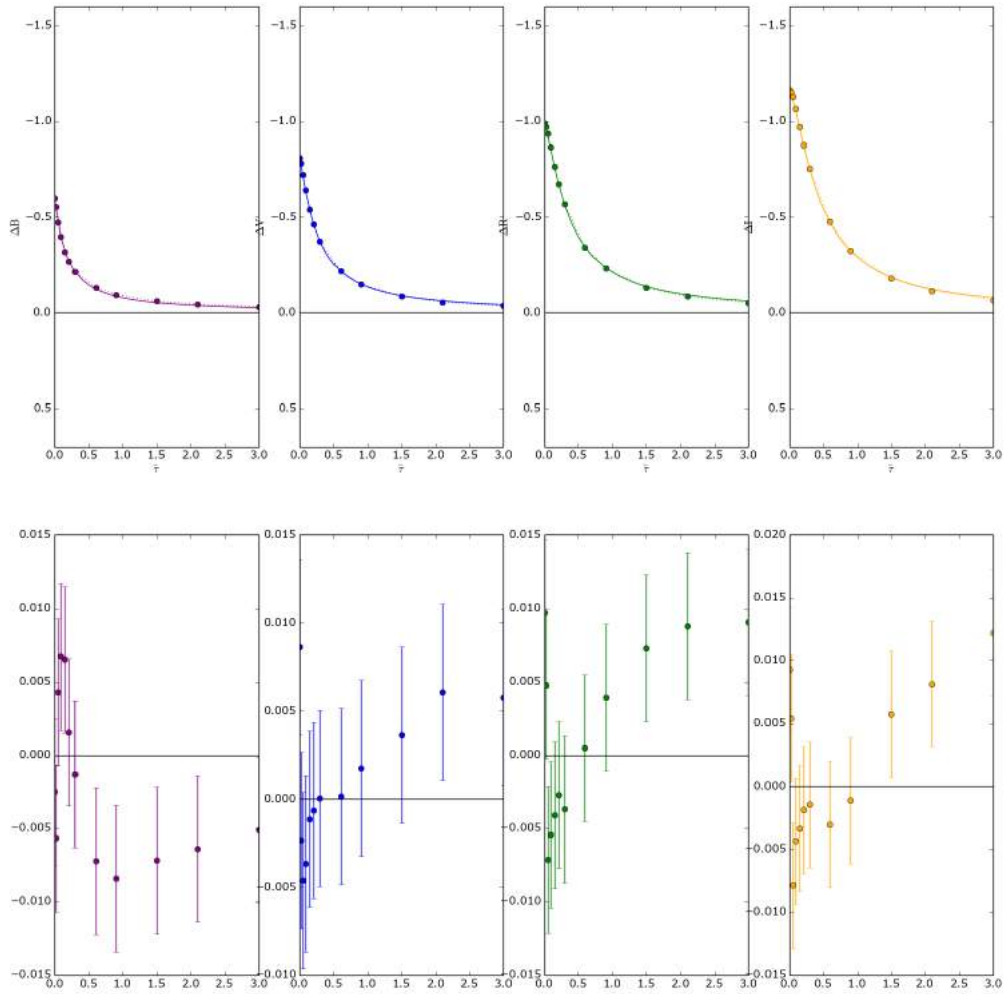


Figure B.12: $(\text{Star}, i, \Sigma_0, \tilde{\tau}_{\text{bu}}) = (\text{Star 2}, 38.2 \text{ deg}, 2.50 \text{ g cm}^{-2}, \mathbf{6})$

B.2.2 (Star, i , Σ_0 , $\tilde{\tau}_{\text{bu}}$) = (Star 2, 38.2 deg, **1.01 g cm⁻²**, *)

Three examples of fittings for $\Sigma_0 = 1.01 \text{ g cm}^{-2}$.

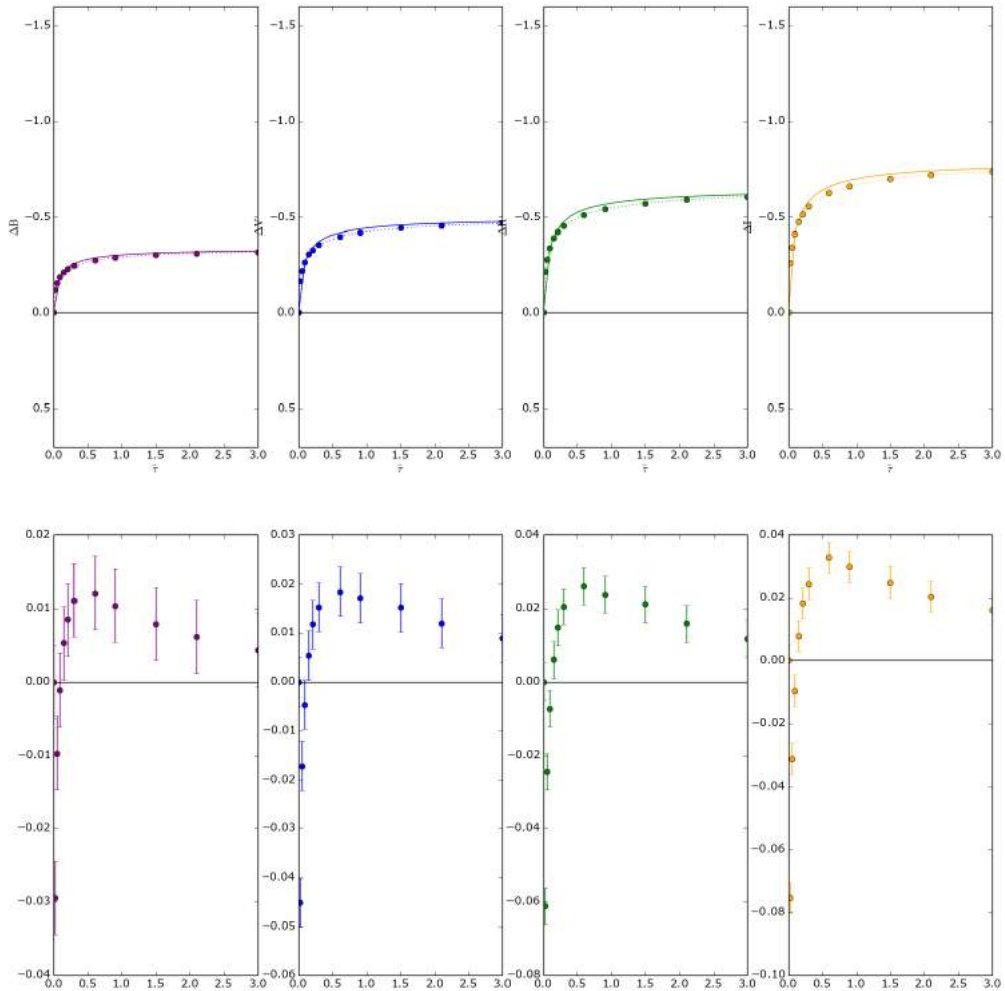


Figure B.13: (Star, i , Σ_0 , $\tilde{\tau}_{\text{bu}}$) = (Star 2, 38.2 deg, 1.01 g cm⁻², bu)

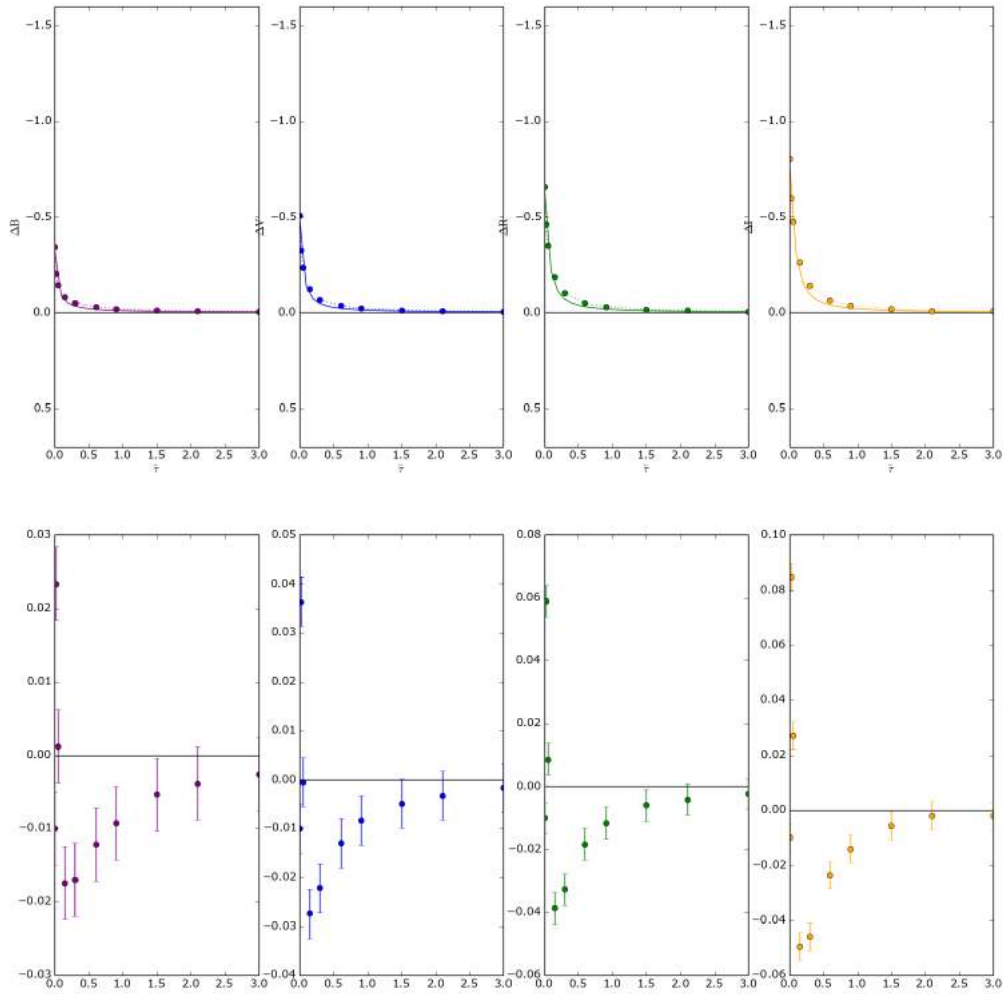


Figure B.14: $(\text{Star}, i, \Sigma_0, \tilde{\tau}_{\text{bu}}) = (\text{Star 2}, 38.2 \text{ deg}, 1.01 \text{ g cm}^{-2}, \mathbf{1.5})$

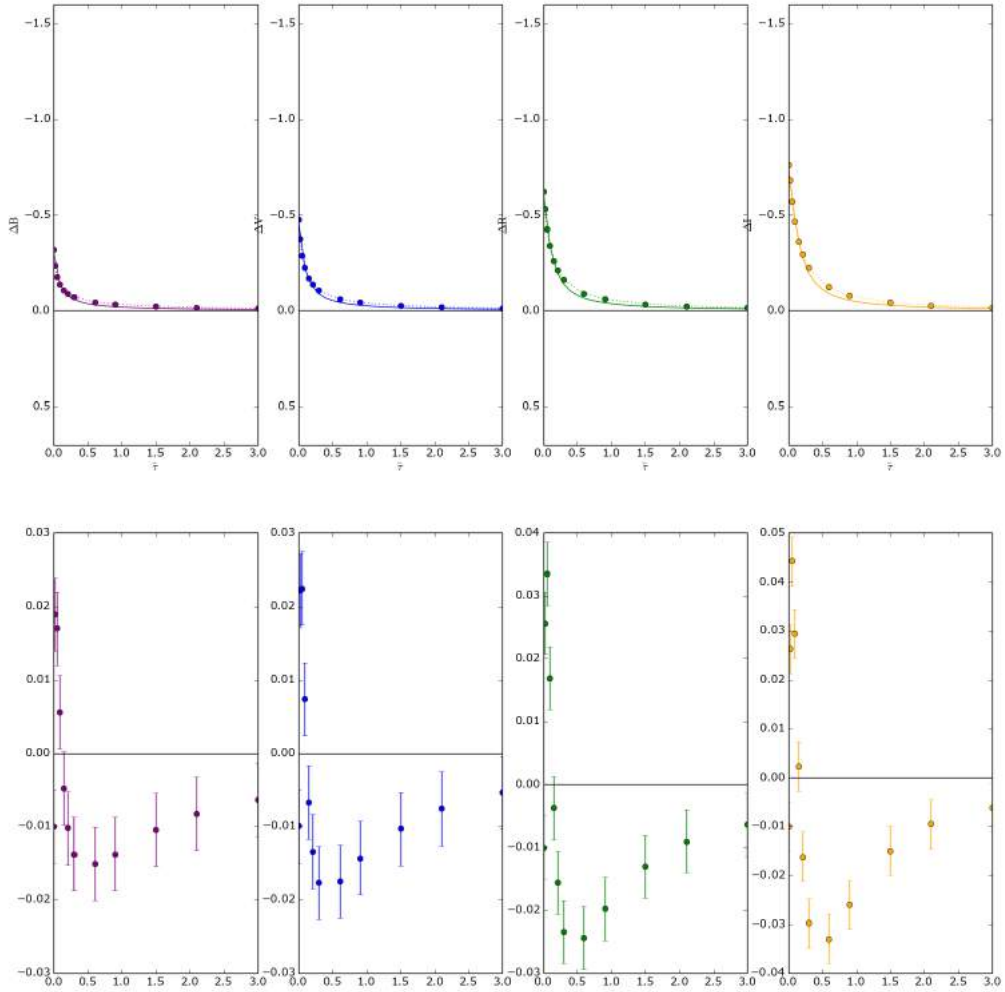


Figure B.15: (Star, i , Σ_0 , $\tilde{\tau}_{\text{bu}}$) = (Star 2, 38.2 deg, 1.01 g cm^{-2} , **6**)

B.2.3 (Star, i , Σ_0 , $\tilde{\tau}_{\text{bu}})$ = (Star 2, 38.2 deg, 0.41 g cm^{-2} , *)

Three examples of fittings for $\Sigma_0 = 0.41 \text{ g cm}^{-2}$.

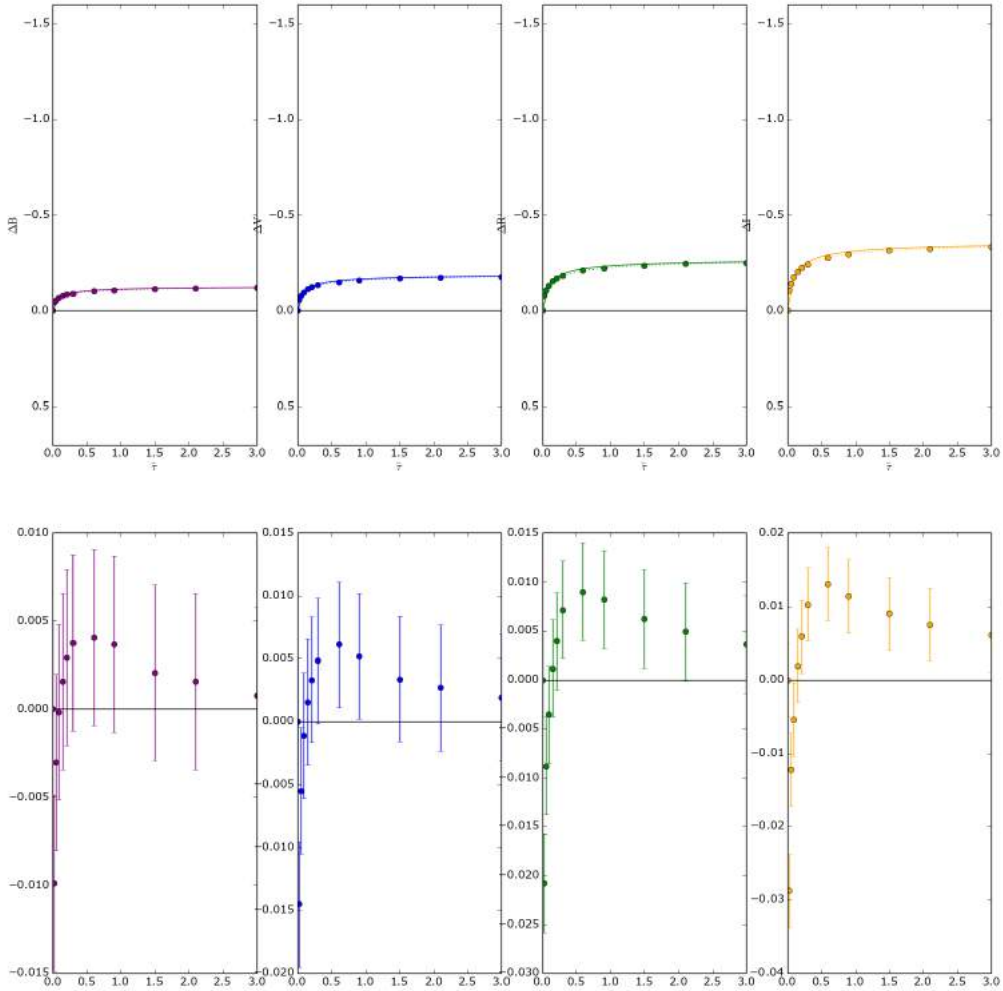


Figure B.16: (Star, i , Σ_0 , $\tilde{\tau}_{\text{bu}})$ = (Star 2, 38.2 deg, 0.41 g cm^{-2} , bu)

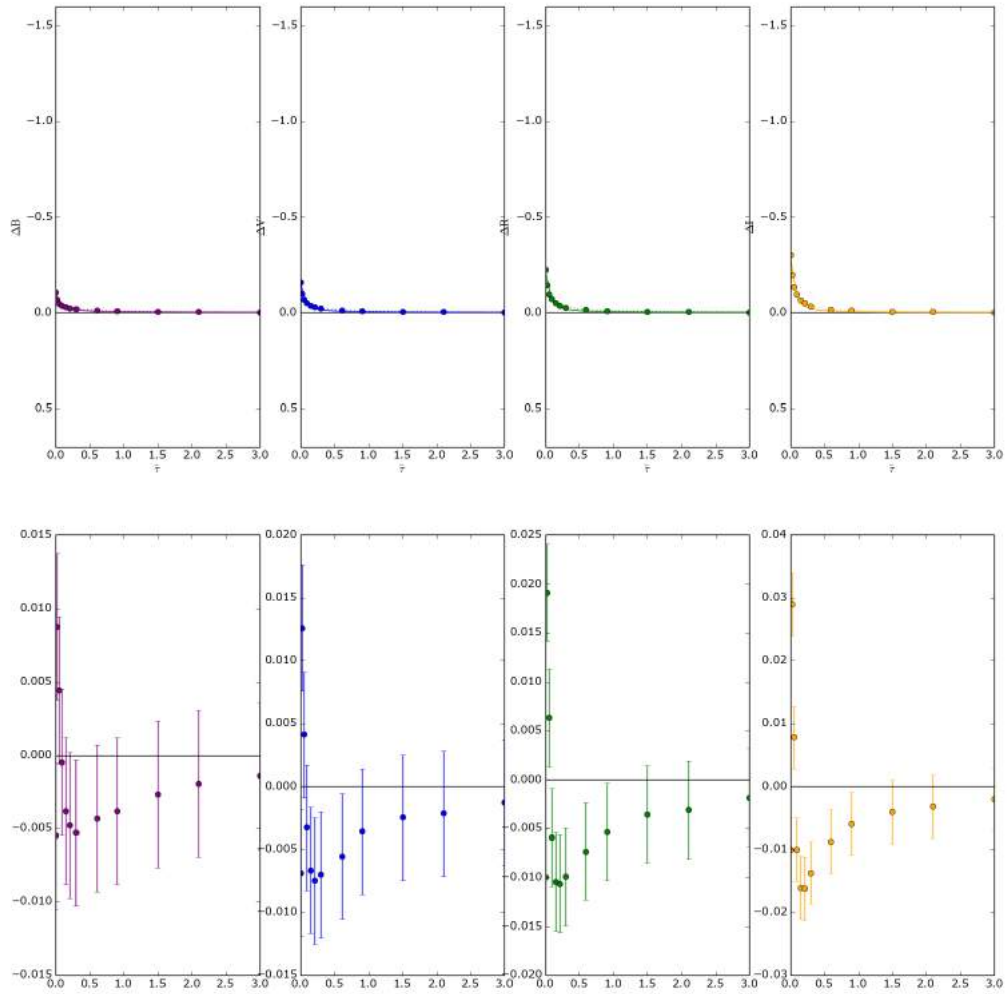


Figure B.17: $(\text{Star}, i, \Sigma_0, \tilde{\tau}_{\text{bu}}) = (\text{Star 2}, 38.2 \text{ deg}, 0.41 \text{ g cm}^{-2}, 1.5)$

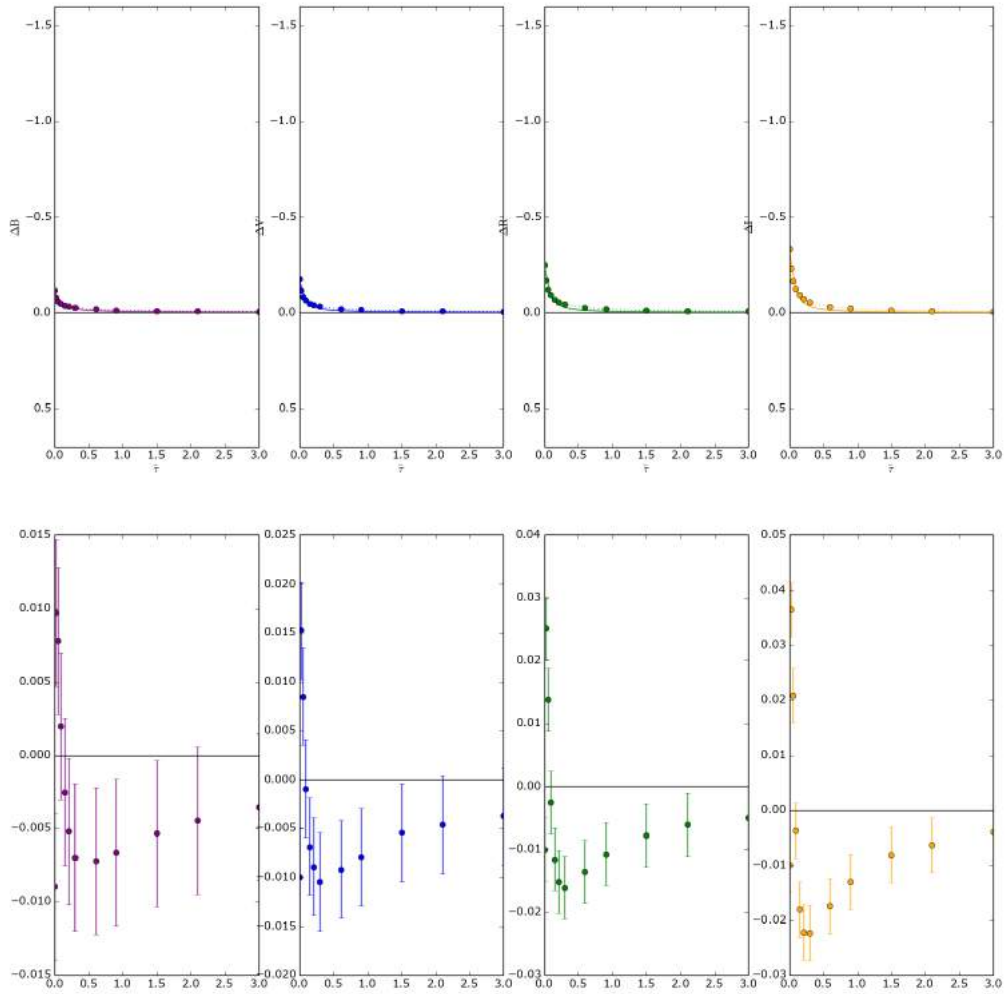


Figure B.18: $(\text{Star}, i, \Sigma_0, \tilde{\tau}_{\text{bu}}) = (\text{Star 2}, 38.2 \text{ deg}, 0.41 \text{ g cm}^{-2}, \mathbf{6})$

Appendix C

Scientific paper

The life cycles of Be viscous decretion discs: fundamental disc parameters of 54 SMC Be stars

L. R. Rímulo,^{1*} A. C. Carciofi,¹ R. G. Vieira,¹ Th. Rivinius,² D. M. Faes,¹
M. R. Ghoreyshi,¹ J. E. Bjorkman,³ I. Soszyński⁴

¹*Instituto de Astronomia, Geofísica e Ciências Atmosféricas, Universidade de São Paulo,
Rua do Matão 1226, Cidade Universitária, 05508-900 São Paulo, SP, Brazil*

²*ESO, European Organization for Astronomical Research in the Southern Hemisphere, Chile*

³*Ritter Observatory, Department of Physics & Astronomy, Mail Stop 113, University of Toledo, Toledo, OH 43606, US*

⁴*Warsaw University Observatory, Al. Ujazdowskie 4, 00-478 Warszawa, Poland*

Accepted XXX. Received YYY; in original form ZZZ

ABSTRACT

Be stars are main-sequence massive stars with emission features in their spectrum, which originates from a circumstellar gaseous disc. Even though the viscous decretion disc (VDD) model can satisfactorily explain most observations, two important physical ingredients, namely the magnitude of the viscosity (α) and the disk mass injection rate, remain poorly constrained. The light curves of Be stars that undergo events of disc formation and dissipation offer an opportunity to constrain these quantities. A pipeline was developed to model these events that uses a grid of synthetic light curves, computed from detailed hydrodynamic simulations combined with radiative transfer calculations. Comparison between model and data was made possible by empirical laws that closely match the photometric behaviour of the events. A sample of 54 Be stars from the OGLE survey of the Small Magellanic Cloud (SMC) was selected for this study. Because of the way our sample was selected (bright stars with clear disc events), it likely represents the densest discs found in the SMC. Like their siblings in the Galaxy, the mass of the disc in the SMC increases with the mass of the star. The typical mass and angular momentum loss rates associated with the disk events are of the order of $\sim 10^{-10} M_{\odot} \text{ yr}^{-1}$ and $\sim 5 \times 10^{36} \text{ g cm}^2 \text{ s}^{-2}$, respectively. The values of α found in this work are typically of a few tenths, consistent with recent results in the literature and with the ones found in dwarf novae, but larger than the current theory predicts. Considering the sample as a whole, the viscosity parameter is roughly two times larger at build-up ($\langle \alpha_{\text{bu}} \rangle = 0.63$) than at dissipation ($\langle \alpha_{\text{d}} \rangle = 0.29$). Further work is necessary to verify whether this trend is real or a result of some of the model assumptions. If real, this is a phenomenon worth further investigation, as it may lead to clues as to the origin of anomalous viscosity in astrophysical discs.

Key words: circumstellar matter – radiative transfer – stars: emission-line, Be – stars: mass-loss – techniques: photometric – hydrodynamics

1 INTRODUCTION

In a classical, observational, and quite broad definition, a Be star is a hot, massive star, with a B spectral type (mass ranging roughly from 3 to 17 M_{\odot}), non-supergiant, whose spectrum has, or had at some time, one or more Balmer lines in emission (Jaschek et al. 1981; Collins 1987). In a more modern and theoretically-oriented definition, a Be star is a very rapidly rotating and non-radially pulsating B star that forms a geometrically thin *viscous decretion disc* (VDD) composed of an outwardly diffusing, viscosity driven gaseous Keplerian disc that is fed by mass ejected from the central

star (Rivinius et al. 2013), and a possibly non-negligible line-driven wind (Kee et al. 2016). There is no evidence of large scale magnetic fields in Be stars (Rivinius et al. 2013). Fast stellar rotation lowers the effective gravity near the stellar equator and a second mechanism, likely to be stellar pulsation (Rivinius et al. 1998; Baade et al. 2016; Rivinius et al. 2016), is responsible for pushing this near equatorial matter into orbit in the inner disc. Once in orbit, a viscous mechanism takes place, diffusing matter and angular momentum outwards, thus making the disc grow.

Be stars are usually quite variable in all observables and in several timescales (days, weeks, months or even years). The variability observed in Be stars indicates that the injection of matter and angular momentum into the disc is frequently quite erratic, with sudden

* E-mail: lrrimulo@usp.br

outbursts of mass injection and periods of no or negligible mass injection. Rivinius et al. (2016) propose a terminology, which will be used here, in which a star that possesses a disc is said to be active and, conversely, when there is no detectable disc, the star is inactive. Two additional terms are used to distinguish the phases of active disc formation (outbursting Be star) and dissipation (dissipating Be star).

It has been demonstrated (e.g., Haubois et al. 2012) that a Be disc fed roughly at a constant rate, and for a sufficiently long time (a few to several years, depending on the value of the viscosity), reaches a quasi-steady state in which the density is nearly constant in time. If the gas temperature is properly taken into consideration, the radial density profile is typically a complicated function of the distance from the star (e.g., Carciofi & Bjorkman 2008). However, a usual approximation is to consider the gas to be isothermal, in which case the density profile assumes a power-law form. This simple steady-state VDD has been successful in describing the main observed features of individual Be discs (Carciofi et al. 2006, 2007; Jones et al. 2008b; Carciofi et al. 2009; Klement et al. 2015, *ress*) and samples of Be stars (Silaj et al. 2010; Touhami et al. 2011; Vieira et al. 2017). However, despite its great success, there are several open and intriguing theoretical questions about the VDD model. Besides the fact that a good description of the mechanism responsible for putting stellar material into orbit is still needed, a complete physical understanding of the forces that drive these discs is also lacking. It has been commonly assumed that the forces operating on the discs are the gravity from the central star and the forces that come from the gradient of pressure and from viscosity, the latter being the one capable of producing torque. Recently, Kee et al. (2016) showed that radiative line forces may also generate a non-negligible torque, at least for gaseous discs with Solar metallicity. In this work we will proceed with the assumption that line-driven forces are negligible. We mitigate this potential issue by choosing to study Be stars in the SMC, whose low metallicity will greatly decrease the strength of the line forces.

In the alpha-disc formalism, the kinematic viscosity is scaled with the α parameter, defined such that the $R\phi$ component of the stress tensor is proportional to the gas pressure: $\tau_{R\phi} = -\alpha P$. The most reliable and direct way of estimating α is to study the time-dependent disc behaviour, where the diffusive effect of viscosity will have clear observational counterparts. Therefore, light curves of long temporal coverage, such as the ones given by microlensing or planetary transit surveys, are excellent instruments to study the dynamical processes in action on the disc, as it builds-up and dissipates.

Dynamical studies of Be star viscous discs are still quite scarce. Jones et al. (2008a), using a 1-D time-dependent treatment of the alpha-disc and a non-LTE radiative transfer code, studied the temperature and density profiles of a dynamical disc and their respective $H\alpha$ line profiles. Haubois et al. (2012) studied the theoretical photometric effects of time variable mass injection rates on the structure of the disc also using a 1-D time-dependent treatment of the alpha-disc, associated with the Monte Carlo radiative transfer code HDUST (Carciofi & Bjorkman 2006, 2008). Carciofi et al. (2012), by fitting these dynamical models to a dissipating portion in the light curve of the Be star 28 CMa (which passed from an outbursting phase, that lasted from 2001 to 2003, to a dissipating phase at the end of 2003), estimated the value of the α parameter for the Be disc of 28 CMa to be $\alpha = 1.0 \pm 0.2$. Later, however, it was realised that a proper consideration of the previous history of the disc must be taken into consideration even when fitting the dissipating portion of the light

curve, and this quite high value has been revisited to be closer to $\alpha = 0.2$ (Ghoreyshi & Carciofi 2017).

Another intriguing issue regarding Be stars is how they acquired such high rotation rates (typically 80% of break-up, Rivinius et al. 2013). As the rotating B star evolves, core contraction and internal angular momentum redistribution generally tends to enhance surface angular rotation (Ekström et al. 2008; Granada et al. 2013). Another scenario (e.g., Pols et al. 1991) would involve a past mass-transfer phase in a binary system, during which the primary donates mass and angular momentum to the secondary. The left-over of such a system would be a fast-spinning Be star (the former mass gainer) and a subdwarf O or B star (sdO/sdB, the former mass donor). Regardless of how they were spun-up, it has been proposed (Krtićka et al. 2011) that the discs of Be stars may provide natural mechanisms for removing large quantities of angular momentum from the fast rotating stars, preventing them to reach the rotation critical limit. The evolutionary models of Granada et al. (2013) assumed the appearance of completely formed viscous discs every time their models reached a near-critical rotation. The mass density and the rate of angular momentum loss of their discs were roughly similar to the ones estimated by Vieira et al. (2017), who modelled the spectral energy distribution (SED) of 80 Be stars using the VDD model, provided that values of α of at least a few tenths were assumed in both approaches.

The main objective of this paper is to build upon the previous dynamical studies of Be discs and provide, for the first time, a detailed study of the temporal evolution of a large sample of Be stars from the Small Magellanic Cloud (SMC). By studying a large sample of stars, we may begin to answer several open questions related to Be stars and their discs, namely: i) What is the typical value of the viscosity in these discs? ii) Is there any significant evidence for a dependence of α with parameters such as the density of the disc, the spectral type of the star, etc.? iii) What are the typical rates of mass and angular momentum loss in these stars? To reach these goals we developed a new method for modelling the light curves of Be stars, described in Sects. 2 and 3. The sample of studied light curves is described in Sect. 4, and the model results are discussed in Sect. 5, followed by the conclusions.

2 VISCOUS DECRETION DISCS AROUND BE STARS

The optical light curves of early-type Be stars (with spectral type ranging roughly from B0 to B4) are usually quite variable in timescales of days to years, with amplitudes of up to tenths of mag (Rivinius et al. 2013). The majority of them show very irregular variability. Most present clear single bump-like features, characterised by a fast rise in brightness followed by a slower fading. Frequently, between the brightening and the fading phases some sort of plateau of nearly constant brightness is seen. Sometimes these bumps are reversed, so that an initial fast fading is followed by a slow recovering of the stellar brightness. Two examples of light curves showing these dips are presented in Fig. 1, taken from OGLE-II (Udalski et al. 1997) and OGLE-III (Udalski et al. 2008) data, for two Be star candidates from the SMC, based on the selection made by Menickent et al. (2002). Object SMC_SC1 75701 shows two bumps, while SMC_SC6 128831 shows a dip.

These bumps and dips resemble the photometric features shown in Haubois et al. (2012, e.g., their Fig. 14), where a circumstellar viscous disc builds up as a result of a mass injection into the disc at a constant rate, and then dissipates after the mass injection ceases. Haubois et al. (2012) studied several disc feeding scenarios

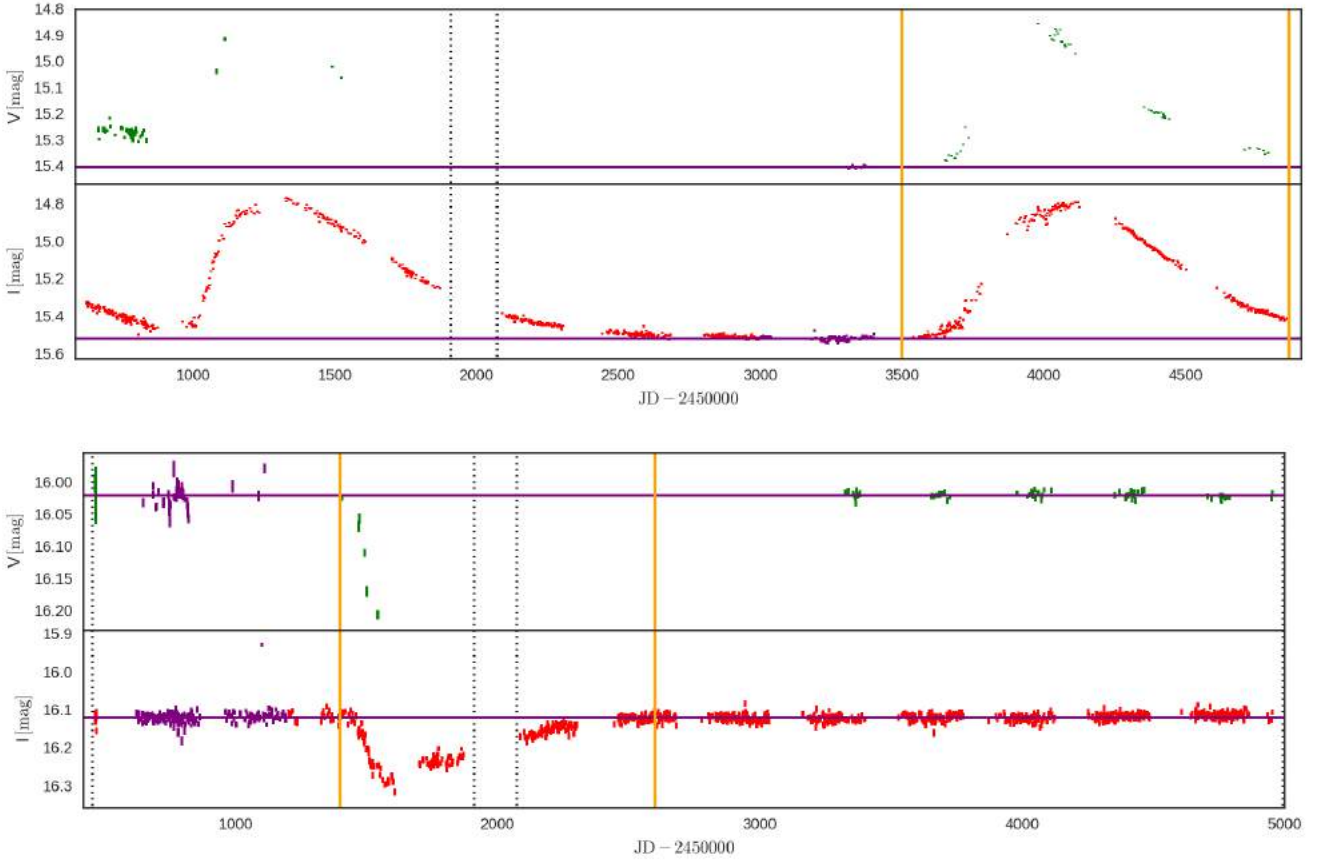


Figure 1. Two light curves, in photometric bands V (green), and I (red), selected from the OGLE-II and OGLE-III photometric surveys. *Above:* light curve of SMC_SC1 75701, showing two bumps. *Below:* light curve of SMC_SC6 128831, showing a dip. The pair of vertical dotted straight lines near $\text{JD} - 2450000 = 2000$ separates OGLE-II from OGLE-III data. The measurements shown in purple are assumed to represent the inactive (discless) brightness level of the Be star. Their mean is given by the horizontal purple straight lines. The pairs of vertical orange straight lines bracket our visually selected bumps. These bumps are modelled in Figs. 8 and 9.

(constant, cyclic, and outburst) and their photometric counterparts, and demonstrated that the bumps are disc formation/dissipation events of active Be stars seen at near pole-on inclination angles ($i \lesssim 70$ deg), while the dips are associated with near edge-on Be stars (often called shell stars, $i \gtrsim 70$ deg). The inclination angle plays an important role on how the stellar brightness is modified by the presence of disc because, in the second case (edge-on), the disc is seen projected against the stellar disc, thus causing an attenuation of the stellar radiation. This attenuation does not happen for the pole-on case, where the net effect of the disc is to increase the optical brightness as a result of free-bound and free-free radiation from the gas (Gehrz et al. 1974; Vieira et al. 2015).

In this section, we describe the basic hydrodynamical concepts of gaseous VVDs, with a focus on how to model the aforementioned events of disc construction and dissipation responsible for the bumps seen in the light curves of active Be stars. The evolution of the surface density,

$$\Sigma(R, t) = \int_{-\infty}^{\infty} \rho(R, z, t) dz, \quad (1)$$

of thin circumstellar axisymmetric discs of Be stars is described by

the following equation (Papaloizou & Lin 1995)

$$\frac{\partial \Sigma}{\partial t} + \frac{1}{R} \frac{\partial}{\partial R} (R \Sigma v_R) = S_{\Sigma}, \quad (2)$$

where R and z are cylindrical coordinates, $R \Sigma v_R$ is the mass flux crossing radius R per azimuthal angle, S_{Σ} represents the sources and sinks of mass in the disc per unit of area (see below), and ρ is the mass density. In Be discs with azimuthal symmetry, as assumed in this work, the mass flux at a given radius ($2\pi R \Sigma v_R$) can switch between a positive (decretion) and negative (accretion) value, in response to changes in S_{Σ} . In the circumstellar alpha-disc formulation, the mass flux is given by

$$2\pi R \Sigma v_R = -4\pi \left(\frac{R}{GM} \right)^{\frac{1}{2}} \frac{\partial}{\partial R} (R^2 \alpha c_s^2 \Sigma), \quad (3)$$

where $c_s^2 = kT_{\text{disc}}/\mu m_H$ is the isothermal sound speed and α is the viscosity parameter.

The orbital velocity of the disc, v_{ϕ} , is assumed to be Keplerian ($v_{\phi} = v_K = v_{\text{orb}} \tilde{R}^{-1/2}$, with $v_{\text{orb}} = (GM/R_{\text{eq}})^{1/2}$ and $\tilde{R} = R/R_{\text{eq}}$, where R_{eq} is the stellar equatorial radius). This assumption holds as long as the gravitational force is much larger than the force due to the pressure gradient, which is generally true for distances from

the star of dozens to a few hundreds of stellar radii (Okazaki 2001), as long as $(c_s/v_K)^2 \ll 1$.

The function S_Σ is the rate of mass injected into (or removed from) the disc per unit of area. It represents the variable mass exchange between the star, the disc and the outer medium. We consider that, during outbursts, mass is put into orbit along a very thin ring of radius R_{inj} close to the stellar equator. Therefore, we assume

$$S_\Sigma = \dot{M}_{\text{inj}}(t) \frac{\delta(R - R_{\text{inj}})}{2\pi R} + \text{boundaries}, \quad (4)$$

where $\dot{M}_{\text{inj}}(t)$ is the mass injection rate from the star into the disc at R_{inj} .

In addition, mass can flow away from the disc through its boundaries. Mass can fall back into the star through the inner boundary at R_{eq} , or it can leave the system at an outer boundary, R_{out} . The outer boundary can be interpreted as the limiting radius of the disc due to a binary companion (e.g., Okazaki et al. 2002) or due to the photoevaporation of the disc (e.g., Okazaki 2001). We consider that all mass that eventually reaches the stellar equator R_{eq} is totally absorbed. The same is assumed for the mass that eventually reaches an outer radius R_{out} (see below for the definition of R_{out}). Therefore, the boundaries consist of $\Sigma(R_{\text{eq}}, t) = \Sigma(R_{\text{out}}, t) = 0$.

For the hydrodynamical simulations, we assume the disc to be isothermal, with $T_{\text{disc}} = 0.6T_{\text{eff}}$, following Carciofi & Bjorkman (2006). We further assume that the α parameter is constant with R , but we allow it to possibly be time-dependent, as there is evidence that it might happen in discs of Be stars (Ghoreyshi & Carciofi 2017). Consequently, Eqs. (2)–(4) can be scaled in the following way

$$\frac{\partial \Sigma}{\partial t} = \frac{1}{\tau} \left\{ \frac{2}{\tilde{R}} \frac{\partial}{\partial \tilde{R}} \left[\tilde{R}^{\frac{1}{2}} \frac{\partial}{\partial \tilde{R}} (\tilde{R}^2 \Sigma) \right] + \tau S_\Sigma \right\}, \quad (5)$$

where we introduce the *timescale parameter*, $\tau(t)$, given by

$$\tau(t) = \frac{1}{\alpha(t)} \left(\frac{R_{\text{eq}}^3}{GM} \right)^{\frac{1}{2}} \frac{v_{\text{orb}}^2}{c_s^2}, \quad (6)$$

and distances from the star are expressed by the dimensionless parameter $\tilde{R} = R/R_{\text{eq}}$. The timescale parameter is proportional to the viscous timescale at the stellar equator, which is given by $t_{\text{vis}} = R^2/\nu$, where the viscosity ν is given by $\nu = (2/3)\alpha c_s^2 R/v_K$. Since we are in the thin disc limit ($c_s^2/v_K^2 \ll 1$), we see that τ is much larger than the orbital period at the stellar equator, given by $2\pi(R_{\text{eq}}^3/GM)^{1/2}$.

The solution of Eq. 5 is scaled in time by the timescale parameter, which controls how fast matter is distributed throughout the disc and, consequently, its observational counterparts. It follows that by fitting observed light curves of Be stars, this parameter can be estimated, and once other parameters are known (R_{eq} , M , T_{disc}), the α value can be determined (e.g., Carciofi et al. 2012).

In order to generate models that do not depend on the time-dependent form of $\alpha(t)$ and also on the parameters R_{eq} , M and T_{disc} , which are related to the central star, we define a *time parameter*, $\tilde{\tau}(t)$, such that

$$d\tilde{\tau} = \frac{dt}{\tau(t)}, \quad (7)$$

which allows us to solve Eq. (5) in terms of $\tilde{\tau}$ instead of the physical time t . The advantage of using this new variable is that it separates the problem of the time dependency of $\alpha(t)$ from the problem of solving Eq. (5). Consequently, it allows us to create a grid of solutions of that equation that is independent of $\alpha(t)$, R_{eq} , M and T_{disc} (see Sect. 3)

In this work, Eq. (5) is solved numerically by the 1-D thin-disc code SINGLEBE (Okazaki 2007). At selected time parameters $\tilde{\tau}$, the solution $\Sigma(\tilde{R}, \tilde{\tau})$ enters as input for the Monte Carlo 3-D radiative transfer code HDUST (Carciofi et al. 2004; Carciofi & Bjorkman 2006, 2008) that calculates the emergent spectrum of the star+disc system. To convert between surface density and mass density (Eq. 1), it is assumed that the disc is vertically sustained by hydrostatic pressure, in which case the vertical density profile is a Gaussian, and

$$\rho(\tilde{R}, z, \tilde{\tau}) = \frac{\Sigma(\tilde{R}, \tilde{\tau})}{\sqrt{2\pi}H} e^{-\frac{z^2}{2H^2}}, \quad (8)$$

where

$$\frac{H}{R_{\text{eq}}} = \left(\frac{c_s}{v_{\text{orb}}} \right) \tilde{R}^{\frac{3}{2}} \quad (9)$$

is the scale height.

Before moving on to the modelling of bump-like events such as the ones of Fig. 1, we introduce in the next section some important parameters of the dynamical discs implied in the equations shown above.

2.1 Dynamical disc parameters

The radius of mass injection divides the disc in two regions: a narrow region between the inner boundary and the radius of mass injection ($1 \leq \tilde{R} \leq \tilde{R}_{\text{inj}}$), and the much wider region between the radius of mass injection and the outer boundary ($\tilde{R}_{\text{inj}} \leq \tilde{R} \leq \tilde{R}_{\text{out}}$). The steady-state solution of Eq. (5) corresponds to the limiting case of a disc that has been fed at a constant rate for an infinitely long time. It is obtained by setting $\partial \Sigma / \partial t = 0$ and assuming that α and \dot{M}_{inj} are time-independent. The surface density in the steady-state is given by

$$\Sigma_{\text{steady}}(\tilde{R}) = \begin{cases} \frac{\Sigma_0}{\tilde{R}^2} \left(\frac{\tilde{R}^{\frac{1}{2}} - 1}{\tilde{R}_{\text{inj}}^{\frac{1}{2}} - 1} \right) \Upsilon, & 1 \leq \tilde{R} < \tilde{R}_{\text{inj}} \\ \frac{\Sigma_0}{\tilde{R}^2} \left(\frac{\tilde{R}_{\text{out}}^{\frac{1}{2}} - \tilde{R}^{\frac{1}{2}}}{\tilde{R}_{\text{out}}^{\frac{1}{2}} - 1} \right), & \tilde{R}_{\text{inj}} \leq \tilde{R} \leq \tilde{R}_{\text{out}} \end{cases}, \quad (10)$$

where $\Upsilon = (\tilde{R}_{\text{out}}^{1/2} - \tilde{R}_{\text{inj}}^{1/2}) / (\tilde{R}_{\text{out}}^{1/2} - 1)$ is a number usually very close to 1 for any Be disc.

The physical quantity Σ_0 represents the surface density at R_{eq} , obtained by extrapolating Σ_{steady} in the domain $\tilde{R}_{\text{inj}} \leq \tilde{R} \leq \tilde{R}_{\text{out}}$ to R_{eq} . We will refer to this physical quantity as the *asymptotic surface density*, as it is the asymptotic value reached after an infinitely long disc build-up under a constant \dot{M}_{inj} . It is easily shown that Σ_0 is related to \dot{M}_{inj} by the following equation

$$2\pi R_{\text{eq}} \Sigma_0 \left(\frac{R_{\text{eq}}}{\tau} \right) = \dot{M}_{\text{inj}} \left(\tilde{R}_{\text{inj}}^{\frac{1}{2}} - 1 \right) \equiv \left(-\frac{\partial M}{\partial t} \right)_{\text{typ}}, \quad (11)$$

where $(\partial M / \partial t)_{\text{typ}}$ is defined below.

We may extend Eq. (11) to the general case of a time-dependent $\dot{M}_{\text{inj}}(\tilde{\tau})$, which would define, by the same equation, a time dependent asymptotic surface density, $\Sigma_0(\tilde{\tau})$. The function $\Sigma_0(\tilde{\tau})$, therefore, is just another way of specifying the history of mass injection from the star into the disc. It has, however, the advantage of being a surface density, which is a quantity that may be determined from, e.g. SED analyses, in contrast to the mass injection rate and the radius of mass injection, which are parameters that cannot be observationally determined.

The steady-state solution (Eq. 10) shows that, in the wider

domain $\tilde{R}_{\text{inj}} \leq \tilde{R} \leq \tilde{R}_{\text{out}}$, the density profile of the disc is not altered if \tilde{R}_{inj} is changed, provided that \dot{M}_{inj} is also changed in order to maintain Σ_0 fixed, according to Eq. (11). In fact, we verified that the time-dependent solutions of Eq. (5) in the domain $\tilde{R}_{\text{inj}} \leq \tilde{R} \leq \tilde{R}_{\text{out}}$ are negligibly affected by the particular choice of \tilde{R}_{inj} or $\dot{M}_{\text{inj}}(\tilde{\tau})$, as long as the quantity $\Sigma_0(\tilde{\tau})$ is kept fixed. This is a consequence of the fact that the dynamical solutions reach a near steady-state very quickly in the vicinity of the injection radius (Haubois et al. 2012). Furthermore, provided that mass is injected not too far from the stellar photosphere (i.e., assuming $\tilde{R}_{\text{inj}} \gtrsim 1$), the domain $1 \leq \tilde{R} \leq \tilde{R}_{\text{inj}}$ is much narrower than the region where the continuum visual flux of Be stars is generated (Carciofi 2011), which means that the emission from this region can be ignored. Consequently, we conclude that $\Sigma_0(\tilde{\tau})$ (with the assumption that $\tilde{R}_{\text{inj}} \gtrsim 1$) is a much better parameter for describing the mass injection history of the disc than the pair of parameters $\dot{M}_{\text{inj}}(\tilde{\tau})$ and \tilde{R}_{inj} .

The time-dependent solutions of Eq. (5) generally show that, for Be stars dynamically feeding the disc but still far from steady-state, the mass flux close to \tilde{R}_{inj} has absolute values of the order of $(-\partial M/\partial t)_{\text{typ}}$, defined by Eq. (11). Therefore, we refer to this quantity as the *typical decretion rate*, which depends on parameters relatively easy to estimate from SEDs of Be stars.

In our simulations, since the values of \dot{M}_{inj} and \tilde{R}_{inj} are of no interest, and the value of \tilde{R}_{out} is quite uncertain, we arbitrarily chose $\tilde{R}_{\text{inj}} = 1.017$ and $\tilde{R}_{\text{out}} = 1000$ (we discuss below how this choice of \tilde{R}_{out} might affect our results). Eq. 11, therefore, shows that the typical decretion rate is much smaller than the mass injection rate $\dot{M}_{\text{inj}}(\tilde{\tau})$. In our case, the typical decretion rate is only $8.46 \times 10^{-3} \dot{M}_{\text{inj}}$. This means that the majority of the injected mass flows inwards and is absorbed by the inner boundary at the stellar equator, and only a small remaining fraction of the injected mass is responsible for the growth of the disc. These results were first obtained from SPH simulations of Be discs by Okazaki et al. (2002), who found that only about 0.1% of the injected material flows outward, as a direct result of their choice for R_{inj} .

It can be shown, by substitution of Eqs. (10) and (11) in Eq. (3) that, in steady-state, only the fraction of the injected mass given by $\dot{M}_{\text{inj}}(1 - \Upsilon)$ is flowing outwards through the disc and crossing the outer radius R_{out} , thus leaving the system. For our assumed values for \tilde{R}_{inj} and \tilde{R}_{out} , $1 - \Upsilon = 2.84 \times 10^{-4}$. Since the mass of the disc is not varying in steady-state, the mass flux given by $\dot{M}_{\text{inj}}(1 - \Upsilon)$ is actually the rate of mass being lost by the star, which we will indicate by $(-\partial M/\partial t)_{\text{steady}}$. It is easily seen that it is related to the typical decretion rate by the following equation

$$\left(-\frac{\partial M}{\partial t}\right)_{\text{steady}} = \frac{\Lambda}{\tilde{R}_{\text{out}}^{\frac{1}{2}}} \left(-\frac{\partial M}{\partial t}\right)_{\text{typ}}, \quad (12)$$

where $\Lambda = 1/(1 - \tilde{R}_{\text{out}}^{-1/2})$ is a number very close to 1 for any Be disc in general.

In steady-state, the angular momentum escaping the system at the outer boundary (and also being lost by the star) is $(GM R_{\text{out}})^{1/2} \dot{M}_{\text{inj}}(1 - \Upsilon)$, and is written as

$$\left(-\frac{\partial J}{\partial t}\right)_{\text{steady}} = \Lambda (GM R_{\text{eq}})^{\frac{1}{2}} \left(-\frac{\partial M}{\partial t}\right)_{\text{typ}}. \quad (13)$$

From Eq. (12) we see that knowing \tilde{R}_{out} is essential for estimating the rate of mass being lost by the star. Interestingly, this is not the case for the rate of angular momentum being lost by the star, given by Eq. (13).

2.2 The Mass Reservoir Effect

It is important to stress that the solution $\Sigma(\tilde{R}, \tilde{\tau})$ is shaped not just by the mass injection rate $\Sigma_0(\tilde{\tau})$ at the specific instant $\tilde{\tau}$, but by the whole mass injection history before the instant $\tilde{\tau}$. Therefore, the advantage of studying the relatively isolated bumps like the ones exemplified in Fig. 1, which started after a clear inactive phase, is that there is no disc present when the bump starts developing; thus, no previous history of mass injection has to be taken into account in the beginning of their modelling.

The light curves of several Be stars show that the duration of the build-up phase, which we refer to as the *build-up time*, is variable between Be stars and even between different bumps from the same star, ranging from a few days to years. The following phase of disc dissipation, however, contrary to the build-up phase, depends of the previous history of mass injection. For this reason, the modelling of the dissipation phase must not be disconnected from the modelling of the build-up phase that happened before it.

One of the main consequences of this fact is the *mass reservoir effect* (see also Ghoreyshi & Carciofi 2017). Basically, discs that had a longer build-up phase necessarily transported more matter and angular momentum outwards and created a larger external reservoir of mass and angular momentum in its outer regions, which usually extend far beyond the first few stellar radii where the visible photometric observables are formed. It is common, for instance, that some bumps reach plateaus during the build-up phase. The plateau indicates that the density in the inner disc has reached near-steady-state values and, consequently, there is little photometric variation in the visible wavelengths. The outer disc, however, will likely be far from steady-state and thus will continue to increase in density and mass. When mass injection ceases, the dissipation phase begins. Re-accretion occurs and, due to the more massive outer disc, the inner disc remains relatively denser for a longer time. This makes the dissipation of the disc to appear slower in the observed light curves. Conversely, a disc that had a small build-up time would dissipate much faster.

The importance of the mass reservoir effect can be assessed by the reevaluation of the α parameter in 28 CMa by Ghoreyshi & Carciofi (2017). Carciofi et al. (2012) modelled the 2003 dissipation phase of 28 CMa by considering a very long previous build-up time, and found that a high value of α was necessary (1.0 ± 0.2) to match the observed dissipation rate. Ghoreyshi & Carciofi have shown that when the previous build-up phase is properly accounted for in the modelling, the value of α required to match the dissipation rate is much smaller (0.21 ± 0.05).

3 A MODEL GRID OF DISC FORMATION AND DISSIPATION EVENTS

In this section we describe the method we developed for fitting the light curves associated with events of disc formation and dissipation. The method consists of precomputing a large grid of dynamical models of the time-dependent disc structure, covering the entire range of observed scenarios (Sect. 3.1) and performing the radiative transfer in these models to produce synthetic light curves (Sect. 3.2). The observed light curves are then fitted by the synthetic one using the procedure described in Sects. 3.3 and Sect. 3.4.

3.1 Dynamical model grid

For building a comprehensive grid of dynamical models that are solutions of Eq. 5, we used the definitions of Sect. 2 that allow us to write the solution $\Sigma(\tilde{R}, \tilde{\tau})$ in terms of $\Sigma_0(\tilde{\tau})$ and the dimensionless parameter $\tilde{\tau}$.

As discussed in Sect. 2.2, the advantage of studying relatively isolated bumps like the ones exemplified in Fig. 1, which started after a clear inactive phase, is that there is no previous history of mass injection to be taken into account for the modelling, so that during build-up the shape of the curve is controlled solely by $\Sigma_0(\tilde{\tau})$ and $\tilde{\tau}$, while for dissipation the previous disc build-up time should also be considered (Sect. 2.2). By using the time parameter (Eq. 7) instead of the physical time, our dynamical models are independent of the specific physical parameters M , T_{eff} , R_{eq} and $\alpha(t)$ of the Be star under consideration (Eq. 6). Also, from the linearity of Eq. 5, it follows that multiplying $\Sigma_0(\tilde{\tau})$ by some constant results in the solution $\Sigma(\tilde{R}, \tilde{\tau})$ multiplied by the same constant. Consequently, only one value of Σ_0 during the build-up phase is necessary.

For our grid of dynamical models, we therefore assume that our Be stars start discless. At instant $\tilde{\tau} = 0$, mass injection into the disc begins at an arbitrary constant rate ($\Sigma_0 > 0$) that lasts until $\tilde{\tau} = \tilde{\tau}_{\text{bu}}$, which we refer to as the *scaled build-up time*, since it is related to the above mentioned build-up time, but scaled by the timescale parameter. After that ($\tilde{\tau} > \tilde{\tau}_{\text{bu}}$), mass injection no longer occurs ($\Sigma_0 = 0$) and the disc dissipates. In Appendix A, we further discuss the properties of these dynamical models.

We chose 11 values of $\tilde{\tau}_{\text{bu}}$, listed in Table 1. Since the timescale parameter (Eq. 6) is roughly given by $\sim (100\text{--}200)/\alpha$ days for early Be stars in the main sequence with $\alpha \lesssim 1$, these values correspond to real build-up times of at least 15 days, which brackets the observed build-up times of the sample described below (Sect. 4, Table 5). In this study, we decided not to model the bumps with observed build-up times lower than about 15 days, usually referred to as flickers (Keller et al. 2002).

3.2 Radiative transfer models

Having selected a set of suitable hydrodynamic bump models, the next step is to produce photometric light curves of these models. The radiative transfer part of the problem requires a stellar model, which will be the primary source of radiation. The stellar model depends on the physical parameters M , R_{eq} and T_{eff} , which were left unspecified in the dynamical model grid. In addition, three other parameters must be specified: the viewing angle, i ($i = 0$ means pole-on orientation), the distance to the star, d , and the interstellar reddening.

One important feature of the central stars of Be stars is that they are fast rotators. Fast rotation causes the star to be oblate, with hotter poles and colder equatorial regions. Rotation is specified by the ratio of the rotation velocity at the equator to the Keplerian velocity at the equator, $W = v_{\text{eq}}/v_{\text{orb}}$. The ratio between the equatorial radius to the polar radius is given by $R_{\text{eq}}/R_{\text{pole}} = 1 + W^2/2$ for a Roche-shaped star. All these parameters evolve in time as a consequence of stellar evolution, and Be stars can be found in luminosity classes from V to III (Rivinius et al. 2013). We adopt the Geneva evolutionary tracks (Georgy et al. 2013) to determine R_{eq} and T_{eff} given M and the age in the main sequence, t_{MS} .

The current version of HDUST allows for a spheroidal rotationally oblate star, with the latitude-dependent surface temperature being given by $T_{\text{surf}} \propto g_{\text{eff}}^{\beta}$ (Carciofi et al. 2008). Here, the coefficient $\beta(W)$ is calculated by fitting a straight line to the gradient

Table 1. Parameters of the grid of photometric models of bumps

Star	i [deg]	Σ_0 [g cm^{-2}]	$\tilde{\tau}_{\text{bu}}$
Star 1	00.0	0.30	00.15
Star 2	21.8	0.41	00.45
Star 3	31.0	0.56	00.75
	38.2	0.75	01.50
	44.4	1.01	02.25
	50.0	1.37	03.00
	55.2	1.85	04.50
	60.0	2.50	06.00
	64.6		09.00
	69.1		15.00
	73.4		30.00
	77.6		
	81.8		
	85.9		
	90.0		

Table 2. Parameters of the stellar models of Table 1

Star	Z	M [M_{\odot}]	W	t/t_{MS}	$\alpha\tau$ [d]
Star 1	0.002	7	0.81	0.5	90.4
Star 2	0.002	11	0.81	0.5	103.3
Star 3	0.002	15	0.81	0.5	118.9

$\partial \ln T_{\text{surf}} / \partial \ln g_{\text{eff}}$ given by the flux theory of Espinosa Lara & Rieutord (2011). For the disc scale height (Eq. 9), we assume an isothermal disc with $T_{\text{disc}} = 0.6T_{\text{eff}}$, where T_{eff} is the effective temperature of the star, defined by $T_{\text{eff}} = (L_*)^{1/4} (\sigma S_*)^{-1/4}$, with S_* being the surface area of the star.

In order to generate synthetic absolute magnitudes from the computed SEDs, we used the standard *BVRI* Johnson-Cousins passbands from Bessell (1990) and the Vega flux from Castelli & Kurucz (1994) as standard of calibration.

A grid of model light curves was computed using the 11 dynamical models described in Sect. 3.1, with 8 different values of Σ_0 (third column of Table 1). For each of these disc models, radiative transfer models were calculated with HDUST at 17 different time parameters (not shown in the table) and 15 equally-spaced values of $\cos i$ (second column). This whole process was done for 3 different stellar models (“Star 1”, “Star 2” and “Star 3”, first column of Table 1). Details on the stellar models are given in Table 2. They were chosen to represent early B-type stars from the SMC ($Z = 0.002$), in the middle of their life in the main sequence, with the rotation parameter given by the mean value obtained for Be stars ($W = 0.81$, Rivinius et al. 2006). In the sixth column of Table 2, we present the values of $\alpha\tau$ (Eq. 6) for the discs of these stars (with the assumption that $T_{\text{disc}} = 0.6T_{\text{eff}}$). In short, a single light curve is specified by taking one element of each column of Table 1. The end result was a grid of $3 \times 15 \times 8 \times 11 = 3960$ light curves, for each of the *BVRI* bands.

A grid of inactive (discless) stellar models was also calculated. Because these models can be computed much faster than the bump models, we were able to cover a much finer grid of stellar parameters (Table 3), aiming at a better determination of the stellar parameters. The grid is composed by models for 12 different masses (second column), 6 different rotation rates (third column), 5 equally spaced values for the age in the main sequence (fourth column) and 10 equally spaced values of $\cos i$ (fifth column), resulting in a total of

[!t]

Table 3. Parameters of the grid of photometric models of discless stars

Z	M/M_{\odot}	W	t/t_{MS}	i [deg]
0.002	2.50	0.600	0.00	00.0
	3.68	0.699	0.25	27.3
	4.85	0.770	0.50	38.9
	6.00	0.833	0.75	48.2
	7.15	0.901	1.00	56.3
	8.29	0.990		63.6
	9.42			70.5
	10.54			77.2
	11.66			83.6
	12.78			90.0
	13.89			
	15.00			

$12 \times 6 \times 5 \times 10 = 3600$ photometric models for each of the *BVRI* bands.

3.3 Empirical law

In order to facilitate the comparison of the synthetic light curves (Sect. 3.2) with the observed ones (Sect. 4), we developed two empirical laws that match quite closely the synthetic light curves for build-up and dissipation. The usefulness of these formulae will become clear in the next section.

In our discussion of the features of the light curves, it is useful to separate them in three groups: (i) *pole-on light curves*, of stars seen at small inclination angles ($0 \leq i \lesssim 70$ deg), which should statistically correspond to the majority of the observed light curves; (ii) *edge-on light curves*, of shell stars ($i \approx 90$ deg); and, (iii) *intermediate light curves*, of stars seen at intermediate angles ($70 \lesssim i \lesssim 85$ deg – the extension of this intermediate region varies depending the photometric band under consideration and will be defined below). Pole-on light curves show an increase in apparent brightness, due to the additional flux coming from the disc. Conversely, edge-on light curves show a decrease in apparent brightness, due to obscuration of the star by the disc. The intermediate case shows the smallest variations in apparent brightness, and frequently the light curve has a more complicated shape, as it is influenced by variable amounts of disc emission/absorption.

A computed light curve is a sequence of absolute magnitudes for a set of time parameters, in a given photometric band X , given by

$$M_X(\tilde{\tau}) = M_{X*} + \Delta X(\tilde{\tau}),$$

where M_{X*} is the absolute magnitude of the inactive Be star at band X , and $\Delta X(\tilde{\tau})$ is the magnitude difference caused by the disc ($\Delta X(\tilde{\tau})$ can be either positive or negative). M_{X*} can be estimated from the light curve during the inactive phase (e.g., the purple points of Fig. 1). A build-up light curve (for $\tilde{\tau} - \tilde{\tau}_{\text{bu}} < 0$) is denoted by $\Delta X_{\text{bu}}(\tilde{\tau})$. Its limiting value, if the build-up phase were to have an infinite duration, is denoted by $\Delta X_{\text{bu}}^{\infty}$ – the photometric excess of the disc when in steady-state. A dissipation light curve (for $\tilde{\tau} - \tilde{\tau}_{\text{bu}} \geq 0$) is denoted by $\Delta X_{\text{d}}(\tilde{\tau})$. Its value at the beginning of the dissipation ($\tilde{\tau} = \tilde{\tau}_{\text{bu}}$) is given by ΔX_{d}^0 . Since every dynamical model starts from a discless state and asymptotically ends at a discless state, it follows that, regardless of the viewing angle, for every build-up light curve the quantity $\Delta X_{\text{bu}}(\tilde{\tau})/\Delta X_{\text{bu}}^{\infty}$ is a function that goes from 0 to 1 as $\tilde{\tau}$ goes from 0 to ∞ , and for every dissipation light curve, the quantity

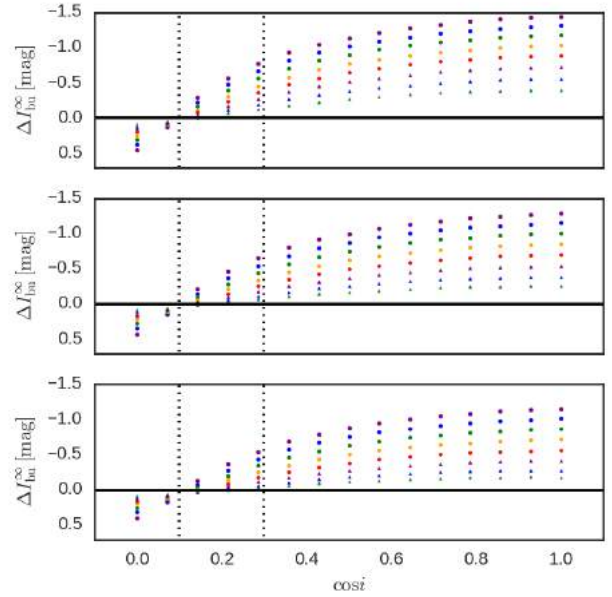


Figure 2. The values of $\Delta I_{\text{bu}}^{\infty}$ versus $\cos i$ for our grid. From top to bottom, the results are for Star 1, Star 2 and Star 3, respectively. Purple, blue, green, orange and red circles correspond to $\Sigma_0 = 2.50, 1.85, 1.37, 1.01, 0.75 \text{ g cm}^{-2}$. Purple, blue and green triangles correspond to $\Sigma_0 = 0.56, 0.41, 0.30 \text{ g cm}^{-2}$. Vertical dotted lines define the region of intermediate angles for the *I*-band ($73 \lesssim i \lesssim 84$ deg).

$\Delta X_{\text{d}}(\tilde{\tau})/\Delta X_{\text{d}}^0$ is a function that goes from 1 to 0 as $\tilde{\tau} - \tilde{\tau}_{\text{bu}}$ goes from 0 to ∞ . In Appendix B, we show examples of light curves that accompany the conclusions drawn on this section.

The values of $\Delta I_{\text{bu}}^{\infty}$ for our grid are shown in Fig. 2, plotted against $\cos i$. The values for the *BVR* bands show qualitatively similar patterns to the ones presented in this figure. Each panel shows the results for a different star, and all 8 values of Σ_0 (Table 1) are represented in the figure by different colours and symbols. The curves monotonically increase with $\cos i$, starting with negative values at edge-on orientation and reaching a maximum for pole-on viewing. The angle for which $\Delta X_{\text{bu}}^{\infty} = 0$, where the disc excess emission is exactly matched by the absorption of photospheric light by the disc, depends both on the density scale (as shown in the figure) and (most importantly) on the band pass.

An analysis of our model grid allowed us to determine the ranges in inclination angle for which the light curve displays the intermediate behaviour described above. They were determined by visual inspection of our model grid, as the angles for which the light curves present more complex shapes (see, e.g., the *I*-band light curves seen at $i = 81.8$ deg and $i = 77.6$ deg in Fig. B1 of Appendix B). Their adopted values are 53–78 deg, 60–78 deg, 66–84 deg and 73–84 deg for the *BVRI* bands, respectively.

For pole-on orientations, the observed excess is given by $\Delta X \approx -2.5 \log(1 + F_{\text{disc}}/F_*) \approx -F_{\text{disc}}/F_*$. Vieira et al. (2015) studied the continuum emission from gaseous discs, and showed that it can be approximated by the sum of the flux coming from an optically thick inner part (the so-called pseudophotosphere) with the contribution from an optically thin outer part, i.e.,

$$F_{\text{disc}} \propto F_{\text{thick}} \cos i + F_{\text{thin}}. \quad (14)$$

If the contribution of the optically thin part of the disc were negli-

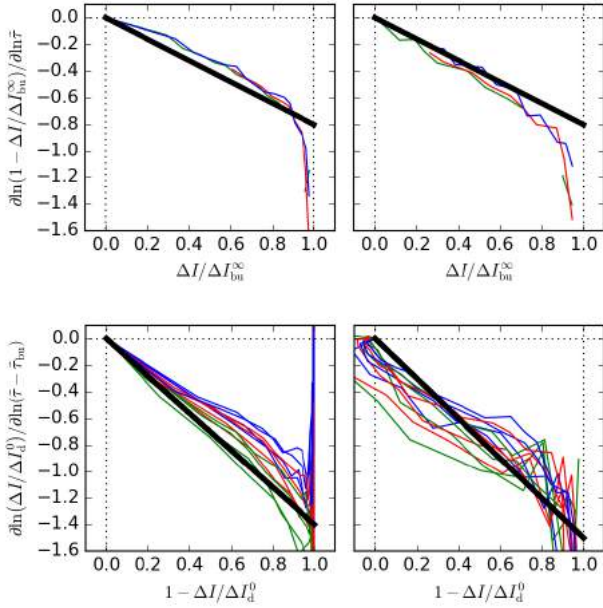


Figure 3. Comparison of the empirical law (black straight lines) with the computed light curves for build-up and dissipation. *Top panels:* log – log derivative of $1 - \Delta I_{\text{bu}}(\tilde{\tau})/\Delta I_{\text{bu}}^\infty$ vs. $\Delta I_{\text{bu}}(\tilde{\tau})/\Delta I_{\text{bu}}^\infty$. *Bottom panels:* log – log derivative of $\Delta I_{\text{d}}/\Delta I_{\text{d}}^0$ vs. $1 - \Delta I_{\text{d}}/\Delta I_{\text{d}}^0$, for values of $\tilde{\tau}_{\text{bu}}$ equal to 0.45, 1.5, 6 and 30. The results are shown for Star 2 at two inclination angles: $i = 0$ deg (*left*), and $i = 90$ deg (*right*). The green, red and blue curves correspond to Σ_0 equal to 1.37, 0.75 and 0.41 g cm^{-2} .

gible and the stellar flux, F_* , did not depend on $\cos i$, ΔX would be a linear function of $\cos i$. Clearly this is not the case for the entire range of $\cos i$, and both the optically thin and thick parts of the disc contributes to observed behaviour of ΔX vs. $\cos i$. This pseudophotosphere concept will be important to understand the growth and decay rates of the light curves, discussed below.

Figure 2 also shows that the excesses increase a little when moving from a low- to a high-mass star, for discs with the same other features. This is a consequence of the fact that the stellar flux relative to the disc flux increases with the luminosity of the star.

Both the pole-on and edge-on light curves have functions $\Delta X_{\text{bu}}(\tilde{\tau})/\Delta X_{\text{bu}}^\infty$ and $\Delta X_{\text{d}}(\tilde{\tau})/\Delta X_{\text{d}}^0$ that are qualitatively similar to each other, suggesting that they could be approximated by simple and general formulas of $\tilde{\tau}$. This is illustrated in Fig. 3, where we compare the values of $\Delta I_{\text{bu}}(\tilde{\tau})/\Delta I_{\text{bu}}^\infty$ and $\Delta I_{\text{d}}(\tilde{\tau})/\Delta I_{\text{d}}^0$ (in the horizontal axis) with their log – log derivatives (in the vertical axis). As the panels exemplify, the curves are similar to each other in a wide range parameters ($\cos i$, Σ_0 and $\tilde{\tau}_{\text{bu}}$), and they can be roughly approximated by straight lines (shown in black). Therefore, the build-up and dissipation light curves (for inclinations not in the intermediate region) should roughly obey the following differential equations:

$$\frac{\partial \ln}{\partial \ln \tilde{\tau}} \left(1 - \frac{\Delta X_{\text{bu}}}{\Delta X_{\text{bu}}^\infty} \right) \approx -\eta_{\text{bu}} \frac{\Delta X_{\text{bu}}}{\Delta X_{\text{bu}}^\infty}, \quad (15)$$

and

$$\frac{\partial \ln}{\partial \ln (\tilde{\tau} - \tilde{\tau}_{\text{bu}})} \frac{\Delta X_{\text{d}}}{\Delta X_{\text{d}}^0} \approx -\eta_{\text{d}} \left(1 - \frac{\Delta X_{\text{d}}}{\Delta X_{\text{d}}^0} \right), \quad (16)$$

Table 4. Adopted values for the η exponent of Eqs. 17 and 18

		<i>B</i>	<i>V</i>	<i>R</i>	<i>I</i>
η_{bu}	(edge-on)	0.8	0.8	0.8	0.8
	(pole-on)	0.8	0.8	0.8	0.8
η_{d}	(edge-on)	1.5	1.5	1.5	1.5
	(pole-on)	1.1	1.2	1.3	1.4

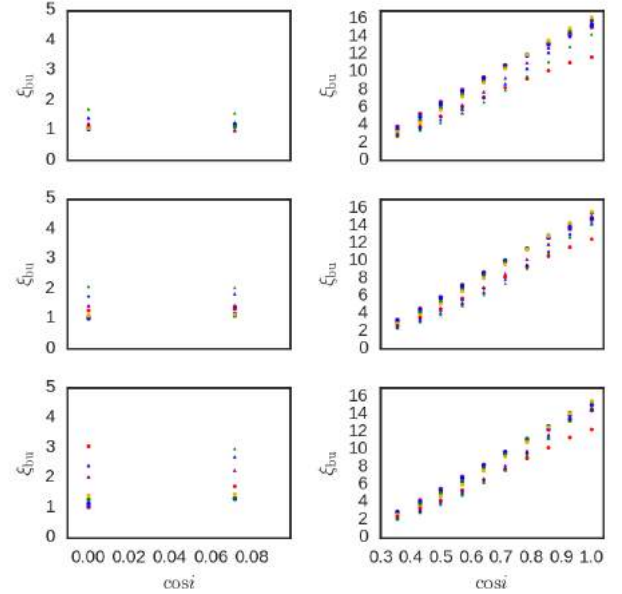


Figure 4. The *I*-band values of ξ_{bu} for our grid vs. $\cos i$. *Left:* Edge-on models. *Right:* Pole-on models. From top to bottom, the results for Star 1, 2, and 3, respectively. The markers are the same as in Fig. 2.

whose solutions are, respectively,

$$\Delta X_{\text{bu}} = \Delta X_{\text{bu}}^\infty \left[m 1 - \frac{1}{1 + (\xi_{\text{bu}} \tilde{\tau})^{\eta_{\text{bu}}}} \right], \quad (17)$$

and

$$\Delta X_{\text{d}} = \Delta X_{\text{d}}^0 \left[\frac{1}{1 + (\xi_{\text{d}} (\tilde{\tau} - \tilde{\tau}_{\text{bu}}))^{\eta_{\text{d}}}} \right]. \quad (18)$$

The continuity condition requires

$$\Delta X_{\text{d}}^0 = \Delta X_{\text{bu}}^\infty \left[1 - \frac{1}{1 + (\xi_{\text{bu}} \tilde{\tau}_{\text{bu}})^{\eta_{\text{bu}}}} \right]. \quad (19)$$

The parameters ξ_{bu} and ξ_{d} are constants of integration whose values must be determined by fitting the above formulae to the computed light curves. The values of the exponents η_{bu} and η_{d} were empirically determined to best match the model light curves (Table 4). It was found that good fits for the whole set of parameters ($\cos i$, Σ_0 and $\tilde{\tau}_{\text{bu}}$) could be obtained for certain fixed values of η_{bu} and η_{d} for each photometric band.

Representative *I*-band values of ξ_{bu} and ξ_{d} for our grid are shown in Figs. 4, 5 and 6 (the values of ξ_{bu} and ξ_{d} for the *BVR* bands show qualitatively similar patterns to the ones presented in these figures). Each row shows the results for a different star. The left (right) panels are for edge-on (pole-on) models. The values of ξ

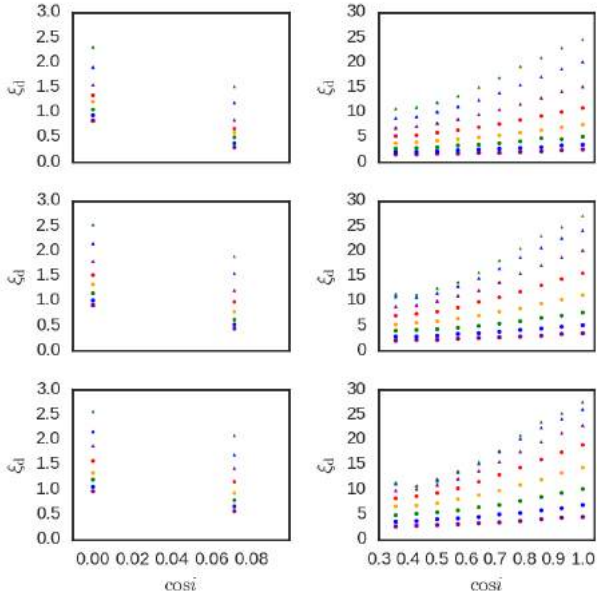


Figure 5. Selected I -band values of ξ_d for our grid vs. $\cos i$. The scaled build-up time was fixed to $\bar{\tau}_{bu} = 2.25$. *Left:* Edge-on models. *Right:* Pole-on models. From top to bottom, the results for Star 1, 2, and 3, respectively. The markers are the same as in Fig. 2.

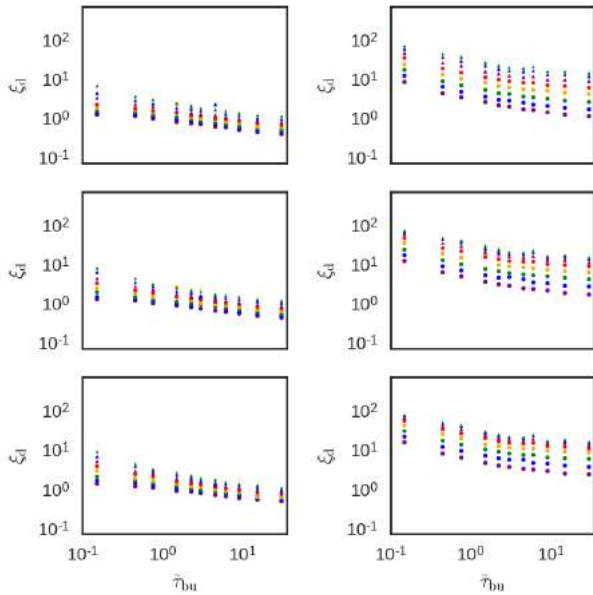


Figure 6. Selected I -band values of ξ_d for our grid vs. $\bar{\tau}_{bu}$. *Left:* Edge-on models with $i = 90$ deg. *Right:* Pole-on models with $i = 0$ deg. From top to bottom, the results for Star 1, 2, and 3, respectively. The markers are the same as in Fig. 2.

are directly related to the rate of photometric variations: the smaller the ξ , the slower the variation (see Eqs. 17 and 18).

Figure 4 exemplifies the strong variation of ξ_{bu} with i , for the pole-on case. This is probably due to the fact that, in the build-up process, the density grows from the inside out (see Appendix A), which means that the optically thick part of the disc (an expanding pseudo-photosphere) forms first, and the optically thin part takes longer to be built. Since the optical excess of the disc is given by $\Delta X \propto F_{thick} \cos i + F_{thin}$, it follows that, as we move from pole-on to edge-on angles, only the optically thick contribution (proportional to $\cos i$) varies. As a consequence, the observed rate of increase in flux moves from being more to less optically thick dominated.

In the dissipation process, the density rapidly adjusts to a self-similar dissipation pattern in the inner disc (Appendix A). Therefore, the flux from the disc is the result of the decrease and disappearance of the optically thick region - transformed into an optically thin region - and the diminishing of the whole optically thin region. The pole-on values of ξ_d (right panels of Fig. 5) are affected by $\cos i$ to a less extent, when compared to the values of ξ_{bu} . In the dissipation process, by the same reasoning applied to the build-up process, since the optically thick emission is attenuated by the effect of $\cos i$, its disappearance has a reduced effect for more inclined discs and, therefore, the disc should apparently disappear at a slower rate.

The values of ξ_d also show great variation with the asymptotic surface density (Figs. 5 and 6). More specifically, increasing Σ_0 results in a light curve with a slower decay rate. This is probably due to different levels of saturation in the optically thick region. The denser the optically thick region, the bigger its optical depth and the greater the amount of time for it to turn into an optically thin region.

In addition, Fig. 6 shows that ξ_d strongly depends on the scaled build-up time. As expected from the mass reservoir effect (Sect. 2.2), increasing $\bar{\tau}_{bu}$ results in smaller values of ξ_d , which implies slower decay rates.

From the above an important conclusion can be drawn: viscosity is not the only parameter affecting the rate of photometric variations in a Be light curve. The stellar parameters, the asymptotic surface density, as well as the inclination angle, all affect the observed shape of the light curve. Thus, extracting α from light curves, one of the main goals of this paper, cannot be done without some knowledge about these parameters.

3.4 Fitting pipeline

So far, our model light curves were given in terms of the adimensional time parameter, $\bar{\tau}$. Thus, an equation is necessary to transform from the physical time t to $\bar{\tau}$, in order to connect the real light curves to our simulated ones.

A variation in the time parameter, $d\bar{\tau}$, is related to a variation in physical time by $d\bar{\tau} = dt/\tau(t)$, where $\tau(t)$ depends on 3 stellar parameters (M , R_{eq} , T_{eff}) and the viscous parameter $\alpha(t)$ (Eq. 6). For a given Be star, the build-up phase starts at t_1 , and ends at t_2 , when dissipation begins. Thus, the build-up time is given by $t_2 - t_1$. In this work, following the results of Ghoreyshi & Carciofi (2017), we explore the possibility that the viscosity parameter may be different at build-up ($\alpha(t) = \alpha_{bu}$, for $t_1 \leq t < t_2$) and dissipation ($\alpha(t) = \alpha_d$, for $t \geq t_2$). Therefore, the transformation equation from t to $\bar{\tau}$ is

$$\bar{\tau} = \begin{cases} \alpha_{bu} \frac{t-t_1}{\alpha\tau}, & t_1 \leq t < t_2 \\ \alpha_{bu} \frac{t_2-t_1}{\alpha\tau} + \alpha_d \frac{t-t_2}{\alpha\tau}, & t \geq t_2 \end{cases}, \quad (20)$$

which is such that, as t goes from t_1 to t_2 , $\bar{\tau}$ goes from 0 to $\bar{\tau}_{bu} = \alpha_{bu}(t_2 - t_1)/\alpha\tau$, and for t larger than t_2 , we see that $\bar{\tau} > \bar{\tau}_{bu}$. Recall

that $\alpha\tau$, defined in Eq. 6, is a quantity dependent only on the stellar parameters and the disc temperature.

Substitution of Eq. (20) into Eqs. (17), (18) and (19), gives the following equation for fitting an observed bump

$$\Delta X(t) = \begin{cases} \Delta X_{\text{bu}}^{\infty} \left(1 - \frac{1}{1+[C_{\text{bu}}(t-t_1)]^{\eta_{\text{bu}}}}\right), & t_1 \leq t < t_2 \\ \Delta X_{\text{bu}}^{\infty} \left(1 - \frac{1}{1+[C_{\text{bu}}(t_2-t_1)]^{\eta_{\text{bu}}}}\right) \frac{1}{1+[C_{\text{d}}(t-t_2)]^{\eta_{\text{d}}}}, & t \geq t_2 \end{cases}$$

where

$$C_{\text{bu}} = \alpha_{\text{bu}} \frac{\xi_{\text{bu}}}{\alpha\tau}, \quad (22)$$

and

$$C_{\text{d}} = \alpha_{\text{d}} \frac{\xi_{\text{d}}}{\alpha\tau} \quad (23)$$

are coefficients related to the rate of photometric variations. The values of the parameters $\Delta X_{\text{bu}}^{\infty}$, ξ_{bu} and ξ_{d} were tabulated in Sect. 3.3, by fitting the respective empirical laws to the model grid.

Our goal is to fit an observed light curve with Eq. 21, in order to obtain, in a self-consistent way, all the stellar and disc parameters of interest. For that, the following chain of procedures is adopted:

- (i) Find a light curve of a Be star that contains at least one clear inactive phase and one complete photometric bump.
- (ii) Obtain the magnitudes X_* at the inactive phase. Subtract these magnitudes from the light curve and obtain the excesses $\Delta X(t)$.

Without a clear inactive phase, it is not possible to obtain the pure photospheric level (e.g., the horizontal purple straight lines in Fig. 1) and, consequently, it is not possible to know how much of the observed bumps represent the disc contribution to the total flux. In addition, the photometric bump must contain a completely identified build-up phase, from which the instants t_1 and t_2 can be extracted, and a considerable extension of the dissipation phase.

- (iii) Fit Eq. (21) to the selected bumps, obtaining the coefficients $\Delta X_{\text{bu}}^{\infty}$, C_{bu} and C_{d} , as well as the times t_1 and t_2 for the onsets of build-up and dissipation.

- (iv) Transform the magnitudes at the inactive phase, X_* , to absolute magnitudes, M_{X_*} , by correcting for the distance to the star and reddening at each observed band.

Given the theoretical dependence of the coefficients in Eq. 21 on the stellar parameters, the absolute magnitudes are required to estimate the stellar parameters (M , W and t/t_{MS}). From them, the parameter $\alpha\tau$ (see Eq. 6) can be estimated. Clearly, if the stellar parameters are known from some other way (e.g., by spectroscopic analysis), this requirement is no longer necessary. Unfortunately, this is not the case for our sample.

- (v) Estimate the stellar parameters, the geometric parameter ($\cos i$) and the bump parameters (Σ_0 , α_{bu} and α_{d} , for each bump) that best reproduce the fitted stellar (M_{X_*}) and bump ($\Delta X_{\text{bu}}^{\infty}$, C_{bu} and C_{d}) parameters (see Eqs. 22 and 23 and the parameters $\Delta X_{\text{bu}}^{\infty}$, ξ_{bu} and ξ_{d} from Sect. 3.3).

In practice, the above process involves several complications (e.g., estimating the goodness of the fit) that are described in the next section.

3.5 Fitting using a MCMC sampling

The task of fitting the measured stellar absolute magnitude (M_{X_*}) and bump parameters ($\Delta X_{\text{bu}}^{\infty}$, C_{bu} and C_{d}) for estimating the model

parameters – step 5, above – was done using the Markov-Chain Monte Carlo (MCMC) sampling technique. We used the Python MCMC sampler *emcee* (Foreman-Mackey et al. 2013). The code samples a large collection of models by varying all model parameters within a pre-specified range. The sampler provides a distribution of model parameters according to a posterior distribution $p(\text{model} | \text{data}) \propto L(\text{data} | \text{model}) \pi(\text{model})$, where L and π are the likelihood and the prior distributions, respectively.

In our fitting procedure, there are $4 + 5N_{\text{bumps}}$ model parameters for each light curve containing N_{bumps} identified bumps. There are 3 stellar parameters (M , t/t_{MS} , W) and one geometric parameter ($\cos i$), and, for each bump in the light curve, there are 5 parameters: the initial times of the build-up and dissipation phases (t_1 and t_2), the asymptotic surface density (Σ_0), and the viscosity parameters during the build-up and dissipation phases (α_{bu} and α_{d}).

We assume that the errors of the observations follow a Gaussian distribution and, therefore, the likelihood of a Be star with certain model parameters, given the observed data, is given by

$$L(\text{data} | \text{model}) \propto e^{-\frac{1}{2}\chi^2}, \quad (24)$$

where

$$\chi^2 = \chi_{\text{discless}}^2 + \chi_{\text{bump}}^2, \quad (25)$$

and

$$\chi_{\text{discless}}^2 = \sum_{\text{bands}} \frac{(M_{X_*}^{\text{model}} - M_{X_*}^{\text{obs}})^2}{\sigma^2(M_{X_*}^{\text{obs}})}, \quad (26)$$

and

$$\chi_{\text{bump}}^2 = \sum_{\text{bands}} \sum_{\text{bumps}} \frac{1}{N_t} \sum_{i=1}^{N_t} \frac{(\Delta X_i^{\text{model}} - \Delta X_i^{\text{obs}})^2}{\sigma^2(\Delta X_i^{\text{obs}})}, \quad (27)$$

where N_t is the number of data points for a given bump at a given photometric band.

The prior distribution π represents our prior knowledge of the distribution of Be stars. We assume it to be

$$\pi(\text{model}) \propto M^{-2.3} f_{\text{Be}}(M) e^{-\frac{(W-\langle W \rangle)^2}{2\sigma_W^2}}, \quad (28)$$

where the factor $M^{-2.3}$ is the initial mass function (IMF) of Kroupa (2001), and $f_{\text{Be}}(M)$ represents the fraction of Be stars relative to the number of B stars, estimated by Martayan et al. (2007a, their Fig. 6). Finally, the Gaussian factor comes from the distribution of rotational velocities in the sample of Be stars, here estimated from Rivinius et al. (2006), assuming $\langle W \rangle = 0.81$ and $\sigma_W = 0.12$.

For the parameter sampling, we have chosen hundreds of “walkers”¹, proportional to the number of $4 + 5N_{\text{bumps}}$ model parameters. For a randomly chosen set of parameters sampled by *emcee* in the course of the simulation, the corresponding stellar and bump observables are calculated by a multidimensional linear interpolation of the model grid. During the raffle of parameters the prior probability was set to zero if one of the values were sampled outside of the allowed range of a given parameter (Tables 1 and 3). The simulation consists of two steps, the so-called “burn-in phase” and the sampling phase. We verified that 1000 iterations in the burn-in phase were sufficient for the convergence of all our models. For each parameter, the best-fitting values were chosen to be the median of distribution of the posterior probabilities, with upper (lower)

¹ Each walker can be viewed as a separated Markov Chain in the sample, although the walkers influence each another (Foreman-Mackey et al. 2013).

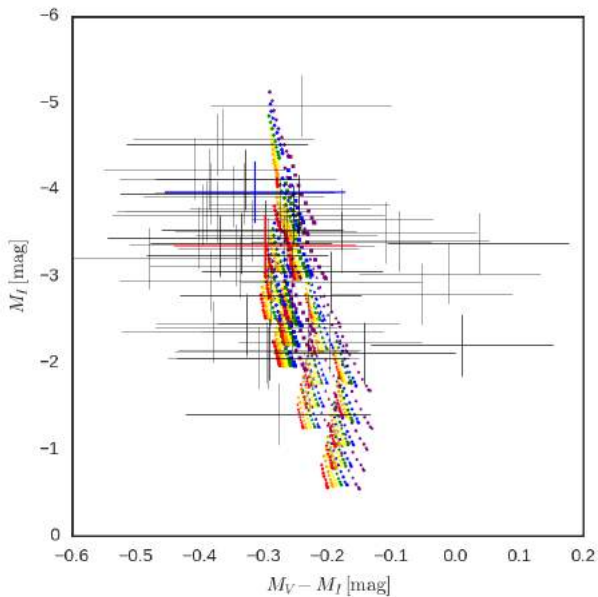


Figure 7. Color-magnitude diagram of simulated discless stars (Table 3). Circles, triangles, squares and diamonds correspond to stellar models with $M = 6.0, 8.3, 11.7, 15.0 M_{\odot}$, respectively. The colours red, orange, yellow, green, blue and purple correspond, respectively, to the 6 values of W in increasing order. The 5 different stellar ages are seen as the groups of points move in the upper-right direction. For each star, the effect of going from 90 deg to 0 deg is to move in the upper-left direction. Also shown, as error bars, is the position of our selected stars (see eighth and ninth columns of Table 5). The blue and red error bars mark the positions of SMC_SC1 75701 and SMC_SC6 128831, respectively.

uncertainties estimated from the differences between 84%(16%) of the sample and the median

In Sect. 4 we present a selection of light curves of Be stars from the SMC, and measure their stellar and bump quantities (steps 1 to 4 of the pipeline). Later, in Sect. 5, we apply step 5 of the pipeline, as described in this section, in order to estimate the relevant parameters of the selected Be stars.

4 OGLE LIGHT CURVES OF BE STAR CANDIDATES

Mennickent et al. (2002) selected roughly one thousand Be star candidates from the SMC, by studying light curve variations using the OGLE-II database (Udalski et al. 1997). They classified the morphologies found in the light curves into four categories. The majority of the light curves ($\sim 65\%$) belonged to their type-4 category, composed by the light curves showing irregular and non-periodic variations. These light curves should correspond to Be stars showing episodes of mass injection more complicated than the simple build-up followed by dissipation scenario described in Sect. 3.

Most interesting for us is the type-1 group ($\sim 13\%$ of the sample), composed by light curves that show single sharp or hump-like bumps, like the bumps of the light curve of SMC_SC1 75701 (Fig. 1). These bumps should be the result of single nearly continuous episodes of mass injection followed by dissipation of the disc, like the theoretical scenario explored in Sect. 3.

The type-2 group ($\sim 14\%$ of the sample), containing light curves showing high and low plateaus, also has some interesting

cases for our purposes. High plateaus are usually the photometric result of a longer build-up process in which a near steady-state has been reached in the inner disc. The low plateaus are frequently the portions of the light curve during inactive phases.

Sabogal et al. (2005) selected roughly two thousand Be star candidates from the LMC and classified their light curves into the same four categories described by Mennickent et al. (2002). Previously, Keller et al. (2002) also studied light curves from the LMC using the MACHO survey. They spectroscopically analysed a subsample of their Be star candidates and found that 90% of them were Be stars. They also classified morphologically their light curves in a slightly different manner. Their so called “bumper events” and “flicker events” more or less correspond to the bumps of type-1 light curves, but also to features of the more irregular type-4 light curves. The bumpers have duration of a few hundred days, while the flicker events are faster, with durations of a few dozens of days. Dips like the one exemplified by the light curve of SMC_SC6 128831 (Fig. 1) were called “fading events”. The frequency of these events was quite smaller than the bumpers, in accordance to the picture that fading events are associated with the less numerous shell stars.

Paul et al. (2012) studied the spectral properties of stars from the catalogues of Mennickent et al. (2002) and Sabogal et al. (2005). For the candidates from the SMC, they found that the majority of type-1 and type-2 light curves belong to early B type stars with emission features characteristic of circumstellar material (Paul et al. 2012). Therefore, these light curves are very likely to be from Be stars.

In this work, we selected light curves from the catalogue of Be star candidates from the SMC of Mennickent et al. (2002). In order to have light curves of a longer time baseline, we combined OGLE-II data with OGLE-III (Udalski et al. 2008) Due to a calibration issue between OGLE-II and OGLE-III, namely a shift in the zero points present in some of the light curves, it was necessary to find inactivity intervals in both the OGLE-II and OGLE-III portions of these light curves to measure and correct the problem.

The light curves were visually inspected according to the criteria of item 1, Sect. 3.4, i.e., light curves with at least one clear inactive phase and one bump. In this initial work we focussed on well-behaved light curves with clear bumps. We also avoided the short events (flickers, with build-up times $\lesssim 15$ days), due to the fact that most of them are poorly sampled. The end result was a sample of 54 stars, containing 81 selected bumps, shown in Table 5. In the table, horizontal lines separate the data for each of the 54 stars. Each row in the table contain the data for each of the 81 selected bumps. The fifth and sixth columns in the table contain the beginning and ending of the selected inactive interval for the light curve. The seventh, eighth and ninth columns contain the $B_*V_*I_*$ magnitudes obtained at the inactive phase for the light curve. Due to the nature of the OGLE survey, the B_*V_* are not available for all sources. The eleventh column contains the bands that were considered in the fitting process of the specific bumps, depending on the availability of measurements in each band. The last two columns are initial visual estimates of t_1 and t_2 , which were used as input for emcee.

As explained in Sect. 3.4, the magnitudes at the inactive phase are necessary to set the baseline level of the light curves and to provide an estimate of stellar parameters. In order to do the latter, these apparent magnitudes must be colour-corrected and converted to absolute magnitudes by the standard formula $M_{X_*} = X_* - (5 \log d - 5) - A_X$. We adopted as the distance to the SMC $d = 60.3 \pm 3.8$ kpc from Hilditch et al. (2005). The mean V -band reddening of the bright stars over the whole SMC

is $A_V = 0.470 \pm 0.326$ (Zaritsky et al. 2004). The reddening in the other bands were obtained by the relations A_X/A_V given by Gordon et al. (2003).

The colour-magnitude diagram (CMD) of Fig. 7 compares the grid of discless models (Table 3) to our sample of Be stars. Most of the stars lie in the upper right corner of the CMD, which means that the majority of our sample is comprised of early-type Be stars, as further discussed in Sect. 5.2.1.

5 RESULTS

In this section, the results obtained by applying the pipeline to the stars and bumps of our sample are described. Initially, the results for the two objects of Fig. 1 are examined in detail (Sect. 5.1), followed by an analysis of the results obtained for the entire sample (Sect. 5.2).

5.1 SMC_SC1 75701 and SMC_SC6 128831

The results for SMC_SC1 75701 and SMC_SC6 128831 are shown in Figs. 8 and 9, respectively. For SMC_SC1 75701 there was enough data for both the I and V bands to allow these two light curves to be fitted simultaneously. For SMC_SC6 128831, however, only I -band data was available. The times for the beginning of the build-up (t_1) and dissipation (t_2) are fitted quantities in the pipeline, but an initial estimate for them is provided to `emcee` by graphically analysing each light curve. These estimates are shown as the purple and orange segments in the horizontal straight lines in the figure. In the MCMC sampling, after a sufficient number of iterations, a stationary sample is obtained, for which the model parameters are more concentrated in the regions of higher posterior probability. In the plots we show 100 sets of randomly selected model curves obtained after the stationary sample was reached. The dispersion of the curves gives a visual measure of the goodness of the fits.

The goodness of the fit can be quantitatively assessed from the distribution of the posterior probabilities of each fitted parameter shown in Figs. 8 and 9. The main diagonal of the triangular diagram plots the distributions of the stellar (M , t/t_{MS} and W), geometrical ($\cos i$), and bump (Σ_0 , α_{bu} and α_d) parameters, and they can be used to assess how well-constrained each parameter is. The images below the diagonal show how the parameters correlate with each other.

The stellar parameters (M , t/t_{MS} and W) are mainly constrained by the magnitudes at the inactive phase. In Fig. 8, the three leftmost histograms along the diagonal have broad distributions, which means that these parameters are not well constrained. The first histogram shows that SMC_SC1 75701 is an early Be star, probably even more massive than the available stellar models (Table 3). This agrees with the position of the star in the CMD (Fig. 7). The mass is anti-correlated with the main sequence age (see $t/t_{MS} \times M$ plane), as expected from the fact that a less massive but more evolved star can have a similar absolute magnitude of a younger, more massive star.

The bump parameters (Σ_0 , α_{bu} and α_d) are mainly constrained by the shape of the observed bump. Roughly, the amplitude of the bump depends mostly on Σ_0 (and $\cos i$, see Fig. 2), while the value of viscosity parameter in each phase controls the rate of brightness variation. For SMC_SC1 75701, Σ_0 has a broad distribution peaking around $\sim 1.5 \text{ g cm}^{-2}$, indicating a quite dense disc, close to the densest cases in the sample of Vieira et al. (2017) for the same spectral

type. This fact can also be inferred from Fig. 2, given the large observed ΔI_{bu}^{∞} . The best-fit viscosity parameters are $\alpha_{bu} = 0.24^{+0.18}_{-0.08}$ and $\alpha_d = 0.11^{+0.08}_{-0.05}$.

Of the three bump parameters derived for SMC_SC1 75701, Σ_0 and α_d clearly anti-correlate with $\cos i$, while α_{bu} shows no signs of correlation. In fact, an anti-correlation of these three parameters with $\cos i$ is expected, as a consequence of the dependency of ΔX_{bu}^{∞} , ξ_{bu} and ξ_d , defined in Sect. 3.3, on $\cos i$. Fig. 2 shows that, if the star is seen more pole-on (higher values of $\cos i$), smaller values of Σ_0 are required in order to obtain the fitted ΔX_{bu}^{∞} , hence the strong anti-correlation seen in the $\Sigma_0 \times \cos i$ plane. Eq. (22) shows that the fitted coefficient C_{bu} is proportional to the product of α_{bu} and ξ_{bu} , and it was shown (Fig. 4) that discs seen more pole-on (higher values of $\cos i$) appear to build-up faster (having higher values of ξ_{bu}). Therefore, for higher values of $\cos i$, smaller values of α_{bu} are required to obtain the fitted C_{bu} , which explains the anti-correlation in the $\alpha_{bu} \times \cos i$ plane. Finally, Eq. (23) shows that the C_d is proportional to the product of α_d and ξ_d , and it was shown in Fig. 5 that the more pole-on and the less dense the disc, the faster the rate of brightness variation in the dissipation, thus the anti-correlation expected in the $\alpha_d \times \cos i$ plane. Even though this last anti-correlation was not observed for SMC_SC1 75701, it is clearly seen for many objects of our sample, for instance, SMC_SC3 71445 (Fig. C11) and SMC_SC3 125899 (Fig. C13).

The results for SMC_SC6 128831 (Fig. 9) point to a less massive star ($M = 12.2^{+2.7}_{-2.2} M_{\odot}$) surrounded by a much more massive disc ($\Sigma_0 = 2.6^{+0.5}_{-0.6} \text{ g cm}^{-2}$). SMC_SC6 128831 is an example of a dip, which means that this Be star is seen at a near edge-on angles. The very steep build-up phase of SMC_SC6 128831 hints to large mass injection rate and viscosity during build-up, as confirmed by the fifth and sixth histograms along the diagonal of Fig. 9. The viscosity parameter during dissipation was found to be $\alpha_d = 0.69^{+0.34}_{-0.27}$. The plane $\alpha_d \times \Sigma_0$ shows a correlation, just as for the case of SMC_SC1 75701, which is a consequence of the decrescent relationship between ξ_d with Σ_0 , also expected for near-edge-on inclinations (see Fig. 5).

For SMC_SC6 128831 a positive correlation between Σ_0 , α_{bu} and α_d with $\cos i$ was observed. Fig. 2 shows that, if the star moves away from the edge-on case ($\cos i = 0$), bigger values of Σ_0 are required in order to obtain the fitted ΔX_{bu}^{∞} , hence the correlation seen in the $\Sigma_0 \times \cos i$ plane. Fig. 4 shows that, for the edge-on case there is no strong variation of ξ_{bu} with $\cos i$. However, there is the trend that a more tenuous discs appear to build-up faster, specially for a hotter star. Therefore, since Eq. 22 shows that $C_{bu} \propto \alpha_{bu} \xi_{bu}$, it follows that, with the increase of Σ_0 with $\cos i$, the function ξ_{bu} decreases and, hence, α_{bu} increases. Finally, Eq. 23 shows that $C_d \propto \alpha_d \xi_d$ and Fig. 6 shows that ξ_d decreases with $\cos i$ and Σ_0 . Therefore, as Σ_0 increases with $\cos i$, it follows that ξ_d decreases and, hence, α_d must increase. Similar trends were found for the other two edge-on stars in our sample (SMC_SC1 92262, Figs. C4 and C5, and SMC_SC4 179053 (Fig. C34).

In general, the histograms of Fig. 9 are broader than the ones in Fig. 8, indicating that parameters are worse constrained than for SMC_SC1 75701. There are two main reasons for this. First, only I -band data was available for this star, which has a negative impact on the pipeline's ability to constrain the stellar parameters. The MCMC method ensures that the uncertainties in the stellar parameters are properly propagated into the other model parameters. Second, the fact that the dips have smaller amplitudes than the bumps of pole-on stars, even for higher values of Σ_0 , is a great disadvantage,

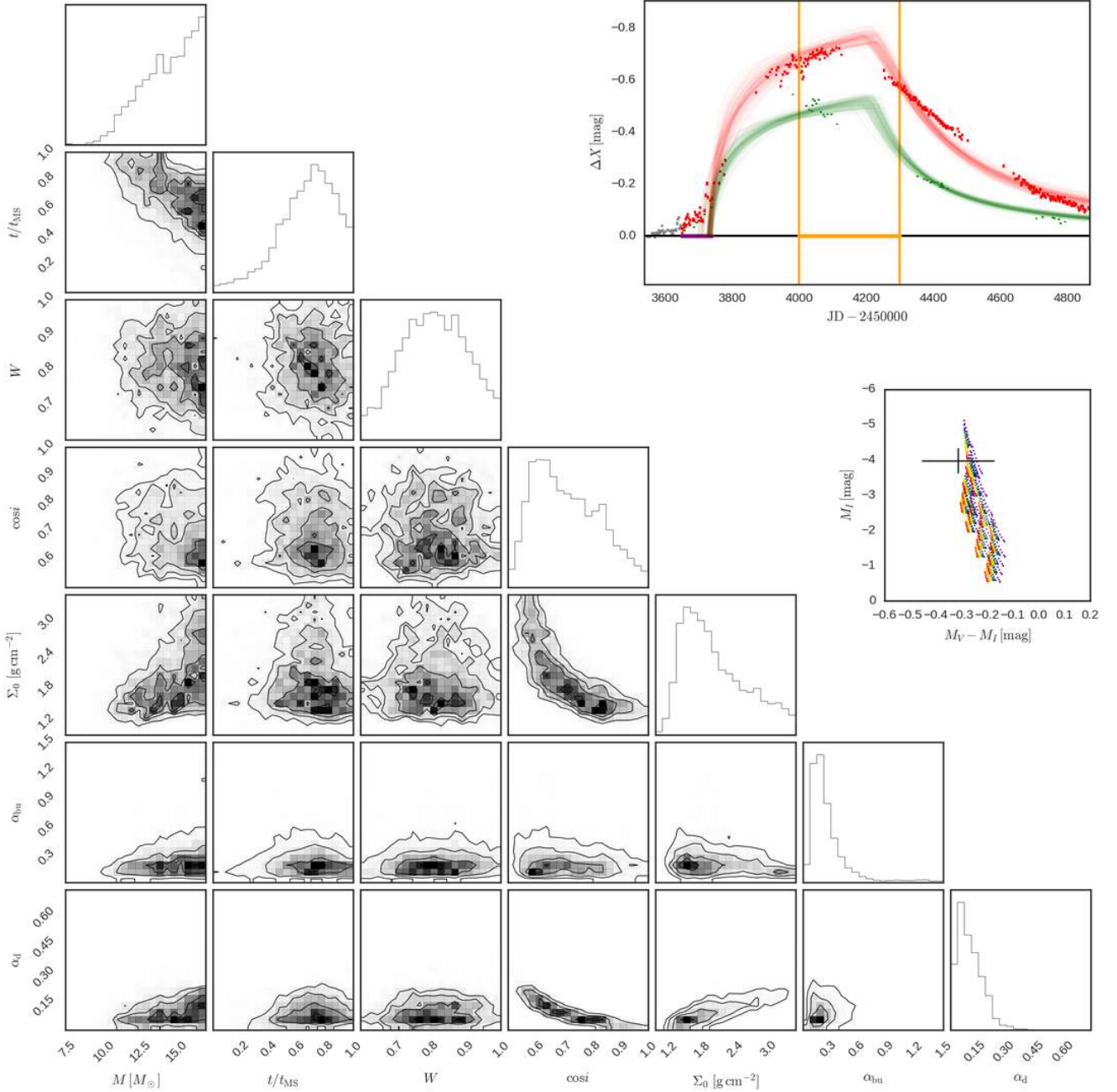


Figure 8. *Upper-right:* Light curve of SMC_SC1 75701. Thin lines: 100 model curves randomly selected from the stationary sample of the `emcee` code. The red (green) colour indicates the I (V) band. The purple and orange time intervals marked in the horizontal straight lines are the allowed intervals for the model parameters t_1 and t_2 , respectively. *Middle-right:* CMD displaying the model grid of inactive Be stars and the position of SMC_SC1 75701 (see Fig. 7 for details). *Below:* Results of the `emcee` run for SMC_SC1 75701. Histogram distributions of the posterior probabilities (top panels) and two-by-two correlations of the stellar (M , t/t_{MS} and W), geometrical ($\cos i$), and bump (Σ_0 , α_{bu} and α_d) parameters (off-diagonal panels). The parameters t_1 and t_2 were not shown for convenience. The normalised density levels shown in the off-diagonal panels are 12%, 39%, 68%, 87% of the peak probability.

because the bump amplitude is much closer to the noise level of the measurements.

The results of the pipeline for all stars in Table 5 are shown in Figs. C1 to C79, available electronically only. The best-fit model parameters for all stars and bumps are listed in Table 6.

5.2 Results for the whole sample

As seen previously, the scarcity of information about the central star (one, two, or at most 3 photometric bands only) causes a poor determination of its fundamental stellar parameters, which, owing to the nature of the MCMC method, propagates onto the disc parameters. The main result of this work, therefore, does not lie on

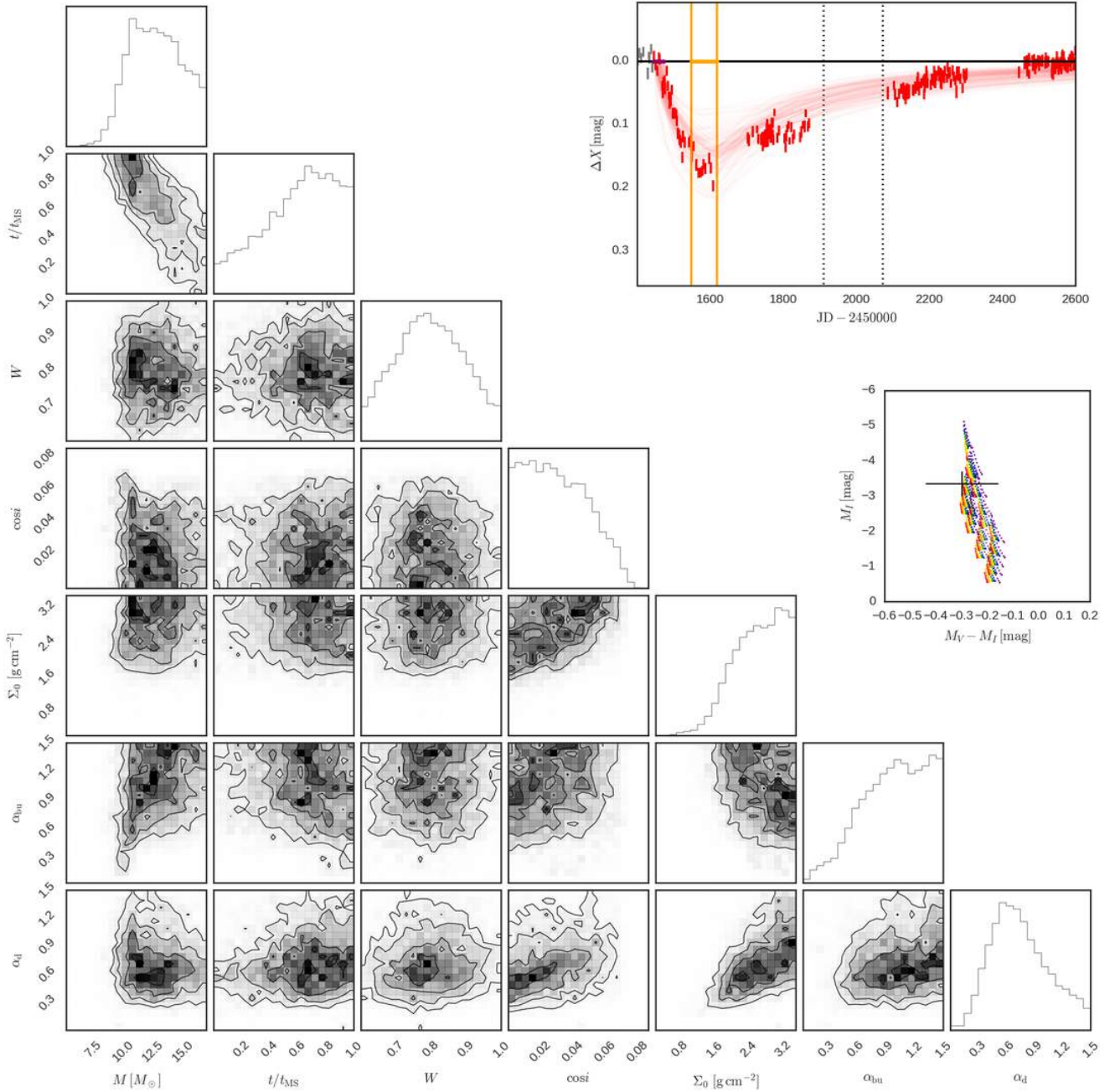


Figure 9. Same as Fig. 8 for SMC_SC6 128831.

the individual determination of the bump parameters, but on the statistical properties of the sample as a whole.

5.2.1 Mass distribution

Let us initially discuss the properties of our sample, in order to determine whether it represents a typical population of Be stars in SMC, or whether one or more selection biases were introduced.

Our selection of stars and bumps comes from the catalogue of visual photometric Be star candidates of Mennickent et al. (2002), where the candidate stars were selected according to the expected

location of Be stars in colour-magnitude diagrams and according to the observed variability in the light curves. In Fig. 10, we show the sum of the posterior probabilities of parameter M for all our sample of stars (solid line). Clearly, most of our stars are early-type Be stars, in agreement to the position of our sample in the CMD (Fig. 7). We also show the factor $\propto M^{-2.3} f_{\text{Be}}(M)$ of Eq. 28 (dashed line). We recall that this factor was assumed as a prior in the MCMC fitting, and it represents our current knowledge about the populations of Be stars in the SMC. The green curve shows that, although the fraction of Be stars over B stars ($f_{\text{Be}}(M)$), estimated by Martayan et al. (2007a) from a cluster of the SMC) generally increases with

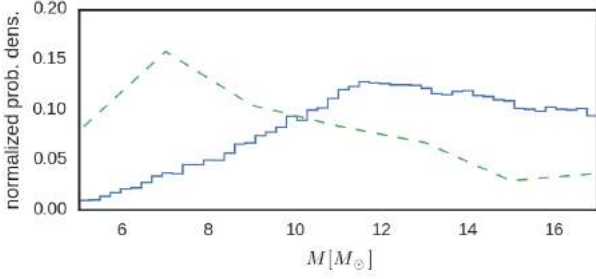


Figure 10. *Solid line:* Histogram of the sum of the posterior probabilities of parameter M for all stars in our sample. *Dashed line:* IMF of Kroupa (2001) weighed by the fraction of Be stars over B stars of Martayan et al. (2007a), given by the factor $M^{-2.3} f_{\text{Be}}(M)$ in Eq. (28).

M , the higher probability of the formation of less massive stars expressed in the IMF of Kroupa (2001) results in a bigger incidence of late type over early type Be stars. Our sample, therefore, is biased towards more massive stars.

This bias likely have several reasons:

- (i) The typical apparent I -band magnitudes of a B0 and B9 star in the SMC are ~ 15.5 and ~ 19.5 , with rms uncertainties given by $\gtrsim 0.005$ and $\gtrsim 0.15$, respectively (Wyrzykowski et al. 2009). Therefore, the threshold of detectability of a good bump increases for late type Be stars.
- (ii) Late-type Be stars tend to have more tenuous discs than early-type ones (Vieira et al. 2017, see also next subsections), and therefore should develop bumps with much smaller amplitudes.
- (iii) Late-type Be stars tend to show less variability (Rivinius et al. 2013, see also next subsections), which would make it less probable to identify bumps in their light curves.

5.2.2 Asymptotic surface density

In the upper panel of Fig. 11 we show how Σ_0 varies with stellar mass in our sample, demonstrating a clear tendency of denser discs around the more massive stars. Vieira et al. (2017) have shown that, for the Be stars in the Galaxy, the incidence of denser discs increases with the mass of the stars. Comparison of our results with the ones of Vieira et al. are done in Fig. 12. While our sample is biased towards large masses, their sample is more evenly distributed in mass. Another difference is that our results are all concentrated in a region of high disc density, while theirs cover a much wider range of densities for all spectral types. The reason for this lies in fact that for this initial study we selected light curves with large and well-defined bumps, disregarding low-amplitude and short-duration ones. In fact, the detection of tenuous discs by Vieira et al. was only possible because they studied the SED in the IR (typically between 9 and 60 μm), where the disc emission is much stronger than in the visible range. Therefore, all but the most dense of their discs would be too tenuous to generate appreciable photometric excesses in visual photometric bands, suitable for our fitting procedure.

We conclude that our sample of visual bumps should represent the upper limit for the densities found in the discs of SMC Be stars. In the Galaxy, these large densities are only found in early type Be stars. The median of the Σ_0 for our sample is $\langle \Sigma_0 \rangle = 1.44_{-0.75}^{+1.01} \text{ g cm}^{-2}$. Furthermore, there may be some indication that the Be stars in the SMC may have more massive discs, on average, than their

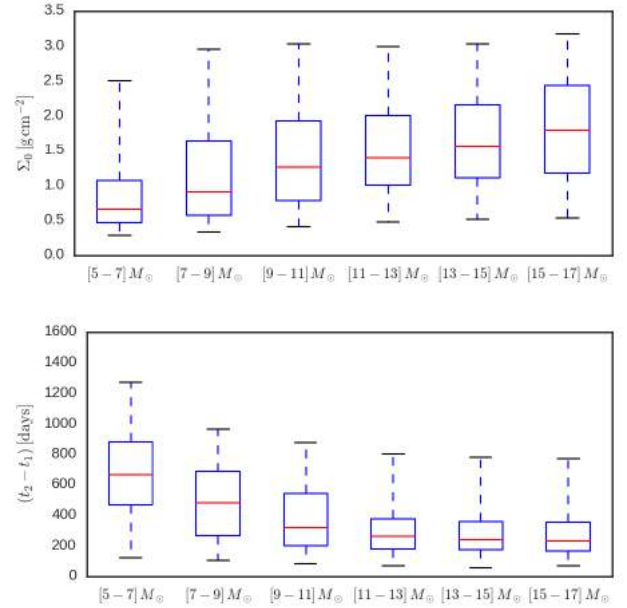


Figure 11. Boxplots of Σ_0 (above) and $t_2 - t_1$ (below) for the summed posterior probabilities of our sample of bumps, separated in six equal intervals of mass, ranging from 5 to 17 solar masses. The middle line of the boxes mark the median (50%) of the samples. The lower and upper ends of the boxes mark 25% and 75% of the samples. The lower and upper whiskers mark 5% and 95% of the samples.

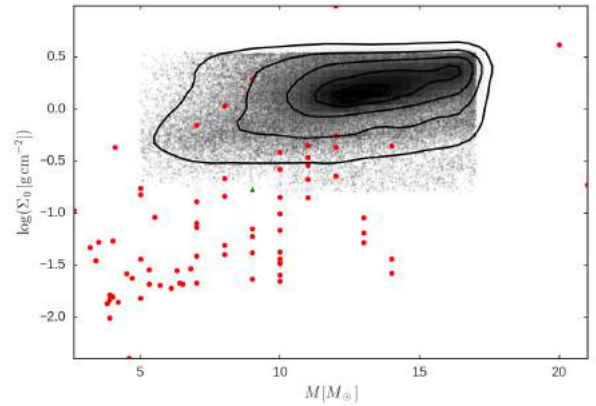


Figure 12. Distribution of the parameters M and Σ_0 for our sample. The contour levels are the same as in Fig. 8. The red dots correspond to the surface densities at the base of the disc of Galactic Be stars, measured by Vieira et al. (2017). The green triangle corresponds to the initial state of the ablating disc model of Kee et al. (2016) for a B2e star.

galactic counterparts, in line with results from the literature that report higher $H\alpha$ equivalent widths in the SMC Be stars than in the Galaxy (Martayan et al. 2007b). This last point, however, should be view with some caution given the large biases present in our sample.

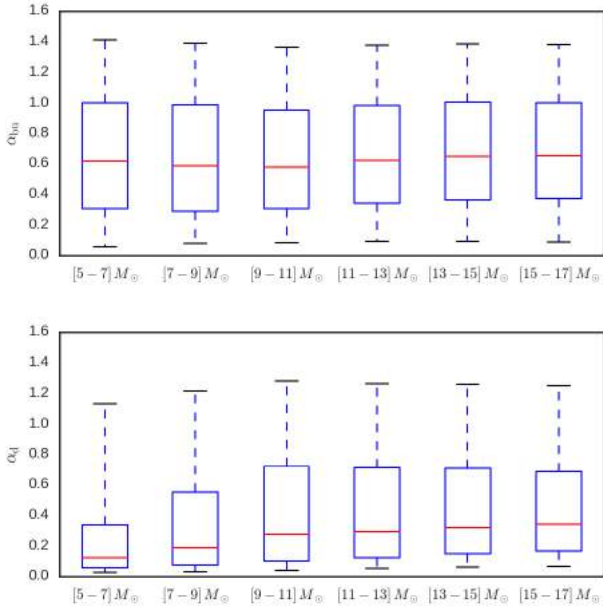


Figure 13. Same as Fig. 11 for α_{bu} (above) and α_{d} (below).

5.2.3 Disc life cycles

In the lower panel of Fig. 11, we plot the distribution of the build-up time, $t_2 - t_1$, versus the stellar mass. We see that the duration of the bump is much shorter for massive stars, which indicates that these stars are much more variable than their late type siblings. Similar findings were reported in the Galaxy (e.g. Rivinius et al. 2013). For a complete characterisation of the disc life cycles it would be required a census of the number of bumps present during the timespan of OGLE-II and OGLE-III observations (roughly 12 years). Unfortunately, this cannot be done for our sample because in this study we focused only on the well-defined bumps. The median of the build-up time for our sample is $\langle t_2 - t_1 \rangle = 305^{+351}_{-171}$ days.

5.2.4 Viscosity parameter

The majority of our determinations of the viscosity parameter had broad uncertainty distributions, and it was found that the errors in the determinations of α_{bu} were generally greater than those of α_{d} . Considering the sample as a whole, we find that there is no variation of α_{bu} with the stellar mass (Fig. 13, top), but there is a slight hint that α_{d} may grow with the stellar mass (Fig. 13, bottom). Furthermore, we find that on average the viscosity parameter is roughly two times larger at build-up than at dissipation ($\langle \alpha_{\text{bu}} \rangle = 0.63^{+0.52}_{-0.39}$ vs. $\langle \alpha_{\text{d}} \rangle = 0.29^{+0.61}_{-0.20}$).

Lamers et al. (1995) identified two bi-stability jumps in stellar winds, one strong jump at $T_{\text{eff}} \approx 22,000$ K, and a weaker one at $T_{\text{eff}} \approx 10,000$ K. These jumps are associated with rapid changes of the ionisation and excitation state of the gas in stellar winds around these temperatures, which in turn modify the line opacity. If radiative ablation were a relevant disc driving mechanism, we would expect that the jumps would cause changes in the line forces, thus affecting disc ablation and the observed timescales of disc dissipation. The absence of any structure around $T_{\text{eff}} \approx 22,000$ K (roughly $10 M_{\odot}$) in Fig. 13 argues against ablation as a strong driving mechanism in the discs of our sample.

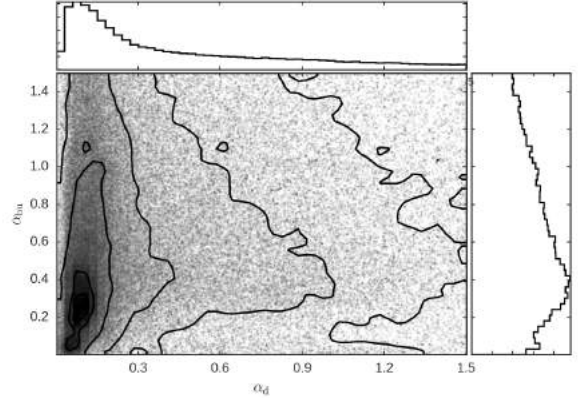


Figure 14. Distribution of the two viscosity parameters α_{bu} and α_{d} . The histograms above and on the right are the projections for α_{d} and α_{bu} , respectively. The contour levels are the same as in Fig. 8.

The estimated values of α in the range of a few tenths to one is in agreement with the usual values obtained for the hot and variable discs of dwarf novae (King et al. 2007; Kotko & Lasota 2012), as well as with the values obtained for the Be star 28 CMA by Ghoreyshi & Carciofi (2017). They are, however, an order of magnitude or more above the usual values obtained in magnetohydrodynamic (MHD) simulations, where the magnetorotational instability (MRI, Balbus & Hawley 1991) is the main theoretical assumption for the mechanism that generates the necessary viscosity (King et al. 2007).

In Fig. 14, we show the distributions of α_{bu} (right) and α_{d} (above) and the distribution in the $\alpha_{\text{bu}} \times \alpha_{\text{d}}$ plane. We found that, for most of the bumps, there was a correlation between α_{bu} and α_{d} , with values of α_{bu} greater than values of α_{d} being more likely. This trend can be seen in the darker areas of the $\alpha_{\text{bu}} \times \alpha_{\text{d}}$ plane. Ghoreyshi & Carciofi (2017) found the same trend for 28 CMA.

It is unclear whether the higher likelihood of $\alpha_{\text{bu}} > \alpha_{\text{d}}$ is real a phenomenon or a result of the approximations employed in this work. One key approximation made in our model is that the hydrodynamical equations are solved assuming that the entire disc is isothermal. Earlier studies (e.g., Jones et al. 2004; Carciofi & Bjorkman 2006) have shown the disc to be highly non-isothermal, which means that c_s in Eq. 3 is a complicated function both of R and time. Another approximation is that the possible effects of line forces were neglected. Recently, Kee et al. (2016) simulated the effects of a line-driven wind from early B-type stars over a non-viscous gaseous disc of solar metallicity and typical density. They showed that the line-driven wind was able to destroy the disc in timescales compatible with the observed large-amplitude photometric variations of Be stars. They argued that the presence of the line-driven wind might be the cause of the apparent abnormal value estimated for α by Carciofi et al. (2012), Ghoreyshi & Carciofi (2017), and this work. Future work must explore if the viscous force and the line force working together can produce the variability of Be stars with smaller values of α .

The line force of an outwardly diffusing near-Keplerian optically thin disc under irradiation by the hot star will have a positive component in the azimuthal direction, giving angular momentum to the gas (Gayley et al. 2001). It is possible that this additional source of angular momentum may help viscosity in pushing material outwards during the build-up phase and oppose to the reaccretion of the inner disc in the dissipation, thus contributing to the observed

trend of $\alpha_{\text{bu}} > \alpha_{\text{d}}$. We expect, however, that for our low-metallicity SMC Be stars, the possible effect of the line force will be greatly diminished. Furthermore, so far all studies of the effects of line forces in gaseous Keplerian discs assumed that the gas is optically thin, which is not the case for our inner discs near the disc plane. The green triangle in Fig. 12 marks the mass and density at the stellar equator of the initial state of the ablating disc model of Kee et al. (2016) for a B2e star. Our calculations show that their initial state would generate only a modest excess $\Delta I = -0.1$ mag, if seen pole-on.

On the other hand, it is possible that an opposite scenario might happen. The line force might operate ablating the tenuous material above the disc plane. These regions would receive radiation from the stellar surface and radiation reprocessed by the optically thick disc, behaving as a sink of mass and angular momentum of the disc (e.g. Krtićka et al. 2011). In that case, the line-driven wind would actually slow down the build-up phase, because it would take a longer time for the disc to reach a near steady-state, and would speed up the dissipation phase. If the above were true, that would result in $\alpha_{\text{bu}} < \alpha_{\text{d}}$, contrary to the results of Ghoreysli & Carciofi (2017) and in this work.

We end this section by speculating about another possible cause for the observed trend $\alpha_{\text{bu}} > \alpha_{\text{d}}$. The disc formation is probably a mechanically violent process, with outbursts of matter injecting mechanical energy into the disc that is likely to disrupt its hydrostatic equilibrium and induce further turbulent motion. The dissipation, on the other hand, is expected to be a more gentle process, much less perturbed by stellar activity. The mechanically-driven turbulence during outburst might account for the larger values of α at these phases.

5.2.5 Mass and angular momentum loss

Although the discs of Be stars in our sample are generally not in steady-state, their steady-state mass and angular momentum loss rates (Eqs. 12 and 13) are useful estimates of the actual quantities that are lost by the star after the bump event ends (see Appendix A). The panels of Fig. 15 show our distributions of the steady-state mass (above) and angular momentum (below) loss rates. For the calculation of $(-\partial M/\partial t)_{\text{steady}}$, we considered the radius of the outer boundary to be given by the radius at which the disc outflow becomes angular momentum conserving (which can be seen as an outer radius of the viscous disc), estimated as $\tilde{R}_{\text{out}} = 0.3(v_{\text{orb}}/c_s)^2$ by Krtićka et al. (2011). The red dots (upper panel) are the estimates of $(-\partial M/\partial t)_{\text{steady}}$ made from the results of Vieira et al. (2017) for Galactic Be stars, assuming that $\alpha = 1$.

The steady-state mass and angular momentum loss rates for our densest bumps are of the order of $\sim 10^{-10} M_{\odot} \text{ yr}^{-1}$ and $\sim 5 \times 10^{36} \text{ g cm}^2 \text{ s}^{-2}$, respectively. The typical decretion rate, which estimates the flux of mass in the disc near the stellar equator, is an order of magnitude higher than $(-\partial M/\partial t)_{\text{steady}}$, being of the order of $\sim 10^{-9} M_{\odot} \text{ yr}^{-1}$, which also corresponds to the upper limit of the observed wind mass loss rate of B stars (Snow 1981; Puls et al. 2008). Values of the typical decretion rate and steady-state angular momentum loss rate are given in the eleventh and twelfth columns of Table 6, respectively. The total angular momentum lost by the star as a consequence of the bump, $-\Delta J_*$, is given by $(-\partial J/\partial t)_{\text{steady}}$ times the build-up time (Eq. A4), and the total mass lost is simply $-\Delta M_* = -\Delta J_*/(GM R_{\text{out}})^{1/2}$, if we still approximate the VDD as a Keplerian disc at R_{out} . If we consider that a typical bump has a build-up time of roughly one year, then the mass and angular

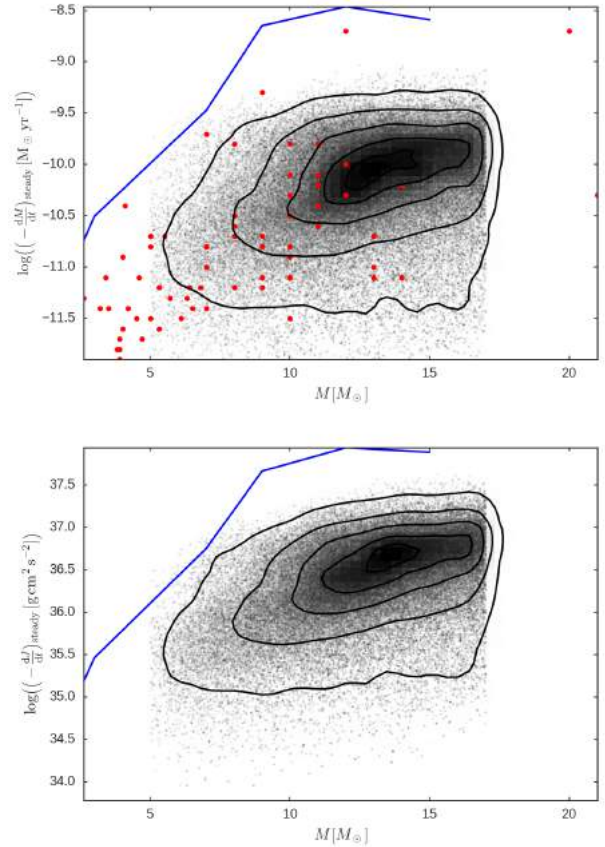


Figure 15. Distributions of the steady-state mass (above) and angular momentum (below) loss rates for our sample. The contour levels are the same as in Fig. 8. The red dots (upper panel) are the values of $(-\partial M/\partial t)_{\text{steady}}$, calculated from the results of Vieira et al. (2017) for galactic Be stars. The blue curves are the estimations made by Granada et al. (2013) of the steady-state mass and angular momentum loss of their $Z = 0.002$ stars during their episodes of disc formation.

momentum lost by the star as a consequence of one dense complete bump are of the order of $\sim 10^{-10} M_{\odot}$ and $\sim 10^{44} \text{ g cm}^2 \text{ s}^{-1}$ (or ~ 0.01 Moon masses and $\sim 10^{-3}$ times Earth’s orbital angular momentum around the Sun, respectively). The VDD is, thus, a physical mechanism capable of extracting a large quantity of angular momentum from the outer layers of the star, without requiring the loss of too much mass. It is, therefore, a breaking mechanism of the outer layers. The angular momentum lost by the star for each individual bump is given in the thirteenth column of Table 6.

It was proposed (e.g., Krtićka et al. 2011) that, with the evolution of the star, the formation of the VDD might be a natural mechanism to extract angular momentum from the outer layers of the star, preventing it to exceed the break up velocity. Granada et al. (2013) assumed the appearance of a steady-state VDD in the Geneva stellar evolution code every time the outer layers of the star reached $W > 0.88$ (or $\omega > 0.99$, in their notation, where $\omega = \Omega/(8GM/27R_{\text{pole}}^3)^{1/2}$). The blue curves in Fig. 15 are the estimates made by Granada et al. (2013) of the steady-state mass and angular momentum loss of their $Z = 0.002$ stars during their episodes of disc formation. The fact that the curves of Granada et al. (2013) lie up to one order of magnitude above our results and the

ones of [Vieira et al.](#) suggests that their assumed discs were made much too dense to be able to remove the needed angular momentum.

Although the Be phenomenon is probably a powerful velocity breaking mechanism for the outer layers of the star, its effect on the star as a whole is expected to be modest. Our determinations of angular momentum loss show that, even if the Be phenomenon happened during $\sim 30\%$ of the stellar main sequence lifetime, and the integrated time of all the build-up phases was $\sim 30\%$ of that time, that would lead to the removal of $\sim 1\%$ of the initial angular momentum of the star, which, for fast rotating stars of masses from $7M_{\odot}$ to $15M_{\odot}$ is of $8 - 30 \times 10^{51} \text{ g cm}^2 \text{ s}^{-1}$ ([Granada et al. 2013](#)).

In conclusion, light-curve modelling offers a reliable way to measure directly the amount of angular momentum lost by disc formation events in Be stars. Coupling this information with future studies about the fraction of the main-sequence lifetime a Be star spends in outburst will allow us to estimate the total amount of angular momentum that is lost by the disc during the main sequence. To obtain the total angular momentum lost we must sum the amount lost by the stellar wind. This quantity, hitherto unknown, will provide an essential constraint on stellar evolution models, in effect allowing for calibration of the core-surface angular momentum coupling of a star.

6 CONCLUSIONS

We present a new method to model the light curves of Be stars with the goal of extracting quantitative information about the fundamental parameters of their discs, such as the viscosity parameter, α , and the asymptotic surface density (Σ_0 , which is related to the disc mass injection rate). The method uses a large pre-computed grid of synthetic Be light curves, calculated using detailed hydrodynamic calculations coupled with three-dimensional NLTE radiative transfer calculations. The comparison between the model grid and the observed light curves was made possible by the identification of two empirical laws, that consists of simple formulas that closely match the photometric behaviour during disc build-up and dissipation.

An initial analysis of our model grid allowed us to draw important conclusions about the properties of viscous decretion discs (VDD) around Be stars, and their effect on the stellar SED as they evolve in time:

- The viscosity parameter α is the most important parameter controlling the observed rate of photometric variations in Be light curves, but it is not the only one. Stellar parameters (mass, radius and effective temperature), as well as the disc viewing angle and density level, all concur to change the rate of brightness variations in complicated ways, which means that if meaningful information about α is to be extracted from the data, these parameters must be somehow estimated;

- We identified a previously unknown effect, dubbed mass-reservoir effect, which also controls the rate of photometric variations during phases of disc dissipation. This effect is a consequence of the fact that VDDs build a mass reservoir at their outer regions, which is unnoticed at short wavelengths (e.g., visible). The longer the build-up phase of a disc, the bigger its mass reservoir. When mass injection from the star stops and reaccrion occurs, the reservoir feeds the inner disc with mass. Clearly, the larger the reservoir, the longer it will be able to supply mass to the inner disc, and the slower the photometric dissipation will appear.

We applied our fitting pipeline to a sample of light curves of 54 Be star candidates from the SMC ([Mennickent et al. 2002](#))

containing 81 clearly identified events of disc formation/dissipation (here referred to as bumps). The light curves come from OGLE-II and OGLE-III data, covering roughly 12 years. A Markov Chain Monte Carlo technique was used to properly estimate the posterior probabilities of each fitted parameter.

It was found that our sample is biased towards early type Be stars, likely because these stars are more variable and their discs are denser, resulting in clearer bumps. Also, photometric uncertainties increase for late type Be stars. Since our sample was selected based on the appearance of their bumps, we conclude that our Be discs must be among the densest found for Be stars in the SMC. We verified an increase of Σ_0 with the stellar mass and the median for our whole sample is $\langle \Sigma_0 \rangle = 1.44_{-0.75}^{+1.01} \text{ g cm}^{-2}$. Our results may suggest that Be discs in the SMC are denser than their siblings in the Galaxy, in line with $H\alpha$ surveys that found stronger line emission in the SMC than in our Galaxy.

The durations of the build-up phases become shorter for more massive stars, which indicates that, as it was already observed in the Galaxy, late-type Be stars are less variable than early-type ones. The median of the build-up time for our sample is $\langle t_2 - t_1 \rangle = 305_{-171}^{+351}$ days.

We obtained, for the first time, estimates of α for a statistically significant sample of Be stars. In our work, we explored the possibility that the viscosity parameter might be different at build-up (α_{bu}) and dissipation (α_{d}). We found no significant variation of α_{bu} with the stellar mass (Fig. 13, top), but some evidence points to a correlation between α_{d} with M (Fig. 13, bottom). Furthermore, we find that on average the viscosity parameter is sensibly larger at build-up than at dissipation. Our medians of the two viscosity parameters are $\langle \alpha_{\text{bu}} \rangle = 0.63_{-0.39}^{+0.52}$ and $\langle \alpha_{\text{d}} \rangle = 0.29_{-0.20}^{+0.61}$. These values are in agreement in magnitude with the determinations of [Carciofi et al. \(2012\)](#) and [Ghoreyshi & Carciofi \(2017\)](#) for the Galactic Be star 28 CMA. They are also similar to the values of α usually found in cataclysmic variables ([King et al. 2007](#); [Kotko & Lasota 2012](#)).

The trend that $\alpha_{\text{bu}} > \alpha_{\text{d}}$ was also seen by [Ghoreyshi & Carciofi \(2017\)](#) in the different cycles of activity of the Be star 28 CMA. Further work is necessary to establish whether this trend is real or simply a result of our model assumptions. In particular, two important physical effects were ignored in this work, namely the fact that Be discs are non-isothermal and the line forces known to act on the disc material. This last point, however, is likely of little importance for Be stars in the SMC, given their low metallicity.

It must be further emphasised that in this work what is really measured are the timescales for disc build-up and dissipation. Under the assumption that viscosity is the only driving mechanism operating on the disc, these timescales can in turn be converted to estimates of the viscosity parameter. The presence of other driving mechanisms (such as the aforementioned ablation) might affect the determination of α in unpredictable ways.

The steady-state mass and angular momentum loss rates for the studied bumps are of the order of $\sim 10^{-10} M_{\odot} \text{ yr}^{-1}$ and $\sim 5 \times 10^{36} \text{ g cm}^2 \text{ s}^{-2}$, respectively. The typical decretion rate is of the order of $\sim 10^{-9} M_{\odot} \text{ yr}^{-1}$. These values are in agreement with the upper limit of the observed wind mass loss rate of B stars ([Snow 1981](#); [Puls et al. 2008](#)). In addition, these values roughly agree in magnitude with the work of [Vieira et al. \(2017\)](#), who studied a sample of 80 Galactic Be stars.

Future perspectives for this work are threefold. First, an effort must be made to remove the biases of our current sample, by including late-type Be stars and smaller-amplitude bumps. Second, the availability of a great number of past and current automated surveys (e.g., MACHO – [Alcock et al. 1997](#), EROS – [Aubourg et al. 1993](#),

ASAS – [Pojmanski 1997](#), VISTA-VVV – [Minniti et al. 2010](#), KELT – [Pepper et al. 2007](#)) will allow us not only to greatly increase the number of Be stars studied, but also to explore the Be phenomenon and associated disc properties in other metallicities (Galaxy, LMC, etc.). Finally, also important is to obtain a better estimate of the central star properties, e.g., via spectroscopic modelling or using stars belonging to clusters with known age. Our current analysis was bound by the limited amount of information available on the central stars.

The α determinations made in this work should help investigating the physical mechanisms originating the anomalous viscosity in circumstellar discs environments. In addition, the estimates of the net mass and angular momentum loss rates are important for understanding the conditions in which the Be phenomenon appears, and its consequences for the evolution of B-type stars.

Table 5. List of Be stars and their respective bumps selected for this study

Field	OGLE-II ID	OGLE-III Field	OGLE-III ID	diskless interval (JD-2450000)		B_*	V_*	I_*	Bump ID	Bands	Bump interval (JD-2450000)	
SMC_SC1	7612	SMC133.4	8877	600	1300	15.926±0.01	16.164±0.009	16.443±0.009	01 02	<i>I</i> <i>I</i>	1420 3250	2000 3800
SMC_SC1	60553	SMC128.6	57	3000	3500	—	15.418±0.003	15.601±0.007	01	<i>V I</i>	3500	5000
SMC_SC1	75701	SMC125.7	20383	3000	3500	—	15.397±0.003	15.51±0.006	01	<i>V I</i>	3650	5000
SMC_SC1	92262	SMC128.6	147	3500	3800	—	15.623±0.003	15.811±0.007	01 02	<i>I</i> <i>V I</i>	2600 3900	3100 5000
SMC_SC2	94939	SMC125.3	52	1000	1100	15.832±0.008	15.991±0.013	16.126±0.007	01	<i>I</i>	1100	2000
SMC_SC3	5719	SMC125.1	20231	2980	3020	—	—	16.233±0.01	01	<i>I</i>	1200	4500
SMC_SC3	15970	SMC125.2	28056	700	750	15.282±0.01	15.412±0.006	15.541±0.006	01 02 03	<i>B V I</i> <i>I</i> <i>V I</i>	750 2200 4000	2000 3500 5000
SMC_SC3	71445	SMC125.2	34818	700	800	16.227±0.01	16.425±0.009	16.608±0.012	01 02	<i>I</i> <i>I</i>	1450 4400	2400 4700
SMC_SC3	125899	SMC125.2	6200	3500	3750	—	15.837±0.004	15.956±0.008	01	<i>I</i>	2320	3400
SMC_SC3	197941	SMC125.3	25034	4000	4060	—	15.671±0.003	15.724±0.006	01	<i>V I</i>	2350	4000
SMC_SC4	22859	SMC125.4	22723	700	1200	17.068±0.013	17.133±0.012	17.129±0.015	01	<i>V I</i>	1200	3500
SMC_SC4	71499	SMC100.7	34896	1000	1450	15.414±0.011	15.553±0.007	15.597±0.006	01 02	<i>V I</i> <i>V I</i>	1430 2900	2400 4400
SMC_SC4	120783	SMC100.6	7129	4250	4500	—	14.401±0.003	14.442±0.005	01	<i>V I</i>	2750	4500
SMC_SC4	127840	SMC100.6	38372	3500	4500	—	14.853±0.003	15.026±0.006	01	<i>I</i>	2800	3500
SMC_SC4	156248	SMC100.8	14683	1000	1200	15.91±0.01	15.964±0.007	15.852±0.006	01	<i>I</i>	1320	2300
SMC_SC4	156251	SMC100.8	14642	600	680	14.881±0.005	15.13±0.007	15.338±0.005	01 02 03	<i>B V I</i> <i>V I</i> <i>V I</i>	650 3170 3770	1200 3600 4600
SMC_SC4	159829	SMC100.8	37214	4450	4500	—	15.895±0.005	15.959±0.009	01 02	<i>I</i> <i>V I</i>	2600 3430	3000 4500
SMC_SC4	159857	SMC100.8	45127	3000	3500	—	15.626±0.004	15.8±0.008	01 02	<i>I</i> <i>V I</i>	780 3600	1400 4300
SMC_SC4	163828	SMC100.7	8813	600	700	17.171±0.009	17.164±0.009	16.953±0.013	01	<i>B V I</i>	700	2400
SMC_SC4	167554	SMC100.7	51098	3000	4500	—	17.258±0.009	17.2±0.016	01 02	<i>I</i> <i>V I</i>	1620 4700	1900 5000

Table 5 – continued List of Be stars and their respective bumps selected for this study

	OGLE-II Field	OGLE-III Field	diskless interval (JD-2450000)		B_*	V_*	I_*	Bump ID	Bands	Bump interval (JD-2450000)	
SMC_SC4	171253	SMC100.7	42620	700 1200	15.674±0.01	15.714±0.009	15.691±0.006	01 02	<i>I</i> <i>V I</i>	1410 3245	1900 4000
SMC_SC4	175272	SMC100.6	7362	3950 4000	—	16.579±0.005	16.431±0.009	01	<i>I</i>	2600	3800
SMC_SC4	179053	SMC100.6	38443	0 1000	16.304±0.009	16.339±0.009	16.148±0.008	01	<i>I</i>	1300	2400
SMC_SC5	11453	SMC100.8	14734	3300 3400	—	15.871±0.004	15.779±0.008	01	<i>I</i>	3400	5000
SMC_SC5	21117	SMC100.8	52883	3650 3750	—	16.051±0.004	16.143±0.009	01 02 03 04	<i>V I</i> <i>I</i> <i>I</i> <i>V I</i>	970 2200 2900 3850	2000 2800 3400 5000
SMC_SC5	21134	SMC100.8	45175	1000 1500	15.994±0.013	16.023±0.006	16.091±0.007	01	<i>I</i>	1600	2000
SMC_SC5	32377	SMC100.7	50838	4050 4100	—	15.844±0.003	15.941±0.008	01 02	<i>I</i> <i>I</i>	3030 4350	3400 5000
SMC_SC5	43650	SMC100.6	15248	1400 2000	17.177±0.013	17.214±0.01	17.305±0.017	01 02	<i>V I</i> <i>V I</i>	750 2550	2000 5000
SMC_SC5	54851	SMC100.5	14725	600 850	16.264±0.01	16.311±0.009	16.366±0.008	01 02 03	<i>B V I</i> <i>I</i> <i>V I</i>	850 2120 3650	2000 3600 5000
SMC_SC5	65500	SMC101.8	21127	1000 1500	16.034±0.011	15.981±0.007	15.959±0.006	01	<i>B V I</i>	600	1000
SMC_SC5	129535	SMC100.6	53957	4700 4800	—	16.923±0.008	16.953±0.013	01	<i>V I</i>	3300	5000
SMC_SC5	145724	SMC101.8	21370	3000 3200	—	—	17.116±0.019	01	<i>I</i>	3230	5000
SMC_SC5	180034	SMC100.1	27826	3900 4100	—	16.436±0.005	16.431±0.009	01	<i>V I</i>	4120	5000
SMC_SC5	260841	SMC100.1	36050	800 900	15.858±0.011	16.013±0.008	16.182±0.008	01 02	<i>I</i> <i>V I</i>	1500 3800	2200 4800
SMC_SC5	260957	SMC100.1	36101	1200 1700	16.747±0.009	16.917±0.009	17.043±0.015	01	<i>V I</i>	3620	5000
SMC_SC5	266088	SMC100.2	9240	700 750	17.227±0.012	17.315±0.01	17.408±0.016	01	<i>B V I</i>	750	2000
SMC_SC5	276982	SMC100.3	9403	4400 4500	—	15.993±0.005	15.757±0.008	01	<i>V I</i>	3030	4500
SMC_SC5	282963	SMC100.3	9408	1000 1500	15.431±0.009	15.591±0.006	15.665±0.005	01	<i>I</i>	1600	4300
SMC_SC6	11085	SMC100.1	36096	700 1100	15.52±0.01	15.667±0.007	15.863±0.006	01 02	<i>V I</i> <i>V I</i>	1400 3900	2000 5000
SMC_SC6	17538	SMC100.2	9240	0 750	17.213±0.012	17.315±0.013	17.424±0.015	01	<i>V I</i>	800	3000
SMC_SC6	42440	SMC100.3	56046	700 1100	16.867±0.012	17.01±0.011	17.19±0.017	01	<i>I</i>	1400	3500

Table 5 – *continued* List of Be stars and their respective bumps selected for this study

Field	OGLE-II ID	OGLE-III Field ID	diskless interval (JD-2450000)		B_*	V_*	I_*	Bump ID	Bands	Bump interval (JD-2450000)	
SMC_SC6	99991	SMC100.1	43700	1300 1800	15.755±0.007	15.923±0.007	16.126±0.009	01 02 03 04	<i>I</i> <i>I</i> <i>I</i> <i>I</i>	650 1400 1800 2500 3150 4000 4200 5000	
SMC_SC6	105368	SMC100.2	17645	600 1200	16.462±0.011	16.592±0.008	16.681±0.011	01 02	<i>V I</i> <i>I</i>	1150 2000 2700 4000	
SMC_SC6	116294	SMC100.2	49901	0 900	16.775±0.012	16.958±0.01	17.085±0.013	01	<i>I</i>	985 2000	
SMC_SC6	128831	SMC100.3	55954	600 1200	15.849±0.009	16.018±0.007	16.116±0.007	01	<i>I</i>	1445 2600	
SMC_SC6	199611	SMC100.3	29080	600 1300	15.265±0.011	15.447±0.008	15.594±0.006	01	<i>I</i>	1500 2000	
SMC_SC6	272665	SMC106.6	26640	1000 1500	17.784±0.016	17.962±0.016	18.04±0.029	01	<i>I</i>	1620 4500	
SMC_SC7	57131	SMC105.6	33029	1200 2000	16.037±0.015	16.127±0.008	16.269±0.008	01	<i>I</i>	2780 3500	
SMC_SC8	183240	SMC105.2	32029	3000 4000	—	14.783±0.003	14.946±0.005	01	<i>V I</i>	4150 4800	
SMC_SC9	105383	SMC110.6	114	1000 1300	16.115±0.01	16.264±0.007	16.4±0.009	01 02	<i>V I</i> <i>V I</i>	1240 3500 3780 4800	
SMC_SC9	168422	SMC113.7	6330	4700 4850	—	17.002±0.009	17.057±0.014	01	<i>V I</i>	2700 4850	
SMC_SC10	8906	SMC110.6	22338	4500 5000	—	15.253±0.003	15.382±0.006	01 02	<i>I</i> <i>V I</i>	2935 3300 3650 3710	
SMC_SC11	28090	SMC113.2	4458	4500 5000	—	15.248±0.004	15.433±0.006	01	<i>V I</i>	2300 4500	
SMC_SC11	46587	SMC110.3	16096	600 1000	17.087±0.013	17.248±0.01	17.343±0.021	01	<i>I</i>	1110 4500	

Table 6. Results of the pipeline for each star and bump of the sample

OGLE-II ID	Bump ID	$M [M_{\odot}]$	t/t_{MS}	W	$\cos i$	Σ_0 [g cm^{-2}]	α_{bu}	α_{d}	τ_{bu}	$\left(-\frac{\partial M}{\partial t}\right)_{\text{yp}}$ [$10^{-5} \times M_{\odot} \text{ yr}^{-1}$]	$\left(-\frac{\partial J}{\partial t}\right)_{\text{sd}}$ [$10^{36} \times \text{g cm}^2 \text{ s}^{-2}$]	$-\Delta J$ [$10^{44} \times \text{g cm}^2 \text{ s}^{-1}$]
SMC_SC1 7612	01	$12.8^{+2.6}_{-2.6}$	$0.5^{+0.3}_{-0.3}$	$0.81^{+0.11}_{-0.11}$	$0.36^{+0.11}_{-0.04}$	$1.1^{+1.3}_{-0.6}$	$0.33^{+0.68}_{-0.24}$	$0.65^{+0.54}_{-0.41}$	$0.15^{+0.32}_{-0.11}$	$0.62^{+0.65}_{-0.38}$	$1.09^{+1.35}_{-0.68}$	$0.07^{+0.08}_{-0.04}$
	02					$1.3^{+1.2}_{-0.7}$	$0.38^{+0.64}_{-0.27}$	$0.62^{+0.53}_{-0.4}$	$0.15^{+0.28}_{-0.1}$	$0.77^{+0.8}_{-0.45}$	$1.35^{+1.66}_{-0.81}$	$0.07^{+0.08}_{-0.04}$
SMC_SC1 60553	01	$12.7^{+2.8}_{-1.9}$	$0.7^{+0.2}_{-0.3}$	$0.81^{+0.1}_{-0.11}$	$0.66^{+0.12}_{-0.1}$	$1.6^{+0.7}_{-0.4}$	$1.25^{+0.18}_{-0.25}$	$0.09^{+0.04}_{-0.05}$	$2.76^{+0.5}_{-0.57}$	$4.32^{+2.2}_{-1.54}$	$8.24^{+5.62}_{-3.31}$	$2.63^{+1.73}_{-1.05}$
SMC_SC1 75701	01	$14.7^{+1.7}_{-1.9}$	$0.7^{+0.2}_{-0.2}$	$0.81^{+0.1}_{-0.11}$	$0.7^{+0.15}_{-0.1}$	$1.9^{+0.8}_{-0.4}$	$0.24^{+0.18}_{-0.08}$	$0.11^{+0.08}_{-0.05}$	$0.66^{+0.48}_{-0.22}$	$1.15^{+1.06}_{-0.52}$	$2.47^{+2.62}_{-1.24}$	$1.03^{+1.08}_{-0.52}$
SMC_SC1 92262	01	$12.7^{+2.5}_{-1.8}$	$0.6^{+0.2}_{-0.3}$	$0.8^{+0.11}_{-0.09}$	$0.03^{+0.03}_{-0.02}$	$1.5^{+1.0}_{-0.9}$	$0.47^{+0.6}_{-0.29}$	$0.84^{+0.4}_{-0.38}$	$0.53^{+0.63}_{-0.56}$	$1.07^{+1.62}_{-0.86}$	$2.01^{+2.83}_{-1.06}$	$0.31^{+0.4}_{-0.16}$
	02					$2.4^{+0.4}_{-0.5}$	$0.99^{+0.26}_{-0.23}$	$0.94^{+0.33}_{-0.3}$	$1.2^{+0.38}_{-0.37}$	$4.42^{+2.72}_{-1.42}$	$8.36^{+6.38}_{-3.24}$	$1.51^{+1.01}_{-0.62}$
SMC_SC2 94939	01	$12.2^{+2.7}_{-2.3}$	$0.6^{+0.2}_{-0.3}$	$0.81^{+0.1}_{-0.11}$	$0.45^{+0.13}_{-0.05}$	$2.4^{+0.7}_{-0.8}$	$0.88^{+0.42}_{-0.45}$	$0.69^{+0.43}_{-0.33}$	$1.15^{+0.53}_{-0.56}$	$3.44^{+2.61}_{-1.75}$	$6.05^{+5.42}_{-3.17}$	$1.06^{+0.92}_{-0.56}$
SMC_SC3 5719	01	$12.3^{+2.7}_{-2.3}$	$0.6^{+0.3}_{-0.3}$	$0.81^{+0.1}_{-0.11}$	$0.38^{+0.11}_{-0.05}$	$2.6^{+0.5}_{-0.8}$	$0.72^{+0.42}_{-0.33}$	$0.47^{+0.36}_{-0.22}$	$3.83^{+2.41}_{-1.72}$	$3.25^{+2.3}_{-1.77}$	$5.73^{+4.5}_{-3.18}$	$4.09^{+3.25}_{-2.27}$
SMC_SC3 15970	01	$13.5^{+1.5}_{-1.3}$	$0.8^{+0.1}_{-0.2}$	$0.87^{+0.07}_{-0.09}$	$0.63^{+0.05}_{-0.03}$	$1.1^{+0.2}_{-0.1}$	$0.89^{+0.31}_{-0.45}$	$0.13^{+0.05}_{-0.04}$	$1.64^{+0.67}_{-0.79}$	$2.52^{+1.15}_{-1.14}$	$5.31^{+3.1}_{-2.54}$	$1.55^{+0.95}_{-0.74}$
	02					$1.4^{+0.2}_{-0.2}$	$0.85^{+0.29}_{-0.31}$	$0.17^{+0.04}_{-0.04}$	$1.92^{+0.77}_{-0.84}$	$2.89^{+1.38}_{-1.03}$	$6.17^{+3.61}_{-2.92}$	$2.24^{+1.22}_{-0.92}$
	03					$1.2^{+0.2}_{-0.1}$	$1.1^{+0.31}_{-0.3}$	$0.12^{+0.04}_{-0.05}$	$2.62^{+0.83}_{-0.9}$	$3.27^{+1.03}_{-1.12}$	$6.97^{+3.75}_{-2.73}$	$2.62^{+1.66}_{-1.18}$
SMC_SC3 71445	01	$11.2^{+2.7}_{-2.3}$	$0.5^{+0.3}_{-0.3}$	$0.81^{+0.1}_{-0.11}$	$0.43^{+0.09}_{-0.06}$	$2.5^{+0.6}_{-0.6}$	$0.57^{+0.41}_{-0.25}$	$0.75^{+0.37}_{-0.31}$	$1.11^{+0.8}_{-0.48}$	$2.14^{+1.74}_{-1.0}$	$3.42^{+3.2}_{-1.7}$	$0.83^{+0.77}_{-0.41}$
	02					$1.4^{+0.5}_{-0.5}$	$0.65^{+0.53}_{-0.34}$	$1.05^{+0.91}_{-0.38}$	$0.47^{+0.24}_{-0.24}$	$1.38^{+0.94}_{-0.61}$	$2.19^{+1.74}_{-1.02}$	$0.2^{+0.17}_{-0.09}$
SMC_SC3 125899	01	$13.4^{+2.3}_{-2.4}$	$0.6^{+0.2}_{-0.3}$	$0.82^{+0.1}_{-0.11}$	$0.37^{+0.17}_{-0.06}$	$1.7^{+0.9}_{-0.7}$	$0.7^{+0.54}_{-0.44}$	$0.41^{+0.33}_{-0.22}$	$0.89^{+0.7}_{-0.53}$	$2.14^{+2.11}_{-1.32}$	$4.04^{+4.74}_{-2.55}$	$0.73^{+0.88}_{-0.46}$
SMC_SC3 197941	01	$12.0^{+2.5}_{-1.8}$	$0.8^{+0.2}_{-0.2}$	$0.82^{+0.1}_{-0.11}$	$0.57^{+0.15}_{-0.05}$	$0.8^{+0.3}_{-0.2}$	$0.4^{+0.52}_{-0.23}$	$0.1^{+0.04}_{-0.04}$	$1.43^{+1.79}_{-0.81}$	$0.69^{+0.82}_{-0.38}$	$1.3^{+1.69}_{-0.75}$	$0.66^{+0.85}_{-0.38}$
SMC_SC4 22859	01	$9.5^{+2.5}_{-2.1}$	$0.4^{+0.3}_{-0.3}$	$0.81^{+0.1}_{-0.11}$	$0.64^{+0.19}_{-0.1}$	$0.4^{+0.2}_{-0.1}$	$0.66^{+0.57}_{-0.51}$	$0.04^{+0.64}_{-0.02}$	$3.5^{+3.15}_{-2.71}$	$0.27^{+0.26}_{-0.19}$	$0.35^{+0.42}_{-0.25}$	$0.21^{+0.25}_{-0.15}$
SMC_SC4 71499	01	$14.5^{+1.8}_{-2.2}$	$0.7^{+0.2}_{-0.2}$	$0.82^{+0.1}_{-0.09}$	$0.54^{+0.07}_{-0.03}$	$1.3^{+0.5}_{-0.3}$	$0.7^{+0.46}_{-0.35}$	$0.25^{+0.11}_{-0.08}$	$0.96^{+0.66}_{-0.47}$	$2.15^{+1.3}_{-0.94}$	$4.6^{+3.3}_{-2.36}$	$0.94^{+0.67}_{-0.46}$
	02					$1.5^{+0.3}_{-0.3}$	$0.64^{+0.47}_{-0.34}$	$0.19^{+0.06}_{-0.06}$	$1.16^{+0.83}_{-0.63}$	$2.18^{+1.77}_{-1.0}$	$4.59^{+3.38}_{-2.23}$	$1.26^{+1.19}_{-0.61}$
SMC_SC4 120783	01	$15.2^{+1.2}_{-1.8}$	$0.9^{+0.1}_{-0.1}$	$0.84^{+0.09}_{-0.1}$	$0.64^{+0.2}_{-0.11}$	$0.7^{+0.2}_{-0.2}$	$0.63^{+0.54}_{-0.43}$	$0.11^{+0.06}_{-0.05}$	$1.56^{+1.33}_{-1.06}$	$1.47^{+1.37}_{-0.93}$	$3.67^{+3.63}_{-2.41}$	$1.53^{+1.46}_{-1.01}$
SMC_SC4 127840	01	$14.3^{+1.7}_{-1.8}$	$0.9^{+0.1}_{-0.2}$	$0.83^{+0.09}_{-0.11}$	$0.6^{+0.15}_{-0.09}$	$2.6^{+0.5}_{-0.6}$	$0.4^{+0.23}_{-0.15}$	$0.85^{+0.4}_{-0.41}$	$0.54^{+0.3}_{-0.19}$	$3.19^{+2.4}_{-1.53}$	$7.35^{+6.28}_{-3.72}$	$1.6^{+1.3}_{-0.8}$
SMC_SC4 156248	01	$12.3^{+2.8}_{-1.9}$	$0.7^{+0.2}_{-0.3}$	$0.81^{+0.09}_{-0.1}$	$0.07^{+0.02}_{-0.04}$	$1.3^{+1.4}_{-0.9}$	$0.5^{+0.73}_{-0.34}$	$0.78^{+0.43}_{-0.41}$	$1.44^{+1.98}_{-1.0}$	$0.83^{+3.31}_{-0.56}$	$1.6^{+6.2}_{-1.07}$	$0.63^{+2.39}_{-0.43}$
SMC_SC4 156251	01	$15.3^{+1.2}_{-1.7}$	$0.7^{+0.1}_{-0.2}$	$0.83^{+0.1}_{-0.1}$	$0.76^{+0.08}_{-0.07}$	$2.2^{+0.4}_{-0.4}$	$0.4^{+0.16}_{-0.11}$	$0.78^{+0.4}_{-0.33}$	$0.37^{+0.14}_{-0.15}$	$2.52^{+1.17}_{-0.91}$	$5.83^{+3.14}_{-2.42}$	$0.86^{+0.48}_{-0.37}$
	02					$1.5^{+0.2}_{-0.2}$	$0.65^{+0.29}_{-0.18}$	$0.61^{+0.35}_{-0.21}$	$0.62^{+0.25}_{-0.16}$	$2.7^{+1.46}_{-0.98}$	$6.27^{+3.88}_{-2.6}$	$0.94^{+0.57}_{-0.39}$
	03					$2.5^{+0.4}_{-0.4}$	$0.8^{+0.42}_{-0.33}$	$0.49^{+0.18}_{-0.13}$	$0.96^{+0.47}_{-0.36}$	$5.27^{+2.84}_{-2.16}$	$11.98^{+7.6}_{-5.13}$	$2.31^{+1.45}_{-0.92}$
SMC_SC4 159829	01	$13.1^{+2.6}_{-2.3}$	$0.6^{+0.3}_{-0.3}$	$0.8^{+0.11}_{-0.1}$	$0.61^{+0.1}_{-0.07}$	$2.0^{+0.7}_{-0.5}$	$1.07^{+0.28}_{-0.34}$	$0.25^{+0.1}_{-0.08}$	$1.47^{+0.48}_{-0.48}$	$3.91^{+1.91}_{-1.44}$	$7.21^{+4.56}_{-3.27}$	$1.37^{+0.84}_{-0.56}$
	02					$2.1^{+0.6}_{-0.4}$	$0.96^{+0.36}_{-0.36}$	$0.67^{+0.31}_{-0.24}$	$2.26^{+0.83}_{-0.77}$	$3.64^{+1.99}_{-1.56}$	$6.74^{+3.84}_{-3.15}$	$2.18^{+1.39}_{-1.0}$
SMC_SC4 159857	01	$13.7^{+1.9}_{-2.3}$	$0.7^{+0.2}_{-0.3}$	$0.81^{+0.1}_{-0.11}$	$0.55^{+0.08}_{-0.03}$	$0.6^{+1.0}_{-0.2}$	$0.42^{+0.64}_{-0.32}$	$0.66^{+0.46}_{-0.32}$	$0.28^{+0.45}_{-0.32}$	$0.62^{+0.5}_{-0.36}$	$1.22^{+1.15}_{-0.73}$	$0.12^{+0.11}_{-0.07}$
	02					$1.0^{+0.6}_{-0.2}$	$0.7^{+0.48}_{-0.43}$	$0.34^{+0.28}_{-0.16}$	$0.42^{+0.28}_{-0.27}$	$1.38^{+0.94}_{-0.65}$	$2.7^{+2.24}_{-1.36}$	$0.22^{+0.19}_{-0.11}$
SMC_SC4 163828	01	$9.7^{+2.4}_{-2.0}$	$0.4^{+0.4}_{-0.3}$	$0.79^{+0.11}_{-0.1}$	$0.71^{+0.14}_{-0.08}$	$0.7^{+0.2}_{-0.1}$	$0.53^{+0.58}_{-0.33}$	$0.06^{+0.05}_{-0.02}$	$3.42^{+3.83}_{-2.13}$	$0.43^{+0.5}_{-0.25}$	$0.59^{+0.78}_{-0.36}$	$0.44^{+0.58}_{-0.26}$
SMC_SC4 167554	01	$9.9^{+2.4}_{-2.1}$	$0.4^{+0.3}_{-0.2}$	$0.82^{+0.1}_{-0.1}$	$0.63^{+0.12}_{-0.09}$	$0.9^{+0.7}_{-0.3}$	$0.54^{+0.51}_{-0.36}$	$0.6^{+0.45}_{-0.29}$	$0.45^{+0.42}_{-0.3}$	$0.59^{+0.46}_{-0.31}$	$0.82^{+0.76}_{-0.46}$	$0.08^{+0.08}_{-0.04}$
	02					$1.6^{+0.7}_{-0.5}$	$0.42^{+0.47}_{-0.21}$	$0.86^{+0.41}_{-0.37}$	$0.42^{+0.5}_{-0.2}$	$0.86^{+0.82}_{-0.41}$	$1.19^{+1.44}_{-0.61}$	$0.14^{+0.15}_{-0.07}$

Table 6 – *continued* Results of the pipeline for each star and bump of the sample

OGLE-II ID	Bump ID	$M [M_{\odot}]$	t/t_{MS}	W	$\cos i$	Σ_0 [g cm^{-2}]	α_{bu}	α_{d}	τ_{bu}	$\left(-\frac{\partial M}{\partial t}\right)_{\text{yp}}$ [$10^{-5} \times M_{\odot} \text{ yr}^{-1}$]	$\left(-\frac{\partial J}{\partial t}\right)_{\text{sd}}$ [$10^{36} \times \text{g cm}^2 \text{ s}^{-2}$]	$-\Delta J$ [$10^{44} \times \text{g cm}^2 \text{ s}^{-1}$]
SMC_SC4 171253	01	$14.3^{+1.9}_{-2.5}$	$0.6^{+0.2}_{-0.3}$	$0.81^{+0.11}_{-0.11}$	$0.58^{+0.13}_{-0.06}$	$0.3^{+1.2}_{-0.1}$	$0.29^{+0.74}_{-0.28}$	$0.81^{+0.44}_{-0.49}$	$0.24^{+0.6}_{-0.23}$	$0.16^{+0.3}_{-0.12}$	$0.35^{+0.65}_{-0.23}$	$0.04^{+0.07}_{-0.03}$
	02					$0.3^{+0.8}_{-0.1}$	$0.48^{+0.66}_{-0.44}$	$0.64^{+0.52}_{-0.42}$	$0.31^{+0.45}_{-0.29}$	$0.29^{+0.32}_{-0.2}$	$0.58^{+0.7}_{-0.4}$	$0.05^{+0.06}_{-0.04}$
SMC_SC4 175272	01	$12.1^{+2.8}_{-2.4}$	$0.5^{+0.3}_{-0.3}$	$0.81^{+0.1}_{-0.1}$	$0.38^{+0.12}_{-0.06}$	$1.8^{+0.8}_{-0.7}$	$0.75^{+0.49}_{-0.39}$	$0.48^{+0.29}_{-0.23}$	$2.31^{+1.52}_{-1.21}$	$2.07^{+1.73}_{-1.16}$	$3.52^{+3.33}_{-2.05}$	$1.37^{+1.31}_{-0.8}$
SMC_SC4 179053	01	$12.6^{+2.6}_{-2.3}$	$0.6^{+0.3}_{-0.4}$	$0.8^{+0.11}_{-0.11}$	$0.02^{+0.02}_{-0.02}$	$2.1^{+0.7}_{-0.6}$	$0.96^{+0.37}_{-0.52}$	$1.1^{+0.27}_{-0.32}$	$2.14^{+1.11}_{-1.16}$	$3.1^{+1.84}_{-1.32}$	$5.5^{+4.29}_{-2.58}$	$1.74^{+1.19}_{-0.86}$
SMC_SC5 11453	01	$13.6^{+2.2}_{-2.3}$	$0.7^{+0.2}_{-0.3}$	$0.81^{+0.11}_{-0.11}$	$0.38^{+0.12}_{-0.06}$	$1.8^{+0.7}_{-0.7}$	$0.9^{+0.38}_{-0.4}$	$0.26^{+0.15}_{-0.11}$	$4.17^{+1.82}_{-1.74}$	$3.3^{+2.78}_{-1.81}$	$6.49^{+6.33}_{-3.7}$	$4.41^{+4.36}_{-2.51}$
SMC_SC5 21117	01	$13.5^{+1.9}_{-1.7}$	$0.7^{+0.1}_{-0.2}$	$0.84^{+0.09}_{-0.1}$	$0.52^{+0.04}_{-0.02}$	$1.3^{+0.3}_{-0.2}$	$0.5^{+0.32}_{-0.17}$	$0.61^{+0.48}_{-0.32}$	$0.64^{+0.39}_{-0.23}$	$1.46^{+1.04}_{-0.57}$	$2.97^{+2.63}_{-1.34}$	$0.56^{+0.47}_{-0.26}$
	02					$1.8^{+0.5}_{-0.4}$	$0.58^{+0.4}_{-0.28}$	$0.17^{+0.08}_{-0.05}$	$0.85^{+0.55}_{-0.38}$	$2.44^{+1.63}_{-1.04}$	$4.99^{+3.88}_{-2.39}$	$1.08^{+0.78}_{-0.51}$
	03					$1.9^{+0.6}_{-0.5}$	$0.57^{+0.28}_{-0.19}$	$0.35^{+0.23}_{-0.13}$	$0.57^{+0.28}_{-0.18}$	$2.53^{+1.94}_{-1.01}$	$5.13^{+3.32}_{-2.31}$	$0.76^{+0.51}_{-0.35}$
	04					$1.3^{+0.2}_{-0.2}$	$0.87^{+0.36}_{-0.3}$	$0.16^{+0.07}_{-0.05}$	$3.11^{+1.25}_{-1.03}$	$2.65^{+1.36}_{-1.09}$	$5.36^{+3.31}_{-2.46}$	$2.83^{+1.58}_{-1.29}$
SMC_SC5 21134	01	$12.7^{+2.5}_{-2.4}$	$0.6^{+0.2}_{-0.3}$	$0.8^{+0.11}_{-0.09}$	$0.38^{+0.15}_{-0.03}$	$0.8^{+1.4}_{-0.4}$	$0.4^{+0.68}_{-0.33}$	$0.18^{+0.26}_{-0.11}$	$0.34^{+0.59}_{-0.28}$	$0.54^{+0.58}_{-0.36}$	$0.97^{+1.22}_{-0.66}$	$0.12^{+0.15}_{-0.08}$
SMC_SC5 32377	01	$13.3^{+2.3}_{-2.2}$	$0.7^{+0.2}_{-0.3}$	$0.81^{+0.1}_{-0.11}$	$0.34^{+0.06}_{-0.03}$	$1.9^{+0.9}_{-0.7}$	$0.71^{+0.45}_{-0.41}$	$0.66^{+0.48}_{-0.33}$	$0.3^{+0.28}_{-0.17}$	$2.53^{+2.18}_{-1.38}$	$4.93^{+4.81}_{-2.77}$	$0.31^{+0.3}_{-0.17}$
	02					$2.2^{+0.6}_{-0.6}$	$0.51^{+0.38}_{-0.24}$	$0.32^{+0.15}_{-0.12}$	$0.84^{+0.69}_{-0.38}$	$2.31^{+1.89}_{-1.12}$	$4.49^{+3.77}_{-2.34}$	$1.08^{+1.03}_{-0.56}$
SMC_SC5 43650	01	$10.7^{+3.0}_{-2.6}$	$0.4^{+0.3}_{-0.3}$	$0.81^{+0.1}_{-0.11}$	$0.55^{+0.09}_{-0.04}$	$0.5^{+1.2}_{-0.2}$	$0.35^{+0.75}_{-0.3}$	$0.39^{+0.71}_{-0.3}$	$0.61^{+1.32}_{-0.53}$	$0.24^{+0.33}_{-0.16}$	$0.35^{+0.59}_{-0.23}$	$0.07^{+0.12}_{-0.05}$
	02					$0.6^{+0.2}_{-0.2}$	$0.72^{+0.33}_{-0.53}$	$0.53^{+0.67}_{-0.42}$	$6.35^{+4.94}_{-4.65}$	$0.5^{+0.45}_{-0.33}$	$0.71^{+0.83}_{-0.46}$	$0.74^{+0.92}_{-0.47}$
SMC_SC5 54851	01	$11.7^{+1.6}_{-1.5}$	$0.7^{+0.1}_{-0.1}$	$0.78^{+0.1}_{-0.08}$	$0.62^{+0.04}_{-0.01}$	$1.3^{+0.3}_{-0.2}$	$0.38^{+0.35}_{-0.14}$	$0.11^{+0.04}_{-0.03}$	$0.82^{+0.73}_{-0.42}$	$1.06^{+0.78}_{-0.42}$	$1.95^{+1.69}_{-0.9}$	$0.59^{+0.5}_{-0.28}$
	02					$1.3^{+0.2}_{-0.2}$	$0.48^{+0.32}_{-0.23}$	$0.12^{+0.04}_{-0.03}$	$1.19^{+0.99}_{-0.58}$	$1.28^{+1.07}_{-0.58}$	$2.33^{+2.28}_{-1.38}$	$0.8^{+0.79}_{-0.41}$
	03					$1.1^{+0.2}_{-0.1}$	$0.51^{+0.23}_{-0.2}$	$0.05^{+0.01}_{-0.01}$	$2.11^{+0.99}_{-0.8}$	$1.12^{+0.78}_{-0.49}$	$2.04^{+1.38}_{-0.97}$	$1.19^{+0.88}_{-0.57}$
SMC_SC5 65500	01	$12.1^{+2.9}_{-2.4}$	$0.6^{+0.2}_{-0.3}$	$0.81^{+0.1}_{-0.1}$	$0.71^{+0.13}_{-0.08}$	$1.7^{+0.6}_{-0.4}$	$0.7^{+0.38}_{-0.34}$	$0.26^{+0.13}_{-0.1}$	$0.44^{+0.24}_{-0.19}$	$2.07^{+1.66}_{-1.02}$	$3.7^{+3.62}_{-2.05}$	$0.32^{+0.34}_{-0.17}$
SMC_SC5 129535	01	$9.4^{+2.2}_{-2.0}$	$0.5^{+0.3}_{-0.3}$	$0.81^{+0.1}_{-0.11}$	$0.58^{+0.13}_{-0.06}$	$0.7^{+0.2}_{-0.2}$	$0.65^{+0.52}_{-0.37}$	$0.25^{+0.36}_{-0.13}$	$3.88^{+3.02}_{-2.29}$	$0.58^{+0.54}_{-0.32}$	$0.8^{+0.86}_{-0.46}$	$0.56^{+0.6}_{-0.33}$
SMC_SC5 145724	01	$9.2^{+2.1}_{-1.8}$	$0.5^{+0.3}_{-0.3}$	$0.81^{+0.1}_{-0.11}$	$0.4^{+0.13}_{-0.06}$	$2.6^{+0.7}_{-1.0}$	$0.88^{+0.4}_{-0.46}$	$0.16^{+0.19}_{-0.08}$	$3.87^{+1.89}_{-1.98}$	$2.6^{+2.03}_{-1.55}$	$3.46^{+3.23}_{-2.12}$	$1.79^{+1.7}_{-1.11}$
SMC_SC5 180034	01	$12.6^{+2.6}_{-2.6}$	$0.4^{+0.3}_{-0.3}$	$0.8^{+0.1}_{-0.11}$	$0.62^{+0.17}_{-0.09}$	$1.0^{+0.5}_{-0.3}$	$0.4^{+0.65}_{-0.25}$	$0.22^{+0.17}_{-0.09}$	$0.97^{+1.54}_{-0.57}$	$0.68^{+0.81}_{-0.4}$	$1.17^{+1.57}_{-0.71}$	$0.36^{+0.47}_{-0.22}$
SMC_SC5 260841	01	$12.7^{+2.4}_{-2.0}$	$0.6^{+0.2}_{-0.3}$	$0.83^{+0.09}_{-0.1}$	$0.54^{+0.08}_{-0.03}$	$0.6^{+0.4}_{-0.1}$	$0.8^{+0.42}_{-0.49}$	$0.07^{+0.58}_{-0.93}$	$1.42^{+0.81}_{-0.93}$	$0.86^{+0.71}_{-0.45}$	$1.58^{+1.61}_{-0.9}$	$0.38^{+0.38}_{-0.22}$
02						$0.5^{+0.1}_{-0.2}$	$0.78^{+0.4}_{-0.41}$	$0.08^{+0.78}_{-0.04}$	$2.49^{+1.47}_{-1.38}$	$0.78^{+0.6}_{-0.41}$	$1.44^{+1.39}_{-0.82}$	$0.64^{+0.64}_{-0.36}$
SMC_SC5 260957	01	$9.4^{+2.5}_{-1.9}$	$0.5^{+0.3}_{-0.3}$	$0.82^{+0.1}_{-0.11}$	$0.58^{+0.13}_{-0.06}$	$1.3^{+0.4}_{-0.3}$	$0.64^{+0.46}_{-0.3}$	$0.05^{+0.02}_{-0.02}$	$2.41^{+1.92}_{-1.1}$	$1.07^{+0.89}_{-0.57}$	$1.48^{+1.49}_{-0.85}$	$0.66^{+0.68}_{-0.38}$
SMC_SC5 266088	01	$8.8^{+2.4}_{-2.1}$	$0.4^{+0.4}_{-0.3}$	$0.8^{+0.1}_{-0.11}$	$0.71^{+0.14}_{-0.08}$	$0.7^{+0.4}_{-0.2}$	$0.29^{+0.73}_{-0.22}$	$0.07^{+0.07}_{-0.03}$	$1.53^{+3.83}_{-1.17}$	$0.23^{+0.46}_{-0.15}$	$0.31^{+0.58}_{-0.21}$	$0.18^{+0.34}_{-0.12}$
SMC_SC5 276982	01	$15.2^{+1.3}_{-2.0}$	$0.5^{+0.2}_{-0.2}$	$0.81^{+0.1}_{-0.11}$	$0.78^{+0.11}_{-0.11}$	$1.0^{+0.4}_{-0.3}$	$0.05^{+0.18}_{-0.03}$	$0.06^{+0.05}_{-0.02}$	$0.25^{+0.8}_{-0.13}$	$0.13^{+0.26}_{-0.06}$	$0.26^{+0.57}_{-0.14}$	$0.17^{+0.34}_{-0.09}$
SMC_SC5 282963	01	$13.8^{+2.1}_{-2.4}$	$0.7^{+0.2}_{-0.3}$	$0.82^{+0.1}_{-0.11}$	$0.37^{+0.11}_{-0.05}$	$1.5^{+0.7}_{-0.5}$	$0.69^{+0.47}_{-0.35}$	$0.44^{+0.29}_{-0.19}$	$5.52^{+3.69}_{-2.75}$	$2.46^{+1.98}_{-1.47}$	$5.05^{+4.7}_{-3.2}$	$6.01^{+5.53}_{-3.82}$
SMC_SC6 11085	01	$15.7^{+1.0}_{-2.0}$	$0.6^{+0.2}_{-0.3}$	$0.82^{+0.09}_{-0.1}$	$0.69^{+0.07}_{-0.07}$	$2.3^{+0.6}_{-0.4}$	$0.63^{+0.47}_{-0.26}$	$0.16^{+0.09}_{-0.05}$	$0.87^{+0.63}_{-0.36}$	$3.17^{+2.3}_{-1.35}$	$6.76^{+5.89}_{-3.13}$	$1.39^{+1.2}_{-0.65}$
	02					$2.5^{+0.6}_{-0.6}$	$0.65^{+0.43}_{-0.24}$	$0.34^{+0.22}_{-0.1}$	$1.04^{+0.63}_{-0.36}$	$3.66^{+2.39}_{-1.49}$	$7.79^{+6.18}_{-3.49}$	$1.82^{+1.43}_{-0.8}$
SMC_SC6 17538	01	$8.8^{+2.5}_{-2.1}$	$0.3^{+0.3}_{-0.2}$	$0.81^{+0.1}_{-0.1}$	$0.62^{+0.17}_{-0.1}$	$0.8^{+0.4}_{-0.2}$	$0.63^{+0.55}_{-0.45}$	$0.1^{+0.12}_{-0.05}$	$3.15^{+2.77}_{-2.3}$	$0.5^{+0.49}_{-0.29}$	$0.61^{+0.74}_{-0.36}$	$0.33^{+0.41}_{-0.2}$
SMC_SC6 42440	01	$9.4^{+2.6}_{-2.1}$	$0.4^{+0.4}_{-0.3}$	$0.8^{+0.11}_{-0.11}$	$0.37^{+0.14}_{-0.06}$	$1.8^{+0.8}_{-0.8}$	$0.76^{+0.49}_{-0.41}$	$0.2^{+0.16}_{-0.11}$	$2.4^{+1.65}_{-1.29}$	$1.5^{+1.6}_{-0.83}$	$2.01^{+2.62}_{-1.15}$	$0.75^{+0.97}_{-0.44}$

Table 6 – continued Results of the pipeline for each star and bump of the sample

SMC_SC6 99991	01	13.0 ^{+2.2} _{-2.2}	0.7 ^{+0.2} _{-0.2}	0.82 ^{+0.1} _{-0.1}	0.34 ^{+0.04} _{-0.03}	1.6 ^{+0.6} _{-0.5}	0.53 ^{+0.41} _{-0.22}	0.94 ^{+0.33} _{-0.38}	0.64 ^{+0.51} _{-0.73}	1.82 ^{+1.03} _{-0.72}	3.54 ^{+2.38} _{-1.84}	0.61 ^{+0.41} _{-0.35}
	02					1.8 ^{+0.5} _{-0.4}	0.67 ^{+0.32} _{-0.32}	0.75 ^{+0.26} _{-0.26}	1.07 ^{+0.49} _{-0.49}	2.42 ^{+1.06} _{-1.06}	4.68 ^{+1.84} _{-2.34}	1.09 ^{+0.85} _{-0.82}
	03					1.8 ^{+0.5} _{-0.4}	0.51 ^{+0.4} _{-0.22}	0.82 ^{+0.33} _{-0.27}	0.81 ^{+0.63} _{-0.34}	1.89 ^{+1.26} _{-0.77}	3.64 ^{+2.95} _{-1.66}	0.82 ^{+0.65} _{-0.36}
	04					1.7 ^{+0.6} _{-0.5}	0.42 ^{+0.33} _{-0.18}	0.94 ^{+0.28} _{-0.26}	0.78 ^{+1.0} _{-0.36}	1.56 ^{+1.05} _{-0.66}	3.04 ^{+2.29} _{-1.44}	0.8 ^{+0.61} _{-0.37}
SMC_SC6 105368	01	12.4 ^{+2.7} _{-2.5}	0.5 ^{+0.2} _{-0.3}	0.82 ^{+0.11} _{-0.1}	0.53 ^{+0.05} _{-0.03}	1.0 ^{+0.4} _{-0.2}	0.56 ^{+0.5} _{-0.32}	0.2 ^{+0.12} _{-0.07}	1.03 ^{+0.9} _{-0.59}	0.89 ^{+0.79} _{-0.45}	1.52 ^{+1.66} _{-0.81}	0.36 ^{+0.39} _{-0.19}
	02					1.5 ^{+0.7} _{-0.5}	0.24 ^{+0.45} _{-0.12}	0.22 ^{+0.2} _{-0.09}	0.56 ^{+1.02} _{-0.27}	0.65 ^{+0.76} _{-0.31}	1.17 ^{+1.53} _{-0.63}	0.34 ^{+0.43} _{-0.18}
SMC_SC6 116294	01	9.2 ^{+2.3} _{-1.8}	0.5 ^{+0.3} _{-0.3}	0.81 ^{+0.1} _{-0.11}	0.4 ^{+0.14} _{-0.06}	2.6 ^{+0.7} _{-1.0}	0.89 ^{+0.38} _{-0.38}	0.18 ^{+0.19} _{-0.09}	2.39 ^{+1.03} _{-1.09}	2.67 ^{+2.3} _{-1.5}	3.63 ^{+3.66} _{-2.09}	1.13 ^{+1.13} _{-0.65}
SMC_SC6 128831	01	12.2 ^{+2.7} _{-2.2}	0.6 ^{+0.2} _{-0.3}	0.8 ^{+0.11} _{-0.09}	0.03 ^{+0.02} _{-0.02}	2.6 ^{+0.5} _{-0.6}	0.98 ^{+0.35} _{-0.4}	0.69 ^{+0.34} _{-0.27}	0.82 ^{+0.32} _{-0.36}	4.18 ^{+2.2} _{-1.72}	7.47 ^{+4.69} _{-3.44}	0.84 ^{+0.61} _{-0.4}
SMC_SC6 199611	01	13.8 ^{+2.1} _{-2.0}	0.8 ^{+0.2} _{-0.3}	0.81 ^{+0.1} _{-0.1}	0.37 ^{+0.12} _{-0.06}	1.4 ^{+1.4} _{-0.7}	0.47 ^{+0.62} _{-0.33}	0.34 ^{+0.34} _{-0.18}	0.35 ^{+0.48} _{-0.25}	1.48 ^{+1.51} _{-0.91}	3.03 ^{+3.73} _{-1.93}	0.34 ^{+0.42} _{-0.21}
SMC_SC6 272665	01	7.0 ^{+1.8} _{-1.2}	0.4 ^{+0.3} _{-0.3}	0.8 ^{+0.11} _{-0.1}	0.37 ^{+0.14} _{-0.05}	0.7 ^{+0.4} _{-0.2}	0.68 ^{+0.54} _{-0.46}	0.08 ^{+0.25} _{-0.05}	5.97 ^{+5.43} _{-4.09}	0.37 ^{+0.37} _{-0.22}	0.4 ^{+0.46} _{-0.24}	0.37 ^{+0.42} _{-0.24}
SMC_SC7 57131	01	12.1 ^{+2.6} _{-2.2}	0.6 ^{+0.3} _{-0.3}	0.81 ^{+0.1} _{-0.1}	0.39 ^{+0.12} _{-0.06}	2.0 ^{+0.7} _{-0.7}	0.78 ^{+0.45} _{-0.39}	0.74 ^{+0.41} _{-0.35}	1.69 ^{+0.98} _{-0.81}	2.48 ^{+1.97} _{-1.36}	4.32 ^{+3.9} _{-2.46}	1.26 ^{+1.11} _{-0.73}
SMC_SC8 183240	01	14.7 ^{+1.6} _{-1.8}	0.8 ^{+0.1} _{-0.2}	0.82 ^{+0.1} _{-0.11}	0.64 ^{+0.18} _{-0.11}	0.7 ^{+0.3} _{-0.2}	0.63 ^{+0.51} _{-0.38}	0.25 ^{+0.21} _{-0.12}	1.1 ^{+0.86} _{-0.63}	1.37 ^{+1.24} _{-0.8}	3.2 ^{+3.22} _{-1.94}	0.92 ^{+0.89} _{-0.54}
SMC_SC9 105383	01	13.2 ^{+2.6} _{-2.5}	0.5 ^{+0.2} _{-0.3}	0.83 ^{+0.09} _{-0.1}	0.56 ^{+0.08} _{-0.05}	1.9 ^{+0.8} _{-0.5}	0.52 ^{+0.5} _{-0.25}	0.1 ^{+0.04} _{-0.03}	1.17 ^{+1.2} _{-0.58}	1.82 ^{+1.58} _{-0.86}	3.36 ^{+3.43} _{-1.76}	1.01 ^{+1.07} _{-0.51}
	02					1.8 ^{+0.3} _{-0.4}	0.86 ^{+0.38} _{-0.39}	0.1 ^{+0.08} _{-0.03}	1.76 ^{+0.73} _{-0.75}	2.58 ^{+1.86} _{-1.15}	4.75 ^{+4.14} _{-2.38}	1.3 ^{+1.12} _{-0.62}
SMC_SC9 168422	01	9.4 ^{+2.3} _{-2.0}	0.4 ^{+0.3} _{-0.3}	0.82 ^{+0.1} _{-0.11}	0.61 ^{+0.16} _{-0.08}	0.5 ^{+0.4} _{-0.2}	0.56 ^{+0.62} _{-0.45}	0.08 ^{+0.12} _{-0.04}	2.15 ^{+2.35} _{-1.71}	0.33 ^{+0.41} _{-0.22}	0.44 ^{+0.63} _{-0.3}	0.2 ^{+0.29} _{-0.13}
SMC_SC10 8906	01	13.9 ^{+2.0} _{-2.1}	0.8 ^{+0.1} _{-0.2}	0.81 ^{+0.11} _{-0.1}	0.58 ^{+0.1} _{-0.05}	2.0 ^{+1.0} _{-0.7}	0.79 ^{+0.44} _{-0.39}	0.47 ^{+0.26} _{-0.18}	0.16 ^{+0.1} _{-0.07}	3.88 ^{+2.17} _{-1.57}	8.2 ^{+5.63} _{-3.7}	0.26 ^{+0.19} _{-0.12}
	02					1.8 ^{+0.7} _{-0.6}	0.81 ^{+0.39} _{-0.35}	0.92 ^{+0.33} _{-0.32}	0.06 ^{+0.03} _{-0.02}	3.39 ^{+2.05} _{-1.5}	7.26 ^{+3.01} _{-3.55}	0.09 ^{+0.06} _{-0.04}
SMC_SC11 28090	01	13.7 ^{+2.1} _{-2.1}	0.8 ^{+0.1} _{-0.2}	0.83 ^{+0.09} _{-0.11}	0.56 ^{+0.12} _{-0.05}	1.7 ^{+0.8} _{-0.5}	0.1 ^{+0.1} _{-0.05}	0.12 ^{+0.05} _{-0.05}	0.41 ^{+0.37} _{-0.18}	0.48 ^{+0.41} _{-0.23}	1.02 ^{+1.01} _{-0.54}	0.64 ^{+0.64} _{-0.34}
SMC_SC11 46587	01	9.0 ^{+2.5} _{-2.1}	0.4 ^{+0.4} _{-0.3}	0.81 ^{+0.1} _{-0.11}	0.39 ^{+0.19} _{-0.07}	0.9 ^{+0.7} _{-0.4}	0.6 ^{+0.57} _{-0.43}	0.36 ^{+0.51} _{-0.22}	4.02 ^{+3.88} _{-2.89}	0.55 ^{+0.58} _{-0.34}	0.72 ^{+0.91} _{-0.47}	0.55 ^{+0.7} _{-0.36}

ACKNOWLEDGEMENTS

This work made use of the computing facilities of the Laboratory of Astroinformatics (IAG/USP, NAT/Unicisul), whose purchase was made possible by the Brazilian agency FAPESP (grant 2009/54006-4) and the INCT-A. L. R. R. acknowledges the support from FAPESP (grant 2012/21518-5) and from CNPq (grant 142411/2011-6). A. C. C. acknowledges the support from CNPq (grant 307594/2015-7) and FAPESP (grant 2015/17967-7). D. M. F. acknowledges the support from FAPESP (grant 2016/16844-1). R. G. V. acknowledges the support from FAPESP (grant 2012/20364-4). M. R. G. acknowledges the support from CAPES PROEX Programa Astronomia. J. E. B. was supported by NSF grant AST-1412135. The OGLE project has received funding from the National Science Centre, Poland, grant MAESTRO 2014/14/A/ST9/00121.

REFERENCES

- Alcock C., et al., 1997, *ApJ*, **486**, 697
Aubourg E., et al., 1993, *Nature*, **365**, 623
Baade D., et al., 2016, *A&A*, **588**, A56
Balbus S. A., Hawley J. F., 1991, *ApJ*, **376**, 214
Bessell M. S., 1990, *PASP*, **102**, 1181
Carciofi A. C., 2011, in Neiner C., Wade G., Meynet G., Peters G., eds, IAU Symposium Vol. 272, Active OB Stars: Structure, Evolution, Mass Loss, and Critical Limits. pp 325–336 ([arXiv:1009.3969](https://arxiv.org/abs/1009.3969)), doi:10.1017/S1743921311010738
Carciofi A. C., Bjorkman J. E., 2006, *ApJ*, **639**, 1081
Carciofi A. C., Bjorkman J. E., 2008, *ApJ*, **684**, 1374
Carciofi A. C., Bjorkman J. E., Magalhães A. M., 2004, *ApJ*, **604**, 238
Carciofi A. C., et al., 2006, *ApJ*, **652**, 1617
Carciofi A. C., Magalhães A. M., Leister N. V., Bjorkman J. E., Levenhagen R. S., 2007, *ApJ*, **671**, L49
Carciofi A. C., Domiciano de Souza A., Magalhães A. M., Bjorkman J. E., Vakili F., 2008, *ApJ*, **676**, L41
Carciofi A. C., Okazaki A. T., Le Bouquin J.-B., Štefl S., Rivinius T., Baade D., Bjorkman J. E., Hummel C. A., 2009, *A&A*, **504**, 915
Carciofi A. C., Bjorkman J. E., Otero S. A., Okazaki A. T., Štefl S., Rivinius T., Baade D., Haubois X., 2012, *ApJ*, **744**, L15
Castelli F., Kurucz R. L., 1994, *A&A*, **281**, 817
Collins II G. W., 1987, in Slettebak A., Snow T. P., eds, IAU Colloq. 92: Physics of Be Stars. pp 3–19
Ekström S., Meynet G., Maeder A., Barblan F., 2008, *A&A*, **478**, 467
Espinosa Lara F., Rieutord M., 2011, *A&A*, **533**, A43
Foreman-Mackey D., Hogg D. W., Lang D., Goodman J., 2013, *PASP*, **125**, 306
Gayley K. G., Ignace R., Owocki S. P., 2001, *ApJ*, **558**, 802
Gehrz R. D., Hackwell J. A., Jones T. W., 1974, *ApJ*, **191**, 675
Georgy C., Ekström S., Granada A., Meynet G., Mowlavi N., Eggenberger P., Maeder A., 2013, *A&A*, **553**, A24
Ghoreyshi M. R., Carciofi A. C., 2017, in Miroshnichenko A., Zharikov S., Korčáková D., Wolf M., eds, Astronomical Society of the Pacific Conference Series Vol. 508, Astronomical Society of the Pacific Conference Series. p. 323 ([arXiv:1702.06982](https://arxiv.org/abs/1702.06982))
Gordon K. D., Clayton G. C., Misselt K. A., Landolt A. U., Wolff M. J., 2003, *ApJ*, **594**, 279
Granada A., Ekström S., Georgy C., Krtićka J., Owocki S., Meynet G., Maeder A., 2013, *A&A*, **553**, A25
Haubois X., Carciofi A. C., Rivinius T., Okazaki A. T., Bjorkman J. E., 2012, *ApJ*, **756**, 156
Hilditch R. W., Howarth I. D., Harries T. J., 2005, *MNRAS*, **357**, 304
Jaschek M., Slettebak A., Jaschek C., 1981, Be star terminology., Be Star Newsletter
Jones C. E., Sigut T. A. A., Marlborough J. M., 2004, *MNRAS*, **352**, 841
Jones C. E., Sigut T. A. A., Porter J. M., 2008a, *MNRAS*, **386**, 1922
Jones C. E., Tycner C., Sigut T. A. A., Benson J. A., Hutter D. J., 2008b, *ApJ*, **687**, 598
Kee N. D., Owocki S., Sundqvist J. O., 2016, *MNRAS*, **458**, 2323
Keller S. C., Bessell M. S., Cook K. H., Geha M., Syphers D., 2002, *AJ*, **124**, 2039
King A. R., Pringle J. E., Livio M., 2007, *MNRAS*, **376**, 1740
Klement R., et al., 2015, *A&A*, **584**, A85
Klement R., Carciofi A. C., Rivinius T., in press, *MNRAS*
Kotko I., Lasota J.-P., 2012, *A&A*, **545**, A115
Kroupa P., 2001, *MNRAS*, **322**, 231
Krtićka J., Owocki S. P., Meynet G., 2011, *A&A*, **527**, A84
Lamers H. J. G. L. M., Snow T. P., Lindholm D. M., 1995, *ApJ*, **455**, 269
Martayan C., Frémat Y., Hubert A.-M., Floquet M., Zorec J., Neiner C., 2007a, *A&A*, **462**, 683
Martayan C., Floquet M., Hubert A. M., Gutiérrez-Soto J., Fabregat J., Neiner C., Mekkas M., 2007b, *A&A*, **472**, 577
Mennickent R. E., Pietrzyński G., Gieren W., Szewczyk O., 2002, *A&A*, **393**, 887
Minniti D., et al., 2010, *New Astron.*, **15**, 433
Okazaki A. T., 2001, *PASJ*, **53**, 119
Okazaki A. T., 2007, in Okazaki A. T., Owocki S. P., Stefl S., eds, Astronomical Society of the Pacific Conference Series Vol. 361, Active OB-Stars: Laboratories for Stellare and Circumstellar Physics. p. 230
Okazaki A. T., Bate M. R., Ogilvie G. I., Pringle J. E., 2002, *MNRAS*, **337**, 967
Papaloizou J. C. B., Lin D. N. C., 1995, *ARA&A*, **33**, 505
Paul K. T., Subramaniam A., Mathew B., Mennickent R. E., Sabogal B., 2012, *MNRAS*, **421**, 3622
Pepper J., et al., 2007, *PASP*, **119**, 923
Pojmanski G., 1997, *Acta Astron.*, **47**, 467
Pols O. R., Cote J., Waters L. B. F. M., Heise J., 1991, *A&A*, **241**, 419
Puls J., Vink J. S., Najarro F., 2008, *A&ARv*, **16**, 209
Rivinius T., Baade D., Stefl S., Stahl O., Wolf B., Kaufer A., 1998, *A&A*, **333**, 125
Rivinius T., Štefl S., Baade D., 2006, *A&A*, **459**, 137
Rivinius T., Carciofi A. C., Martayan C., 2013, *A&ARv*, **21**, 69
Rivinius T., Baade D., Carciofi A. C., 2016, *A&A*, **593**, A106
Sabogal B. E., Mennickent R. E., Pietrzyński G., Gieren W., 2005, *MNRAS*, **361**, 1055
Silaj J., Jones C. E., Tycner C., Sigut T. A. A., Smith A. D., 2010, *ApJS*, **187**, 228
Snow Jr. T. P., 1981, *ApJ*, **251**, 139
Touhami Y., Gies D. R., Schaefer G. H., 2011, *ApJ*, **729**, 17
Udalski A., Kubiak M., Szymanski M., 1997, *Acta Astron.*, **47**, 319
Udalski A., Szymanski M. K., Soszynski I., Poleski R., 2008, *Acta Astron.*, **58**, 69
Vieira R. G., Carciofi A. C., Bjorkman J. E., 2015, *MNRAS*, **454**, 2107
Vieira R. G., Carciofi A. C., Bjorkman J. E., Rivinius T., Baade D., Rímulo L. R., 2017, *MNRAS*, **464**, 3071
Wyrzykowski Ł., et al., 2009, *MNRAS*, **397**, 1228
Zaritsky D., Harris J., Thompson I. B., Grebel E. K., 2004, *AJ*, **128**, 1606

APPENDIX A: PROPERTIES OF THE HYDRODYNAMICAL SOLUTIONS OF THE VDD MODEL

A particular bump model (Sect. 3.1) with arbitrary density Σ_0 and scaled build-up time $\tilde{\tau}_{\text{bu}} = 30$ is used to illustrate features of the bump models in Fig. A1. The top panel shows the amount of angular momentum in the disc, given by

$$J_{\text{disc}} = \int (GMR)^{\frac{1}{2}} \Sigma 2\pi R dR, \quad (\text{A1})$$

and the amount of angular momentum that is lost by the star, given by the angular momentum that is injected at the radius of mass injection minus the angular momentum that falls back to the stellar equator. By the continuity of angular momentum, the difference

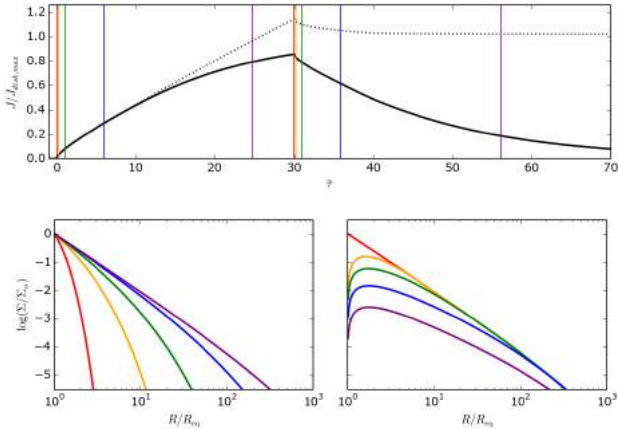


Figure A1. Dynamical bump model with $\tilde{\tau}_{\text{bu}} = 30$. *Top*: the amount of angular momentum in the disc (solid black curve) and the amount of angular momentum that is lost by the star (dotted black curve). Colored vertical straight lines mark the 5 instants $\tilde{\tau} = 0, 0.2, 1, 6, 25$ (during the build-up phase), and the 5 instants $\tilde{\tau} = 30, 30.2, 31, 36, 55$ (during the dissipation phase). Surface density profiles are shown at the first 5 instants (*bottom left*) and at the last 5 instants (*bottom right*).

between the dotted and the solid curves is the angular momentum that escapes the system through the outer boundary at R_{out} . All values were scaled by the maximum angular momentum supported by the disc, which is

$$J_{\text{disc,max}} = \int (GMR)^{\frac{1}{2}} \Sigma_{\text{steady}} 2\pi R dR. \quad (\text{A2})$$

The plot shows that, as the build-up process occurs, the disc mass and angular momentum content increase continuously. Eventually (in our example, roughly after $\tilde{\tau} = 10$), a non-negligible amount of angular momentum starts to reach the outer radius $R_{\text{out}} = 1000R_{\text{eq}}$, leaving the system through the outer boundary. After the end of the build-up phase (which, in our example, happens at $\tilde{\tau} = 30$), the disc starts to dissipate: the black curve shows that the disc loses angular momentum until it reaches zero. However, as the dotted curve shows, only a fraction of the angular momentum of the disc returns to the star by re-accretion. The dotted curve tends to a non-zero value, which is the angular momentum that was lost by the star in the whole process. This non-zero total angular momentum lost by the star was verified in our simulations to be given exactly by

$$-\Delta J_* = \int_0^{\tilde{\tau}_{\text{bu}}} \tau(t) \left(-\frac{\partial J}{\partial t} \right)_{\text{steady}} d\tilde{\tau}, \quad (\text{A3})$$

or, in the case of a constant α in time during build-up (Eq. 20),

$$-\Delta J_* = \left(-\frac{\partial J}{\partial t} \right)_{\text{steady}} (t_2 - t_1). \quad (\text{A4})$$

This quantity, therefore, is nearly independent of R_{out} .

The bottom panels of Fig. A1 show surface density radial profiles at the specify instants marked in the top panel. During build-up, the disc grows in an inside out pattern, with the inner regions reaching a near stationary regime earlier than the outer parts. During dissipation, however, the disc becomes less and less dense as a whole, more or less self-similar way, because the entire disc is coupled by viscous forces.

APPENDIX B: EXAMPLES OF MODEL LIGHT CURVES

Figure B1 shows examples of I -band light curves from our grid (see Table 1 and Sects. 3.2 and 3.3). The dashed black curves correspond to $\Delta I_{\text{bu}}/\Delta I_{\text{bu}}^{\infty}$ versus $\tilde{\tau}$. The solid curves correspond to $\Delta I_{\text{d}}/\Delta I_{\text{d}}^0$ versus $\tilde{\tau} - \tilde{\tau}_{\text{bu}}$ for four dissipating light curves with increasing scaled build-up times. Since $\Delta I_{\text{bu}}^{\infty}$ is the limiting magnitude of the build-up light curves and ΔI_{d}^0 is the magnitude at the instant of the beginning of dissipation, it follows that all $\Delta I_{\text{bu}}/\Delta I_{\text{bu}}^{\infty}$ curves go from 0 to 1 and all $\Delta I_{\text{d}}/\Delta I_{\text{d}}^0$ curves go from 1 to 0.

The build-up and dissipation light curves of the edge-on (upper-left panel) and nearly-pole-on cases (right panels) can be approximated by the mathematical formulae given by Eqs. 17 and 18, respectively. The light curves at intermediate angles like the ones of the middle-left and lower-left panels show more complex forms that cannot be described by Eqs. 17 and 18. The light curves show that, at $\tilde{\tau} \approx 1$, the simulated bump has reached a significant fraction of its limiting value, and, at $\tilde{\tau} - \tilde{\tau}_{\text{bu}} \approx 1$, the bump has already fallen considerably from its previous magnitude before the beginning of the dissipation.

Furthermore, dissipating curves with larger scaled build-up times dissipate at slower rates, as a result of the mass reservoir effect (Sect. 2.2). Also, as discussed in Sect. 3.3, both the dissipation and growth rates depend on the viewing angle.

APPENDIX C: ONLINE FIGURES

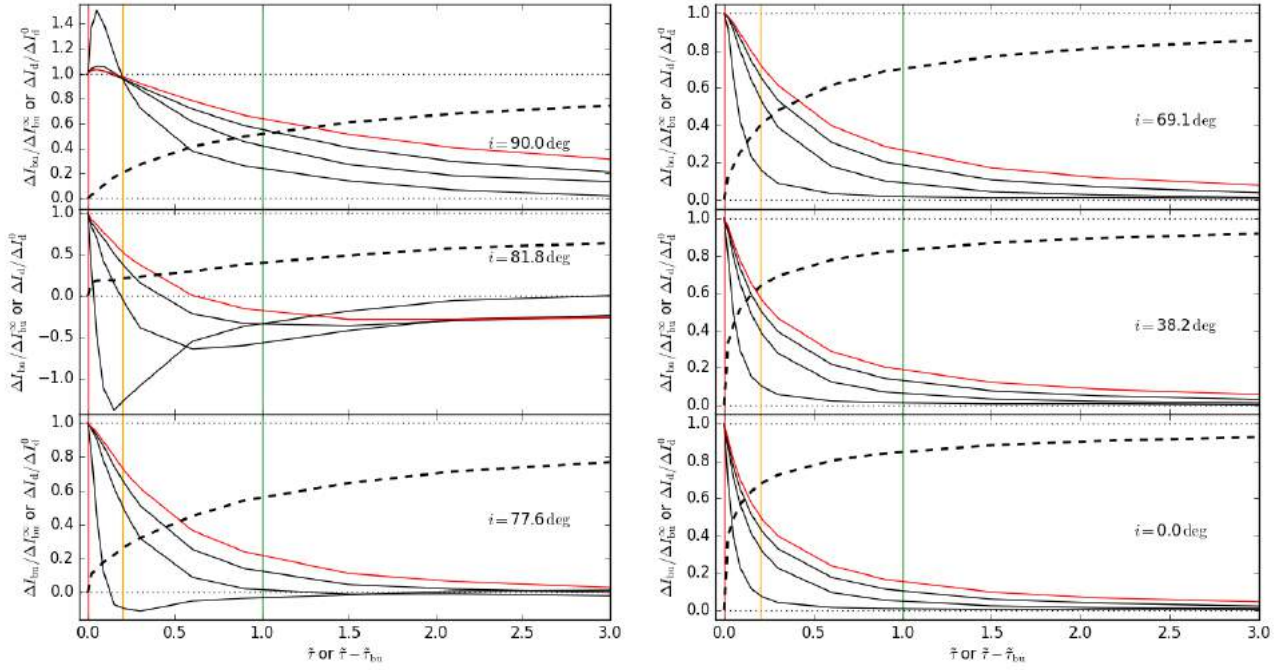


Figure B1. Examples of model *I*-band light curves. Each panel shows the results for different inclination angles, as indicated. The dashed black curves correspond to $\Delta I_{\text{bu}}/\Delta I_{\text{bu}}^{\infty}$ versus $\bar{\tau}$, and the solid curves correspond to $\Delta I_d/\Delta I_d^0$ versus $\bar{\tau} - \bar{\tau}_{\text{bu}}$, for four dissipating light curves with scaled build-up times given by $\bar{\tau}_{\text{bu}} = 0.15, 1.5, 6$ (in black) and $\bar{\tau}_{\text{bu}} = 30$ (in red). Vertical colored straight lines mark the instants $\bar{\tau}$ or $\bar{\tau} - \bar{\tau}_{\text{bu}} = 0, 0.2, 1$ (same color-code as in Fig. A1). All light curves are from Star 2 and $\Sigma_0 = 1.37 \text{ g cm}^{-2}$.

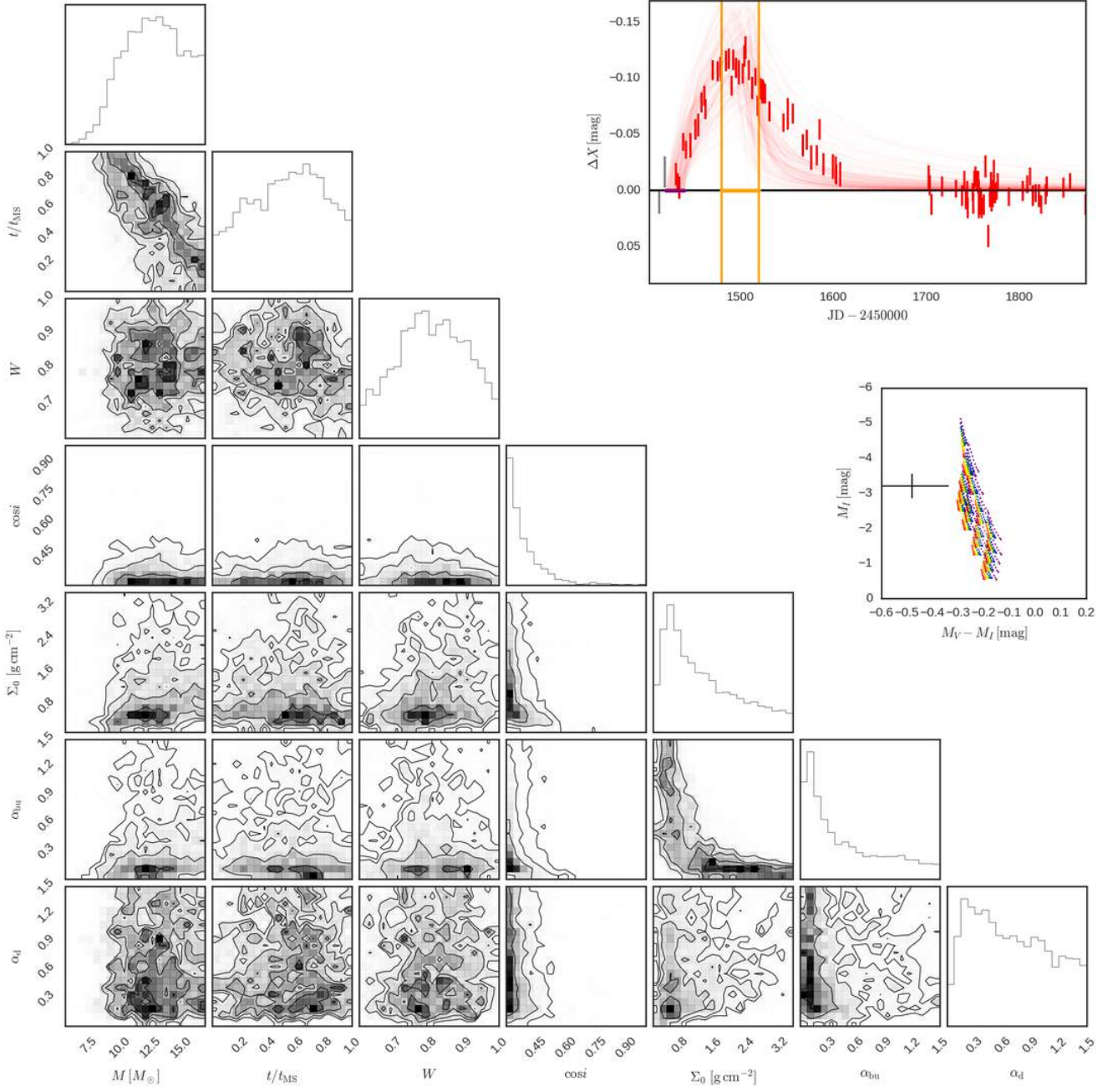


Figure C1. Same as Fig. 8 for SMC_SC1 7612 and bump ID 01.

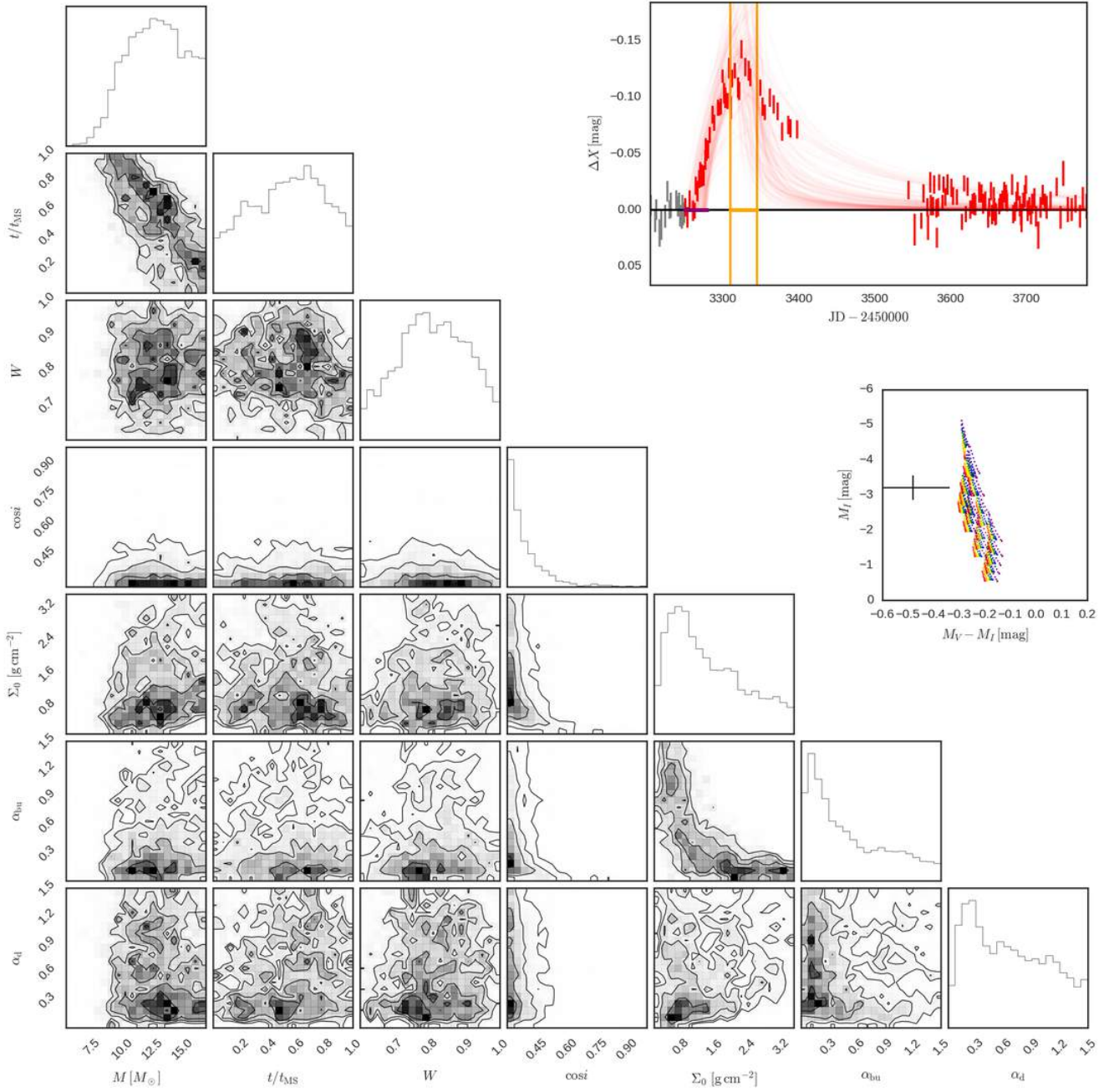


Figure C2. Same as Fig. 8 for SMC_SC1 7612 and bump ID 02.

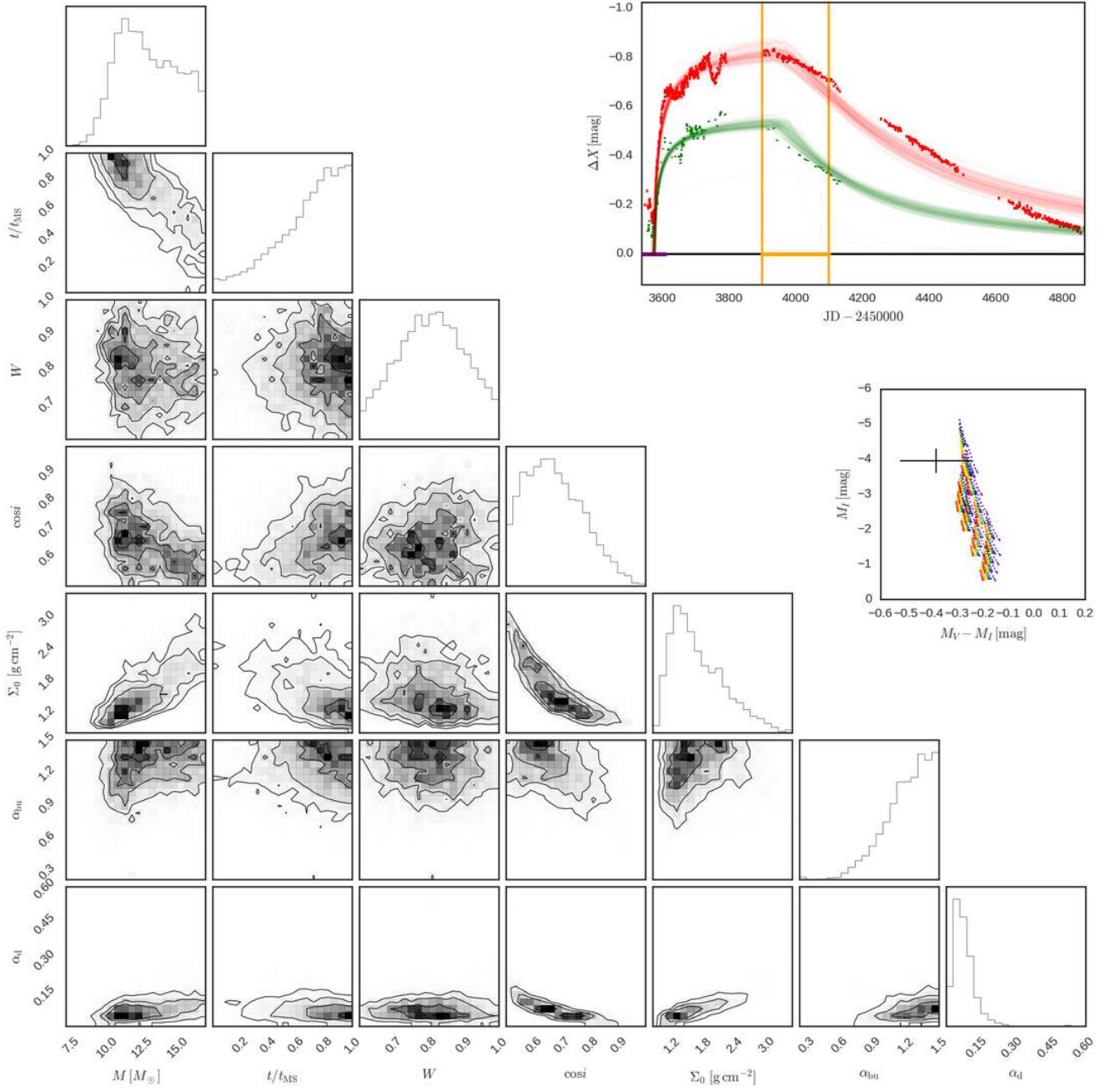


Figure C3. Same as Fig. 8 for SMC_SC1 60553 and bump ID 01.

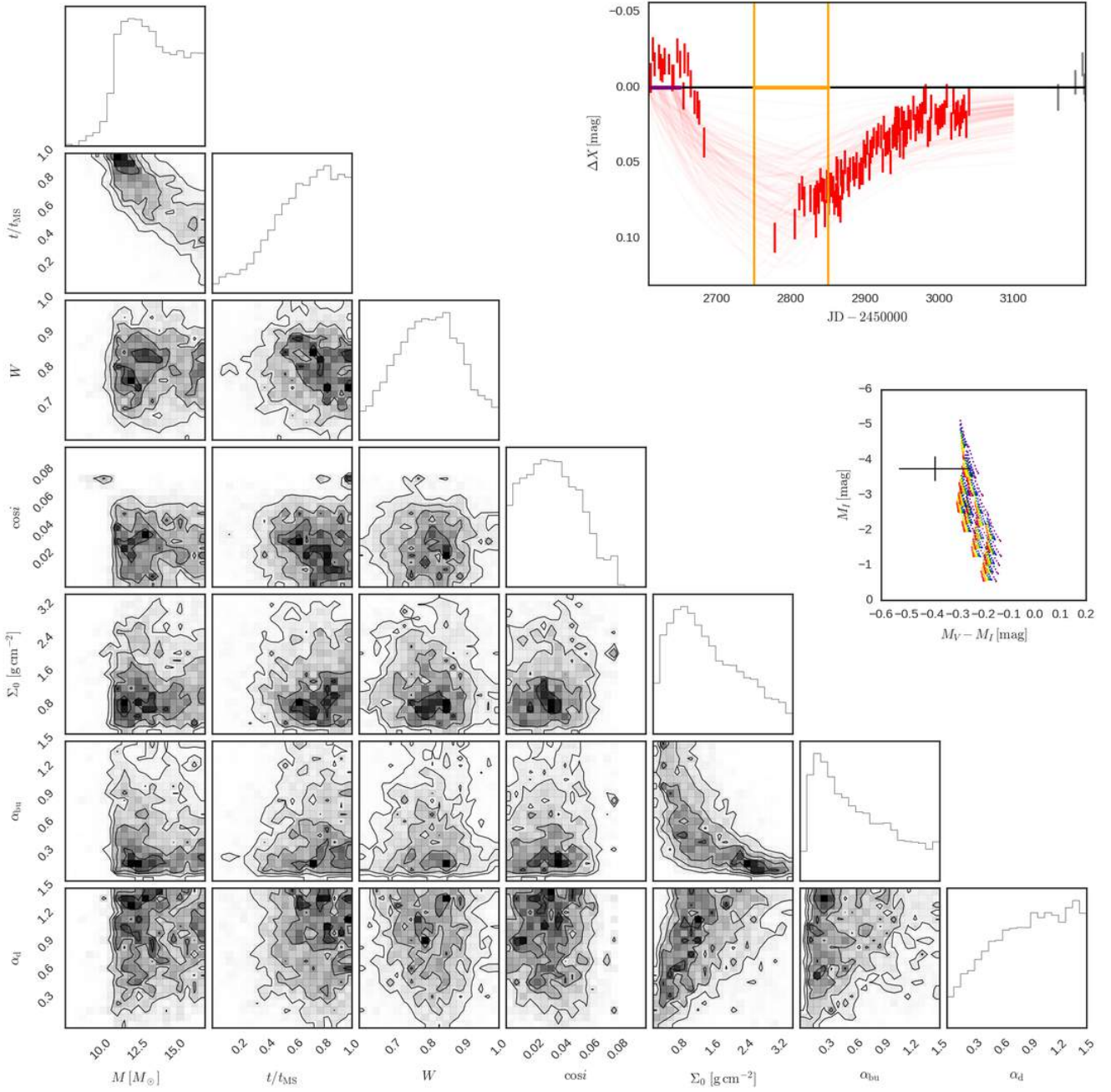


Figure C4. Same as Fig. 8 for SMC_SC1 92262 and bump ID 01.

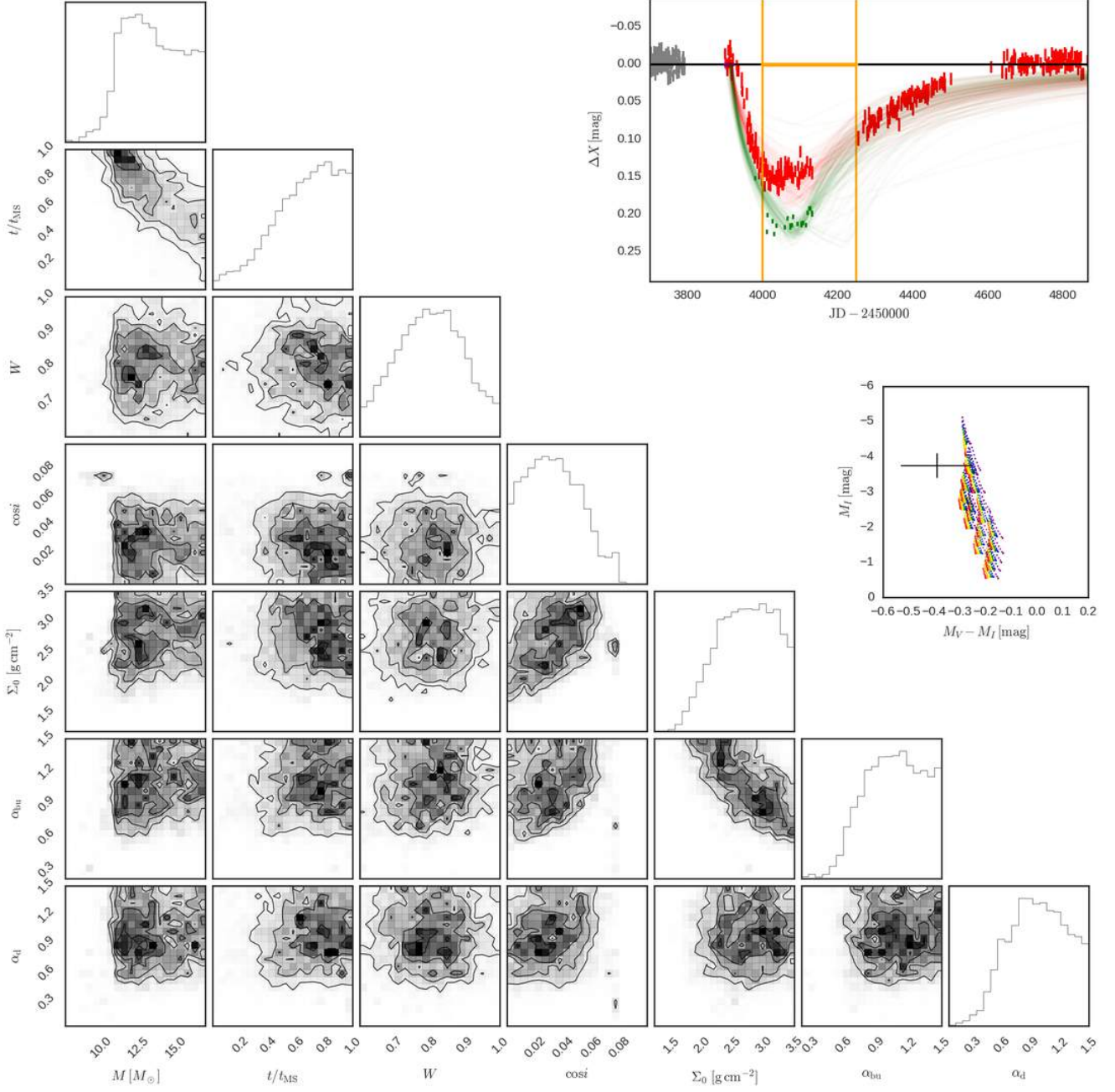


Figure C5. Same as Fig. 8 for SMC_SC1 92262 and bump ID 02.

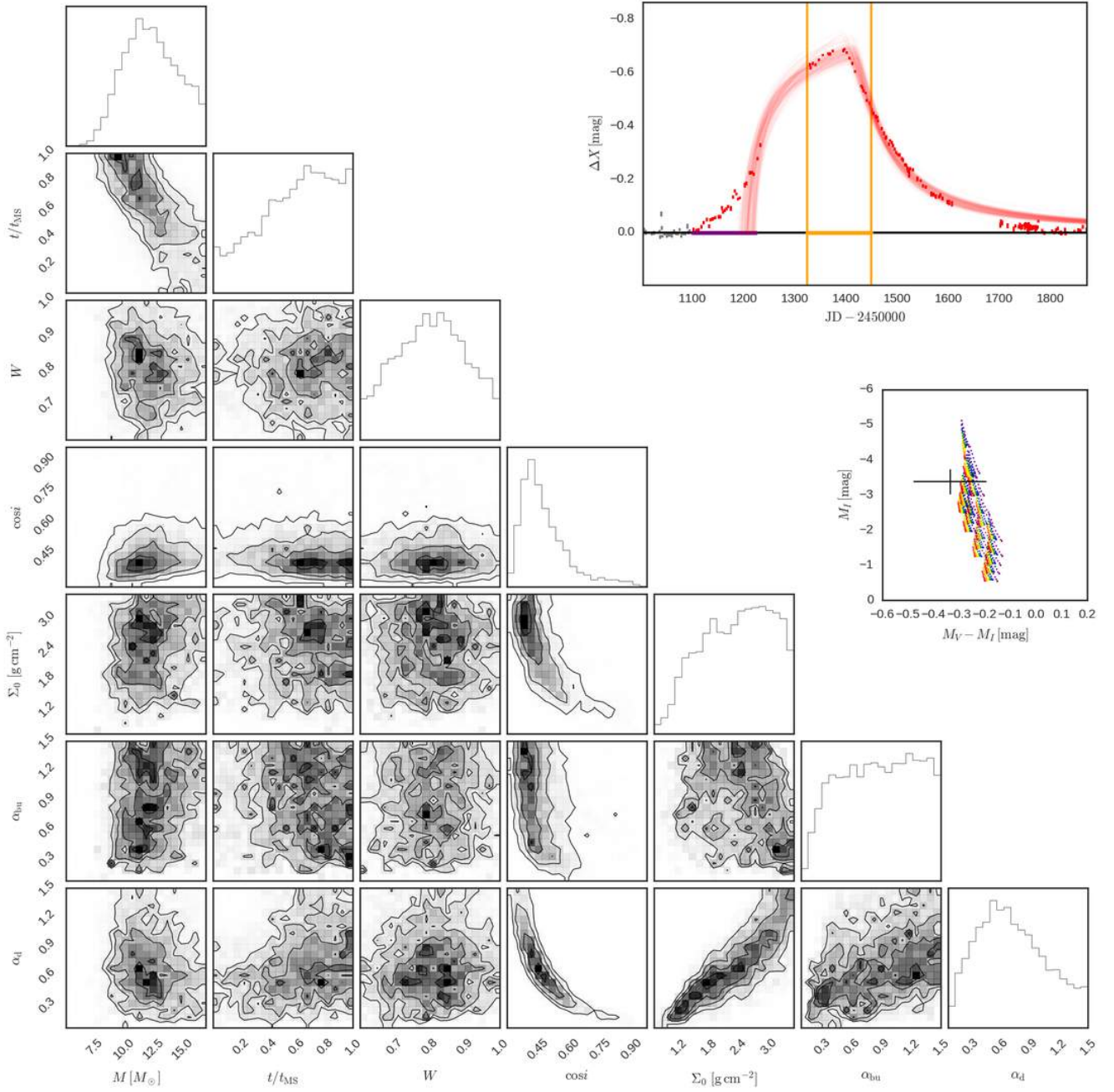


Figure C6. Same as Fig. 8 for SMC_SC2 94939 and bump ID 01.

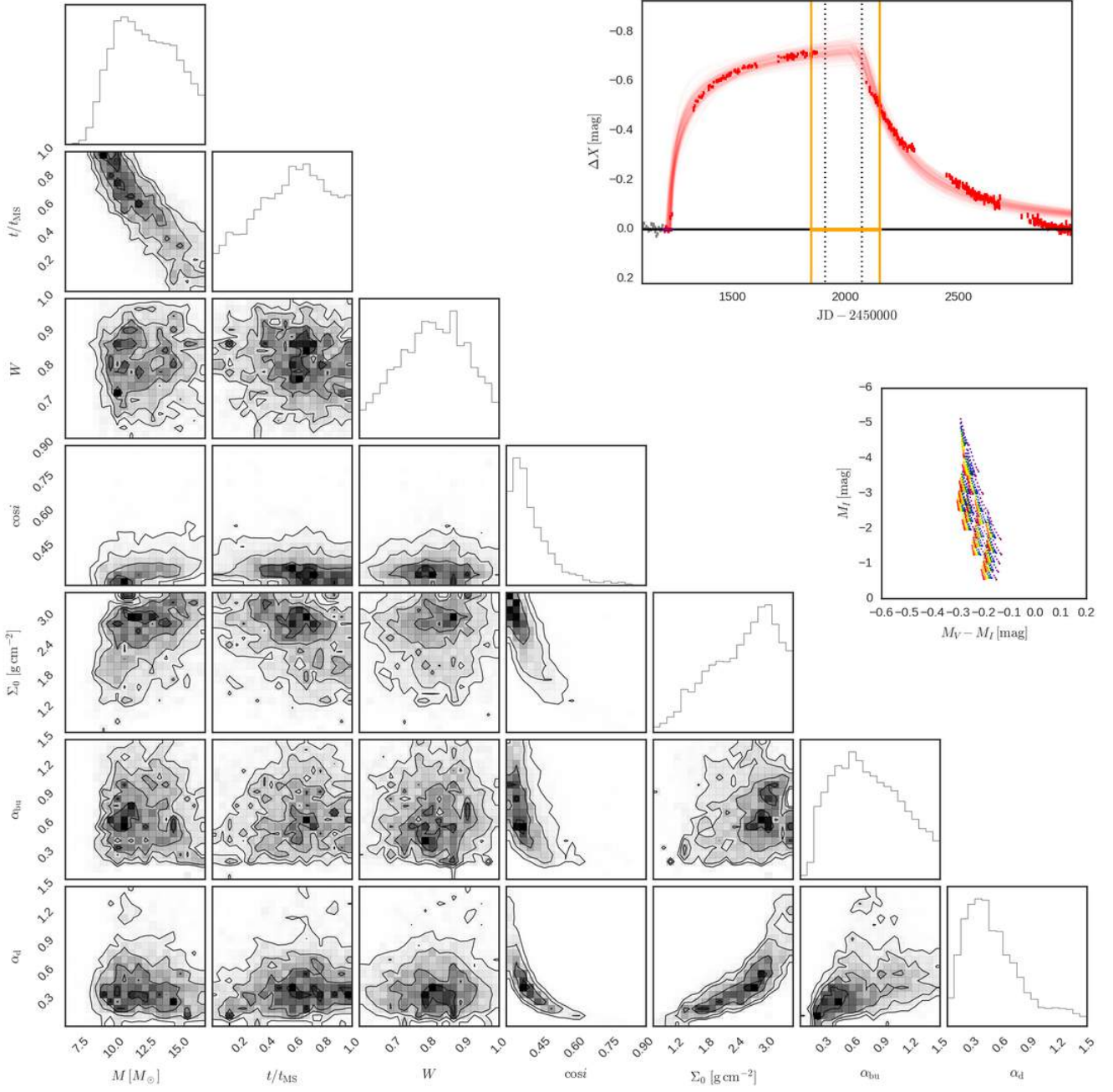


Figure C7. Same as Fig. 8 for SMC_SC3 5719 and bump ID 01.

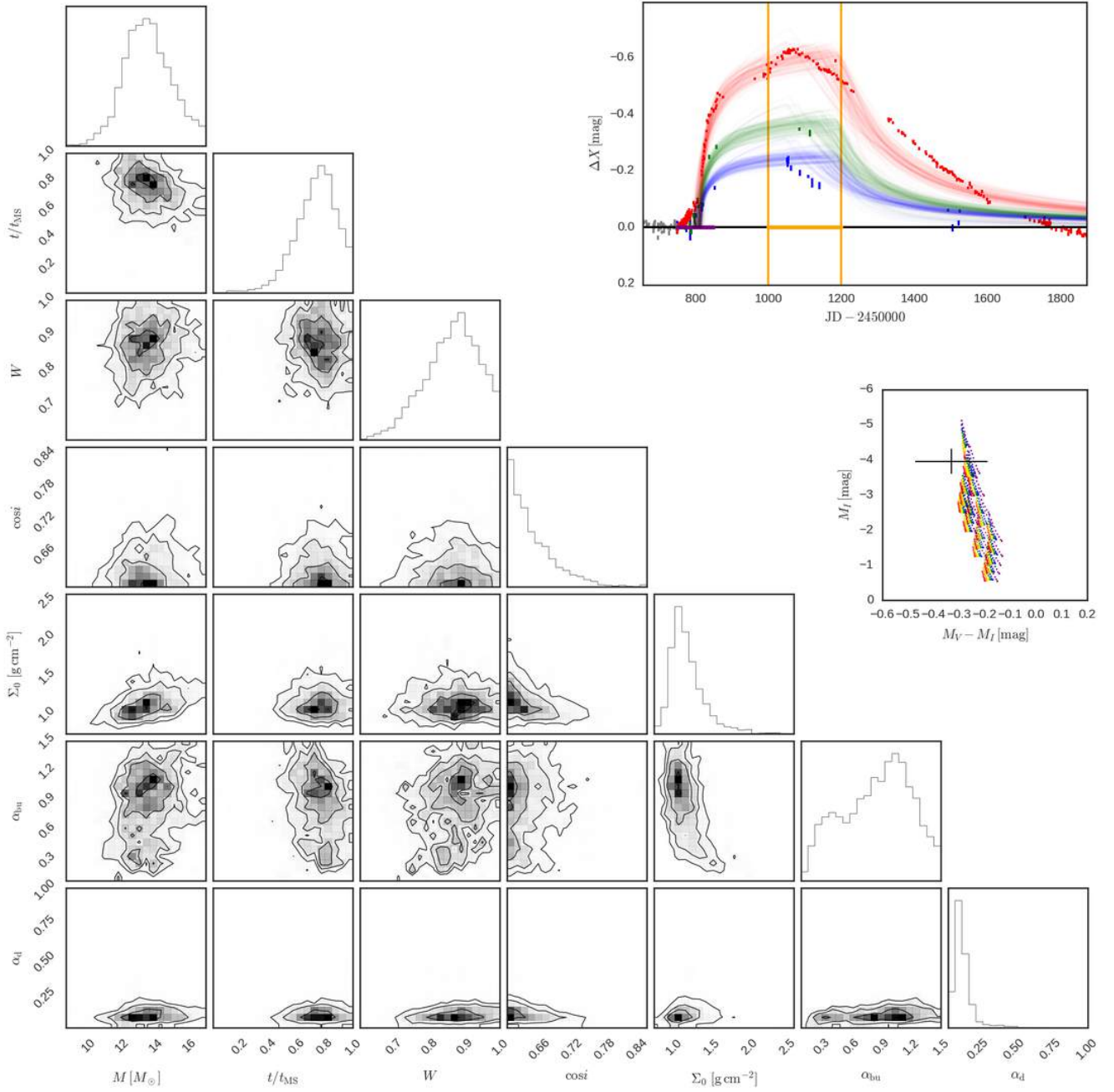


Figure C8. Same as Fig. 8 for SMC_SC3 15970 and bump ID 01.

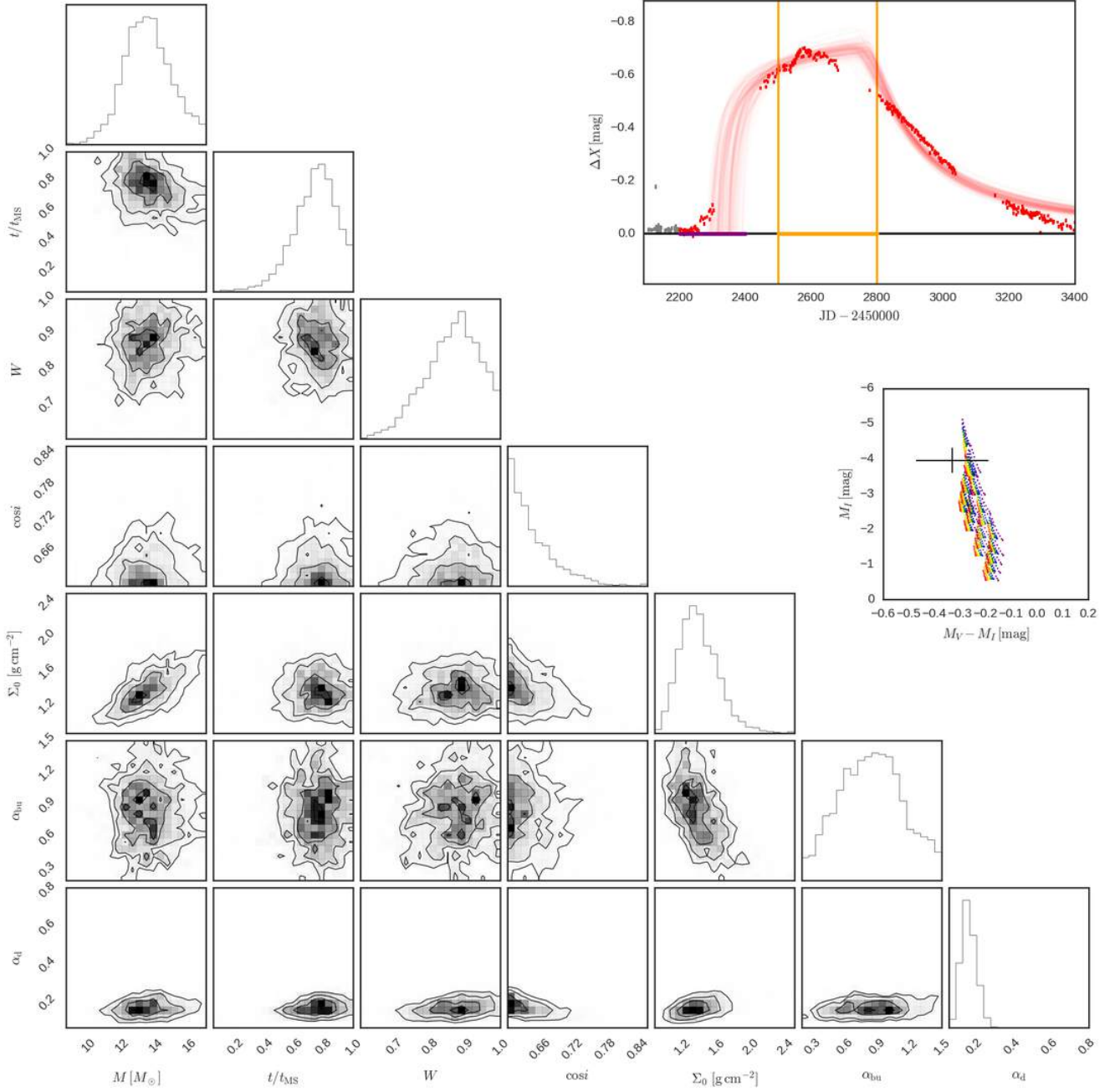


Figure C9. Same as Fig. 8 for SMC_SC3 15970 and bump ID 02.

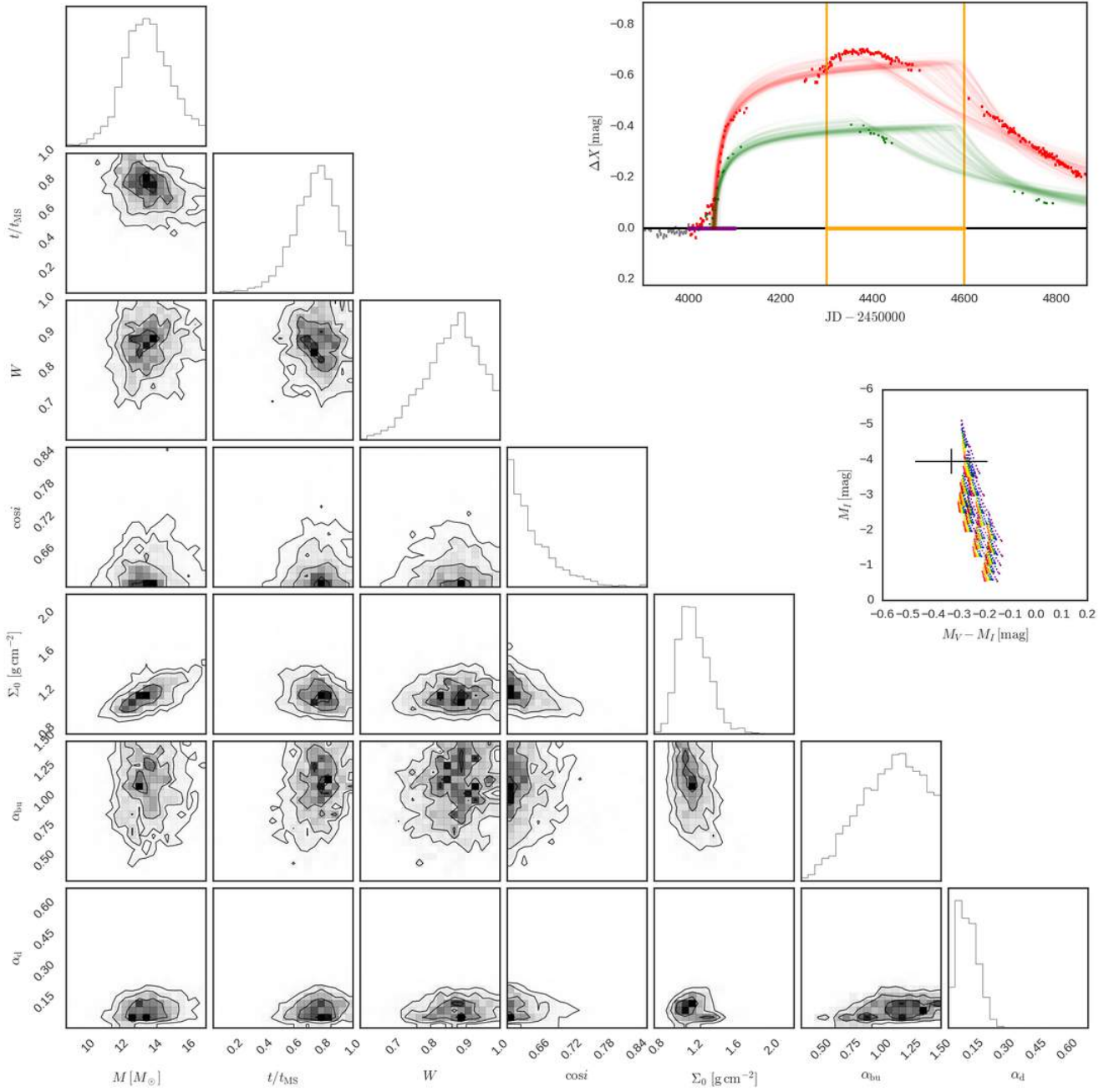


Figure C10. Same as Fig. 8 for SMC_SC3 15970 and bump ID 03.

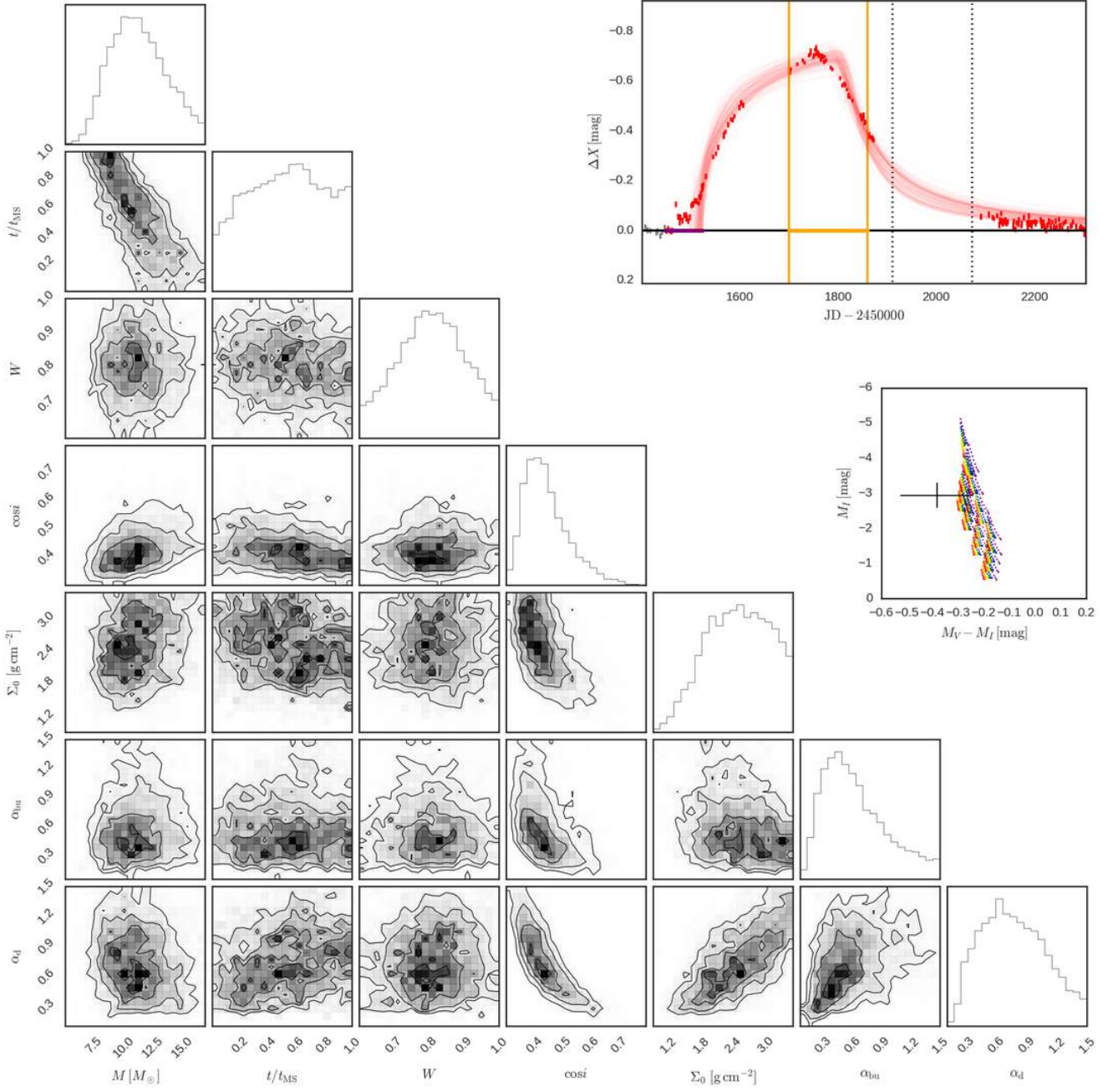


Figure C11. Same as Fig. 8 for SMC_SC3 71445 and bump ID 01.

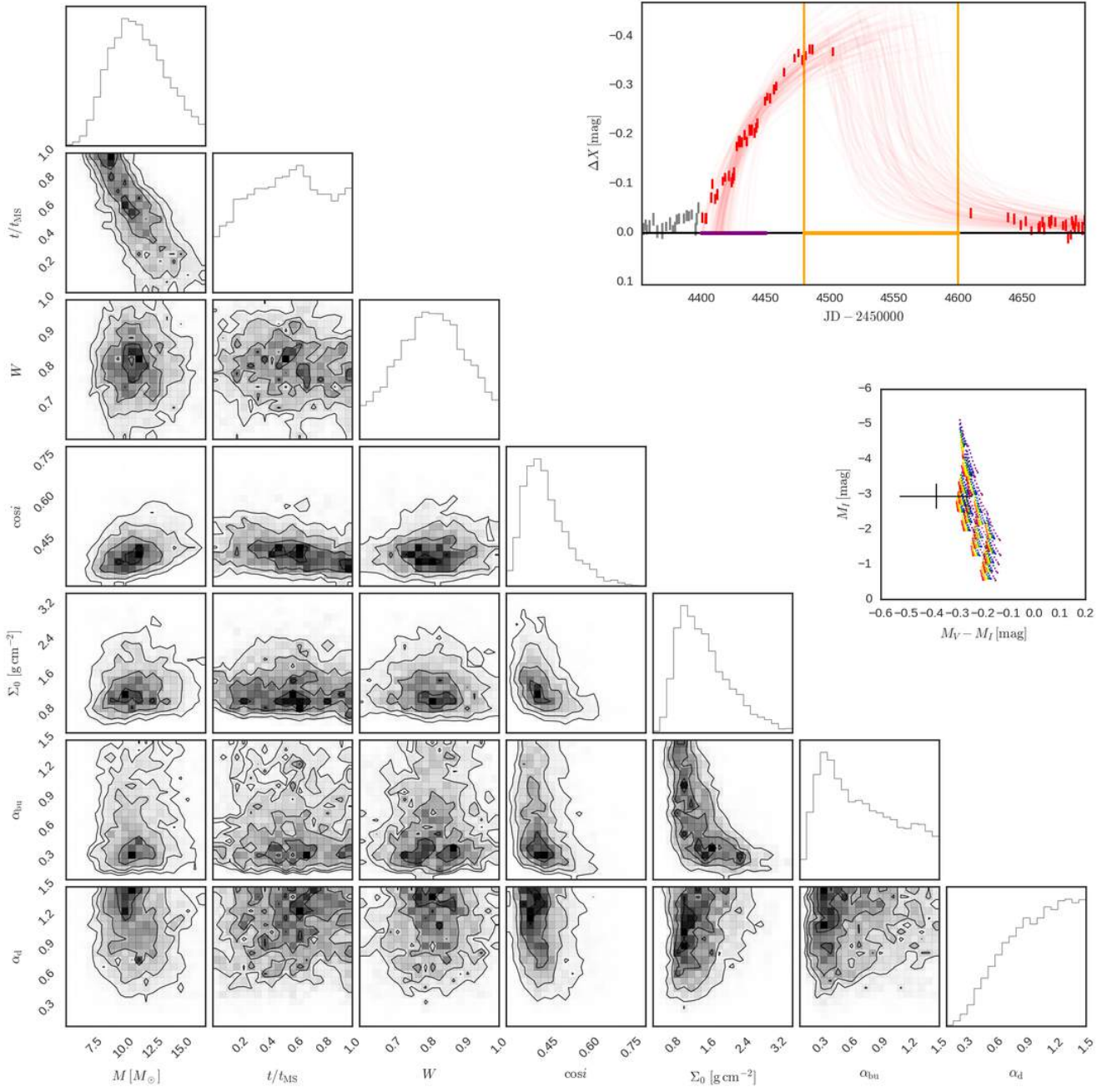


Figure C12. Same as Fig. 8 for SMC_SC3 71445 and bump ID 02.

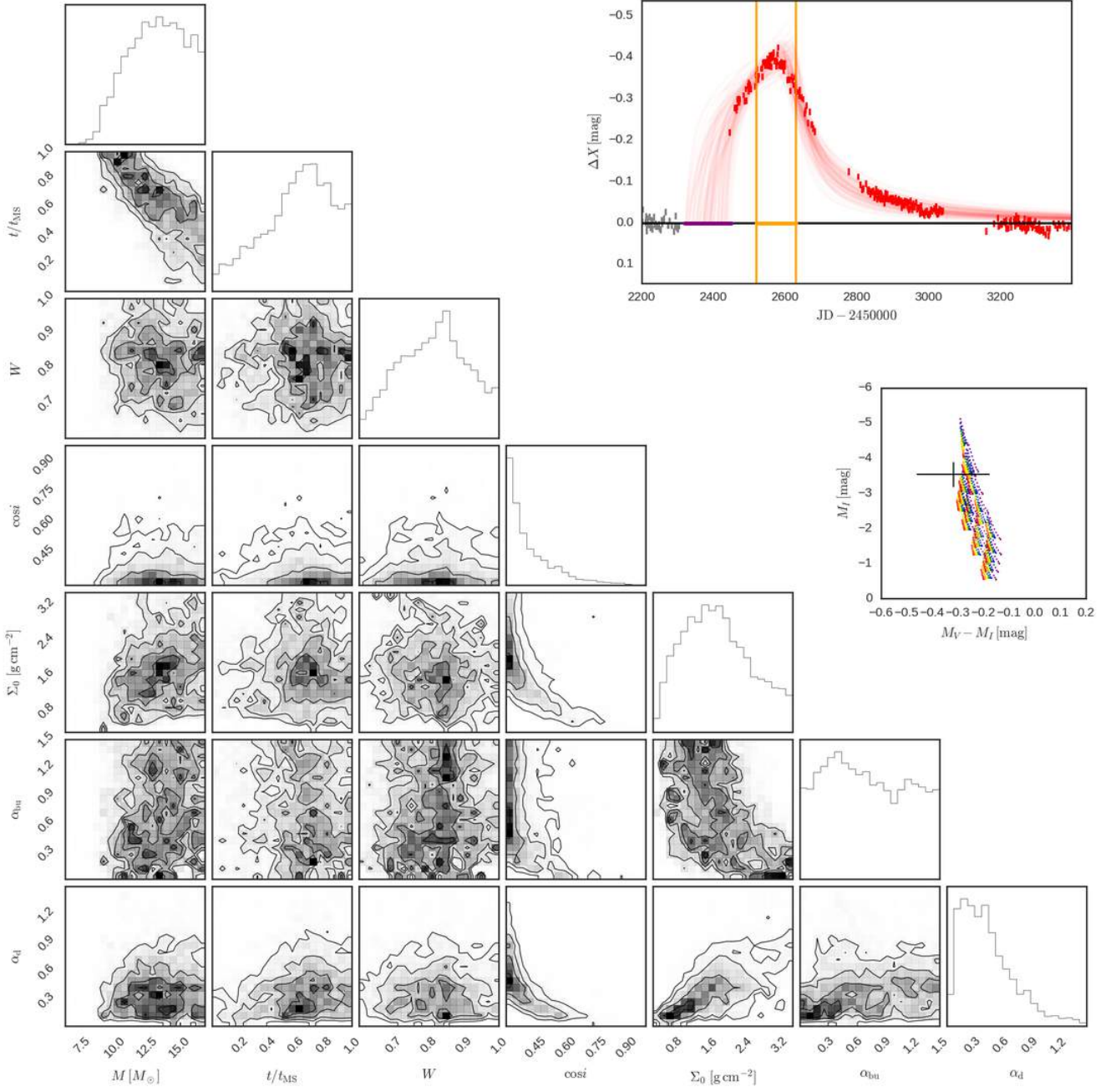


Figure C13. Same as Fig. 8 for SMC_SC3 125899 and bump ID 01.

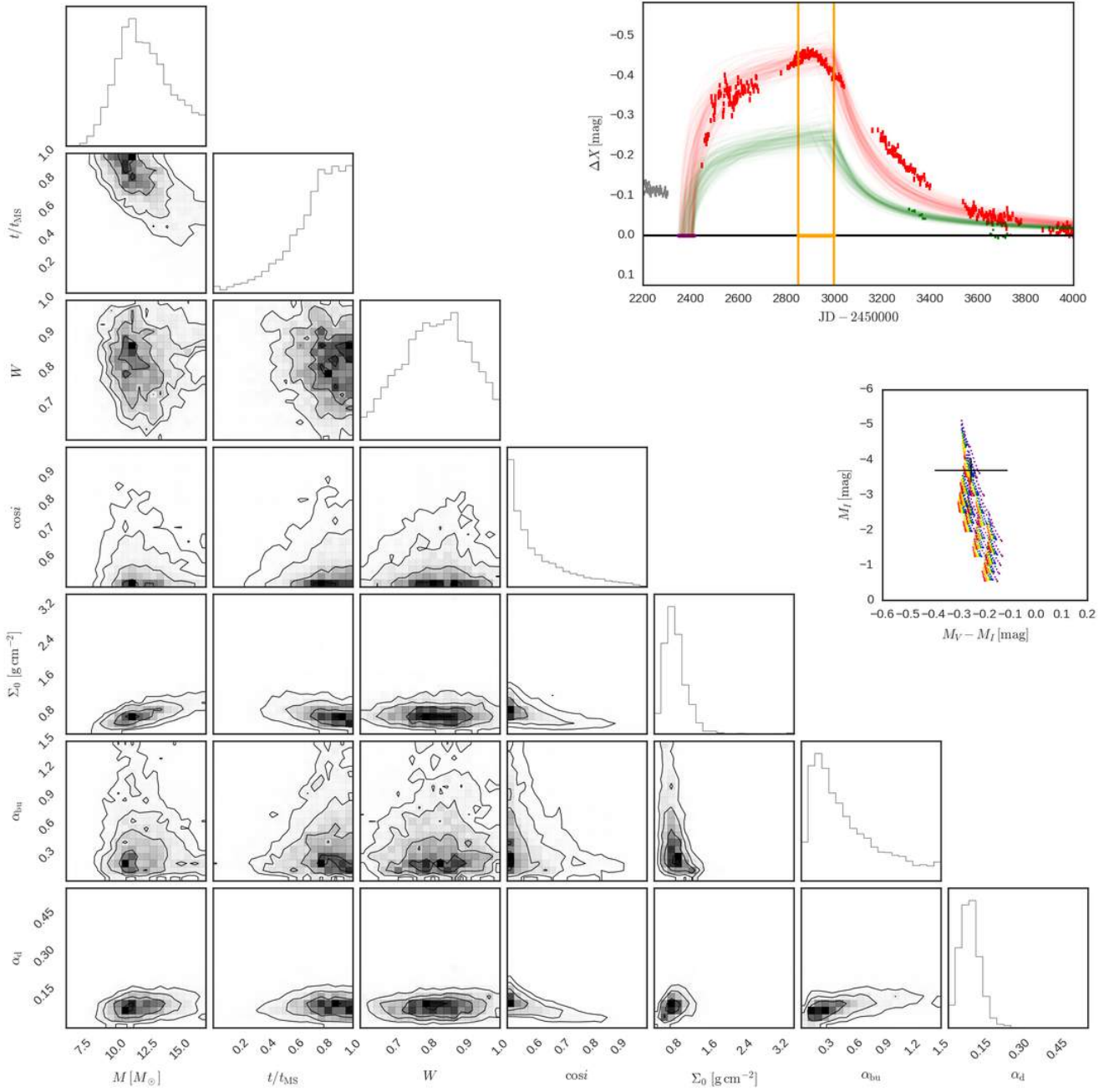


Figure C14. Same as Fig. 8 for SMC_SC3 197941 and bump ID 01.

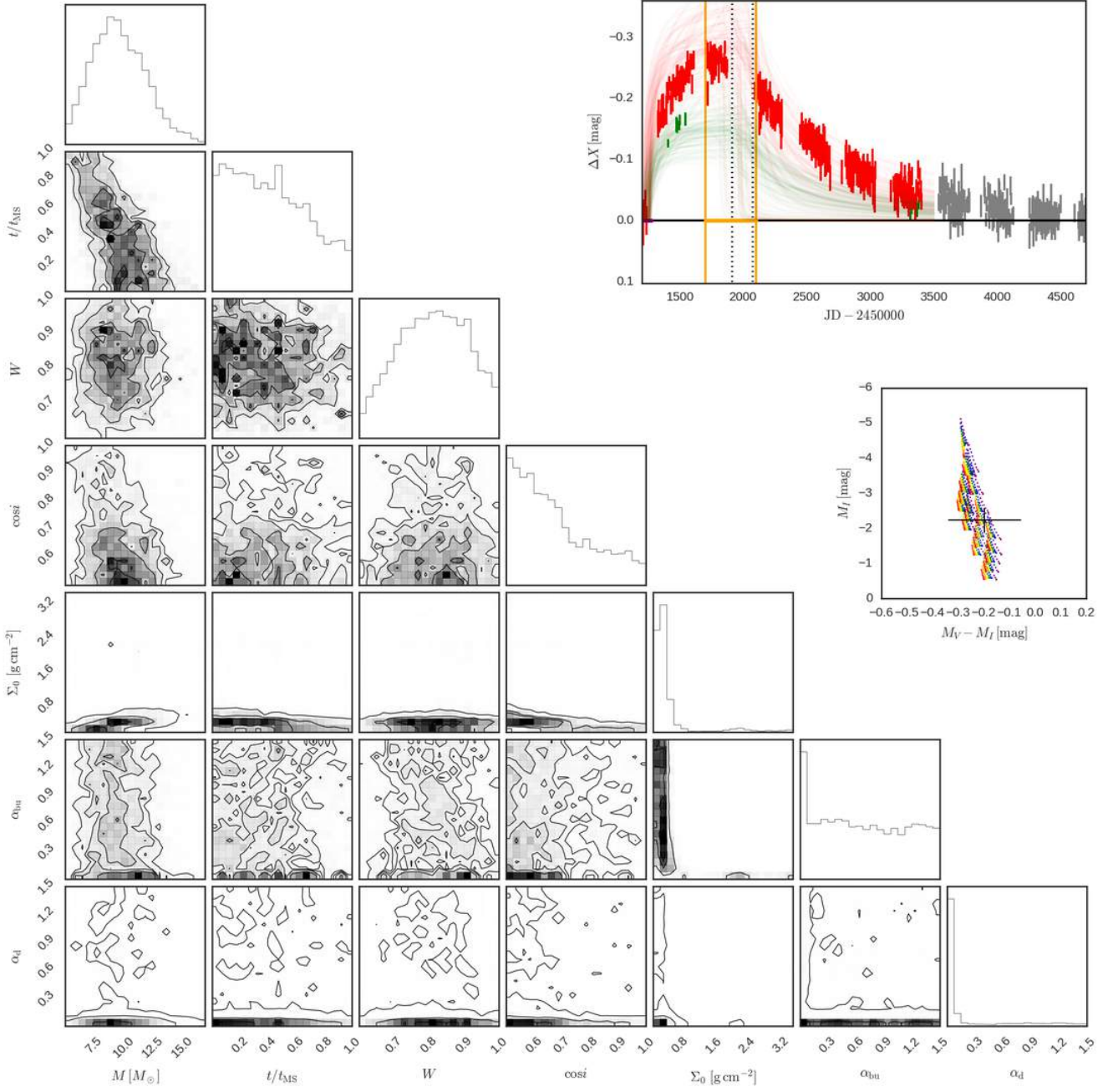


Figure C15. Same as Fig. 8 for SMC_SC4 22859 and bump ID 01.

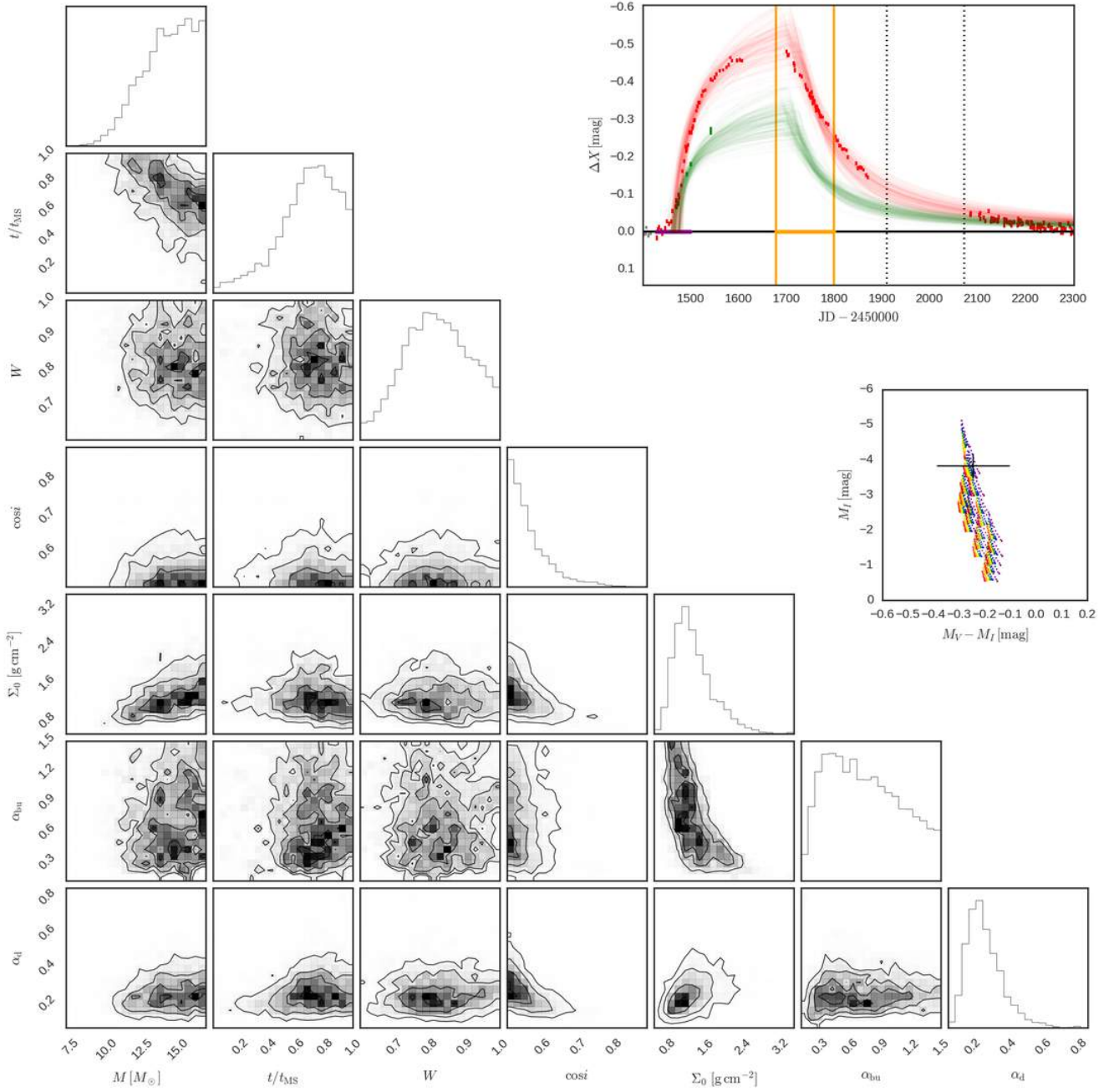


Figure C16. Same as Fig. 8 for SMC_SC4 71499 and bump ID 01.

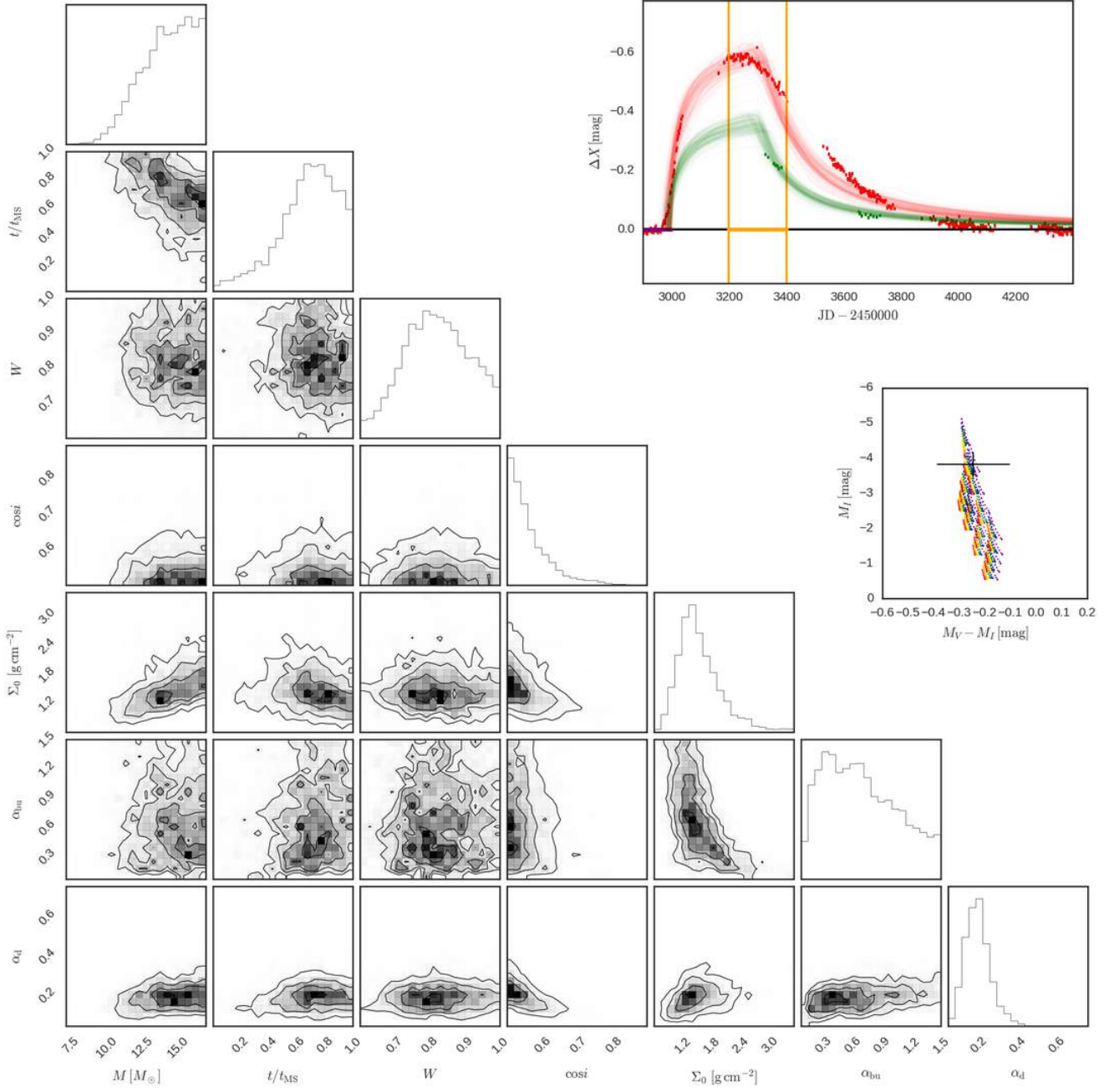


Figure C17. Same as Fig. 8 for SMC_SC4 71499 and bump ID 02.

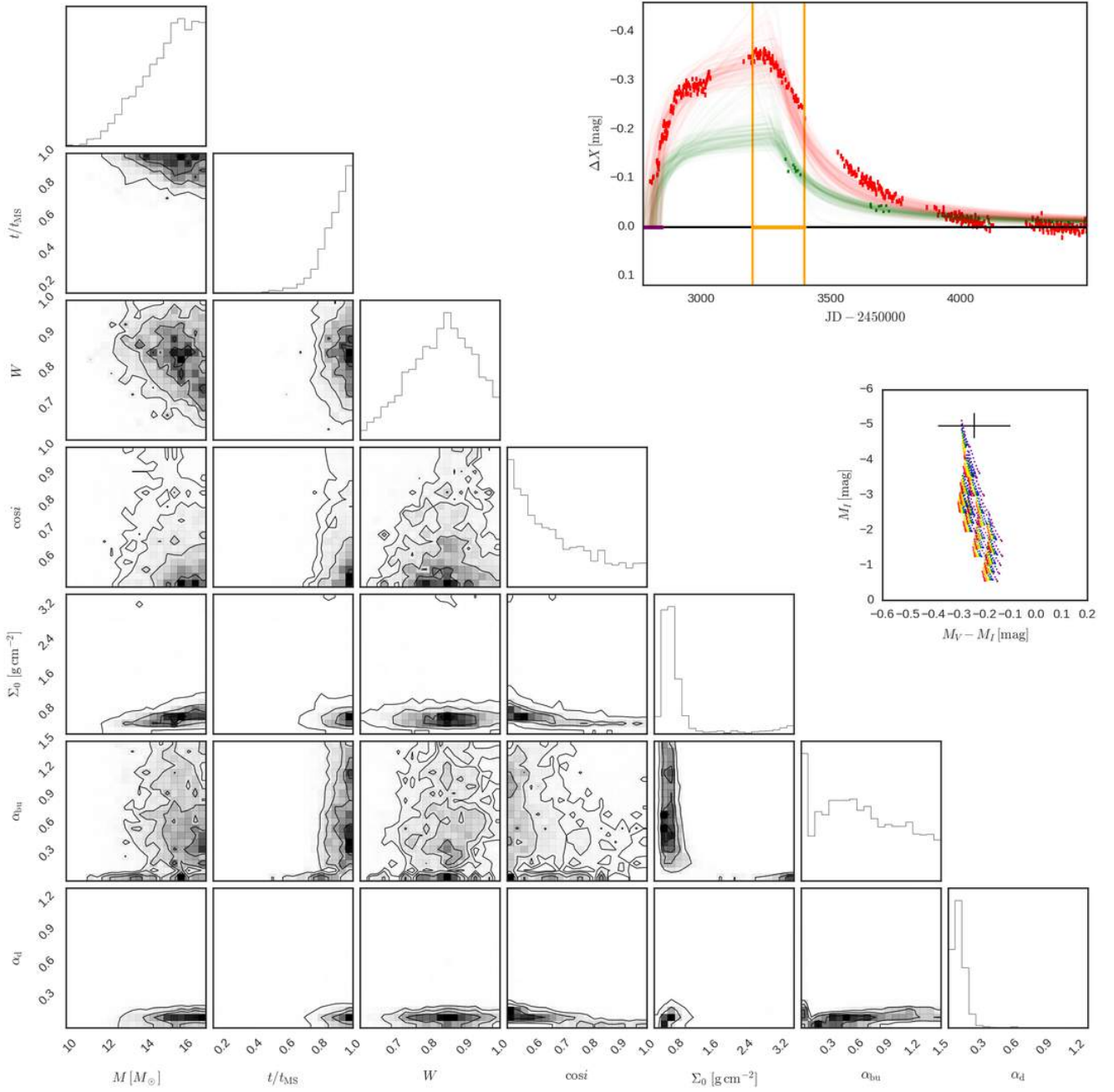


Figure C18. Same as Fig. 8 for SMC_SC4 120783 and bump ID 01.

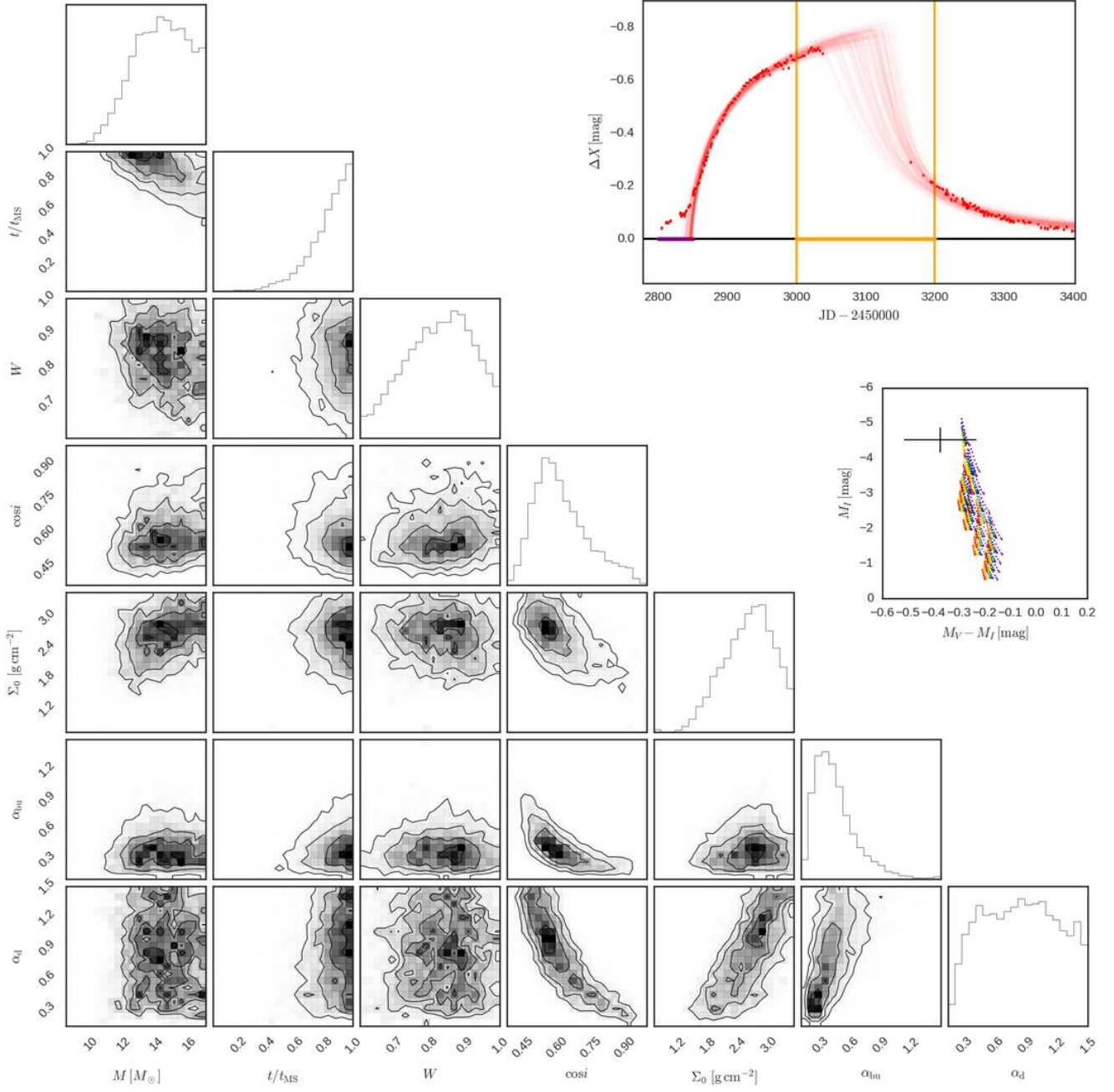


Figure C19. Same as Fig. 8 for SMC_SC4 127840 and bump ID 01.

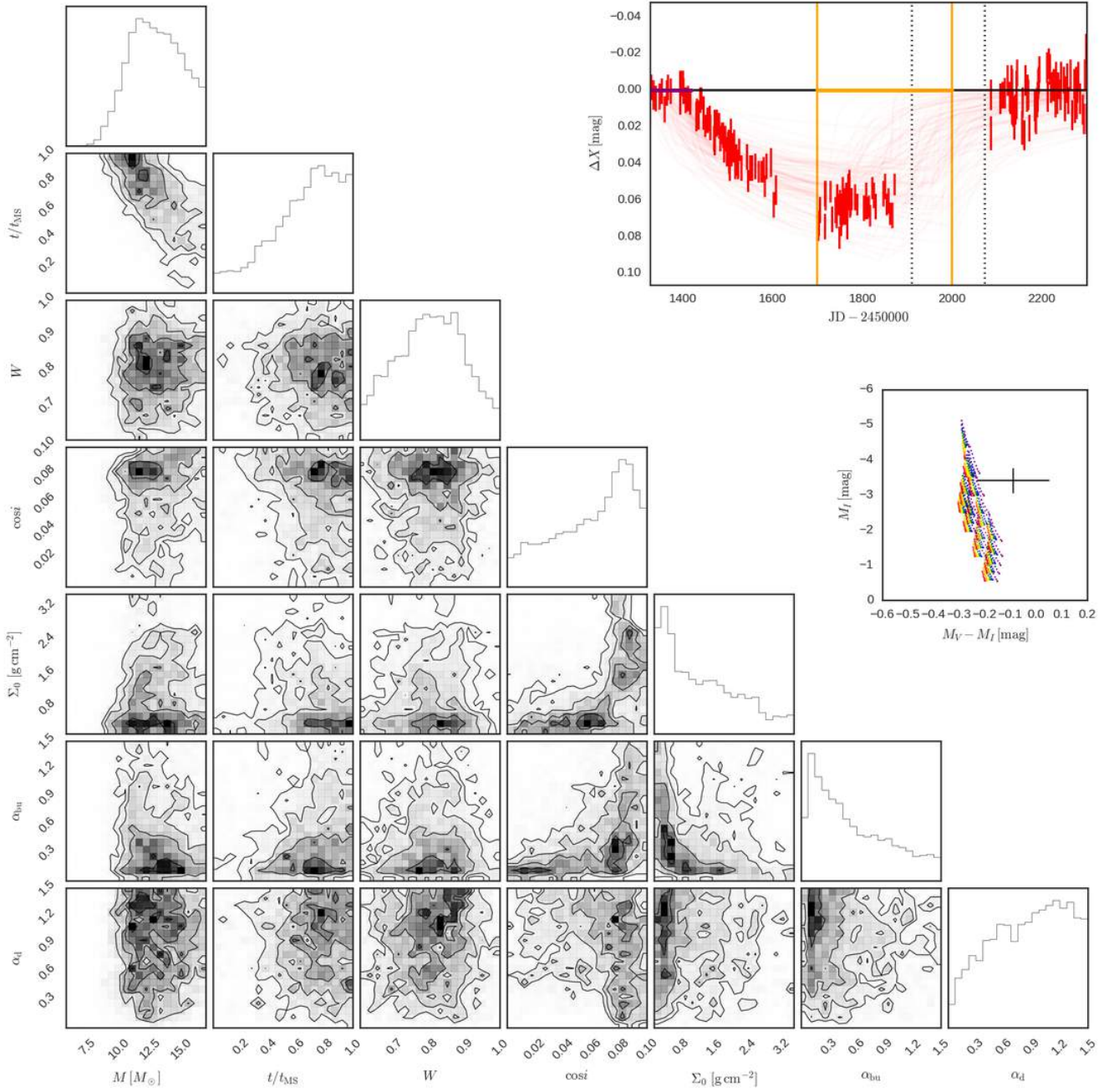


Figure C20. Same as Fig. 8 for SMC_SC4 156248 and bump ID 01.

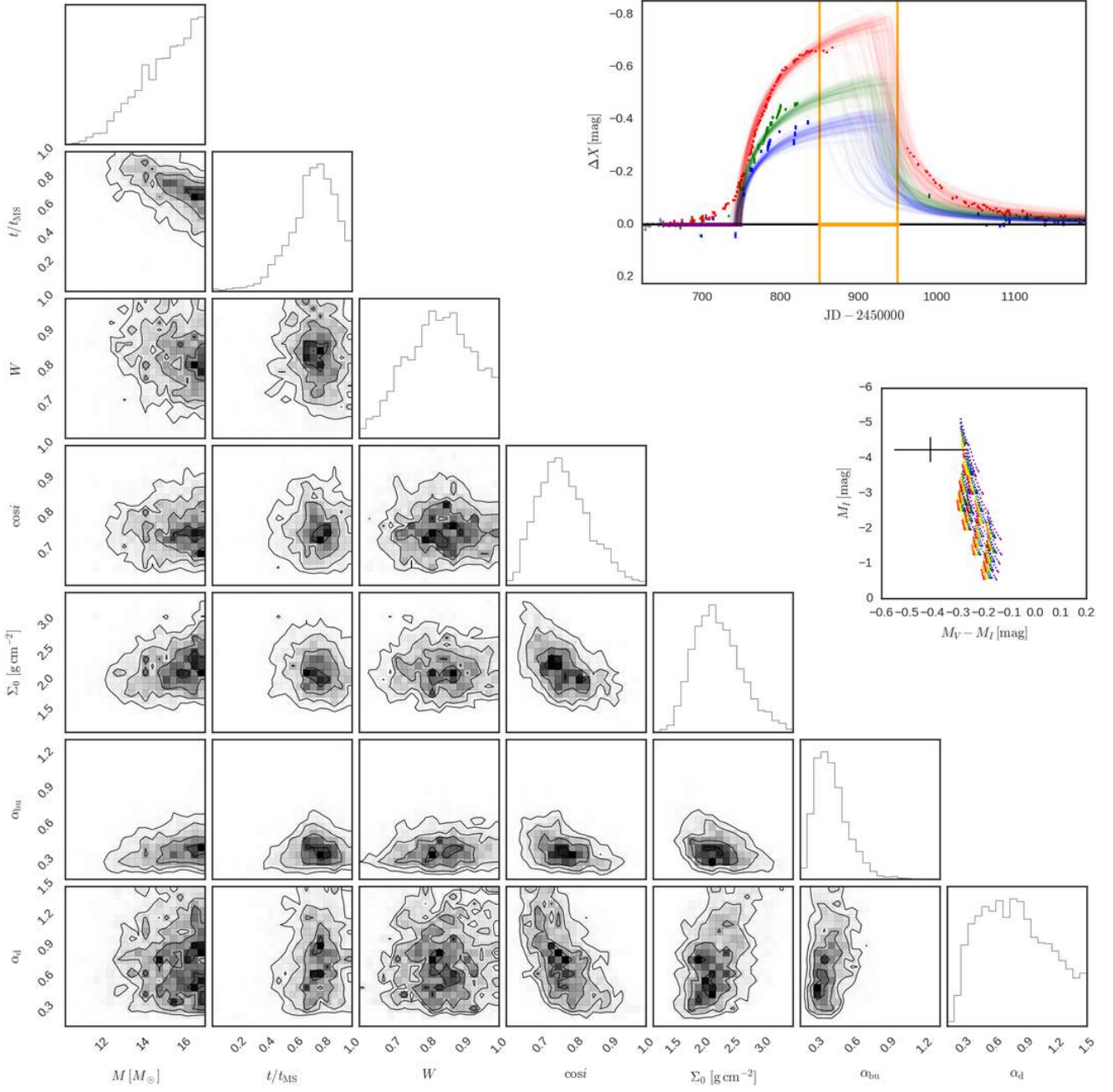


Figure C21. Same as Fig. 8 for SMC_SC4 156251 and bump ID 01.

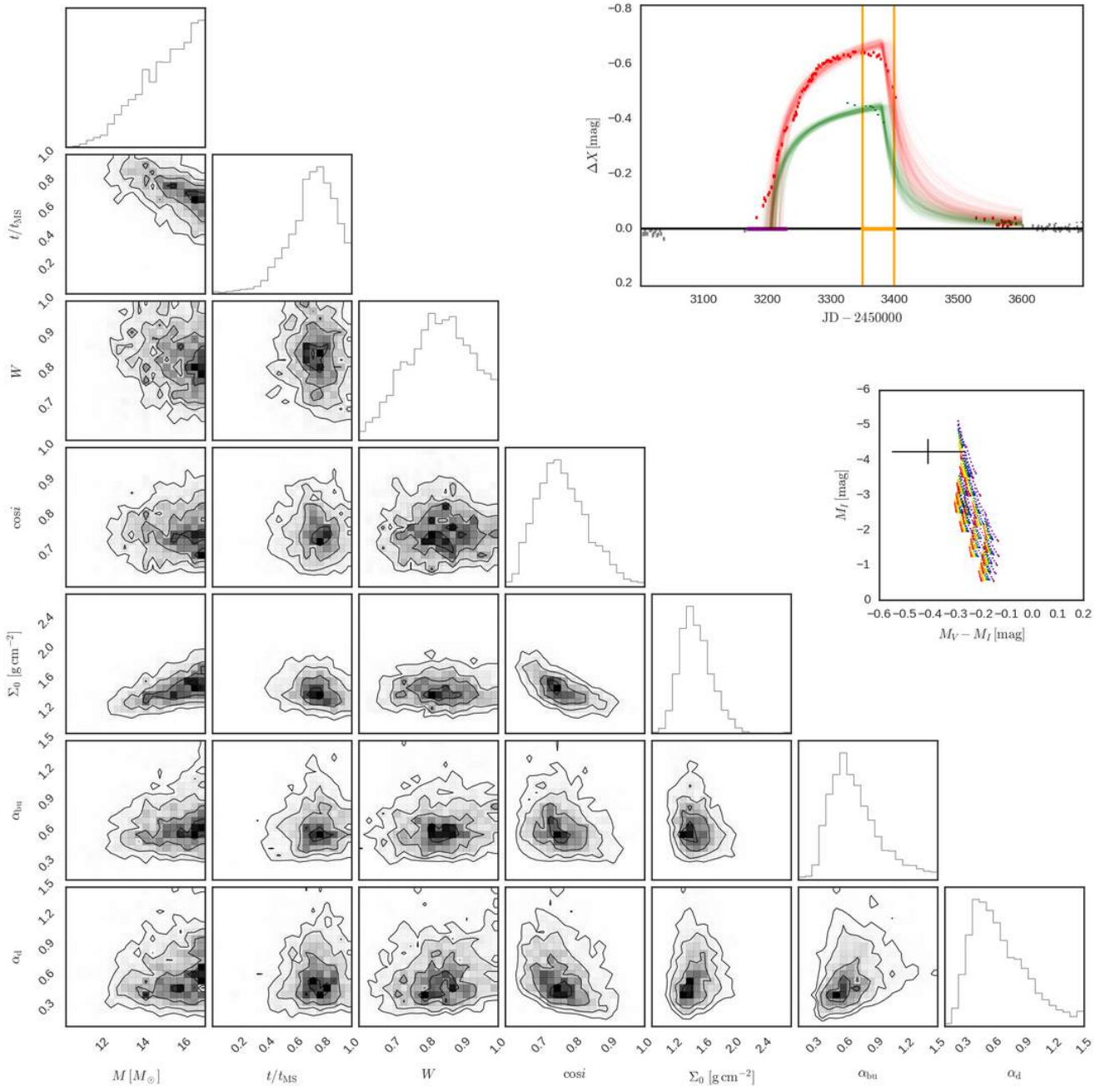


Figure C22. Same as Fig. 8 for SMC_SC4 156251 and bump ID 02.

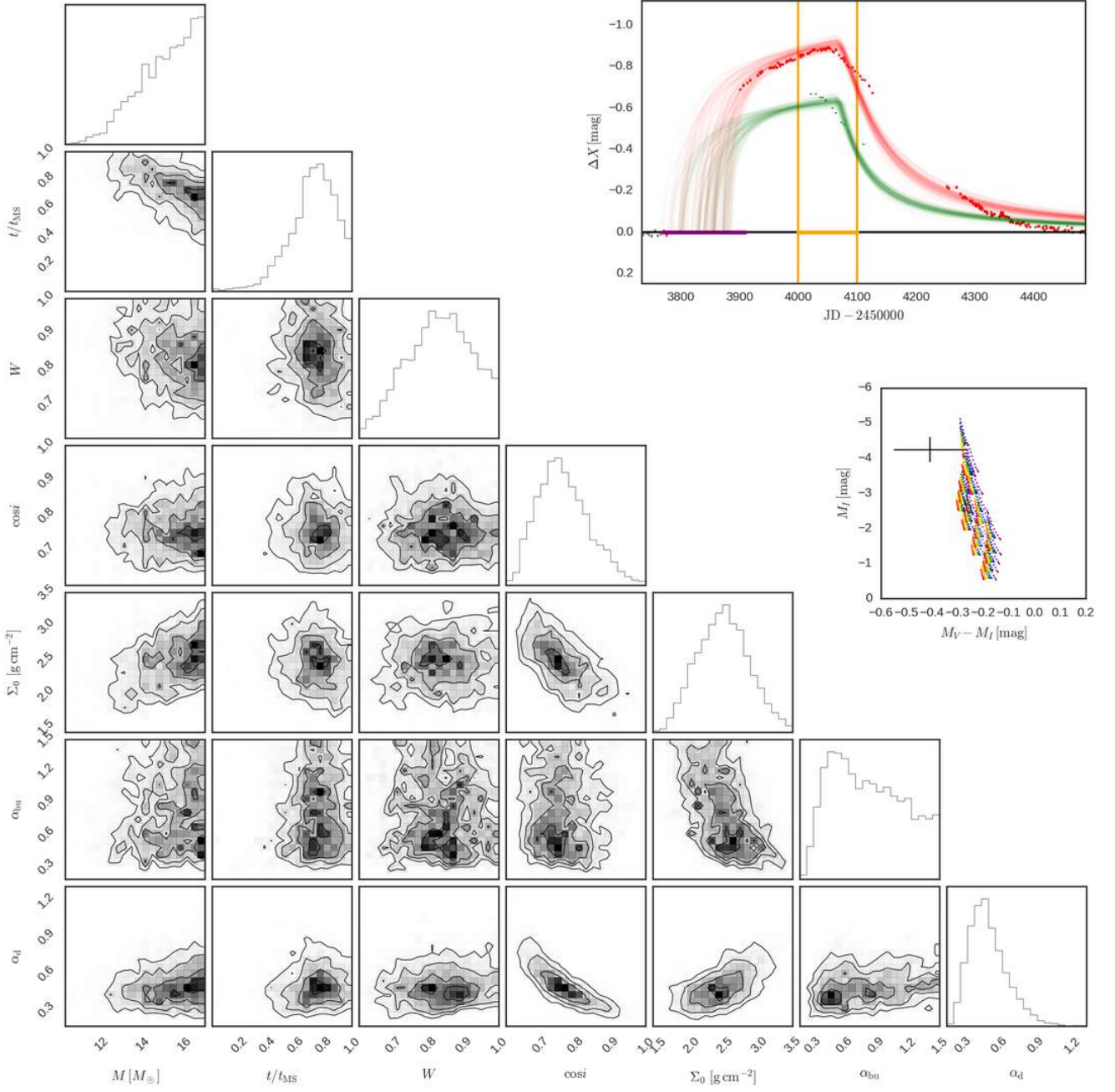


Figure C23. Same as Fig. 8 for SMC_SC4 156251 and bump ID 03.

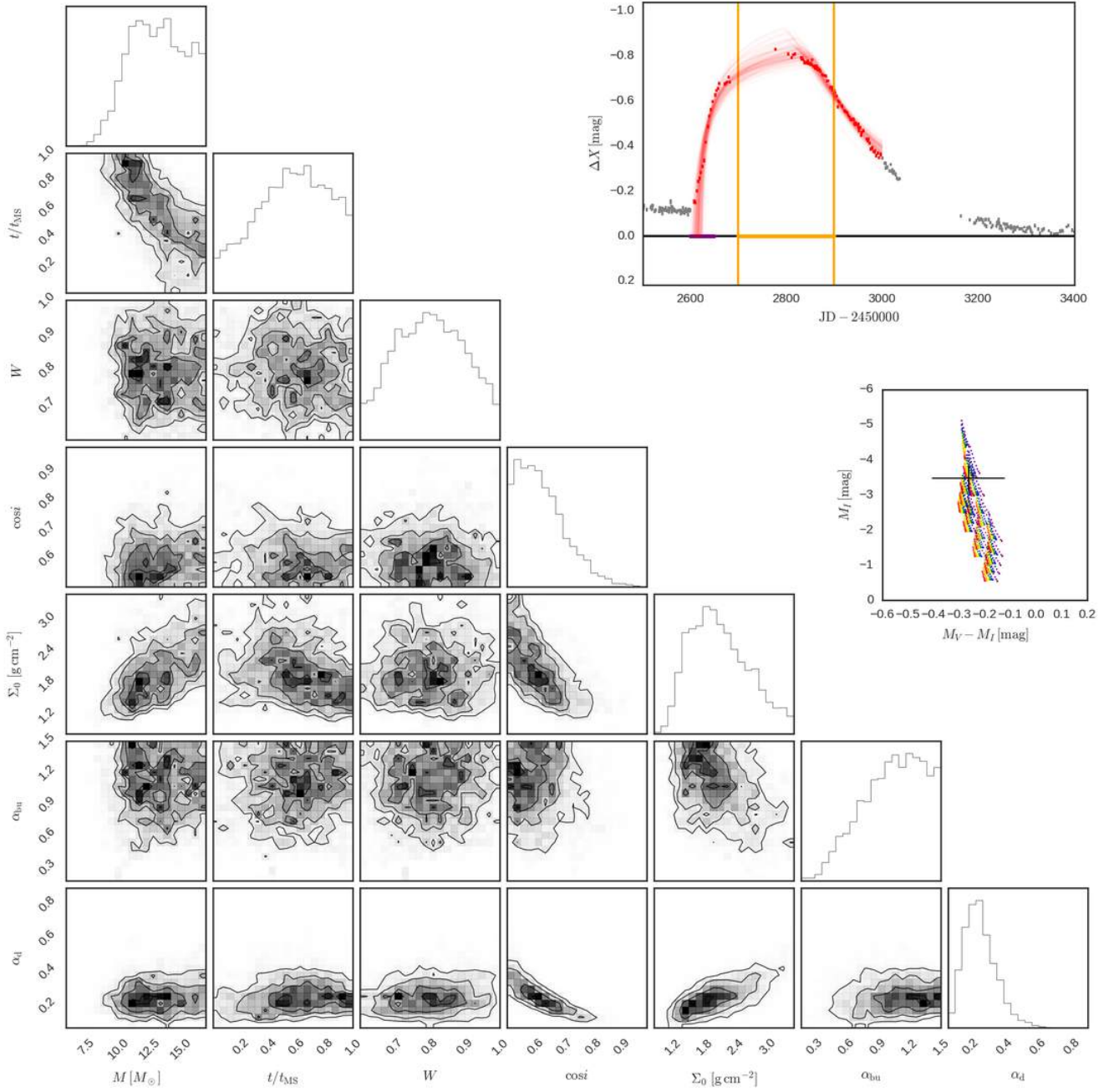


Figure C24. Same as Fig. 8 for SMC_SC4 159829 and bump ID 01.

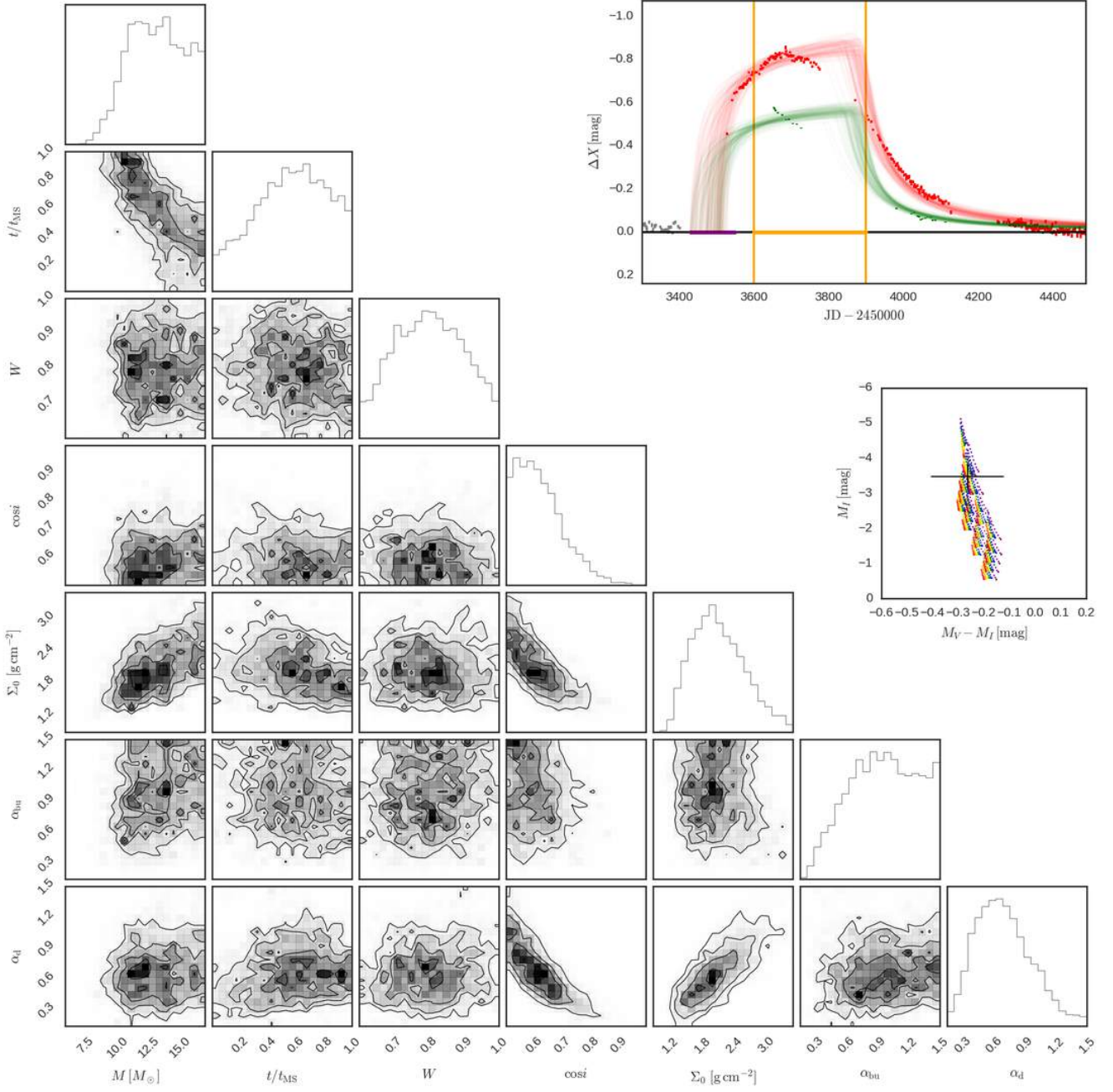


Figure C25. Same as Fig. 8 for SMC_SC4 159829 and bump ID 02.

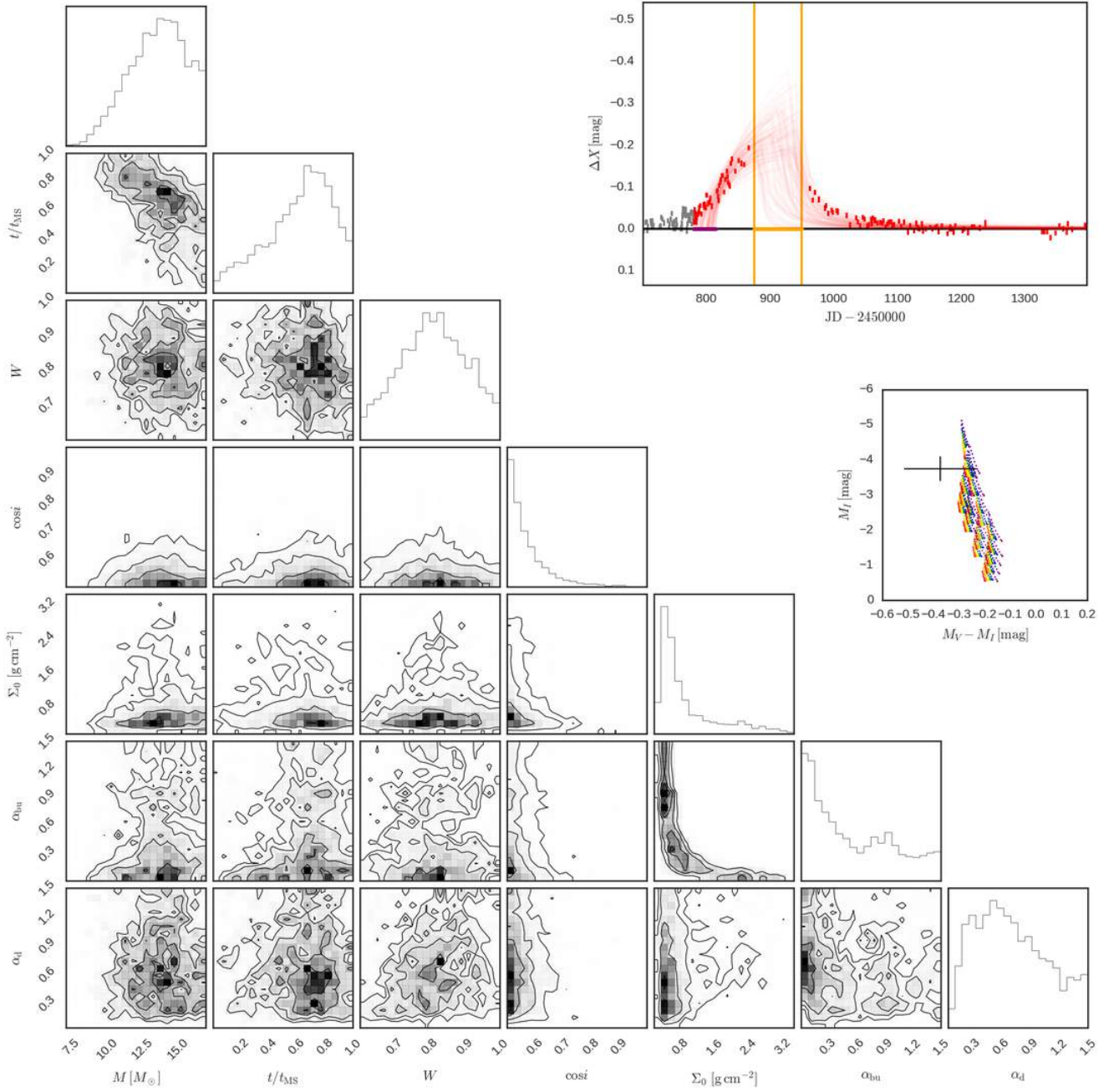


Figure C26. Same as Fig. 8 for SMC_SC4 159857 and bump ID 01.

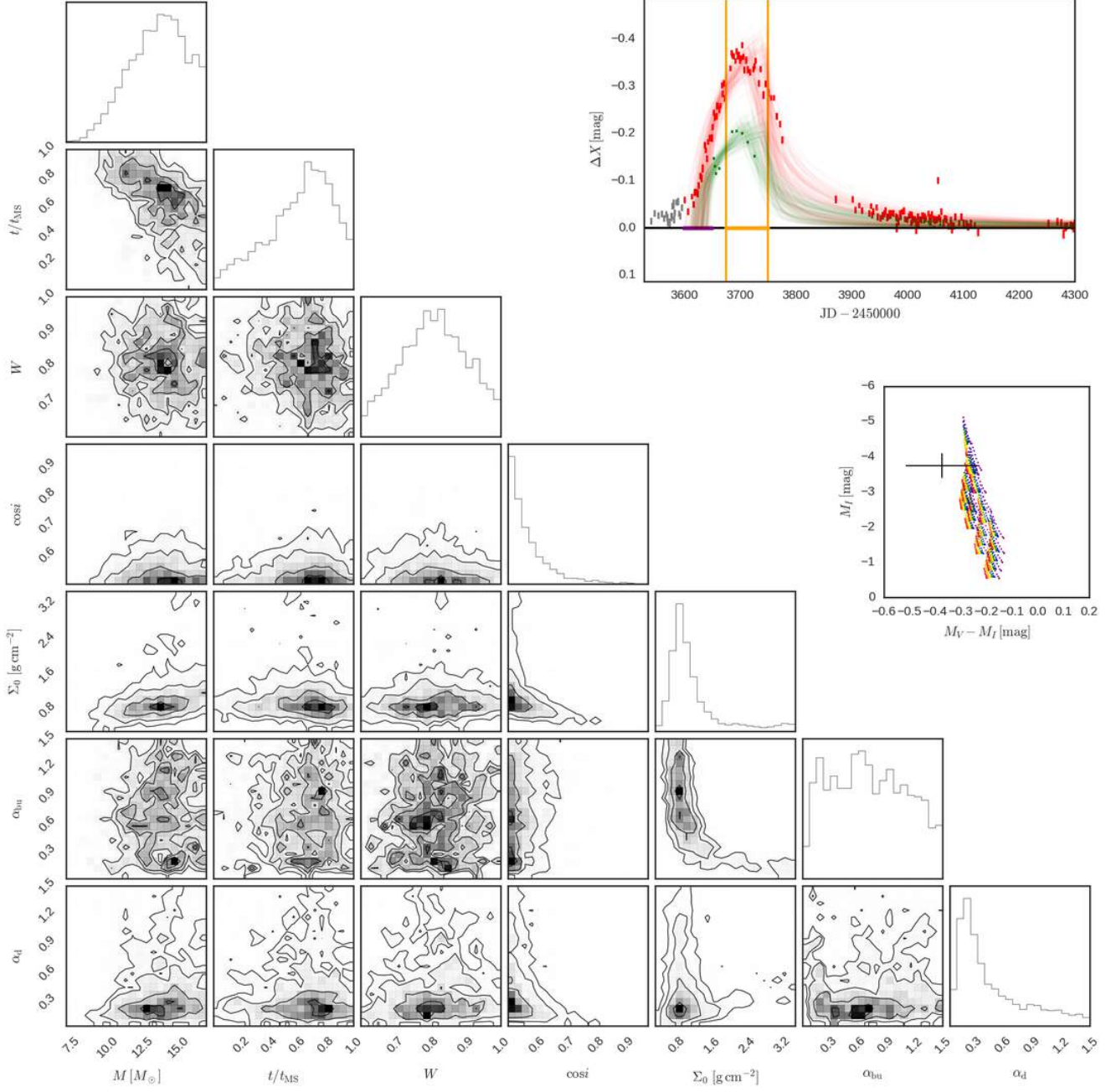


Figure C27. Same as Fig. 8 for SMC_SC4 159857 and bump ID 02.

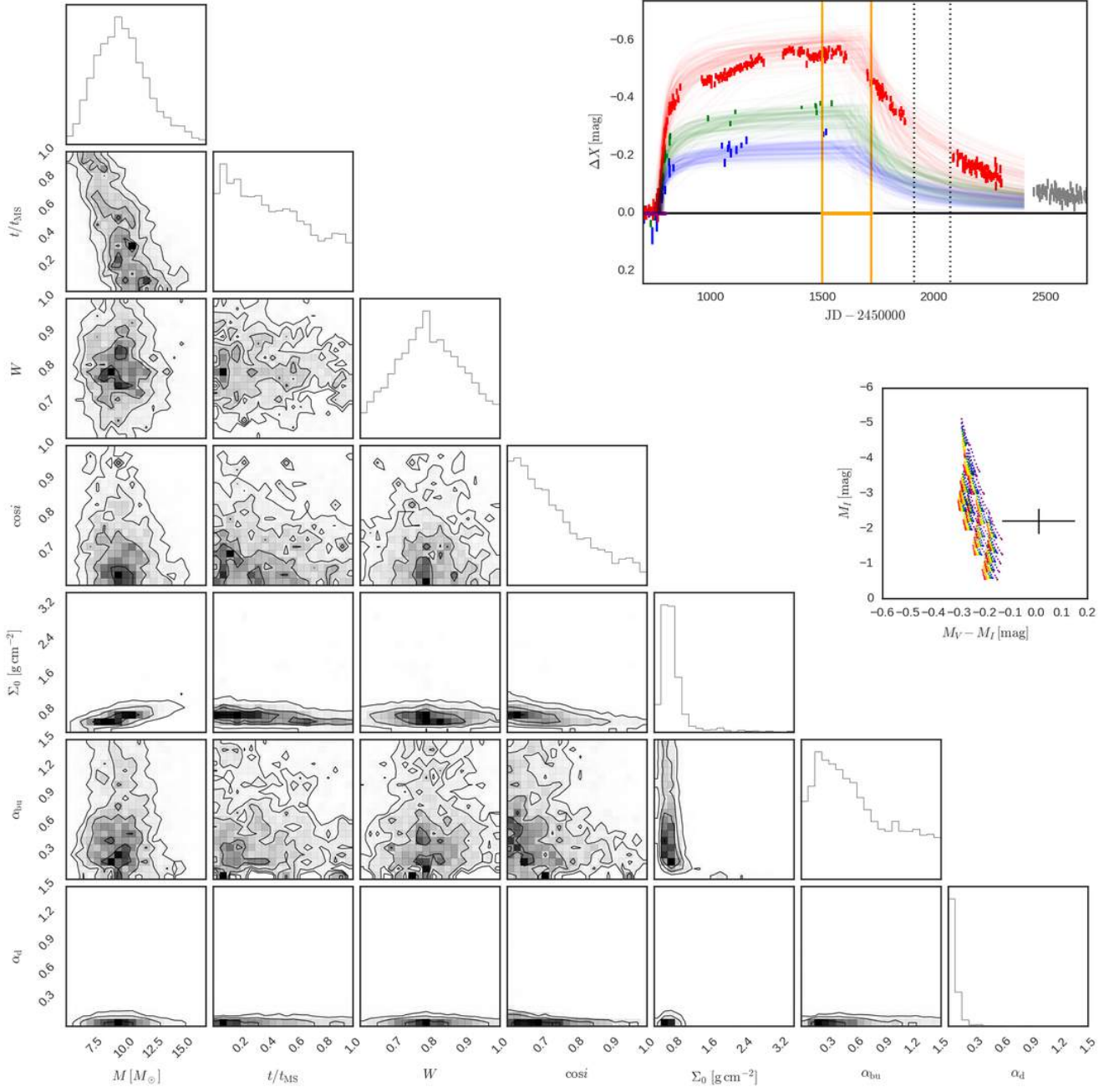


Figure C28. Same as Fig. 8 for SMC_SC4 163828 and bump ID 01.

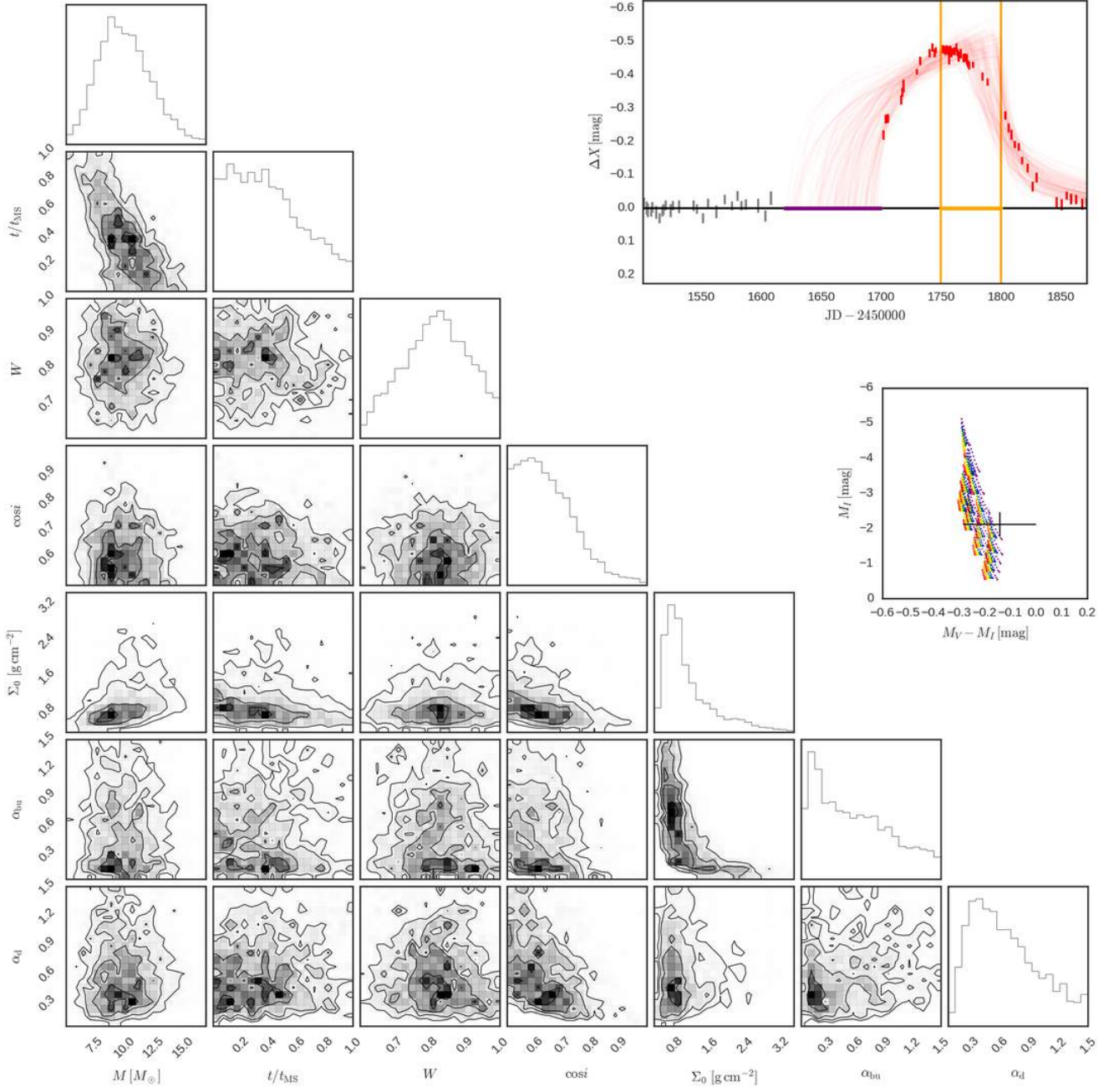


Figure C29. Same as Fig. 8 for SMC_SC4 167554 and bump ID 01.

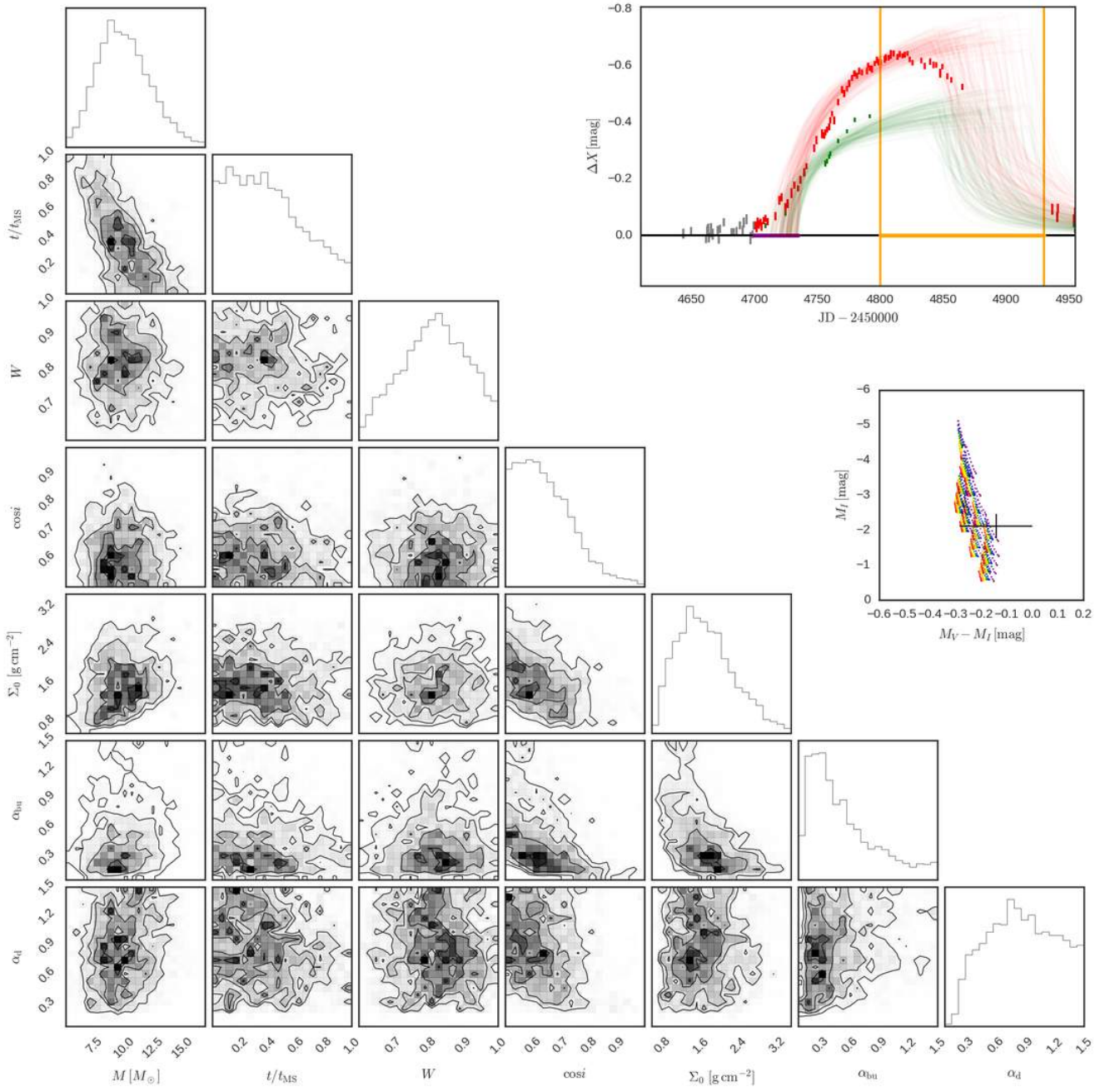


Figure C30. Same as Fig. 8 for SMC_SC4 167554 and bump ID 02.

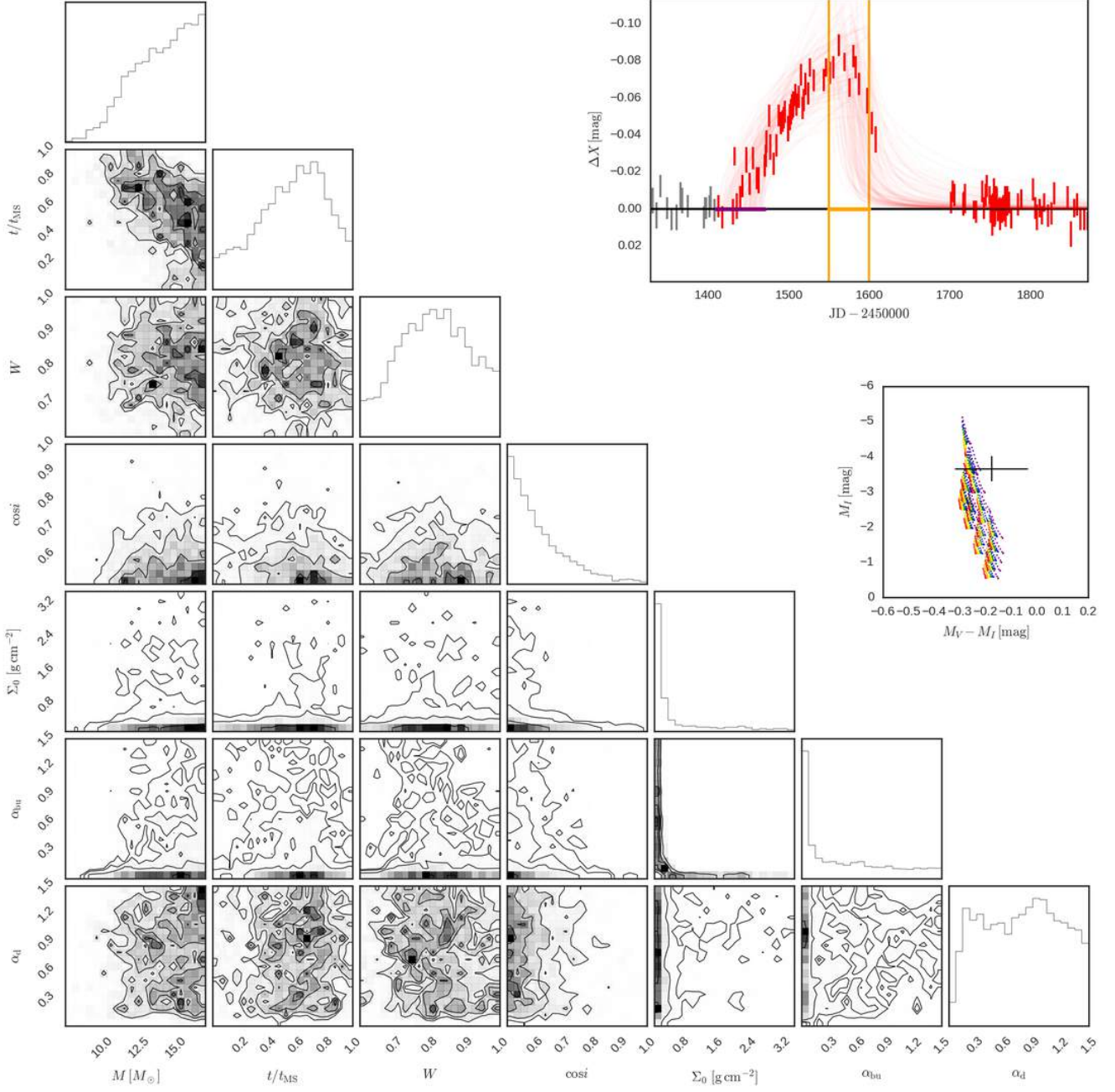


Figure C31. Same as Fig. 8 for SMC_SC4 171253 and bump ID 01.

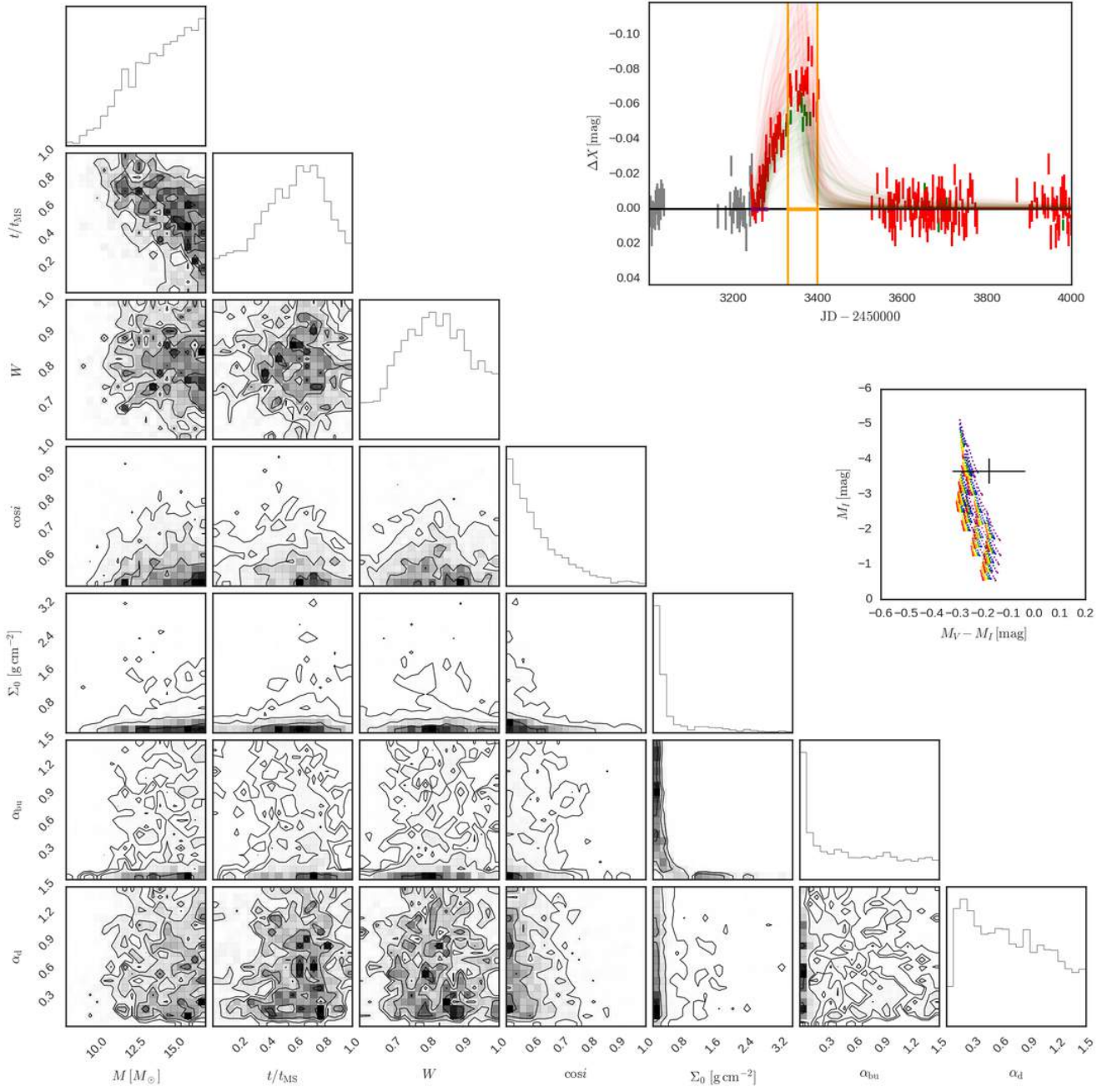


Figure C32. Same as Fig. 8 for SMC_SC4 171253 and bump ID 02.

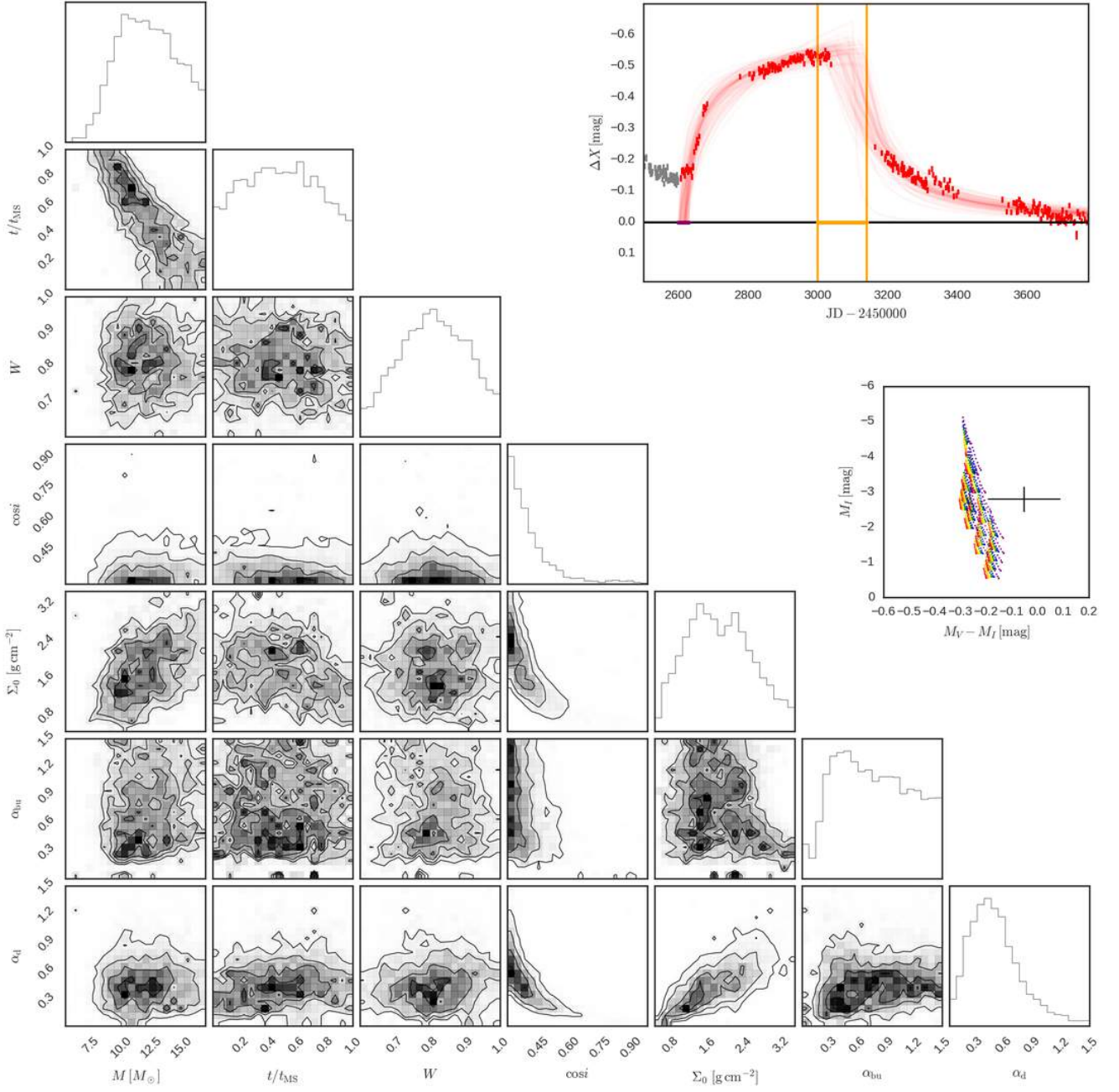


Figure C33. Same as Fig. 8 for SMC_SC4 175272 and bump ID 01.

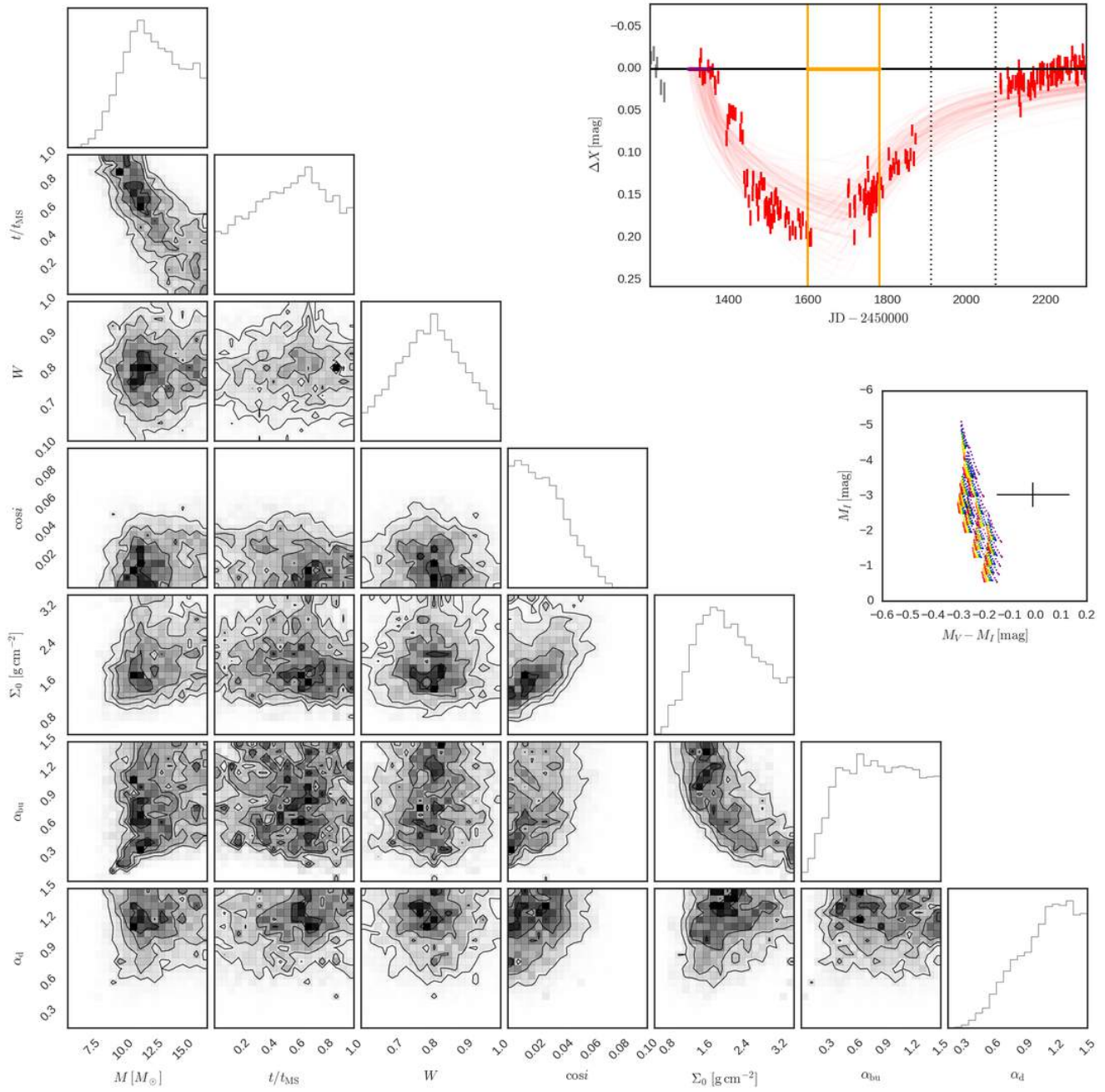


Figure C34. Same as Fig. 8 for SMC_SC4 179053 and bump ID 01.

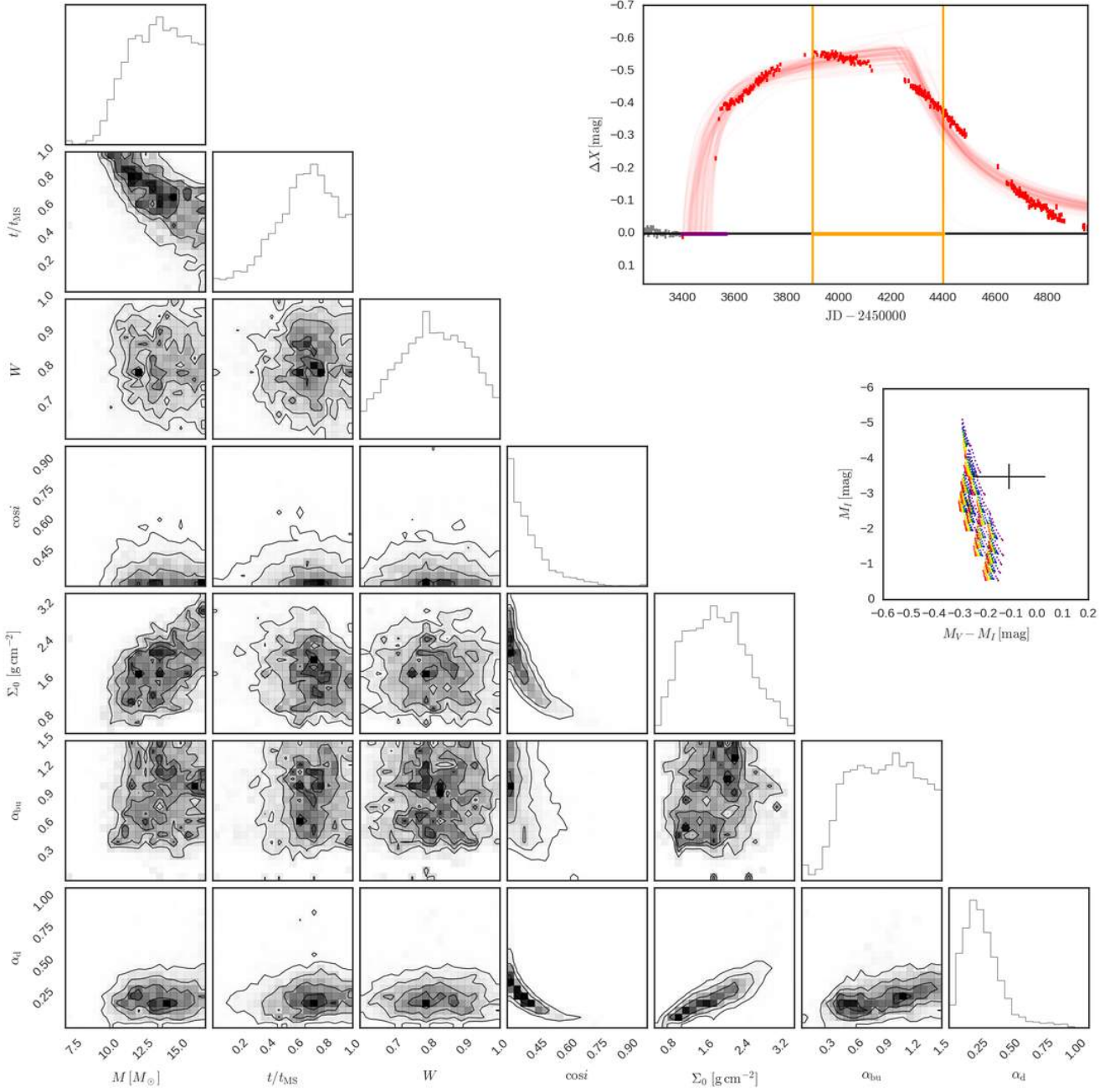


Figure C35. Same as Fig. 8 for SMC_SC5 11453 and bump ID 01.

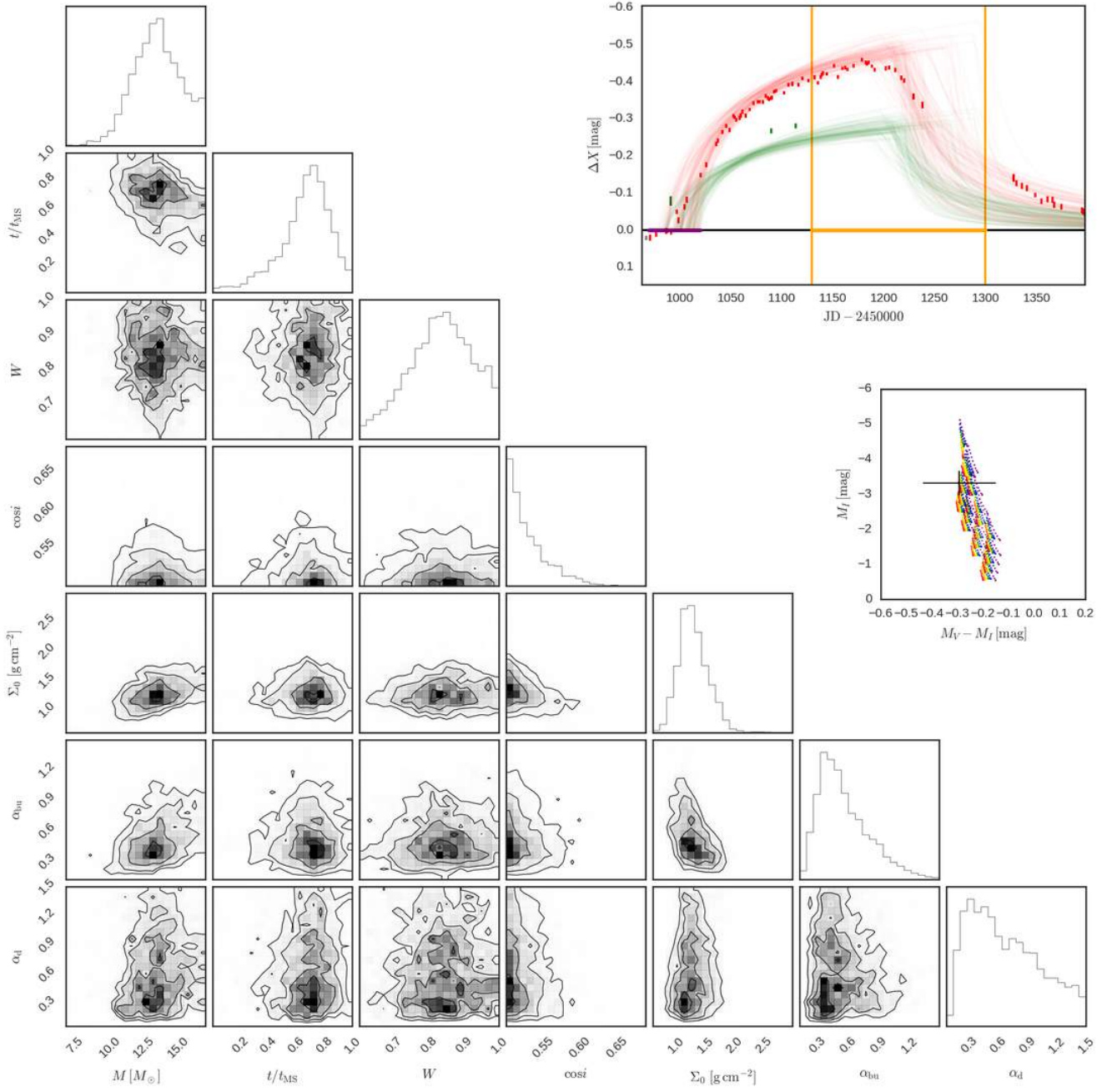


Figure C36. Same as Fig. 8 for SMC_SC5 21117 and bump ID 01.

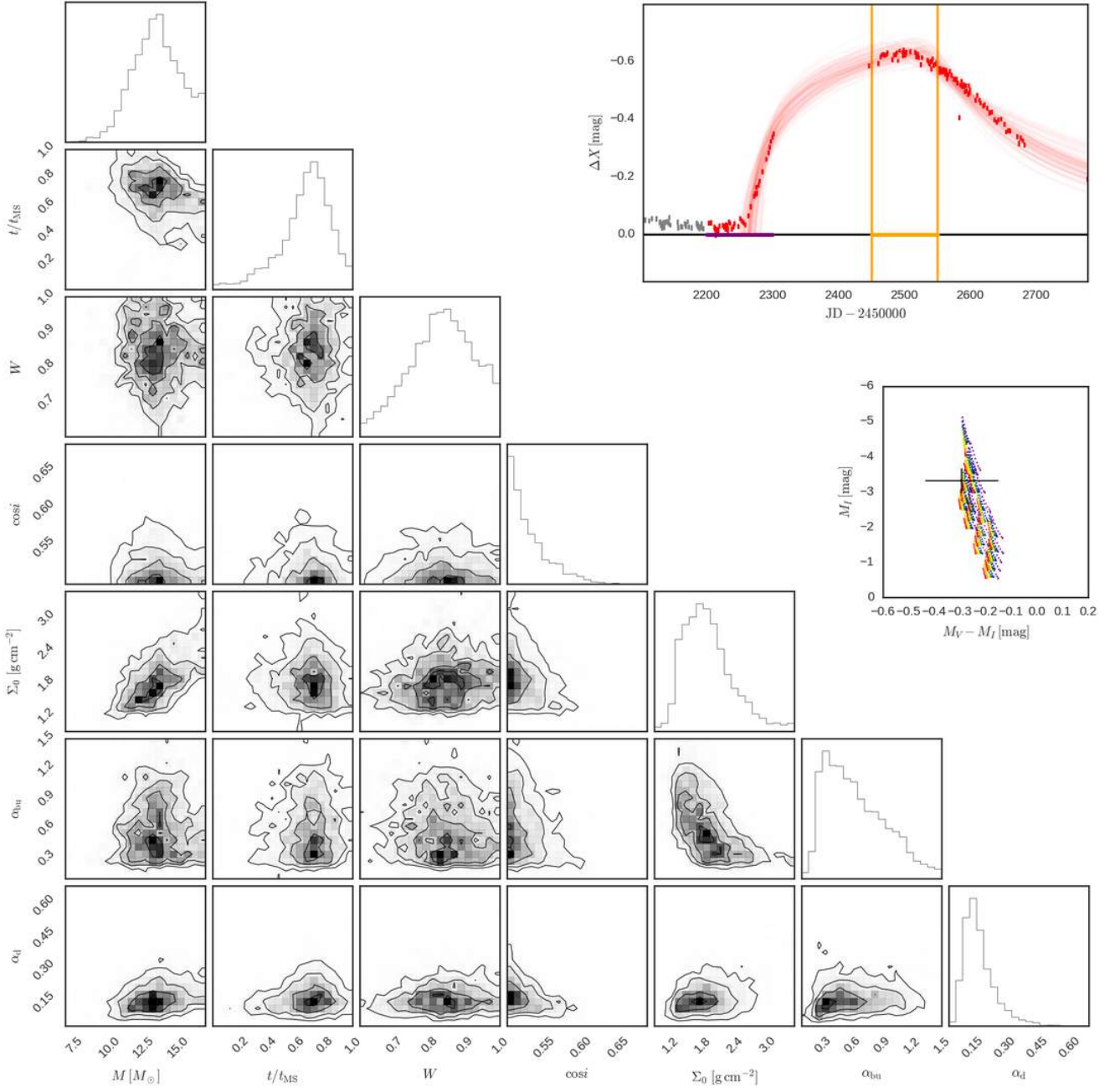


Figure C37. Same as Fig. 8 for SMC_SC5 21117 and bump ID 02.

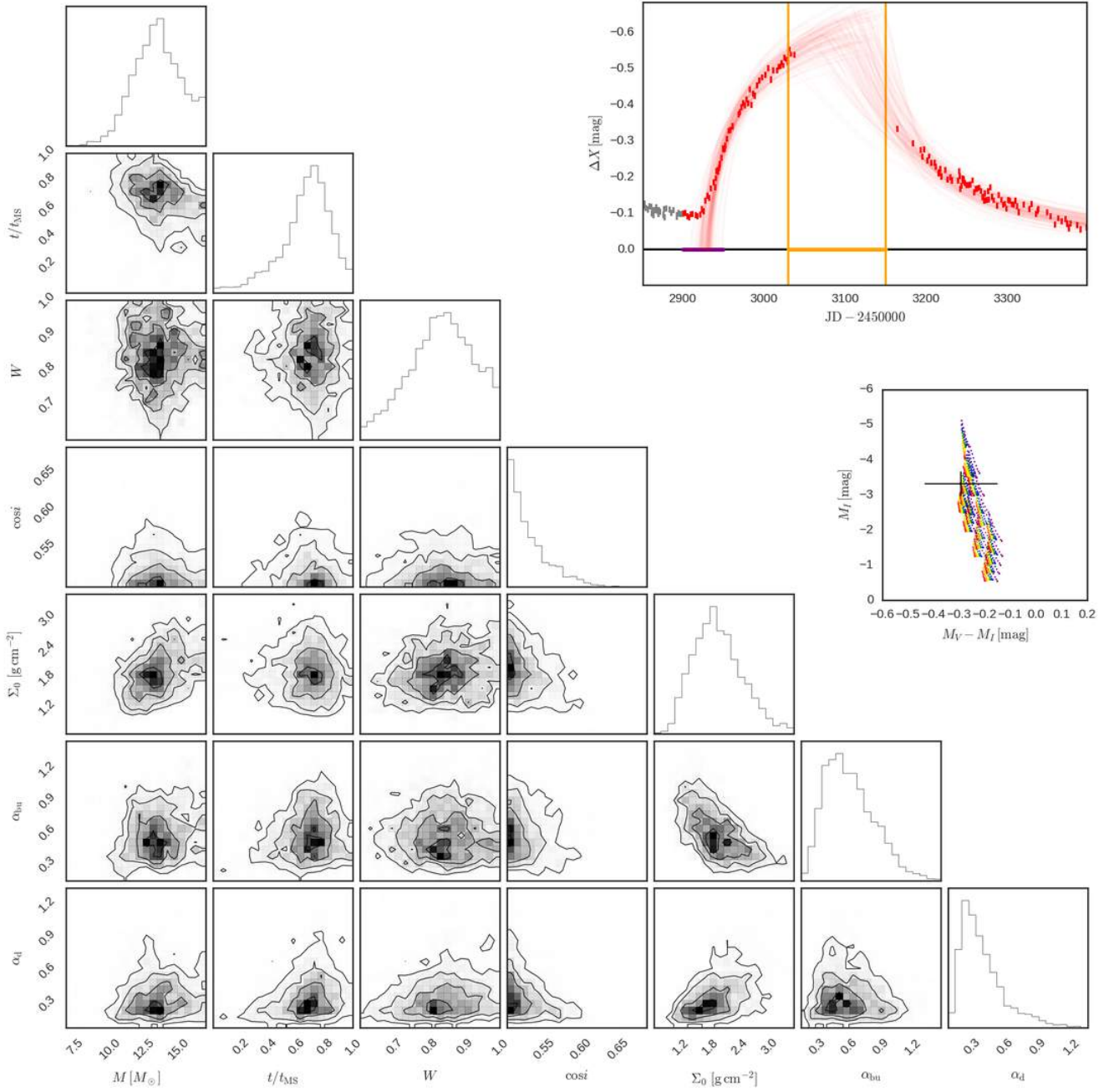


Figure C38. Same as Fig. 8 for SMC_SC5 21117 and bump ID 03.

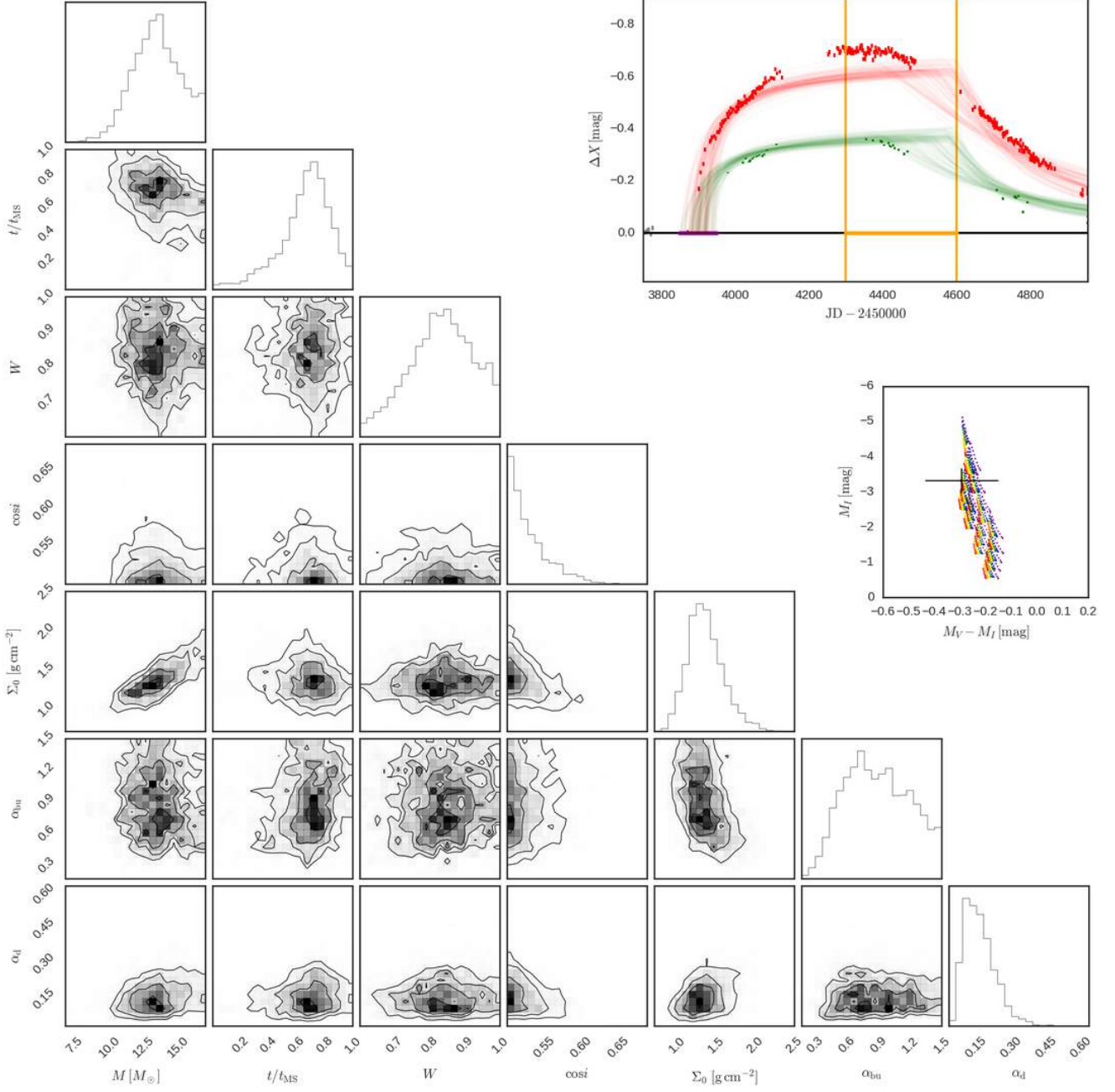


Figure C39. Same as Fig. 8 for SMC_SC5 21117 and bump ID 04.

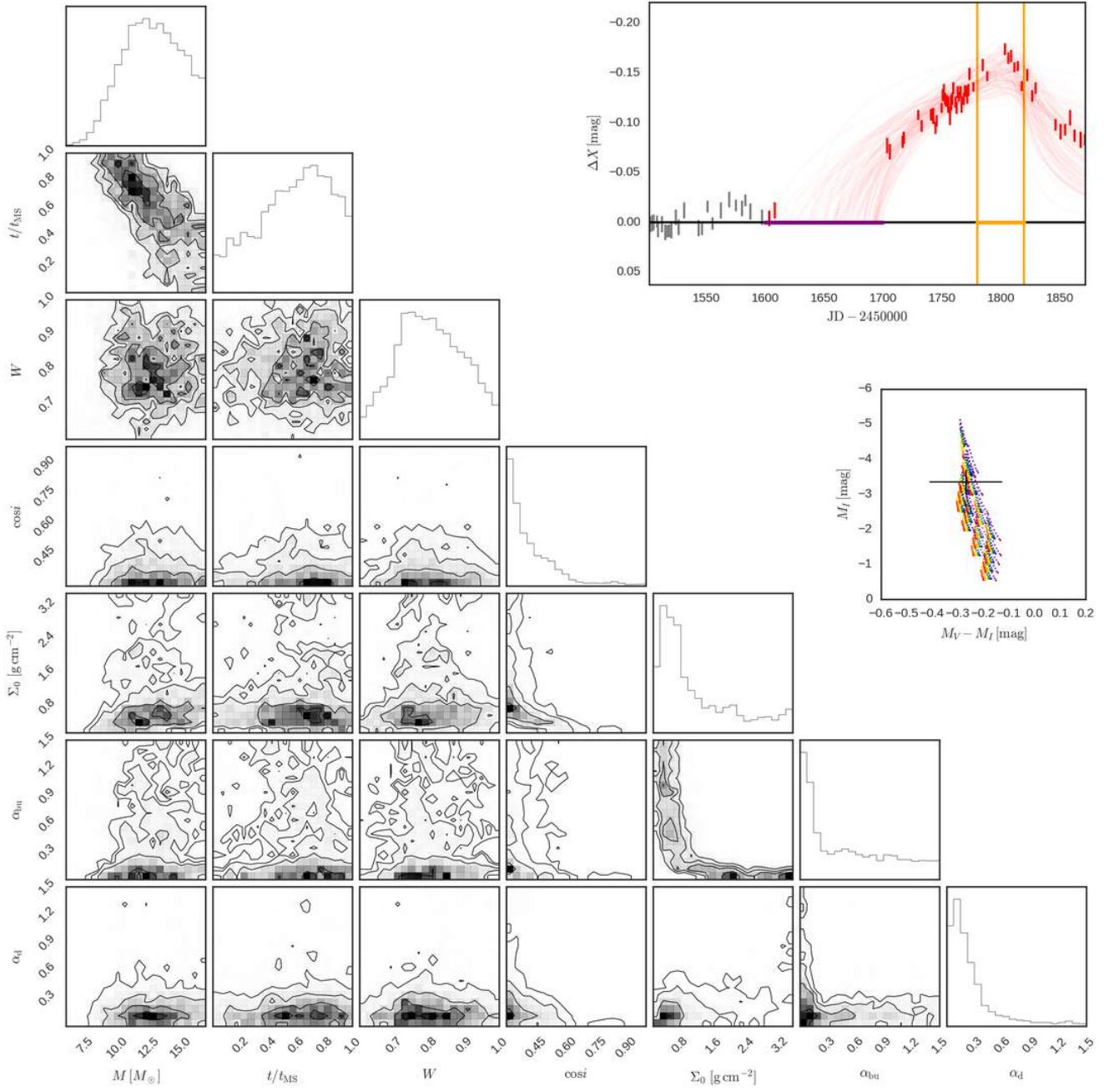


Figure C40. Same as Fig. 8 for SMC_SC5 21134 and bump ID 01.

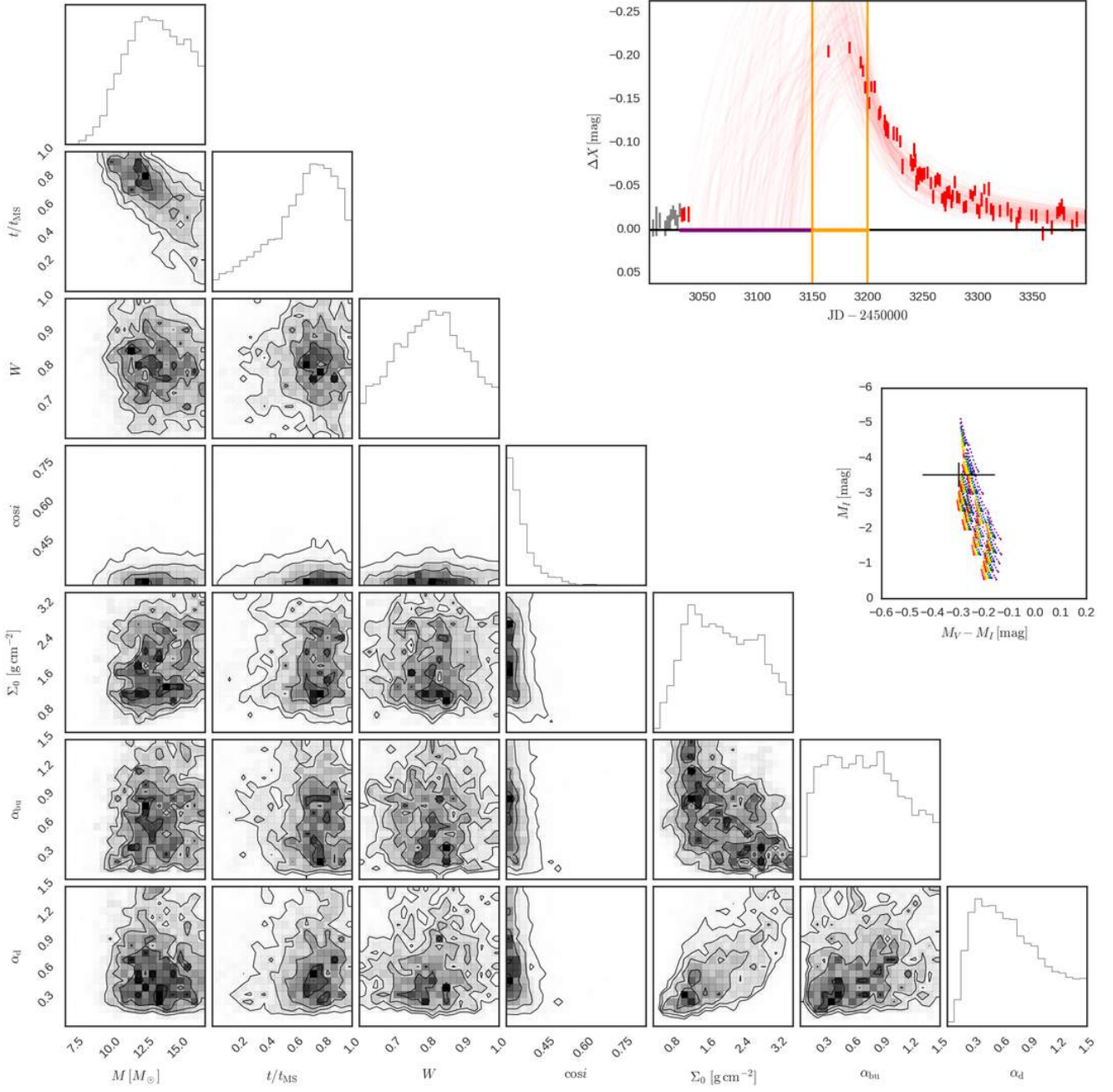


Figure C41. Same as Fig. 8 for SMC_SC5 32377 and bump ID 01.

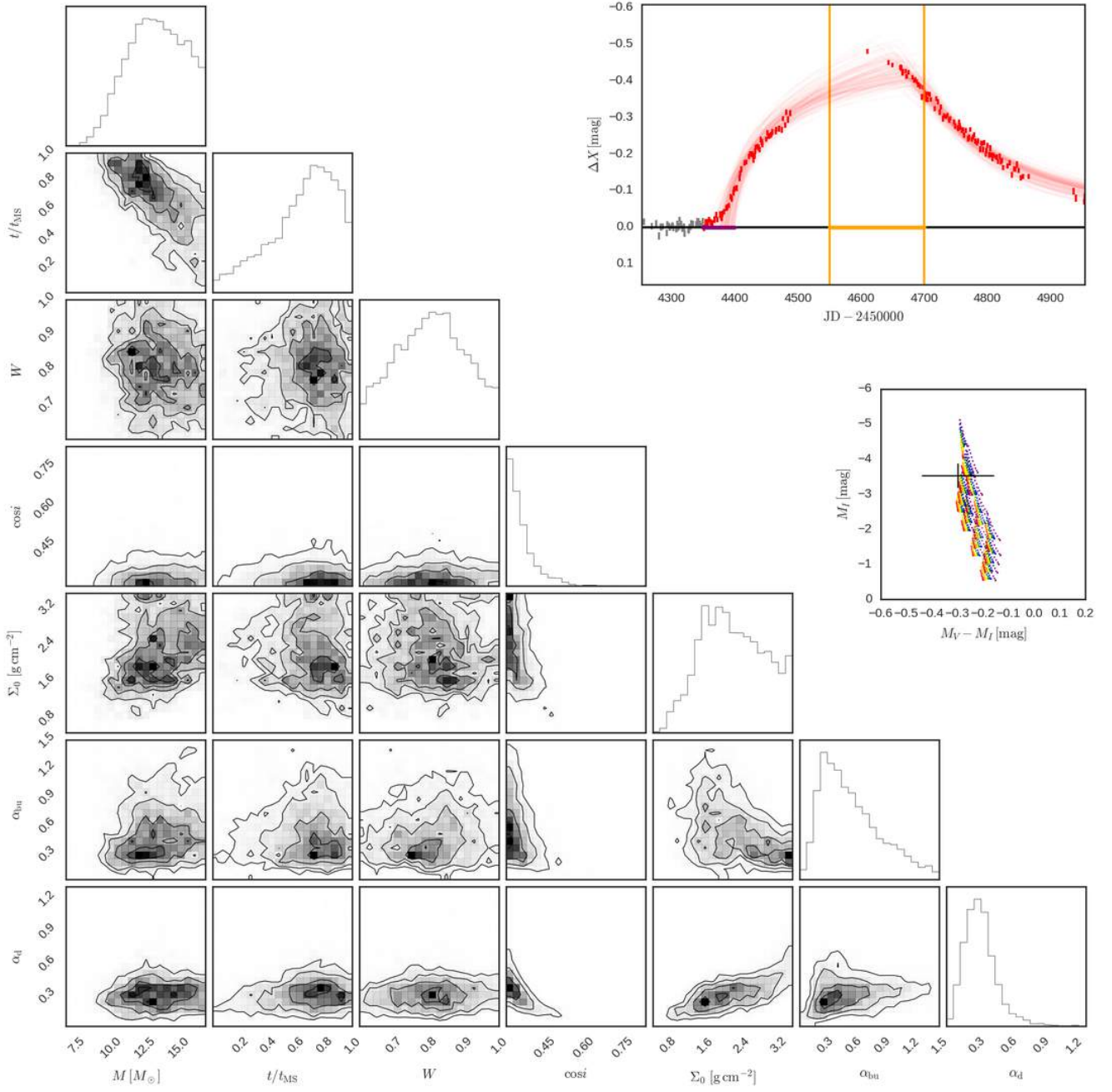


Figure C42. Same as Fig. 8 for SMC_SC5 32377 and bump ID 02.

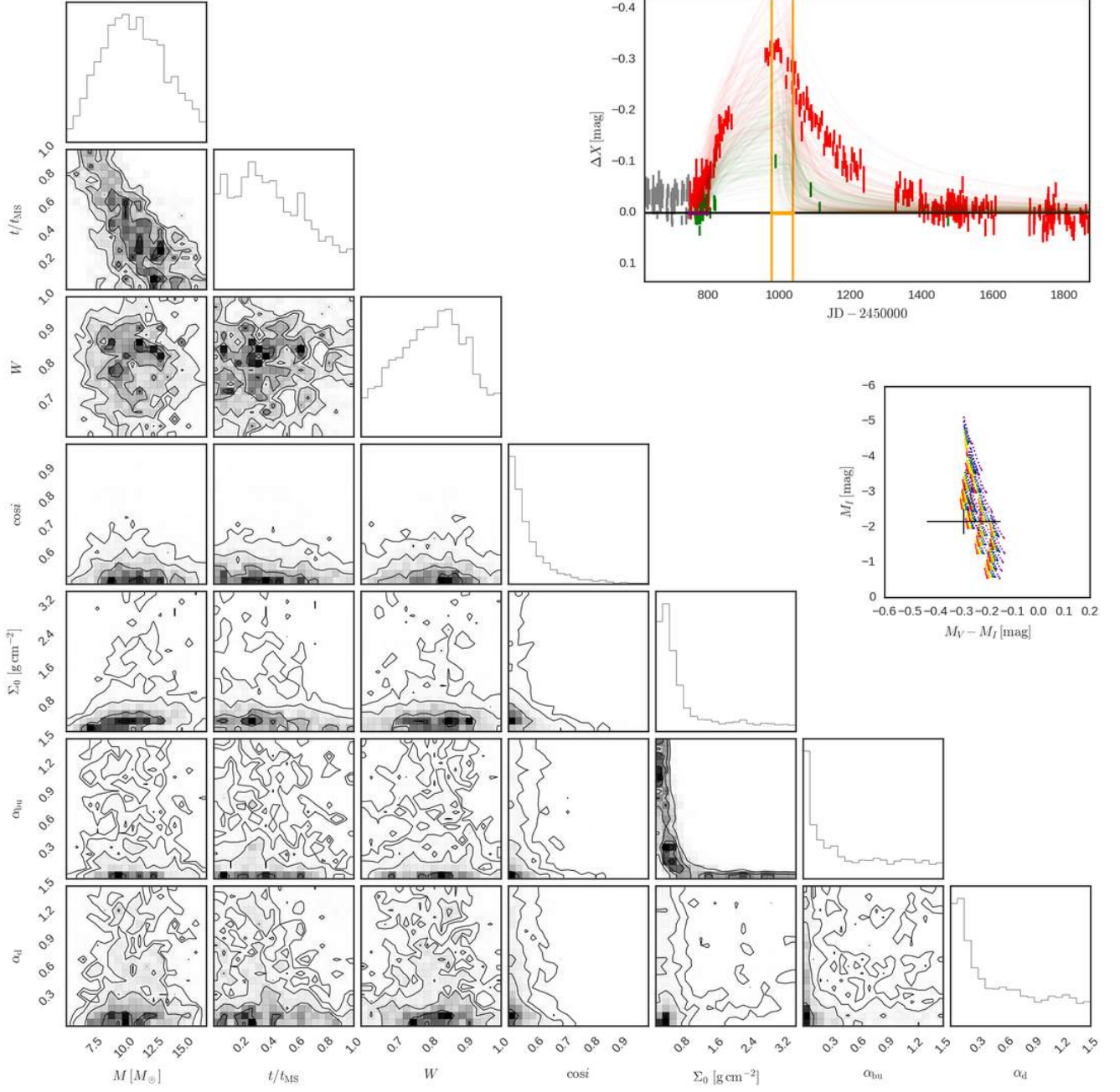


Figure C43. Same as Fig. 8 for SMC_SC5 43650 and bump ID 01.

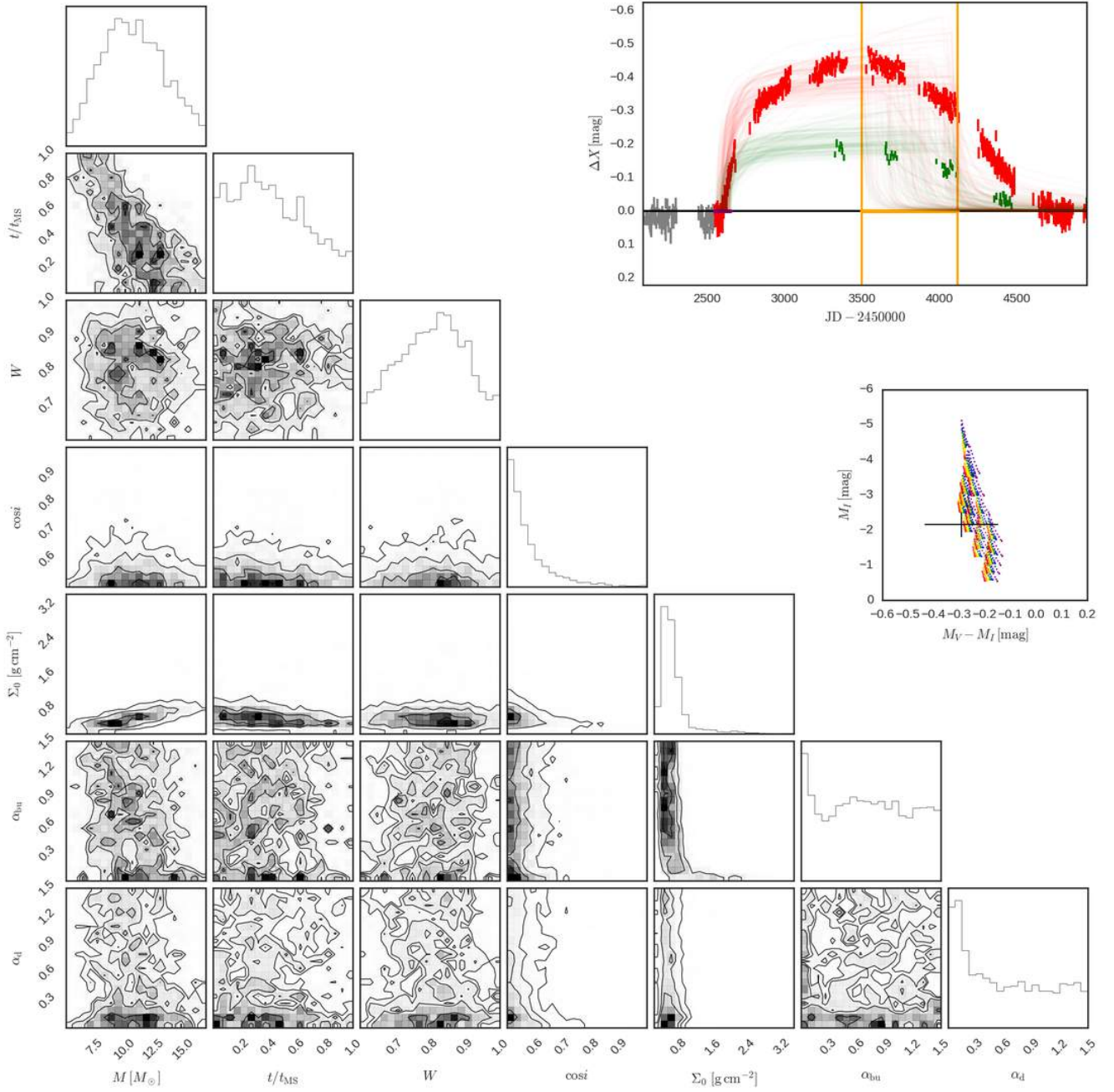


Figure C44. Same as Fig. 8 for SMC_SC5 43650 and bump ID 02.

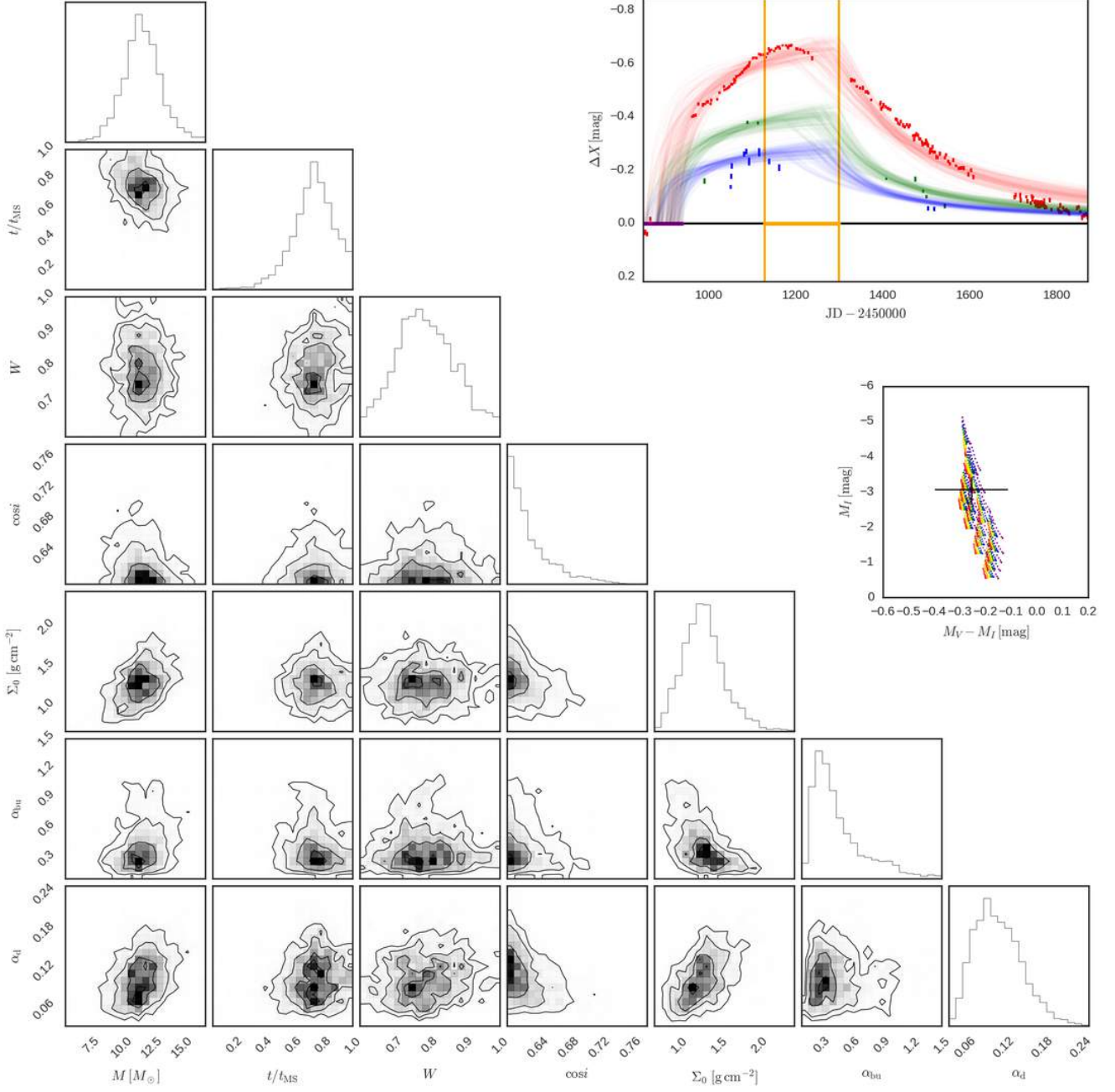


Figure C45. Same as Fig. 8 for SMC_SC5 54851 and bump ID 01.

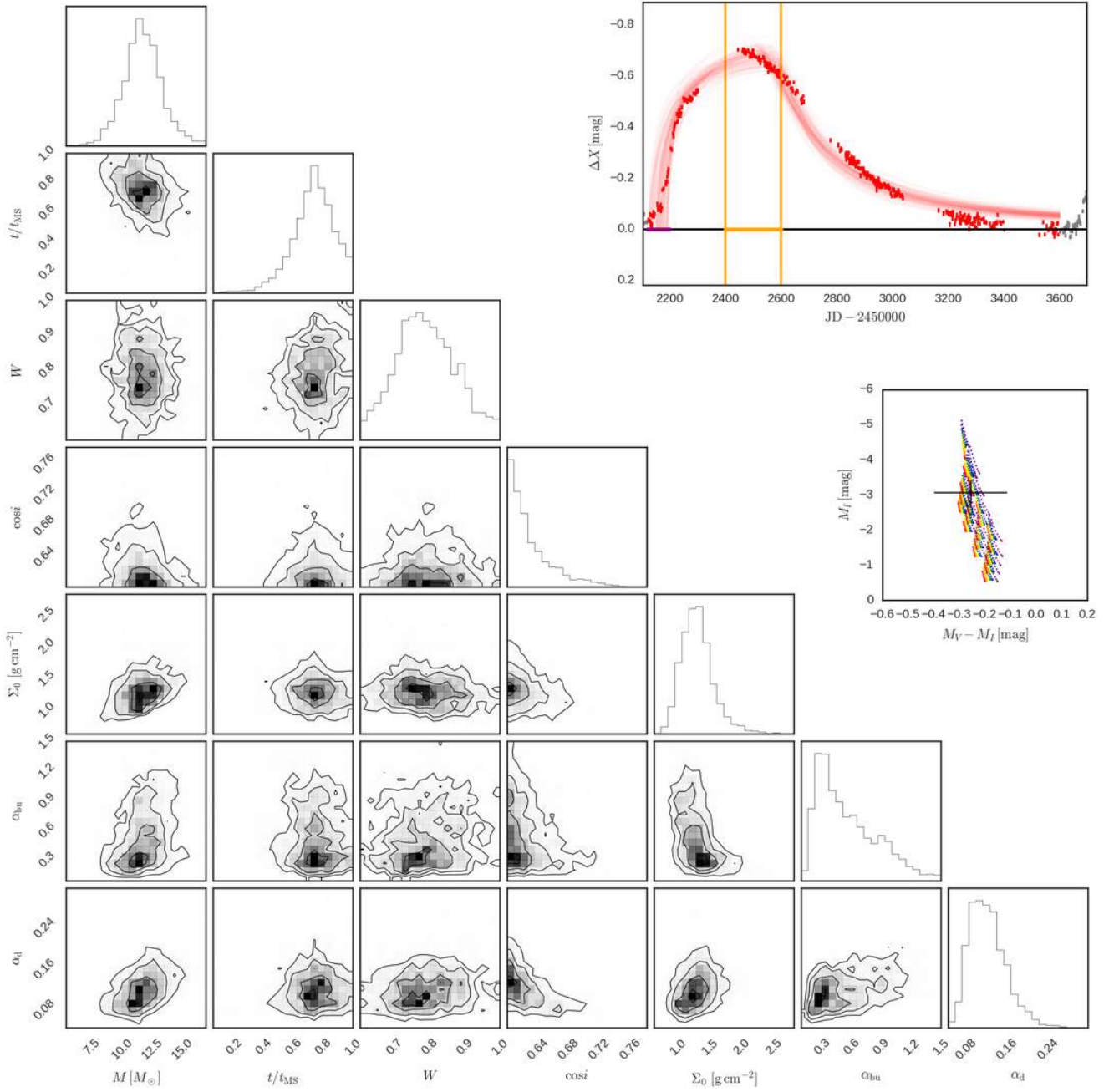


Figure C46. Same as Fig. 8 for SMC_SC5 54851 and bump ID 02.

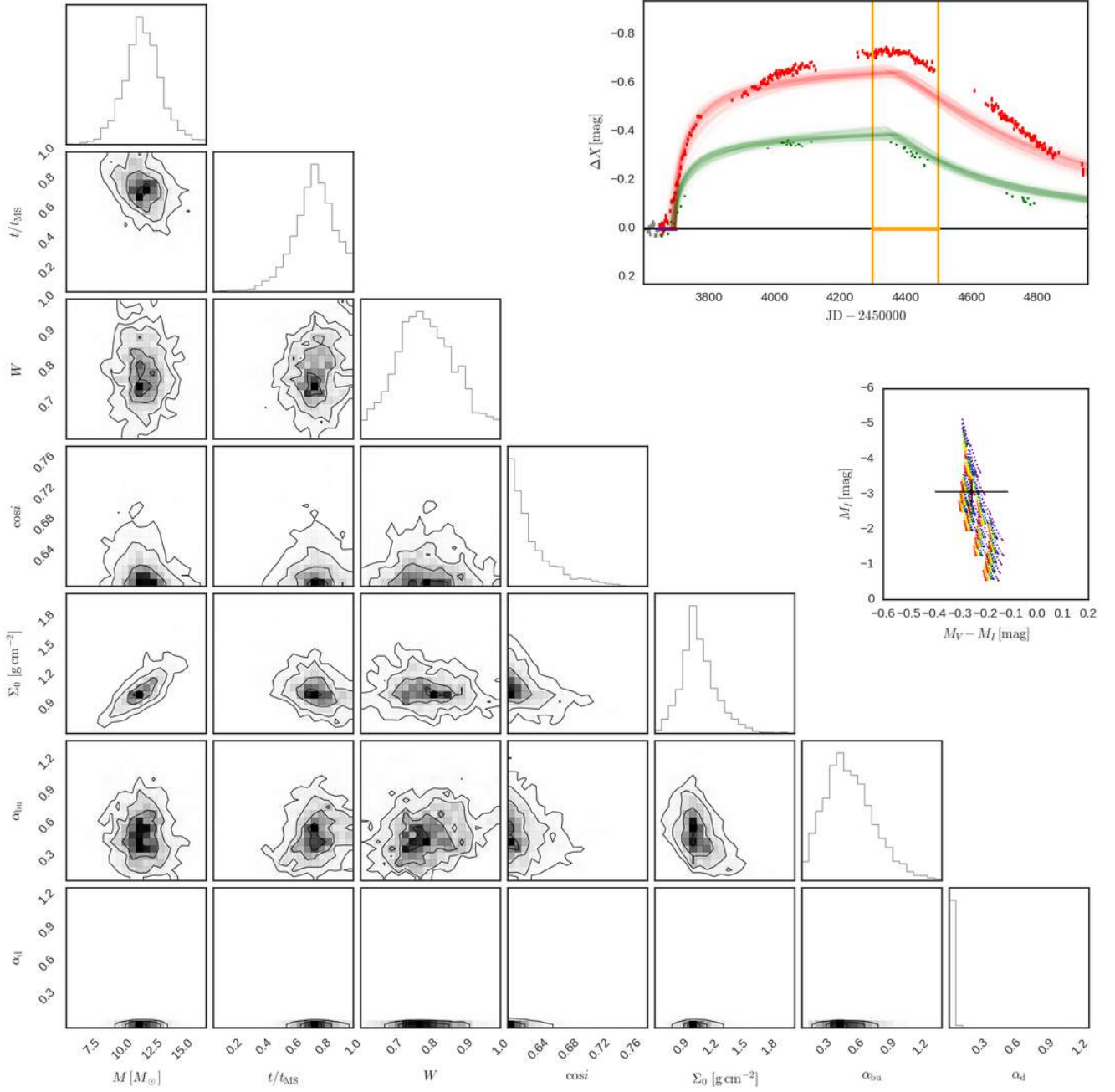


Figure C47. Same as Fig. 8 for SMC_SC5 54851 and bump ID 03.

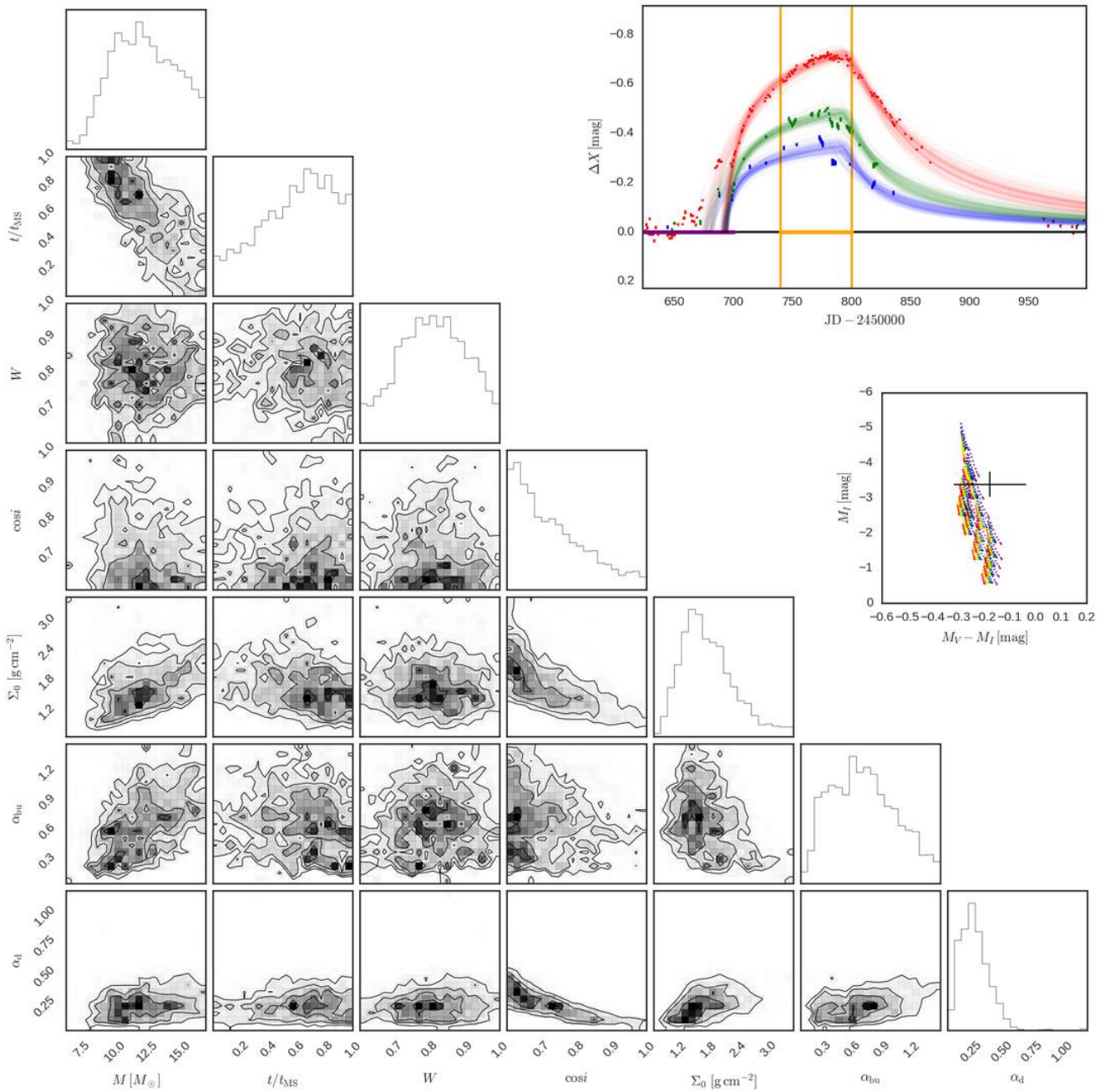


Figure C48. Same as Fig. 8 for SMC_SC5 65500 and bump ID 01.

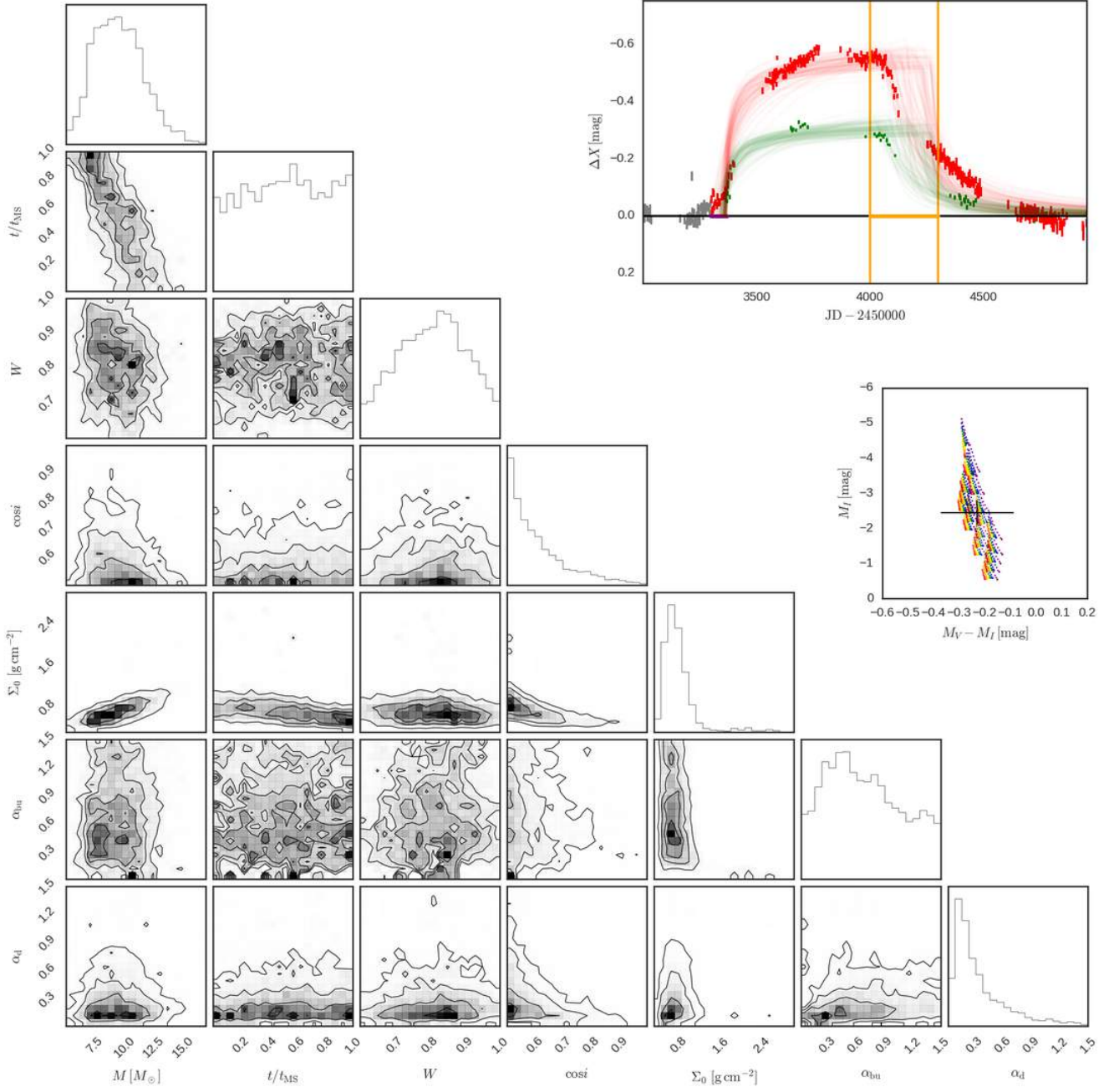


Figure C49. Same as Fig. 8 for SMC_SC5 129535 and bump ID 01.

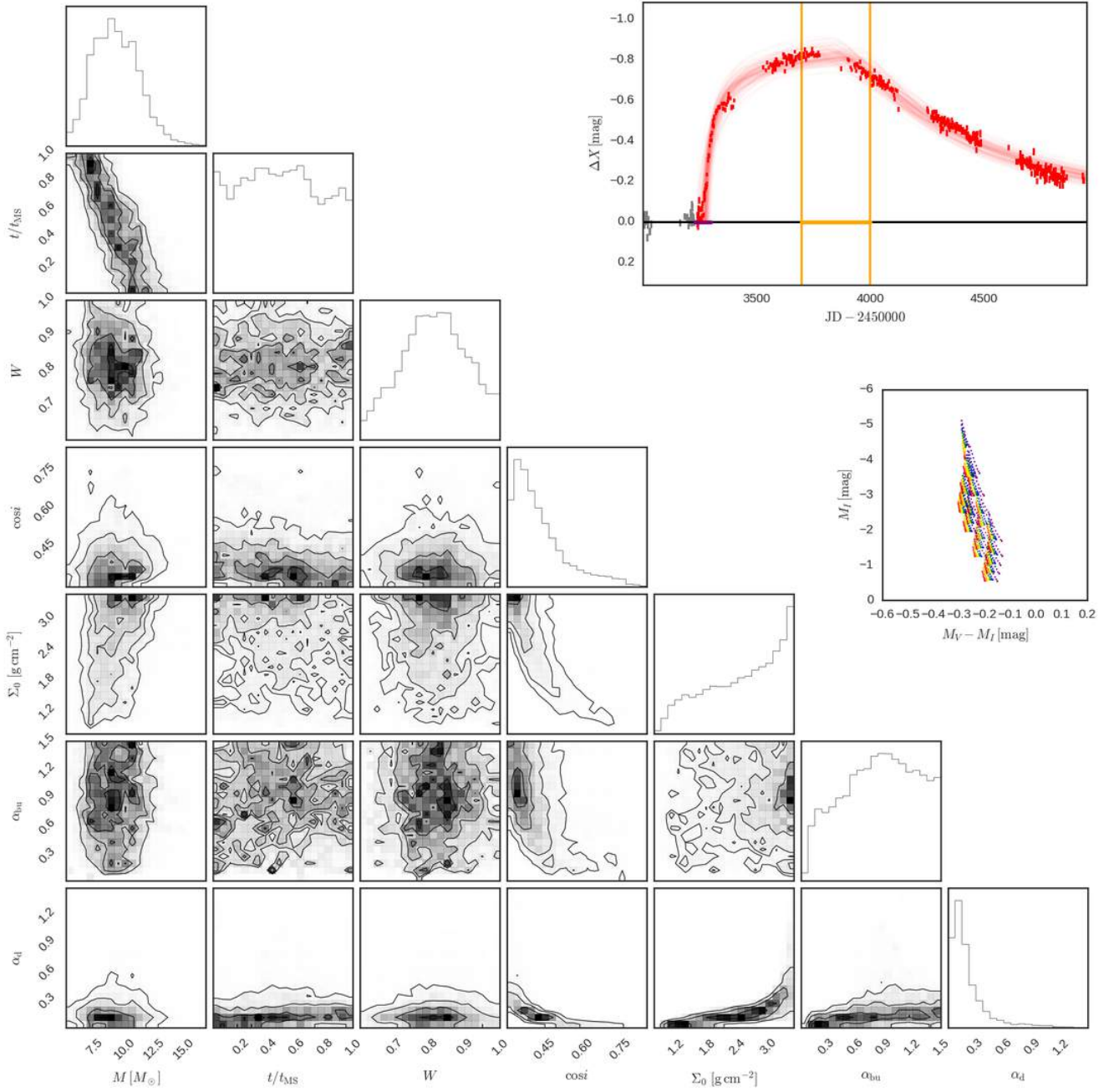


Figure C50. Same as Fig. 8 for SMC_SC5 145724 and bump ID 01.

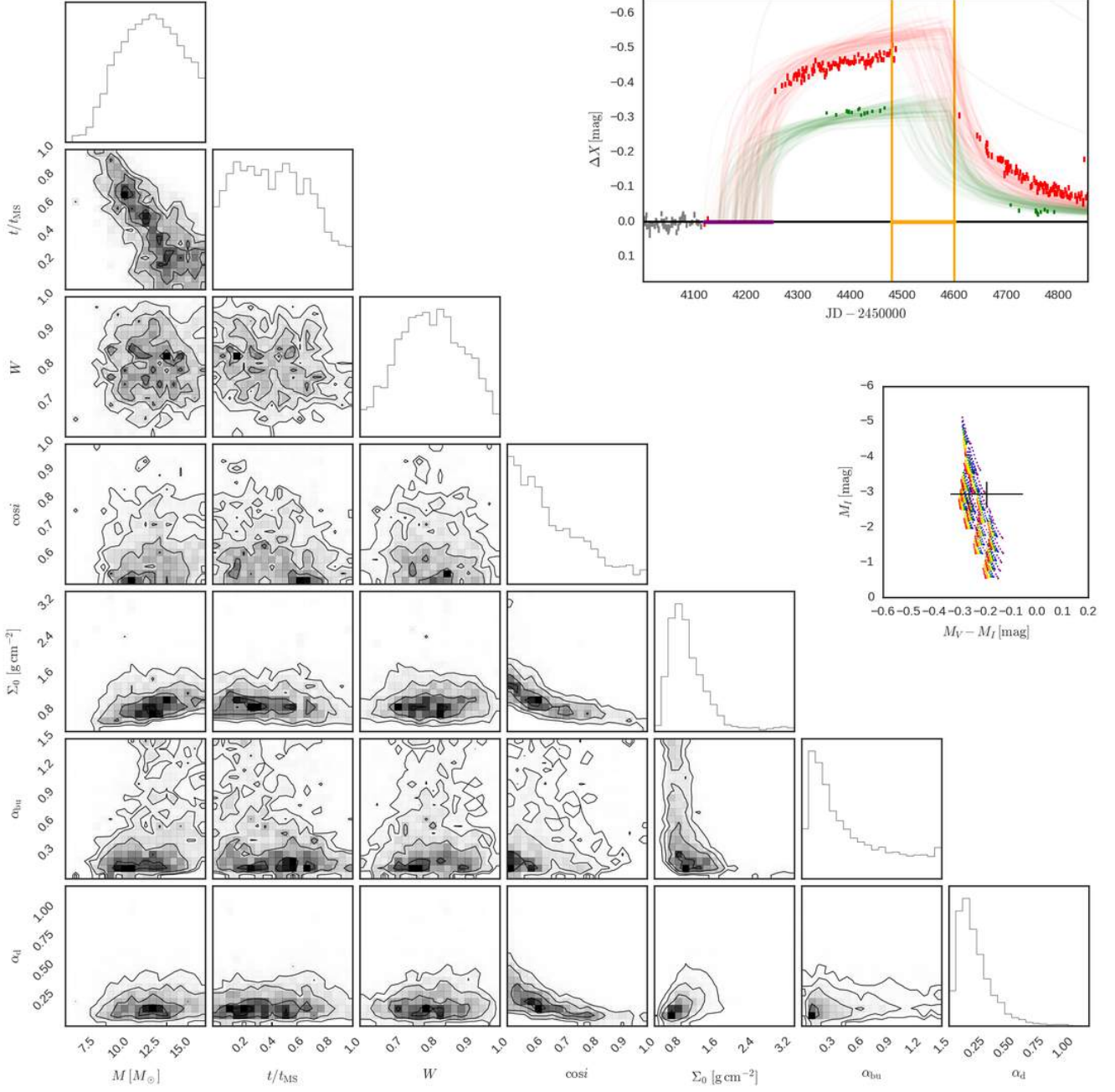


Figure C51. Same as Fig. 8 for SMC_SC5 180034 and bump ID 01.

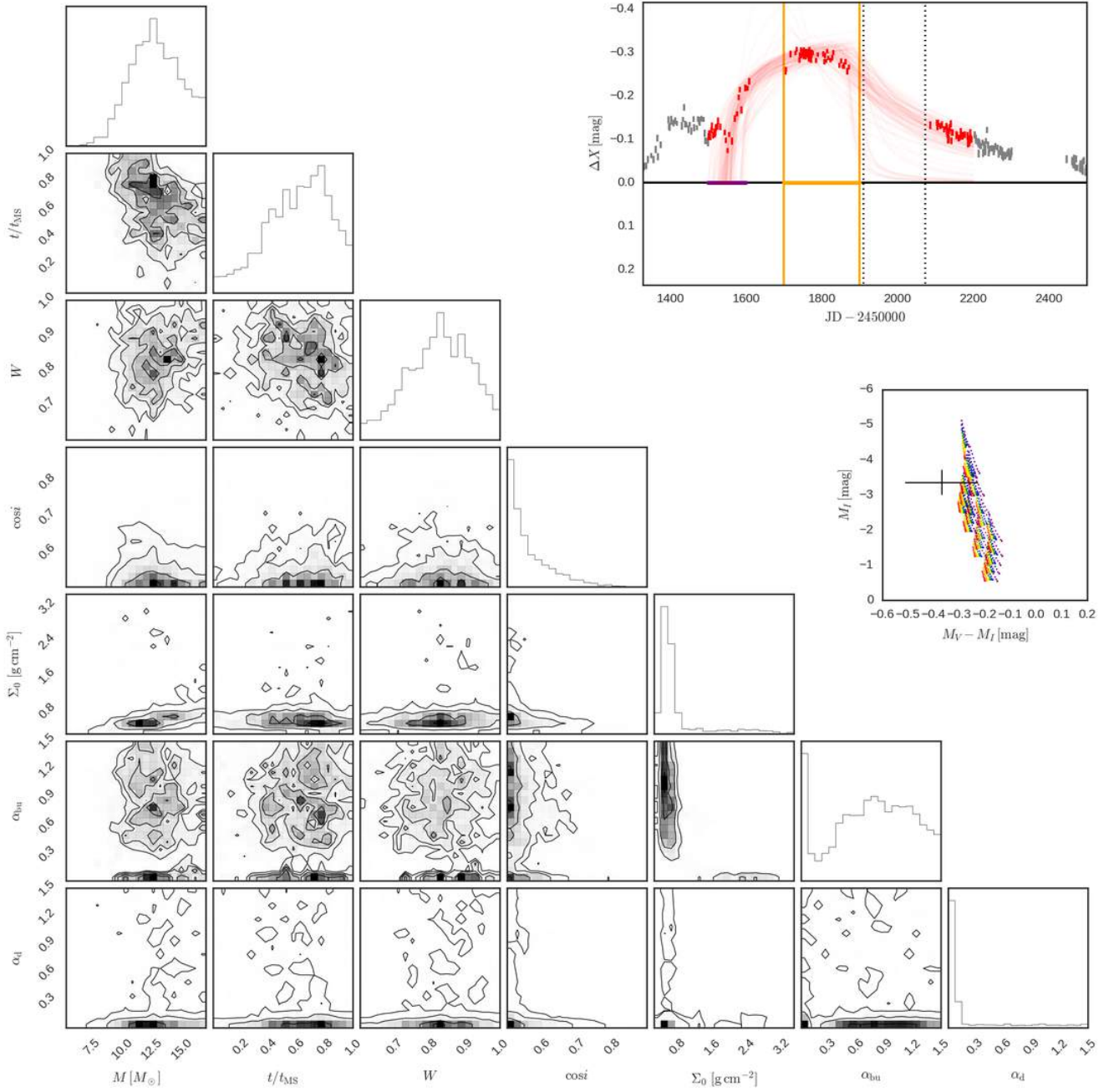


Figure C52. Same as Fig. 8 for SMC_SC5 260841 and bump ID 01.

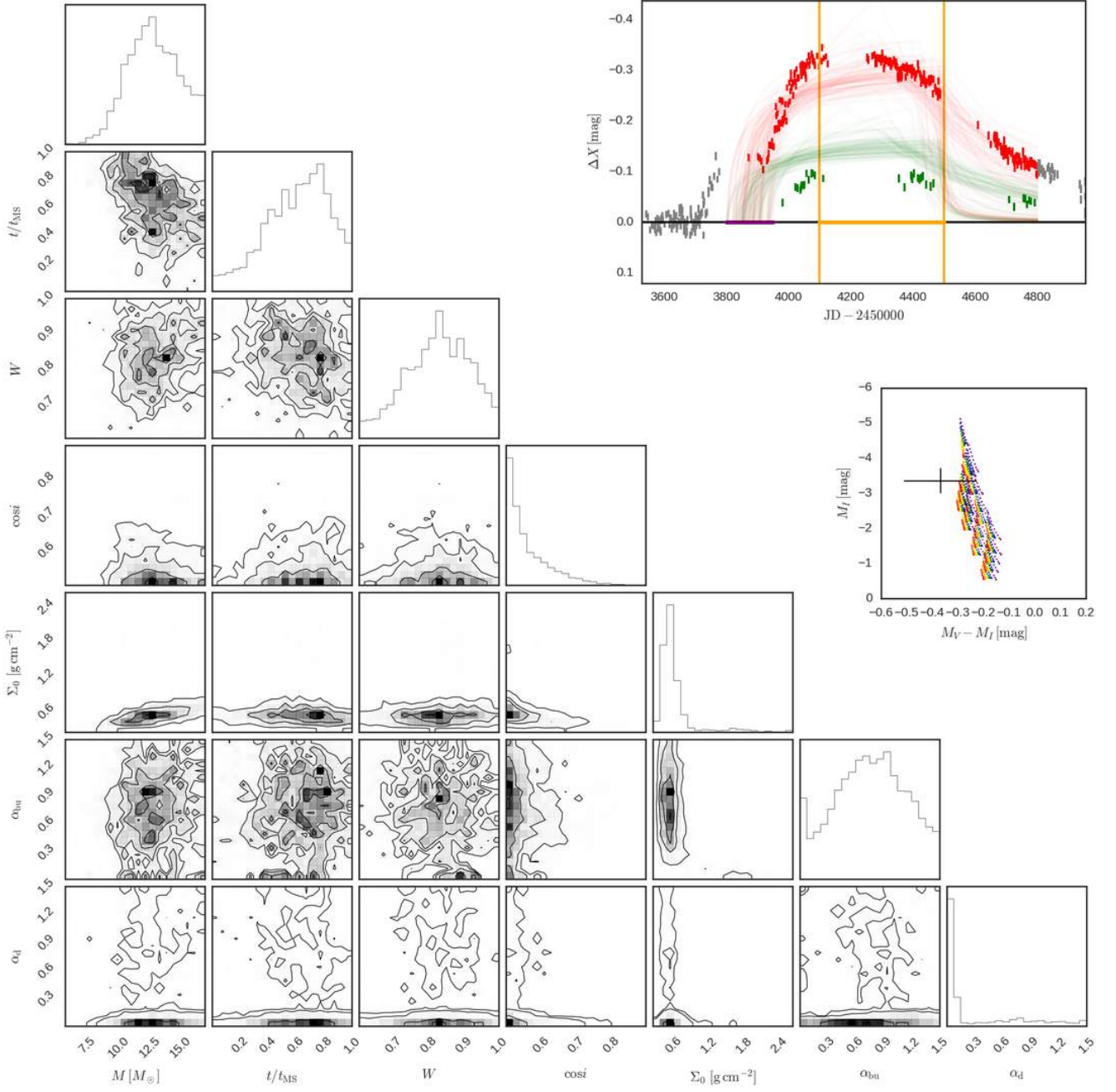


Figure C53. Same as Fig. 8 for SMC_SC5 260841 and bump ID 02.

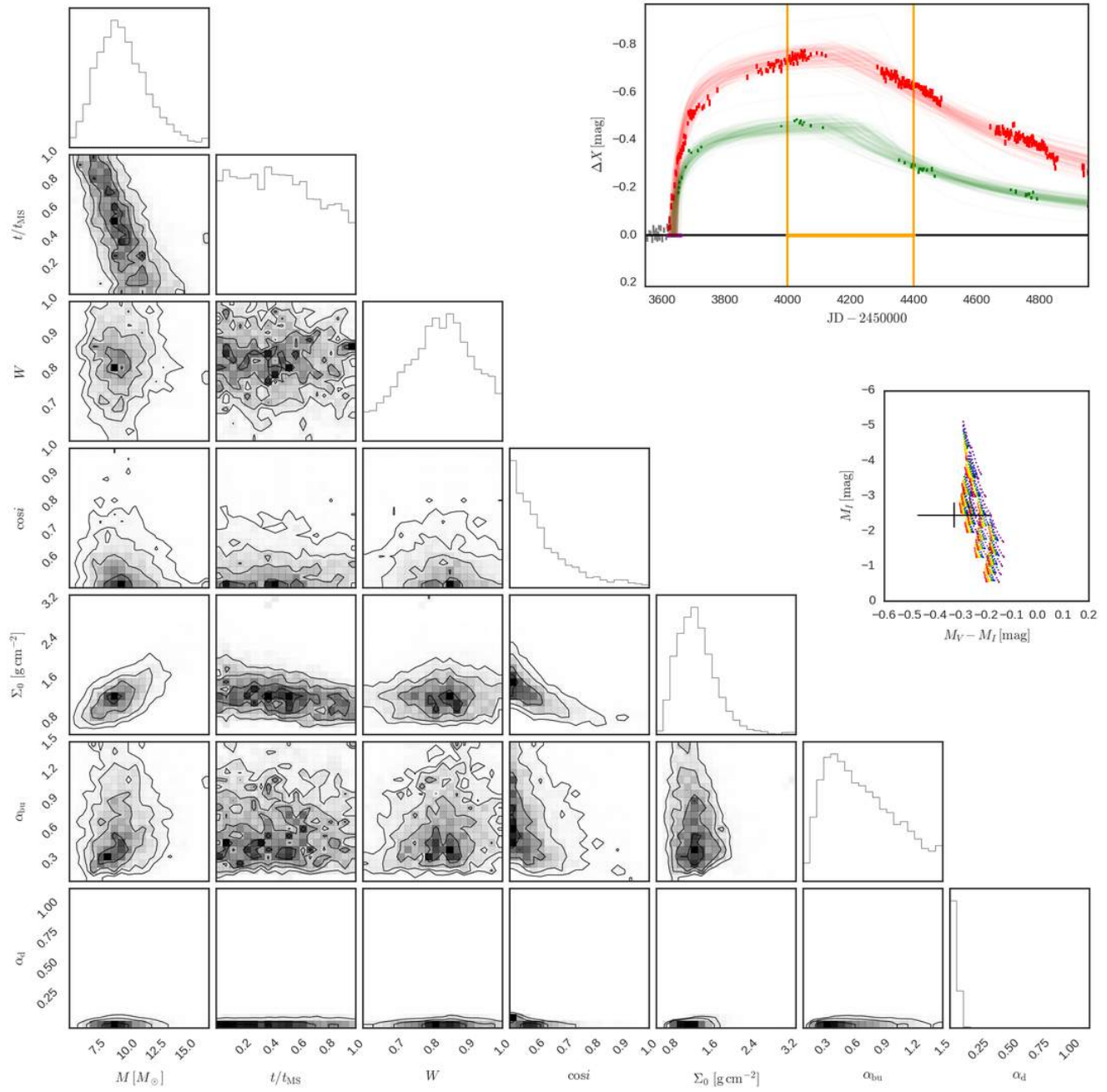


Figure C54. Same as Fig. 8 for SMC_SC5 260957 and bump ID 01.

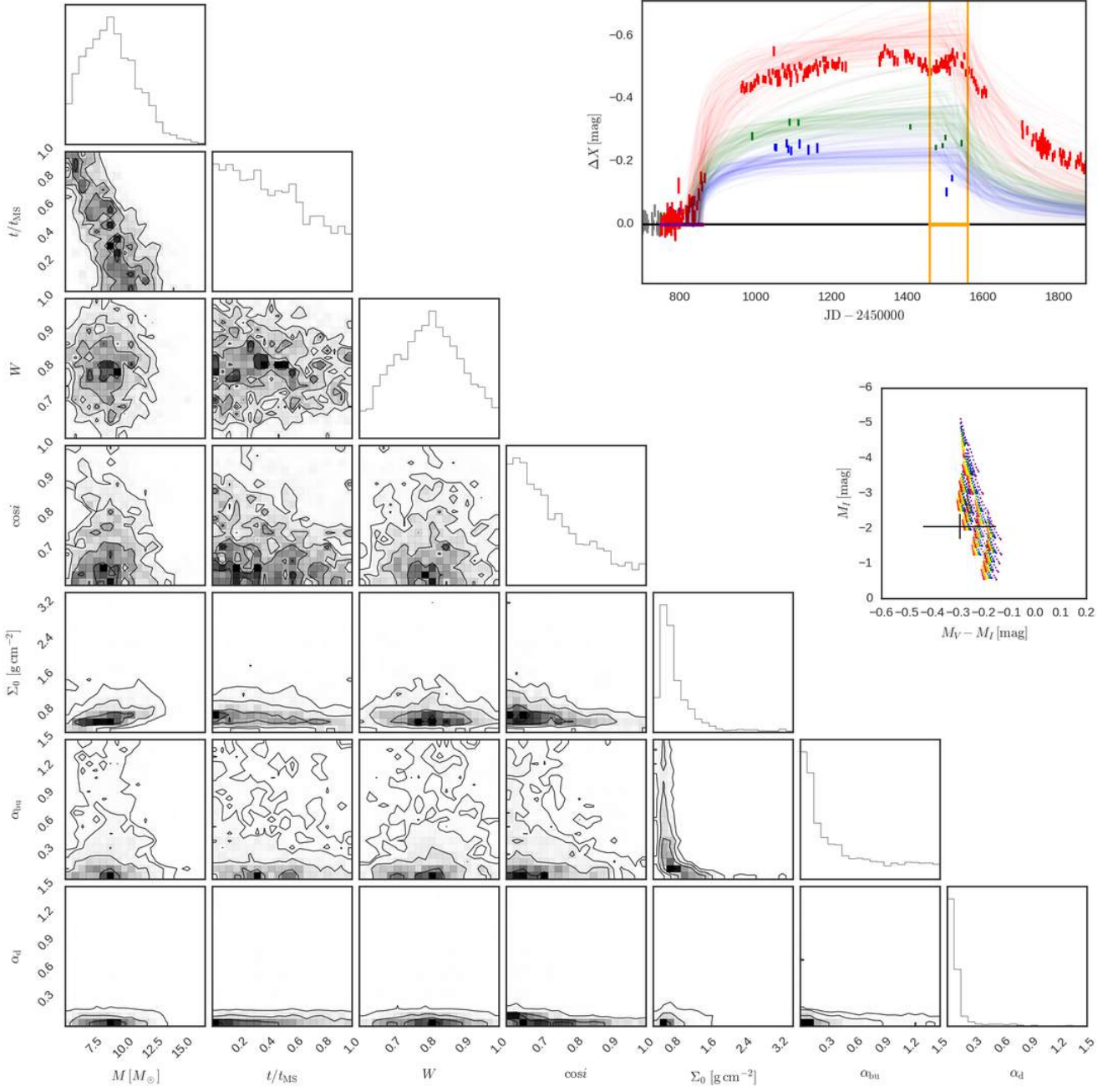


Figure C55. Same as Fig. 8 for SMC_SC5 266088 and bump ID 01.

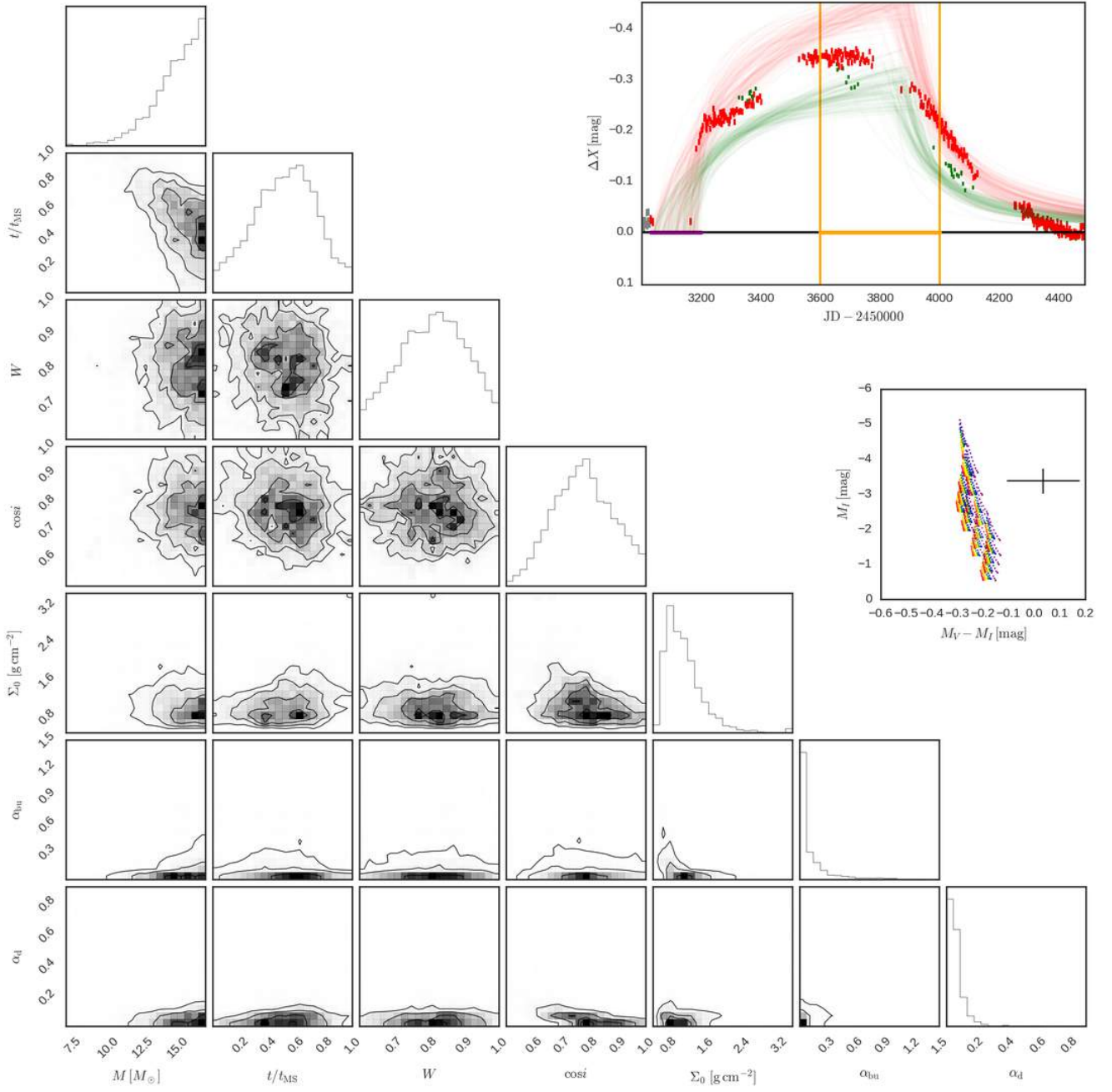


Figure C56. Same as Fig. 8 for SMC_SC5 276982 and bump ID 01.

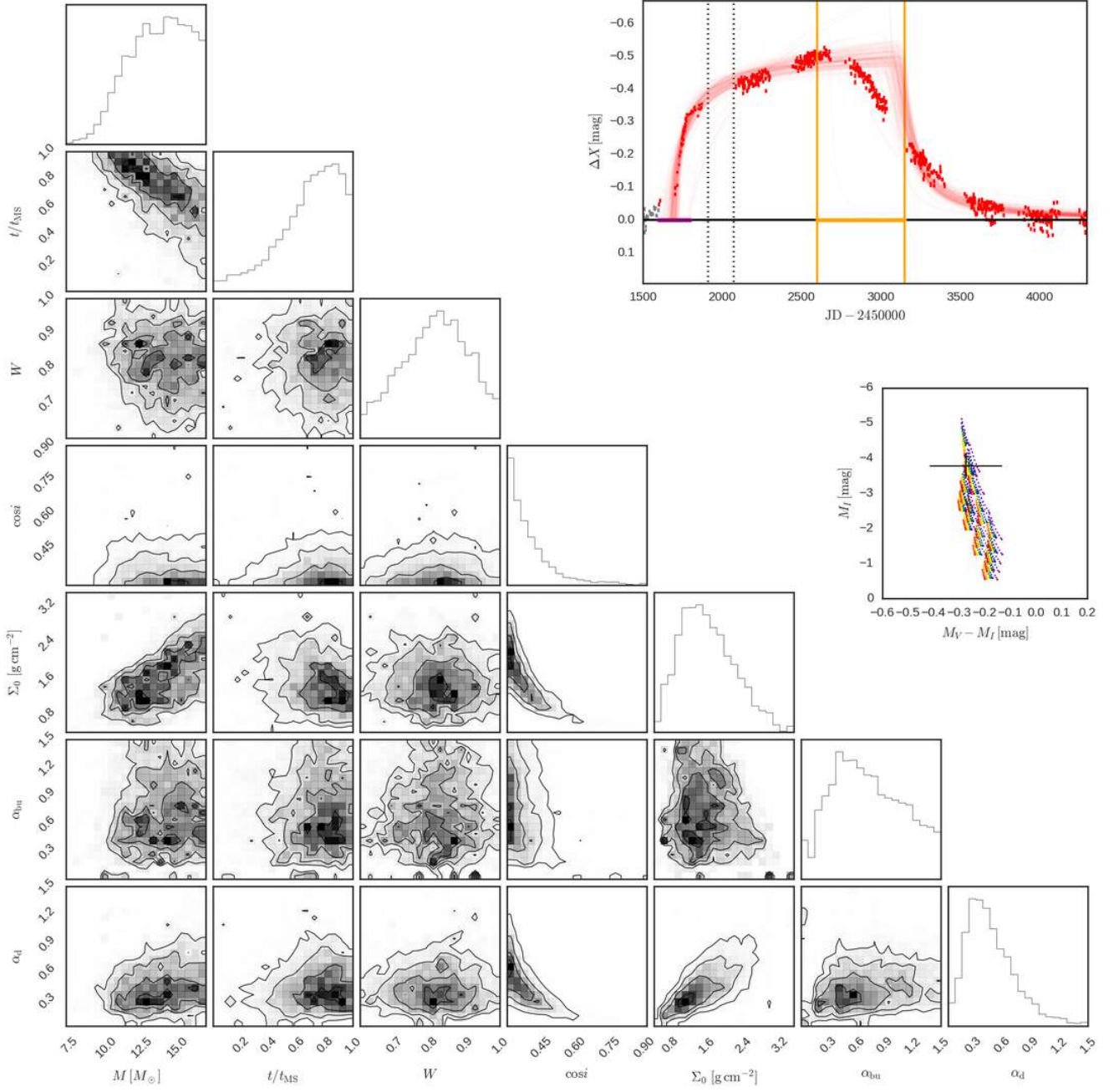


Figure C57. Same as Fig. 8 for SMC_SC5 282963 and bump ID 01.

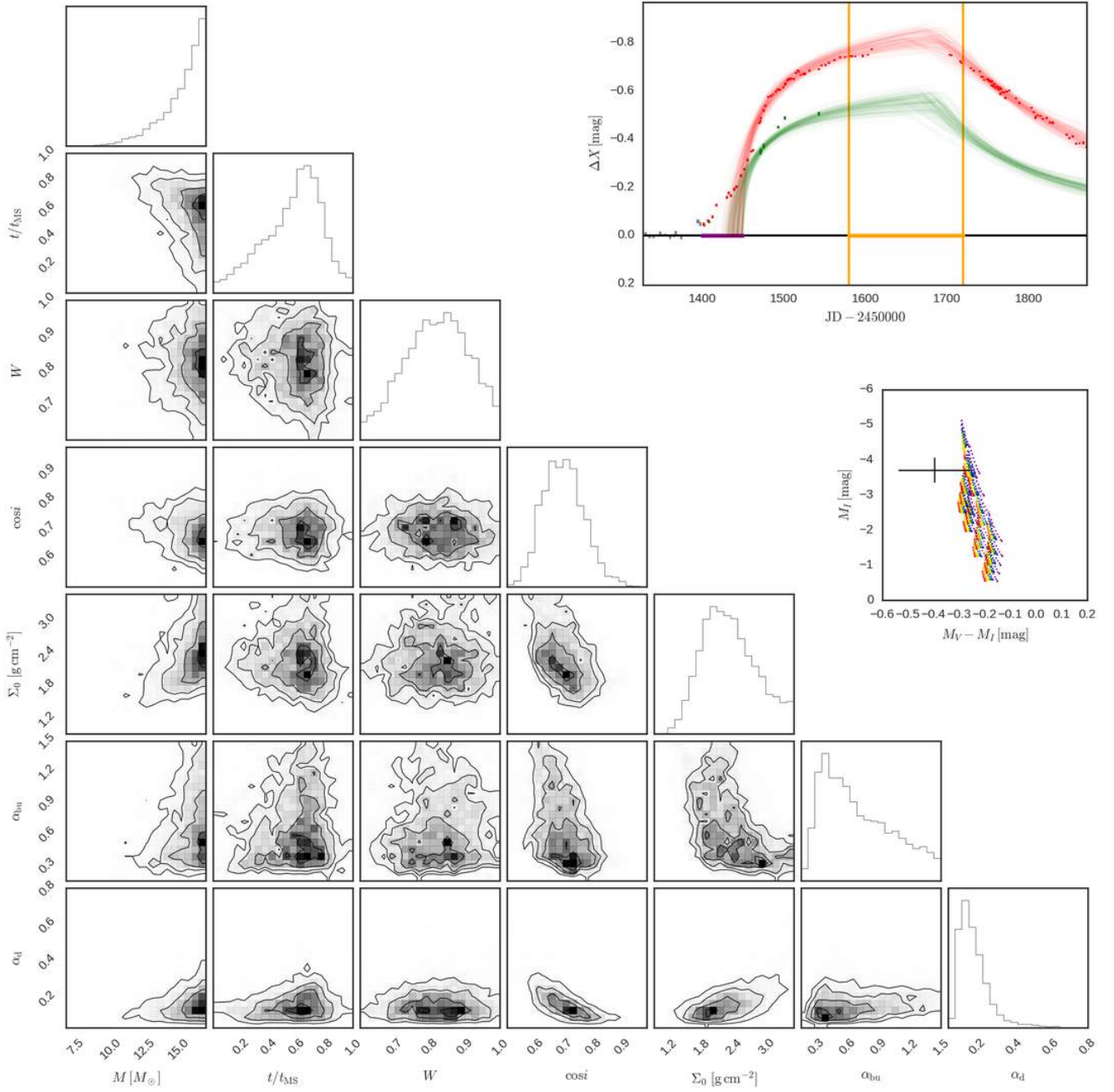


Figure C58. Same as Fig. 8 for SMC_SC6 11085 and bump ID 01.

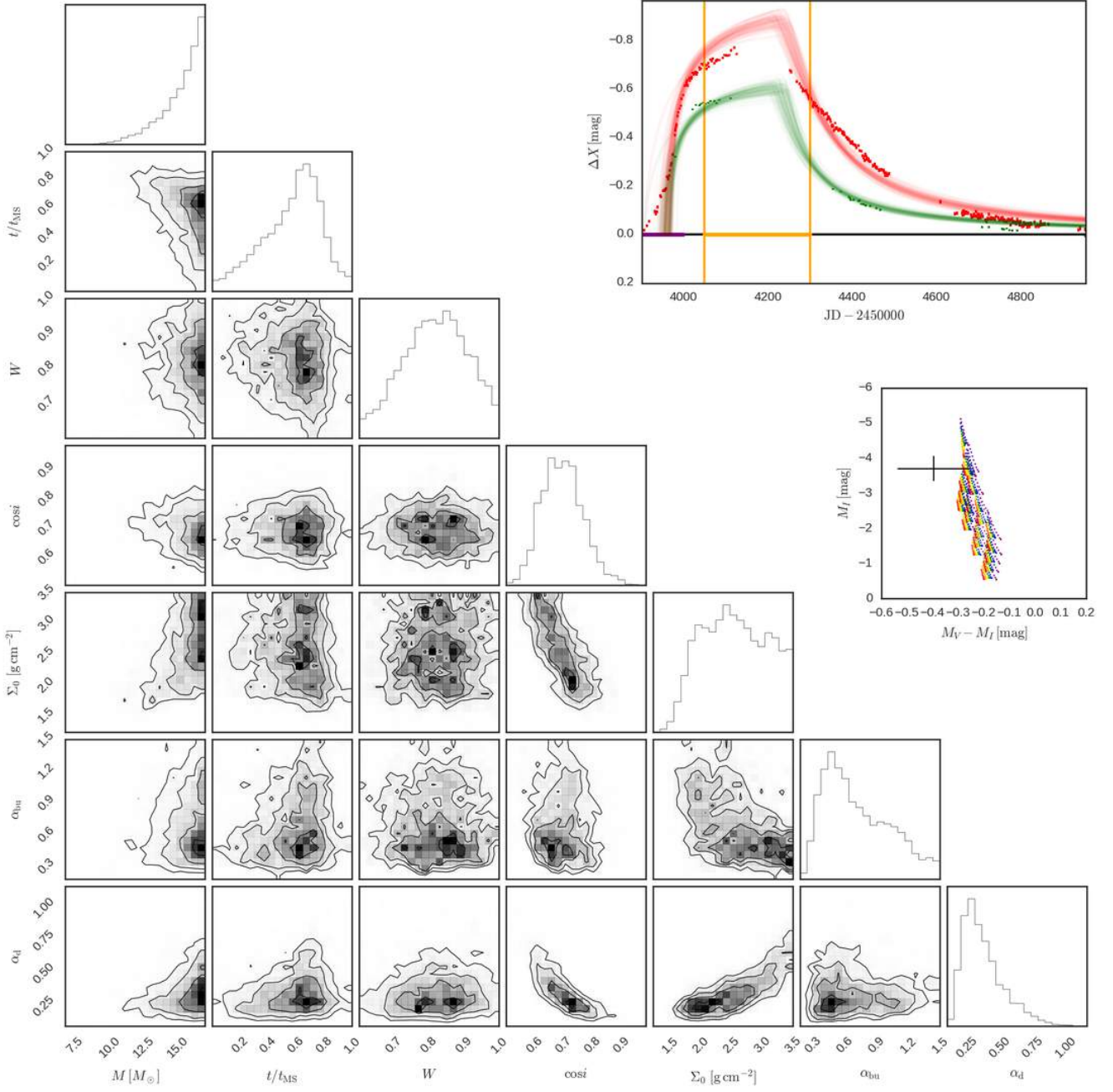


Figure C59. Same as Fig. 8 for SMC_SC6 11085 and bump ID 02.

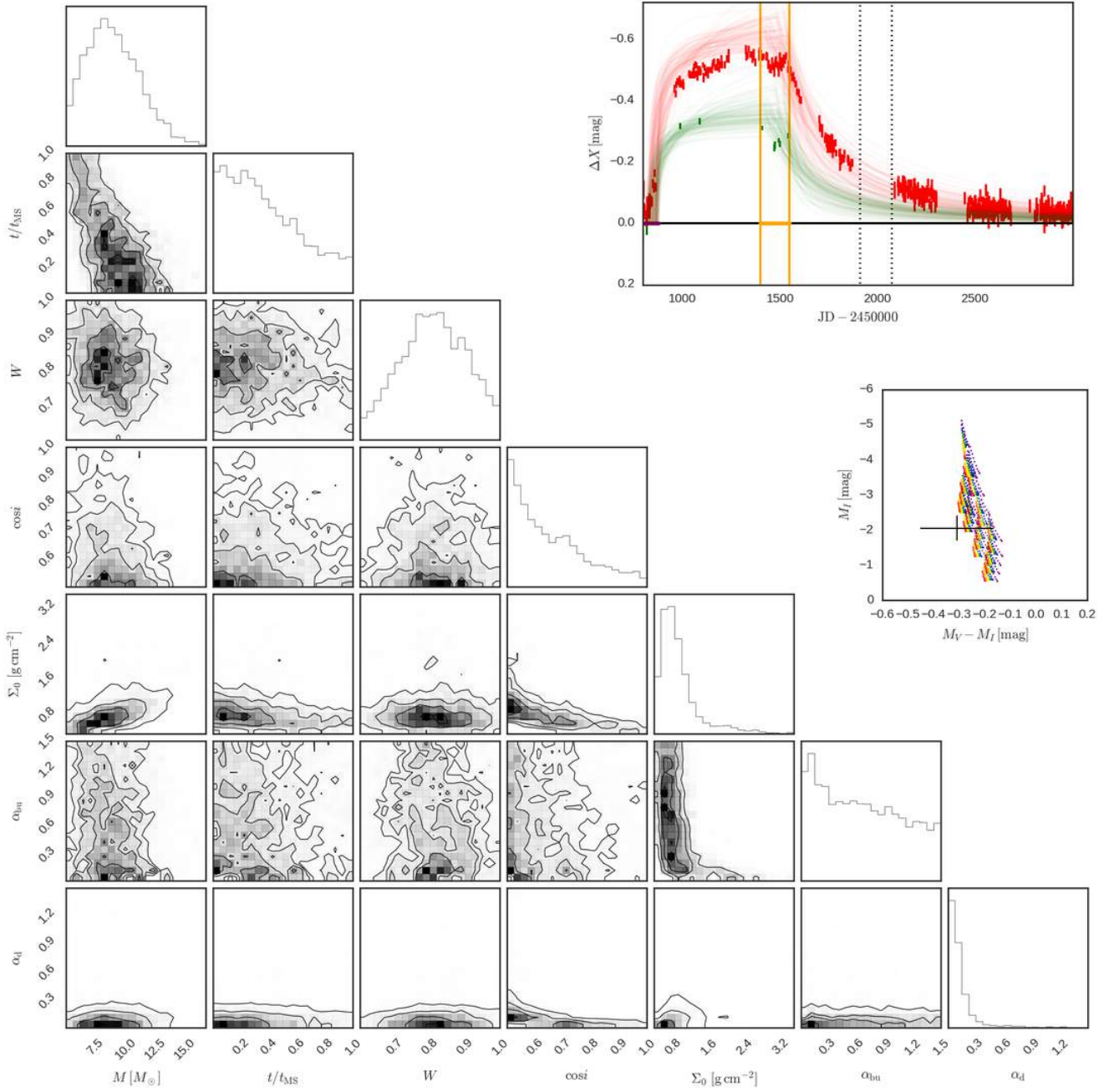


Figure C60. Same as Fig. 8 for SMC_SC6 17538 and bump ID 01.

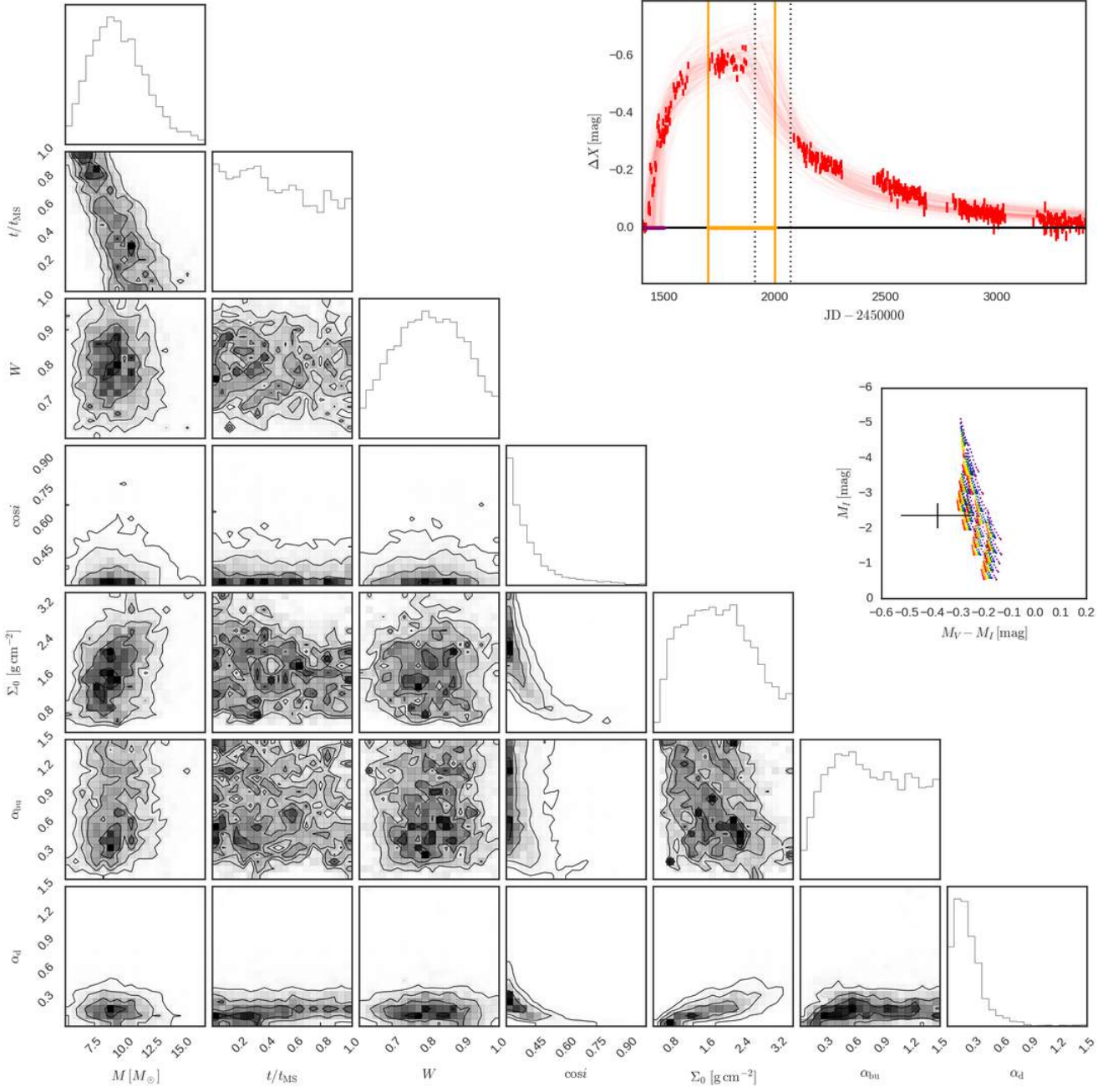


Figure C61. Same as Fig. 8 for SMC_SC6 42440 and bump ID 01.

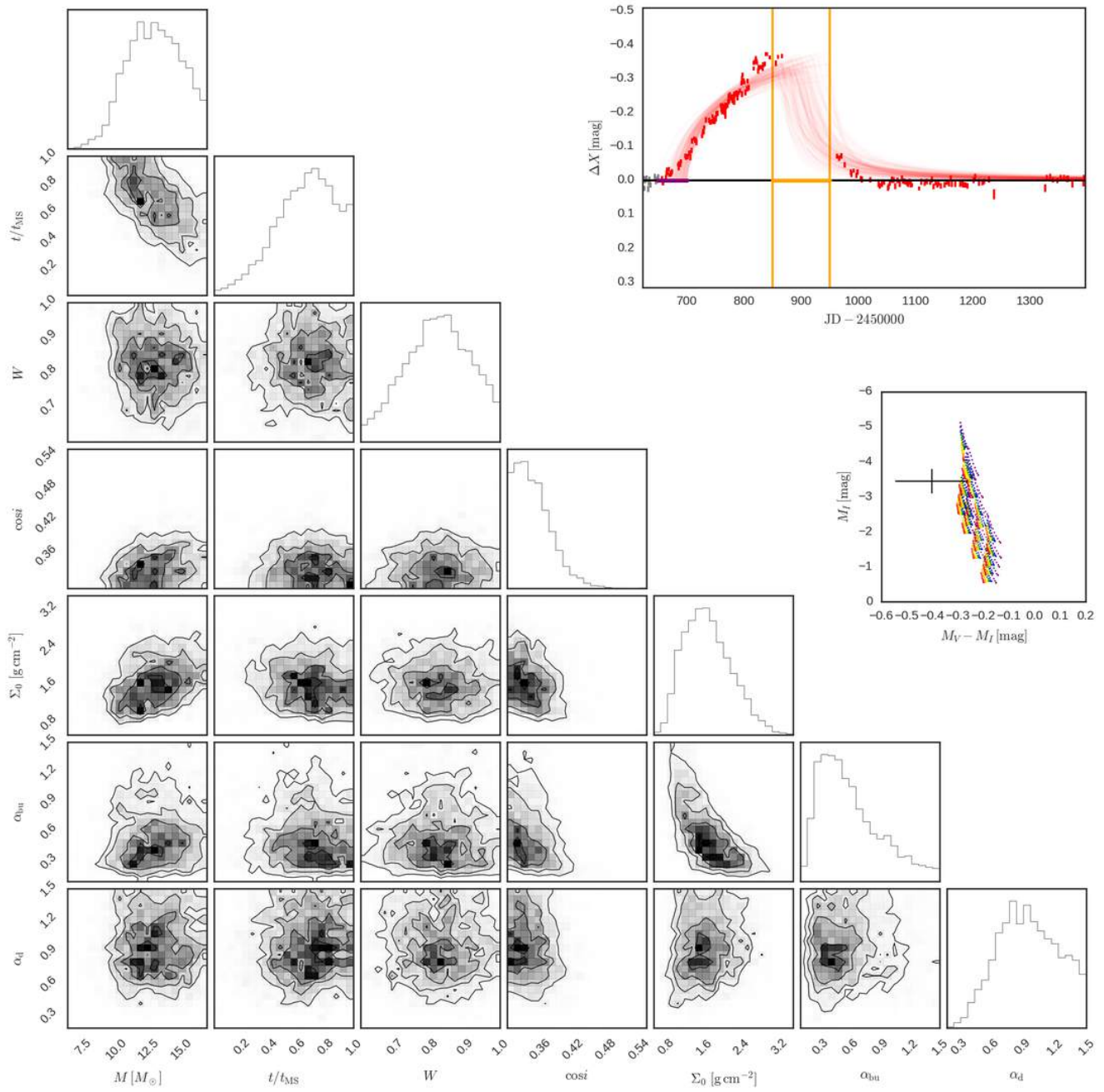


Figure C62. Same as Fig. 8 for SMC_SC6 99991 and bump ID 01.

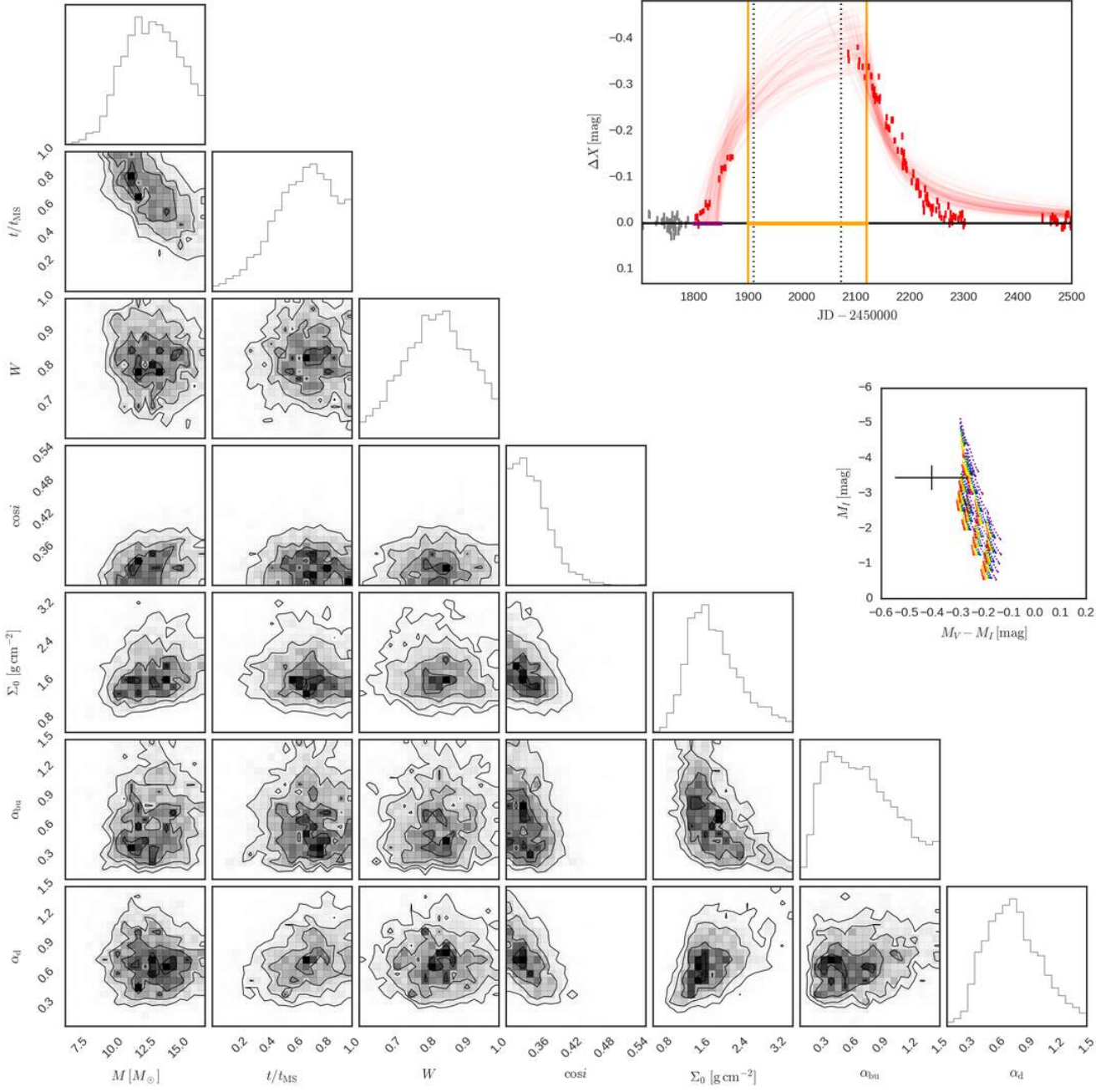


Figure C63. Same as Fig. 8 for SMC_SC6 99991 and bump ID 02.

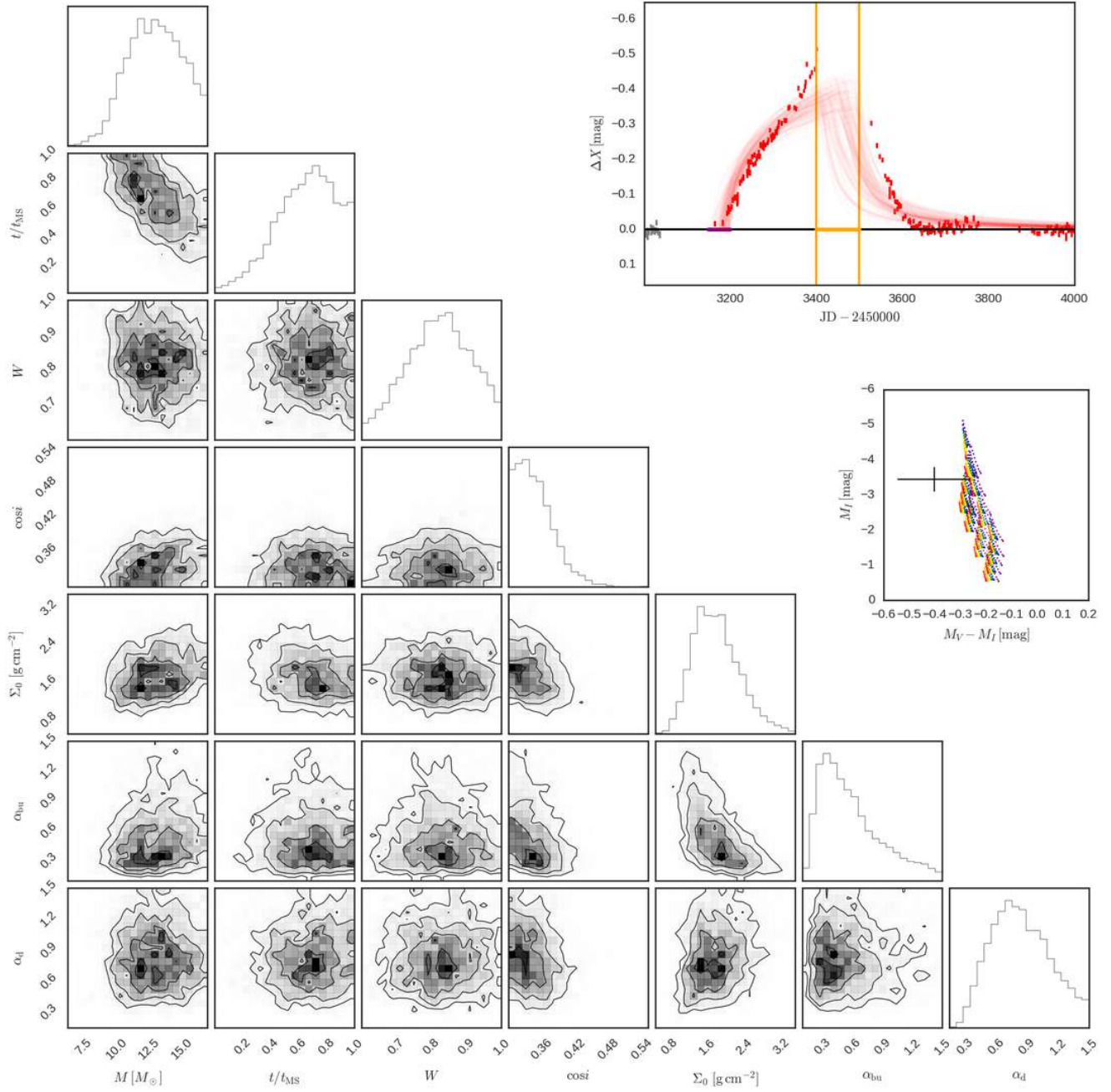


Figure C64. Same as Fig. 8 for SMC_SC6 99991 and bump ID 03.

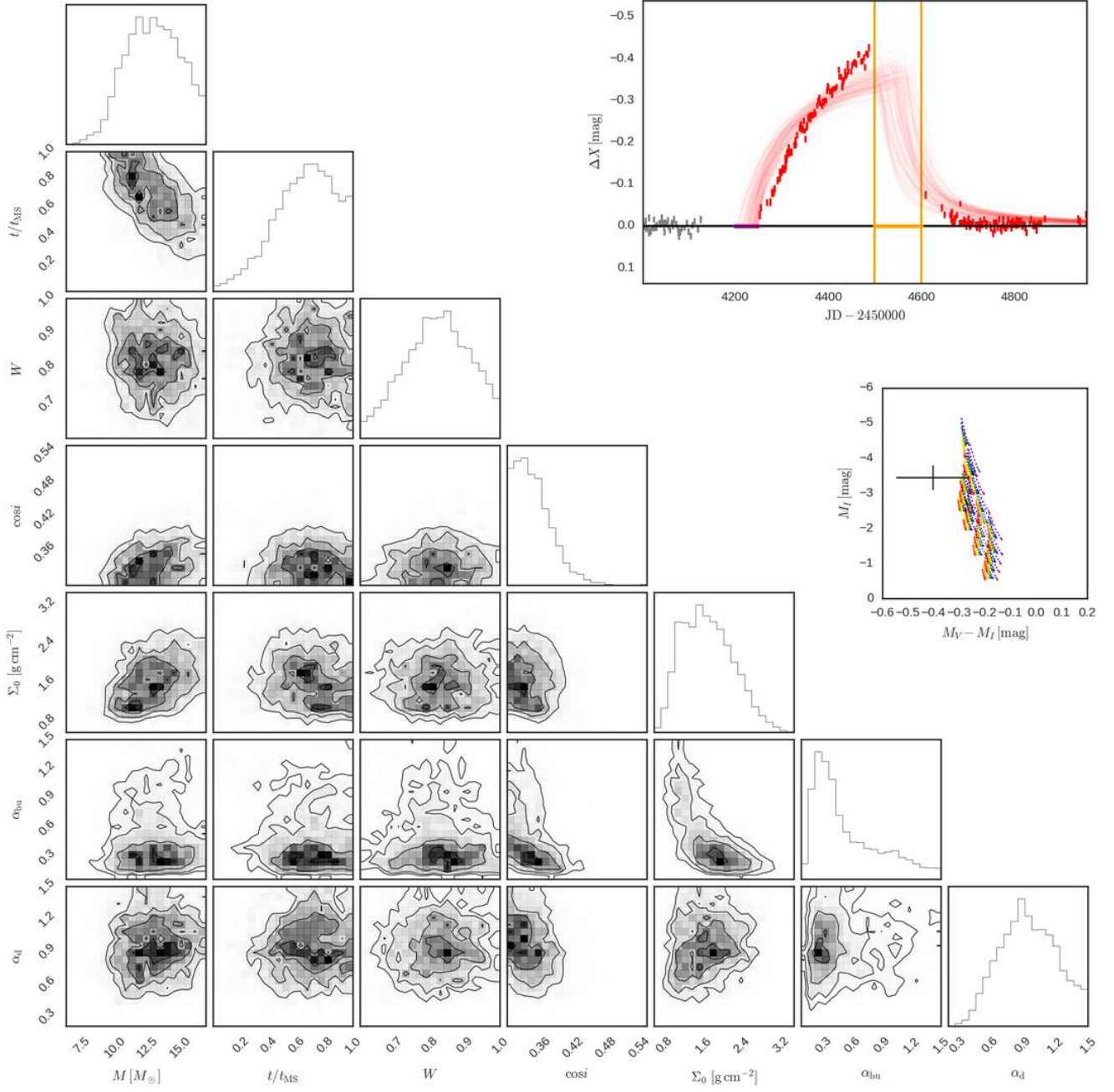


Figure C65. Same as Fig. 8 for SMC_SC6 99991 and bump ID 04.

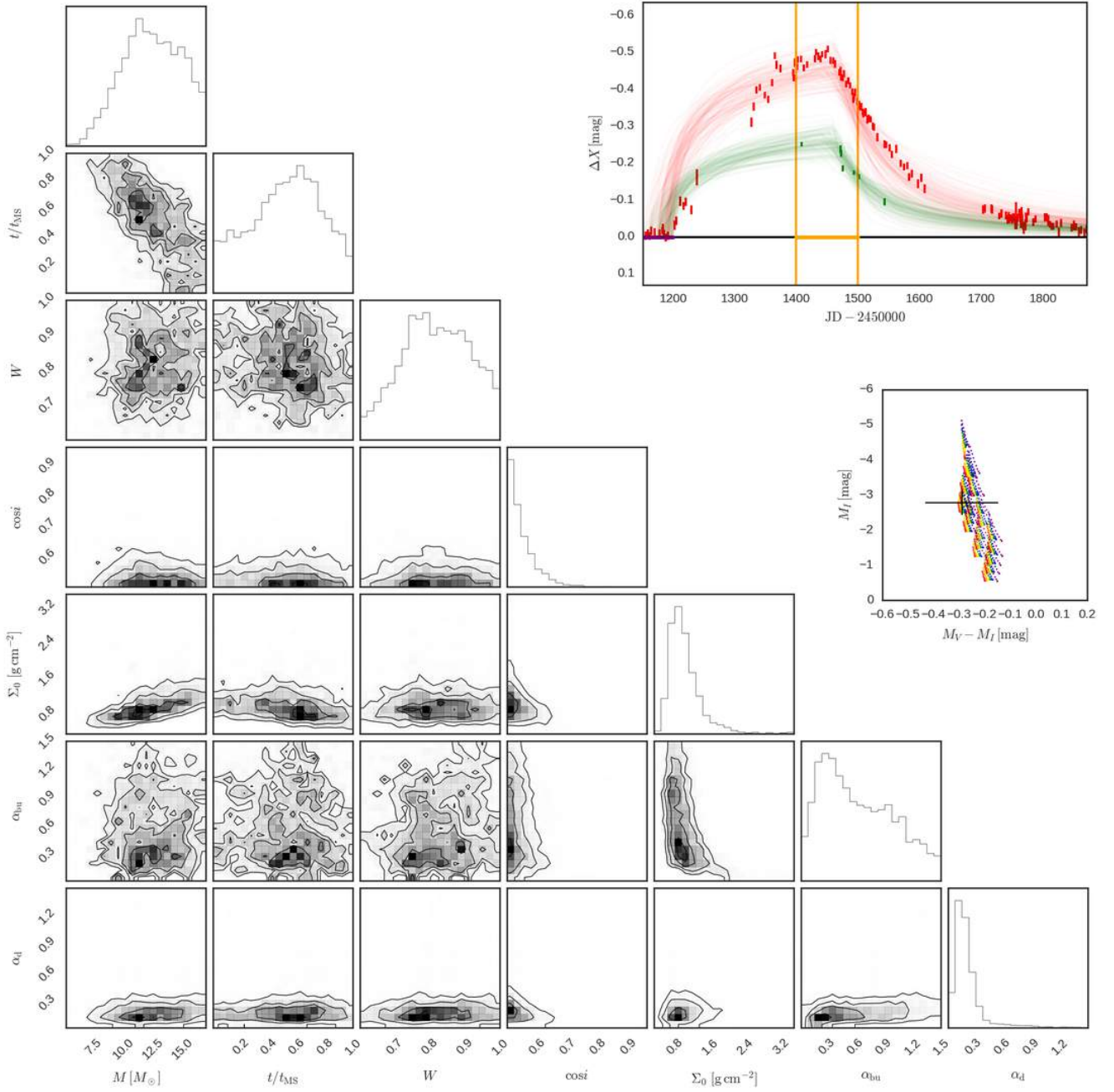


Figure C66. Same as Fig. 8 for SMC_SC6 105368 and bump ID 01.

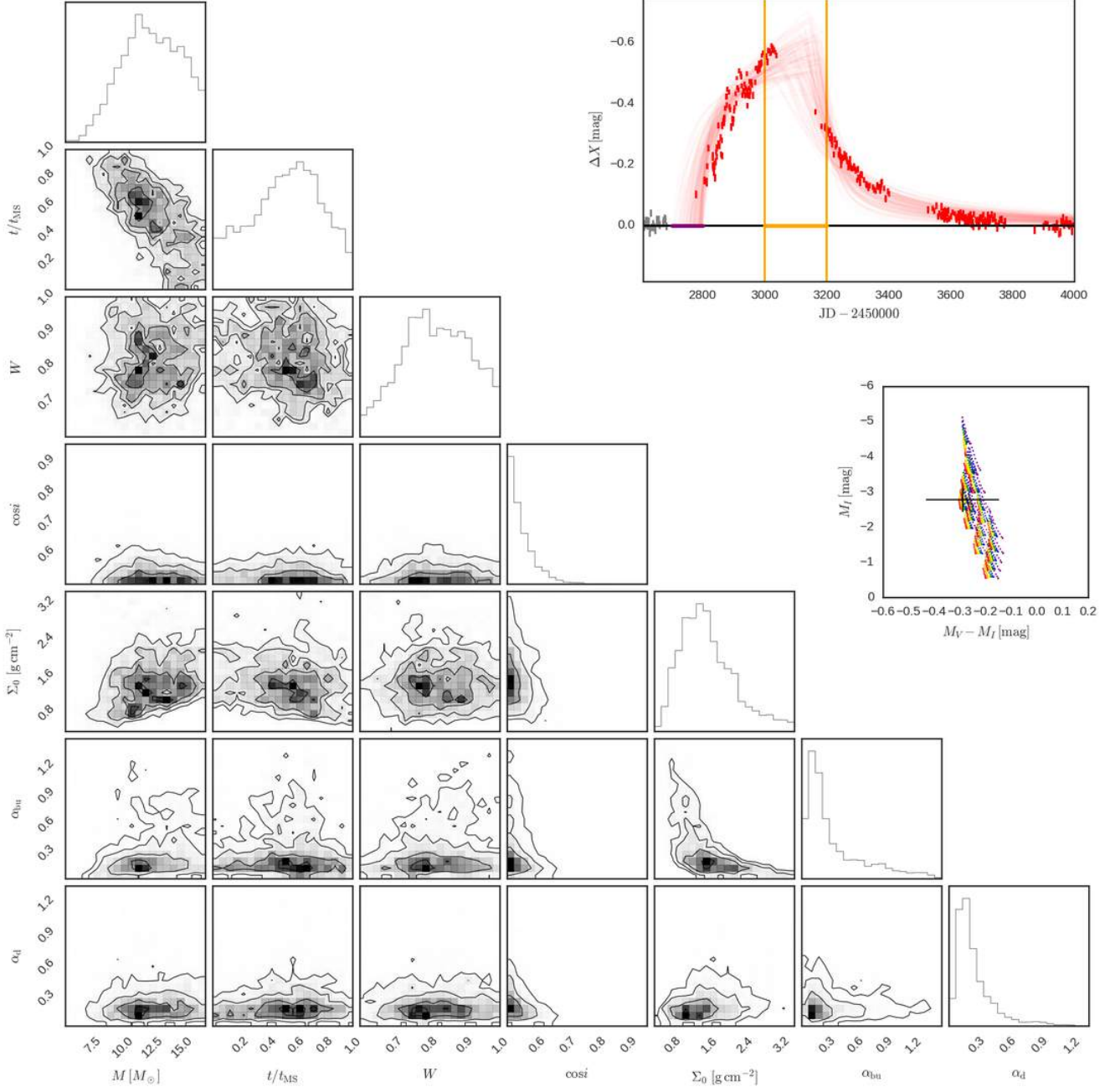


Figure C67. Same as Fig. 8 for SMC_SC6 105368 and bump ID 02.

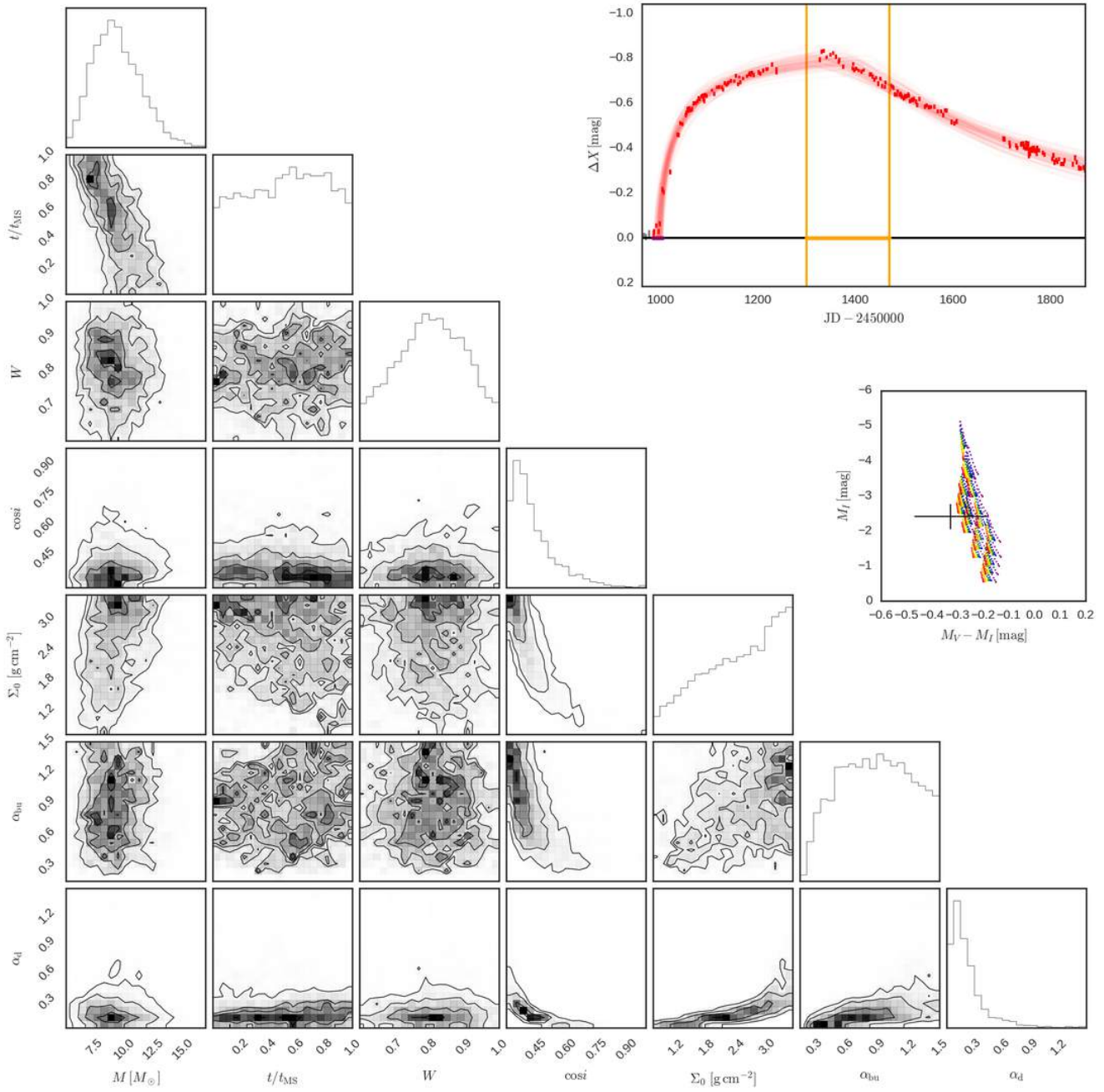


Figure C68. Same as Fig. 8 for SMC_SC6 116294 and bump ID 01.

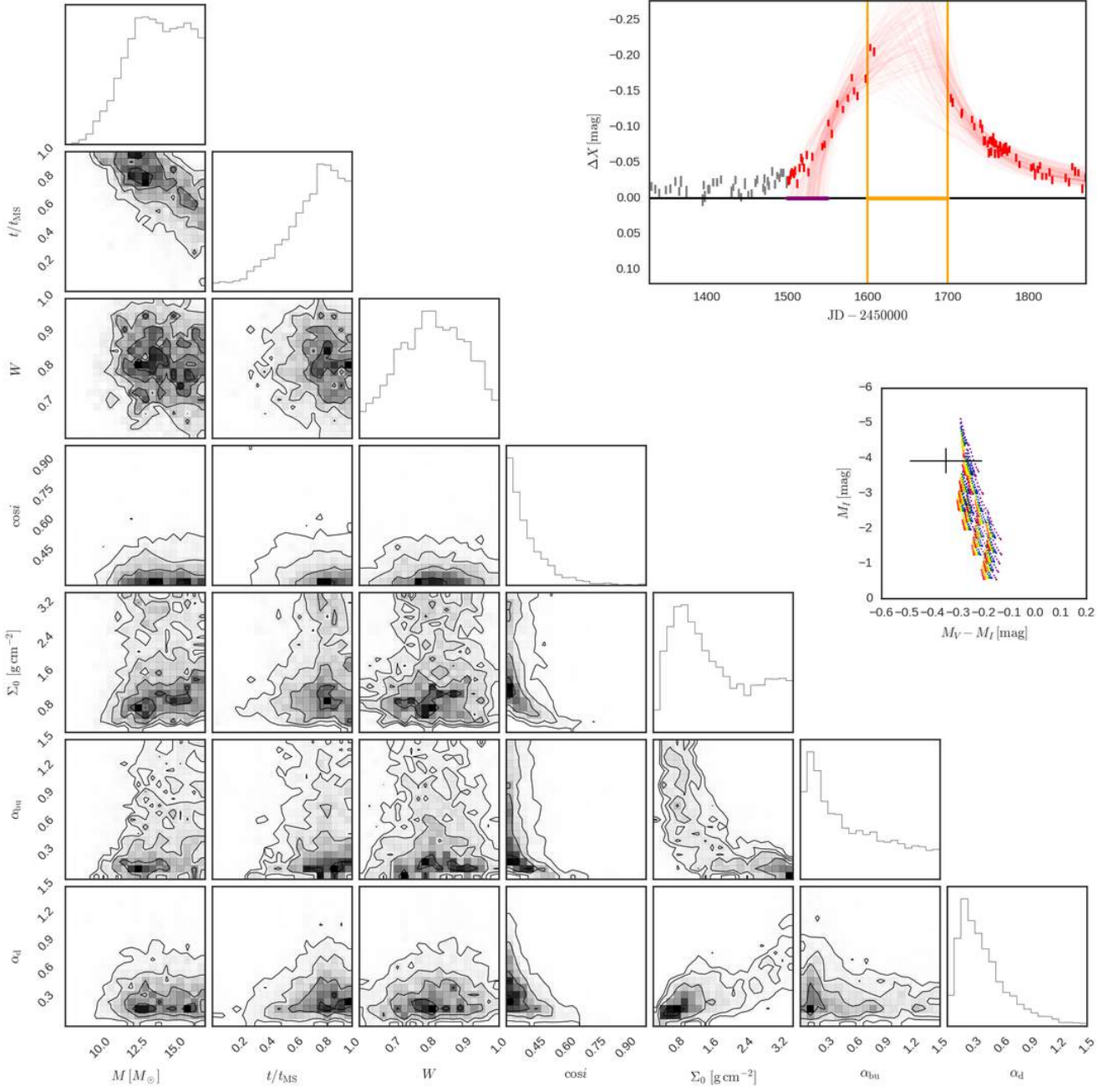


Figure C69. Same as Fig. 8 for SMC_SC6 199611 and bump ID 01.

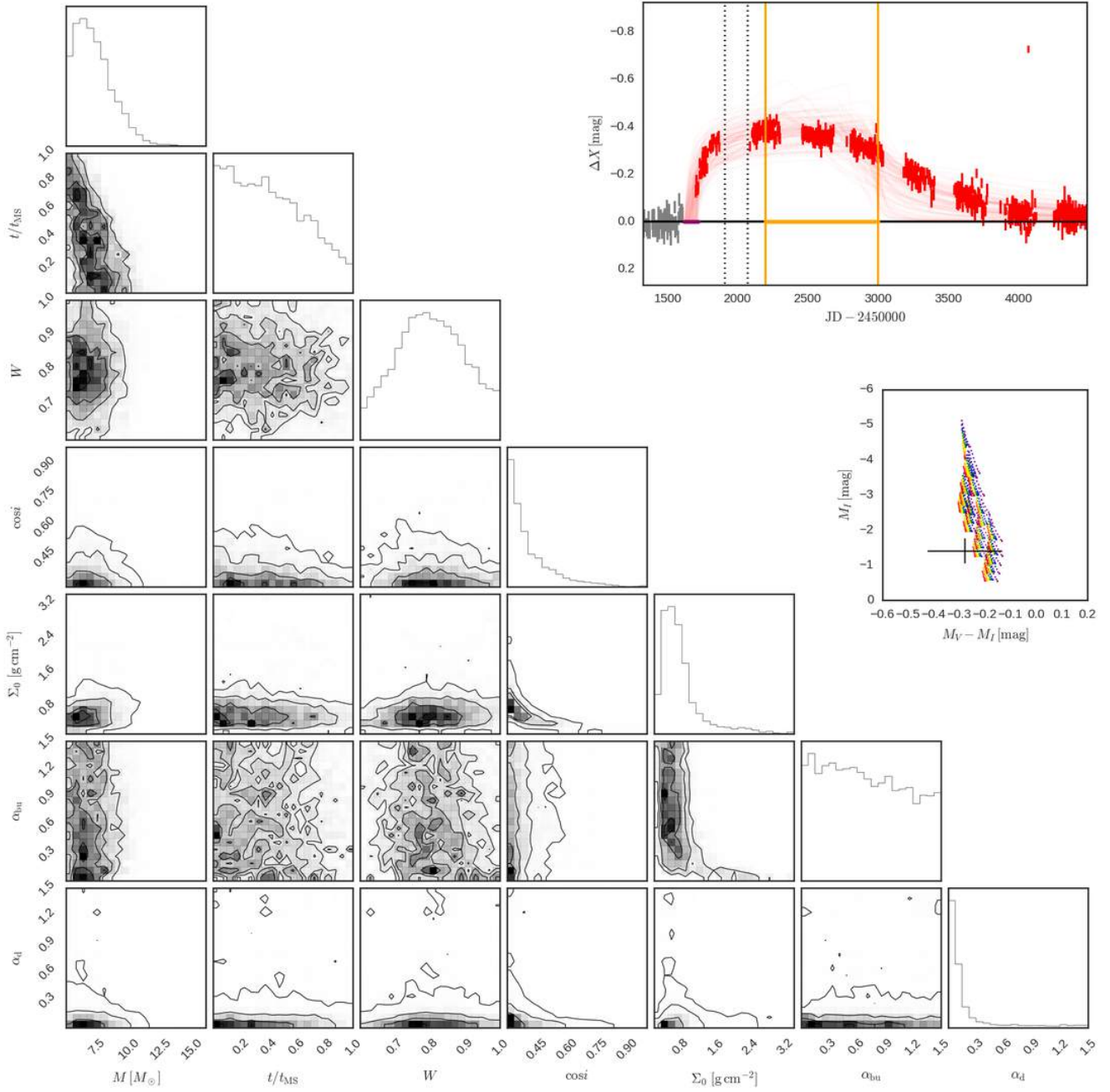


Figure C70. Same as Fig. 8 for SMC_SC6 272665 and bump ID 01.

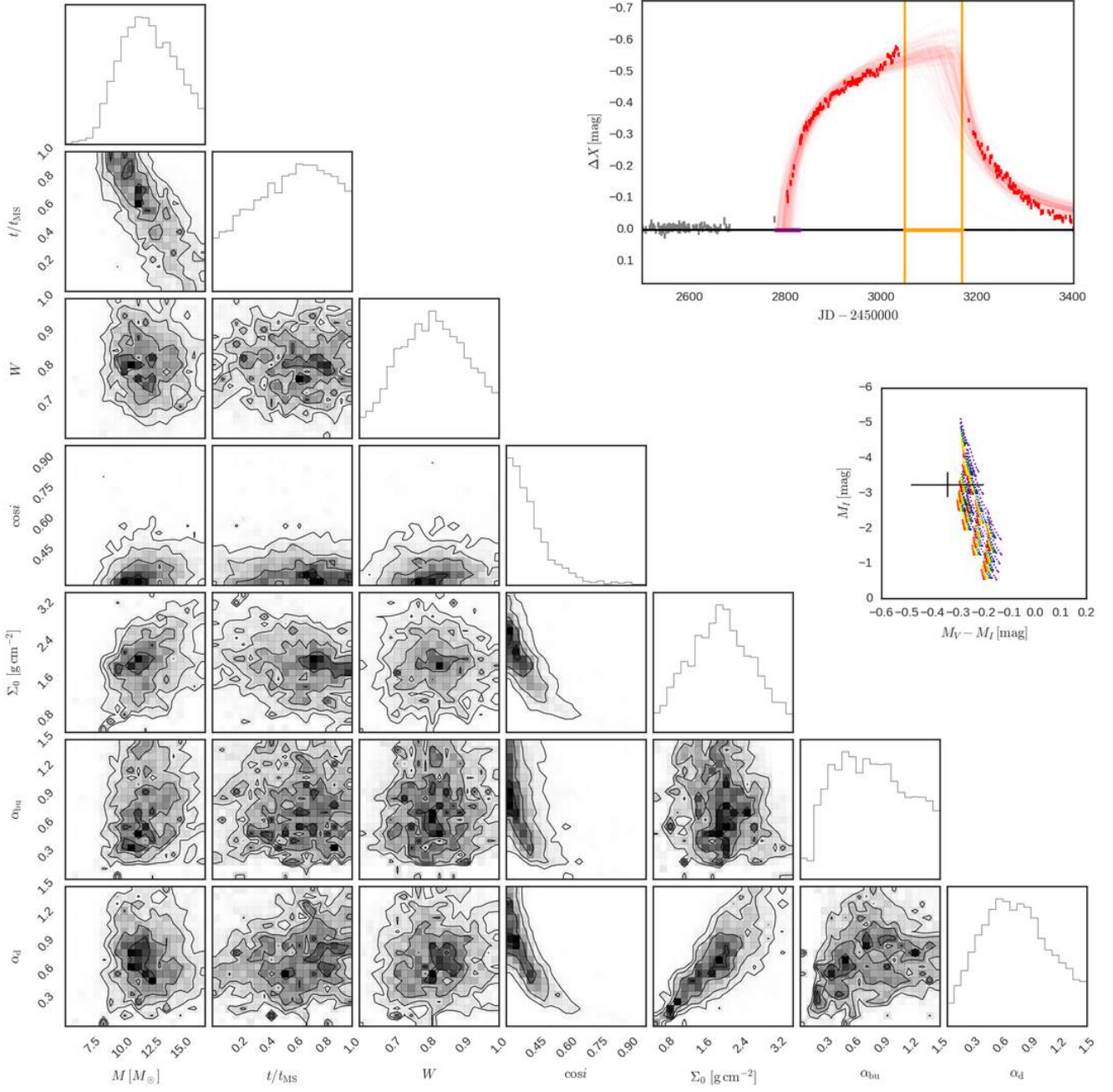


Figure C71. Same as Fig. 8 for SMC_SC7 57131 and bump ID 01.

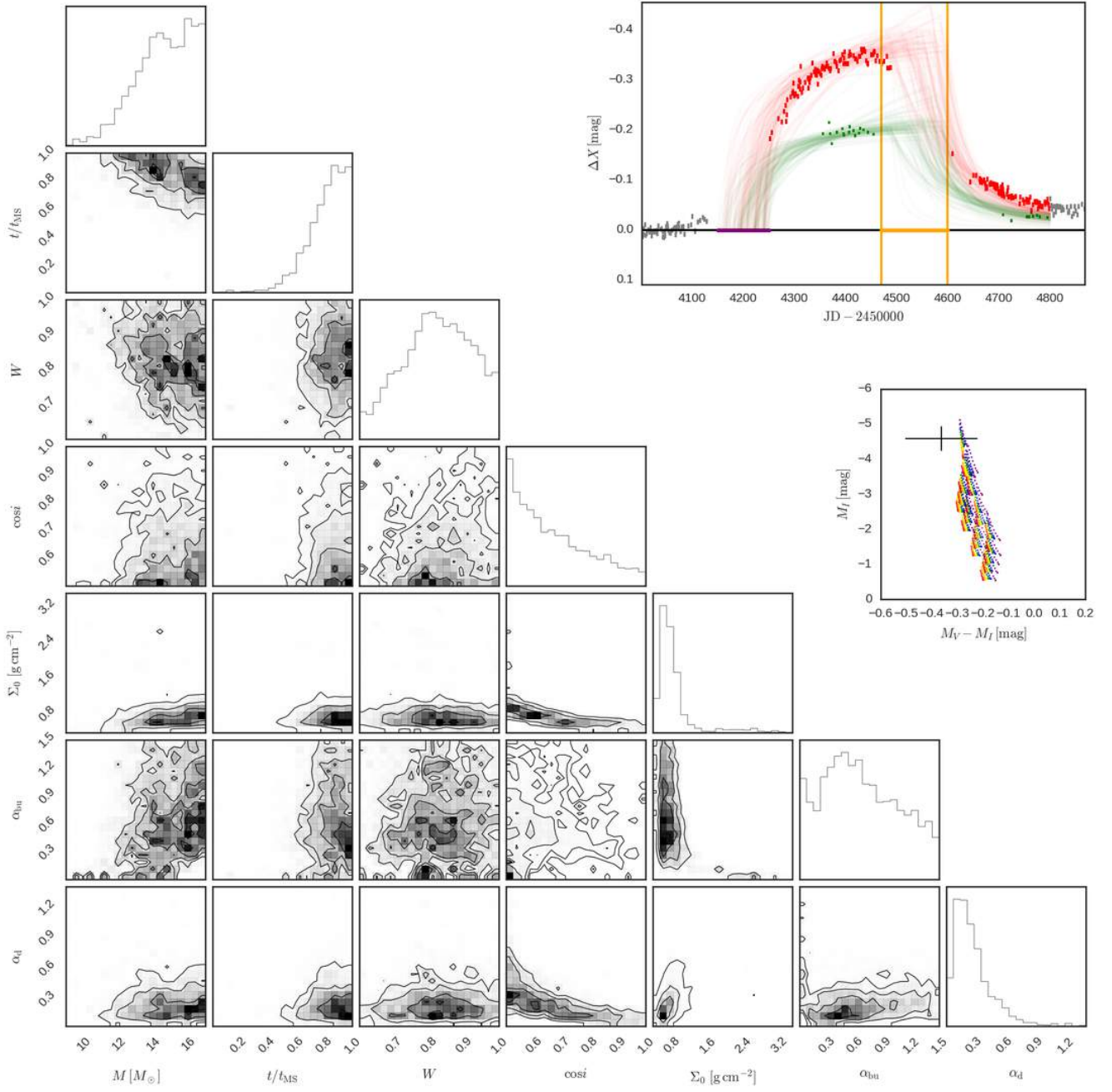


Figure C72. Same as Fig. 8 for SMC_SC8 183240 and bump ID 01.

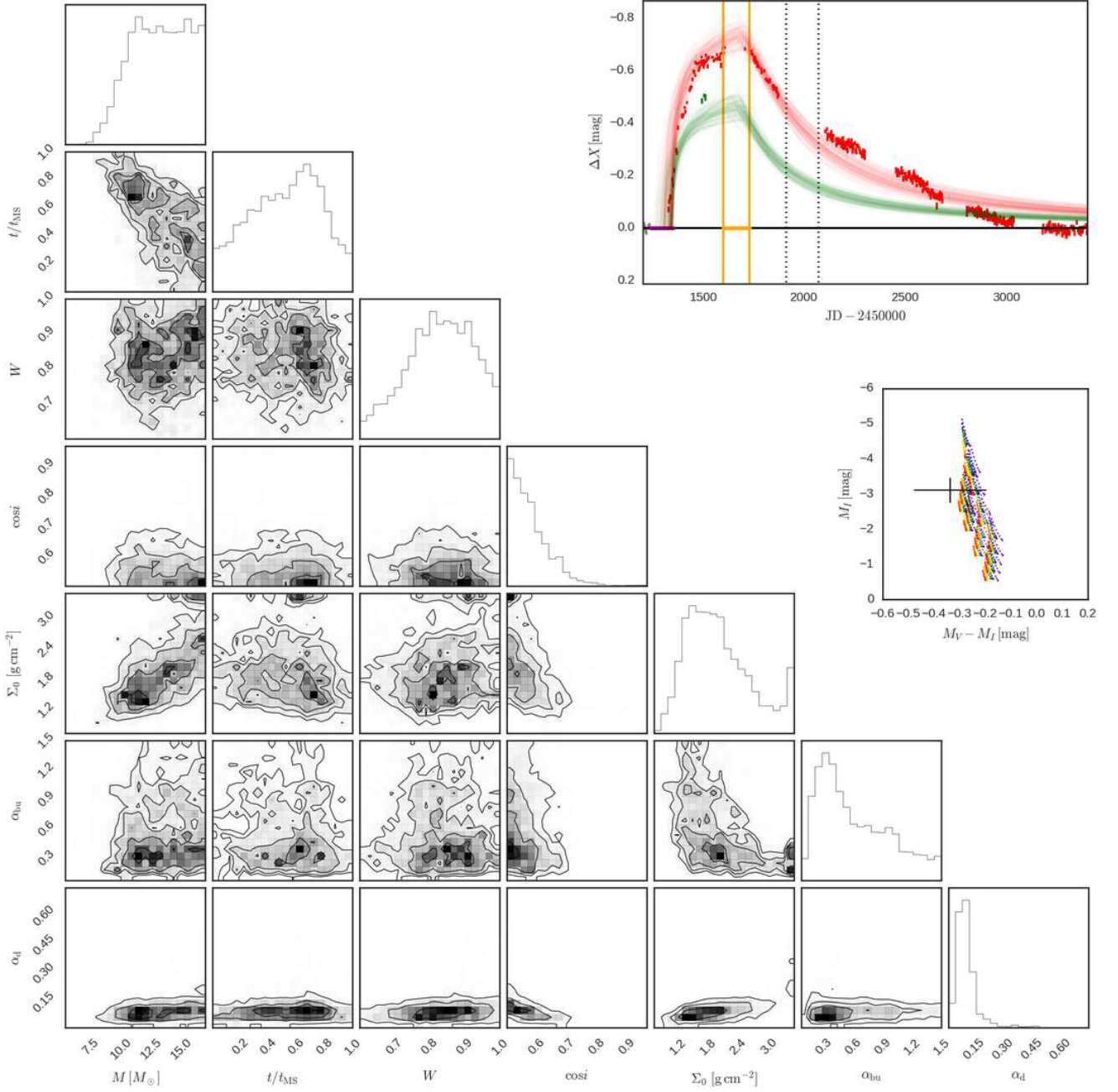


Figure C73. Same as Fig. 8 for SMC_SC9 105383 and bump ID 01.

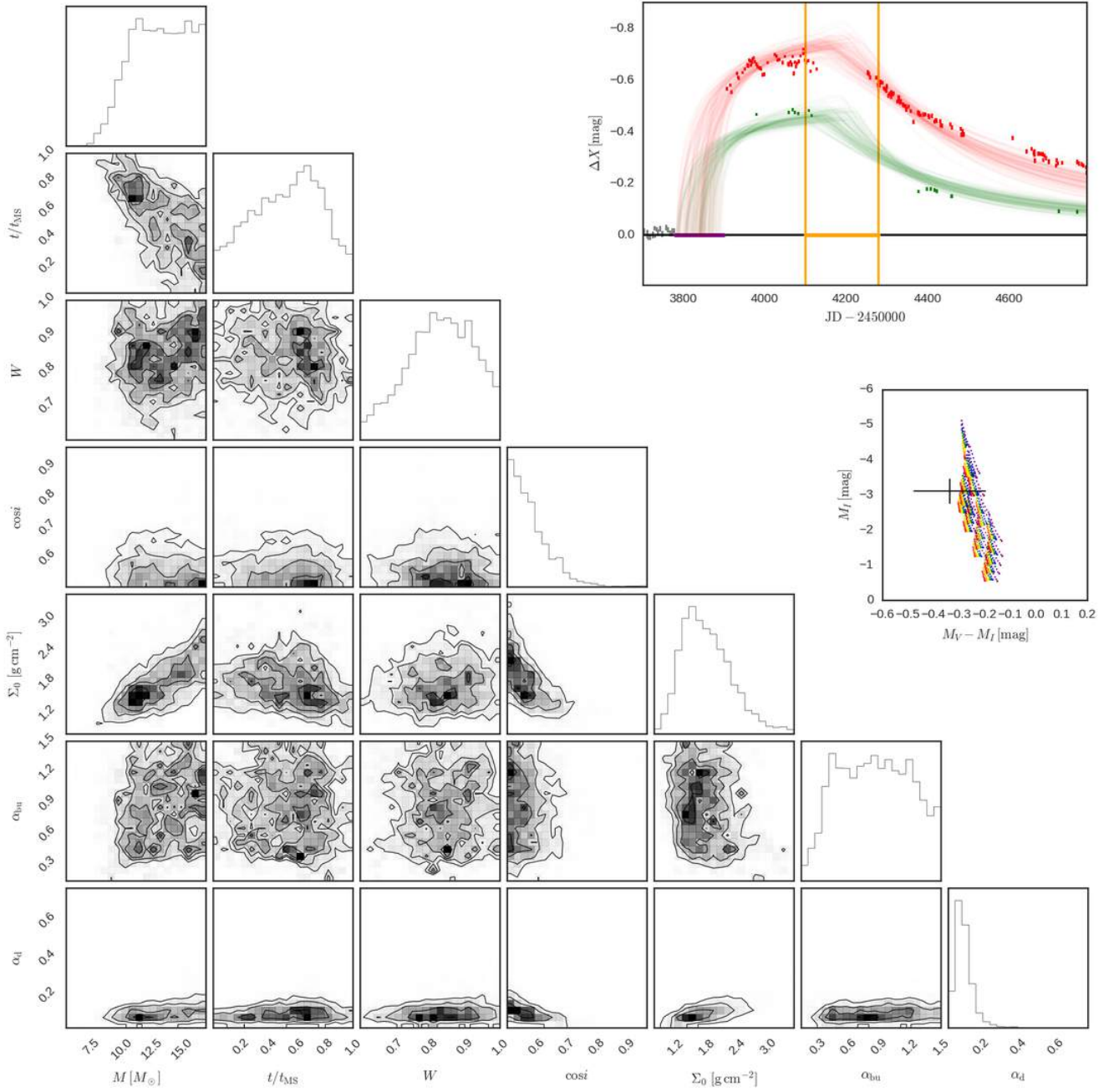


Figure C74. Same as Fig. 8 for SMC_SC9 105383 and bump ID 02.

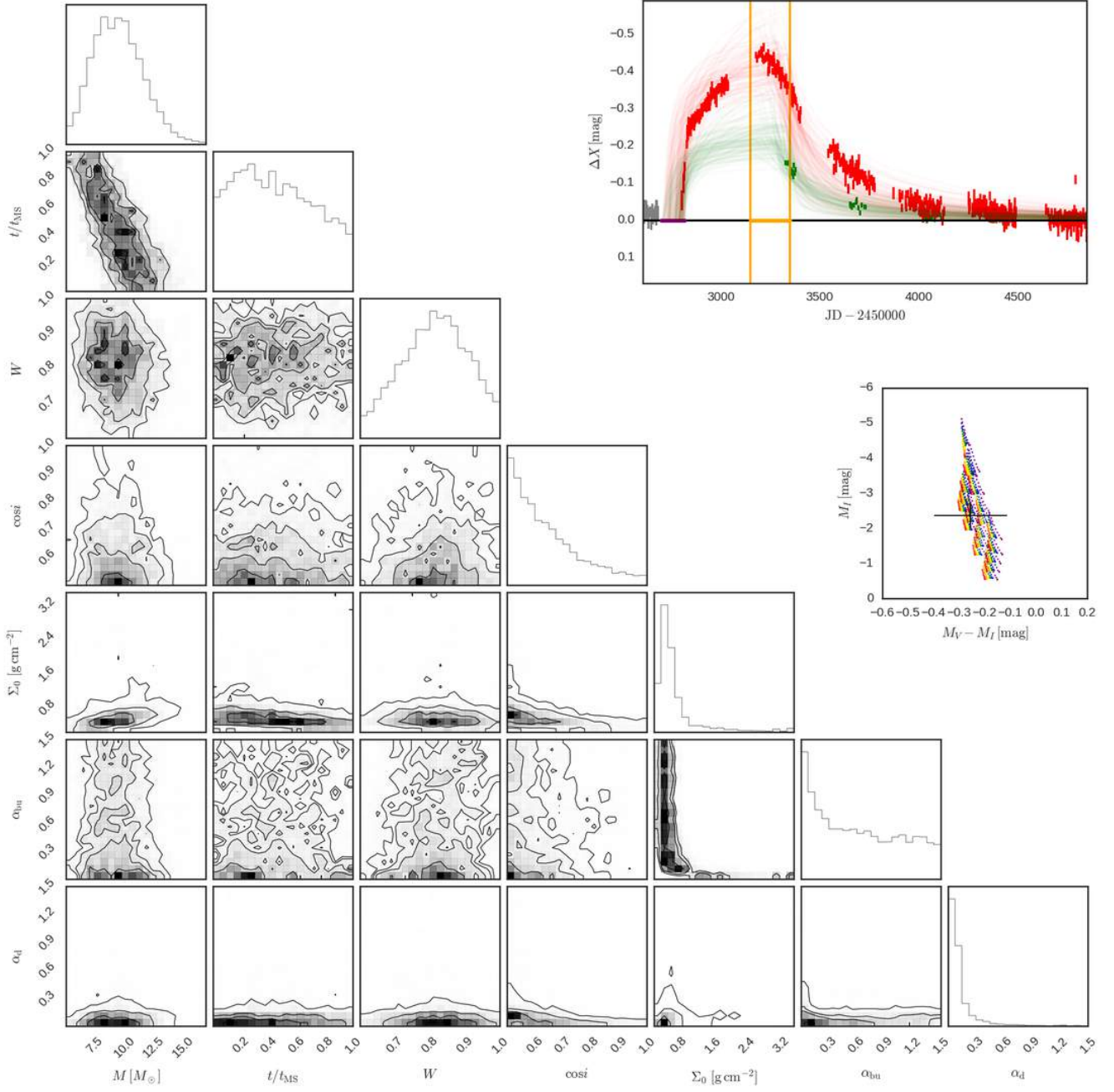


Figure C75. Same as Fig. 8 for SMC_SC9 168422 and bump ID 01.

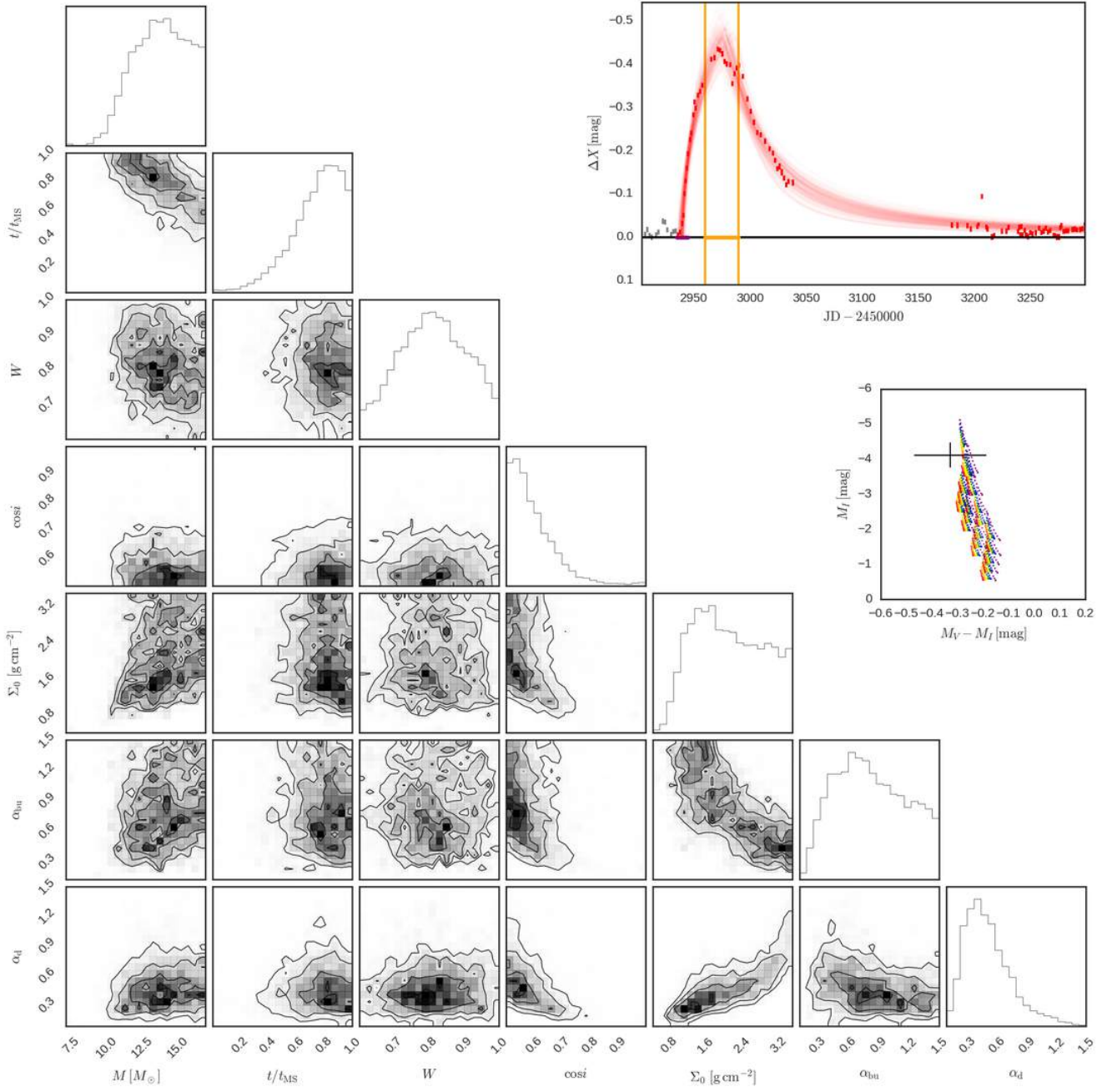


Figure C76. Same as Fig. 8 for SMC_SC10 8906 and bump ID 01.

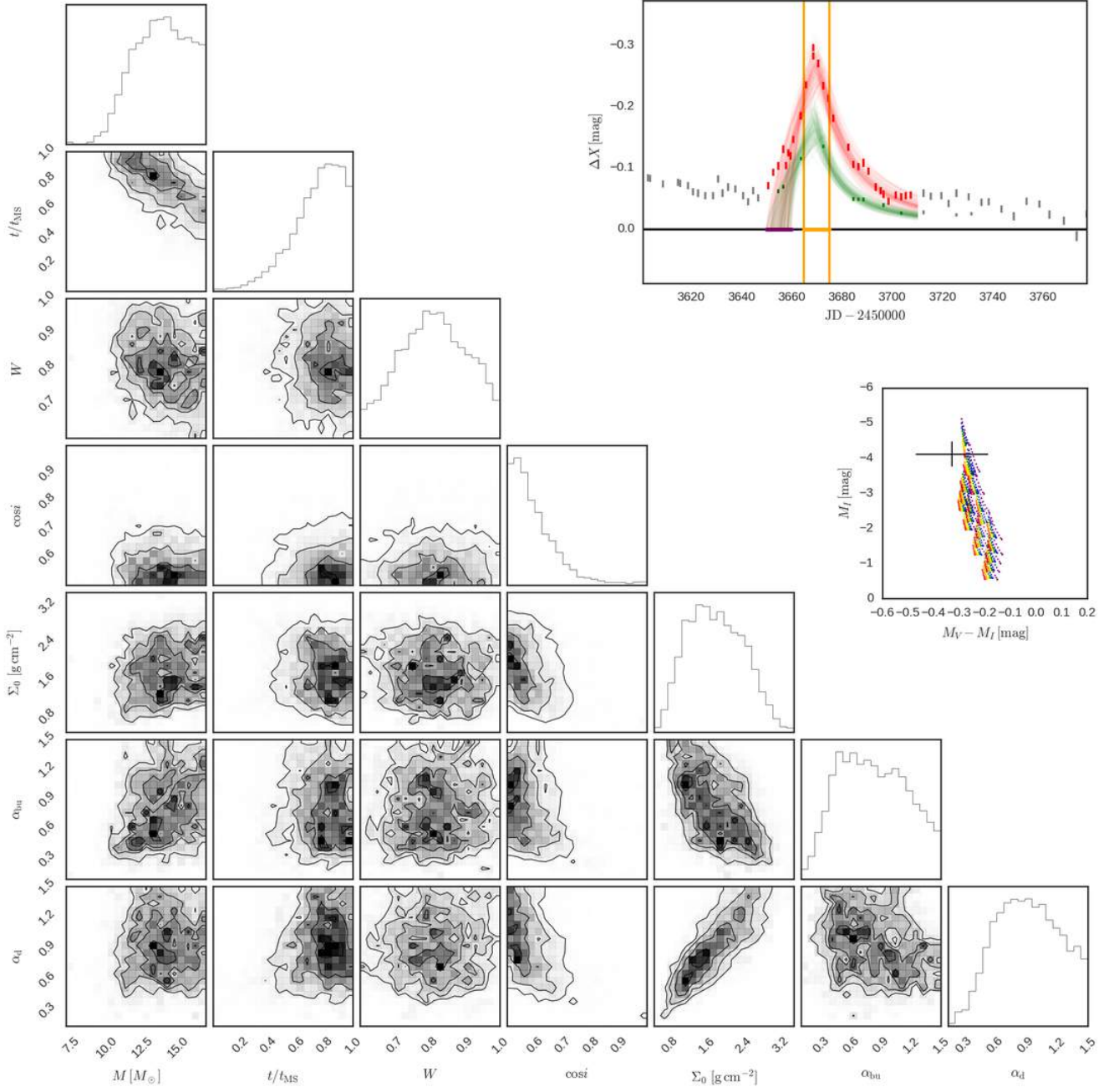


Figure C77. Same as Fig. 8 for SMC_SC10 8906 and bump ID 02.

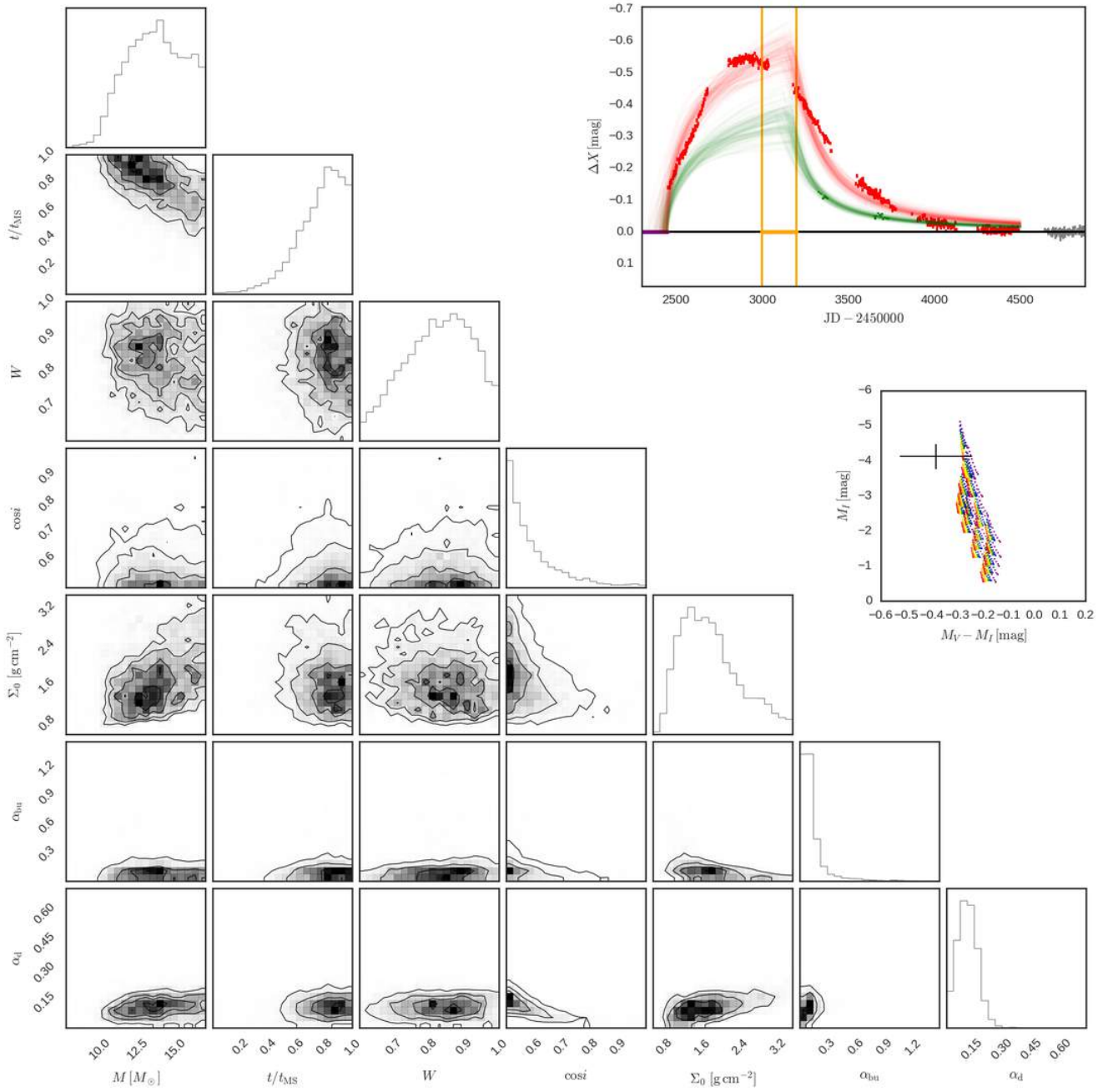


Figure C78. Same as Fig. 8 for SMC_SC11 28090 and bump ID 01.

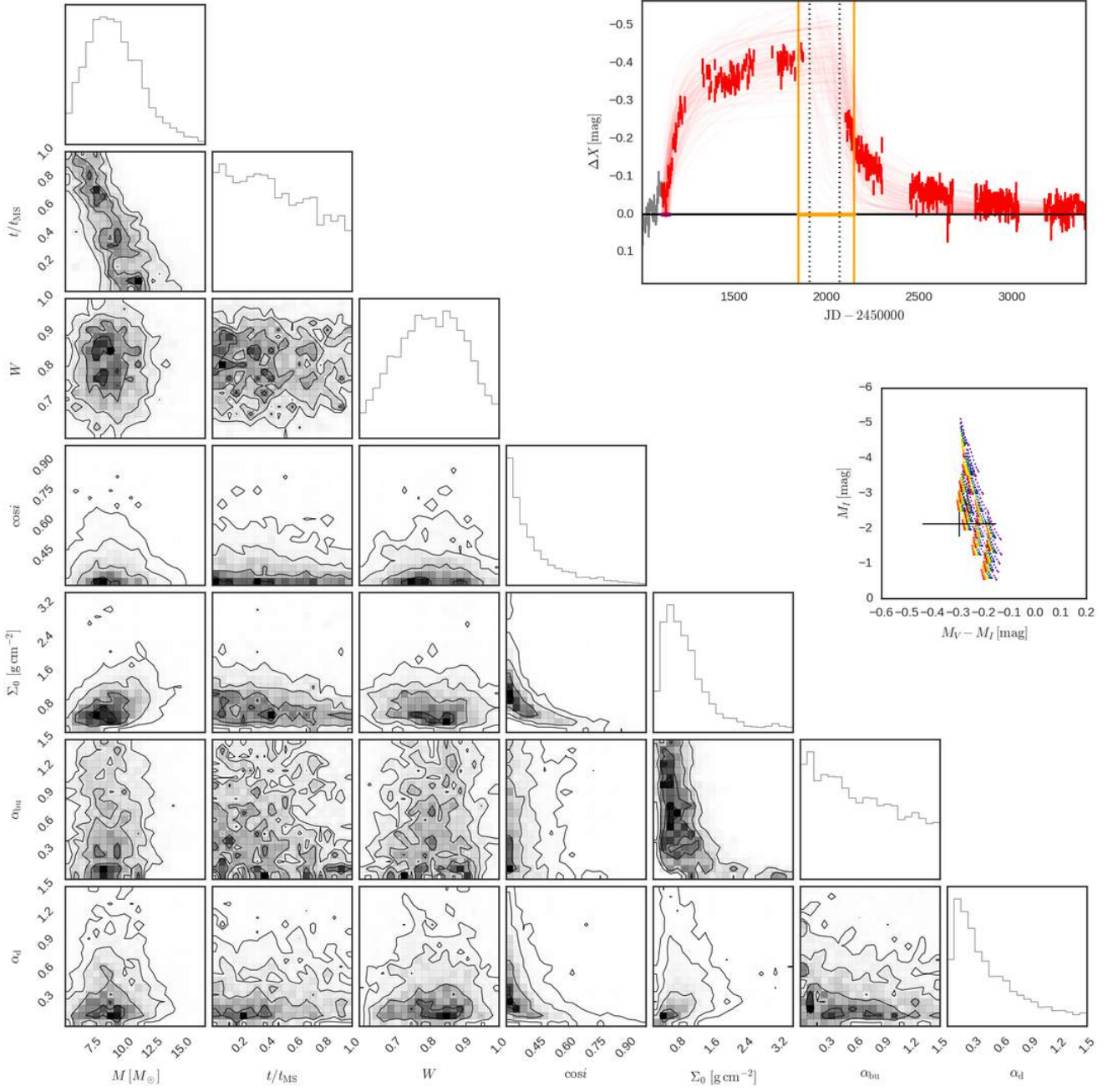


Figure C79. Same as Fig. 8 for SMC_SC11 46587 and bump ID 01.

This paper has been typeset from a \TeX/L\TeX file prepared by the author.